frontiers | Research Topics

Human digital twins for medical and product engineering

Edited by
Jörg Miehling, Anne D. Koelewijn and Julie Choisne

Published in
Frontiers in Bioengineering and Biotechnology

ISSN 1664-8714
ISBN 978-2-8325-5604-7
DOI 10.3389/978-2-8325-5604-7

About Frontiers

Frontiers is more than just an open access publisher of scholarly articles: it is a pioneering approach to the world of academia, radically improving the way scholarly research is managed. The grand vision of Frontiers is a world where all people have an equal opportunity to seek, share and generate knowledge. Frontiers provides immediate and permanent online open access to all its publications, but this alone is not enough to realize our grand goals.

Frontiers journal series

The Frontiers journal series is a multi-tier and interdisciplinary set of open-access, online journals, promising a paradigm shift from the current review, selection and dissemination processes in academic publishing. All Frontiers journals are driven by researchers for researchers; therefore, they constitute a service to the scholarly community. At the same time, the *Frontiers journal series* operates on a revolutionary invention, the tiered publishing system, initially addressing specific communities of scholars, and gradually climbing up to broader public understanding, thus serving the interests of the lay society, too.

Dedication to quality

Each Frontiers article is a landmark of the highest quality, thanks to genuinely collaborative interactions between authors and review editors, who include some of the world's best academicians. Research must be certified by peers before entering a stream of knowledge that may eventually reach the public - and shape society; therefore, Frontiers only applies the most rigorous and unbiased reviews. Frontiers revolutionizes research publishing by freely delivering the most outstanding research, evaluated with no bias from both the academic and social point of view. By applying the most advanced information technologies, Frontiers is catapulting scholarly publishing into a new generation.

What are Frontiers Research Topics?

Frontiers Research Topics are very popular trademarks of the *Frontiers journals series*: they are collections of at least ten articles, all centered on a particular subject. With their unique mix of varied contributions from Original Research to Review Articles, Frontiers Research Topics unify the most influential researchers, the latest key findings and historical advances in a hot research area.

Find out more on how to host your own Frontiers Research Topic or contribute to one as an author by contacting the Frontiers editorial office: frontiersin.org/about/contact

Human digital twins for medical and product engineering

Topic editors

Jörg Miehling — Friedrich-Alexander-Universität Erlangen-Nürnberg, Germany
Anne D. Koelewijn — Friedrich-Alexander-Universität Erlangen-Nürnberg, Germany
Julie Choisne — University of Auckland, New Zealand

Citation

Miehling, J., Koelewijn, A. D., Choisne, J., eds. (2024). *Human digital twins for medical and product engineering*. Lausanne: Frontiers Media SA.
doi: 10.3389/978-2-8325-5604-7

Table of contents

frontiers | Frontiers in Bioengineering and Biotechnology

TYPE Editorial
PUBLISHED 16 October 2024
DOI 10.3389/fbioe.2024.1489975

OPEN ACCESS

EDITED AND REVIEWED BY
Markus O. Heller,
University of Southampton, United Kingdom

*CORRESPONDENCE
Jörg Miehling,
joerg.miehling@fau.de

RECEIVED 02 September 2024
ACCEPTED 07 October 2024
PUBLISHED 16 October 2024

CITATION
Miehling J, Choisne J and Koelewijn AD (2024) Editorial: Human digital twins for medical and product engineering.
Front. Bioeng. Biotechnol. 12:1489975.
doi: 10.3389/fbioe.2024.1489975

Editorial: Human digital twins for medical and product engineering

Jörg Miehling[1]*, Julie Choisne[2] and Anne D. Koelewijn[3]

[1]Engineering Design, Department of Mechanical Engineering, Friedrich-Alexander-Universität Erlangen-Nürnberg, Erlangen, Germany, [2]Auckland Bioengineering Institute, The University of Auckland, Auckland, New Zealand, [3]Chair of Autonomous Systems and Mechatronics, Department of Electrical Engineering, Friedrich-Alexander-Universität Erlangen-Nürnberg, Erlangen, Germany

KEYWORDS

biomechanics, personalized musculoskeletal modelling and simulation, human-technology interaction, sensorization, state estimation

Editorial on the Research Topic
Human digital twins for medical and product engineering

1 Introduction

The current trend towards digitalization of human-centred engineering processes in conjunction with advances in (bio-) mechanistic modelling, high-performance computing, artificial intelligence (AI) and sensor technology leads to unprecedented transformation potentials in medical, product and human factors engineering. These advancements are significantly enhancing human-technology interaction and improving medical treatment outcomes. Biomechanical simulations hold high potential by revealing the processes and inner strain conditions of the human body. For reliable simulation results, a suitable model is required, as well as a measurement, estimation, or prediction approach to analyse human motion behaviour, its interaction with the environment and, if present, its interaction with technology. In this context, we refer to a human digital twin as a virtual representation or digital replica of an individual, created using data from various sources, including sensors, medical records, and other digital inputs. This digital twin mirrors certain physical and behavioural characteristics of the person, enabling simulations, predictions, and analyses. If interactions between humans and technology are considered, the concept of digital twin couples is applicable. This concept facilitates the use of human digital twins and digital product twins (within its environment) in conjunction with different data streams, which can be measured on the human, on the product, or at their interface. The combined use of different data streams may enable a more accurate estimation of the states within the overall human-technology system in terms of a model-based systems engineering approach. This subsequently allows to optimize physical human-technology interactions based on simulations, estimations, or predictions with the digital twin couples as well as data transfer between virtual and physical instances of human and technology.

The goal of this Research Topic was to explore human digital twins as personalized biomechanical models for person-specific simulations and their application in human-centred engineering. Such simulations allow for computing biomechanical variables from wearable or unobtrusive sensors instead of requiring expensive gold standard lab-based equipment. Portable equipment and automatic processes lead to easily accessible biomechanical analysis for clinical applications, to permanent monitoring of usage scenarios, or to direct use of simulation-based

information during the interaction between the human and a product. Digital product twins may be included, if observation, simulation or prediction of product behaviour is necessary in the prospective human-technology interaction use case.

Current biomechanical models are often generic and only scaled based on full bodyweight and marker data. Personalised medicine allows to customize biomechanical models to the patient-specific information allowing for more accurate prediction. For example, statistical shape models are replacing musculoskeletal generic models. Moreover, crucial factors such as muscle strength or range of motion are usually not personalized in a scaling-based generic model. In-depth patient-specific modelling from medical image data is often implemented for limited body regions, for which such data is available. Medical imaging is usually indicated for conditions that cause larger bone deformities, such as in cerebral palsy or for orthopaedic surgery planning. However, when medical imaging and standard motion capture data are unavailable, alternative methods for personalized modelling are needed.

2 Tackling the challenges in the design, implementation and application of human digital twin technology

The Research Topic Human Digital Twins for Medical and Product Engineering encompasses a broad overview of this research area through eleven excellent contributions which include one systematic review, one brief research report and nine original research articles. These theoretical, computational and experimental studies can be grouped into the following focus areas of the Research Topic.

2.1 Approaches towards motion data processing with digital human models

The systematic review by Wechsler et al. provides a comprehensive overview and recommendations for minimizing the sim2real gap – the discrepancy that commonly exists between musculoskeletal simulation outputs and real-world observations. This information supports those researchers using musculoskeletal models in conjunction with movement measurement data for both medical and product engineering applications. Moghadam et al. investigated the feasibility of predicting joint kinematics and kinetics with IMU sensors in conjunction with personalized machine learning models. This study proposes a promising personalized approach for gait time series prediction in children, involving an RF model and two IMUs on the feet. Michaud et al. created digital twins for patellar tracking and treatment prediction. This study considers two different approaches: the use of 3D models and contact detection algorithms. Eventually, simulation results were compared with experimental measurements from a sensorized 3D-printed test bench under pathological and treatment scenarios.

2.2 Parameter identification and modelling procedures for detailed person-specific modelling and simulation

Zot et al. studied the mechanical effects of lumbar disc arthroplasty on the facet joints by creating patient-specific finite element models of the intact and post-arthroplasty lumbar spine based on CT-scans of lumbar spine specimens. These models have been applied to compare the mechanical response of both ball-and-socket and elastic protheses under physiological loadings. Remus et al. conducted experimental human abdominal *in vivo* macro-indenter measurements to derive soft tissue material properties based on time-of-flight sensors for 3D displacement measurement of the body hull and surface electromyography (sEMG) to monitor muscle activation levels. Inverse finite element analysis was used to approximate the nonlinear material parameters of the soft tissue. Baier et al. simulated functional electric stimulation (FES) protocols on the forearm with muscle-specific activation resolution with a human digital twin consisting of an anatomically based 3D volume conductor, muscle specific nerve fibre arrangement and a specific nerve model. This approach can eventually be applied to determine the optimal procedure for neurological rehabilitation. Ortiz-Puerta et al. conducted a morphometric study of the proximal airways based on geometrical measures associated with the different airway generations. Accurate representation and characterization of the airway luminal surface and volume was informed by CT images of the respiratory tree and was applied to compare smoking pre-COPD and COPD individuals.

2.3 Evaluation criteria and test procedures

Nölle et al. investigated tendon strains in jersey finger load cases using a finite element neuromuscular model in conjunction with a newly defined injury criterion. Jersey finger injury occurs through an eccentric overextension of the distal interphalangeal joint leading to an avulsion of the connected FDP tendon. Achour et al. developed a biomechanical test bench for investigation of implant failure of different osteosynthesis systems on the mandible.

2.4 Predictive approaches

Van der Kruk and Geijtenbeek investigated the effects of muscle weakness and pain avoidance in individuals with unilateral knee pain on trunk flexion while standing up using a predictive neuromuscular simulation study. Killen et al. investigated *in silico* techniques to facilitate optimal personalized prescription of shoe insoles based on measured motion capture, inverse musculoskeletal modelling and forward dynamic simulation to predict the kinematic adaption to specific insole designs. The approach was subsequently used to study healthy participants and flatfoot patients.

3 Conclusion and future perspectives

The published articles provide valuable contributions towards personalized biomechanical modelling and simulation including model parameter identification, novel sensor data processing, and state prediction and evaluation based on musculoskeletal models. These results will gradually pave the way towards a productive applicability of human digital twins in the context of medical, product and human factors engineering. Nevertheless, some

further aspects need to be researched in order to exploit the full potential of human digital twin application in bioengineering processes.

An ongoing challenge in biomechanics remains the identification of person-specific model parameters, such as muscle and material parameters for multibody and finite element simulations. Therefore, rethinking the paradigms concerning the choice of muscle and material parameters is of outstanding importance for the whole community (Nölle et al.; Remus et al.). On this basis, novel workflows need to prove clinical usability and the ability to optimize clinical outcome focussing on automated applicability, speed of use, use of more accessible data and possibly use of highly-accessible software for clinically applied human digital twin technology leading to effective and efficient patient-specific surgical and rehabilitation strategies (Zot et al.; Michaud et al.; Killen et al.; Baier et al.; Remus et al.). Generally spoken, simple and robust applicability is necessary for successful implementation also in non-clinical application areas. Predictive simulations offer valuable insights into the mechanisms behind altered movement strategies, potentially guiding more targeted treatment (Van der Kruk and Geijtenbeek; Killen et al.) and optimized human-technology systems. Moreover, multimodal approaches tracking kinematic and dynamic measurements may be one possible solution to handle the discrepancies between simulation results and real-world observations, reducing the sim2real gap (Wechsler et al.). In this context also novel experimental measurement setups and sensor technology are needed to accurately determine empirical reference values (Achour et al.; Remus et al.).

Author contributions

JM: Writing–original draft, Writing–review and editing. JC: Writing–review and editing. AK: Writing–review and editing.

Funding

The author(s) declare that financial support was received for the research, authorship, and/or publication of this article. The authors wish to thank the following support given by: Deutsche Forschungsgemeinschaft (DFG, German Research Foundation) under Grant SFB 1483 – Project-ID 442419336 and Grant MI 2608/2-1 – Project-ID 450307023. We would like to also acknowledge the support from the New Zealand Ministry of Business Innovation and Employment catalyst grant 12 Labours.

Acknowledgments

The guest editors gratefully acknowledge the contributions to this Research Topic and the support of all referees who volunteered to review the submitted manuscripts.

Conflict of interest

The authors declare that the research was conducted in the absence of any commercial or financial relationships that could be construed as a potential conflict of interest.

Publisher's note

frontiers | Frontiers in Bioengineering and Biotechnology

TYPE Original Research
PUBLISHED 21 November 2023
DOI 10.3389/fbioe.2023.1287197

OPEN ACCESS

EDITED BY
Jörg Miehling,
Friedrich-Alexander-Universität Erlangen-Nürnberg, Germany

REVIEWED BY
Christian Liebsch,
Ulm University Medical Center, Germany
Robin Remus,
Ruhr University Bochum, Germany

*CORRESPONDENCE
François Zot,
francois.zot@univ-poitiers.fr

RECEIVED 01 September 2023
ACCEPTED 01 November 2023
PUBLISHED 21 November 2023

CITATION
Zot F, Ben-Brahim E, Severyns M, Ledoux Y, Mesnard M, Caillé L, Swennen C, Teyssédou S, Moufid A-Y, Germaneau A and Vendeuvre T (2023), Study of mechanical effects of lumbar disc arthroplasty on facet joints at the index level/adjacent levels by using a validated finite element analysis. *Front. Bioeng. Biotechnol.* 11:1287197. doi: 10.3389/fbioe.2023.1287197

Study of mechanical effects of lumbar disc arthroplasty on facet joints at the index level/adjacent levels by using a validated finite element analysis

François Zot[1]*, Estelle Ben-Brahim[1,2], Mathieu Severyns[1,3], Yann Ledoux[4], Michel Mesnard[4], Laëtitia Caillé[1], Cécile Swennen[2], Simon Teyssédou[2], Abdollah-Yassine Moufid[2], Arnaud Germaneau[1] and Tanguy Vendeuvre[1,2]

[1]Institut Pprime, UPR 3346 CNRS—Université de Poitiers, Poitiers, France, [2]CHU de Poitiers, Department of Orthopaedic Surgery and Traumatology, Poitiers, France, [3]Orthopaedic and Traumatology Department, Clinique Porte Océane, Les Sables d'Olonne, France, [4]Univ. Bordeaux, I2M, CNRS, Talence, France

Introduction: Lumbar disc arthroplasty is a surgical procedure designed to treat degenerative disc disease by replacing the affected disc with a mobile prosthesis. Several types of implants fall under the term total disc replacement, such as ball-and-socket, mobile core or elastic prostheses. Some studies have shown that facet arthritis can develop after arthroplasty, without much precision on the mechanical impact of the different implant technologies on the facet joints. This study aims to create validated patient-specific finite element models of the intact and post-arthroplasty lumbar spine in order to compare the mechanical response of ball-and-socket and elastic prostheses.

Methods: Intact models were developed from CT-scans of human lumbar spine specimens (L4-S1), and arthroplasty models were obtained by replacing the L4-L5 disc with total disc replacement implants. Pure moments were applied to reproduce physiological loadings of flexion/extension, lateral bending and axial rotation.

Results: Models with ball-and-socket prosthesis showed increased values in both range of motion and pressure at the index level and lower values at the adjacent level. The mechanical behaviour of the elastic prosthesis and intact models were comparable. The dissipated friction energy in the facet joints followed a similar trend.

Conclusion: Although both implants responded to the total disc replacement designation, the mechanical effects in terms of range of motion and facet joint loads varied significantly not only between prostheses but also between specimens. This confirms the interest that patient-specific surgical planning using finite element analysis could have in helping surgeons to choose the appropriate implant for each patient.

KEYWORDS

lumbar spine, arthroplasty, biomechanics, finite element, patient-specific

1 Introduction

The management of degenerative phenomena of the lumbar spine and the resulting pathologies, such as radiculalgia and low back pain, represents a public health problem (Adams and Roughley, 2006; Karran et al., 2020). Low back pain is acknowledged as the primary cause of disability worldwide (Hoy et al., 2012; Vos et al., 2016; Wu et al., 2020) and has significant economic consequences in many countries (Dagenais et al., 2008; Fatoye et al., 2023). Several works have indicated that low back pain could be caused by intervertebral disc degeneration (Cheung et al., 2009; Simon et al., 2014) and facet joint degeneration (Manchikanti, 2002; Kalichman et al., 2008; Bashkuev et al., 2020). Also, it has been highlighted that the mechanical environment is linked to the pathogenesis of low back pain (Iatridis et al., 2013; Iorio et al., 2016).

Two main surgical procedures exist to treat Degenerative Disc Disease (DDD), which are arthrodesis and arthroplasty. Only the latter can retain some of the natural mobilities of the spine. This is achieved by removing the degenerated disc and replacing it with a mobile prosthesis. Multiple studies have shown that arthroplasty represents a pertinent alternative to arthrodesis to treat DDD, and could provide an improvement of the quality of life to the patient over the longer term (Cui et al., 2018; Mu et al., 2018; Zigler et al., 2018; Formica et al., 2020). Various arthroplasty implant technologies exist, encompassing ball-and socket prostheses featuring a fixed core with 3 Degrees of Freedom (DoF), mobile core prostheses offering 4 to 6 DoF, and elastic prosthesis providing 6 DoF (Abi-Hanna et al., 2018).

Despite the benefits of lumbar Total Disc Replacement (TDR) surgery, researches have demonstrated that 34% of patients may develop facet arthritis at the index level within 2 years of the surgery (Furunes et al., 2020; M.-H; Shin et al., 2013). Facet arthritis can lead to severe pain (Gellhorn et al., 2013) and require revision surgery to stabilise the affected level, with higher morbidity rates. To prevent facet arthritis occurrence at the index level following lumbar TDR, it is necessary to identify its causes from a biomechanical approach. For several years, numerous Finite Element (FE) studies were performed to analyse biomechanical responses associated with lumbar spine issues (Shin et al., 2007; Schmidt et al., 2012; Demir et al., 2020; Biswas et al., 2023). Some studies, either experimental or numerical, have shown significant increases in both loads in the facet joints and Range of Motion (ROM) at the index level after lumbar arthroplasty (Wilke et al., 2012; Choi et al., 2017). However, it remains unclear whether different types of TDR implants, used under the same surgical denomination, can involve different loading effects on the facet joints at the index and the adjacent levels under physiological loads (Sandhu et al., 2020). Although arthroplasty has shown beneficial effects on adjacent-level disc preservation, some studies showed that index level facet joints degeneration was higher than other levels involving a negative impact on ROM (Siepe et al., 2010). For some solutions, it was noted that the main cause of the unsatisfactory results where degeneration of facet joints at the index levels or neighbouring levels, in addition to subsidence and migration of the prosthesis (Ooij et al., 2003). Some experimental studies have also shown that using an artificial ball and socket disc can lead to higher load in the facets (Dooris et al., 2001).

The objective of this work was to quantify the mechanical effects involved by a TDR on the facet joints according to the arthroplasty solution and the inter-subject differences. For this, patient specific FE models of the lumbar spine were developed to assess mechanical effects in pressure, sliding, and dissipated energy in the facet joints at the index and inferior adjacent level.

2 Materials and methods

The protocol used to carry out the study is detailed in the flow chart shown in Figure 1. Each step of this protocol will be described in detail.

2.1 Reference models

To develop the patient-specific FE models of the initial lumbar spine, 2 fresh-frozen cadaveric human lumbosacral spinal segments (L4-S1) extracted from 2 male donors (age: 77 and 86 years old) were used (step 1 in Figure 1). The dissections were carried out by experienced surgeons, who also verified the quality of the specimens to select those presenting the least degeneration signs

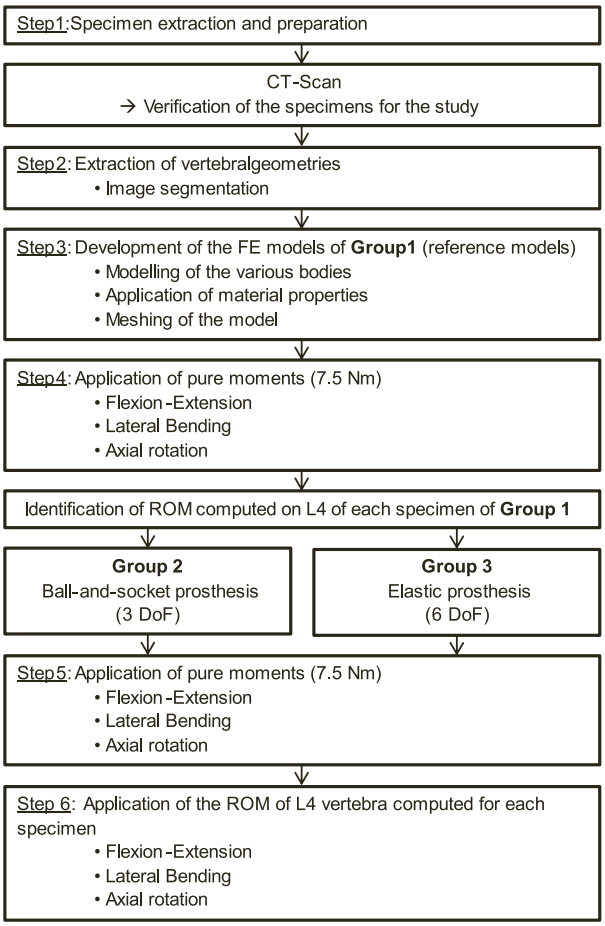

FIGURE 1
Flow chart presenting the protocol of this study.

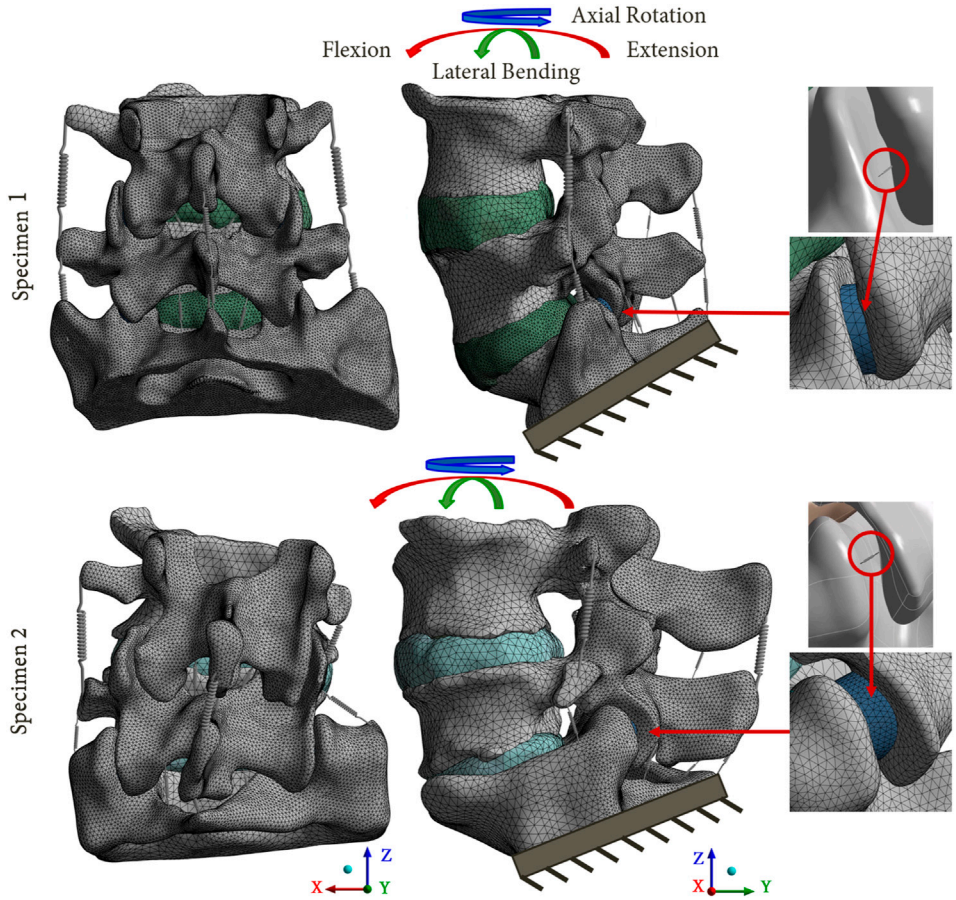

FIGURE 2
Reference FE models based on the 2 lumbosacral specimens. The mesh refinement on the posterior parts of the models is shown. A focus on the facet joints is presented, with the cartilaginous body (blue body) representing the articular cartilage, and the equivalent spring used to model the capsular ligaments.

on the zygapophyseal joints. These anatomical segments were provided by the anatomy laboratory (ABS Lab) of the University of Poitiers (Ministry of Education and Research No. DC-2008-137). The choice of using 2 lumbar specimens to perform this study was made to account for anatomical variability between each spinal segment. Also, it allowed the mechanical effects of various lumbar arthroplasty prostheses on the facet joints to be determined for 2 specimens, each presenting different anatomical geometries. The 2 lumbar specimens were then digitised using a medical CT-scan (Aquilion One, Genesis Edition, Canon, Japan). The resulting images were composed of voxels of $0.468 \times 0.468 \times 0.250\ mm^3$ in size. A FE model was developed from the geometrical characteristics of each specimen including vertebrae and intervertebral discs, which were extracted by the means of 3D Slicer software (Version 4.11, Kitware, France; step 2 in Figure 1). These geometries were then imported into Ansys Mechanical software (Version 2023R1, Ansys Inc., United States) for FE modelling.

Homogeneous material properties were assumed to model the vertebrae. The intervertebral discs were composed of an annulus fibrosus (green body in Figure 2) and a central nucleus pulposus assuming linear elastic material properties (Peng et al., 2018; Demir et al., 2020; Chemmami et al., 2021; Qin et al., 2021). In addition, two cartilaginous endplates were included above and below the intervertebral discs, making contact with the adjacent vertebrae (step 3 in Figure 1).

The ligaments of the lumbar spine (i.e., anterior longitudinal ligament, posterior longitudinal ligament, ligamentum flavum, transverse ligament, capsular ligament, interspinous ligament and supraspinous ligament), were modelled by uniaxial springs (COMBIN39 elements) assuming a non-linear behaviour (Nikkhoo et al., 2020), as shown in the Figure 3 (Shirazi-Adl et al., 1986). Some degrees of freedom are allowed to the spring elements, so it is possible for them to adapt to the orientation of the loading. To model the capsular ligaments, insertions were imposed by selecting the faces located on the periphery of the superior and inferior articular processes. It is therefore an 'equivalent' spring that simulates the behaviour of the ligament capsule. The other ligaments insertions were determined according to the anatomy of the lumbar spine (Kapandji, 2019).

To model the articular cartilages of the facet joints, cartilaginous endplates were placed in contact between the inferior and superior articular processes (blue body in Figure 2) (Qin et al., 2021; Remus et al., 2021). The upper surface of the cartilage was designed using a

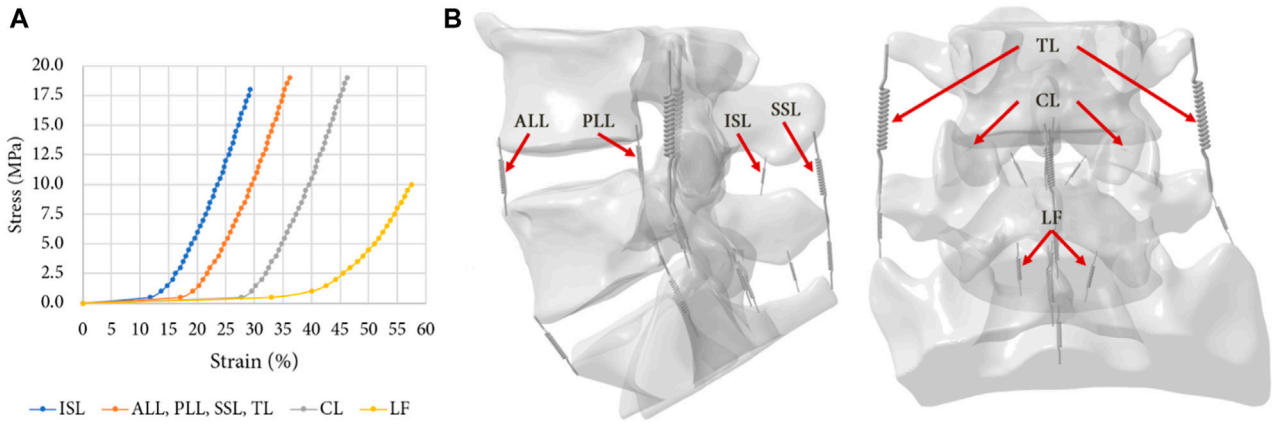

FIGURE 3
(A) Non-linear behaviour of the ligaments of the FE model: Anterior Longitudinal Ligament (ALL), Posterior Longitudinal Ligament (PLL), Ligamentum Flavum (LF), Transverse Ligament (TL), Capsular Ligament (CL), Interspinous Ligament (ISL), Supraspinous Ligament (SSL) (Shirazi-Adl, Ahmed, et Shrivastava, 1986); **(B)** Ligaments insertions on the specimens.

TABLE 1 Mechanical properties of the bodies composing the FE models.

Component	Elastic Modulus (MPa)	Poisson ratio	Reference
Bone	12,000	0.3	(Park, Kim, et Kim, 2013)
Cartilaginous endplate	23.8	0.42	(Finley et al., 2018)
Articular cartilage	10	0.3	(John, Saravana Kumar, et Yoganandan, 2019)
Annulus fibrosus	2	0.45	(Lavaste et al., 1992)
Nucleus pulposus	1	0.49	(D. S. Shin, Lee, et Kim, 2007)
Prodisc-L endplates	187,000	0.3	
Prodisc-L core	927.9	0.42	
LP-ESP endplates	107,000	0.32	
LP-ESP annulus	23.93	0.49	(Nic An Ghaill et Little, 2008)
LP-ESP core	3.9	0.47	

boolean geometrical operation that involved cutting the cartilaginous body in relation to the geometry of the articular process of the adjacent vertebra. To simulate the behaviour of the facet joint, a bonded contact condition was imposed between the inferior articular process and the cartilage, whereas a frictionless contact condition was imposed between the cartilage and the superior articular process (Mengoni, 2020). The three-dimensional models of the intact spines were developed using 2 mm sized quadratic tetrahedral elements (TET10). A refinement of the mesh was performed on the posterior part of the vertebrae and on the articular cartilages, in order to improve the accuracy of the results for these zones. A mesh convergence study was carried out on a single spinal functional unit (L4-L5) using quadratic tetrahedral mesh with a size varying from 0.5mm to 3 mm. An optimal compromise was achieved using a mesh size of 2 mm and a posterior refinement of 1 mm. This balance ensured a computation time of less than 1 h while maintaining error variation below 5% for pressure and 1% for slip in the facet joints compared to results obtained with the most refined mesh (with a size of 0.5 mm but requiring more than 12 h for computation). All material properties used in the FE models are listed in Table 1.

In the computations, an iterative solver was selected in Ansys, utilizing large deformations and incorporating low stiffness springs to aid simulation convergence.

2.2 Arthroplasty models

To develop the arthroplasty FE models (group 2 and 3), 3D models of each prosthesis (Prodisc-L and LP-ESP) were created. Three families of lumbar arthroplasty prostheses exist (Abi-Hanna et al., 2018), which can be distinguished by the number of Degrees-Of-Freedom (DoF). The two prostheses selected for this study belong to the families with the least DoF (ball-and-socket implants) and the most DoF (elastic implants). Prodisc-L (ball-

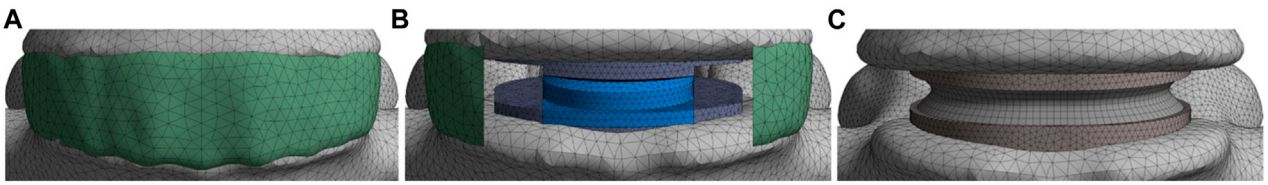

FIGURE 4
Presentation of the various models; **(A)** Group 1: reference models; **(B)** Group 2: models implanted with a ball-and-socket prosthesis with 3 DoF; **(C)** Group 3: models implanted with an elastic prosthesis with 6 DoF.

and-socket prosthesis), which is one of the most widely used TDR implants, consisted of two CoCrMo (Cobalt-Chromium-Molybdenum alloy) endplates and a UHMWPE (Ultra-High Molecular Weight Polyethylene) core. The lower endplate was fixed to the core, and a frictionless contact was imposed between the core and the upper endplate. LP-ESP (elastic prosthesis) consisted of four parts: two Ti 6Al-4V (titanium alloy) endplates, a silicone core, and a Bionate 80A annulus. Both endplates were fixed to the annulus and core.

The reference FE models (group 1) were modified to simulate the arthroplasty models (Figures 4A, B). The positioning of the prosthesis was set with the guidance of experienced spine surgeons. The anterior longitudinal ligament, posterior longitudinal ligament and nucleus pulposus of the L4-L5 level were removed in accordance with real-life surgical technique. In addition, the annulus fibrosus was either partially or completely removed (respectively for groups 2 and 3, Figures 4B, C). The L4-L5 level was selected as the index level due to its high incidence of degenerative disc pathology with 59.6% of the patients having DDD at this spinal level (Mostofi, 2015). To model the secondary stability around the prosthesis endplates, the artificial discs were rigidly fixed to the vertebrae.

2.3 Study design

3 groups of 2 specimens leading to specific FE models were considered (Figure 1).

- Group 1: reference models based on the native geometries of the lumbar spines
- Group 2: lumbar spines implanted with a ball-and-socket prosthesis with 3 DoF (Prodisc-L, Centinel Spine, United States)
- Group 3: lumbar spines implanted with an elastic prosthesis with 6 DoF (LP-ESP, Spine Innovation, France)

40 simulations were conducted (20 for each specimen). For the reference models, pure moments of 7.5 Nm were applied to the upper vertebra while the lower extremity of the sacrum was fixed (step 4 in Figure 1), replicating physiological movements of flexion-extension, lateral bending and axial rotation (Wilke et al., 2012; Germaneau et al., 2016; Jaramillo et al., 2017; Demir et al., 2020). As for the arthroplasty models, 2 loading types were considered. First, a pure moment was applied on the upper vertebra, similarly to the intact models (step 5 in Figure 1). However, it is important to note that for the patient, the main objective of the surgery is to restore the mobility of the spine. Thus, a second set of arthroplasty models was developed for each specimen where the observed rotation of the L4 vertebra from the intact models was imposed to obtain the same segmental amplitude for each model (step 6 in Figure 1). ROM at each level and resulting moments were analysed.

The ROM values of each level were determined and compared with literature results from experimental and numerical studies (Panjabi et al., 1994; Dreischarf et al., 2014; Sutterlin et al., 2016; Rana et al., 2020; Zhang et al., 2021; Nikkhoo et al., 2023) to assess the validity of the developed models. This comparison is presented in the Figure 5. Also, the pressure and sliding between the articular cartilage and the superior articular process were measured for each movement, both at the index level and adjacent level, and the maximum and average values were recorded. The dissipated energy in the facet joints was then calculated by multiplying the pressure and sliding values at each mesh node by the contact area.

For each of these data, we computed standardised values corresponding to ratios between results obtained for intact and operated models.

3 Results

3.1 Validation of patient-specific FE models

The validity of the developed FE models was assessed comparing the numerical results of ROM of the intact models to the results of previously published studies. Figure 5 presents a comparison of the articular amplitudes at L4-L5 and L5-S1 levels observed for imposed moments of 7.5 Nm reproducing physiological movements of flexion-extension, lateral bending and axial rotation. For the lateral bending and axial rotation movements, the results present the combined amplitude of the right and left movements.

For movements of lateral bending and axial rotation, the ROM of both spinal levels were within the corridor established by previously published studies. For the movement of flexion-extension, it could be observed that the spinal segments were stiffer than the specimens used in the other studies, although the ROM of the L5-S1 level was comparable to that of the stiffer specimens of the study of Nikkhoo et al. (Nikkhoo et al., 2023). This high stiffness may be caused by the vertebral and discal geometries of the specimens used in the present study.

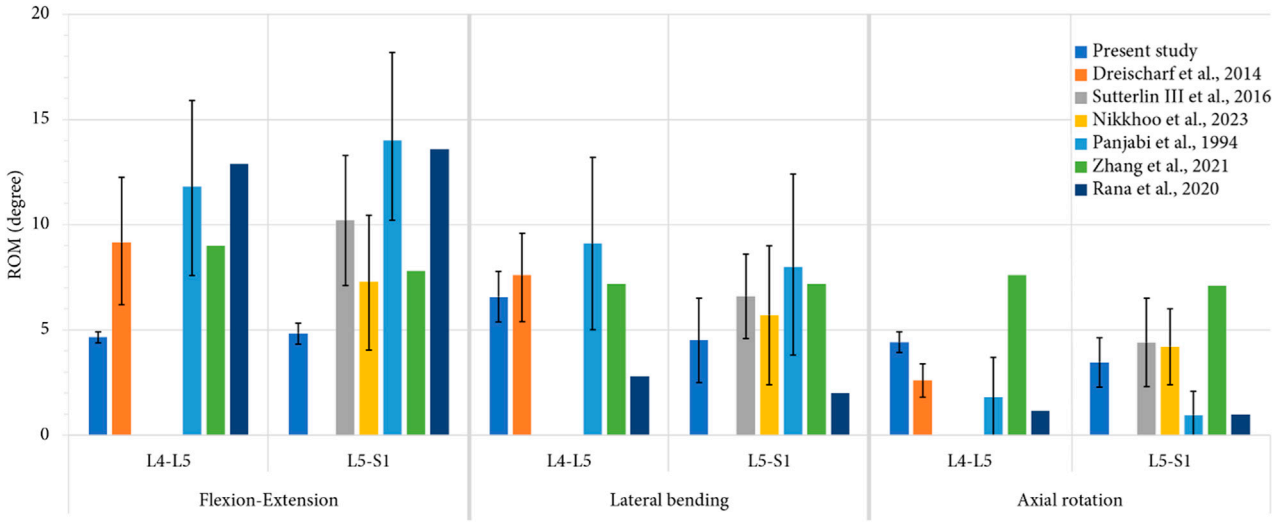

FIGURE 5
Comparison of mean values of ROM, computed for each level during each movement, with previous numerical studies (Dreischarf et al., 2014; Nikkhoo et al., 2023; Zhang et al., 2021; Rana et al., 2020) and *in vitro* studies (Panjabi et al., 1994; Sutterlin et al., 2016) for an imposed pure moment of 7.5 Nm. For the present study, the error bars represent the minimal and the maximal value of ROM observed for all the specimens, whereas for the previous studies, they represent the standard deviation.

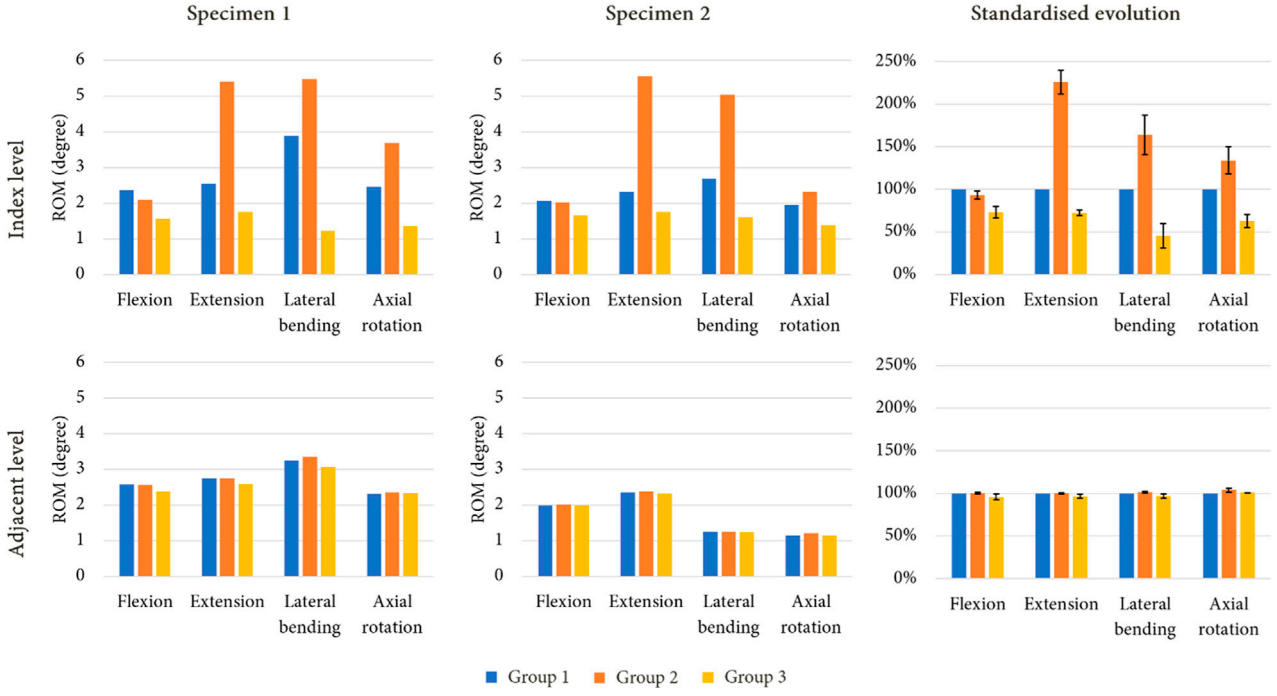

FIGURE 6
ROM evolution under imposed pure moments on the upper vertebra for both specimen after simulated lumbar arthroplasty, with standardised ROM evolution shown to summarise the results of each model (mean values of ROM in percent; error bars presenting the minimum and maximum values).

3.2 Ranges of motion (ROM)

Figure 6 presents the ROM of each model for the imposed moment of 7.5 Nm. During flexion, both arthroplasty models led to reduced ROM at the index level compared to the intact levels, with a mobility decrease of 7% for group 2, and of 27% for group 3. Group 2 presented higher ROM for movements of extension (+126%), lateral bending (+64%) and axial rotation (+34%). The mobility of

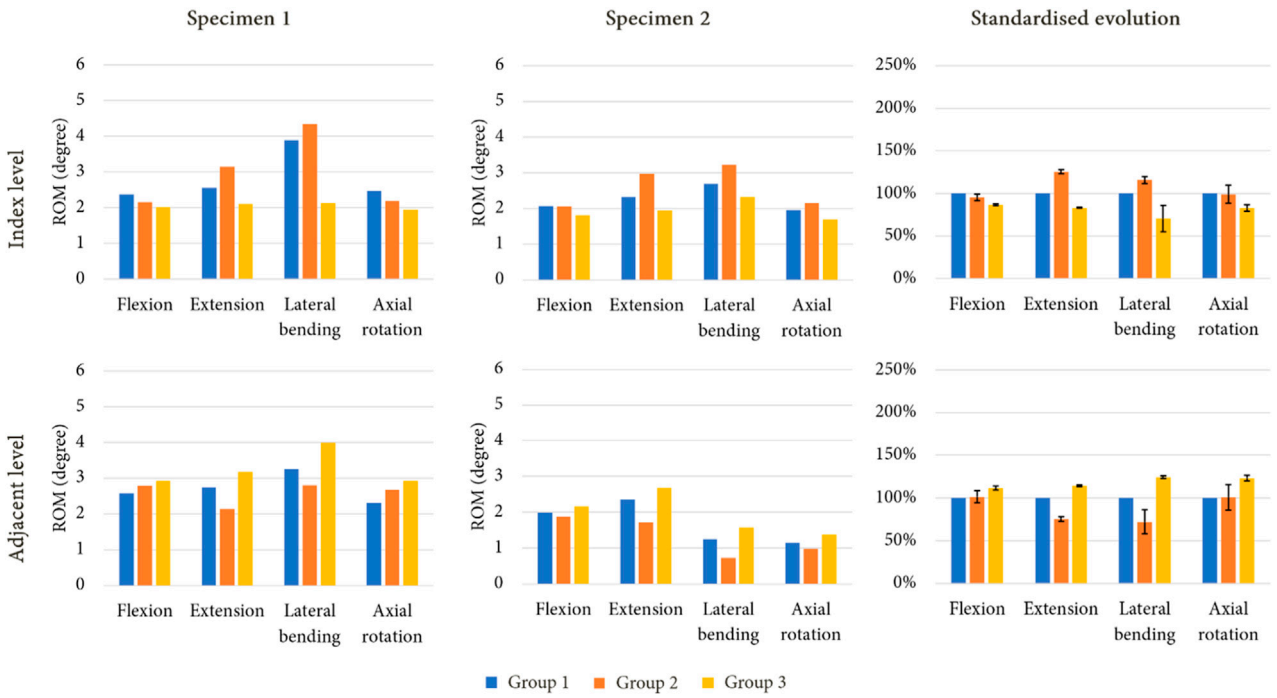

FIGURE 7
ROM evolution under imposed rotation on the upper vertebra for both specimen after simulated arthroplasty, with standardised ROM evolution to shown to summarise the results of each model (mean values of ROM in percent; error bars presenting the minimum and maximum values).

TABLE 2 Moment values observed for the maximum amplitude of each movement under imposed rotation reproducing the movement of the intact models.

Group	Specimen 1				Specimen 2			
	Flexion	Extension	Lateral bending	Axial rotation	Flexion	Extension	Lateral bending	Axial rotation
Group 1	7.5 Nm	7.5 Nm	7.5 Nm	7.5 Nm	7.5 Nm	7.5 Nm	7.5 Nm	7.5 Nm
Group 2	7.2 Nm	3.8 Nm	9.4 Nm	7.7 Nm	7.4 Nm	4.1 Nm	2.8 Nm	5.6 Nm
Group 3	10.1 Nm	10.1 Nm	12.9 Nm	11.1 Nm	13.1 Nm	13.1 Nm	10.0 Nm	10.5 Nm

group 3 decreased for each movement, with a reduction of 28% in extension, 56% during lateral bending, and 37% for axial rotation. At the adjacent level however, no difference was observed between the various models.

Figure 7 presents the ROM of each model for an imposed rotation reproducing the movement of the intact specimens. With this loading condition, little to no variation in ROM could be observed at the index level and at the adjacent level for group 2 during flexion and axial rotation. However, an increase of mobility was noticed for extension (+25%) and lateral bending (+16%) at the index level, whereas decreases of 25% and 28% were observed for these movements at the adjacent level. For group 3, a reduction of mobility was witnessed during every movement at the index level (−14% in flexion, −17% in extension, −30% in lateral bending, and −17% in axial rotation). At the adjacent level, an increase in ROM was observed for each movement, with +12% in flexion, +14% in extension, +24% in lateral bending, and +23% in axial rotation.

Table 2 presents the values of required moment in the arthroplasty models to obtain the same displacement as those observed for group 1. For group 2, we observed that for flexion and extension, the moment was approximately similar or lower than that of group 1. For group 3, an increase of moment values was remarked for each movement.

3.3 Mechanical effects in the facet joints

As illustrations, Figures 8, 9 present the pressure distribution and sliding in the facet joints at the index level (upper level) and adjacent level (lower level) for each model of one specimen (specimen 1) during all 4 movements. The results revealed that the pressure and sliding distributions in groups 2 and 3 were similar to those observed in group 1 for movements of lateral bending and axial rotation. For group 2, it seems that the contact zone was similar during flexion to that of group 1, although there was an increase in

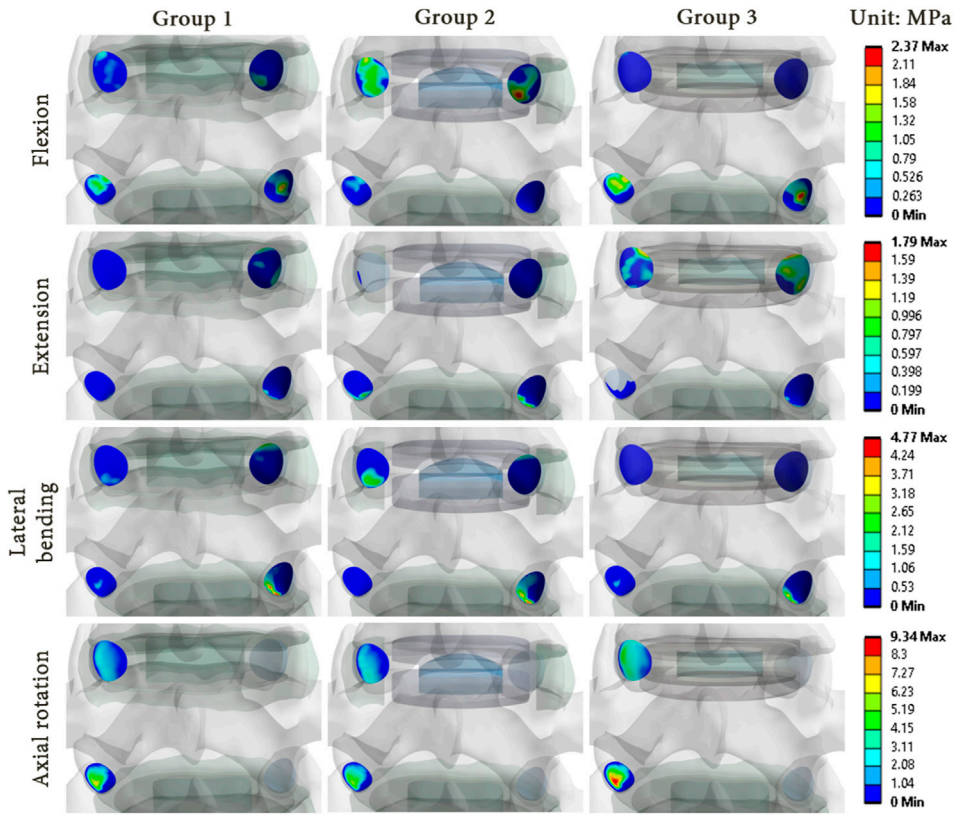

FIGURE 8
Pressure distribution in the facet joints for each model of specimen 1 during each movement reproduced by imposed rotation on the upper vertebra (upper level: index level; lower level: adjacent level).

both pressure and sliding values at the index level. During extension, no contact pressure nor sliding were observed on one of the facet joints of the index level. For group 3, the contact zones remain similar to that of the group 1, and an increase of pressure and sliding was observed at the adjacent level.

The results showed that there were differences in the pressure and sliding values between the three groups. While the pressure and sliding values observed in group 3 were similar to those of group 1, a notable increase was observed in the index level of group 2 for all loading configurations. At the adjacent level, the maximum values of pressure and sliding were lower, which implied a load transfer from the adjacent level to the index level as observed in the ROM results. These observations suggest that the prosthesis type could affect the pressure distribution and sliding in the facet joints, and could therefore have an impact on the long-term wear of the facet joints.

Figure 10 presents the mechanical behaviour of each model for all of the reproduced movements, both at the index level and the adjacent level. At the index level, group 2 showed higher values of pressure compared to group 1, particularly during flexion (+300%) and lateral bending (+35%), whereas a pressure decrease was noted during extension (−55%) and axial rotation (−27%). At the adjacent level, a decrease of pressure was observed during flexion (−74%) and axial rotation (−26%). An increase was remarked during extension (+196%). For group 3, at the index level, an increase of pressure was observed during extension (+288%) and axial rotation (+40%), whereas a decrease was noted for the other movement (−62% in flexion, −67% in lateral bending). At the adjacent level, the pressure values observed during flexion and axial rotation increased (respectively +39% and +19%), whereas during extension and lateral bending, the values remained close to that of group 1.

For each arthroplasty group, the evolution of sliding at the index level followed a similar trend to those of results of pressure for the same groups. At the adjacent level, a decrease of sliding was observed during extension for group 2 (−12%), whereas an increase was noted for group 3 (+107%).

The dissipated energy in the facet joints for each model was analysed to evaluate the mechanical behaviour of the implants. Group 2 showed higher dissipated energy in the facet joints at the index level compared to groups 1 and 3, especially during flexion (+706%) and lateral bending (+16%). In contrast, a reduction was observed at the adjacent level, particularly during flexion (−68%), lateral bending (−35%), and axial rotation (−63%). Group 3 presented an increase of dissipated energy during extension and axial rotation (respectively +270% and +54%), whereas a reduction was observed during flexion (−61%) and lateral bending (−71%). At the adjacent level, the behaviour was similar to that of group 1 for each movement.

4 Discussion

This study used FE analysis to show that for the same TDR implant designation, the mechanical effects in terms of ROM and

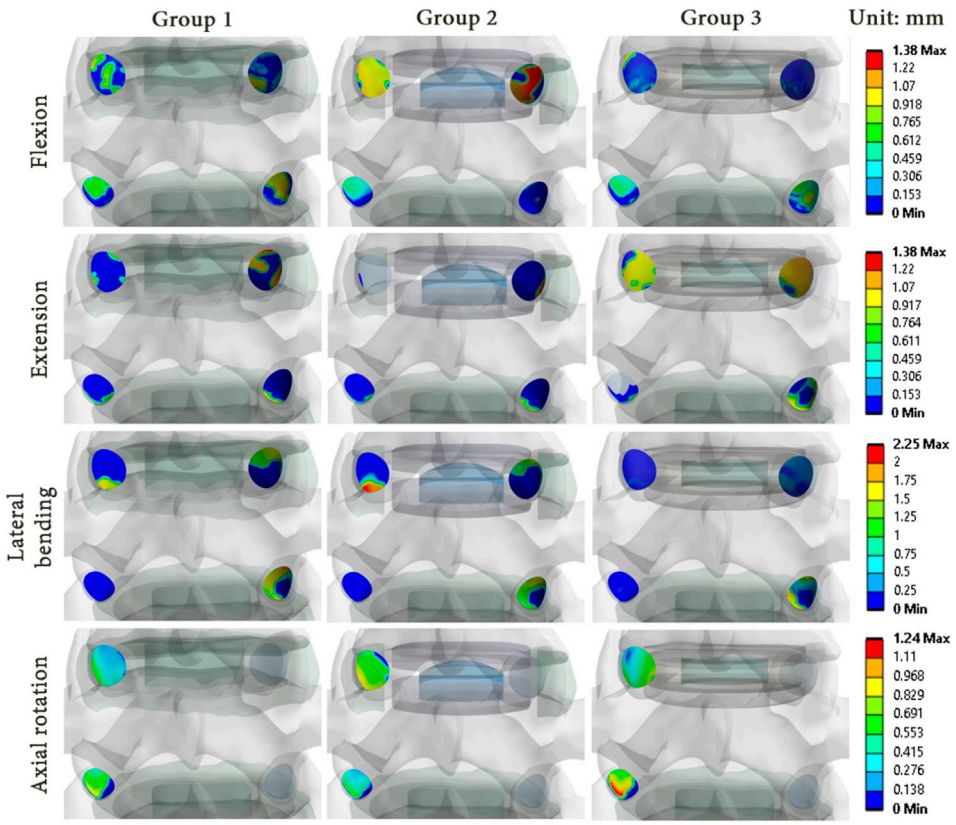

FIGURE 9
Sliding distribution in the facet joints for each model of specimen 1 during each movement reproduced by imposed rotation on the upper vertebra (upper level: index level; lower level: adjacent level).

facet joint loads can vary greatly not only between different TDR designs, but also among different patients. These findings highlight the potential benefits of using patient-specific FE analysis to assist surgeons in selecting the most appropriate surgical solution for each patient.

Most FE studies of the lumbar spine focus on ROM (Shin et al., 2007; Le Huec et al., 2010; Coombs et al., 2017), on intradiscal pressures (Rohlmann et al., 2006; Zhang et al., 2021) or on forces in the facet joints (Choi et al., 2017; Schmidt et al., 2009; Turbucz et al., 2022). We assumed that facet arthritis could be caused by an increase of both pressure and sliding in the facet joints after arthroplasty. To compare the mechanical response of the different models to physiological loadings (pure moments reproducing movements of flexion, extension, lateral bending and axial rotation), we investigated changes in intervertebral ROM, pressure, sliding and dissipated energy in the facet joints. It is, in our knowledge, the first study that focuses on this set of parameters, especially dissipated friction energy, based on the contribution of both pressure and sliding.

The stiffness of the models was found to be higher than that reported in most studies, in particular for flexion-extension movements (Figure 4). This stiffness difference could be attributed to the fact that our specimens were from aged donors with some degree of arthritis and DDD. This is consistent with previous studies which suggested DDD is associated with hypomobility of the lower lumbar segments (Passias et al., 2011; Yao et al., 2013). This increase of stiffness could also be attributed to the fact that in the developed models, all ligaments contribute to limit movements of flexion and extension, whereas for lateral bending and axial rotation movements, only 3 groups of ligaments were activated (TL, LF, CL).

Although all TDR implants were intended to treat the same indication, the mechanical behaviour of different implant types varied significantly. The ball-and-socket prosthesis (Prodisc-L) appeared to increase the ROM and the loads at the index level, while preserving the adjacent level, which is consistent with the results of previously published studies (Schmidt et al., 2009). Therefore, intact facet joint cartilages at the index level seems essential before implantation of such a prosthesis, as intended for the Prodisc-L. The elastic prosthesis (LP-ESP) tended to preserve or reduce ROM at the index level while increasing it at the adjacent level. The same general trend was observed for loadings on the facet joints. Although this study focused only on ball-and-socket and elastic prostheses, the same protocol could be applied for other implants, such as mobile core prostheses or arthrodesis implants. In future works, *in vivo* studies could be envisaged to understand the acceptable level of increased loads for facet joint cartilages. It would be interesting to define a threshold of stress that increases the risk of facet joint arthritis, which could have important implications for the development of prostheses and surgical planning.

This study presents some limitations, the first of which consists in the fact that the validation of the FE models presented in this work

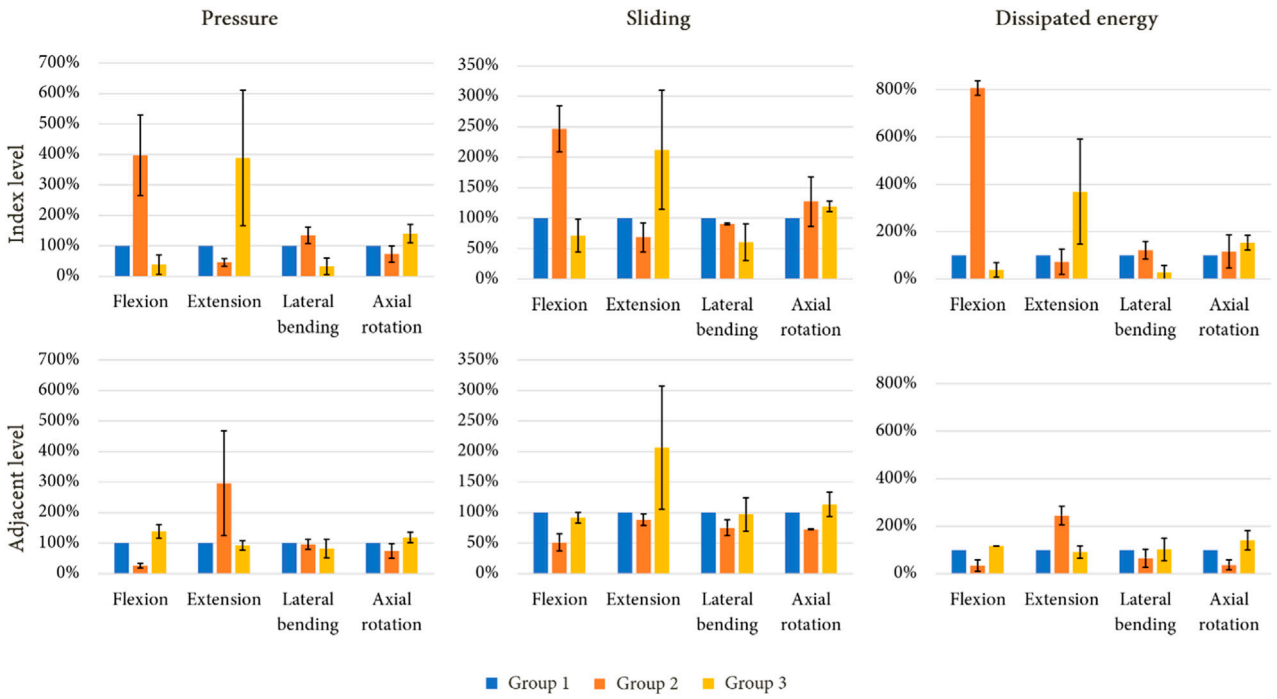

FIGURE 10
Standardised evolution of mean pressure, mean sliding and dissipated energy in the facet joints of the index level and adjacent level under imposed rotation after a simulated lumbar arthroplasty (mean values for each mechanical field in percent; error bars presenting the minimum and maximum values).

were only performed by comparison of the computed ROM to previous kinematic data presented in the literature. To improve this, experiments could be done on the specimens to assess their real behaviour, allowing for a specimen specific validation by a coupled approach of experimental and numerical testing. Also, it would be interesting to validate the computed pressure results by inserting pressure sensors in the facet joints of the real specimens. However, this method would be very invasive and could be difficult to perform.

Specific models were developed from CT scans. However, it was not possible to accurately construct facet joint cartilage. For future studies, it would be interesting to have access to an MRI facility with sufficient resolution to construct accurate cartilage surfaces and combine MRI and CT data to generate a complete patient-specific model.

Furthermore, elastic behaviour was assumed to model the intervertebral discs, whereas most current tend to model the discs with hyperelastic behaviours (Jaramillo et Garcia, 2017; Guldeniz et al., 2022; Vinyas et al., 2023). Xie et al. showed that this modelling approach can lead to higher ROM for the spinal segments. However, the use of hyperelastic material properties lead to highly increased computation times.

Another limitation of this work is that the results are valid only under the assumption of perfect stability after bone remodelling around the prosthesis, which may not always be the case in clinical practice due to different efficacy of the anchoring systems and physiological differences between patients.

In addition, this work focused only on the effect of arthroplasty on the index level and the inferior adjacent level. The same methodology could be applied to perform the same analyses on the superior adjacent levels.

Also, these models could be modified to consider more types of spinal implants. Indeed, it would be interesting to determine the effects on the facet joints of mobile core prosthesis, which correspond to the third family of arthroplasty implants, or of implants destined to other types of surgeries, such as arthrodesis cages or posterior stabilisation devices based on pedicular screws.

Finally, this study did not investigate the effects of antero-posterior misalignment of the different implants according to specimen geometry. It has been shown that this can significantly influence the results (Le Huec et al., 2010) but it would be interesting to evaluate the optimal placement for various spinal segments. These limitations will be addressed in future studies.

5 Conclusion

In this work, we developed patient specific FE models to analyse mechanical effects linked to arthroplasty in lumbar levels. Elastic prostheses seem to be a promising option for arthroplasty due to their mechanical behaviour similar to a disc in particular, in case of degenerated discs and relatively stiff spinal units. On the other hand, for patients without arthrosis disease, ball-and-socket prostheses reduce loads at the lower adjacent level and increases ROM at the index level. These findings confirm the contribution of a surgical planning built from a patient-specific FE analysis. FE models integrating patient characteristics (age, native mobility, presence of arthrosis, etc.) could provide quantitative data to surgeons to optimise the choice of the implant. Further research coupled with clinical observations would be needed to determine the long-term

effects of these implants on adjacent and surgical spinal segments, as well as to explore other potential solutions that balance the benefits of increased mobility and reduced loads.

Data availability statement

The raw data supporting the conclusion of this article will be made available by the authors, without undue reservation.

Ethics statement

The studies involving humans were approved by the Ethics committee of the French Ministry of Health under the number: DC-2019-3704 Universite de Poitiers, ABSLAb F-86000 Poitiers, France. The studies were conducted in accordance with the local legislation and institutional requirements. The human samples used in this study were acquired from gifted from another research group. Written informed consent for participation was not required from the participants or the participants' legal guardians/next of kin in accordance with the national legislation and institutional requirements.

Author contributions

FZ: Conceptualization, Data curation, Formal Analysis, Investigation, Methodology, Software, Validation, Writing–original draft. EB-B: Conceptualization, Data curation, Methodology, Writing–original draft, Writing–review and editing. MS: Conceptualization, Data curation, Methodology, Visualization, Writing–review and editing. YL: Conceptualization, Methodology, Software, Supervision, Validation, Writing–review and editing. MM: Conceptualization, Methodology, Supervision, Writing–review and editing. LC: Data curation, Formal Analysis, Software, Writing–review and editing. CS: Conceptualization, Investigation, Methodology, Writing–review and editing. ST: Conceptualization, Investigation, Methodology, Writing–review and editing. A-YM: Conceptualization, Investigation, Methodology, Writing–review and editing. AG: Conceptualization, Formal Analysis, Funding acquisition, Investigation, Methodology, Project administration, Supervision, Writing–original draft. TV: Conceptualization, Formal Analysis, Methodology, Project administration, Resources, Supervision, Writing–review and editing.

Funding

The author(s) declare financial support was received for the research, authorship, and/or publication of this article. This work was supported by Région Nouvelle-Aquitaine under grant number AAPR 2020-2019-8410610.

Acknowledgments

The authors would like to thank the Anatomy Laboratory of the University of Poitiers (ABS Lab) for the anatomical segments. In addition, we thank the companies Centinel Spine and Spine Innovations for providing their prostheses.

Conflict of interest

The authors declare that the research was conducted in the absence of any commercial or financial relationships that could be construed as a potential conflict of interest.

Publisher's note

References

Abi-Hanna, D., Kerferd, J., Phan, K., Rao, P., and Mobbs, R (2018). Lumbar disk arthroplasty for degenerative disk disease: literature review. *World Neurosurg.* 109 (janvier), 188–196. doi:10.1016/j.wneu.2017.09.153

Adams, M. A., and Roughley, P. J. (2006). What is intervertebral disc degeneration, and what causes it? *Spine* 31 (18), 2151–2161. doi:10.1097/01.brs.0000231761.73859.2c

Bashkuev, M., Reitmaier, S., and Schmidt, H. (2020). Relationship between intervertebral disc and facet joint degeneration: a probabilistic finite element model study. *J. Biomechanics* 102, 109518. doi:10.1016/j.jbiomech.2019.109518

Biswas, J. K., Banerjee, A., Mondal, N., and Rana, M. (2023). A finite element based comparative study of lumbosacral pedicle screw fixation and artificial disc replacement. *J. Eng. Sci. Med. Diagnostics Ther* 6 (3), 030902. doi:10.1115/1.4056953

Chemmami, A., Aour, B., Zahaf, S., Dahmane, M., Mehdi, I. B. G., and Boutchicha, D. (2021). Biomechanical comparison of three total artificial discs: sb-charite iii®, prodisc-l® and maverick® reinforced by a posterior fixation system in the spinal column: a three-dimensional finite element analysis. *Struct Integr Life* 21, 65–83.

Cheung, K. M. C., Karppinen, J., Chan, D., Ho, D. W. H., Song, Y.-Q., Sham, P., Cheah, K. S. E., John, C., et al. (2009). Prevalence and pattern of lumbar magnetic resonance imaging changes in a population study of one thousand forty-three individuals. *Spine* 34 (9), 934–940. doi:10.1097/BRS.0b013e3181a01b3f

Choi, J., Shin, D.-A., and Kim, S. (2017). Biomechanical effects of the geometry of ball-and-socket artificial disc on lumbar spine: a finite element study. *Spine* 42 (6), E332–E339. doi:10.1097/BRS.0000000000001789

Coombs, D. J., Rullkoetter, P. J., and Laz, P. J. (2017). Efficient probabilistic finite element analysis of a lumbar motion segment. *J. Biomechanics* 61 (août), 65–74. doi:10.1016/j.jbiomech.2017.07.002

Cui, X.-D., Li, H.-T., Zhang, W., Zhang, L.-L., Luo, Z.-P., and Yang, H. L. (2018). Mid- to long-term results of total disc replacement for lumbar degenerative disc disease: a systematic review. *J. Orthop. Surg. Res.* 13 (1), 326. doi:10.1186/s13018-018-1032-6

Dagenais, S., Caro, J., and Haldeman, S. (2008). A systematic review of low back pain cost of illness studies in the United States and internationally. *Spine J.* 8 (1), 8–20. doi:10.1016/j.spinee.2007.10.005

Demir, E., Eltes, P., Castro, A.P., Lacroix, D., and Toktaş, İ. (2020). Finite element modelling of hybrid stabilization systems for the human lumbar spine. *Proc. Institution Mech. Eng. Part H J. Eng. Med.* 234 (12), 1409–1420. doi:10.1177/0954411920946636

Dooris, A. P., Goel, V. K., Grosland, N. M., Gilbertson, L. G., and Wilder, David.G. (2001). Load-sharing between anterior and posterior elements in a lumbar motion segment implanted with an artificial disc. *Spine* 26 (6), E122–E129. doi:10.1097/00007632-200103150-00004

Dreischarf, M., Zander, T., Shirazi-Adl, A., Puttlitz, C. M., Adam, C. J., Chen, C. S., et al. (2014). Comparison of eight published static finite element models of the intact lumbar spine: predictive power of models improves when combined together. *J. Biomechanics* 47 (8), 1757–1766. doi:10.1016/j.jbiomech.2014.04.002

Fatoye, F., Gebrye, T., Mbada, C. E., and Useh, U. (2023). Clinical and economic burden of low back pain in low- and middle-income countries: a systematic review. *BMJ Open* 13 (4), e064119. doi:10.1136/bmjopen-2022-064119

Finley, S. M., Darrel, S. B., Spina, N. T., DeDen, C. A., and Ellis, B.J. (2018). FEBio finite element models of the human lumbar spine. *Comput. Methods Biomechanics Biomed. Eng.* 21 (6), 444–452. doi:10.1080/10255842.2018.1478967

Formica, C., Zanirato, A., Divano, S., Basso, M., Cavagnaro, L., Alessio Mazzola, M., et al. (2020). Total disc replacement for lumbar degenerative disc disease: single centre 20 Years experience. *Eur. Spine J.* 29 (7), 1518–1526. doi:10.1007/s00586-019-06100-3

Furunes, H., Berg, L., Espeland, A., Thoresen, H., Neckelmann, G., Helga, M. B., Cvancarova Småstuen, M., Ivar Brox, J., Storheim, K., and Hellum, C. (2020). Facet arthropathy following disc replacement versus rehabilitation: a prospective study with 8-year follow-up. *Spine* 45 (21), 1467–1475. doi:10.1097/BRS.0000000000003600

Gellhorn, A. C., Katz, J. N., and Suri, P. (2013). Osteoarthritis of the spine: the facet joints. *Nat. Rev. Rheumatol.* 9 (4), 216–224. doi:10.1038/nrrheum.2012.199

Germaneau, A., Vendeuvre, T., Saget, M., Doumalin, P., Dupré, J. C., Brémand, F., et al. (2016). A novel approach for biomechanical spine analysis: mechanical response of vertebral bone augmentation by kyphoplasty to stabilise thoracolumbar burst fractures. *J. Mech. Behav. Biomed. Mater.* 59 (juin), 291–303. doi:10.1016/j.jmbbm.2016.02.002

Guldeniz, O., Yesil, O. B., and Okyar, F. (2022). Yeditepe spine mesh: finite element modeling and validation of a parametric CAD model of lumbar spine. *Med. Eng. Phys.* 110 (décembre), 103911. doi:10.1016/j.medengphy.2022.103911

Hoy, D., Bain, C., Williams, G., March, L., Brooks, P., Blyth, F., et al. (2012). A systematic review of the global prevalence of low back pain. *Arthritis and Rheumatism* 64 (6), 2028–2037. doi:10.1002/art.34347

Iatridis, J. C., Steven, B. N., Michalek, A. J., Walter, B. A, and Gupta, M. S. (2013). Role of Biomechanics in intervertebral disc degeneration and regenerative therapies: what needs repairing in the disc and what are promising biomaterials for its repair? *Spine J* 13 (3), 243–262. doi:10.1016/j.spinee.2012.12.002

Iorio, J. A., Jakoi, A. M., and Singla, A. (2016). Biomechanics of degenerative spinal disorders. *Asian Spine J* 10 (2), 377. doi:10.4184/asj.2016.10.2.377

Jaramillo, H. E., and Garcia., J. J. (2017). elastic constants influence on the L4-L5-S1 annuli fibrosus behavior, A probabilistic finite element analysis. *Acta of bioengineering and Biomechanics* 19, 4. doi:10.5277/ABB-00949-2017-02

John, J. D., Gurunathan, S. K., and Narayan, Y. (2019). Cervical spine morphology and ligament property variations: a finite element study of their influence on sagittal bending characteristics. *J. Biomechanics* 85 (mars), 18–26. doi:10.1016/j.jbiomech.2018.12.044

Kalichman, L., Li, L., Kim, D. H., Ali, G., Berkin, V., O'Donnell, C. J., et al. (2008). Facet joint osteoarthritis and low back pain in the community-based population. *Spine* 33 (23), 2560–2565. doi:10.1097/BRS.0b013e318184ef95

Kapandji, I. A. (2019). *The physiology of the joints: the spinal column, pelvic girdle and head*. London, England, UK: Handspring Publishing Limited.

Karran, E. L., Grant, A. R., and Moseley, G. L. (2020). Low back pain and the social determinants of health: a systematic review and narrative synthesis. *Pain* 161 (11), 2476–2493. doi:10.1097/j.pain.0000000000001944

Lavaste, F., Skalli, W., Robin, S., Roy-Camille, R., and Mazel, C. (1992). Three-dimensional geometrical and mechanical modelling of the lumbar spine. *J. Biomechanics* 25 (10), 1153–1164. doi:10.1016/0021-9290(92)90071-8

Le Huec, Jean-Charles, Lafage, V., Bonnet, X., Lavaste, F., Josse, L., et al. (2010). Validated finite element analysis of the maverick total disc prosthesis. *J. Spinal Disord. Tech.* 23 (4), 249–257. doi:10.1097/BSD.0b013e3181a5db24

Manchikanti, L. 2002. « Review of chronic low back pain of facet joint origin ». *Pain Physician*;5 (1;1): 83–101. doi:10.36076/ppj.2002/5/83

Mengoni, M. (2020). biomechanical modelling of the facet joints: a review of methods and validation processes in finite element analysis. *Biomechanics and Modeling in mechanobiology* 20, 389–401. doi:10.1007/s10237-020-01403-7

Mostofi, K. (2015). Total disc arthroplasty for treating lumbar degenerative disc disease. *Asian Spine J.* 9 (1), 59. doi:10.4184/asj.2015.9.1.59

Mu, X., Wei, J., Jiancuo, A., Li, Z., and Ou, Y. (2018). the short-term efficacy and safety of artificial total disc replacement for selected patients with lumbar degenerative disc disease compared with anterior lumbar interbody fusion: a systematic review and meta-analysis. *Édité Par Giovanni Grasso. PLOS ONE* 13 (12), e0209660. doi:10.1371/journal.pone.0209660

Nic An Ghaill, N., and Little, E. G. (2008). Determination of the mechanical properties of bionate 80A and bionate 75D for the stress analysis of cushion form bearings. *Proc. Institution Mech. Eng. Part H, J. Eng. Med.* 222 (5), 683–694. doi:10.1243/09544119JEIM372

Nikkhoo, M., Chen, W.-C., Lu, M.-L., Fu, C.-J., Niu, C.-C., Lien, H. Y., and Cheng, C. H. (2023). Anatomical parameters alter the biomechanical responses of adjacent segments following lumbar fusion surgery: personalized poroelastic finite element modelling investigations. *Front. Bioeng. Biotechnol.* 11, 1110752. doi:10.3389/fbioe.2023.1110752

Nikkhoo, M., Khoz, Z., Cheng, C.-H., Niu, C.-C., El-Rich, M., and Khalaf, K. (2020). Development of a novel geometrically-parametric patient-specific finite element model to investigate the effects of the lumbar lordosis angle on fusion surgery. *J. Biomechanics* 102, 109722 doi:10.1016/j.jbiomech.2020.109722

Ooij, A., Oner, F. C., and Verbout, A. J. (2003). Complications of artificial disc replacement. *J. Spinal Disord.* 16 (4). doi:10.1097/00024720-200308000-00009

Panjabi, M. M., Oxland, T. R., Yamamoto, I., and Crisco, J. J. (1994). Mechanical behavior of the human lumbar and lumbosacral spine as shown by three-dimensional load-displacement curves. *JBJS* 76 (3), 413. doi:10.2106/00004623-199403000-00012

Park, W. M., Kim, K., and Kim, Y. H. (2013). Effects of degenerated intervertebral discs on intersegmental rotations, intradiscal pressures, and facet joint forces of the whole lumbar spine. *Comput. Biol. Med.* 43 (9), 1234–1240. doi:10.1016/j.compbiomed.2013.06.011

Passias, P. G., Wang, S., Kozanek, M., Xia, Q., Li, W., Grottkau, B., et al. (2011). Segmental lumbar rotation in patients with discogenic low back pain during functional weight-bearing activities. *J. Bone Jt. Surg.* 93 (1), 29–37. doi:10.2106/JBJS.I.01348

Peng, Yi, Du, X., Huang, L., Li, J., Zhan, R., Wang, W., et al. (2018). Optimizing bone cement stiffness for vertebroplasty through biomechanical effects analysis based on patient-specific three-dimensional finite element modeling. *Med. Biol. Eng. Comput.* 56 (11), 2137–2150. doi:10.1007/s11517-018-1844-x

Qin, D.-P., Zhang, X.-G., Son, M., Zhang, H., Cao, L.-Z., Zhao, W.-T., et al. (2021). Effect of different attributes of the mimic human lumbar spine Biomechanics material structure change by finite element analysis. *SN Appl. Sci.* 3 (12), 880. doi:10.1007/s42452-021-04857-1

Rana, M., Roy, S., Biswas, P., Biswas, S. K., and Biswas, J. K. (2020). Design and development of a novel expanding flexible rod device (frd) for stability in the lumbar spine: a finite-element study. *Int. J. Artif. Organs* 43 (12), 803–810. doi:10.1177/0391398820917390

Remus, R., Lipphaus, A., Neumann, M., and Bender, B. (2021). calibration and validation of a novel hybrid model of the lumbosacral spine in ArtiSynth–the passive structures. *Édité par kevin mattheus moerman. PLOS ONE* 16 (4), e0250456. doi:10.1371/journal.pone.0250456

Rohlmann, A., Zander, T., Schmidt, H., Wilke, H.-J., and Bergmann, G. (2006). Analysis of the influence of disc degeneration on the mechanical behaviour of a lumbar motion segment using the finite element method. *J. Biomechanics* 39 (13), 2484–2490. doi:10.1016/j.jbiomech.2005.07.026

Sandhu, F. A., Dowlati, E., and Garica, R. (2020). Lumbar arthroplasty: past, present, and future. *Neurosurgery* 86 (2), 155–169. doi:10.1093/neuros/nyz439

Schmidt, H., Galbusera, F., Rohlmann, A., Zander, T., and Wilke, H.-J. (2012). Effect of multilevel lumbar disc arthroplasty on spine kinematics and facet joint loads in flexion and extension: a finite element analysis. *Eur. Spine J.* 21 (S5), 663–674. doi:10.1007/s00586-010-1382-1

Schmidt, H., Midderhoff, S., Adkins, K., and Wilke, H.-J. (2009). The effect of different design concepts in lumbar total disc arthroplasty on the range of motion, facet joint forces and instantaneous center of rotation of a L4-5 segment. *Eur. Spine J.* 18 (11), 1695–1705. doi:10.1007/s00586-009-1146-y

Shin, M.-H., Ryu, K.-S., Hur, J.-W., Kim, J.-S., and Park, C.-K. (2013). Association of facet tropism and progressive facet arthrosis after lumbar total disc replacement using ProDisc-L®. *Eur. Spine J.* 22 (8), 1717–1722. doi:10.1007/s00586-012-2606-3

Shin, Dong, S., Lee, K., and Kim, D. (2007). Biomechanical study of lumbar spine with dynamic stabilization device using finite element method. *Computer-Aided Des.* 39 (7), 559–567. doi:10.1016/j.cad.2007.03.005

Shirazi-Adl, A., Ahmed, A. M., and Suresh, C. S. (1986). Mechanical response of a lumbar motion segment in axial torque alone and combined with compression. *Spine* 11 (9), 914–927. doi:10.1097/00007632-198611000-00012

Siepe, C. J., Zelenkov, P., Sauri-Barraza, J.-C., Szeimies, U., Grubinger, T., Alexander, T., et al. (2010). The fate of facet joint and adjacent level disc degeneration following total lumbar disc replacement: a prospective clinical, X-ray, and magnetic resonance imaging investigation. *Spine* 35 (22), 1991–2003. doi:10.1097/BRS.0b013e3181d6f878

Simon, J., McAuliffe, M., Shamim, F., Vuong, N., and Tahaei, A. (2014). Discogenic low back pain. *Phys. Med. Rehabilitation Clin. N. Am.* 25 (2), 305–317. doi:10.1016/j.pmr.2014.01.006

Sutterlin, III, Chester, E., Field, A., Ferrara, L. A., Freeman, A. L., and Phan, K. (2016). Range of motion, sacral screw and rod strain in long posterior spinal constructs: a biomechanical comparison between S2 alar iliac screws with traditional fixation strategies. *J. Spine Surg.* 2 (4), 266–276. doi:10.21037/jss.2016.11.01

Turbucz, M., Jakab Pokorni, A., György Szőke, Hoffer, Z., Rita Maria, K., Lazary, A., and Eltes, P. E. (2022). Development and validation of two intact lumbar spine finite element models for *in silico* investigations: comparison of the bone modelling approaches. *Appl. Sci.* 12 (20), 10256. doi:10.3390/app122010256

Vinyas, Bhat, S. K., Adhikari, R., and Shy Bhat, N. (2023). In-silico model development and validation of the L5-S1 spinal unit. *Cogent Eng.* 10 (1), 2184446. doi:10.1080/23311916.2023.2184446

Vos, T., Allen, C., Arora, M., Barber, R. M., Bhutta, Z. A., Brown, A., et al. (2016). Global, regional, and national incidence, prevalence, and years lived with disability for

310 diseases and injuries, 1990–2015: a systematic analysis for the global burden of disease study 2015. *Lancet* 388 (10053), 1545–1602. doi:10.1016/S0140-6736(16)31678-6

Wilke, H.-J., Schmidt, R., Richter, M., Werner, S., Reichel, H., and Cakir, B. (2012). The role of prosthesis design on segmental Biomechanics: semi-constrained versus unconstrained prostheses and anterior versus posterior centre of rotation. *Eur. Spine J.* 21 (S5), 577–584. doi:10.1007/s00586-010-1552-1

Wu, A., March, L., Zheng, X., Huang, J., Wang, X., Zhao, J., et al. (2020). Global low back pain prevalence and years lived with disability from 1990 to 2017: estimates from the global burden of disease study 2017. *Ann. Transl. Med.* 8 (6), 299–299. doi:10.21037/atm.2020.02.175

Yao, Qi, Wang, S., Shin, J.-H., Li, G., and Wood, K. (2013). Motion characteristics of the lumbar spinous processes with degenerative disc disease and degenerative spondylolisthesis. *Eur. Spine J.* 22 (12), 2702–2709. doi:10.1007/s00586-013-2918-y

Zhang, C., Shi, J., Chang, M., Yuan, X., Zhang, R., Huang, H., et al. (2021). Does osteoporosis affect the adjacent segments following anterior lumbar interbody fusion? A finite element study. *World Neurosurg.* 146 (février), e739-46. doi:10.1016/j.wneu.2020.11.005

Zhang, L., Li, H.-M., Zhang, R., Zhang, H., and Shen, C. L. (2021). Biomechanical changes of adjacent and fixed segments through cortical bone trajectory screw fixation versus traditional trajectory screw fixation in the lumbar spine: a finite element analysis. *World Neurosurg.* 151 (juillet), e447-56. doi:10.1016/j.wneu.2021.04.061

Zigler, J., Gornet, M. F., Ferko, N., Cameron, C., Schranck, F. W., and Patel, L. (2018). Comparison of lumbar total disc replacement with surgical spinal fusion for the treatment of single-level degenerative disc disease: a meta-analysis of 5-year outcomes from randomized controlled trials. *Glob. Spine J.* 8 (4), 413–423. doi:10.1177/2192568217737317

frontiers | Frontiers in Bioengineering and Biotechnology

TYPE Original Research
PUBLISHED 14 December 2023
DOI 10.3389/fbioe.2023.1293705

OPEN ACCESS

EDITED BY
Jörg Miehling,
Friedrich-Alexander-Universität Erlangen-Nürnberg, Germany

REVIEWED BY
Sigrid Leyendecker,
University of Erlangen Nuremberg, Germany
Magnus Gislason,
Reykjavík University, Iceland

*CORRESPONDENCE
Lennart V. Nölle,
lennart.noelle@imsb.uni-stuttgart.de

RECEIVED 13 September 2023
ACCEPTED 01 December 2023
PUBLISHED 14 December 2023

CITATION
Nölle LV, Alfaro EH, Martynenko OV and Schmitt S (2023), An investigation of tendon strains in jersey finger injury load cases using a finite element neuromuscular human body model. *Front. Bioeng. Biotechnol.* 11:1293705. doi: 10.3389/fbioe.2023.1293705

An investigation of tendon strains in jersey finger injury load cases using a finite element neuromuscular human body model

Lennart V. Nölle[1]*, Eduardo Herrera Alfaro[1], Oleksandr V. Martynenko[1] and Syn Schmitt[1,2]

[1]Institute for Modelling and Simulation of Biomechanical Systems, University of Stuttgart, Stuttgart, Germany, [2]Stuttgart Center for Simulation Science, University of Stuttgart, Stuttgart, Germany

Introduction: A common hand injury in American football, rugby and basketball is the so-called jersey finger injury (JFI), in which an eccentric overextension of the distal interphalangeal joint leads to an avulsion of the connected musculus flexor digitorum profundus (FDP) tendon. In the field of automotive safety assessment, finite element (FE) neuromuscular human body models (NHBMs) have been validated and are employed to evaluate different injury types related to car crash scenarios. The goal of this study is to show, how such a model can be modified to assess JFIs by adapting the hand of an FE-NHBM for the computational analysis of tendon strains during a generalized JFI load case.

Methods: A jersey finger injury criterion (JFIC) covering the injury mechanisms of tendon straining and avulsion was defined based on biomechanical experiments found in the literature. The hand of the Total Human Model for Safety (THUMS) version 3.0 was combined with the musculature of THUMS version 5.03 to create a model with appropriate finger mobility. Muscle routing paths of FDP and musculus flexor digitorum superficialis (FDS) as well as tendon material parameters were optimized using literature data. A simplified JFI load case was simulated as the gripping of a cylindrical rod with finger flexor activation levels between 0% and 100%, which was then retracted with the velocity of a sprinting college football player to forcefully open the closed hand.

Results: The optimization of the muscle routing node positions and tendon material parameters yielded good results with minimum normalized mean absolute error values of 0.79% and 7.16% respectively. Tendon avulsion injuries were detected in the middle and little finger for muscle activation levels of 80% and above, while no tendon or muscle strain injuries of any kind occurred.

Discussion: The presented work outlines the steps necessary to adapt the hand model of a FE-NHBM for the assessment of JFIs using a newly defined injury criterion called the JFIC. The injury assessment results are in good agreement with documented JFI symptoms. At the same time, the need to rethink commonly asserted paradigms concerning the choice of muscle material parameters is highlighted.

KEYWORDS

finite element analysis, injury criteria, jersey finger injury, muscle modelling, tendon strain injury

1 Introduction

Many sporting activities put great stress on the upper appendages with around 25% of sports related injuries involving the hand or the wrist (Amadio, 1990; Rettig, 2003). A common hand injury in American football, rugby and basketball is the so-called jersey finger injury (JFI). This type of injury is caused by an eccentric overextension of the distal interphalangeal (DIP) joint, as can occur during the forceful release of one player's grip on another player's jersey or a finger getting caught on the rim of a basketball hoop, and leads to an avulsion of the connected *musculus flexor digitorum profundus* (FDP) tendon (Murphy and Mass, 2005; Gaston and Loeffler, 2015; Avery et al., 2016). This injury has been studied extensively in clinical studies, for example, in the work of Tempelaere et al. (Tempelaere et al., 2017), while computational investigations have thus far been focused on the modelling of general hand models (Joaquin et al., 2011), singular digits (Wu et al., 2008; Vigouroux et al., 2009; Fok and Chou, 2010; Wu et al., 2010) or the finger pulley system (Roloff et al., 2006; Vigouroux et al., 2008). In the field of automotive safety assessment, finite element (FE) neuromuscular human body models (NHBMs) created for the use with the FE-solver LS-DYNA (Ansys, Canonsburg, PA, United States) such as the Global Human Body Models Consortium (GHBMC) (Devane et al., 2019) or the Total Human Model for Safety (THUMS) (Kato et al., 2017; Kato et al., 2018) have been validated and are mainly employed to evaluate a host of different injury types related to car crash scenarios (GHBMC, 2016; Toyota Motor Corporation, and Toyota Central R&D Labs. Inc, 2021). Examples of these validation efforts are given by Kato et al. (Kato et al., 2018) where the THUMS model of version 6.0 was validated against several sets of test data derived from post-mortem human subjects (Cavanaugh et al., 1986; Cesari and Bouquet, 1990; Bolte et al., 2003; Foster et al., 2006; Rupp et al., 2008; Kroell et al., 2009; Shaw et al., 2009; Viano, 2009). The goal of this study is to show how a FE-NHBM can be modified to assess injuries not only found in car crashes, specific to the automotive domain, by adapting the hand of the THUMS AM50 occupant model of academic version 3.0 (Iwamoto et al., 2007) for the computational analysis of tendon strains during generalized JFI load cases. To this end, a Jersey Finger Injury Criterion (JFIC) covering the injury mechanisms of tendon straining and avulsion is first defined based on biomechanical experiments found in the literature. Next, FE-NHBM choice and necessary modification steps, including the routing and parameter tuning of newly introduced Hill-type muscles, will be outlined. Finally, a simulation study is performed to ensure both a sensible model behavior, and to tackle the question of how varying muscle activation levels and resulting maximum muscle forces impact the risk of sustaining a JFI in a representative injury scenario.

2 Materials and methods

2.1 Definition of a jersey finger injury criterion

JFI scenarios are characterized by the forced opening of an otherwise closed grip resulting in two distinct injury mechanisms. The main injury mechanism of the JFI is the avulsion of the FDP tendon caused by a hyperextension of the DIP joint (Gaston and Loeffler, 2015; Avery et al., 2016). Measurements of the forces necessary to induce such an injury are described in both the works of Holden and Northmore-Ball (Holden and Northmore-Ball, 1975) as well as those of Manske and Lesker (Manske and Lesker, 1978). To err on the side of caution, the lowest reported avulsion load of 10.8 kg (Manske and Lesker, 1978) was converted to Newtons and set as the resulting avulsion force threshold of 105.91 N. While not classically associated with the JFI, it is well known that eccentric muscle contraction can cause considerable damage to the affected tissue, with injuries ranging from minor strains to the complete rupture of the muscle-tendon-unit (MTU) (Noonan and Garrett, 1999; Maffulli, 2005). The eccentric lengthening of the finger flexor muscle groups was thus identified as a secondary injury mechanism to be represented in the JFIC. Studies of tendon material properties have shown that the severity of a sustained tendon strain injury can be linked to the deformation stages of the tendon's stress-strain curve (Maffulli, 2005; Wang, 2006). Consequently, three distinct tendon strain injury thresholds were defined, with the minor injury threshold set at the start of the strain hardening region, the major injury threshold at the start of the necking region, and rupture threshold at the point of material failure. Tendon strains appropriate for the deformation regions of positional tendons as defined by Kaya et al. (Kaya et al., 2019) were derived from the literature (Maganaris et al., 2004; Wang, 2006; Stauber et al., 2019) and there thus used to define a secondary injury criterion called the Tendon Strain Injury Criterion (TSIC). A summary of the avulsion injury and TSIC threshold values, which together form the JFIC, is given in Table 1. The occurrence and severity of muscle strain injury was assessed using the Muscle Strain Injury Criterion (MSIC) analogously defined by Nölle et al. (Nölle et al., 2022b). An injury assessment using the JFIC and MSIC was performed for the FDP and the *musculus flexor digitorum superficialis* (FDS). All abbreviations used in the paper are listed in Supplementary Table S1.

2.2 Model selection and modification

The main selection criterion for the choice of an FE-NHBM was deemed to be the maximally achievable finger mobility, as simulating a gripping motion prior to the forced eccentric opening of the hand was considered to be essential for the reconstruction of JFI load cases. After evaluating the hand models of the THUMS AM50 occupant models version 3.0 (Iwamoto et al., 2007), version 4.1 (Shigeta et al., 2009), version 5.03 (Iwamoto and Nakahira, 2015) and version 6.1 (Kato et al., 2018), we arrived at the conclusion that no single model would be able to deliver a sufficient range of finger motion in their default states, as the mesh geometry and hand structures of all models limited the finger mobility to flexion movements only. Consequently, we decided to combine the properties of multiple models into one. THUMS version 3.0 was chosen as the base model because of the detailed modelling of the finger bone structure, while the muscle elements necessary for the generation of a flexion movement as well as the overall kinematic modelling approach were adopted from THUMS version 5.03. Both models were acquired under academic license from DYNAmore Gesellschaft für FEM Ingenieurdienstleistungen mbH, Stuttgart, Germany. All model modifications described in the following were performed on the right hand of the THUMS version 3.0. As a first modification step, the interphalangeal ligaments were removed to ensure

TABLE 1 List of JFIC and TSIC threshold values.

Type of injury	Injury criterion	Threshold value	References
Minor Injury	JFIC, TSIC	4% strain	Maganaris et al. (2004), Wang (2006), Stauber et al. (2019)
Major Injury	JFIC, TSIC	8% strain	Maganaris et al. (2004), Wang (2006), Stauber et al. (2019)
Rupture	JFIC, TSIC	10% strain	Maganaris et al. (2004), Wang (2006), Stauber et al. (2019)
Avulsion	JFIC	105.91 N	Manske and Lesker (1978)

Abbreviations: JFIC, Jersey Finger Injury Criterion; TSIC, Tendon Strain Injury Criterion.

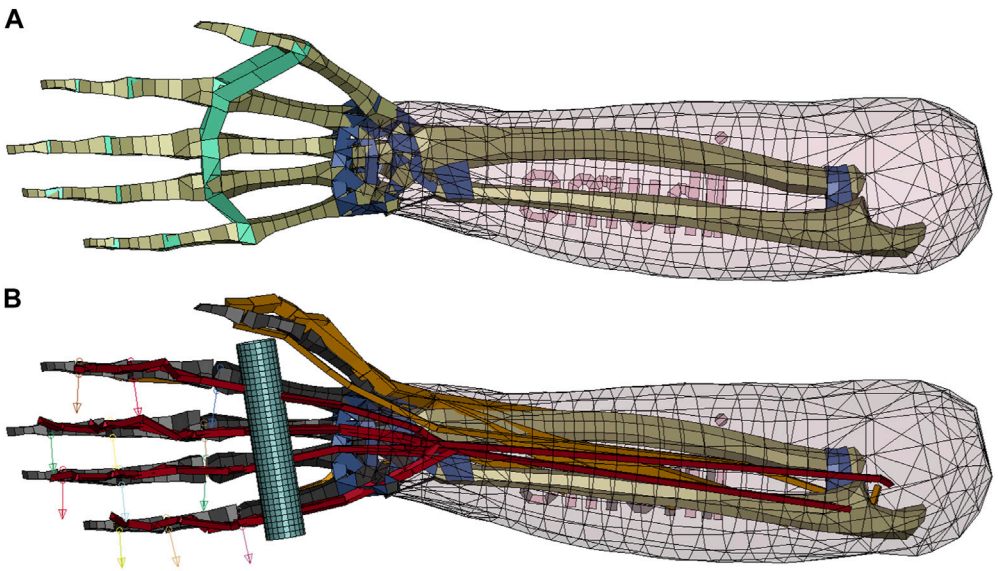

FIGURE 1
Comparison of the original and the modified THUMS version 3.0 hand models. **(A)** Original THUMS version 3.0 hand model, removed ligaments marked in green, kept ligaments marked in dark blue; **(B)** Modified THUMS version 3.0 hand model, rigid bones marked in black, manually routed muscles marked in orange, muscles with optimized routing marked in red, rod marked in light blue and revolute joint axes in the DIP, PIP and MCP joints marked with arrows.

appropriate finger movement capabilities. Second, the phalanges, metacarpals and carpals of the fingers were made rigid to allow for the insertion of kinematic revolute joints between the phalanges and metacarpals. To increase numerical stability, joint stiffness values taken from THUMS version 5.03 and joint range of motion limits described by Hirt et al. (Hirt, 2016) were implemented in a third step. Relevant flexor and extensor muscles of the hand were added based on the muscle modelling present in THUMS version 5.03 (Iwamoto and Nakahira, 2015) (Supplementary Table S2). Originally, these muscles are modelled using truss elements with the default LS-DYNA Hill-type muscle material *MAT_MUSCLE (LSTC, 2016b), while tendons are represented by seatbelt elements. To allow for a better assessment of tendon strain injury severity, *MAT_MUSCLE was replaced with a more biophysiological Hill-type muscle material developed by (Günther et al., 2007) and Haeufle et al. (Haeufle et al., 2014), which is available in LS-DYNA as a user-defined material named the extended Hill-type material (EHTM). The EHTM was initially implemented in LS-DYNA by Kleinbach et al. (Kleinbach et al., 2017) and updated to its most current version by Kleinbach et al. (Kleinbach, 2019), Martynenko et al. (Martynenko et al., 2023) and Wochner et al. (Wochner et al., 2022). Compared to *MAT_MUSCLE, the EHTM material has the additional benefit of including the tendon as a distinct element called the serial elastic element (SEE) (Haeufle et al., 2014), eliminating the need for combining muscle and seatbelt elements to form the MTU. However, one limitation of this modelling approach is that MTUs with a single muscle body and multiple connected tendons, as is the case for many muscles in the hand and lower arm, cannot be modelled as such but instead need be split up into discrete truss elements for each separate tendon path. For example, the FDP, a muscle with tendons reaching into fingers 2 to 5, was modelled as 4 parallel truss elements. A comparison of the original THUMS version 3.0 hand model and the modified version presented in this work is given in Figure 1.

2.3 Muscle routing and validation through moment arm optimization

The finger extensor muscle groups as well as the *musculus flexor pollicis longus* were manually routed using the via-point method (Delp et al., 1990; Hoy et al., 1990; Günther and Ruder,

2003) along anatomical landmarks, while special attention was given to the most injury-relevant flexors, FDP and FDS, whose routing paths across the DIP, proximal interphalangeal (PIP) and metacarpophalangeal (MCP) joint were additionally validated by adjusting them to fit moment arm curves compiled by Boots et al. (Boots et al., 2020) to ensure physiologically valid grip strength production and finger flexion mobility. Moment arms of FDP and FDS for the index finger were originally measured by Fowler et al. (Fowler et al., 2001), while data on the middle to ring finger were taken from Koh et al. (Koh et al., 2006). The nodal positions defining the muscle routing paths were optimized using the least-squares optimization functionality "lsqcurvefit" provided in the MATLAB R2022a Optimization Toolbox (Mathworks, Natick, MA, United States). The boundary conditions for the optimization were defined such that the routing nodes were placed on a plane which is normal to the revolute joint axes and intersects with the joint center. This condition was implemented to ensure that the force generated by the muscle elements could fully contribute to the resulting joint torque instead of partially dissipating by acting on a degree of freedom locked by the revolute joint. Additionally, nodes needed be placed on the medial palm side of the hand to avoid an overlap of the muscle trusses and the finger bones. The quality of the moment arm curves resulting from the optimized node placement was evaluated using the mean absolute error (Willmott and Matsuura, 2005) (Eq. (1)) normalized to the mean of the measured moment arm data (Eq. (2)).

$$MAE(\hat{y}, y) = \sum_{i=1}^{n} \frac{|\hat{y}_i - y_i|}{n} \tag{1}$$

$$NMAE(\hat{y}, y) = \frac{MAE(\hat{y}, y)}{\frac{1}{n}\sum_{i=1}^{n}|y_i|} \tag{2}$$

where MAE is the mean absolute error, $NMAE$ is the normalized mean absolute error, $\hat{y}$ is the predicted value, y is the measured value and n is the number of data points.

A total number of 20 moment arm curves, with the FDP spanning 4 digits over 3 joints and the FDS spanning 4 digits over 2 joints, were derived with the help of the routing path optimization. All optimized moment arm curves are shown in Supplementary Figures S1, S2. A detailed description of the moment arm optimization methodology is provided in Supplementary Chapter S3.

2.4 Tendon material parameter optimization

An assessment of JFI severity can only be reliably performed if the material parameters of the tendons are set within sensible bounds. On the one hand, overly compliant tendons would be a poor fit for the deformation characteristics of positional tendons and would limit finger movement capabilities, as the contractions of the muscles located in the lower arm could not be mechanically transferred to the fingers through the tendons but would instead be compensated for by an elongation of the tendon itself (Maffulli, 2005). On the other hand, overly stiff tendons would lead to an overestimation of MTU forces, which, in turn, would trigger the defined avulsion injury threshold (Table 1) erroneously. To avoid these issues, experimental data on the stress-strain characteristics of unembalmed human tendons collected by Benedict et al. (Benedict et al., 1968) were used for the manual tuning of the material parameters defining the tendon properties of the EHTM. These parameters are the force at the non-linear linear transition point $\Delta F_{SEE,0}$, the relative stretch at non-linear-linear transition in $F_{SEE}(l_{SEE})$, $\Delta U_{SEE,nll}$, and the relative stretch in the linear part for force increase of $\Delta F_{SEE,0}$, $\Delta U_{SEE,l}$. A graphical explanation of these parameters can be found in the work of Günther et al. (Günther et al., 2007). Data on the maximum isometric force F_{max} and the tendon cross-sectional area CSA, required for calculating equivalent stress-strain-curves with the EHTM, were taken from the works of Morales-Orcajo et al. (Morales-Orcajo et al., 2016) and Saraswat et al. (Saraswat et al., 2010). The curve fit quality for different parts of the stress-strain curve was assessed using two $NMAE$ values, $NMAE_3$ covering the range of tendon strains between 0% and 3% and $NMAE_5$ for strains between 0% and 5% (Figure 3). Additionally, the Young's modulus E was calculated from the linear parts of the resulting curves. All other non-generic muscle parameters of the EHTM were derived by converting the parameters of *MAT_MUSCLE with an adapted version of the method presented in the EHTM manual (Nölle et al., 2022a) and the work of Wochner et al. (Wochner et al., 2022). The aim of this method is to achieve a length equilibrium state during the initial simulation timestep in which the following condition holds true (Eq. (3)):

$$l_{MTU,i} = l_{CE,i} + l_{SEE,i} = l_{CE,opt} + l_{SEE,0} \tag{3}$$

where $l_{MTU,i}$ is the initial length of the MTU, $l_{CE,i}$ is the initial length of the EHTM contractile element CE, $l_{SEE,i}$ is the initial length of the EHTM serial elastic element SEE, $l_{CE,opt}$ is the optimal muscle fibre length and $l_{SEE,0}$ is the resting tendon length.

To account for the fact that the fingers of the THUMS version 3.0 model are straightened in its initial position and deviate from a relaxed hand position (Mount et al., 2003) in which the condition outlined in Eq. 3 could be assumed, we introduced an additional scaling factor $c_{e,f}$ to artificially shorten or elongate $l_{MTU,i}$ for the extensor and flexor muscle groups to represent their initially compressed or stretched state (Eq. (4)). The factor $c_{e,f}$ was manually set to achieve a MTU length equilibrium in which the hand of the model would close slightly on its own even when no external muscle activation was applied to reflect a neutral hand position (Mount et al., 2003).

$$c_{e,f}\, l_{MTU,i} = l_{CE,i} + l_{SEE,i}; \qquad c_{e,f} = \begin{cases} 0.95, & extensors \\ 1.05, & flexors \end{cases} \tag{4}$$

where $c_{e,f}$ is the extensor-flexor scaling factor.

Additionally, the maximum isometric force of the muscles was scaled in cases where complex geometries of singular muscles had to be recreated with multiple parallel elements (Eq. (5)).

$$F_{max,s} = \frac{F_{max,T}}{n_s} \tag{5}$$

where $F_{max,s}$ is the maximum isometric force of the muscle strand, $F_{max,T}$ is the original F_{max} value found in THUMS version 5.03 and n_s is the number of muscle strands.

A complete list of all EHTM material parameters used in the presented model can be found in Supplementary Tables S2, S3.

2.5 Simulated load case

A simplified JFI load case was defined by substituting the opponent's jersey with a cylindrical rigid rod of 100 mm length and a diameter of 20 mm placed in the palm of the THUMS version 3.0 hand (Figure 1). Each JFI simulation included two consecutive stages (Supplementary Figure S3). In the first stage, covering the time interval of 0–100 ms, FDP and FDS were activated and given time to reach their flexion state in order to grab the rigid rod. The interaction between the hand and the rod was modelled using the an automatic surface-to-surface contact with static and dynamic friction values of 0.4 and 0.3 respectively (LSTC, 2016a). Additionally, a tied surface-to-surface contact with the same friction values (LSTC, 2016a) was activated after 80 ms to ensure that the rection forces of the surface-to-surface contact would not push the fingers apart to loosen the grip before the retraction of the rod. Once the rod gripping movement was completed, the ulna and radius were fully constrained in space to eliminate noise factors such as elbow extension or shoulder rotation during the rod pulling stage and to make sure that the entire stress caused by the JFI load case is placed on the finger flexors. In the second stage from t_R = 100 ms to the simulation end time of 200 ms, the gripped rod was pulled out of the hand with a semi-instantaneous velocity of 11.615 m/s calculated using accelerations of sprinting college football players reported by (Brechue et al., 2010). The velocity and acceleration curves of the rod retraction are depicted in Supplementary Figure S4.

Eight JFI simulations at FDP and FDS muscle activation levels 0%, 20%, 40%, 60%, 70%, 80%, 90% and 100% were performed (simulations 1 to 8 in Table 3). An additional model check simulation (simulation 9 in Table 3) was done at 100%, in which the rod was not retracted, to ensure that the maximal muscle contraction alone did not cause injury by itself, for a total of 9 simulations. Muscle activation levels for all other muscles were kept at the minimum activation level defined by (Günther, 1997) to reflect their relaxed state. The effectiveness of the muscle material parameter dependent transfer between muscle activation a and the resulting MTU force F_{MTU} was determined for FDP and FDS by calculating the muscle activation effectiveness η_a (Eq. (6)).

$$\eta_a(a) = \frac{\bar{F}_{MTU,f,a}}{\bar{F}_{max,f}} \tag{6}$$

where η_a is the muscle activation effectiveness [0. . .100%] at muscle activation level a, $\bar{F}_{MTU,f,a}$ is the mean maximum muscle force of FDP and FDS for the time interval from 0 ms to 100 ms at muscle activation level a and $\bar{F}_{max,f}$ is the mean maximum isometric muscle force of FDP and FDS.

All simulations were performed with a user-compiled double precision (DP) symmetric multiprocessing (SMP) version of LS-DYNA R9.3.1 (Ansys, Canonsburg, PA, United States) including EHTM version 3.2.04 (Nölle et al., 2022a). The simulations were run on a high-performance workstation equipped with an AMD Ryzen Threadripper 3990X 64-core processor (AMD, Santa Clara, CA, United States) using 32 SMP threads. The timestep size was automatically calculated with the timestep size for mass scaled solutions set to −6.000e-07 s. Simulation runtimes ranged between 4 h 31 m 25 s for simulation 5 and 7 h 12 m 58 s ± 3 m 16 s for all other simulations.

3 Results

3.1 Moment arm curve fit quality

The optimization of the muscle routing node positions for FDP and FDS using moment arm data derived from the literature (Fowler et al., 2001; Koh et al., 2006; Boots et al., 2020) yielded good results with all moment arm curves showing $NMAE$ values below 25% and 12 of the 20 optimized moment arm curves staying below $NMAE$ = 5% (Figure 2A). An exemplary moment arm curve comparison for the FDP spanning the DIP joint is given in Figure 2B. A complete list of all moment arm curves can be found in Supplementary Figures S1, S2.

3.2 Optimized tendon material parameters

The manual tuning of EHTM tendon material properties to curves reported by Benedict et al. (Benedict et al., 1968) resulted in a greatly improved curve fit for tendon strains of up to 3%, with the tuned EHTM tendon material parameters scoring $NMAE$ values of $NMAE_3$ = 7.16% compared to those of the default EHTM tendon parameters with $NMAE_3$ = 92.21% (Table 2). As such, the experimentally determined tendon stress-strain behavior is well represented by the tuned EHTM for this strain range. For higher tendon strains, the curve fit quality of the tuned EHTM decreases to $NMAE_5$ = 18.84% while still outperforming the default EHTM at $NMAE_5$ = 84.99%. The tuned tendon parameters are reflective of a much stiffer tendon than is commonly assumed for Hill-type muscles and differ greatly from the default material parameters of the EHTM (Nölle et al., 2022a) (Table 2), with a Young's modulus of 2.4 GPa for both the tuned EHTM and the literature reference compared to E = 0.7 GPa for the default EHTM. The achieved curve fit is pictured in Figure 3.

3.3 Tendon and muscle strain injury assessment

The analysis of the MTU forces F_{MTU} and the tendon strains ε_{SEE} for simulations 1 to 9 was performed with two goals in mind. The first goal was to determine if the muscle material parameters of the modified THUMS version 3.0 hand model were set well and if the model itself yielded sensible injury assessment results by running the model check simulation 9. The results of model check simulation 9 (Table 3) show that the muscle parameters yield physiologically valid simulation results as the muscle activation of a = 100% is translated to an η_a of 95.6% ± 1.3%, indicating that maximal muscle activation results in near maximal muscle force output. Additionally, the maximum muscle contraction on its own does not result in injury of any kind when assessed with both the MSIC and JFIC, confirming that the lower injury thresholds are set correctly in the sense that they do not register injuries during physiologically plausible muscle-driven gripping scenarios without external loads. Similarly, the results of simulations 1 to 5 (Table 3), covering the muscle activations of 0%–70% and η_a values of 0.7% ± 0.6% to 68.0% ± 1.2%, show that the JFI loading scenario does not result in FDP or FDS injury, if insufficient muscle activation and thus

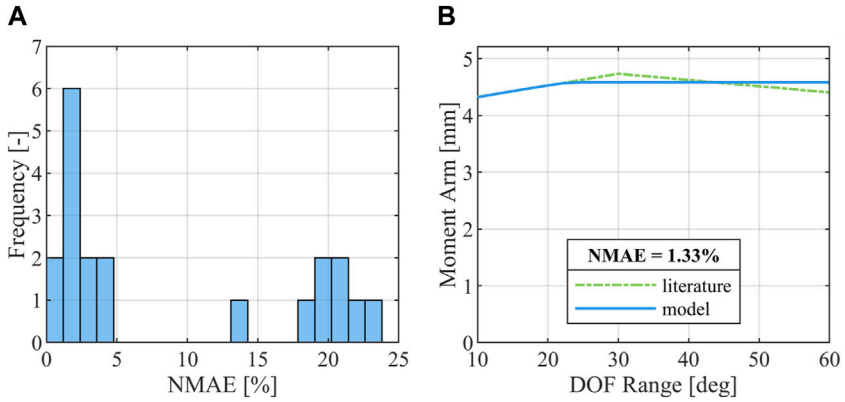

FIGURE 2
Results of the moment arm optimization. **(A)** Distribution of ***NMAE*** across all 20 optimized moment arm curves; **(B)** Comparison of moment arm curve reported in the literature (Fowler et al., 2001; Koh et al., 2006; Boots et al., 2020) and the model moment arm curve derived from optimization for FDP over the DIP joint in the index finger.

TABLE 2 EHTM tendon material parameters and curve fit quality metrics.

Variable	Unit	EHTM tuned	EHTM default
$\Delta F_{SEE,0}$	[N]	0.8 F_{max}	0.4 F_{max}
$\Delta U_{SEE,nll}$	[-]	0.02	0.0425
$\Delta U_{SEE,l}$	[-]	0.01	0.0170
$NMAE_3$	[%]	7.16	92.21
$NMAE_5$	[%]	18.84	84.99
E	[GPa]	2.4	0.7

Abbreviations: EHTM, extended Hill-type material.

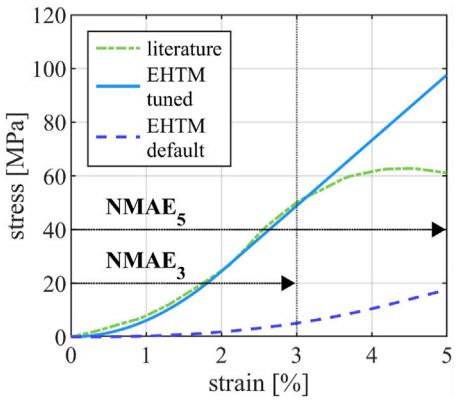

FIGURE 3
Comparison of the tendon stress-strain-curve reported in the literature (Benedict et al., 1968), the stress-strain curve of the EHTM tendon achieved through manual parameter fit and the stress-strain curve of the EHTM tendon using the default material parameters (Nölle et al., 2022a). Curve sections used for the calculation of $NMAE_3$ and $NMAE_5$ are indicated with arrows.

reduced gripping force is applied. The first injury is detected in simulation 6 (a = 80%, η_a = 78.0 ± 1.5%) where the JFIC tendon avulsion injury threshold is crossed by the FDS of the middle finger after the rod retraction at t_R (Table 3; Supplementary Figures S5, S6). The number of detected injuries further increases in Simulations 7 (a = 90%, η_a = 87.4 ± 1.5%) and 8 (a = 100%, η_a = 95.6 ± 1.3%) where additional avulsion injuries of the middle finger FDP (Table 3; Figure 4) and little finger FDP (Table 3; Supplementary Figures S5, S6) are detected. Overall, a clear relationship between muscle activity, resulting finger flexor muscle force and JFI occurrence can be established, with activation levels above 80% resulting in FDP and FDS avulsion injuries.

4 Discussion

The simulation-based reconstruction of sports injuries such as a JFI and the definition of criteria to assess such injuries is a challenging task, as numerous methodological approaches (Krosshaug et al., 2005) such as motion analysis, cadaver studies or athlete interviews yield insufficiently detailed information necessary for the one-to-one reconstruction of an injury. Additionally, only few instances of sports injuries during biomechanical experiments are described in the literature (Zernicke et al., 1977; Barone et al., 1999; Heiderscheit et al., 2005; Schache et al., 2009) with, to the authors' knowledge, no documented case of an *in-vivo* JFI occurring in an experimental setup. Likewise, tendon strains and avulsion are not currently tracked in publicly available injury databases (Compton, 2002), further limiting the pool of load cases useable to define an injury criterion by conventional statistical means. The JFIC is thus based on the biomechanical properties of the human tendon instead of the statistical derivation of a risk index from documented injury cases. The tendon-strain-based injury thresholds of the TSIC were defined with the aim to represent the properties of positional tendons (Kaya et al., 2019), which are comparatively stiff and serve to transfer forces from the muscle to the bone with minimal force dissipation. As functional requirements influence the material properties of the tendon (Quigley et al., 2018), TSIC threshold values may need to be adjusted if applied to tendons which are known to be subjected to

TABLE 3 List of simulations and injury assessment results.

Simulation No.	a [%]	η_a[a] [%]	Rod retraction	No. of injuries	Type of injury	Injured MTU
1	0	0.7 ± 0.6	Yes	0	-	-
2	20	17.8 ± 1.8	Yes	0	-	-
3	40	39.4 ± 2.6	Yes	0	-	-
4	60	58.4 ± 1.8	Yes	0	-	-
5	70	68.0 ± 1.2	Yes	0	-	-
6	80	78.0 ± 1.5	Yes	1	Tendon Avulsion	FDS 3
7	90	87.4 ± 1.5	Yes	3	Tendon Avulsion	FDP 3, FDS 3, FDP 5
8	100	95.6 ± 1.3	Yes	3	Tendon Avulsion	FDP 3, FDS 3, FDP 5
9	100	95.6 ± 1.3	No	0	-	-

[a]Data are represented as mean ± SD.
Abbreviations: FDP, musculus flexor digitorum profundus; FDS, musculus flexor digitorum superficialis; MTU, muscle-tendon-unit. Notes: Fingers are denoted according to the following numbering scheme: 1 = Thumb; 2 = Index Finger; 3 = Middle Finger; 4 = Ring Finger; 5 = Little Finger.

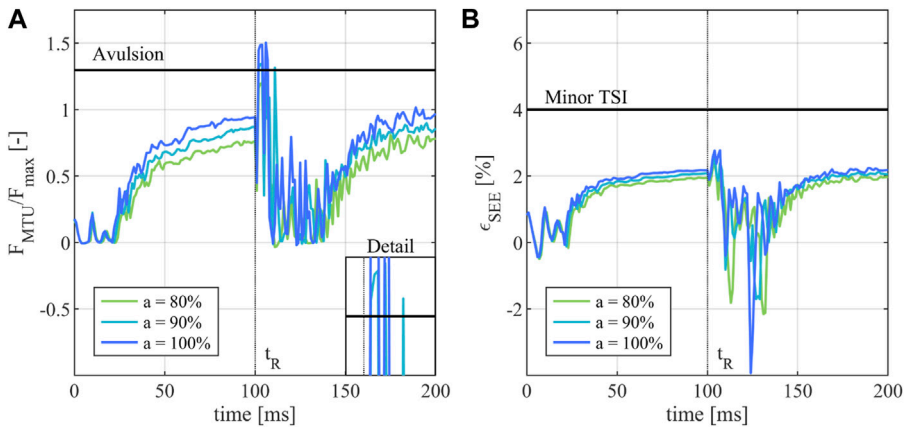

FIGURE 4
Injury assessment of the of the FDP in the middle finger during a JFI loading scenario. **(A)** Activity dependent normalized muscle force F_{MTU}/F_{max} compared to the JFIC avulsion injury threshold; **(B)** Resulting tendon strain ε_{SEE} compared to the minor TSI threshold. The start of the rod retraction is denoted as t_R.

larger strain ranges such as the Achilles tendon. Similarly, the force-based JFIC avulsion threshold is only valid when applied to human finger flexor MTUs as the underlying experiments by Manske and Lesker (Manske and Lesker, 1978) were limited to the FDP tendon insertion only. Given that the JFIC was defined for the use with Hill-type muscle models such as the EHTM, tendon properties such as fatigue (Ker et al., 2000) or tendon creep (Maganaris, 2002; Maganaris et al., 2004) were not included in the definition of the injury criterion, as the used muscle model is not able to reflect these effects properly. Numerical instabilities common to Hill-type muscles as described by Yeo et al. (Yeo et al., 2023) were mitigated in this study by not routing muscles in series and by keeping muscle co-contraction levels to a minimum as the finger extensor muscles were only activated with a minimum physiological activity level (Günther, 1997). The modified THUMS version 3.0 hand model itself is well suited for the assessment of MTU forces and strains as is necessary for the proposed JFI assessment. Other anatomical structures such as the finger pulley system, the joint capsules or the soft tissues surrounding the phalanges are however not represented in the current model and offer room for further improvement of the model quality in future studies. Additionally, the previous validation efforts of both THUMS version 3.0 (Iwamoto et al., 2007) and 5.03 (Iwamoto and Nakahira, 2015) did not include specific validation cases for the lower arm or hand regions. The validity of the FE-NHBMs used in this study is thus transitively assumed, as the models performed well in the described whole-body validation cases, whose outcomes partly depend on the correct behavior of the upper extremities. The quality of the moment arm curve fit was determined using the $NMAE$ as this metric provides an unweighted percentage result, meaning that the joint torque given as F_{MTU} times moment arm length will deviate from the mean literature moment arm by the same $NMAE$ percentage as the model moment arm itself. The achieved moment arm curve fit quality (Figure 2A) thus indicates that the majority of

joint torques will be simulated with less than 5% error. The 8 worst moment arm curve fits ($NMAE$ between 13.87% and 23.72%) all occurred at the PIP joint, possibly indicating poor phalange geometry or inappropriately placed revolute joint axes in the PIP region. However, even the maximum $NMAE$ of 23.72% (Supplementary Figure S1) is comparable to the standard deviations present in the reference literature data with Koh et al. (Koh et al., 2006) reporting FDP moment arm lengths over the MCP joint of 9.7 ± 2.0 mm equivalent to a deviation of 20.62%. While a good moment arm curve fit quality could thus be achieved, results might further be improved by implementing more advance routing methods such as the ellipse-based muscle routing proposed by Hammer et al. (Hammer et al., 2019) or by refining the positions of the finger joint axes. To the authors' knowledge, no published data on the stress-strain behavior of unenbalmed human finger and lower arm tendons exist in the literature. Because of the similar anatomical structure, experimental data derived from the human lower extremities (Benedict et al., 1968) were used as a reference instead. The tuning of the tendon material parameters resulted in an EHTM tendon stress-strain behavior which is in good agreement with the literature data (Benedict et al., 1968) for tendon strains up to 3% ($NMAE_3$ = 7.16%) but decreased in fit quality for larger strains ($NMAE_5$ = 18.84%). This is due to the fact that the EHTM SEE only partially accounts for the deformation characteristics of a biological tendon as only the non-linear toe-region and an indefinitely continued linear elastic curve region are modelled (Günther et al., 2007). This means that tendon stress is overestimated for high tendon strains, which was deemed acceptable for the assessment of the presented JFI load case as the observed tendon strains never exceeded the minor TSIC threshold of 4% strain. Other muscle material models might however be needed to reliably determine tendon injury for load cases in which plastic tendon deformation is expected. Paradoxically, this overestimation of tendon forces in the EHTM could mitigate a common limitation of Hill-type muscles which are otherwise known to produce unphysiologically low forces in the eccentric muscle contraction range (Yeo et al., 2023). The Young's modulus achieved through parameter optimization matched the literature reference (Benedict et al., 1968) exactly (E = 2.4 GPa). This value is among the upper bound of vertebrate tendon stiffnesses described in the literature, where Young's moduli ranging from 0.3 GPa (Maganaris et al., 2008) to 2.54 GPa (Ker et al., 1986) are reported. The modelled finger tendons can thus be described as very stiff, which is appropriate considering their mechanical function. The default EHTM tendon (E = 0.7 GPa), while well suited to describe the passive mechanical properties of tendons found, for example, in the patella region (Wang, 2006), would thus not have been able to properly represent the finger tendons observed in this study. The simulated JFI load case is a simplified reconstruction of real-life injury scenarios, in which the jersey of an American football player has been replaced with a simple rod. This generalization is likely to reduce the detected injury severity, as the rod will always be cleanly released from the hand whereas the fabric of a jersey might catch on the fingers and subject the MTUs to even larger stresses. Future studies might focus on a more precise representation of JFI load cases. The results of the JFI assessment are congruent with JFIs as they are described in the literature (Tempelaere et al., 2017), given that the observed MTU forces under specific loads and muscle activations are high enough to register as tendon avulsions but do not trigger any of the other JFIC or MSIC thresholds. This means that the tendon and muscle body sustain no injury themselves but rather that the tendon insertion point is the weak link of the MTU chain. The detected dependency of injury occurrence and muscle activation can be explained by the synchronous rise in FDP and FDS muscle forces (Table 3) which place a larger stress on the tendon insertion before the eccentric rod retraction further increases the injury load. Translating this abstract description to a real-life injury scenario leads to the intuitive conclusion, that a stronger grip equates to an increased JFI severity. Contrary to JFI cases described in medical literature, JFI was only detected in the middle and little finger instead of the most injury-prone ring finger (Leddy and Packer, 1977; Manske and Lesker, 1978; Lunn and Lamb, 1984; Leddy, 1985; Bynum and Gilbert, 1988). This might be caused by several factors. First, the parallel muscle routing approach needed for the use of the EHTM, in which otherwise connected tendons operate as individual mechanical structures, might influence the loads acting on the now separated MTUs. Second, the simplifications of the load case and the model structure outlined above, while needed, will certainly impact the outcome of the simulations evaluated in the presented study. Finally, the muscle parameters which were adapted from the THUMS version 5.03 model might not be entirely representative of the average JFI patient. Muscle material parameters may vary greatly from person to person (Scovil and Ronsky, 2006) and the hand created by combining the hand geometry of THUMS version 3.0 and the musculature of THUMS version 5.03 might simply be representative of a person who belongs to the smaller group of people who suffer from JFI in less commonly injured digits (Murphy and Mass, 2005). In general, the topic of muscle material parameter choice should be considered if the MTU forces and strains are to be evaluated for injury assessment purposes, as they influence the detected injury severity most severely. Finetuning material parameters which are otherwise considered to be generic across all muscles, as is the case for the default EHTM tendon material parameters (Nölle et al., 2022a), may thus be needed to ensure a reliable injury detection.

4.1 Conclusion

The presented work outlines the steps necessary to successfully adapt the hand model of a FE-NHBMs for the assessment of JFIs using a newly defined injury criterion called the JFIC based on biomechanical data found in the literature, which, together with the previously established MSIC (Nölle et al., 2022b), forms a next step in creating a wholistic injury criterion for strain injuries of the MTU. The injury assessment results achieved with the JFIC are in good agreement with JFI symptoms as described in the medical field, showing a clear dependency between finger flexor activation, gripping force and JFI severity. At the same time, the need to rethink commonly asserted paradigms concerning the choice of muscle material parameters, in which only few parameters are assumed to be muscle specific, is highlighted, as material properties across all muscle structures need to be closely matched to the physiological demands of the muscle to ensure a reliable MTU injury assessment. Additionally, modelling choices and load case

conditions should be representative of the real-life injury scenario, as to not subject the MTU to unrealistic loads. This work emphasizes the benefit of using neuromuscular human body models together with literature data and experiments to improve our understanding of how mechanical loads may cause tissue damage and thus, how to predict potential sources of injury. The authors hope to inspire further scientific cooperation between all fields of injury biomechanics with this interdisciplinary work of applying models commonly used in the automotive sector in a sports science context.

Data availability statement

The original contributions presented in the study are included in the article/Supplementary Material, further inquiries can be directed to the corresponding author.

Author contributions

LN: Conceptualization, Methodology, Software, Visualization, Writing–original draft. EA: Data curation, Software, Writing–review and editing. OM: Conceptualization, Funding acquisition, Supervision, Writing–review and editing. SS: Conceptualization, Funding acquisition, Supervision, Writing–review and editing.

Funding

The author(s) declare financial support was received for the research, authorship, and/or publication of this article. This work was supported by the Deutsche Forschungsgemeinschaft (DFG, German Research Foundation) under Germany's Excellence Strategy—EXC 2075—390740016 (SimTech) and by the Federal Ministry for Economic Affairs and Climate Action of Germany (Bundesministerium für Wirtschaft und Klimaschutz) through the project "Artificial Intelligence for Real-Time Injury Prediction (ATTENTION)," grant number 19A21027D.

Conflict of interest

The authors declare that the research was conducted in the absence of any commercial or financial relationships that could be construed as a potential conflict of interest.

Publisher's note

All claims expressed in this article are solely those of the authors and do not necessarily represent those of their affiliated organizations, or those of the publisher, the editors and the reviewers. Any product that may be evaluated in this article, or claim that may be made by its manufacturer, is not guaranteed or endorsed by the publisher.

Supplementary material

The Supplementary Material for this article can be found online at: https://www.frontiersin.org/articles/10.3389/fbioe.2023.1293705/full#supplementary-material

References

Amadio, P. C. (1990). Epidemiology of hand and wrist injuries in sports. *Hand Clin.* 6, 379–381. doi:10.1016/S0749-0712(21)00880-5

Avery, D. M., Rodner, C. M., and Edgar, C. M. (2016). Sports-related wrist and hand injuries: a review. *J. Orthop. Surg. Res.* 11, 99. doi:10.1186/s13018-016-0432-8

Barone, M., Senner, V., and Schaff, P. (1999). "ACL Injury Mechanism in Alpine Skiing: Analysis of an Accidental ACL Rupture" in Skiing trauma and safety: 12th volume: contains papers presented at the 12th International Symposium on Skiing Trauma and Safety held in Whistler Blackcomb on May 4–10, 1997. Eds R. J. Johnson and R. J. Johnson (British Columbia, Canada: West Conshohocken: ASTM) 63-63-19.

Benedict, J. V., Walker, L. B., and Harris, E. H. (1968). Stress-strain characteristics and tensile strength of unembalmed human tendon. *J. Biomech.* 1, 53–63. doi:10.1016/0021-9290(68)90038-9

Bolte, J. H., Hines, M. H., Herriott, R. G., McFadden, J. D., and Donnelly, B. R. (2003). Shoulder impact response and injury due to lateral and oblique loading. *Stapp Car Crash J.* 47, 35–53. doi:10.4271/2003-22-0003

Boots, M. T., Hardesty, R., Sobinov, A., Gritsenko, V., Collinger, J. L., Fisher, L. E., et al. (2020). Functional and structural moment arm validation for musculoskeletal models: a study of the human forearm and hand. arXiv.

Brechue, W. F., Mayhew, J. L., and Piper, F. C. (2010). Characteristics of sprint performance in college football players. *J. Strength Cond. Res.* 24, 1169–1178. doi:10.1519/JSC.0b013e3181d68107

Bynum, D. K., and Gilbert, J. A. (1988). Avulsion of the flexor digitorum profundus: anatomic and biomechanical considerations. *J. Hand Surg. Am.* 13, 222–227. doi:10.1016/S0363-5023(88)80053-4

Cavanaugh, J. M., Nyquist, G. W., Goldberg, S. J., and King, A. I. (1986). "Lower abdominal tolerance and response," in *SAE technical paper series SAE International400 commonwealth drive* (Warrendale, PA, United States: SAE International).

Cesari, D., and Bouquet, R. (1990). "Behaviour of human surrogates thorax under belt loading," in *SAE technical paper series SAE International400 commonwealth drive* (Warrendale, PA, United States: SAE International).

Compton, C. P. (2002). "The use of public crash data in biomechanical research," in *Accidental injury: biomechanics and prevention*. Editors A. M. Nahum and J. W. Melvin (New York, NY: Springer New York), 40–71.

Delp, S. L., Loan, J. P., Hoy, M. G., Zajac, F. E., Topp, E. L., and Rosen, J. M. (1990). An interactive graphics-based model of the lower extremity to study orthopaedic surgical procedures. *IEEE Trans. Biomed. Eng.* 37, 757–767. doi:10.1109/10.102791

Devane, K., Johnson, D., and Gayzik, F. S. (2019). Validation of a simplified human body model in relaxed and braced conditions in low-speed frontal sled tests. *Traffic Inj. Prev.* 20, 832–837. doi:10.1080/15389588.2019.1655733

Fok, K. S., and Chou, S. M. (2010). Development of a finger biomechanical model and its considerations. *J. Biomech.* 43, 701–713. doi:10.1016/j.jbiomech.2009.10.020

Foster, C. D., Hardy, W. N., Yang, K. H., King, A. I., and Hashimoto, S. (2006). High-speed seatbelt pretensioner loading of the abdomen. *Stapp Car Crash J.* 50, 27–51. doi:10.4271/2006-22-0002

Fowler, N., Nicol, A., Condon, B., and Hadley, D. (2001). Method of determination of three dimensional index finger moment arms and tendon lines of action using high resolution MRI scans. *J. Biomech.* 34, 791–797. doi:10.1016/S0021-9290(01)00021-5

Gaston, R. G., and Loeffler, B. J. (2015). Sports-specific injuries of the hand and wrist. *Clin. Sports Med.* 34, 1–10. doi:10.1016/j.csm.2014.09.003

GHBMC (2016). *User manual: M50 detailed occupant version 4.5 for LS-DYNA*. Winston-Salem NC: Elemance, LLC.

Günther, M. (1997). *Computersimulationen zur Synthetisierung des muskulär erzeugten menschlichen Gehens unter Verwendung eines biomechanischen Mehrkörpermodells*. Tübingen, Germany: Eberhard-Karls-Universität zu Tübingen.

Günther, M., and Ruder, H. (2003). Synthesis of two-dimensional human walking: a test of the lambda-model. *Biol. Cybern.* 89, 89–106. doi:10.1007/s00422-003-0414-x

Günther, M., Schmitt, S., and Wank, V. (2007). High-frequency oscillations as a consequence of neglected serial damping in Hill-type muscle models. *Biol. Cybern.* 97, 63–79. doi:10.1007/s00422-007-0160-6

Haeufle, D. F. B., Günther, M., Bayer, A., and Schmitt, S. (2014). Hill-type muscle model with serial damping and eccentric force-velocity relation. *J. Biomech.* 47, 1531–1536. doi:10.1016/j.jbiomech.2014.02.009

Hammer, M., Günther, M., Haeufle, D. F. B., and Schmitt, S. (2019). Tailoring anatomical muscle paths: a sheath-like solution for muscle routing in musculoskeletal computer models. *Math. Biosci.* 311, 68–81. doi:10.1016/j.mbs.2019.02.004

Heiderscheit, B. C., Hoerth, D. M., Chumanov, E. S., Swanson, S. C., Thelen, B. J., and Thelen, D. G. (2005). Identifying the time of occurrence of a hamstring strain injury during treadmill running: a case study. *Clin. Biomech.* 20, 1072–1078. doi:10.1016/j.clinbiomech.2005.07.005

Hirt, B. (2016). *Hand and wrist anatomy and biomechanics: a comprehensive guide*. NEW YORK: Thieme.

Holden, C., and Northmore-Ball, M. (1975). The strength of the profundus tendon insertion. *Hand* 7, 238–240. doi:10.1016/0072-968x(75)90059-5

Hoy, M. G., Zajac, F. E., and Gordon, M. E. (1990). A musculoskeletal model of the human lower extremity: the effect of muscle, tendon, and moment arm on the moment-angle relationship of musculotendon actuators at the hip, knee, and ankle. *J. Biomech.* 23, 157–169. doi:10.1016/0021-9290(90)90349-8

Iwamoto, M., and Nakahira, Y. (2015). "Development and validation of the total HUman model for safety (THUMS) version 5 containing multiple 1D muscles for estimating occupant motions with muscle activation during side impacts," in *SAE technical paper series (SAE International400 commonwealth drive* (Warrendale, PA, United States: SAE International).

Iwamoto, M., Nakahira, Y., Tamura, A., Kimpara, H., Watanabe, I., and Miki, K. (2007). "Development of advanced human models in THUMS" in *Proc. 6th European LS-DYNA users' conference* (Toyota Central R&D Labs, Inc), 47–56.

Joaquin, L., Perez-Gonzalez, A., and Vergara, M. (2011). "Towards a realistic and selfcontained biomechanical model of the hand", *in Theoretical biomechanics*. Editor V. Klika (London, United Kingdom: intechOpen).

Kato, D., Nakahira, Y., Atsumi, N., and Iwamoto, M. (2018). "Development of human-body model THUMS Version 6 containing muscle controllers and application to injury analysis in frontal collision after brake deceleration" in *Proceedings of the IRCOBI conference* (Athens, Greece: IRCOBI), 12–14.

Kato, D., Nakahira, Y., and Iwamoto, M. (2017). "A study of muscle control with two feedback controls for posture and reaction force for more accurate prediction of occupant kinematics in low-speed frontal impacts" in *Proceedings of the 25th International technical conference on the enhanced safety of vehicles (ESV)* (Detroit, USA: Toyota Central R&D Labs. Inc).

Kaya, M., Karahan, N., and Yılmaz, B. (2019). "Tendon structure and classification", *in Tendons* (London, United Kingdom: IntechOpen).

Ker, R. F., Dimery, N. J., and Alexander, R. M. (1986). The role of tendon elasticity in hopping in a wallaby (*Macropus rufogriseus*). *J. Zool.* 208, 417–428. doi:10.1111/j.1469-7998.1986.tb01904.x

Ker, R. F., Wang, X. T., and Pike, A. V. (2000). Fatigue quality of mammalian tendons. *J. Exp. Biol.* 203, 1317–1327. doi:10.1242/jeb.203.8.1317

Kleinbach, C., Martynenko, O., Promies, J., Haeufle, D. F. B., Fehr, J., and Schmitt, S. (2017). Implementation and validation of the extended Hill-type muscle model with robust routing capabilities in LS-DYNA for active human body models. *Biomed. Eng. Online* 16, 109. doi:10.1186/s12938-017-0399-7

Kleinbach, C. G. (2019). Simulation of occupant kinematics using active human body models. Dissertation. Düren: Universität Stuttgart.

Koh, S., Buford, W. L., Andersen, C. R., and Viegas, S. F. (2006). Intrinsic muscle contribution to the metacarpophalangeal joint flexion moment of the middle, ring, and small fingers. *J. Hand Surg. Am.* 31, 1111–1117. doi:10.1016/j.jhsa.2006.03.003

Kroell, C. K., Schneider, D. C., and Nahum, A. M. (2009). "Impact tolerance and response of the human thorax II," in *Electronic control module network and data link development and validation using hardware in the loop systems*. Editors D. Williams, J. Allen, and R. Hukkeri (Warrendale, PA: SAE International).

Krosshaug, T., Andersen, T. E., Olsen, O.-E. O., Myklebust, G., and Bahr, R. (2005). Research approaches to describe the mechanisms of injuries in sport: limitations and possibilities. *Br. J. Sports Med.* 39, 330–339. doi:10.1136/bjsm.2005.018358

Leddy, J. P. (1985). Avulsions of the flexor digitorum profundus. *Hand Clin.* 1, 77–83. doi:10.1016/S0749-0712(21)01334-2

Leddy, J. P., and Packer, J. W. (1977). Avulsion of the profundus tendon insertion in athletes. *J. Hand Surg. Am.* 2, 66–69. doi:10.1016/S0363-5023(77)80012-9

LSTC (2016a). *LS-DYNA® keyword USER'S manual volume I: LS-DYNA R9.0 08/29/16 (r:7883)*. Livermore, California Livermore Software Technology Corporation.

LSTC (2016b). *LS-DYNA®KEYWORD USER'S MANUAL VOLUME II material models: LS-DYNA r9.008/31/16 (r:7893)*. Livermore, California Livermore Software Technology Corporation.

Lunn, P. G., and Lamb, D. W. (1984). Rugby finger"--avulsion of profundus of ring finger. *J. Hand Surg. Br.* 9, 69–71. doi:10.1016/0266-7681(84)90020-2

Maffulli, N. (2005). *Tendon injuries: basic science and clinical medicine*. London: Springer.

Maganaris, C. N. (2002). Tensile properties of *in vivo* human tendinous tissue. *J. Biomech.* 35, 1019–1027. doi:10.1016/S0021-9290(02)00047-7

Maganaris, C. N., Narici, M. V., Almekinders, L. C., and Maffulli, N. (2004). Biomechanics and pathophysiology of overuse tendon injuries: ideas on insertional tendinopathy. *Sports Med.* 34, 1005–1017. doi:10.2165/00007256-200434140-00005

Maganaris, C. N., Narici, M. V., and Maffulli, N. (2008). Biomechanics of the Achilles tendon. *Disabil. Rehabil.* 30, 1542–1547. doi:10.1080/09638280701785494

Manske, P. R., and Lesker, P. A. (1978). Avulsion of the ring finger flexor digitorum profundus tendon: an experimental study. *Hand* 10, 52–55. doi:10.1016/S0072-968X(78)80025-4

Martynenko, O. V., Kempter, F., Kleinbach, C., Nölle, L. V., Lerge, P., Schmitt, S., et al. (2023). Development and verification of a physiologically motivated internal controller for the open-source extended Hill-type muscle model in LS-DYNA. *Biomech. Model Mechanobiol.* 22, 2003–2032. doi:10.1007/s10237-023-01748-9

Morales-Orcajo, E., Becerro de Bengoa Vallejo, R., Losa Iglesias, M., and Bayod, J. (2016). Structural and material properties of human foot tendons. *Clin. Biomech. (Bristol, Avon)* 37, 1–6. doi:10.1016/j.clinbiomech.2016.05.014

Mount, F. E., Whitmore, M., and Stealey, S. L. (2003). *Evaluation of neutral body posture on shuttle mission sts-57 (spacehab-1)*. Washington, DC NASA Headquarters.

Murphy, B. A., and Mass, D. P. (2005). Zone I flexor tendon injuries. *Hand Clin.* 21, 167–171. doi:10.1016/j.hcl.2004.12.004

Nölle, L. V., Lerge, P., Martynenko, O., Wochner, I., Kempter, F., Kleinbach, C., et al. (2022a). *EHTM code and manual*. Stuttgart, Germany University of Stuttgart. doi:10.18419/DARUS-1144

Nölle, L. V., Mishra, A., Martynenko, O. V., and Schmitt, S. (2022b). Evaluation of muscle strain injury severity in active human body models. *J. Mech. Behav. Biomed. Mater* 135, 105463. doi:10.1016/j.jmbbm.2022.105463

Noonan, T. J., and Garrett, W. E. (1999). Muscle strain injury: diagnosis and treatment. *J. Am. Acad. Orthop. Surg.* 7, 262–269. doi:10.5435/00124635-199907000-00006

Quigley, A. S., Bancelin, S., Deska-Gauthier, D., Légaré, F., Kreplak, L., and Veres, S. P. (2018). In tendons, differing physiological requirements lead to functionally distinct nanostructures. *Sci. Rep.* 8, 4409. doi:10.1038/s41598-018-22741-8

Rettig, A. C. (2003). Athletic injuries of the wrist and hand. Part I: traumatic injuries of the wrist. *Am. J. Sports Med.* 31, 1038–1048. doi:10.1177/03635465030310060801

Roloff, I., Schöffl, V. R., Vigouroux, L., and Quaine, F. (2006). Biomechanical model for the determination of the forces acting on the finger pulley system. *J. Biomech.* 39, 915–923. doi:10.1016/j.jbiomech.2005.01.028

Rupp, J. D., Miller, C. S., Reed, M. P., Madura, N. H., Klinich, K. D., and Schneider, L. W. (2008). Characterization of knee-thigh-hip response in frontal impacts using biomechanical testing and computational simulations. *Stapp Car Crash J.* 52, 421–474. doi:10.4271/2008-22-0017

Saraswat, P., Andersen, M. S., and Macwilliams, B. A. (2010). A musculoskeletal foot model for clinical gait analysis. *J. Biomech.* 43, 1645–1652. doi:10.1016/j.jbiomech.2010.03.005

Schache, A. G., Wrigley, T. V., Baker, R., and Pandy, M. G. (2009). Biomechanical response to hamstring muscle strain injury. *Gait Posture* 29, 332–338. doi:10.1016/j.gaitpost.2008.10.054

Scovil, C. Y., and Ronsky, J. L. (2006). Sensitivity of a Hill-based muscle model to perturbations in model parameters. *J. Biomech.* 39, 2055–2063. doi:10.1016/j.jbiomech.2005.06.005

Shaw, J. M., Herriott, R. G., McFadden, J. D., Donnelly, B. R., and Bolte, J. H. (2009). "Oblique and lateral impact response of the PMHS thorax," in *Electronic control module network and data link development and validation using hardware in the loop systems*. Editors D. Williams, J. Allen, and R. Hukkeri (Warrendale, PA: SAE International).

Shigeta, K., Kitagawa, Y., and Yasuki, T. (2009). "Development of next generation human FE model capable of organ injury prediction," in *Proceedings of the 21st annual enhanced safety of vehicles*. Washington, DC (National Highway Traffic Safety Administration), 15–18.

Stauber, T., Blache, U., and Snedeker, J. G. (2019). Tendon tissue microdamage and the limits of intrinsic repair. *Matrix Biol.* 85-86, 68–79. doi:10.1016/j.matbio.2019.07.008

Tempelaere, C., Brun, M., Doursounian, L., and Feron, J.-M. (2017). Traumatic avulsion of the flexor digitorum profundus tendon. Jersey finger, a 29 cases report. *Hand Surg. Rehabil.* 36, 368–372. doi:10.1016/j.hansur.2017.06.002

Toyota Motor Corporation, and Toyota Central R&D Labs. Inc (2021). Documentation total human model for safety (THUMS) AM50 occupant model. Version 6.1.

Viano, D. C. (2009). "Biomechanical responses and injuries in blunt lateral impact," in *Electronic control module network and data link development and validation using*

hardware in the loop systems. Editors D. Williams, J. Allen, and R. Hukkeri (Warrendale, PA: SAE International).

Vigouroux, L., Domalain, M., and Berton, E. (2009). Comparison of tendon tensions estimated from two biomechanical models of the thumb. *J. Biomech.* 42, 1772–1777. doi:10.1016/j.jbiomech.2009.03.052

Vigouroux, L., Quaine, F., Paclet, F., Colloud, F., and Moutet, F. (2008). Middle and ring fingers are more exposed to pulley rupture than index and little during sport-climbing: a biomechanical explanation. *Clin. Biomech. (Bristol, Avon)* 23, 562–570. doi:10.1016/j.clinbiomech.2007.12.009

Wang, J. H. C. (2006). Mechanobiology of tendon. *J. Biomech.* 39, 1563–1582. doi:10.1016/j.jbiomech.2005.05.011

Willmott, C. J., and Matsuura, K. (2005). Advantages of the mean absolute error (MAE) over the root mean square error (RMSE) in assessing average model performance. *Clim. Res.* 30, 79–82. doi:10.3354/cr030079

Wochner, I., Nölle, L. V., Martynenko, O. V., and Schmitt, S. (2022). Falling heads': investigating reflexive responses to head-neck perturbations. *Biomed. Eng. Online* 21, 25. doi:10.1186/s12938-022-00994-9

Wu, J. Z., An, K.-N., Cutlip, R. G., and Dong, R. G. (2010). A practical biomechanical model of the index finger simulating the kinematics of the muscle/tendon excursions. *Biomed. Mater Eng.* 20, 89–97. doi:10.3233/BME-2010-0618

Wu, J. Z., An, K.-N., Cutlip, R. G., Krajnak, K., Welcome, D., and Dong, R. G. (2008). Analysis of musculoskeletal loading in an index finger during tapping. *J. Biomech.* 41, 668–676. doi:10.1016/j.jbiomech.2007.09.025

Yeo, S.-H., Verheul, J., Herzog, W., and Sueda, S. (2023). Numerical instability of Hill-type muscle models. *J. R. Soc. Interface* 20, 20220430. doi:10.1098/rsif.2022.0430

Zernicke, R. F., Garhammer, J., and Jobe, F. W. (1977). Human patellar-tendon rupture. *JBJS* 59, 179–183. doi:10.2106/00004623-197759020-00007

frontiers | Frontiers in Bioengineering and Biotechnology

TYPE Original Research
PUBLISHED 19 December 2023
DOI 10.3389/fbioe.2023.1271760

OPEN ACCESS

EDITED BY
Julie Choisne,
University of Auckland, New Zealand

REVIEWED BY
Joyce John,
University of Auckland, New Zealand
Dominik Obrist,
University of Bern, Switzerland

*CORRESPONDENCE
Daniel E. Hurtado,
daniel.hurtado@uc.cl

RECEIVED 02 August 2023
ACCEPTED 07 December 2023
PUBLISHED 19 December 2023

CITATION
Ortiz-Puerta D, Diaz O, Retamal J and Hurtado DE (2023), Morphometric analysis of airways in pre-COPD and mild COPD lungs using continuous surface representations of the bronchial lumen. *Front. Bioeng. Biotechnol.* 11:1271760. doi: 10.3389/fbioe.2023.1271760

Morphometric analysis of airways in pre-COPD and mild COPD lungs using continuous surface representations of the bronchial lumen

David Ortiz-Puerta[1,2], Orlando Diaz[3], Jaime Retamal[3] and Daniel E. Hurtado[1,2]*

[1]Department of Structural and Geotechnical Engineering, School of Engineering, Pontificia Universidad Católica de Chile, Santiago, Chile, [2]Institute for Biological and Medical Engineering, Schools of Engineering, Medicine and Biological Sciences, Pontificia Universidad Católica de Chile, Santiago, Chile, [3]Department of Intensive Care Medicine, Pontificia Universidad Católica de Chile, Santiago, Chile

Introduction: Chronic Obstructive Pulmonary Disease (COPD) is a prevalent respiratory disease that presents a high rate of underdiagnosis during onset and early stages. Studies have shown that in mild COPD patients, remodeling of the small airways occurs concurrently with morphological changes in the proximal airways. Despite this evidence, the geometrical study of the airway tree from computed tomography (CT) lung images remains underexplored due to poor representations and limited tools to characterize the airway structure.

Methods: We perform a comprehensive morphometric study of the proximal airways based on geometrical measures associated with the different airway generations. To this end, we leverage the geometric flexibility of the Snakes IsoGeometric Analysis method to accurately represent and characterize the airway luminal surface and volume informed by CT images of the respiratory tree. Based on this framework, we study the airway geometry of smoking pre-COPD and mild COPD individuals.

Results: Our results show a significant difference between groups in airway volume, length, luminal eccentricity, minimum radius, and surface-area-to-volume ratio in the most distal airways.

Discussion: Our findings suggest a higher degree of airway narrowing and collapse in COPD patients when compared to pre-COPD patients. We envision that our work has the potential to deliver a comprehensive tool for assessing morphological changes in airway geometry that take place in the early stages of COPD.

KEYWORDS

airway characterization, proximal airways, airway morphometry, luminal volume, luminal eccentricity

1 Introduction

Chronic obstructive pulmonary disease (COPD) is the third leading cause of death worldwide, representing a critical public health problem with increasing prevalence (Agustí et al., 2023; GOLD, 2023). COPD genesis has long been related to long-term exposure to inhaled pollutants, with cigarette smoke being the most correlated with the onset and progression of the disease (Ananth and Hurst, 2023). Two essential elements of COPD are emphysematous destruction of the lung parenchyma and chronic airway inflammation. These manifestations are responsible for the loss of pulmonary function, evidenced by reduced expiratory airflow and air trapping (Celli et al., 2022).

Small airway disease represents the first stage of development in COPD, preceding emphysematous changes (McDonough et al., 2011; Koo et al., 2018; Labaki et al., 2019). In explanted lungs from COPD patients, micro-computed tomography and histologic examination of terminal bronchioles in areas with variable emphysema severity showed that the narrowing and loss of these airways occurred before alveolar destruction (McDonough et al., 2011). A significant proportion of terminal and transitional bronchioles were lost in lung samples from patients with COPD without signs of emphysema (McDonough et al., 2011; Koo et al., 2018), while the remaining small airways evidenced remodeling changes (McDonough et al., 2011). Findings from Labaki et al. (2019) support the results of smaller, prior cross-sectional, and short-term longitudinal studies (Galbán et al., 2012; Boes et al., 2015) by demonstrating that baseline functional small airway disease detected on chest computed tomography (CT) images are independently associated with an increase in emphysema 5 years later. In other words, transitioning from normal lungs or lungs with small airway disease to emphysema was the most frequent progression into the whole spectrum of disease from pre-COPD stages (Labaki et al., 2019). Besides, studies have confirmed that lumen narrowing in terminal bronchioles occurs before the alveolar dimensions increase into the emphysematous range (Hogg and Timens, 2009). The observation that bronchiolar destruction precedes emphysema is also consistent with several reports showing that the early appearance of emphysematous lesions predicts a more rapid decline in lung function (Yuan et al., 2009; Hoesein et al., 2011; Vestbo et al., 2011; Nishimura et al., 2012) because it is compatible with the widespread destruction of the terminal and preterminal bronchioles.

From a medical imaging standpoint, the structural alteration of the lung parenchyma has been studied using CT images of the lungs, which allows for the enhanced assessment of COPD subtypes (Bodduluri et al., 2017). The characterization of loss of functional lung tissue from CT images has been widely employed in COPD diagnosis, as a decrease in lung attenuation areas correlates with a reduction in pulmonary function (Bodduluri et al., 2013). In contrast, the radiological assessment of airway remodeling has received far less attention, as image resolution and computational tools to analyze airway morphology still represent a technological challenge (Díaz, 2018). Although small airways with a diameter less than 2 *mm* are too small to be detected in clinical CT images, two particular changes in structural features of large airways have been associated with small airway disease. Firstly, using CT imaging and histological analysis, Nakano et al. (Nakano et al., 2005) showed that the wall area in larger airways correlates to the same measure in small airways with an internal diameter of 1.27 *mm* in non-obstructed and moderately obstructed patients. Secondly, the total airway count (TAC) shows a strong correlation with the number of terminal bronchioles, as observed in micro-CT images in excised lung specimens (Kirby et al., 2020). These findings suggest that the remodeling process that affects the peripheral airways in COPD also affects central airways with diameters greater than 2 *mm*.

The morphological study of central airways in COPD patients has been mainly focused on assessing the lumen area and bronchial wall thickness because these structural parameters are related to airflow limitations (Dudurych et al., 2022). As a result, a close association between reduced lumen area, increased bronchial wall area, and decreased predicted forced expiratory volume after one second (FEV_1%) has been found (Diaz et al., 2016; Bhatt et al., 2019). However, these measurements are estimated by averaging a small selection of cross-section planes perpendicular to the centerline of the airway segment (Coxson, 2008). Such approximations leave out a more precise characterization of the geometry of the airway lumen in terms of irregularities that make it non-circular (Eskandari et al., 2013; 2016), which have been associated with the reduced FEV_1% (Choi et al., 2015; Choi et al., 2017). This has motivated the use of measures considering the total volume of the lumen, as it might better describe the airway morphology. Diaz et al. (2015) studied lumen volume in the estimation of the bronchial size and reported an association of reduced airway volume with decreased expiratory airflow in never-smokers. Further, Koyama et al. (2012b), Koyama et al. (2012a) found a correlation between the reduction of the airway volume and the reduction of expiratory airflow in COPD patients with different levels of severity. Other volumetric measures, such as the surface-area to lumen volume ratio (SA:V), have been proposed to characterize airway remodeling in a 5-year longitudinal study (Bodduluri et al., 2021). The estimation of these metrics considered the entire airway tree, which does not offer a localized analysis to detect regions of substantial morphological changes that may locally affect airflow.

The approach to geometrical modeling of the human airways uses advanced computational geometry techniques (Tawhai et al., 2009). In particular, techniques for generating surface representations of the airway lumen based on CT imaging should capture the irregular lumen shapes found in the airway tree of lungs with COPD (Choi et al., 2017; Bodduluri et al., 2018), and asthma (Eskandari et al., 2015; Miyawaki et al., 2017). Recently, our group has developed a computational framework for the creation of geometric models of the airway tree from CT images that offers arbitrary and flexible lumen geometries using non-uniform rational B-splines (NURBS) (Ortiz-Puerta et al., 2022). This approach, which we have termed Snakes Isogeometric Analysis (SIGA), has shown high accuracy in the surface representation of healthy and COPD airway trees, as measured in terms of DICE scores. Due to its geometrical foundation, the SIGA method enables accurate and flexible surface analysis suitable for studying complex airway morphologies.

In this work, our objective is to study the morphology of the airway tree using flexible surface representations to understand morphological changes in the early stages of COPD. To this end, we leverage the SIGA method to geometrically analyze the airways of a group of smoking pre-COPD subjects and a group of mild COPD [Global Initiative for Chronic Obstructive Lung Disease (GOLD) I]

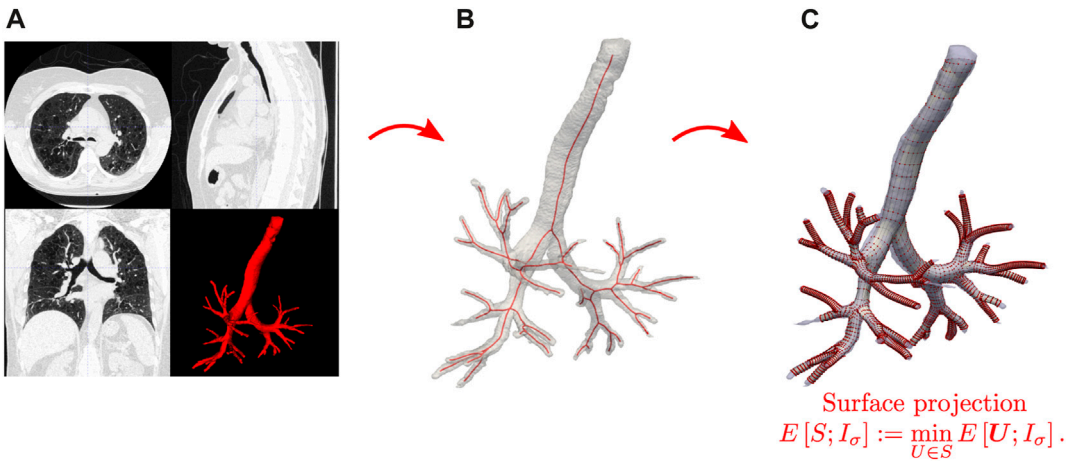

FIGURE 1
Schematic of the SIGA method for creating geometrical models of the airways. **(A)** CT image processing and segmentation. **(B)** Skeletonization of binary airway images. **(C)** Surface construction and projection from solving the Snakes segmentation problem.

patients (Agustí et al., 2023) and assess their differences. In Section 2, we briefly revisit the SIGA method and define morphometric volume, surface, and cross-section measures that capture non-circular features of the lumen. In Section 3, we construct surface representations of the airway trees of each individual in the two study groups, from which we estimate and compare the proposed morphometric measures. We examine our results in Section 4, where we offer a discussion about the main conclusions reached and highlight aspects of this work that can be improved in future contributions.

2 Geometrical modeling and morphometric metrics for the analysis of the respiratory airways

2.1 Airway surface modeling: the Snakes isogeometric analysis (SIGA) method

In the following, we briefly describe the SIGA method for constructing geometrical surface models of the respiratory airways (Ortiz-Puerta et al., 2022), see Figure 1 for a schematic. The first step considers volumetric CT images of the lungs in end-expiration (EE) and end-inspiration (EI) stages, from which we extract binary masks using the image level-set-based segmentation tool provided by the ITK-SNAP software (Yushkevich et al., 2006), see Figure 1A. We perform a visual corroboration of the result to correct possible leakage of the level-set into the parenchyma using the ITK-SNAP editing tools. This leakage can happen mainly in smaller airways with poorly defined bronchial walls due to resolution limitations. Furthermore, considering the voxel size of the images (0.7 *mm*), we established not to segment airways with less than three voxels (2.1 *mm*) in diameter to avoid leakage in smaller airways.

From this step, we obtain binary images I_{seg}: $\Omega \subset \mathbb{R}^3 \rightarrow \{0,1\}$ in NIFTI format with the same voxel size and dimensions as the CT images, where the luminal volume of the airways is marked by ones and the rest by zeroes. Then, using the CGAL library (Gao et al., 2020), we calculate the skeletons from the binary image, see Figure 1B. We identify each airway segment delimited by the bifurcation nodes in the skeleton and recursively identify their child branches to mark them by generation for further spatial grouping. We further implement the approach set forth by Miyawaki et al. (Miyawaki et al., 2017) to post-process the skeleton to identify short branches and create fork-type trifurcations. This methodology involves identifying the child branches from a parent and comparing the proportion between their length and radius, i.e., $p_c = l_c/r_c$, where l_c is the child branch length and r_c is the radius. If one of them is too short with respect to their radius, i.e., $p_c < 0.3$, we transform the bifurcation into a trifurcation by identifying the short branch children and connecting them to the short branch parent through the bifurcation nodes. We refer the reader to Miyawaki et al. (2017) for a detailed description of this post-processing step.

In the next step, the skeleton nodes of each airway branch are used to align octagonal templates containing the spatial control points that will represent cylindrical surfaces. The resulting control points are connected to create the control point mesh necessary to represent the NURBS cylindrical surfaces. These surfaces are then evolved to model the airway boundary by solving variational formulation of the Snakes problem Kass et al. (1988), see Figure 1C. Let $\hat{\Omega} \subset \mathbb{R}^2$ and $\mathcal{S} := [H^2(\hat{\Omega}, \mathbb{R})]^3$ be the space of surface embeddings on the physical domain $\mathbb{R}^3$. Let I_{seg}: $\Omega \subset \mathbb{R}^3 \rightarrow \{0,1\}$ be a volumetric image; The Snakes problem can be stated as follows: Find the optimal surface $\boldsymbol{S} \in \mathcal{S}$ such that

$$E[\boldsymbol{S};I_\sigma] := \min_{\boldsymbol{U}\in\mathcal{S}} \left[\frac{\alpha}{2}\int_{\hat{\Omega}} \left(\|\boldsymbol{U}_{,\xi}\|^2 + \|\boldsymbol{U}_{,\eta}\|^2 \right) d\hat{\Omega} + \frac{\beta}{2}\int_{\hat{\Omega}} \left(\|\boldsymbol{U}_{,\xi\xi}\|^2 + \|\boldsymbol{U}_{,\xi\eta}\|^2 + \|\boldsymbol{U}_{,\eta\eta}\|^2 \right) d\hat{\Omega} - \frac{\lambda}{2}\int_{\hat{\Omega}} \|\nabla\left(G_\sigma * I_{seg}\right)(\boldsymbol{U})\|^2 d\hat{\Omega} \right], \quad (1)$$

where $\alpha, \beta > 0$ are parameters that control the regularizing terms, $\lambda > 0$ is the image energy parameter, $\boldsymbol{U}_{,\mu} := \frac{\partial \boldsymbol{U}}{\partial \mu}$ and $\boldsymbol{U}_{,\mu\nu} := \frac{\partial^2 \boldsymbol{U}}{\partial \mu \partial \nu}$ are the first and second derivatives respect the parametric coordinates $\mu, \nu \in \{\xi, \eta\}$, and $G_\sigma * I_{seg}$ is a Gaussian filter applyed to the binary image I_{seg}.

Note that the Gaussian filter is used to smooth the boundaries of the binary image and not to reduce noise, and in the following, we referred to the filtered image as I_σ. Then, we define the space $\mathcal{S}_t := [H^2(\hat{\Omega}, \mathbb{R})]^3 \times \mathbb{R}^+$, where t is a fictitious time variable, and rate potential $\Psi[\dot{\boldsymbol{U}}] := \frac{1}{2}\int_{\hat{\Omega}} |\dot{\boldsymbol{U}}|^2 d\hat{\Omega}$. Thus, the evolution of the surface can be expressed by the following variational gradient-flow formulation (Hurtado and Henao, 2014): Find $\boldsymbol{S} \in \mathcal{S}_t$ such that

$$\mathcal{D}_{\boldsymbol{v}}\Psi\left[\dot{\boldsymbol{S}}\right] + \mathcal{D}_{\boldsymbol{v}}E[\boldsymbol{S}; I_\sigma] = 0, \quad \forall \boldsymbol{v} \in \mathcal{S}. \tag{2}$$

where $\mathcal{D}_{\boldsymbol{v}}E[\boldsymbol{S}] := \frac{\partial}{\partial \epsilon}E[\boldsymbol{S} + \epsilon \boldsymbol{v}]|_{\epsilon=0}$ is the Gateaux differential of an arbitrary functional E. For the spatial discretization of Eq. 2, we use a multi-patch approach. To this end, we define the NURBS trial and test subspaces in Eq. 3, which read

$$\begin{aligned} \mathcal{S}_t^h &:= \left\{\boldsymbol{S}^h(\cdot, t) \in \left[H^2\left(\hat{\Omega}_\rho, \mathbb{R}\right)\right]^3 \times \mathbb{R}^+ : \boldsymbol{S}^h(\cdot, t)|_{\hat{\Omega}_\rho} \in \mathcal{Q}\left(\hat{\Omega}_\rho\right), \forall \rho = 1, \ldots, n_{pt}\right\}, \\ \mathcal{V}^h &:= \left\{\boldsymbol{v}^h \in \left[H^2\left(\hat{\Omega}_\rho, \mathbb{R}\right)\right]^3 : \boldsymbol{v}^h|_{\hat{\Omega}_\rho} \in \mathcal{Q}\left(\hat{\Omega}_\rho\right), \forall \rho = 1, \ldots, n_{pt}\right\}, \end{aligned} \tag{3}$$

where n_{pt} is the number of patches, $\mathcal{S}_t^h \subset \mathcal{S}_t$, $\mathcal{V}^h \subset \mathcal{S}$, and $\mathcal{Q}(\hat{\Omega}_\rho)$ is the space spanned by isogeometric shape functions that result from the 2-tensor product of 1D NURBS functions. Then, the multi-patch NURBS surface discretization $\boldsymbol{S}^h{}_{\hat{\Omega}_\rho} := \boldsymbol{S}_\rho^h$ and $\boldsymbol{v}^h{}_{\hat{\Omega}_\rho} := \boldsymbol{v}_\rho^h$ with normalized patch domain $\hat{\Omega}_\rho := [0, 1]^2$, takes the form

$$\boldsymbol{S}_\rho^h = \sum_{j=1}^{n_{\rho\eta}} \sum_{i=1}^{n_{\rho\xi}} R_{i,j}^{p,q}\left(\xi_\rho, \eta_\rho\right) \boldsymbol{b}_{i,j}^\rho(t), \tag{4}$$

$$\boldsymbol{v}_\rho^h = \sum_{j=1}^{n_{\rho\eta}} \sum_{i=1}^{n_{\rho\xi}} R_{i,j}^{p,q}\left(\xi_\rho, \eta_\rho\right) \boldsymbol{d}_{i,j}^\rho, \tag{5}$$

where $(\xi_\rho, \eta_\rho) \in \hat{\Omega}_\rho$, $\boldsymbol{b}_{i,j}^\rho$: $(0, T] \to \mathbb{R}^3$ are the spatial control point defined for the patch ρ, and $\boldsymbol{d}_{i,j}^\rho \in \mathbb{R}^3$. The NURBS basis functions are defined in Eq. 6, which take the form

$$R_{i,j}^{p,q}\left(\xi_\rho, \eta_\rho\right) = \frac{N_{i,p}\left(\xi_\rho\right) M_{j,q}\left(\eta_\rho\right) w_{i,j}^\rho}{\sum_{\hat{j}=1}^{n_{\rho\eta}} \sum_{\hat{i}=1}^{n_{\rho\xi}} N_{\hat{i},p}\left(\xi_\rho\right) M_{\hat{j},q}\left(\eta_\rho\right) w_{\hat{i},\hat{j}}^\rho}, \tag{6}$$

where $N_{i,p}$ (ξ_ρ), $M_{j,q}$ (η_ρ) formed by the B-splines basis with polynomial order p, q, calculated with the Cox the Boor recursion formula (Hughes et al., 2005), $w_{i,j} \in \mathbb{R}^+$ the NURBS weights, and $n_{\rho\xi}$, $n_{\rho\eta}$ the number of basis function on each parameter direction. Note that each $\boldsymbol{S}_\rho^h$ in Eq. 4 defines a surface patch ρ in the physical domain and that the spatial control points $\boldsymbol{b}_{i,j}^\rho$ are defined for each patch and evolve on time. Using Eqs 4, 5, we get the spatial discretization of problem (Eq. 2). The result is a semi-discrete system of equations that depends continuously on time. Thus, temporal discretization was carried out using a semi-implicit time integration scheme leading to a linear matrix system. Each time step solution of the linear system is the new spatial position of the control points $\boldsymbol{b}_{i,j}^\rho$ of the expression (Eq. 4), defining the NURBS surface representation $\boldsymbol{S}_\rho^h$ of the airways. See Ortiz-Puerta et al. (2022) for further details of the linear system and temporal integration scheme.

To evaluate the performance of the SIGA method and validate the accuracy of the surface representation, we calculate the DICE coefficient of similarity. To this end, we use the binary image I_{seg} from the initial segmentation step and create the surface-based binary image I_{siga} where voxels with value 1 are inside of the airways NURBS surfaces. The DICE coefficient is defined in Eq. 7, which reads

$$\text{DICE} = 2\frac{|I_{seg} \cap I_{siga}|}{|I_{seg}| + |I_{siga}|}, \quad \text{DICE} \in [0, 1], \tag{7}$$

where $|\cdot|$ is the volume given by the number of voxels with a value equal to 1 of the binary images. The numerator defines the intersection, i.e., the common voxels between both images, and the denominator is the addition of both volumes. This coefficient measures similarity between the images, where DICE = 1 indicates perfectly matching volumes and DICE = 0 indicates no match. Considering that the voxels with value 1 in binary image I_{siga} are defined inside the NURBS surface of each branch, the DICE coefficient also validates the accuracy of the geometrical measures as it is defined directly. Previous studies suggest that DICE ≥ 0.7 can be considered an acceptable threshold to establish similarity (Arrieta et al., 2017).

2.2 Morphometric measures for airway analysis

For the morphometry study, we considered the airways as tubular structures with arbitrary cross-section shapes. Each airway segment is identified using the bifurcation nodes of the skeleton and its corresponding NURBS surfaces as in Eq. 4. Based on these representations, we compute the following parameters:

2.2.1 Total and generation airway count

The total airway count (TAC) is the sum of all segments included in the airway-tree representation for a subject. It measures all visually connected airways from which we can extract morphological information (Kirby et al., 2018). The generation airway count (GAC) is the number of airway segments in a particular generation in the lung of one subject. We note that the sum of all GACs equals the TAC.

2.2.2 Segment luminal volume

Airways luminal volume cannot be directly calculated since the SIGA method only delivers their surface representation. To calculate the volume, we use the parametric model of NURBS surfaces in Eq. 4 and apply the divergence theorem. However, we must close the surface containing the luminal volume to be completely continuous. To this end, we consider the octagonal templates located at each end of the airway and connect them with their corresponding bifurcation node; see Figure 2A. Then, we create the *inlet* $\partial\boldsymbol{S}_{in}$ and *outlet* $\partial\boldsymbol{S}_{out}$ surfaces using the expression in Eq. 4 and the control points defined by the octagonal mesh, and rename the airway lumen surface as $\partial\boldsymbol{S}_{mantle}$. We remark that to guarantee a minimum C^0 continuity of the total surface, it is important that for the new surfaces, the η parametric direction satisfies the same regularity as the $\partial\boldsymbol{S}_{mantle}$ surface. Now, let $\Omega \subset \mathbb{R}^3$ be the airway lumen volume. Its surface boundary is such that $\partial\Omega = \partial\boldsymbol{S}_{in} \cup \partial\boldsymbol{S}_{out} \cup \partial\boldsymbol{S}_{mantle}$, and clearly $\partial\Omega \subset \mathbb{R}^3$. Then, we define the position vector field $\boldsymbol{X}$: $\Omega \to \mathbb{R}^3$ where $[x,y,z]^T = \boldsymbol{X}(\Omega)$ are the position vectors. Taking the divergence of the position vector field $\boldsymbol{X}$ we have

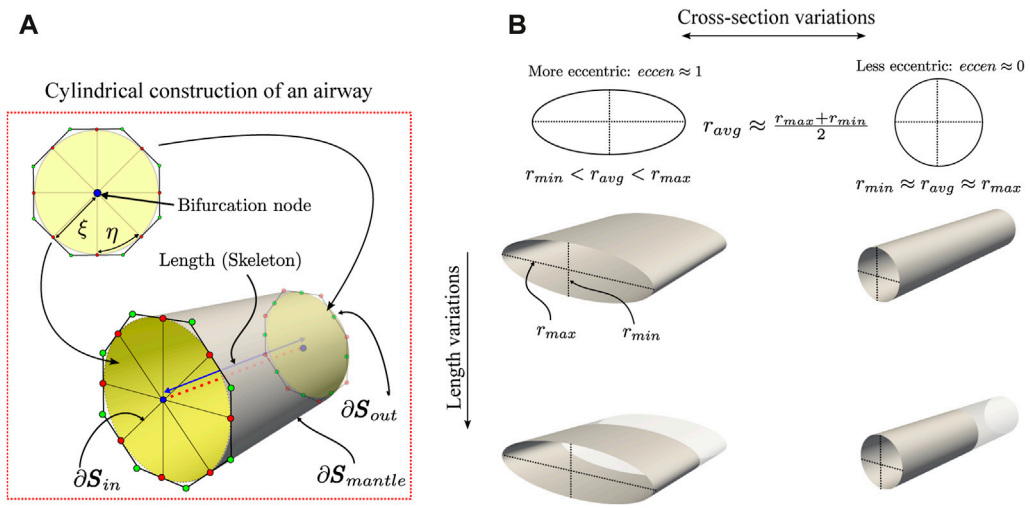

FIGURE 2
Schematic of the geometrical characterization of the airway morphology. In the ideal case of perfectly cylindrical airways **(A)**, its cross-section has an *eccen* = 0 since the minimum and maximum radius are the same, and its length is given by the skeleton. Also, geometrical properties, such as the volume and surface area to volume ratio (SA:V), are easily calculated using NURBS surfaces. However, the airways are far from ideal and exhibit variations in their cross-section and length **(B)**.

$$\boldsymbol{X} = \begin{bmatrix} x \\ y \\ z \end{bmatrix} \Rightarrow \frac{1}{3}\text{div}\boldsymbol{X} = 1. \tag{8}$$

Now, we consider the integral expression to calculate the lumen volume of Ω. Then, replacing Eq. 8 and using the Divergence theorem, the lumen volume is expressed in Eq. 9, which takes the form

$$volume = \int_{\Omega} 1 d\Omega = \frac{1}{3}\int_{\Omega} \text{div}\boldsymbol{X} d\Omega = \frac{1}{3}\int_{\partial\Omega} \boldsymbol{X}\cdot\boldsymbol{n} d\partial\Omega, \tag{9}$$

where $\boldsymbol{n}$ outward pointing unit normal vector defined over $\partial\Omega$. Recalling the union of surfaces boundary $\partial\Omega = \partial\boldsymbol{S}_{in} \cup \partial\boldsymbol{S}_{out} \cup \partial\boldsymbol{S}_{mantle}$ and that each surface is defined parametrically as a NURBS surface patch $\boldsymbol{S}^h_\rho$, where $\rho \in \mathcal{P} := \{in, out, mantle\}$, we have

$$\begin{aligned} volume &= \frac{1}{3}\int_{\partial\Omega} \boldsymbol{X}\cdot\boldsymbol{n} d\partial\Omega \\ &= \frac{1}{3}\sum_{\rho\in\mathcal{P}}\left[\int_{\partial\boldsymbol{S}_\rho} \boldsymbol{X}_\rho \cdot \boldsymbol{n}_\rho d\partial\boldsymbol{S}_\rho\right], \quad \text{with} \quad \boldsymbol{n}_\rho = \frac{\boldsymbol{S}^h_{\rho,\xi}\times\boldsymbol{S}^h_{\rho,\eta}}{\|\boldsymbol{S}^h_{\rho,\xi}\times\boldsymbol{S}^h_{\rho,\eta}\|}, \end{aligned} \tag{10}$$

where $\boldsymbol{S}^h_{\rho,\alpha} := \frac{\partial \boldsymbol{S}^h_\rho}{\partial\alpha}$, is the partial derivative of the surface with respect each parametric coordinate $\alpha \in \{\xi, \eta\}$. Following this, we consider that the dot product $\boldsymbol{X}_\rho \cdot \boldsymbol{n}_\rho$ is defined over the embedded parametrical surfaces $\partial\boldsymbol{S}_\rho$. Then, we use the results from Dedè and Quarteroni (2015) and define the Jacobian determinant $\hat{g}_\rho(\boldsymbol{\xi}_\rho) := \sqrt{det\,(F(\boldsymbol{\xi}_\rho)^T F(\boldsymbol{\xi}_\rho))}$, where $F(\boldsymbol{\xi}_\rho) := \frac{\partial \boldsymbol{X}_\rho}{\partial \boldsymbol{\xi}_\rho}$, and the vectors $\boldsymbol{X}_\rho = (x_\rho, y_\rho, z_\rho)$ and $\boldsymbol{\xi}_\rho = (\xi_\rho, \eta_\rho) \in \hat{\Omega}_\rho$ are the spatial point defined by the NURBS surfaces and the parametric coordinates, respectively. Thus, from Eq. 10, we have

$$volume = \frac{1}{3}\sum_{\rho\in\mathcal{P}}\left[\int_{\hat{\Omega}_\rho} \boldsymbol{X}_\rho \cdot \boldsymbol{n}_\rho \hat{g} d\hat{\Omega}_\rho\right], \qquad \mathcal{P} := \{in, out, mantle\}. \tag{11}$$

In this work, volume results are presented in mm^3.

2.2.3 Surface area to volume ratio (SA:V)

This measure was proposed by Bodduluri et al. (2021) to characterize airway remodeling. It extends the cross-sectional relation between the lumen area and the inner perimeter along the airway extension. We remark that SA:V ratio should increase generation-by-generation until reaching functional tissue as a large alveolar surface area allows for more effective gas exchange (Bodduluri et al., 2021). To estimate this parameter, we calculate the area of the surface boundary $\partial\Omega$ as

$$area = \frac{1}{3}\sum_{\rho\in\mathcal{P}}\left[\int_{\hat{\Omega}_\rho} |\boldsymbol{S}^h_{\rho,\xi} \times \boldsymbol{S}^h_{\rho,\eta}| d\hat{\Omega}_\rho\right], \qquad \mathcal{P} := \{in, out, mantle\}, \tag{12}$$

with the area expressed in mm^2. Volume and area integrals (Eqs 11, 12), respectively, are numerically solved using standard Gauss-Legendre quadrature, as detailed in Ortiz-Puerta et al. (2022). Thus, the surface area to volume ratio is then given by Eq. 13, which reads

$$SA{:}\,V = \frac{area}{volume}, \tag{13}$$

were *area* and *volume* are given by Eqs 11, 12, respectively, and results are presented in mm^{-1}.

2.2.4 Luminal eccentricity

This adimensional measure quantifies the distortion of the cross-section of the airway in terms of the minor and major radii (Oakes et al., 2012). The major and minor radii are calculated from the orthogonal projection of points from the NURBS surfaces to the line segments defined from the internal nodes of the skeleton of each branch. The points on the surface are generated from the parametric

coordinates (ξ, η) in the normalized domain $\hat{\Omega}$ of the mantle surface. Then, for each line segment of the skeleton, we use the orthogonal projection vectors to calculate the minimum, maximum and average distance using the Euclidean norm. Note that in a circular cross-section, these projection vectors have the same size; see Figure 2B. Finally, we calculate the minimum $r_{\min}$, maximum $r_{\max}$, and average r_{avg} radii of the total airway segment by averaging these measures from each skeleton line segment. The luminal eccentricity is then defined in Eq. 14

$$eccen = \sqrt{1 - \left(\frac{r_{min}}{r_{max}}\right)^2}, \quad eccen \in [0, 1). \tag{14}$$

For a circle, we have $eccen = 0$; for an ellipse, the luminal eccentricity will be between 0 and 1, i.e., $eccen \in (0, 1)$.

2.2.5 Airway segment length

It corresponds to the Euclidean distance between two connected skeleton nodes of a segment $\boldsymbol{n}_i \in \mathcal{SN}_b$ that belong to an airway branch b, which is defined in Eq. 15

$$length = \sum_{\boldsymbol{n}_i \in \mathcal{SN}_b} \sqrt{n_i^2 - n_{i+1}^2}. \tag{15}$$

Results are reported in *mm*.

The SIGA method specifically focuses on representing the luminal surface of the airways. Consequently, it is not suitable for measuring bronchial wall thickness. Geometrical measurements are calculated for all available airway segments for inspiratory and expiratory breathing states. In addition, all segments are grouped by generations from generation 0 (trachea) to 5 (subsegmental bronchi). All algorithms and measures presented in this study were implemented in an in-house code using Python 3.9 and on an Intel(R) Core(TM) i7-3770 CPU at 3.40 GHz with 16 GB of RAM workstation.

2.3 Statistical analysis

Statistical analysis was performed using SciPy 1.7.3 (Python 3.9). We used the Shapiro-Wilk test to confirm the non-normal distribution of the data. Then, we used the Mann-Whitney U test for the comparative study to find significant differences between both groups for generations 0 to 5, at EE and EI, and for each measure. While it is important to acknowledge that the Mann-Whitney test can lead to type II errors, we find it the most suitable choice for statistical analysis given the sample size and non-normal data distribution.

3 Morphometric study of the airways of pre-COPD smoking subjects and mild COPD patients

3.1 Experimental groups and image datasets

We analyzed the pulmonary function and image datasets from participants recruited in a study previously reported in the literature (Labarca et al., 2017). We constructed two groups comprising six participants through random selection from a database, with an equal distribution of three males and three females in each group and an age range of 65 ± 6 years. The Control (pre-COPD) group consisted of smokers with no signs of COPD. The COPD group comprised patients diagnosed with COPD at GOLD stages I of severity. We did not conduct a gender-based study, considering the small sample size according to this criterion. Anthropometric and pulmonary function data for these groups are shown in Table 1. Emphysema was measured as the percent of low attenuation areas less than −960 Hounsfield units (LAA%) (Madani et al., 2007).

TABLE 1 Anthropometric and pulmonary function data for the groups under study. Data are presented as median ± IQR. *$p < 0.05$ Mann-Whitney test. mMRC-Dyspnea = modified medical research council, FEV_1pred = predicted forced expiratory volume in one second, TLCpred = predicted total lung capacity, FRCpred = predicted functional residual capacity, DLCOpred = predicted diffusing capacity for carbon monoxide, LAA = low attenuation area, SMWDpred = predicted 6 min walk distance, FEV_1/FVC = rate between forced expiratory volume in one second and forced vital capacity.

Parameters	Control	COPD	*p*-value
Participants, n	6	6	1.00
Female sex, %	50	50	1.00
Age; year	62.0 ± 6.0	64.5 ± 4.5	0.57
Height, cm	159.0 ± 4.5	161.5 ± 8.5	0.47
Weight, kg	62.6 ± 6.3	74.5 ± 15.3	0.15
BMI, kg/cm^2	25.9 ± 4.0	28.7 ± 5.4	0.24
mMRC-Dyspnea	0	1 and 2	**0.002***
TLCpred, %	97.1 ± 17.5	109.4 ± 16.5	0.18
FRCpred, %	87.9 ± 12.8	107.2 ± 20.1	0.18
FEV_1pred, %	118.3 ± 27.9	91.3 ± 22.4	**0.025***
DLCOpred, %	88.8 ± 6.8	68.1 ± 17.0	**0.008***
LAA, %	0.4 ± 1.1	3.3 ± 12.2	**0.013***
SMWDpred, %	95.5 ± 14.3	88.2 ± 8.9	**0.041***
FEV_1/FVC %	79.8 ± 4.5	63.0 ± 12.2	**0.002***

CT images of the thorax at EE and EI for each participant were retrieved and analyzed in this work. The voxel resolution was $0.7mm \times 0.7mm \times 0.5\,mm$. Figure 3 shows coronal planes of representative subjects in each group during EE and EI.

To create the geometric airway models, we adjusted the parameters of the SIGA model so that the best surface representation was achieved. To this end, we considered two surface patches ($\rho = 2$) for each airway segment to reduce the lack of smooth regularity in the interface between two adjacent patches (G^1-continuity) without modifying the control point templates. The accuracy of the representation was measured using the DICE coefficient. We set the polynomial degrees to p, $q = 3$ to guarantee a higher regularity (C^2) inside each patch. Parameters for the energy functional (Eq. 1) were calibrated using the iterative scheme proposed in Ortiz-Puerta et al. (2022), where we sampled the parameter space and picked the point that maximized the DICE coefficient. For the regularity term we used $\alpha = 10^{-2}$, $\beta = 10^{-3}$, for the image energy term, $\lambda = 0.1$, and for the Gaussian filter, $\sigma = 2$. Time steps were kept to $\Delta t = 0.01$ and a

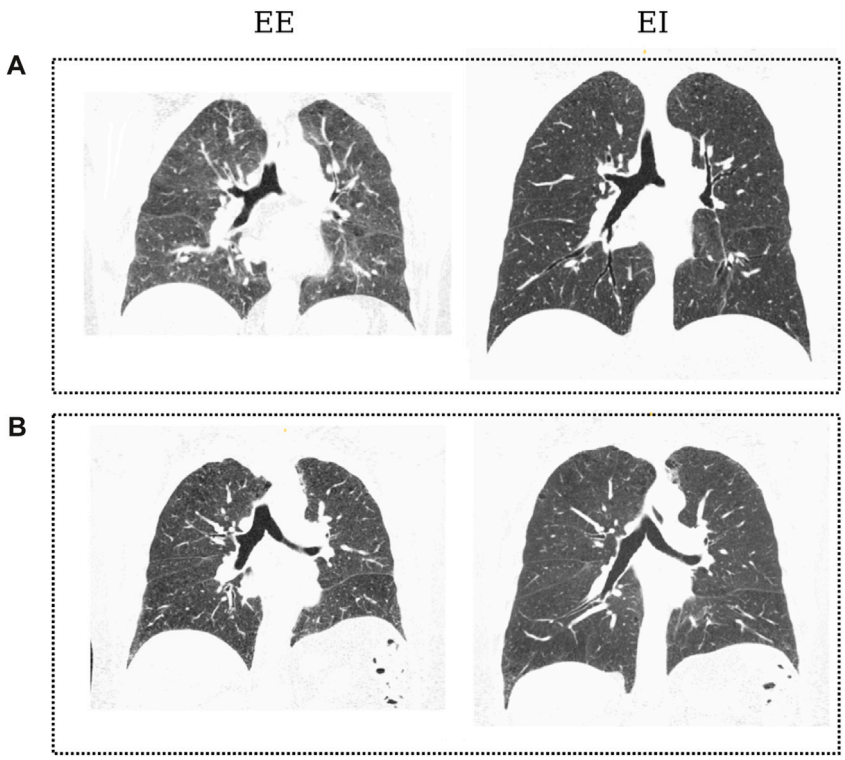

FIGURE 3
Coronal slices of CT images from patients of both groups in the dataset: Control subject **(A)** at EE and EI; COPD patient **(B)** at End of Expiration (EE) and End of Inspiration (EI). Black regions denote aerated areas in the lungs and the airways.

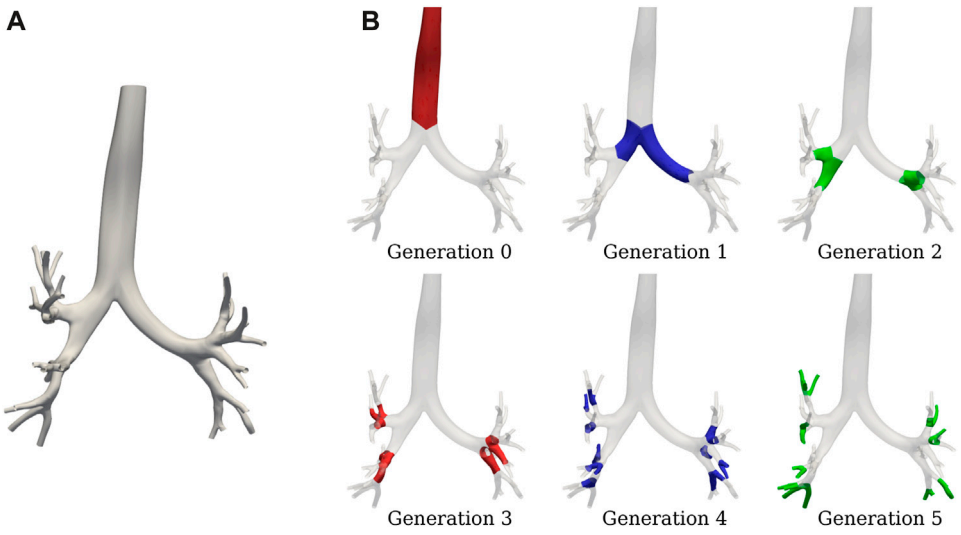

FIGURE 4
SIGA geometrical model for a COPD patient: **(A)** surface results at EE with DICE coefficient of 0.89, and **(B)** airway spatial grouping from generation 0 to 5.

maximum of 35 iterations. These parameters yielded an excellent performance, with DICE >0.88 in all the images for both states and groups. The total time for the workflow presented in Figure 1 is 4.5 h, with steps (a) and (c) being the most time-consuming with about 1 and 3.5 h, respectively. Figure 4 shows the SIGA surface results for a COPD patient at EE with the spatial grouping of the airways by generations. Figure 5 presents the results for two patients in both breathing states.

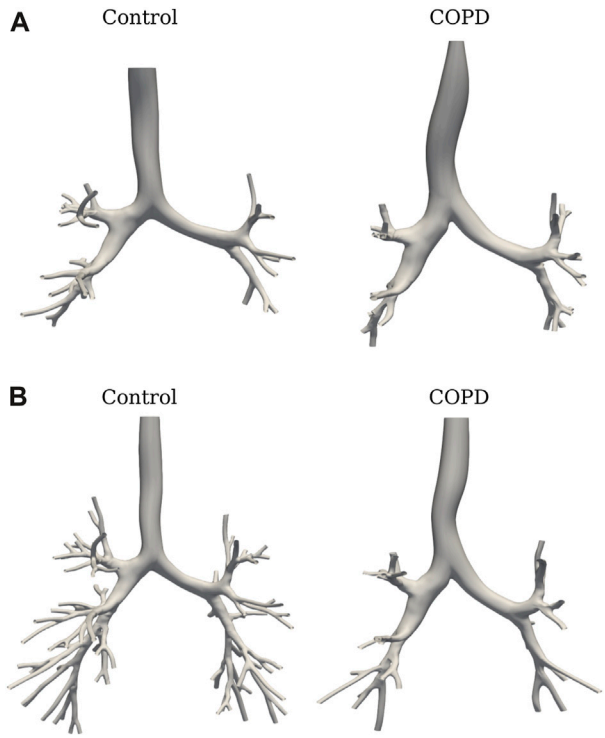

FIGURE 5
SIGA surface models comparison from subjects of both groups: at EE **(A)**, and EI **(B)**.

3.2 Results

Figure 6A shows the TAC comparison. While TAC was similar between groups at EE (49.5 ± 26.4 vs. 53.8 ± 30.5 in Control and COPD groups, respectively), it was significantly higher in the Control group at EI, with values of 139.8 ± 25.6 (Control) and 94.6 ± 21.7 (COPD) (p = 0.015). Figure 6B reports a similar comparison for GAC. At EE, GAC was similar between groups. At EI, GAC in the Control group was significantly different from the COPD group for the 5^{th} (31.8 ± 2.2 vs. 23.8 ± 5.6, p = 0.03), 6^{th} (30.3 ± 7.3 vs. 18.0 ± 6.7, p = 0.03), 7^{th} (20.2 ± 6.4 vs. 9.3 ± 3.3, p = 0.008), and 9^{th} (8.4 ± 2.3 vs. 3.6 ± 2.7, p = 0.03) generations, respectively. See Figure 5 for the airway model of two representative subjects.

Figures 7A, B compare airway luminal volume for each generation at EE and EI, respectively. At EE, luminal volume was lower in the Control group for the 4*th* (103.6 ± 53.5 mm^3 vs. 147.8 ± 90.6 mm^3, $p < 0.001$) and 5*th* (81.6 ± 53.9 mm^3 vs. 119.3 ± 84.6 mm^3, $p < 0.001$) generation. At EI, airway luminal volume was also lower in the Control group for the 4*th* (159.9 ± 69.0 mm^3 vs. 195.6 ± 125.9 mm^3, p = 0.012) and 5*th* (125.1 ± 97.8 mm^3 vs. 148.3 ± 107.4 mm^3, p = 0.043) generation.

Figure 8 shows the airway segment length for each generation in both groups. At EE, airway length was higher in COPD patients for the trachea (148.6 ± 24.1 *mm* vs. 187.8 ± 31.2 *mm*, p = 0.041) and the 5*th* generation (19.0 ± 11.1 *mm* vs. 23.9 ± 13.0 *mm*, p = 0.013). At EI, no significant differences were found for any of the generations.

Results for luminal eccentricity are reported in Figures 9A, B for the EE and EI states, respectively. We placed a horizontal line at 0.86, marking a relation of 1–2 times the radius, i.e., when the maximum radius is two times larger than the minimum radius. At EE, luminal eccentricity was higher in the Control group for the 3rd (0.82 ± 0.06 vs. 0.78 ± 0.05, p = 0.03), 4*th* (0.83 ± 0.06 vs. 0.79 ± 0.04, p = 0.004), and 5*th* (0.83 ± 0.06 vs. 0.81 ± 0.04, p = 0.005) generations. At EI, eccentricity was lower in the Control group but only for the 1st generation 1*st* (0.78 ± 0.05 vs. 0.84 ± 0.03, p = 0.007).

Minimum, average, and maximum radii are shown in Figures 10–12, respectively. Only the minimum radii show significant differences between the Control and COPD groups for the 4*th* (2.2 ± 0.8 *mm* vs. 2.6 ± 0.8 *mm*, p = 0.03) and 5*th* (1.8 ± 0.6 *mm* vs. 2.1 ± 0.7 *mm*, p = 0.009) generations.

Figures 13A, B present the SA:V ratio results at EE and EI, respectively. At EE, the SA: V ratio was significantly higher in the Control group in the 4*th* (1.5 ± 0.2 mm^{-1} vs. 1.3 ± 0.2 mm^{-1}, $p <$ 0.001) and 5*th* (1.7 ± 0.3 mm^{-1} vs. 1.5 ± 0.3 mm^{-1}, p = 0.008) generations. At EI, the SA: V ratio was significantly higher in the Control group but only for the 5*th* generation (1.5 ± 0.3 mm^{-1} vs. 1.4 ± 0.3 mm^{-1}, p = 0.012).

4 Discussion

This study examined the morphological differences in the airway tree among smoking individuals. Our database included smoking subjects divided into Control and COPD groups based on the severity classification criteria outlined in Labarca et al. (2017), Agustí et al. (2023). These groups displayed notable differences in pulmonary function, as reported in Table 1. The Control group, referred to as the pre-COPD group due to their smoking status (Ananth and Hurst, 2023), did not exhibit airflow limitations (FEV_1/FVC ≥70%, post-bronchodilation) or symptoms (mMRC = 0). In contrast, the mild COPD group resulted in airflow obstruction (FEV_1/FVC < 70%, post-bronchodilation) and clear symptoms (mMRC = 1 and 2). It is worth noting that both groups exhibited FEV_1pred values greater than 80%. Consequently, the COPD group falls into the mild stage of disease severity (GOLD I) (GOLD, 2023).

We implemented the SIGA method, which utilizes the variational formulation of the Snakes problem to evolve NURBS surfaces and represent airway lumens, yielding improved performance compared to orthogonal projection techniques like Miyawaki et al. (2017), particularly in terms of the DICE coefficient. See Ortiz-Puerta et al. (2022) for a detailed comparison of these methods. The main findings of this study revealed significant differences in airway characteristics between the Control and COPD groups, particularly during different breathing states (EE and EI) and at specific generations of the airways. Lungs in the Control group displayed a higher TAC than the COPD group when comparing lungs in EI; see Figure 6A. Further reinforcement for this result is the marked reduction in EI GAC from the 5^{th} to 9^{th} generation in patients; see Figure 6B. These observations are consistent with previous studies, where comparisons between mild COPD patients and groups without airflow limitation or symptoms exhibited reductions of 17%–19% in the TAC of patients (McDonough et al., 2011; Kirby et al., 2018). TAC reduction could result from partial or complete airway blockage due to the lack of lung elastic tethering or increased airway stiffness

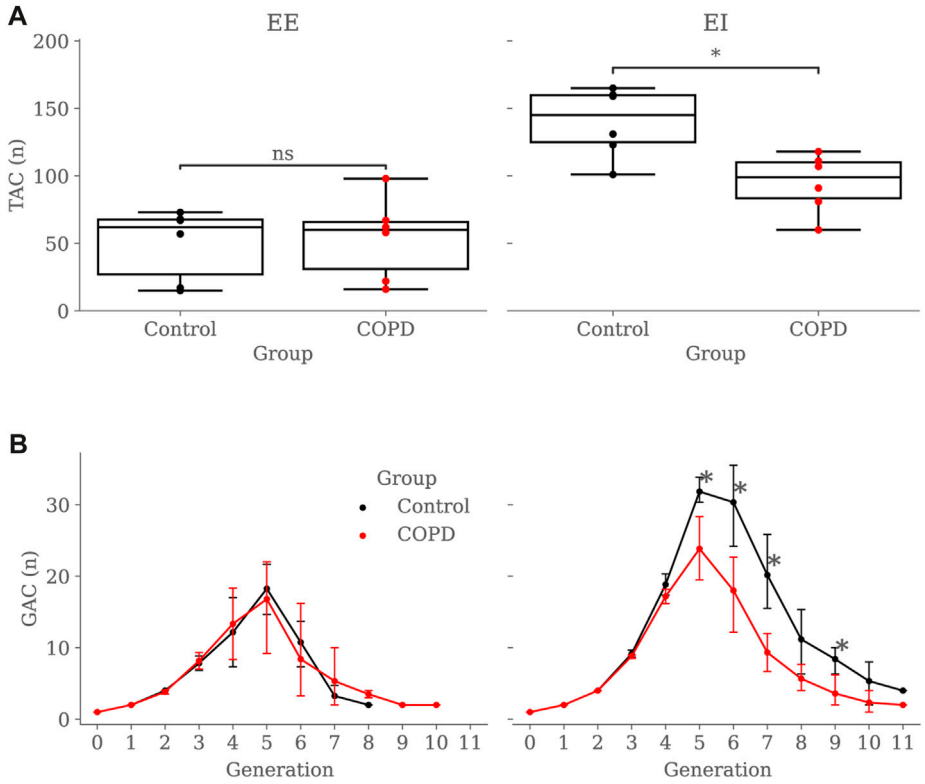

FIGURE 6
Group comparison of airway counts: **(A)** Total Airway Count (TAC) by group and breathing state, **(B)** Generation Airway Count (GAC) by group and breathing state. In subfigure **(B)**, error bars represent confidence intervals. Nomenclature: ns = no significant differences, *$p < 0.05$.

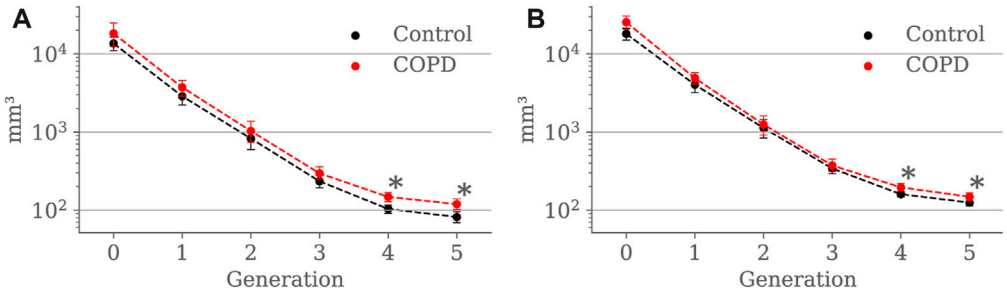

FIGURE 7
Airway luminal volume comparison between the Control and COPD groups from generation 0 to 5: **(A)** at EE, and **(B)** at EI. Dots represent mean values, and the error bars are confidence intervals. Nomenclature: *$p < 0.05$.

resulting from ongoing inflammation in the lumen layers, which has been observed in COPD lungs (Eskandari et al., 2016). Thus, it is plausible that the airways are not missing but rather obliterated to the extent that they are no longer visible on CT scans (Díaz, 2018). Another interesting result is the decreasing number of GAC from generation 5 onwards in both groups. Using a dichotomous branching model of respiratory airways, which delivers an exponential law for GACs (2^n with n the generation number), one could predict a GAC of 32 at the 5*th* generation, which validates the GAC reached in the Control group for that generation (31.83). The limitations of CT resolution can explain the unexpected decreasing trend observed in both groups after the 5*th* generation. In effect, previous contributions have noted a similar tendency, attributing such reduction to the inability of CT images to resolve airways with lumen diameters smaller than the voxel resolution, typically around 1–2 *mm* (Diaz et al., 2015; Kirby et al., 2018).

Our study reveals a substantial increase in lumen volume for the COPD group, particularly for the 4*th* and 5*th* generations, both at EE and EI; see Figure 7. When comparing our findings to previous studies, we identify some discrepancies. Diaz et al. (2015) reported that never smokers experiencing lower FEV_1 have reduced lumen volume, while Koyama et al. (2012b) reported a

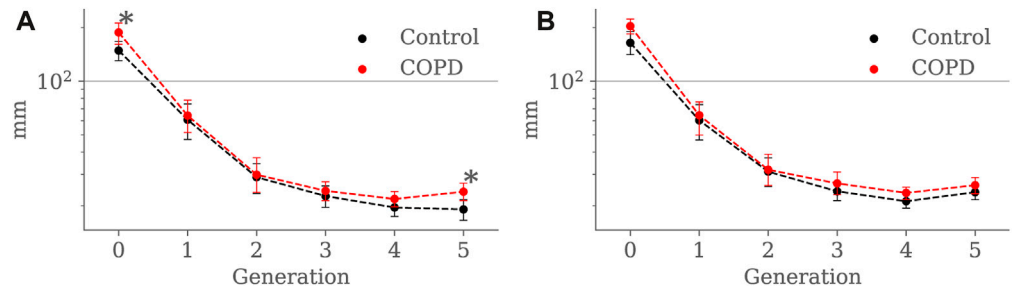

FIGURE 8
Airway segment length comparison between the Control and COPD groups from generation 0 to 5: **(A)** at EE, and **(B)** at EI. Dots represent mean values, and the error bars are confidence intervals. Nomenclature: *$p < 0.05$.

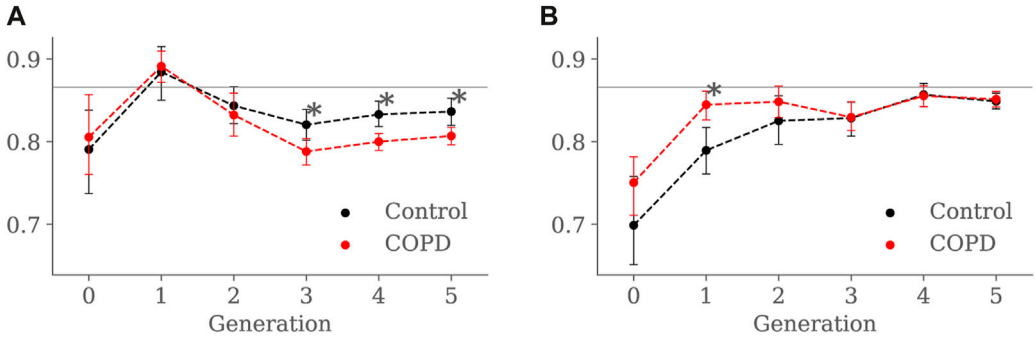

FIGURE 9
Airway luminal eccentricity comparison between the Control and COPD groups from generation 0 to 5: **(A)** at EE, and **(B)** at EI. Dots represent mean values, and the error bars are confidence intervals. Nomenclature: *$p < 0.05$.

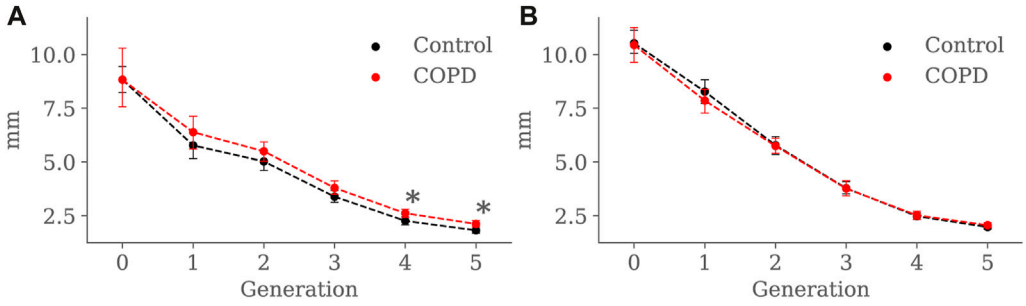

FIGURE 10
Airway minimum radius comparison between the Control and COPD groups from generation 0 to 5: **(A)** at EE, and **(B)** at EI. Dots represent mean values, and the error bars are confidence intervals. Nomenclature: *$p < 0.05$.

reduction of the luminal volume with the progression of the disease in terms of the GOLD classification. These results suggest a correlation between luminal volume reduction, expiratory airflow limitation, and disease severity. Therefore, the greater lumen volume observed in our patients with COPD seems counterintuitive because due to changes in intrinsic lung properties related to emphysema, loss of radial attachments to outer airway walls should produce lower distending forces acting on these peripheral airways, resulting in lower volume (Linhartová et al., 1971). However, thinner airway walls may predispose to airway closure, in which case the increased lumen volume at EE could represent trapped air above the point of collapse (Wilson et al., 1974) with consequent pathologic dilatation of the airways. Since the method used in our study does not allow for assessing airway wall thickness, we can only speculate at this point. Unfortunately, previous histological and imaging studies of proximal airway morphology have yielded conflicting results about airway wall thickness. Some studies on smokers have

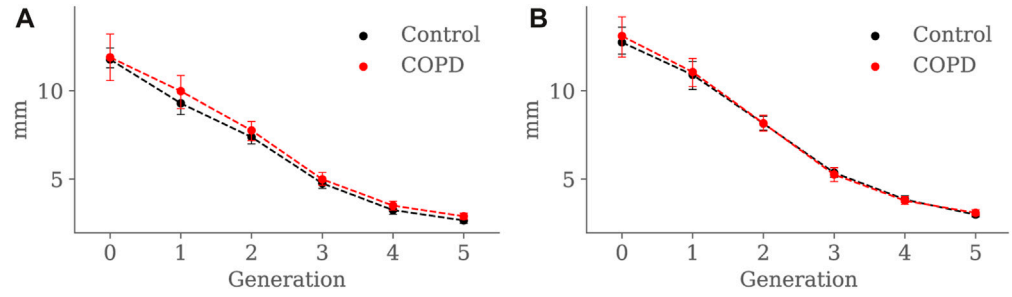

FIGURE 11
Airway average radius comparison between the Control and COPD groups from generation 0 to 5: **(A)** at EE, and **(B)** at EI. Dots represent mean values, and the error bars are confidence intervals. Nomenclature: *$p < 0.05$.

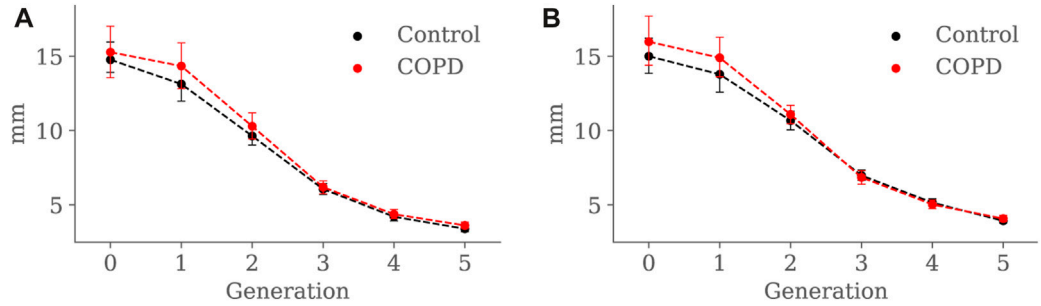

FIGURE 12
Airway maximum radius comparison between the Control and COPD groups from generation 0 to 5: **(A)** at EE, and **(B)** at EI. Dots represent mean values, and the error bars are confidence intervals. Nomenclature: * = $p < 0.05$.

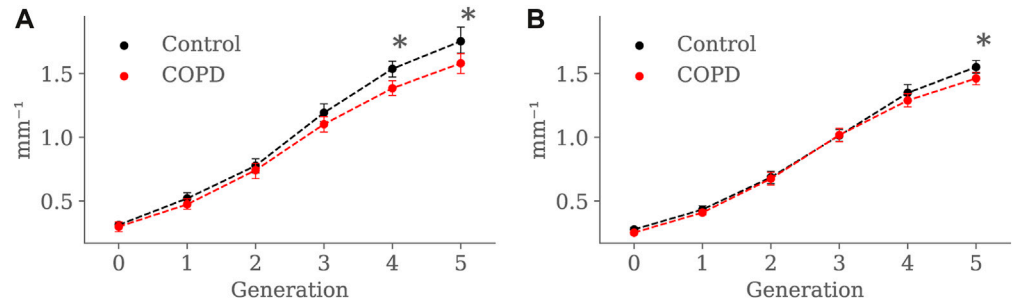

FIGURE 13
Airway SA:V ratio comparison between the Control and COPD groups from generation 0 to 5: **(A)** at EE, and **(B)** at EI. Dots represent mean values, and the error bars are confidence intervals. Nomenclature: * = $p < 0.05$.

demonstrated mural thickening of the proximal airways, particularly in mild COPD (Tiddens et al., 1995; Grydeland et al., 2010). Conversely, more extensive imaging studies, including subjects with a broad spectrum of airflow obstruction, have found thinner-walled proximal airways in patients with COPD compared to Control subjects (Smith et al., 2014; Washko et al., 2014).

Our results indicate that airways in COPD patients tend to be longer than in Controls; see Figure 8. Further, in Table 1, we observe that lung volumes are more prominent in COPD patients than in Control subjects. These findings align with the tendency of lungs affected by COPD to be larger than normal lungs due to loss of lung elastic recoil, and the airways embedded in the lung tissue would elongate as the lung inflates, their length increasing by the cube root of lung volume (Tanabe et al., 2017). Even when some investigators have reported shorter airways in patients with COPD, those findings come from subjects with advanced emphysema (McDonough et al., 2011; Tanabe et al., 2017). In such circumstances, disruption of the acinar fiber networks reduces the tensile forces they exert on the proximal structures, mainly on the terminal and preterminal airways that will retract toward the larger, more central airways, decreasing length; at the same time, they will withdraw from the acinar structures,

thus increasing the acinar space, the hallmark of emphysema (Mitzner, 2011; Weibel, 2013). Nevertheless, we believe that this may not be the case in our study, considering that our COPD group is at an early stage of the disease (GOLD I). Therefore, our patients' airway lengthening could result from higher lung volumes associated with mild emphysema and passive hyperinflation, indicated by the increased LAA% and reduced DLCO; see Table 1.

For the COPD group at EE, less eccentric (i.e., more circular) airways along with higher length may be an expression of less frequent branching patterns at generations 3–5; see Figure 9A and Figure 8A, respectively. In the bronchial tree, the bifurcation point identifies the division of an airway, where the daughter branches separate. Frequent branching could make airway cross sections mostly non-circular (i.e., more eccentric), as shown by Eskandari et al. (2013). However, suppose the collapse of one of the two daughter branches. In that case, a bifurcation point cannot be identified, and the morphology of the remaining daughter branch is considered part of the main branch. The result is a spurious increase in the airway length, volume, and circularity (lower luminal eccentricity).Consequently, the greater volume, length, and circularity found in the airways of COPD patients at EE may represent less frequent branching patterns at generations 3 to 5; see Figure 7A and Figure 8A, respectively. Interestingly, Choi et al. (2015), Choi et al. (2017) reported a positive correlation between length and circularity with airway remodeling by chronic inflammation in COPD and asthma. Note that differences in the expiratory luminal eccentricity are due to the reduced minimum radius in Figure 10A for the same generations, considering that similar values are observed for the average and maximum radius; see Figure 11 and Figure 12, respectively.

When comparing groups at EI, Control subjects displayed less eccentric (more circular) proximal airways than the COPD subjects, see Figure 9B. Furthermore, the luminal eccentricity in the COPD group increased to the same values in the Control group from the 3^{rd} to 5^{th} generations. Consistent with our findings, Choi et al. (2017) reported similar tendencies for their Control and COPD group. In their study, Control subjects had more circular proximal airways, and the circularity was reduced while advancing to the distal generations. Further, they reported that the COPD group presented significantly lesser circularity for the proximal and distal airways but no significant differences for both groups at distal airways. The higher luminal eccentricity in the proximal airways of COPD patients may suggest that chronic bronchitis or inflammation-related airway remodeling affected large airways more than small ones (Choi et al., 2017).

At EE, the Control group exhibited higher SA: V than the COPD group for the 4*th* and 5*th* generations, as observed in Figure 13, but at EI, higher SA:V was only found in the 5*th* generation. As expected, there was a generation-to-generation increase in SA:V in both groups at EE and EI, which can be attributed to a greater loss in luminal volume than surface area as the airways divide towards the periphery, facilitating proper gas exchange (Bodduluri et al., 2021). Despite significant differences in the distal generations, characterizing airway remodeling in terms of narrowing or loss as described in Bodduluri et al. (2021) becomes challenging when studying SA:V by generation. When considering the airways as tubular structures, different combinations of length and radius can result in equivalent surface area and volume. Consequently, the same SA:V value can be obtained in both scenarios: when the airway shortens and thickens (possible loss) and when it lengthens and narrows (possible narrowing).

We perform a global study by adding the SA:V from all available airway segments for each subject and comparing the results for both groups. At EE, the global SA:V was 74.81 ± 42.91 mm^{-1} and 77.33 ± 43.36 mm^{-1} for the Control and COPD group, respectively. At EI, we observed significant differences between the Control and COPD groups, with values of 210.98 ± 39.49 mm^{-1} and 129.52 ± 28.97 mm^{-1} ($p < 0.026$), respectively. In accordance with our global results, Bodduluri et al. (Bodduluri et al., 2021) also reported significant differences for COPD GOLD stages 0 and I-II, which correspond to our Control and COPD groups, respectively. Notably, these global results could be associated with the TAC, as depicted in Figure 6A, where significant differences were exclusively observed at EI. In the same study, Bodduluri et al. found that individuals with predominant airway loss had lower TAC than those with predominant airway narrowing. The link between TAC and global SA:V can be explained by the global measure's reliance on summing this value from each airway. Such a relationship is strengthened when accounting for a larger number of small airways at distal generations, where higher SA:V values are observed; see Figure 13.

The present study has certain limitations that should be addressed in future contributions. First, we considered a small number of patients for each of the groups analyzed. To address this, future research should include a larger cohort, comprising a non-smoking Control group, as well as groups representing various stages of disease progression and severity (GOLD I to IV), as proposed in previous studies by Kirby et al. (2018), Kirby et al. (2021). Furthermore, the Mann-Whitney test is prone to type II errors when used with a reduced sample size. Consequently, expanding the patient cohort can be a practical step to reduce this type of error. Second, our method relies on a semi-automated airway segmentation process using the ITK-SNAP software. Manual seeds are placed on visually identified airways to create the level-set-based binary mask. However, the seed placement may be affected by resolution limitations, posing challenges in accurate airway identification. To enhance precision, researchers should consider alternative approaches involving fully automated tools or commercial software for segmentation, such as the one mentioned in Diaz-Pinto et al. (2022). Third, our approach does not assess bronchial wall thickness to validate our findings. To address this limitation, future studies should incorporate previously used markers such as Wall Area (WA) and Lumen Area (LA) and perform comparative analyses. A feasible approach to assess airway thickness with our SIGA method is by adapting the "Full-width at half maximum" (Coxson, 2008) for airway thickness assessment using NURBS surfaces. This can be achieved by projecting normal vectors from the surface and measuring the image intensity. Moreover, the functional formulation of the SIGA method offers versatility, not only in controlling the surface evolution but also in adapting mechanical-related regularizers for studying bronchial wall mechanical deformation, as demonstrated in recent studies (Cox et al., 2022). Such a study could contribute to regional understanding of deformation in the ariways, as done in the past for the lung tissue Hurtado et al. (2017). Fourth, to avoid marker biases, it is crucial to consider the addition of normalization schemes in our research. This is particularly important as observed in asthma studies where

conflicting results have been reported due to the lack of demographic normalization schemes (Choi et al., 2015). Finally, our study lacks a comparison of the morphology characterization with respect to pulmonary function tests and the quantification of emphysema. Future work should explore correlations between morphological changes, the airflow reduction in the groups under consideration, and the severity of emphysema.

Data availability statement

The original contributions presented in the study are included in the article/Supplementary Material, further inquiries can be directed to the corresponding author.

Ethics statement

The studies involving humans were approved by the ethics committee of the Pontificia Universidad Católica de Chile. The studies were conducted in accordance with the local legislation and institutional requirements. The participants provided their written informed consent to participate in this study.

Author contributions

DO-P: Formal Analysis, Investigation, Methodology, Software, Validation, Visualization, Writing–original draft, Writing–review and editing. OD: Conceptualization, Supervision, Validation, Writing–review and editing. JR: Conceptualization, Supervision, Validation, Writing–review and editing. DH: Conceptualization, Formal Analysis, Funding acquisition, Methodology, Supervision, Writing–original draft, Writing–review and editing.

Funding

The author(s) declare financial support was received for the research, authorship, and/or publication of this article. This work received financial support from the Chilean National Agency for Research and Development (ANID) through grant FONDECYT Regular #1220465 and #1141108.

Acknowledgments

DO-P acknowledges the support of ANID through the Doctoral ANID-Subdireccion de Capital Humano/Doctorado Nacional/2021-21211597.

Conflict of interest

The authors declare that the research was conducted in the absence of any commercial or financial relationships that could be construed as a potential conflict of interest.

The author(s) declared that they were an editorial board member of Frontiers, at the time of submission. This had no impact on the peer review process and the final decision.

Publisher's note

References

Agustí, A., Celli, B. R., Criner, G. J., Halpin, D., Anzueto, A., Barnes, P., et al. (2023). Global initiative for chronic obstructive lung disease 2023 report: gold executive summary. *Am. J. Respir. Crit. Care Med.* 207, 819–837. doi:10.1164/rccm.202301-0106pp

Ananth, S., and Hurst, J. R. (2023). Erj advances: state of the art in definitions and diagnosis of copd. *Eur. Respir. J.* 61, 2202318. doi:10.1183/13993003.02318-2022

Arrieta, C., Uribe, S., Sing-Long, C., Hurtado, D., Andia, M., Irarrazaval, P., et al. (2017). Simultaneous left and right ventricle segmentation using topology preserving level sets. *Biomed. Signal Process. Control* 33, 88–95. doi:10.1016/j.bspc.2016.11.002

Bhatt, S. P., Washko, G. R., Hoffman, E. A., Newell, J. D., Jr, Bodduluri, S., Diaz, A. A., et al. (2019). Imaging advances in chronic obstructive pulmonary disease. insights from the genetic epidemiology of chronic obstructive pulmonary disease (copdgene) study. *Am. J. Respir. Crit. care Med.* 199, 286–301. doi:10.1164/rccm.201807-1351so

Bodduluri, S., Bhatt, S. P., Hoffman, E. A., Newell, J. D., Martinez, C. H., Dransfield, M. T., et al. (2017). Biomechanical ct metrics are associated with patient outcomes in copd. *Thorax* 72, 409–414. doi:10.1136/thoraxjnl-2016-209544

Bodduluri, S., Kizhakke Puliyakote, A., Nakhmani, A., Charbonnier, J.-P., Reinhardt, J. M., and Bhatt, S. P. (2021). Computed tomography–based airway surface area–to-volume ratio for phenotyping airway remodeling in chronic obstructive pulmonary disease. *Am. J. Respir. Crit. care Med.* 203, 185–191. doi:10.1164/rccm.202004-0951oc

Bodduluri, S., Newell, J. D., Jr, Hoffman, E. A., and Reinhardt, J. M. (2013). Registration-based lung mechanical analysis of chronic obstructive pulmonary disease (copd) using a supervised machine learning framework. *Acad. Radiol.* 20, 527–536. doi:10.1016/j.acra.2013.01.019

Bodduluri, S., Puliyakote, A. S. K., Gerard, S. E., Reinhardt, J. M., Hoffman, E. A., Newell, J. D., et al. (2018). Airway fractal dimension predicts respiratory morbidity and mortality in copd. *J. Clin. investigation* 128, 5676–5382. doi:10.1172/jci125987

Boes, J. L., Hoff, B. A., Bule, M., Johnson, T. D., Rehemtulla, A., Chamberlain, R., et al. (2015). Parametric response mapping monitors temporal changes on lung ct scans in the subpopulations and intermediate outcome measures in copd study (spiromics). *Acad. Radiol.* 22, 186–194. doi:10.1016/j.acra.2014.08.015

Celli, B., Fabbri, L., Criner, G., Martinez, F. J., Mannino, D., Vogelmeier, C., et al. (2022). Definition and nomenclature of chronic obstructive pulmonary disease: time for its revision. *Am. J. Respir. Crit. Care Med.* 206, 1317–1325. doi:10.1164/rccm.202204-0671pp

Choi, S., Haghighi, B., Choi, J., Hoffman, E. A., Comellas, A. P., Newell, J. D., et al. (2017). Differentiation of quantitative ct imaging phenotypes in asthma versus copd. *BMJ open Respir. Res.* 4, e000252. doi:10.1136/bmjresp-2017-000252

Choi, S., Hoffman, E. A., Wenzel, S. E., Castro, M., Fain, S. B., Jarjour, N. N., et al. (2015). Quantitative assessment of multiscale structural and functional alterations in asthmatic populations. *J. Appl. physiology* 118, 1286–1298. doi:10.1152/japplphysiol.01094.2014

Cox, A., Ortiz-Puerta, D., Sotelo, J., Uribe, S., and Hurtado, D. E. (2022). Mechanics-informed snakes isogeometric analysis (misiga): an image-based method for the estimation of local deformation and strain in blood vessels. *Eng. Comput.* 38, 4043–4060. doi:10.1007/s00366-022-01738-y

Coxson, H. O. (2008). Quantitative computed tomography assessment of airway wall dimensions: current status and potential applications for phenotyping chronic obstructive pulmonary disease. *Proc. Am. Thorac. Soc.* 5, 940–945. doi:10.1513/pats.200806-057qc

Dedè, L., and Quarteroni, A. (2015). Isogeometric analysis for second order partial differential equations on surfaces. *Comput. Methods Appl. Mech. Eng.* 284, 807–834. doi:10.1016/j.cma.2014.11.008

Díaz, A. A. (2018). The case of missing airways in chronic obstructive pulmonary disease. *Am. J. Respir. Crit. Care Med.* 197, 4–6. doi:10.1164/rccm.201708-1585ed

Diaz, A. A., Estépar, R. S. J., and Washko, G. R. (2016). Computed tomographic airway morphology in chronic obstructive pulmonary disease. remodeling or innate anatomy? *Ann. Am. Thorac. Soc.* 13, 4–9. doi:10.1513/annalsats.201506-371pp

Diaz, A. A., Rahaghi, F. N., Ross, J. C., Harmouche, R., Tschirren, J., San José Estépar, R., et al. (2015). Understanding the contribution of native tracheobronchial structure to lung function: ct assessment of airway morphology in never smokers. *Respir. Res.* 16, 23–29. doi:10.1186/s12931-015-0181-y

Diaz-Pinto, A., Alle, S., Nath, V., Tang, Y., Ihsani, A., Asad, M., et al. (2022). *Monai label: a framework for ai-assisted interactive labeling of 3d medical images*. *arXiv preprint arXiv:2203.12362*.

Dudurych, I., Muiser, S., McVeigh, N., Kerstjens, H. A., van den Berge, M., de Bruijne, M., et al. (2022). Bronchial wall parameters on ct in healthy never-smoking, smoking, copd, and asthma populations: a systematic review and meta-analysis. *Eur. Radiol.* 32, 5308–5318. doi:10.1007/s00330-022-08600-1

Eskandari, M., Javili, A., and Kuhl, E. (2016). Elastosis during airway wall remodeling explains multiple co-existing instability patterns. *J. Theor. Biol.* 403, 209–218. doi:10.1016/j.jtbi.2016.05.022

Eskandari, M., Kuschner, W. G., and Kuhl, E. (2015). Patient-specific airway wall remodeling in chronic lung disease. *Ann. Biomed. Eng.* 43, 2538–2551. doi:10.1007/s10439-015-1306-7

Eskandari, M., Pfaller, M. R., and Kuhl, E. (2013). On the role of mechanics in chronic lung disease. *Materials* 6, 5639–5658. doi:10.3390/ma6125639

Galbán, C. J., Han, M. K., Boes, J. L., Chughtai, K. A., Meyer, C. R., Johnson, T. D., et al. (2012). Computed tomography–based biomarker provides unique signature for diagnosis of copd phenotypes and disease progression. *Nat. Med.* 18, 1711–1715. doi:10.1038/nm.2971

Gao, X., Loriot, S., and Tagliasacchi, A. (2020). "Triangulated surface mesh skeletonization," in CGAL User and reference manual *(CGAL editorial board)*. 5.1 edn.

GOLD (2023). *2023 GOLD report. Global initiative for chronic obstructive lung disease - GOLD*.

Grydeland, T. B., Dirksen, A., Coxson, H. O., Eagan, T. M., Thorsen, E., Pillai, S. G., et al. (2010). Quantitative computed tomography measures of emphysema and airway wall thickness are related to respiratory symptoms. *Am. J. Respir. Crit. care Med.* 181, 353–359. doi:10.1164/rccm.200907-1008oc

Hoesein, F. A. M., de Hoop, B., Zanen, P., Gietema, H., Kruitwagen, C. L., van Ginneken, B., et al. (2011). Ct-quantified emphysema in male heavy smokers: association with lung function decline. *Thorax* 66, 782–787. doi:10.1136/thx.2010.145995

Hogg, J. C., and Timens, W. (2009). The pathology of chronic obstructive pulmonary disease. *Annu. Rev. Pathology Mech. Dis.* 4, 435–459. doi:10.1146/annurev.pathol.4.110807.092145

Hughes, T. J., Cottrell, J. A., and Bazilevs, Y. (2005). Isogeometric analysis: cad, finite elements, nurbs, exact geometry and mesh refinement. *Comput. methods Appl. Mech. Eng.* 194, 4135–4195. doi:10.1016/j.cma.2004.10.008

Hurtado, D. E., and Henao, D. (2014). Gradient flows and variational principles for cardiac electrophysiology: toward efficient and robust numerical simulations of the electrical activity of the heart. *Comput. Methods Appl. Mech. Eng.* 273, 238–254. doi:10.1016/j.cma.2014.02.002

Hurtado, D. E., Villarroel, N., Andrade, C., Retamal, J., Bugedo, G., and Bruhn, A. R. (2017). Spatial patterns and frequency distributions of regional deformation in the healthy human lung. *Biomechanics Model. Mechanobiol.* 16, 1413–1423. doi:10.1007/s10237-017-0895-5

Kass, M., Witkin, A., and Terzopoulos, D. (1988). Snakes: active contour models. *Int. J. Comput. Vis.* 1, 321–331. doi:10.1007/bf00133570

Kirby, M., Smith, B. M., Tanabe, N., Hogg, J. C., Coxson, H. O., Sin, D. D., et al. (2021). Computed tomography total airway count predicts progression to copd in at-risk smokers. *ERJ Open Res.* 7, 00307–02021. doi:10.1183/23120541.00307-2021

Kirby, M., Tanabe, N., Tan, W. C., Zhou, G., Obeidat, M., Hague, C. J., et al. (2018). Total airway count on computed tomography and the risk of chronic obstructive pulmonary disease progression. findings from a population-based study. *Am. J. Respir. Crit. care Med.* 197, 56–65. doi:10.1164/rccm.201704-0692oc

Kirby, M., Tanabe, N., Vasilescu, D. M., Cooper, J. D., McDonough, J. E., Verleden, S. E., et al. (2020). Computed tomography total airway count is associated with the number of micro–computed tomography terminal bronchioles. *Am. J. Respir. Crit. Care Med.* 201, 613–615. doi:10.1164/rccm.201910-1948le

Koo, H.-K., Vasilescu, D. M., Booth, S., Hsieh, A., Katsamenis, O. L., Fishbane, N., et al. (2018). Small airways disease in mild and moderate chronic obstructive pulmonary disease: a cross-sectional study. *Lancet Respir. Med.* 6, 591–602. doi:10.1016/s2213-2600(18)30196-6

Koyama, H., Ohno, Y., Nishio, M., Takenaka, D., Yoshikawa, T., Matsumoto, S., et al. (2012a). Three-dimensional airway lumen volumetry: comparison with bronchial wall area and parenchymal densitometry in assessment of airway obstruction in pulmonary emphysema. *Br. J. Radiology* 85, 1525–1532. doi:10.1259/bjr/22602417

Koyama, H., Ohno, Y., Yamazaki, Y., Onishi, Y., Takenaka, D., Yoshikawa, T., et al. (2012b). Quantitative bronchial luminal volumetric assessment of pulmonary function loss by thin-section mdct in pulmonary emphysema patients. *Eur. J. radiology* 81, 384–388. doi:10.1016/j.ejrad.2010.12.042

Labaki, W. W., Gu, T., Murray, S., Hatt, C. R., Galbán, C. J., Ross, B. D., et al. (2019). Voxel-wise longitudinal parametric response mapping analysis of chest computed tomography in smokers. *Acad. Radiol.* 26, 217–223. doi:10.1016/j.acra.2018.05.024

Labarca, G., Bustamante, A., Valdivia, G., Díaz, R., Huete, Á., Mac Nab, P., et al. (2017). The boundaries of mild chronic obstructive pulmonary disease (copd): design of the searching clinical copd onset (soon) study. *BMJ open* 7, e015731. doi:10.1136/bmjopen-2016-015731

Linhartová, A., Anderson, eA., Jr, and Foraker, A. (1971). Radial traction and bronchiolar obstruction in pulmonary emphysema. observed and theoretical aspects. *Archives pathology* 92, 384–391.

Madani, A., De Maertelaer, V., Zanen, J., and Gevenois, P. A. (2007). Pulmonary emphysema: radiation dose and section thickness at multidetector ct quantification—comparison with macroscopic and microscopic morphometry. *Radiology* 243, 250–257. doi:10.1148/radiol.2431060194

McDonough, J. E., Yuan, R., Suzuki, M., Seyednejad, N., Elliott, W. M., Sanchez, P. G., et al. (2011). Small-airway obstruction and emphysema in chronic obstructive pulmonary disease. *N. Engl. J. Med.* 365, 1567–1575. doi:10.1056/nejmoa1106955

Mitzner, W. (2011). Emphysema: a disease of small airways or lung parenchyma? *N. Engl. J. Med.* 365, 1637–1639. doi:10.1056/nejme1110635

Miyawaki, S., Tawhai, M. H., Hoffman, E. A., Wenzel, S. E., and Lin, C.-L. (2017). Automatic construction of subject-specific human airway geometry including trifurcations based on a ct-segmented airway skeleton and surface. *Biomechanics Model. Mechanobiol.* 16, 583–596. doi:10.1007/s10237-016-0838-6

Nakano, Y., Wong, J. C., de Jong, P. A., Buzatu, L., Nagao, T., Coxson, H. O., et al. (2005). The prediction of small airway dimensions using computed tomography. *Am. J. Respir. Crit. care Med.* 171, 142–146. doi:10.1164/rccm.200407-874oc

Nishimura, M., Makita, H., Nagai, K., Konno, S., Nasuhara, Y., Hasegawa, M., et al. (2012). Annual change in pulmonary function and clinical phenotype in chronic obstructive pulmonary disease. *Am. J. Respir. Crit. care Med.* 185, 44–52. doi:10.1164/rccm.201106-0992oc

Oakes, J. M., Scadeng, M., Breen, E. C., Marsden, A. L., and Darquenne, C. (2012). Rat airway morphometry measured from *in situ* mri-based geometric models. *J. Appl. physiology* 112, 1921–1931. doi:10.1152/japplphysiol.00018.2012

Ortiz-Puerta, D., Cox, A., and Hurtado, D. E. (2022). Snakes isogeometric analysis (siga): towards accurate and flexible geometrical models of the respiratory airways. *Comput. Methods Appl. Mech. Eng.* 394, 114841. doi:10.1016/j.cma.2022.114841

Smith, B. M., Hoffman, E. A., Rabinowitz, D., Bleecker, E., Christenson, S., Couper, D., et al. (2014). Comparison of spatially matched airways reveals thinner airway walls in copd. the multi-ethnic study of atherosclerosis (mesa) copd study and the subpopulations and intermediate outcomes in copd study (spiromics). *Thorax* 69, 987–996. doi:10.1136/thoraxjnl-2014-205160

Tanabe, N., Vasilescu, D. M., McDonough, J. E., Kinose, D., Suzuki, M., Cooper, J. D., et al. (2017). Micro–computed tomography comparison of preterminal bronchioles in centrilobular and panlobular emphysema. *Am. J. Respir. Crit. care Med.* 195, 630–638. doi:10.1164/rccm.201602-0278oc

Tawhai, M. H., Hoffman, E. A., and Lin, C.-L. (2009). The lung physiome: merging imaging-based measures with predictive computational models. *Wiley Interdiscip. Rev. Syst. Biol. Med.* 1, 61–72. doi:10.1002/wsbm.17

Tiddens, H., Pare, P., Hogg, J., Hop, W., Lambert, R., and De Jongste, J. (1995). Cartilaginous airway dimensions and airflow obstruction in human lungs. *Am. J. Respir. Crit. care Med.* 152, 260–266. doi:10.1164/ajrccm.152.1.7599833

Vestbo, J., Edwards, L. D., Scanlon, P. D., Yates, J. C., Agusti, A., Bakke, P., et al. (2011). Changes in forced expiratory volume in 1 second over time in copd. *N. Engl. J. Med.* 365, 1184–1192. doi:10.1056/nejmoa1105482

Washko, G. R., Diaz, A., Kim, V., Barr, R. G., Dransfield, M. T., Schroeder, J., et al. (2014). Computed tomographic measures of airway morphology in smokers and never-smoking normals. *J. Appl. physiology* 116, 668–673. doi:10.1152/japplphysiol.00004.2013

Weibel, E. R. (2013). It takes more than cells to make a good lung. *Am. J. Respir. Crit. care Med.* 187, 342–346. doi:10.1164/rccm.201212-2260oe

Wilson, A., Massarella, G., and Pride, N. (1974). Elastic properties of airways in human lungs post mortem. *Am. Rev. Respir. Dis.* 110, 716–729. doi:10.1164/arrd.1974.110.6P1.716

Yuan, R., Hogg, J. C., Paré, P. D., Sin, D. D., Wong, J., Nakano, Y., et al. (2009). Prediction of the rate of decline in fev1 in smokers using quantitative computed tomography. *Thorax* 64, 944–949. doi:10.1136/thx.2008.112433

Yushkevich, P. A., Piven, J., Hazlett, H. C., Smith, R. G., Ho, S., Gee, J. C., et al. (2006). User-guided 3d active contour segmentation of anatomical structures: significantly improved efficiency and reliability. *Neuroimage* 31, 1116–1128. doi:10.1016/j.neuroimage.2006.01.015

frontiers | Frontiers in Bioengineering and Biotechnology

TYPE Original Research
PUBLISHED 23 February 2024
DOI 10.3389/fbioe.2024.1351403

OPEN ACCESS

EDITED BY
Julie Choisne,
University of Auckland, New Zealand

REVIEWED BY
Qichang Mei,
Ningbo University, China
Maedeh Amirpour,
The University of Auckland, New Zealand

*CORRESPONDENCE
Bryce A. Killen,
bryce.killen@kuleuven.be

RECEIVED 06 December 2023
ACCEPTED 08 February 2024
PUBLISHED 23 February 2024

CITATION
Killen BA, Van Rossom S, Burg F, Vander Sloten J and Jonkers I (2024), *In-silico* techniques to inform and improve the personalized prescription of shoe insoles.
Front. Bioeng. Biotechnol. 12:1351403.
doi: 10.3389/fbioe.2024.1351403

In-silico techniques to inform and improve the personalized prescription of shoe insoles

Bryce A. Killen[1]*, Sam Van Rossom[2], Fien Burg[2], Jos Vander Sloten[3] and Ilse Jonkers[1]

[1]Human Movement Biomechanics Research Group, Department of Movement Sciences, KU Leuven, Leuven, Belgium, [2]Materialise Motion, Materialise, Leuven, Belgium, [3]Biomechanics Section, Department of Mechanical Engineering, Faculty of Engineering Sciences, KU Leuven, Heverlee (Leuven), Belgium

Background: Corrective shoe insoles are prescribed for a range of foot deformities and are typically designed based on a subjective assessment limiting personalization and potentially leading to sub optimal treatment outcomes. The incorporation of *in silico* techniques in the design and customization of insoles may improve personalized correction and hence insole efficiency.

Methods: We developed an *in silico* workflow for insole design and customization using a combination of measured motion capture, inverse musculoskeletal modelling as well as forward simulation approaches to predict the kinematic response to specific insole designs. The developed workflow was tested on twenty-seven participants containing a combination of healthy participants (7) and patients with flatfoot deformity (20).

Results: Average error between measured and simulated kinematics were 4.7 $\pm$ 3.1, 4.5 $\pm$ 3.1, 2.3 $\pm$ 2.3, and 2.3 $\pm$ 2.7° for the chopart obliquity, chopart anterior-posterior axis, tarsometatarsal first ray, and tarsometatarsal fifth ray joints respectively.

Discussion: The developed workflow offers distinct advantages to previous modeling workflows such as speed of use, use of more accessible data, use of only open-source software, and is highly automated. It provides a solid basis for future work on improving predictive accuracy by adapting the currently implemented insole model and incorporating additional data such as plantar pressure.

KEYWORDS

***in-silico*, musculoskeletal, insole ankle foot orthotic, ankle, design methodology**

Introduction

The foot-ankle is a highly intricate collection of bones, and joints supported by a complex system of soft tissues including ligaments, tendons, and muscles (Golanó et al., 2010; Merian et al., 2011). This complex structure is matched by the complex function it performs. The foot-ankle complex forms the connection with the ground and is essential for a majority of tasks of daily living, and all locomotion tasks (Matsui et al., 2017). Due to the complexity and its load bearing role, the foot-ankle is highly prone to injury and by extension dysfunction. Injuries to the foot-ankle complex can be acute in nature such as a lateral ligament tear, however chronic conditions may occur due to foot congenital predisposition, ligament overloading and subsequent laxity, inducing chronic pain and ultimately osteoarthritis (Arnold et al., 2019).

Treatment for many of these chronic conditions involves, in combination with conservative physical therapy, prescription of corrective insoles. Such insoles are common treatment for flatfoot deformity (Glassman et al., 2006; Kido et al., 2014; Su et al., 2017) which aim to correct the structural deformity and support the foot. Other common uses are for diabetes mellitus (Paton et al., 2011) whereby insoles are prescribed to alleviate high pressure concentrations under the foot. Despite their widespread use and prescription, the decision-making within the design process for patient-specific insole design is largely reliant on outdated, and subjective approaches (Bacarin et al., 2009; Paton et al., 2011).

The design of insoles is typically reliant predominantly on clinical experience of the podiatrist prescribing the insole. This clinical design-making is often supplemented by limited quantitative measurements such as static footprints and in some rare cases limited single plane x-ray imaging. These measurements and assessments fail to properly consider the function of the foot under dynamic conditions, where the insole should exert its corrective function. Despite this, attempts are being made to assess foot function more objectively through a range of different methods including video-based 2D movement analysis, dynamic plantar pressure measurement and in some cases 3D motion capture. The analysis of the dynamic motion of the numerous joints of the foot-ankle complex can allow for a deeper understanding of the dynamic deficits of individual patients and supplement the clinicians' decision-making process.

Combing 3D motion capture data with ground reaction force plate data together with musculoskeletal models in so-called inverse workflows allows for the estimation of parameters important for pathology description. These inverse workflows use measured data (i.e., marker trajectories and ground reaction forces) to estimate joint angles and subsequently joint moments using musculoskeletal models. These models are mathematical and physics-based representations of the human body and are used to estimate parameters which cannot be measured such as joint contact loading, and muscle forces. These parameters are often of high clinical interest and already serve to support clinical decision-making in many different clinical use cases (Killen et al., 2020). Related to foot-ankle function, such *in silico* techniques permit to estimate the strain on ligaments and the estimation of muscle forces which could be of particular interest in flatfoot pathologies where ligamentous and muscle dysfunction are often observed (Kaufman et al., 1999; Keegan et al., 2002; Boey et al., 2022). As such the combination of 3D motion capture data, and *in silico* musculoskeletal modelling already provides relevant information on dynamic foot-ankle function potentially prior to, as well as after, insole prescription (Mannisi et al., 2019; Sinclair et al., 2019). However, these approaches do not inform the design process. In fact, the application of the above-mentioned techniques would only be possible if multiple candidate insoles (with different geometries and stiffnesses) were produced, and their effect during dynamic motion subsequently measured and modelled. While this would provide valuable information and potentially the best insole specification, such an approach is infeasible due to increased time as well as cost requirements for manufacturing and testing.

Instead of relying on the manufacturing and testing of multiple insoles, a convenient solution is to instead create an *in silico* representation of the insole which allows for the virtual testing of multiple insole designs without the need to explicitly manufacture them. Previous research has invested in such approaches using highly complex finite-element analysis (Telfer et al., 2014; Telfer et al., 2017). Although these approaches allow integrating highly complex material definitions for the insole as well as the studying the effect on skin tissue pressure, these models often require a specialized and expensive computational infrastructure, infeasible computational times, highly specialized knowledge, and expertise to create and execute, and typically these models do not consider the gait cycle and dynamics of the entire foot-ankle complex.

In this paper we will describe an *in silico* workflow which combines motion capture data, musculoskeletal modelling, and a simplified insole model to predict the effect of a prescribed on a participants' gait pattern, with specific interest in flatfoot deformity. Such a predictive model would permit the optimization of mechanical parameters for insole design to correct the highly complex and dynamic behavior of the foot-ankle during gait.

Materials and equipment

The developed workflow was implemented and tested on twenty-seven participants containing a combination of healthy participants (n = 7) and patients with flatfoot deformity (n = 20). These participants were measured as part of an industry collaboration project (Flemish Government IWT: *Aladyn* project) between KU Leuven and industrial partner Materialise Motion. Each participants' data was collected as part of an extensive insole testing process whereby multiple insoles and highly detailed foot-ankle motion-capture data were collected in different conditions, including barefoot, in a standardized shod condition (i.e., "labshoe" condition), and with two different types of insoles both designed to apply a mid-forefoot correction.

Participants were fitted with an extensive foot-ankle centered motion capture marker set (Figure 1) with the addition to a four-marker cluster on the tibia. Following fitting of the marker set, participants performed a static calibration trial standing in a pre-defined position (Cappozzo et al., 1995) which was captured by a Vicon (*Vicon*, Oxford Metrics, United Kingdom) motion capture system consisting of 16 cameras collecting at 200 Hz. In addition to marker trajectories, ground reaction forces from in-ground force plates (AMTI, 1,000 Hz) were acquired synchronously. For each participant, and each condition, four repeated walking trials were collected and used in the developed workflow. Marker trajectories were exported from motion capture data following standard labelling and gap filling procedures in Vicon Nexus (*Vicon*, Oxford Metrics, United Kingdom). Measured data was first used to define the initial walking gait pattern using data from the shod condition where each participant wore a standardized lab footwear without insoles.

Methods

The developed *in silico* workflow (Figure 2) is implemented in OpenSim (version 3.3). In short, the workflow combines *in-vivo* measured marker trajectories with an extended musculoskeletal model of the foot-ankle complex to determine patient-specific

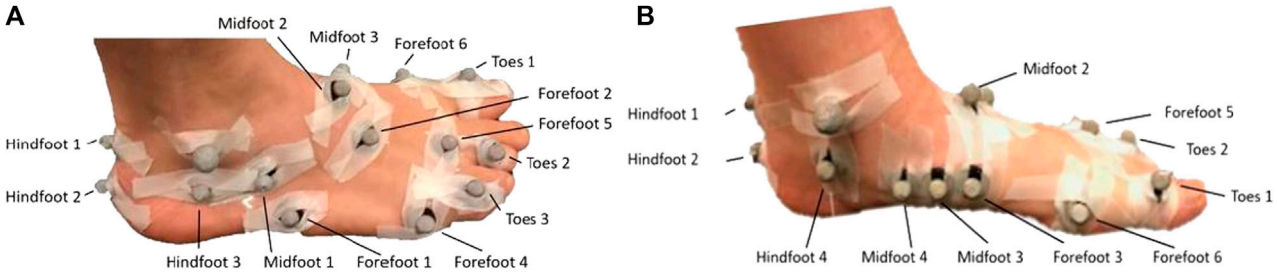

FIGURE 1
View of the lateral aspect **(A)** and medial aspect **(B)** of a participant fit with the extensive foot-ankle centered marker with markers placed on each of the modelled bone segments.

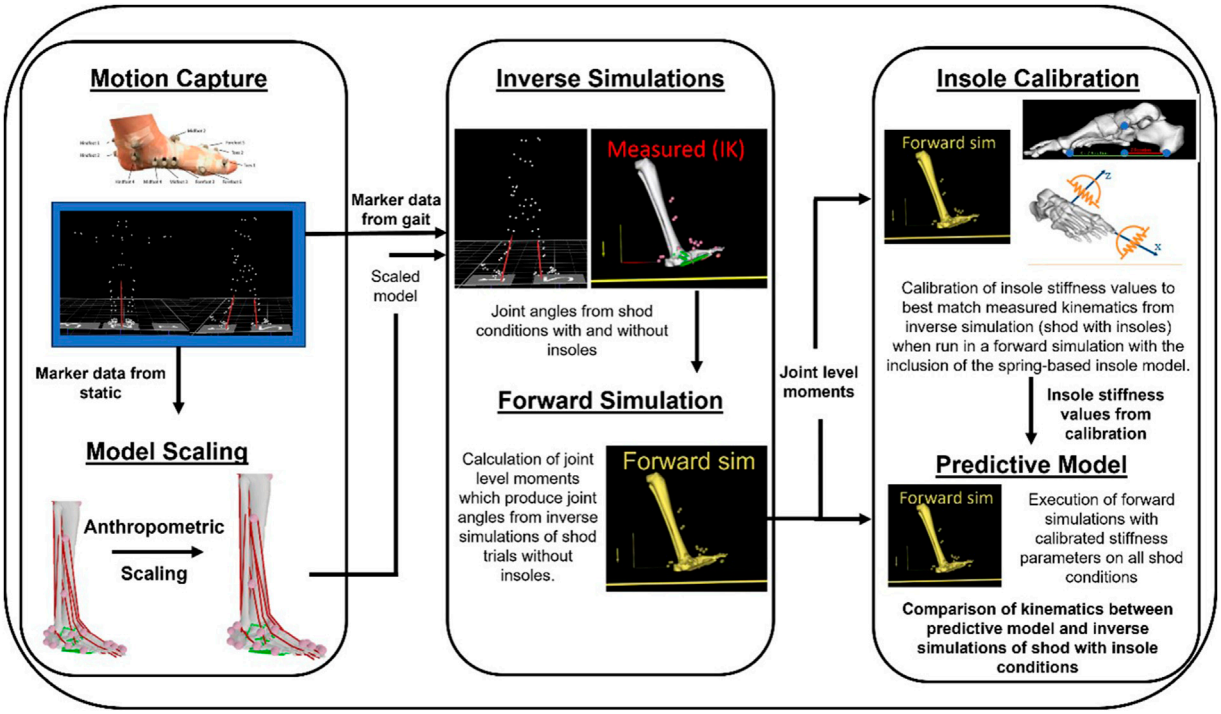

FIGURE 2
Overview schematic of the workflow from data collection (Motion Capture), musculoskeletal model personalization (Model Scaling), estimation of joint kinematics from each condition (Inverse Simulations), calibration of the insole model stiffness values (Insole Calibration), and the combination of forward simulation outputs (i.e, from shod without insole condition) with the calibrated insole model to estimate individual patient responses (Predictive Model).

foot-ankle kinematics and moments. A model of the insole consisting of multiple springs is added to the mid/forefoot segments and a predictive simulation then calculates the estimated change in foot-ankle kinematics. The stiffness of these springs is defined in a calibration step where we iteratively vary spring stiffness constants to best match average measured insole condition. Each of these steps is described in detail in subsequent sections.

Musculoskeletal model

When considering *in silico* applications for insole design, an adequate representation of the complex foot-ankle structure, including different bones, joints and degrees of freedom is vital. Whereas the inclusion of complex hip and knee joint definitions received quite some attention, relatively less attention is paid to include more complex definitions of the ankle and foot joints within musculoskeletal models. Hence, degrees of freedom in the ankle and foot joints are often highly simplified (Figure 3). Specifically, these models often neglect the degrees of freedom of the mid- and forefoot joint, often treating them as a single rigid body. As a result, many musculoskeletal models only have three degrees of freedom, specifically ankle and metatarsal-phalangeal joint plantar-/dorsi-flexion, and subtalar inversion/eversion. While potentially not influential when studying more proximal joints (i.e., knee or hip) these simplifications are a major hurdle when studying the foot and

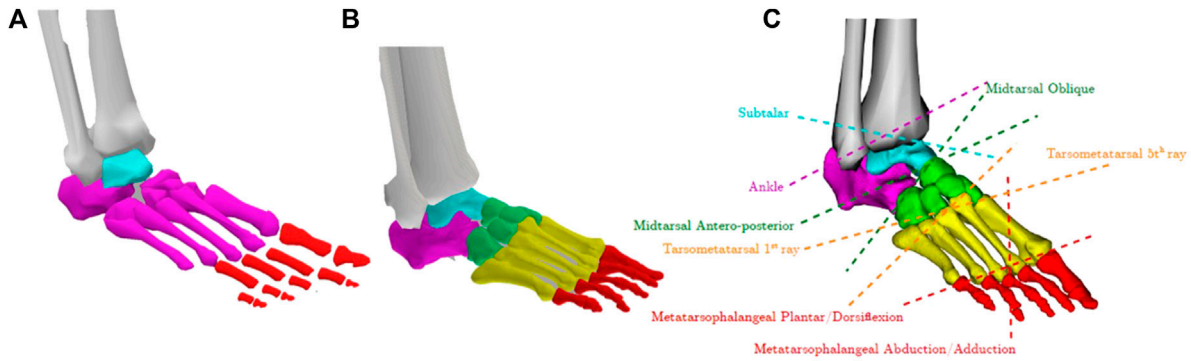

FIGURE 3
(A) Typical representation of a 3 degrees of freedom foot-ankle in many generic musculoskeletal models where each colour represents a different foot segment. **(B)** The previously developed complex foot-ankle musculoskeletal model with **(C)** 8 degree of freedom (Malaquias et al., 2017).

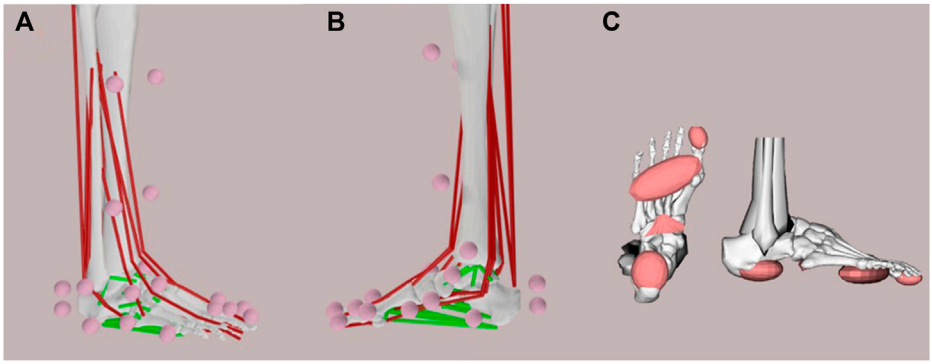

FIGURE 4
(A) Lateral and **(B)** medial view of the extended foot-ankle musculoskeletal model where motion capture markers (pink dots), muscles (red lines), and ligaments (green lines) are visualized. **(C)** Contact surfaces under the foot which model the interaction between the foot and the ground.

ankle, particular in those with potential foot pathologies relating to structural abnormalities and consequent dysfunction. As such researchers have developed more complex foot-ankle musculoskeletal models which contain more physiological and functionally complete representations (Oosterwaal, 2016; Malaquias et al., 2017; Maharaj et al., 2022).

Our workflow for insole design integrated a musculoskeletal model developed in our group (Malaquias et al., 2017) that contains 8 degrees of freedom (Figures 3B, C) and a complex representation of the ligaments and muscles of the foot-ankle complex (Figures 4A, B). For use in forward simulations, our model needs to contain a contact model representing the interaction between the foot (our model) and the ground. To do this, we utilized contact ellipsoids attached to specific foot bones (i.e., Calcaneus, midfoot, forefoot, and toes) and an infinite plane for the ground (Figure 4C). Contact geometries were based on medical imaging from 12 individuals where contacting regions of the foot were extracted (Malaquias, 2022). The average shape and size of these geometries were then added to the generic OpenSim model. Contact between these foot geometries and the ground were modelled using an elastic foundation formulation whereby force was proportional to penetration of the foot geometries and the ground where stiffness values were defined based on values from previous work (Malaquias, 2022). These ground-foot contact forces in turn induce rotational joint moments which can in turn affect the estimation of foot joint kinematics when included in forward simulations (see later sections). They -by default-do not affect the inverse simulations performed here which estimate foot-ankle kinematics using only the marker-based trajectories.

This extended generic musculoskeletal model was then used for all subsequent steps within the developed framework. A personalized version of this model was generated for each participant where marker trajectories from the static trial were used in anthropometric scaling. Specifically, markers pairs were defined and the ratio between model (i.e., on the generic model) and measured (i.e., from motion capture) distances were used to determine scale factors. These scale factors were then applied to the corresponding model segment to match the gross anthropometry of each individual participant.

Inverse simulations

For all acquired gait trials, marker positions were exported as. trc files and used in the open-source OpenSim musculoskeletal modelling platform, to estimate joint angles using a standard

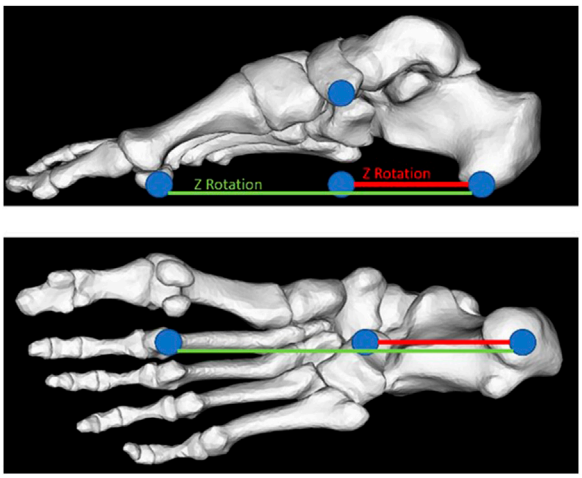

FIGURE 5
Representation of the implemented spring-based insole model. Shown are the two different bushing forces which are implemented, the first (red) spanning the calcaneus and the midfoot, and the second (green) spanning the calcaneus, midfoot, and metatarsals.

Inverse Kinematics (Lu and O'Connor, 1999) approach. Estimated joint angles were restricted to the motion of the tibia (6 degrees of freedom) and the 8 degrees of freedom of the foot-ankle. Gait trials were then limited to only include the stance phase of gait based on measured ground reaction forces and standard thresholding techniques (>10 N).

Preparatory forward simulations

The next step was to ensure that our preparatory forward simulations can recreate estimated joint kinematics from our inverse simulations detailed above. To achieve this goal, we first estimated the joint moments required to produce the measure joint kinematics (using in-built OpenSim tools for moment-driven froward simulations). These joint level moments were then applied and contact forces/moments generated between the foot and ground, in a forward simulation to verify that measured joint kinematics could be recreated. Once we can successfully reproduce our inverse results in our forward simulations—we can then add our insole model to estimate it is kinematic effect. When comparing forward simulation kinematics—to those from inverse kinematics, the average error across all 8 degrees of freedom of the foot-ankle and all participants was 4.69°.

Insole model

We implemented a lumped insole model in OpenSim utilizing Bushing Forces. These can be thought of as translational or rotational springs which span 2 or more bodies. These springs are characterized by a position (on each body), an initial rotational offset (i.e., orientation) as well as multiple stiffness parameters. These stiffnesses can be applied along any of the three axes and can resist either translations, or rotations around these axes. When two bodies, spanned by a bushing force translate/rotate away from their initial position these springs generate either a force or moment to resist such motion, proportional to their stiffness and the amount of translation/rotation. We reduced the tested insoles to a pair of rotational bushing forces. The first (Figure 5 red line) spanned from the calcaneus to the midfoot which aimed to resist plantar/dorsiflexion of the midfoot relative to the calcaneus. The second spring (Figure 5 green) spans from the calcaneus to the metatarsals and aims to support the medial longitudinal arch of the foot in the distal foot segments.

Insole calibration

It was our initial intention to estimate the stiffness of each of these springs from mechanical testing of the specific insoles which participants wore. However, as the insole stiffness and geometry parameters (e.g., arch height) were highly variable across individuals, finding a set of stiffness values which reproduced the observed experimental kinematic effect in our simulations was challenging. This was further complicated by the simplified insole definition that does not explicitly account for geometry, and therefore the contact between the foot and the insole, nor the insole/shoe and the ground. Therefore, to derive an initial set of spring stiffness values (for each individual participant) an optimization routine was first executed to calibrate the insole model for each participant.

Insole model calibration was performed for each participant separately. To this end, a single trial (of the participant being calibrated) from the reference shod condition was used as initial input to find a set of insole stiffness parameters (i.e., stiffness and orientation) which reproduces the measured (i.e., from motion capture) response. Specifically, we use the participants' scaled musculoskeletal model, the joint level moments which produce the kinematics (see Preparatory forward simulations section), and a template insole model (i.e., bushing forces) whose stiffness parameters and orientations will be defined by our calibration process.

Within an optimization routine deployed in Python, we leverage OpenSim API functions to run multiple iterations of forward simulations with differing bushing force (i.e., insole model) parameters. We specifically adjust for both bushing forces, their stiffness (Nm/radian), and orientation. At each iteration the error between predicted (from this specific iteration) and target (average measured insole) kinematics is calculated. Note that despite having gait analysis data throughout the entire stance phase of gait, we focused our error calculations and estimations to the period where the foot was flat on the ground as this is the period where the insole is likely to have the largest effect and the period of interest when assessing corrections. Further, despite estimating a total of 8 degrees of freedom we only consider a subset of foot-ankle kinematics, specifically chopart and tarsometatarsal joint degrees of freedom as these are the joints spanned by our insole model. Each of these joints had two degrees of freedom which were a combination of flexion/extension and inversion/eversion.

This calibration is run until the specific stiffness and orientations which yield the minimum error between the two conditions is found—an example of these results for two participants can be seen below (Figure 6). Specifically, the objective function which is evaluated at each iteration calculates the root mean squared error between the average measured insole kinematics and predicted kinematics for each degree of freedom of interest. The average

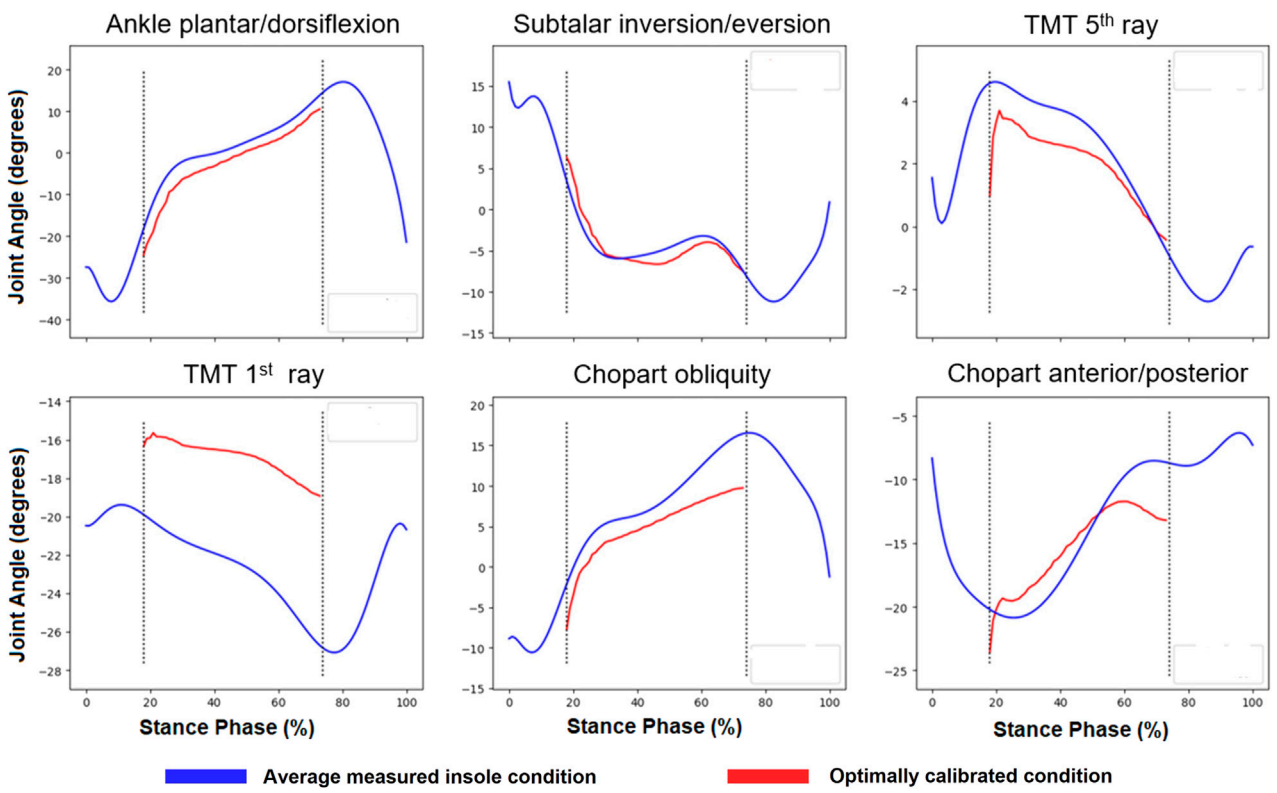

FIGURE 6
Example of calibration results from a single participant where blue lines indicate the average measured insole condition for selected degrees of freedom from inverse kinematics. Red lines show the kinematics from the optimal calibration solution. Note the dotted black vertical lines indicate where error was calculated within the calibration and correspond to the stage where the foot is flat on the ground.

error across the four degrees of freedom, and entire time of interest is then calculated and minimized within the optimization routine. The specific stiffness and orientations yielding the minimum error are then used in the final predictive model and simulations.

Predictive model

In the final predictive simulation, the participant's musculoskeletal model, their calibrated insole model (from above) was combined with joint moments (see Preparatory forward simulations section) from the remaining (i.e., excluding the trail used for calibration) reference lab shoe trials to predict a set of simulated insole kinematics across multiple trials. The average simulated insole kinematics were then compared to measured insole kinematics to determine predictive model accuracy. Again, the time of interest was restricted to the period where the foot is flat on the ground, and to the mid- and fore-foot joints.

Results

When designing this workflow, first, proof of concept simulations were performed to ensure that the implemented insole model which utilizes spring-based bushing forces did alter estimated ankle-foot kinematics, and that these estimations were in fact sensitive to changes in these stiffness parameters (Figure 7). Compared to a reference stiffness as obtained from mechanical testing (black line), increasing or decreasing the insole stiffness effectively alters the estimated kinematics in the targeted degrees of freedom.

Finally, we used the *in silico* workflow for all participants and the average error between measured and predicted kinematics was calculated. Below (Figure 8) are two exemplary participants for which the measured (shod with insole), and simulated (i.e., predictive insole model) conditions are shown. Across the entire cohort, the average root mean squared error ±standard deviation between measured and simulated kinematics were 4.7 ± 3.1, 4.5 ± 3.1, 2.3 ± 2.3, and 2.3 ± 2.7° for the chopart obliquity, chopart anterior-posterior axis, tarsometatarsal first ray, and tarsometatarsal fifth ray respectively. We observed a wide range of errors in the cohort, with maximum and minimum errors of 0.5–11.7, 1.07–13.12, 0.25–9.31, 0.25–12.5° for the chopart obliquity, chopart anterior-posterior axis, tarsometatarsal first ray, and tarsometatarsal fifth ray respectively.

Following the analysis of the prediction error of the developed workflow (above), we additionally assessed 1) if the prediction error (i.e., measured vs. predicted) between the joints of interest were correlated, 2) whether the predicted error was correlated with the measured effect (i.e., difference between shod with and without insoles), finally we assessed whether these relationships were different between healthy participants and flatfoot patients. To determine if prediction error was correlated with the measured

10.3389/fbioe.2024.1351403

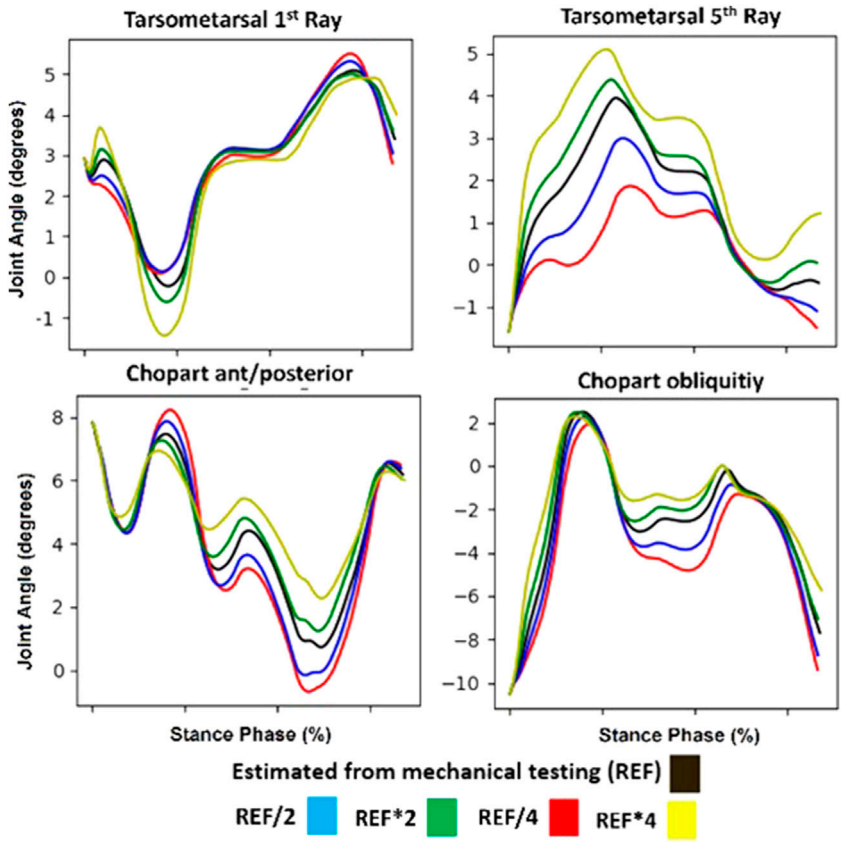

FIGURE 7
Example simulation results for the targeted mid/forefoot degrees of freedom. Specifically shown are the tarsometatarsal first and fifth ray, and chopart anterior-posterior and obliquity degrees of freedom. Shown in black are forward simulation results with reference insole model stiffness. Shown in Blue and Red are forward simulation results with a half and quarter stiffness compared to the reference respectively. Similarly in Green and Yellow are forward simulation results with double and quadruple stiffness compared to the reference respectively.

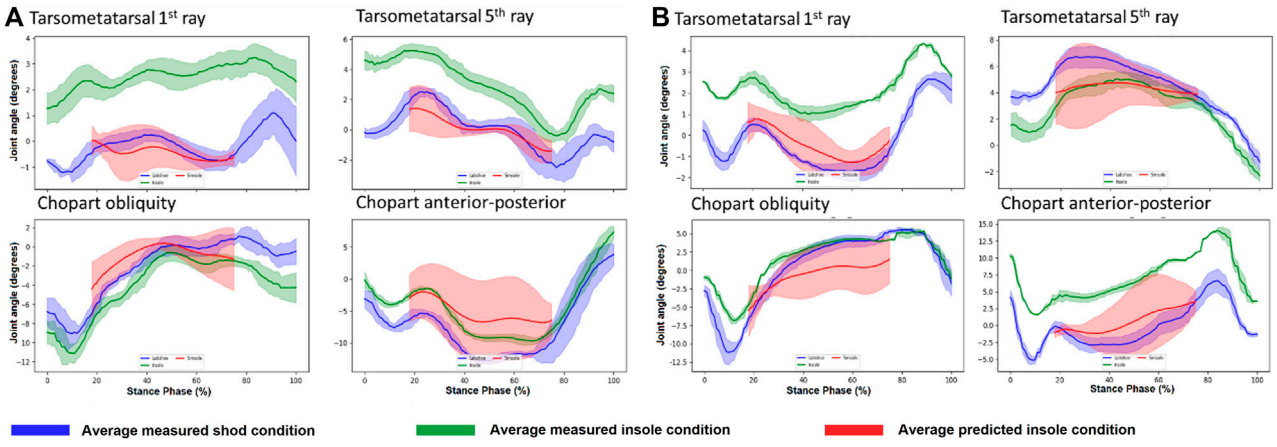

FIGURE 8
Predicted Insole kinematics (red), measured insole (green), and reference (blue) conditions for two participants **(A, B)**. Note the reason the predicted kinematics are in a smaller range compared to the other conditions is because we focused on a time where the foot was flat on the ground which is representative of this period.

insole effect (Figure 9), we graphed measured effect on the *X*-axis for each joint (on a column-by-column basis), the *Y*-axis showing the prediction error (i.e., measured vs. predicted) on a row-by-row basis.

Following graphing, a line of best fit was overlayed for each plot and the Pearsons Correlation calculated. In this analysis, we see only one strong correlation (r^2 0.8) between the error and effect in the

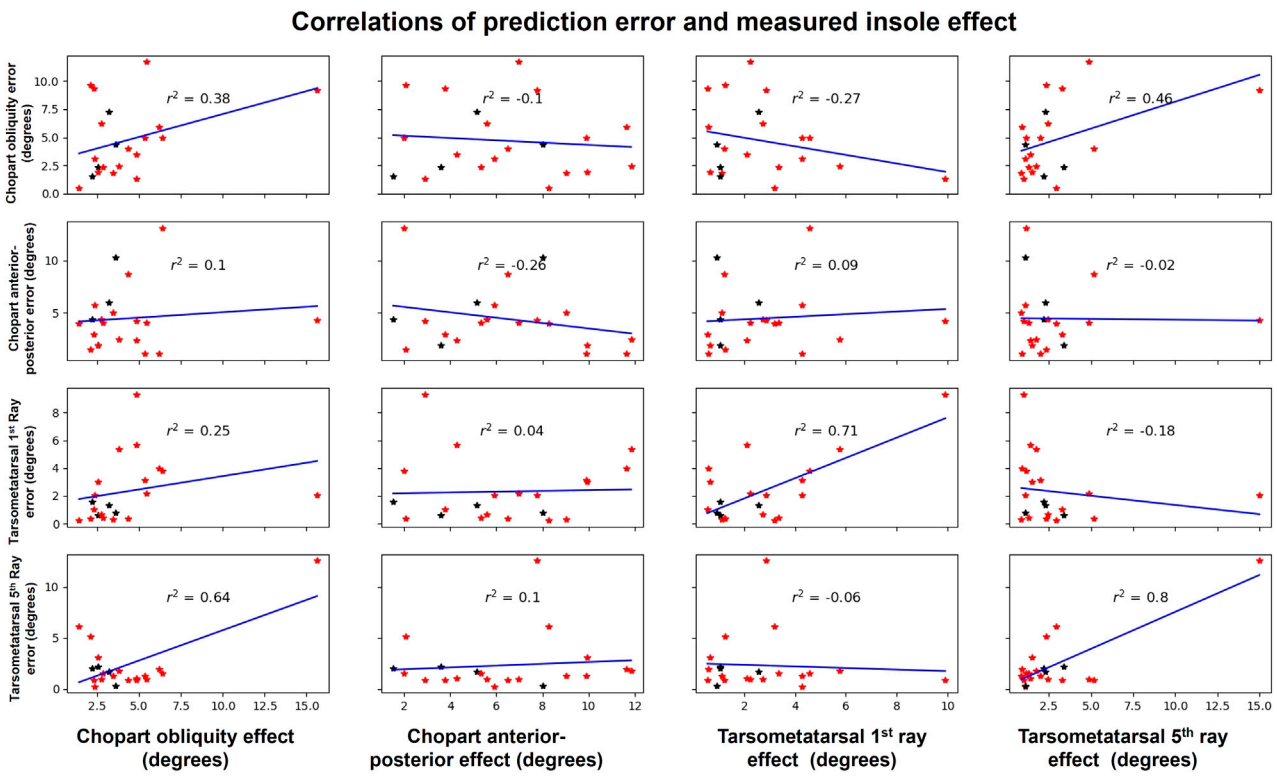

FIGURE 9
Shown are the measured effect of the insole on X axis for each joint (on a column-by-column basis), and the Y axis showing the prediction error (on a row-by-row basis). Each star represents a different participant were red are flatfeet patients and black are healthy participants. This distinction allowed us to further analyse if the relationship is biased by the population.

tarsometatarsal fifth ray, however this seems to be biased by an outlier with a large error and large effect (top right). All remaining correlations were weak or negligible except for two moderation correlations between tarsometatarsal fifth ray error and chopart obliquity effect (r^2 0.64) as well as chopart obliquity error and tarsometatarsal fifth ray effect (r^2 0.46). Examining this relationship in healthy participants (black) and flatfoot patients (red) individually, there appears to be no bias in our workflow between these groups affecting this relationship. The lack of a repeatable relationship suggests that our workflows accuracy is not dependant on a low or high effect, providing confidence in its generalizability.

A similar approach was then applied to determine the correlations between the prediction error (Figure 10) of the different degree of freedom errors (e.g., correlation between chopart obliquity and chopart anterior-posterior). Examining the correlations, only weak and negligible correlations were observed for all comparisons suggesting the error in one degree of freedom in independent of the errors in the remaining degrees of freedom. Similar to the previous comparison, this relationship appears to not be biased or different between the two studied groups.

Discussion

The design and customization of insoles could benefit from computational approaches that help in determining the appropriate mechanical parameters (i.e., stiffness) to provide the most optimal correction for a targeted foot-ankle kinematic dysfunction. In this paper we aimed to develop a workflow to predict individuals' response to a specific corrective insole. The workflow described here, implemented in OpenSim, maximally exploits the added value of 3D motion capture, musculoskeletal modeling of the foot-ankle complex, dynamic simulations together with optimization approaches to define the mechanical properties of a lumped insole model that maximally predicts the foot-ankle kinematics.

In contrast to previous work, this workflow was developed using a rigid body musculoskeletal model in OpenSim. Typical insole model-based workflows assessing corrective insole effects utilize finite-element models that explicitly model contact between the foot and the insole to inform in the first instance on predicted changes in plantar contact pressures. Less often the explicit effect on foot-ankle kinematic predictions is targeted. While this approach permits accounting for complex material models relevant for insole design as well as the effective geometrical shape of the insole its drawback is that the time to develop and execute these models is in the magnitude of numerous hours, complicating their use in the context of a parameter optimization approach as described above. Furthermore, it requires highly specific input data for the material parameters that cannot readily be identified in a sole-specific manner, as well as dedicated expertise to build and execute these simulations. The workflow developed here only requires seconds to execute and does not require highly detailed imaging of the participants foot nor the insole. Additionally, the workflow itself is highly automated making execution simple. An additional

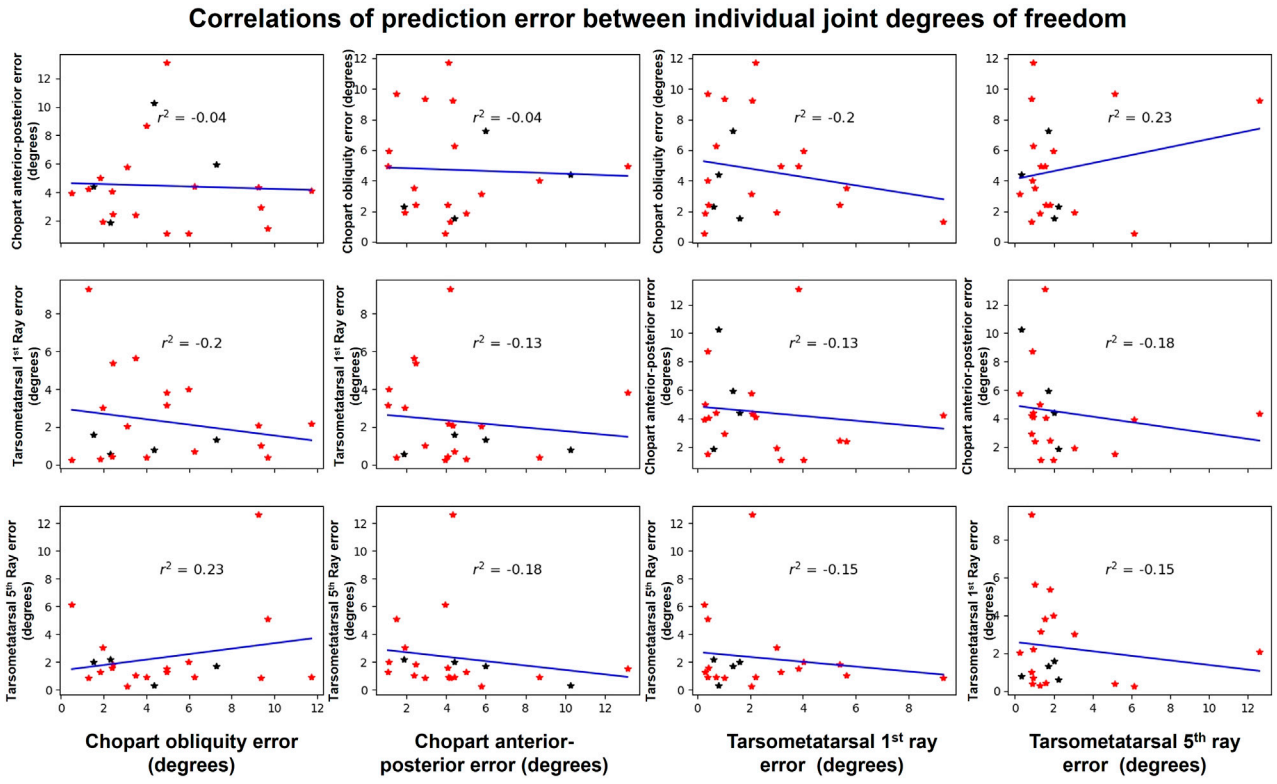

FIGURE 10
Shown are the errors between the measured and predicted kinematics for all participants for each of the joints of interest. From left to right, on the X axis is the Chopart obliquity, chopart anterior-posterior, tarsometatarsal first ray and finally the tarsometatarsal fifth ray. Each star represents a different participant were red are flatfeet patients and black are healthy participants. This distinction allowed us to further analyse if the relationship is biased by the population.

advantage of this OpenSim musculoskeletal modelling approach is that an entire stance phase and numerous gait cycles can be simulated meaning a larger number of trials can be collected, potentially in different environments and speeds meaning the effect of an insole in variable gait conditions can be tested. This contrasts with previously mentioned finite-element modelling approaches that typically only consider a combination of static or quasi-static time points.

The developed musculoskeletal modeling workflow uses measured motion capture data from shod conditions without insoles as a reference condition and predicts the effect of the insole on foot-ankle kinematics during stance phase of gait using a spring-based insole model. Insole models were calibrated based on measured data to improve the predictive ability of the framework. This was a necessary step as initial parameters derived from mechanical testing did not generate a sufficient effect of the predicted kinematics and often yielded the same kinematics as the reference condition. Although a hurdle of the workflow being fully predictive, this is currently required as there is currently no direct way to translate the properties of corrective insoles from the manufacturer to our musculoskeletal modelling framework. However this is a preliminary implementation which we believe can be phased out in later and more developed implementations when a larger cohort can be modelled and considered.

When considering the magnitude of errors between measured and predicted insole conditions (See Results and Figure 8), these are between 2 and 5° for the tarsometatarsal and chopart joints, respectively. These errors also need to be considered in the context of the actual effect of the insole. The effect of the insole to measured kinematics in many cases was highly variable between participants and in many cases is in the range of error in our predictive model. When examining the average effect of the insole in the measured values we see the following: 4.18 ± 2.98, 6.28 ± 3.11, 2.67 ± 2.23, and 2.75 ± 3.05° for the chopart obliquity, chopart anterior-posterior axis, tarsometatarsal first ray, and tarsometatarsal fifth ray respectively. Importantly, the secondary analysis performed shows our model's accuracy is not dependent on the magnitude of the response, nor does it seem to be influenced if it is applied to a healthy participant or flatfoot patient providing confidence in the generalizability of the results.

As with any study, several limitations need to be considered. First, the predictive framework is currently reliant of high-fidelity motion capture data which may limit the scope and application of the current approach. Such equipment is not typically available in clinical practice where such an approach would have the most impact. Second, the use of the calibration steps relies on *a-prior* knowledge of an individual's response which would still require fabrication of numerous insole candidates meaning the framework cannot be run fully predictive.

Future research should focus on reducing the reliance on the use of motion capture data. The use of such data reduces the wider adoption of these approaches as they do not have access to such specialized infrastructure. As this approach is only currently reliant

on accurate estimations of joint kinematics, leveraging of other modalities such as video-based analysis or machine learning may provide a viable alternative to inform such a developed workflow in the future. To this end, current low fidelity approaches such as the use of plantar pressure measurements are becoming more common. Such approaches would allow for the application and translation of such a framework in clinics to facilitate its translation and impact on patients. Future research should focus on improving the simplified spring-based insole model by processing larger data sets with a larger variety of insole designs and mechanical properties potentially augmented and assisted by formal mechanical testing procedures. The improvement of this spring-based model will improve the predictive accuracy of the framework. Following these improvements and refinements, a complete clinical validation including not only quantitative measures of kinematic response, but also patients' subjective outcomes, and clinical outcomes should be done to compare the effectiveness of the *in silico* based workflow for insole design compared to current practice.

This framework serves as an important first step in realizing such an approach not reliant on finite element methods. Examining the results of calibration (Figure 6) using our approach, it is possible to reproduce measured insole gait kinematics using measured shod data (without an insole) and a spring-based insole model. This is a promising outcome as it means that if we can effectively and accurately translate insole design parameters from the manufacturer (e.g., arch support and height, regional stiffness) to spring-based parameters (i.e., bushing force stiffness) the accuracy of this workflow can likely be increased.

Conclusion

The developed workflow provides a solid basis for future *in silico* work to improve the predictive accuracy of the effect of insoles on foot-ankle kinematics, given that the lumped insole model can be further optimized, in terms of mapping the experimental insole mechanical properties and the formulation of the spring-based constants. Combined, a reduced burden of data collection, and improved spring-based model provides an exciting potential for a fully predictive model to assist design and prescription of corrective insoles and improved patient outcomes.

Data availability statement

The datasets presented in this article are not readily available because Data collected in this research were collected by a commercial company who retain the rights to this data. Requests to access the datasets should be directed to BK bryce.killen@kuleuven.be.

Ethics statement

The studies involving humans were approved by UZ Leuven Medical Ethics Committee. The studies were conducted in accordance with the local legislation and institutional requirements. The participants provided their written informed consent to participate in this study.

Author contributions

BK: Conceptualization, Data curation, Formal Analysis, Investigation, Methodology, Software, Visualization, Writing–original draft, Writing–review and editing. SV: Conceptualization, Investigation, Methodology, Project administration, Supervision, Writing–review and editing. FB: Conceptualization, Investigation, Supervision, Writing–review and editing. JV: Conceptualization, Funding acquisition, Project administration, Resources, Supervision, Writing–review and editing. IJ: Conceptualization, Funding acquisition, Investigation, Methodology, Project administration, Resources, Supervision, Writing–original draft, Writing–review and editing.

Funding

The author(s) declare financial support was received for the research, authorship, and/or publication of this article. This work was financially by the In-Silico World (ISW) project. ISW project has received funding from the European Union's Horizon 2020 Research and Innovation Programme, under Grant Agreement n. 101016503.

Conflict of interest

Author SV and FB were employed by the company Materialise.

The remaining authors declare that the research was conducted in the absence of any commercial or financial relationships that could be construed as a potential conflict of interest.

Publisher's note

References

Arnold, J. B., Marshall, M., Thomas, M., Redmond, A., Menz, H., and Roddy, E. (2019). Midfoot osteoarthritis: potential phenotypes and their associations with demographic, symptomatic and clinical characteristics. *Osteoarthr. Cartil.* 27 (4), 659–666. doi:10.1016/j.joca.2018.12.022

Bacarin, T. A., Sacco, I. C. N., and Hennig, E. M. (2009). Plantar pressure distribution patterns during gait in diabetic neuropathy patients with a history of foot ulcers. *Clin. Sci.* 64, 113–120. doi:10.1590/s1807-59322009000200008

Boey, H., Rossom, S. V., Verfaillie, S., Sloten, J. V., and Jonkers, I. (2022). Maximal lateral ligament strain and loading during functional activities: model-based insights for ankle sprain prevention and rehabilitation. *Clin. Biomech. (Bristol, Avon).* 94, 105623. doi:10.1016/j.clinbiomech.2022.105623

Cappozzo, A., Catani, F., Della Croce, U., and Leardini, A. (1995). Position and orientation in space of bones during movement: anatomical frame definition and determination.', *Clinical biomechanics (Bristol, Avon). England* 10 (4), 171–178. doi:10.1016/0268-0033(95)91394-t

Glassman, S. D., Berven, S., Kostuik, J., Dimar, J. R., Horton, W. C., and Bridwell, K. (2006). Nonsurgical resource utilization in adult spinal deformity. *Spine* 31 (8), 941–947. doi:10.1097/01.brs.0000209318.32148.8b

Golanó, P., Vega, J., de Leeuw, P. A. J., Malagelada, F., Manzanares, M. C., Götzens, V., et al. (2010). Anatomy of the ankle ligaments: a pictorial essay. *Knee Surg. sports traumatology, Arthrosc. official J. ESSKA. Ger.* 18 (5), 557–569. doi:10.1007/s00167-010-1100-x

Kaufman, K. R., Brodine, S. K., Shaffer, R. A., Johnson, C. W., and Cullison, T. R. (1999). The effect of foot structure and range of motion on musculoskeletal overuse injuries. *Am. J. sports Med.* 27 (5), 585–593. doi:10.1177/03635465990270050701

Keegan, T. H. M., Kelsey, J. L., Sidney, S., and Quesenberry, C. P. J. (2002). Foot problems as risk factors of fractures. *Am. J. Epidemiol. U. S.* 155 (10), 926–931. doi:10.1093/aje/155.10.926

Kido, M., Ikoma, K., Hara, Y., Imai, K., Maki, M., Ikeda, T., et al. (2014). Effect of therapeutic insoles on the medial longitudinal arch in patients with flatfoot deformity: a three-dimensional loading computed tomography study.', *Clinical biomechanics (Bristol, Avon). England* 29 (10), 1095–1098. doi:10.1016/j.clinbiomech.2014.10.005

Killen, B. A., Falisse, A., De Groote, F., and Jonkers, I. (2020). *In silico*-Enhanced treatment and rehabilitation planning for patients with musculoskeletal disorders: can musculoskeletal modelling and dynamic simulations really impact current clinical practice? *Appl. Sci.* 10, 7255. doi:10.3390/app10207255

Lu, T. W., and O'Connor, J. J. (1999). Bone position estimation from skin marker co-ordinates using global optimisation with joint constraints. *J. biomechanics. U. S.* 32 (2), 129–134. doi:10.1016/s0021-9290(98)00158-4

Maharaj, J. N., Rainbow, M. J., Cresswell, A. G., Kessler, S., Konow, N., Gehring, D., et al. (2022). Modelling the complexity of the foot and ankle during human locomotion: the development and validation of a multi-segment foot model using biplanar videoradiography. *Comput. methods biomechanics Biomed. Eng.* 25 (5), 554–565. doi:10.1080/10255842.2021.1968844

Malaquias, T., Vander Sloten, J., De Groote, F., and Jonkers, I. (2022). *A combined multibody and plantar pressure approach to estimate and predict foot kinematics applied to 3D-printed insoles*'.

Malaquias, T., Silveira, C., Aerts, W., De Groote, F., Dereymaeker, G., Vander Sloten, J., et al. (2017). Extended foot-ankle musculoskeletal models for application in movement analysis. *Comput. Methods Biomechanics Biomed. Eng.* 20 (2), 153–159. doi:10.1080/10255842.2016.1206533

Mannisi, M., Dell'Isola, A., Andersen, M., and Woodburn, J. (2019). Effect of lateral wedged insoles on the knee internal contact forces in medial knee osteoarthritis. *Gait Posture* 68, 443–448. doi:10.1016/j.gaitpost.2018.12.030

Matsui, K., Takao, M., Tochigi, Y., Ozeki, S., and Glazebrook, M. (2017). Anatomy of anterior talofibular ligament and calcaneofibular ligament for minimally invasive surgery: a systematic review. *Knee Surg. sports traumatology, Arthrosc. official J. ESSKA* 25 (6), 1892–1902. doi:10.1007/s00167-016-4194-y

Merian, M., Glisson, R. R., and Nunley, J. A. (2011). Ligament balancing for total ankle arthroplasty: an *in vitro* evaluation of the elongation of the hind- and midfoot ligaments. *Foot ankle Int.* 32 (5), S457–S472. doi:10.3113/FAI.2011.0457

Oosterwaal, M. (2016). The Glasgow-Maastricht foot model: development, repeatability and sources of error of a 26 segment multi-body foot model. *Maastricht Univ.* doi:10.26481/dis.20161123mo

Paton, J., Bruce, G., Jones, R., and Stenhouse, E. (2011). Effectiveness of insoles used for the prevention of ulceration in the neuropathic diabetic foot: a systematic review. *J. diabetes its Complicat.* 25 (1), 52–62. doi:10.1016/j.jdiacomp.2009.09.002

Sinclair, J., Ingram, J., Taylor, P. J., and Chockalingam, N. (2019). Acute effects of different orthoses on lower extremity kinetics and kinematics during running; a musculoskeletal simulation analysis.', *Acta of bioengineering and biomechanics. Poland* 21 (4), 13–25. doi:10.37190/abb-01405-2019-02

Su, S., Mo, Z., Guo, J., and Fan, Y. (2017). The effect of arch height and material hardness of personalized insole on correction and tissues of flatfoot. *J. Healthc. Eng.* 2017, 8614341–8614349. doi:10.1155/2017/8614341

Telfer, S., Erdemir, A., Woodburn, J., and Cavanagh, P. R. (2014). What has finite element analysis taught us about diabetic foot disease and its management? A systematic review', *plos one. Public Libr. Sci.* 9 (10), 1–13. doi:10.1371/journal.pone.0109994

Telfer, S., Woodburn, J., Collier, A., and Cavanagh, P. (2017). Virtually optimized insoles for offloading the diabetic foot: a randomized crossover study. *J. Biomechanics* 60 (1), 157–161. doi:10.1016/j.jbiomech.2017.06.028

frontiers | Frontiers in Bioengineering and Biotechnology

TYPE Original Research
PUBLISHED 23 February 2024
DOI 10.3389/fbioe.2024.1347720

OPEN ACCESS

EDITED BY
Jörg Miehling,
Friedrich-Alexander-Universität Erlangen-Nürnberg, Germany

REVIEWED BY
Jean-Louis Milan,
Aix-Marseille Université, France
Maeruan Kebbach,
University Hospital Rostock, Germany

*CORRESPONDENCE
Florian Michaud,
florian.michaud@udc.es

RECEIVED 01 December 2023
ACCEPTED 13 February 2024
PUBLISHED 23 February 2024

CITATION
Michaud F, Luaces A, Mouzo F and Cuadrado J (2024), Use of patellofemoral digital twins for patellar tracking and treatment prediction: comparison of 3D models and contact detection algorithms.
Front. Bioeng. Biotechnol. 12:1347720.
doi: 10.3389/fbioe.2024.1347720

Use of patellofemoral digital twins for patellar tracking and treatment prediction: comparison of 3D models and contact detection algorithms

Florian Michaud*, Alberto Luaces, Francisco Mouzo and Javier Cuadrado

Laboratory of Mechanical Engineering, CITENI, Campus Industrial de Ferrol, University of La Coruña, Ferrol, Spain

Introduction: Poor patellar tracking can result in painful contact pressures, patella subluxation, or dislocation. The use of musculoskeletal models and simulations in orthopedic surgeries allows for objective predictions of post-treatment function, empowering clinicians to explore diverse treatment options for patients. Although a promising approach for managing knee surgeries, the high computational cost of the Finite Element Method hampers its clinical usability. In anticipation of minimal elastic deformations in the involved bodies, the exploration of the Multibody Dynamics approach emerged as a viable solution, providing a computationally efficient methodology to address clinical concerns related to the knee joint.

Methods: This work, with a focus on high-performance computing, achieved the simulation of the patellofemoral joint through rigid-body multibody dynamics formulations. A comparison was made between two collision detection algorithms employed in the simulation of contact between the patellar and femoral implants: a generic mesh-to-mesh collision detection algorithm, which identifies potential collisions between bodies by checking for proximity or overlap between their discretized mesh surface elements, and an analytical contact algorithm, which uses a mathematical model to provide closed-form solutions for specific contact problems, but cannot handle arbitrary geometries. In addition, different digital twins (3D model geometries) of the femoral implant were compared.

Results: Computational efficiency was considered, and histories of position, orientation, and contact force of the patella during the motion were compared with experimental measurements obtained from a sensorized 3D-printed test bench under pathological and treatment scenarios. The best results were achieved through a purely analytical contact detection algorithm, allowing for clinical usability and optimization of clinical outcomes.

KEYWORDS

multibody dynamics, contact detection, contact forces, digital twin, total knee replacement, patellar tracking, simulation, treatment prediction

1 Introduction

The patella plays a crucial role as a relay, acting as a pulley for the extensor system, which enhances the lever arm of the quadriceps and, consequently, boosts active extension strength in the knee joint. The patellofemoral joint is a part of the knee joint and refers to the articulation between the patella and the femur. It is a gliding joint that allows the patella to move smoothly along the groove at the lower end of the femur called the trochlear groove. The patella acts as a sesamoid bone, embedded within the quadriceps tendon, and plays a crucial role in the functioning of the knee joint. Poor patellar tracking can lead to increased contact pressures, patellar tilt, subluxation, or dislocation. The patellar trajectory refers to the path followed by the kneecap in relation to the femoral groove as the knee undergoes flexion and extension (Katchburian et al., 2003). Evaluating the patellar trajectory has been reliant on the surgeon's subjective assessment, which involves direct visual observation during the surgical procedure (Best et al., 2020). Anatomical factors such as trochlear dysplasia, high-riding patella, ligament laxity, or an increased Q-angle can contribute to patellar instability. In some cases, surgical interventions may be required (Hayat et al., 2023). Total knee replacement (TKR) aims to alleviate pain, improve function, and enhance the overall quality of life for individuals with severe knee joint damage or degeneration (Innocenti et al., 2018). Following the placement of implants within the respective bones, the surgeon manually flexes and extends the knee of the anesthetized patient to witness the joint's range of motion and assess the resulting patellar trajectory after the treatment has been applied. Despite advancements in implant design and surgical techniques for TKR, complications still arise, with around 10% of cases involving patellar issues (Putman et al., 2019) and these complications may require additional surgeries.

To address these challenges and improve treatment outcomes, there has been a growing interest in the use of musculoskeletal models and simulations in orthopedic surgeries (Fregly et al., 2012; Marra et al., 2015; Tischer et al., 2017; Van Rossom et al., 2019; Curreli et al., 2021). These tools enable objective predictions of post-treatment function and empower clinicians to explore different treatment options for patients. By utilizing these tools, the treatment planning process becomes more objective, allowing clinicians to tailor and optimize clinical outcomes according to the specific characteristics of each individual patient. Two main methods can be used for the definition of a mechanical system: Multibody Dynamics (MBD) and the Finite Element Method (FEM) (Gay Neto, 2023). In the Finite Element Method, each geometry is discretized into finite elements, forming a mesh with nodes that represents the physical properties of a mechanical system. Numerous FEM studies have examined the patellofemoral joint (Farrokhi et al., 2011; Aksahin et al., 2016; Islam et al., 2015). However, despite being a promising approach for knee osteoarthritis management, FEM time-intensive process (including pre-processing, processing, and post-processing) hinders its clinical usability (Paz et al., 2021). Consequently, FEM is presently confined to preoperative planning, focusing on aspects like the enhancement of implant design and surgical techniques, which are not subject to time constraints. Given this constraint and the anticipation of minimal elastic deformations in the involved bones, the exploration of the MBD approach emerged as a viable solution, providing a computationally efficient methodology to tackle clinical knee joint concerns (Bei and Fregly, 2004; Geier et al., 2015; Kebbach et al., 2020). This efficiency can potentially provide real-time biofeedback (Lugrís et al., 2023), rapid predictions of post-treatment function, or even time-reduced optimization of the surgical process to the surgeons, paving the way for its intraoperative application in the near future. Nonetheless, one significant computational challenge when integrating contact into a multibody dynamics framework revolves around collision detection (Li et al., 2023). It is challenging to implement methods and algorithms that can effectively and efficiently model the intricate phenomenon of contacting bodies with the necessary realism for MBD simulations. When the colliding bodies have complex 3D geometries, a general collision detection algorithm is required. A comparatively simple alternative is to approximate the freeform surfaces by discretized mesh elements and subsequently verifying proximity or overlap between them (Kebbach et al., 2020; Dopico et al., 2019). Although there are plenty of publications and software tools dealing with polygonal surfaces, in practice both the quality of polygonal surfaces and the efficiency of the tools can differ considerably (Hippmann, 2004). Therefore, when describing certain shapes, mathematical equations provide the optimal solution: both non-uniform rational B-spline (NURBS) surfaces (Bei and Fregly, 2004; Ateshian, 1993) and analytic formulation of 3D geometry (Dopico et al., 2019) have proven to be effective alternatives in previous applications. However, no work on MBD simulation was found that included a comparison of the patella's movement and its forces with experimental results, primarily due to the invasive nature of these experiments.

In this work, due to negligible elastic deformations being expected in the involved bones and high-performance computing being sought, the simulation of the mechanical system was obtained through rigid-body multibody dynamics formulations. A comparison was made between two collision detection algorithms employed for the simulation of contact between rigid bodies: a mesh-to-mesh collision detection algorithm, which discretizes the bodies into triangular mesh surface elements, and an analytical contact algorithm, which uses analytical surface expressions to provide closed-form solutions for this contact problem. In addition, different 3D models of patellar and femoral implants were compared. Computational efficiency was considered, and histories of position, orientation, and pressure of the patella during the motion were compared with experimental measurements obtained from a sensorized 3D-printed test bench under various configurations. While this work does not include tibiofemoral contacts, the authors demonstrate that utilization of the patellofemoral digital twin already enables predictions for treatments addressing patellar stability issues when the tibiofemoral joint and the captured motions of femur and tibia are not affected. This is exemplified with a case study on tibial tuberosity transfer. Moreover, a new potential method for estimating tendon parameters from motion capture and simulation is introduced.

2 Material and methods

2.1 Movement and experimental data collection

To observe the patellar trajectory, two manual passive knee flexions and extensions were performed with the sensorized 3D-printed knee test rig described in (Michaud et al., 2023) which recreates a human leg, thus avoiding ethical issues. Bones were virtually cut and then 3D-printed (Prusa I3 MK3S, Prague, Czech Republic) to attach commercial tibia and femur implants

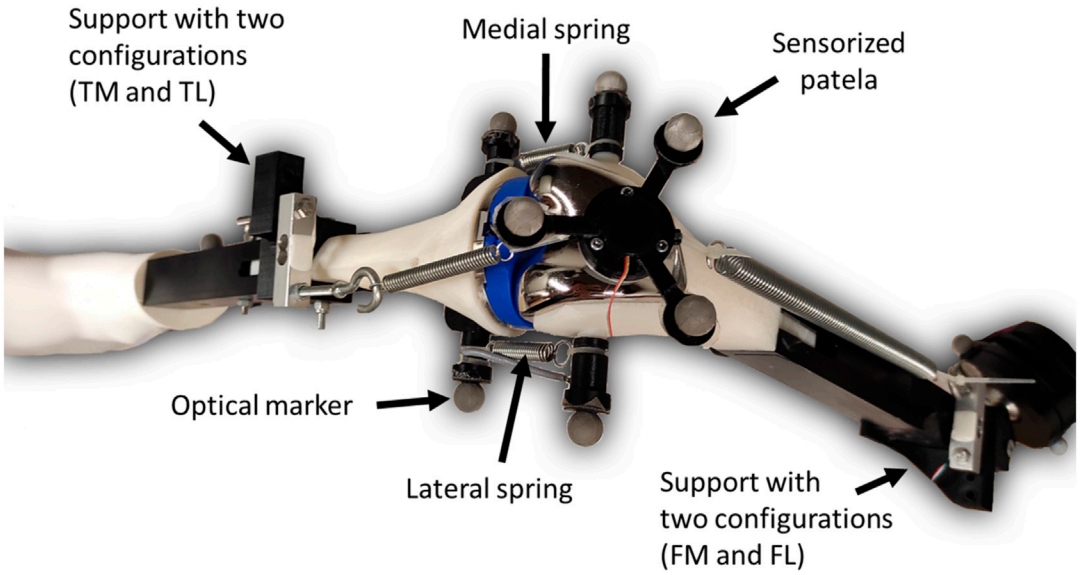

FIGURE 1
Modified sensorized knee test rig.

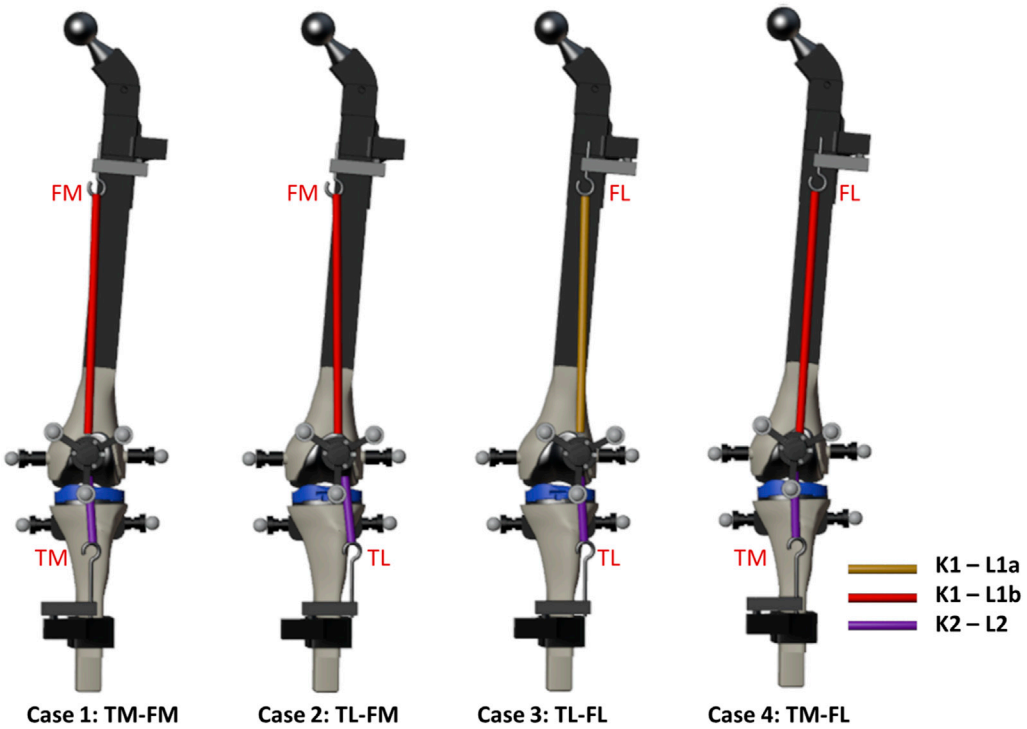

FIGURE 2
Knee anatomical configurations tested.

(Microport®). Springs were used to recreate tendons. The movements of femur, tibia, and patella were obtained from the recorded trajectories of eight optical markers using 18 infrared cameras (OptiTrack FLEX 3, Natural Point, Corvallis, OR, United States) at a sampling frequency of 100 Hz. Additionally, spring tensions of femur and tibia were recorded using two tension load cells (RB-Phi-119, Phidgets, Calgary, Canada), and the contact force between the femur and the patellar prosthetic button was measured using a compact pressure load cell (FX29, TE Connectivity, Wört, Germany), also at a sampling frequency of

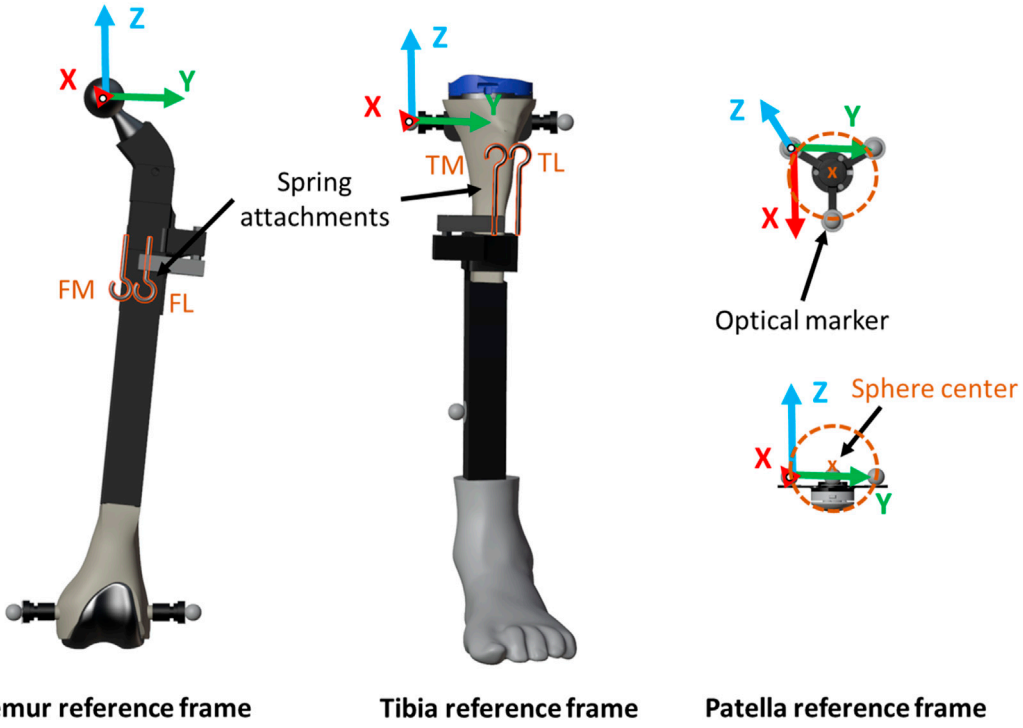

FIGURE 3
Computational model.

100 Hz. A second-order Butterworth filter with a cutoff frequency of 12 Hz was applied to the optically captured marker trajectories (Cuadrado et al., 2021), and a singular spectrum analysis (SSA) (Romero et al., 2015) with a window length of 30 was applied to the force measurements. Motion and force sensors allowed reproduction of the movement in the virtual model, fine-tuning of simulation parameters, and validation of experimental outcomes.

For this study, the knee test rig previously presented by the authors in (Michaud et al., 2023) was modified. The modifications included replacing the simplified hinge knee joint by springs on both sides to offer a more realistic representation of the knee joint. The tibia spring was short and stiff to simulate the patellar tendon (free length L2: 7.14 cm, stiffness K2: 629 N/m), while the femur spring was softer and longer to simulate the quadriceps tendon (free length L1a: 14.32 cm, stiffness K1: 156 N/m). In addition to the support that allows either a medial (FM) or a lateral (FL) attachment point on the femur, a support was also added to the tibia, enabling two configurations: tibia medial (TM) and tibia lateral (TL) (Figures 1–3).

The adjustable attachment points at tibia and femur, and the natural length of the femoral spring, were modified to simulate different knee anatomical configurations (Figure 1). These modifications correspond to altering the tendon laxity, the patellar height and the Q angle, also known as the quadriceps angle, which measures the alignment of the quadriceps muscles and the patella relative to the femur (Khasawneh et al., 2019). Femur and tibia supports provided two different positions each, resulting in a total of four different configurations (see Figure 2). Consequently, four distinct trajectories of the patella were tested. Additionally, the free length of the femoral spring was increased (case 3, Figure 2, L1b) by adding a rigid component of 1.96 cm to introduce an additional variation for simulation. Authors did not intend to reproduce any specific case, they simply wanted to validate their approach with different configurations that offer different patellar tracking to demonstrate that their approach allows to simulate any specific anatomical case.

The movement began with the leg flexed at approximately 45°, and was then flexed and extended twice. Cases 1 and 4 showed experimentally a normal tracking of the patella with different trajectories due to the different Q-angles. In contrast, in cases 2 and 3, a patellar dislocation occurred at complete extension during the experiments, so the leg was only partially extended in the first extension and extended until dislocation in the second extension. In addition, during the flexion of case 2, the patella did not engage with the femoral groove when the knee underwent flexion; instead, it got stuck in the superior part. This phenomenon is usually referred to as high-riding patella, also known as ‘patella alta’ (Tischer et al., 2017; Luyckx et al., 2009).

During TKR, tendon laxity, the patellar height and the Q angle can be corrected by adjusting the angles and heights of the cuts applied to the bones by the surgeon (Wang et al., 2010; Geier et al., 2015). Replicating this would necessitate 3D-printing multiple bones. However, since cases 1 and 2 share the same spring parameters, modifying the tendon attachment at the tibia in case 1 to address the patellar dislocation observed in case 2 can be considered a treatment for patellar issues. The corresponding surgical procedure is known as tibial tuberosity transfer (Clark et al., 2017). For this reason, the authors suggest using case 2 in section 2.6 as a pathological scenario, and case 1 as a potential treatment option (tibial tuberosity medialization) to simulate and validate predictions for a treatment, utilizing a single set of bones.

Due to the manually executed experimental actuation, the imposed motion was not identical for all configurations. The authors made every effort to reproduce the most similar motion; however, it is crucial to highlight that the purpose of this work was not to compare configurations against each other. The significance lies in the comparison between simulation and experimental results. Having different knee motions could be akin to observing different surgeons assessing the patellar trajectory. The recorded motion was used for the simulation, thus facilitating the comparison between simulated and experimental results.

2.2 Computational model

In this study, the leg model under consideration comprised three distinct rigid bodies: the femur, the assembly of tibia and foot, and the patella. The 3D geometries were identical to the physical components, including both the supports and the bones and implants. The femur remained fixed at the hip joint and capable of rotational movement around the three spatial directions. Tibia and patella were considered as two free bodies, each with its six degrees of freedom. This work focused on studying the interaction between patella and femur (using linear springs-dampers as tendons) and, more specifically, the contact of the patella with the femoral implant. The motion of femur and tibia was guided throughout this preliminary study.

The geometrical and physical parameters of the rigid bodies (local coordinates of points, inertias, etc.) were estimated from CAD models created in SolidWorks. These parameters, along with the mechanical constraints of the system, were then introduced into a custom-developed library (Dopico, 2016). The reference frame for the rigid bodies, as identified by the marker positions, is illustrated in Figure 3. The femoral body-fixed reference frame was defined by its "mechanical axis," passing from the center of the knee joint to the center of the femoral head, and its medial-lateral axis, passing through the medial and lateral epicondyle (Y-axis). The sensorized patella body-fixed reference frame was defined by the patellar long axis (X-axis), the patellar medial-lateral axis (Y-axis, parallel to the femoral medial-lateral axis), and the patellar anterior-posterior axis (Z-axis) (Bull et al., 2002). The mechanical parameters of the springs were estimated from the experimentally recorded positions and forces. Utilizing Hooke's Law to describe the spring force and Newton's Law of Motion for the damping force (Sharma et al., 2019), the expression for the linear spring-damper force F_i of spring i is given by the formula:

$$F_i = K_i (L - L_i) - c_i{}^{*}\dot{L} \tag{1}$$

Where K_i is the spring stiffness of spring i, L_i the natural length, L the displacement, $\dot{L}$ its velocity, and $c_i = 0.01{}^{*}K_i$ its damping coefficient.

2.3 Simulation

2.3.1 Formulation

In this work, we utilized the ALI3-P formulation for the dynamics of the multibody system. This formulation, described in (Dopico et al., 2014), has undergone extensive development and evolution over the years, building upon the concepts presented in (Michaud et al., 2023; Cuadrado et al., 2021). The ALI3-P formulation is based on an Augmented Lagrangian approach, more specifically, an index 3 formulation in mixed coordinates (combining natural and relative coordinates). It incorporates velocity and acceleration projections on the constraint subspaces. For a comprehensive understanding of the equations of motion and the projections of velocities and accelerations, we direct the reader to reference (Dopico et al., 2019). The numerical integration was carried out by means of the Newmark integrator (Gavrea et al., 2005), with a time-step size of 1 ms.

2.3.2 Guiding

The positions and orientations of the rigid bodies were determined based on the marker positions captured by the cameras of the motion capture system. To achieve this, the conventional methodology outlined by Vaughan (Vaughan et al., 1999) was applied, involving the following steps: (i) selection of three non-collinear entities, which could be markers or pre-defined joint locations, within each segment; (ii) establishment of an orthogonal reference frame for the corresponding segment using the selected entities; (iii) use of correlation equations to estimate the position and orientation of the rigid body.

The optical motion capture system recorded the movements of femur and tibia, providing the inputs for the simulation. The simulation was guided by the experimentally measured values of all the degrees of freedom of the two rigid bodies. Additionally, the recorded movements of the patella were used for experimental validation of the simulation results (depicted by the red markers in Figure 4) and to approximate the patella to its initial static equilibrium position, which needed to be determined.

2.3.3 Static equilibrium

To conduct a dynamic simulation of a multibody system, it is essential to acquire an initial set of positions and velocities that fulfill the constraint equations at configuration and velocity levels. In multibody systems with a static equilibrium configuration, it is advisable to initiate the simulation from it. This approach prevents the presence of initial high accelerations that could compromise the stability of the simulation. This, in turn, requires solving the static equilibrium equations of the system to determine the equilibrium configuration. Unfortunately, when the system involves bodies in contact, solving the static equilibrium problem becomes highly intricate, and, in some cases, multiple solutions may exist. For solving the nonlinear system, a Newton-Raphson iteration was used, similar to the one used to solve the equations of motion (Dopico et al., 2012).

2.3.4 Contact model

Given that the contact area was lubricated in the experimental setup to mimic the synovial fluid function, the approach to consider the contact between the patella and the femoral implant was limited to the normal forces, excluding tangential forces (friction). The Flores model was selected for the normal force (Flores et al., 2011), its expression being:

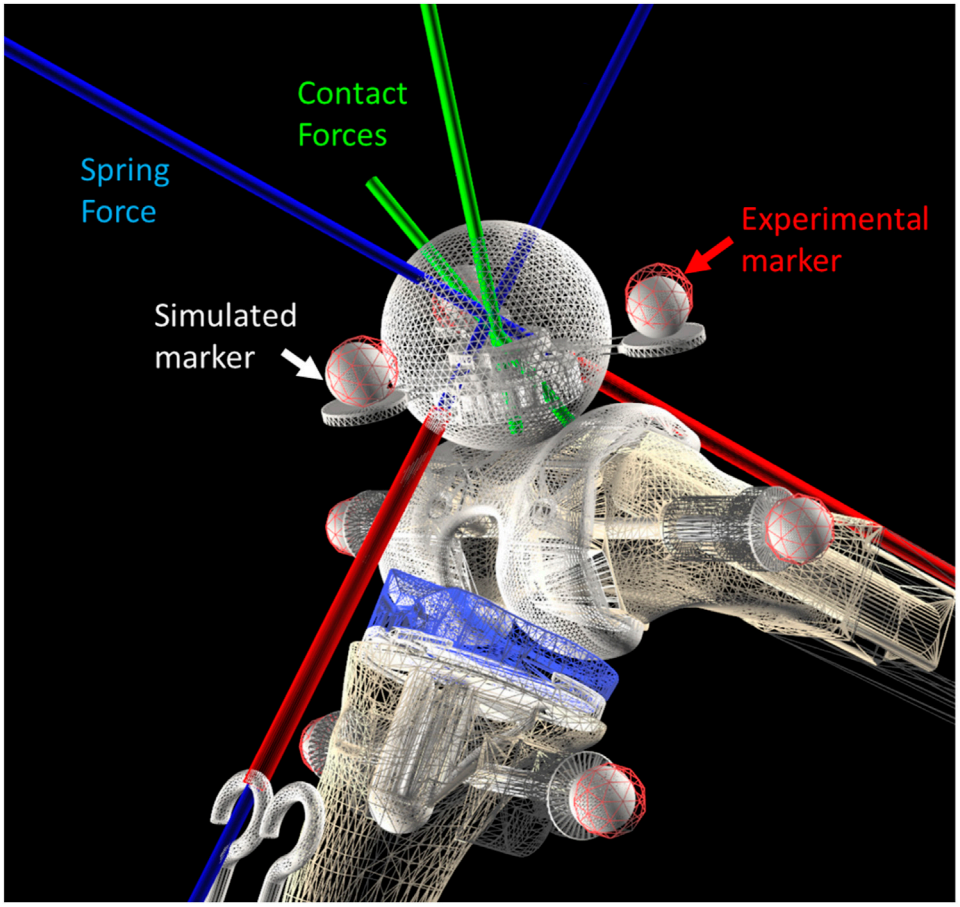

FIGURE 4
Mesh to mesh algorithm.

$$\mathbf{F}_{\mathrm{n}} = k_{\mathrm{n}}\delta^{p}\left(1 + \frac{8(1-\varepsilon)}{5\varepsilon}\frac{\dot{\delta}}{\dot{\delta}_{0}}\right)\mathbf{n}, \tag{2}$$

where k_n is the equivalent contact stiffness, which depends on the shape and the material properties of the colliding bodies, p is the Hertz's exponent, δ is the indentation and $\dot{\delta}$ its temporal derivative, $\dot{\delta}_0$ is the relative normal velocity between the colliding bodies when the contact is detected, ε is the coefficient of restitution, and $\mathbf{n}$ is the direction of the force. The subscript "n" comes from "normal".

2.4 Contact detection

A major computational challenge when incorporating contact into a multibody dynamics framework lies in addressing collision detection. Successfully implementing methods and algorithms that can accurately and efficiently simulate the complex interplay between contacting bodies while maintaining the required realism for multibody system simulations is significantly challenging. Especially when dealing with colliding bodies possessing complex 3D geometries, the demand for a comprehensive collision detection algorithm is required. In this work, two contact detection approaches were implemented in the proprietary development library (Dopico, 2016) and compared.

2.4.1 Mesh to mesh algorithm

A comparatively simple alternative is to approximate the free-form surfaces by discretized mesh elements and subsequently verifying proximity or overlap between them. The triangular meshes of the colliding objects (femur and patellar button) were obtained in obj or stl formats from the native CAD files of the bodies. Due to potential differences in accuracy and efficiency of polygonal surfaces, two meshes were generated to compare these indicators. As shown in Figure 5, the finer mesh (FM, Figure 5B) had a tolerance deviation and angle of 0.006 mm and 0.5°, respectively, while the coarser mesh (CM, Figure 5A) displayed tolerances of 0.1 mm and 1°. A meshed icosphere (Figure 4) with similar mesh sizes was chosen over a meshed model of the patellar button because it possesses regular triangulation and avoids a point intersecting with numerous triangles at its apex.

The algorithm checks for penetration between the triangles and identifies corresponding contact points while calculating the maximum indentation. From this information, for each detected contact, it computes the normal forces (Figure 4, in green) employing the aforementioned contact models.

In order to speed up the collision detection and definition process, it is essential to check only the closest mesh elements. This efficiency is achieved through the utilization of an element classification structure known as the *Axis-Aligned Bounding Box*

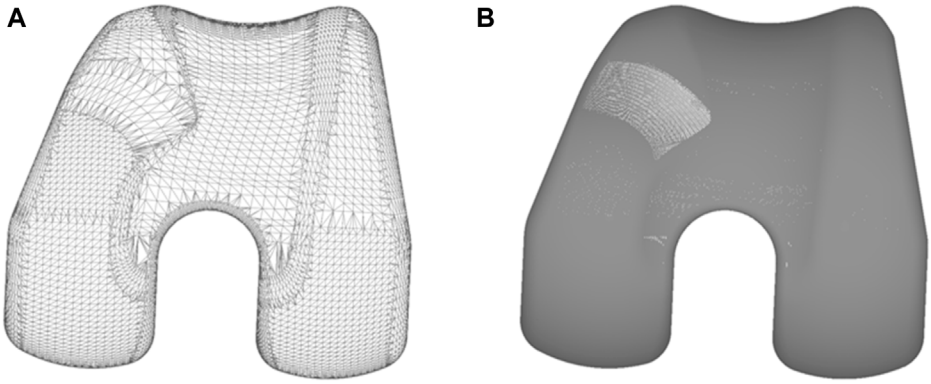

FIGURE 5
(A) Coarse mesh (CM); **(B)** Fine mesh (FM).

Tree (*AABB Tree*). The mesh undergoes a progressive subdivision and classification at each level into pairs of boxes, each approximately covering half of the volume of the previous box. This subdivision continues until the smaller *AABB*s exclusively enclose one element, typically a triangle.

During the collision characterization, the *AABB Tree* is compared against the patella object to determine if each *AABB* is in approximate contact with it. At every step, roughly half of the mesh elements are discarded. If the test is negative for a single *AABB*, its entire sub-tree can be discarded as well. This substantially reduces the number of checks to the order of $\log_2(N)$ instead of N^2, where N is the number of mesh elements.

Once the list of contacting elements is identified, the contact contours are defined by their intersections. Subsequently, the averaged contact point, amount of penetration, and direction of the normal force for each contact can be computed from these contours. For a more detailed and comprehensive description of the algorithm, the reader is referred to (Dopico et al., 2019).

The time-step size for the CM had to be reduced to 0.1 ms for simulating cases 1 to 3 and further reduced to 0.05 ms for case 4.

2.4.2 Analytic formulation

The analytic formulation involves employing mathematical equations to compute distances between the surfaces of geometric primitives. The specific equations used depend on the types of primitives being analyzed. In the scope of this study, only the interaction between the patellar button and the femoral implant was taken into account. The patellar button was represented by a spherical primitive, as only its spherical portion would come into contact with the femur. Similarly, for the femoral implant geometry, a comparable simplification was employed, concentrating solely on the surface that would interact with the patellar component (depicted in orange in Figure 6). Subsequently, a custom-made Matlab program was utilized to approximate this complex surface using a polynomial equation derived from the vertex coordinates. As illustrated in Figure 6, the mesh in the most critical area for patellar luxation was refined to enhance the accuracy of the approximation in this region. The geometry of the femoral implant was approximated using three polynomial equations: second, fourth, and fifth order (Figure 6), referred to as P2, P4, and P5, respectively, throughout the manuscript. This resulted in R-squared values of 91.54%, 99.36%, and 99,71%, respectively.

These equations take into account the position, orientation and size of the primitives. The objective is to ascertain whether two objects are in contact at a given time point. If the distance between the center of the sphere (representing the patellar button) and the femur surface is smaller than the radius of the sphere, it indicates the presence of a collision or contact. Based on this information and for each identified contact, the normal force is calculated (oriented perpendicular to the contact surfaces) utilizing the aforementioned contact model.

2.5 Experimental validation

To compare the results obtained from the computational simulations, the recorded experimental measurements were used as reference. The forces applied on the patella were validated by comparing the forces of the springs with the measurements from the load cells, and the contact force (only the normal component) with that obtained from the pressure load cell. The motion trajectory of the patella was also subjected to validation, achieved by contrasting the coordinates of the center of the patellar prosthetic button (sphere center, Figure 3) against those registered by the optical motion capture system. The latter was performed within the femur reference frame to avoid error accumulation (Figure 3). The tilt, flexion, and roll of the patella (rotations around the X, Y, and *Z*-axes, illustrated in Figure 3, respectively) were also compared with the experimental measurements. The error in the four tested knee anatomical configurations (Figure 2), utilizing the two described contact detection approaches, each of them with several resolution levels (CM, FM, P2, P4, and P5), was assessed by calculating the root mean square error (RMSE) between the respective pairs of data sets.

2.6 Estimation of tendon parameters from motion capture for treatment prediction

The authors employed well-established mechanical parameters of the springs to assess various approaches (CM, FM, P2, P4, and P5)

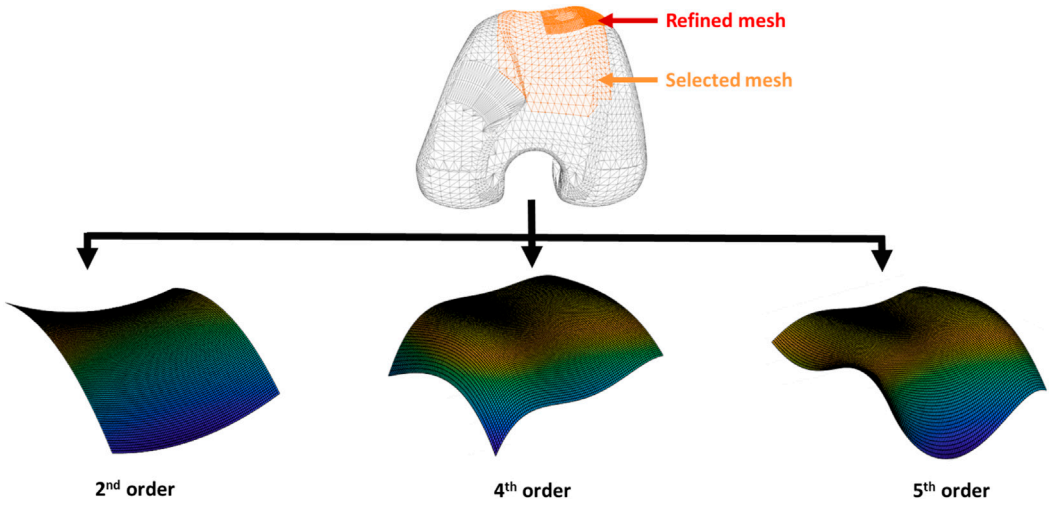

FIGURE 6
Polynomial equations derived from the vertex coordinates.

presented in this work, thus avoiding the introduction of external errors. Following the evaluation, the authors recommend applying the most effective approach, P5 (selected based on accuracy and efficiency comparisons), to simulate a treatment prediction case under real conditions. Since the spring parameters (representing tendon parameters in the real context) are typically unknown, an optimization process was conducted to estimate them. This entailed utilizing the patellofemoral digital twin and conducting contact simulations to match the motion of the recorded patella of the pathological scenario (case 2). The measured forces were not used in this application, as it necessitates additional tools beyond the ones available in contemporary computer-assisted TKR surgeries that capture motion (Shatrov and Parker, 2020). The spring parameters were permitted to fluctuate within a range of 30% above and below their default values. The objective function was formulated as the summation of the RMSE of the distance error in the relative position of the patella. The genetic algorithm (*ga* function) provided by Matlab was employed to estimate the minimum value of this function.

In the current work, the utilization of the patellofemoral digital twin facilitates predictions for treatments that do not impact the tibiofemoral joint and the corresponding captured motion. As mentioned in subsection 2.1, this includes cases like the tibial tuberosity transfer, which entails modifying the tendon attachment at the tibia to address issues with patellar stability. As an example, in this study, the authors suggest using case 2 as a pathological scenario and case 1 as a potential treatment option (tibial tuberosity medialization). After optimizing the parameters with motion capture data from case 2, simulations for cases 1 and 2 were conducted using the novel optimal spring parameters. Experimental measurements from both cases were then used to assess the accuracy of simulating the pathological scenario and its potential treatment option.

2.7 Computational details

The calculations were conducted on a computer equipped with an Intel(R) Core(TM) i7-13700 KF @ 3.40 GHz processor, 32 GB RAM, and a 2 TB SSD running Windows 10 Pro. The analysis was performed using a single-threaded program written in Fortran 2008 and C++. The program was compiled using MSVC 2017 and Intel Fortran 2018. Efficiency was gauged by measuring runtime, distinguishing the time needed for obtaining the initial static equilibrium configuration and for executing the simulation.

3 Results

The discrepancy in the four tested knee anatomical configurations (depicted in Figure 2), employing the two contact detection methods with different resolutions (CM, FM, P2, P4, and P5), was evaluated by computing the RMSE for each pair of corresponding data sets. The mean values of the four configurations by the different approaches are presented in Table 1. P2 yielded the least accurate force estimations and exhibited the highest position errors. CM exhibited notable discrepancies in contact force estimation and patellar orientation, attributed to substantial noise in the results despite reducing the time-step size. The trajectory shown in Figure 7 and the tilt angle shown in Figure 8 for case 4 with CM highlights the altered tilt of the patella due to the inaccurate contact force estimation. On the other hand, P5 exhibited the highest accuracy across all estimated values, with average errors of 2.12 N in force, 2.1° in orientation, and 1.5 mm in position, along all three axes. As highlighted in Figure 8, the primary orientation differences originated from the initial position and then remained constant throughout the knee motion. Besides FM, P5 was the only approach capable of closely replicating the observed high-riding patella phenomenon in case 2 (as depicted in Figures 7, 8), where the patella became wedged instead of sliding along the femur during flexion. Nevertheless, with the exception of P2, all approaches replicated the patellar luxations in cases 2 and 3, albeit some slightly offset in knee flexion (Figure 8).

Regarding the efficiency of the various approaches, the mesh-to-mesh algorithm for contact detection is notably slower than the analytical formulation approach. Despite using a ten-times smaller time-step, the CM discretization was considerably faster than its

TABLE 1 Accuracy and efficiency comparison of the different methods over the four cases (mean values, worst values in red, best values in bold).

		Mean values				
		Mesh to mesh algorithm		Analytic formulation		
		CM	FM	P2	P4	P5
RMSE	Contact Force (N)	4.90	3.44	4.06	3.38	**3.33**
	Tibial Spring Force (N)	1.52	1.39	3.45	1.30	**0.89**
	Femoral Spring Force (N)	1.96	2.01	2.27	**1.96**	2.15
	Int. Rotation (°)	3.72	0.65	**0.45**	0.74	0.59
	Flexion (°)	2.47	1.49	1.82	1.66	**1.38**
	Tilt (°)	11.38	4.85	4.46	6.60	**4.45**
	X-coord. (mm)	2.36	2.02	4.53	2.71	**1.44**
	Y-coord. (mm)	2.16	2.10	3.67	1.88	**1.36**
	Z-coord. (mm)	2.20	2.10	5.81	2.70	**1.70**
Mean error	Distance (mm)	2.98	2.78	7.25	2.99	**2.30**
Initial configuration time (s)		2.37	33.29	**0.51**	0.63	0.72
Runtime (faster than real time)		0.19	0.07	**6.00**	4.97	4.55

TABLE 2 Accuracy of the simulated pathological scenario (case 2) and its treatment (case 1) using estimated tendon parameters from motion capture.

		Pathological scenario	Treatment
RMSE	Contact Force (N)	2.56	3.62
	Tibial Spring Force (N)	1.12	1.16
	Femoral Spring Force (N)	2.45	2.51
	Int. Rotation (°)	0.61	0.67
	Flexion (°)	2.07	0.88
	Tilt (°)	3.63	5.44
	X-coord. (mm)	1.75	1.64
	Y-coord. (mm)	2.22	0.87
	Z-coord. (mm)	0.96	2.17
Mean error	Distance (mm)	1.66	2.61
Initial configuration time (s)		0.75	0.73
Runtime (faster than real time)		4.66	3.95

more accurate counterpart, FM. Although increasing the polynomial order slightly extended the simulation runtimes, the most accurate P5 approach was still 4.55 times faster than real-time, or 2.57 times faster if the time required to obtain the initial equilibrium configuration is included.

This reduced computational time enables optimization using the contact simulation with the P5 approach. The optimization process took 1,233 s to provide an estimation of the spring parameters. Specifically, K1 and L1 were estimated with errors of 8% and 13%, respectively, while K2 and L2 had errors of 5% and 3%. Despite these discrepancies, the simulated pathological scenario and its respective potential treatment option were fairly reproduced (Table 2). Using the parameters optimized from motion captured data, the observed trajectories of the patella were accurately reproduced with mean position errors along all three axes of 1.56 and 1.65 mm, respectively. The high-riding patella and the dislocation were reproduced, and the improved trajectory resulting from tibial tuberosity medialization was also accurately predicted.

4 Discussion

In this study, aiming for computational efficiency and considering the expected negligible elastic deformations of the

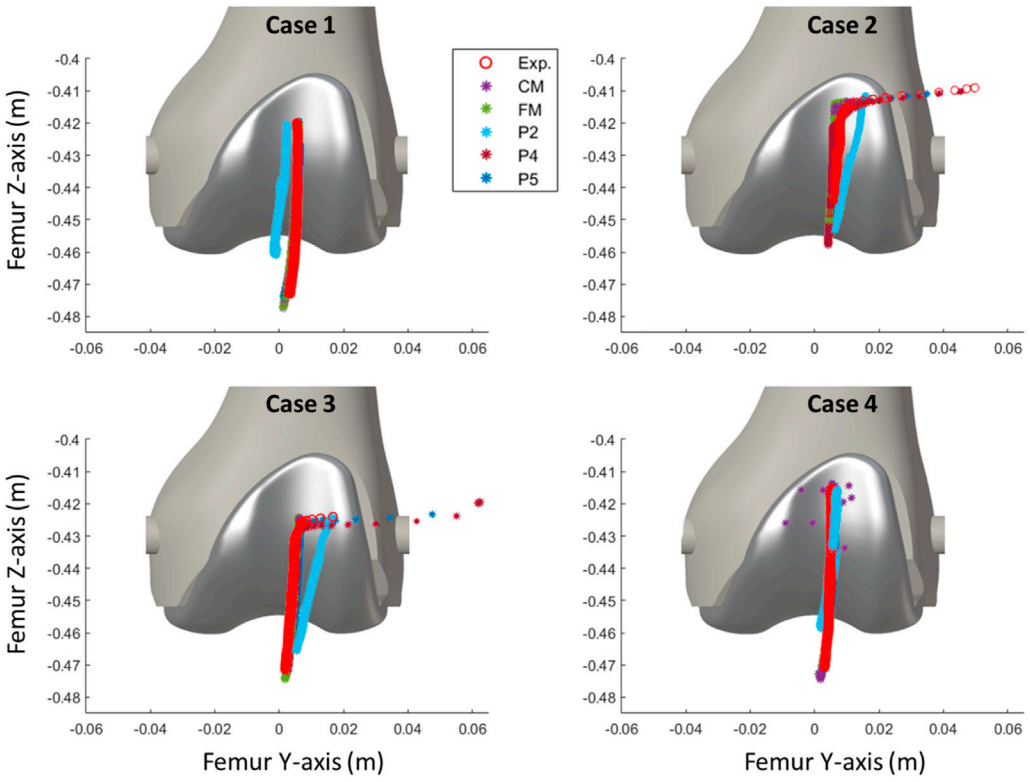

FIGURE 7
Comparison of the simulated patellar tracking using different contact detection algorithms.

bones, the authors employed rigid-body multibody dynamics formulations to simulate the mechanical system. They conducted a comparative analysis between two collision detection algorithms used for simulating contact between rigid bodies: a mesh-to-mesh algorithm, which involves discretizing the surfaces of the bodies into triangular mesh elements, and an analytical algorithm utilizing analytical expressions of the surfaces to provide closed-form solutions for the contact problem. Furthermore, they compared various 3D model geometries of the femoral implant. As observed in (Dopico et al., 2019), the mesh-to-mesh algorithm induces artificial oscillations because the geometry is approximated using a set of triangles. This effect is particularly noticeable with coarse discretization, as the frequency and amplitude of the oscillations are related to the discretization size. Although the approach using the coarse mesh (CM) offered a reasonable approximation, it produced noisy results that require post-processing. Significantly reducing the mesh size almost eliminated the oscillations, but increased proportionally the computational time, thus impeding clinical usability.

The analytical contact detection techniques have proven to be a good alternative, offering reduced computational time. The simplest polynomial approximation (P2) was the fastest approach but also the least accurate. P4 and P5 showed variabilities of few millimeters in position with respect to experimental measurements that might stem from imperfections in 3D-printing, imprecisions in optical measurements magnified in the processing and body motion reconstruction steps, and inaccuracies in the analytical approximation of the femoral implant geometry. On the other hand, discrepancies in force could be attributed to small variabilities in the attachment points. The P5 polynomial approximation provided the best accuracy while maintaining a processing speed 4.5 times faster than real time. This makes it suitable for running optimizations to determine anatomical or treatment parameters and for conducting intraoperative simulations.

In this study, the authors proposed using experimental measurements of case 2 to represent a pathological scenario and those of case 1 as a potential treatment (tibial tuberosity medialization). Since the spring parameters (which mirror tendon characteristics in the real context) are typically unknown, an optimization procedure was carried out to estimate them from case 2 motion capture. Numerous local minima were encountered, complicating the optimization process and prolonging the search for the optimal solution. Nevertheless, the optimization time could certainly be decreased by employing more specialized optimization tools and strategies. As demonstrated in (Michaud et al., 2023), the mechanical system simulation allows for variations in spring parameters while maintaining the force equilibrium. Accurate reproduction of patellar tracking was achieved using the optimized parameters, despite minor deviations from the values of the initial calibration. This implies that the current state of the simulation permits the use of the patellofemoral digital twin to provide predictions for treatments addressing patellar stability issues that do not affect the tibiofemoral joint and the captured motions of femur and tibia, such as tibial tuberosity transfer or trochleoplasty (Nolan et al., 2018).

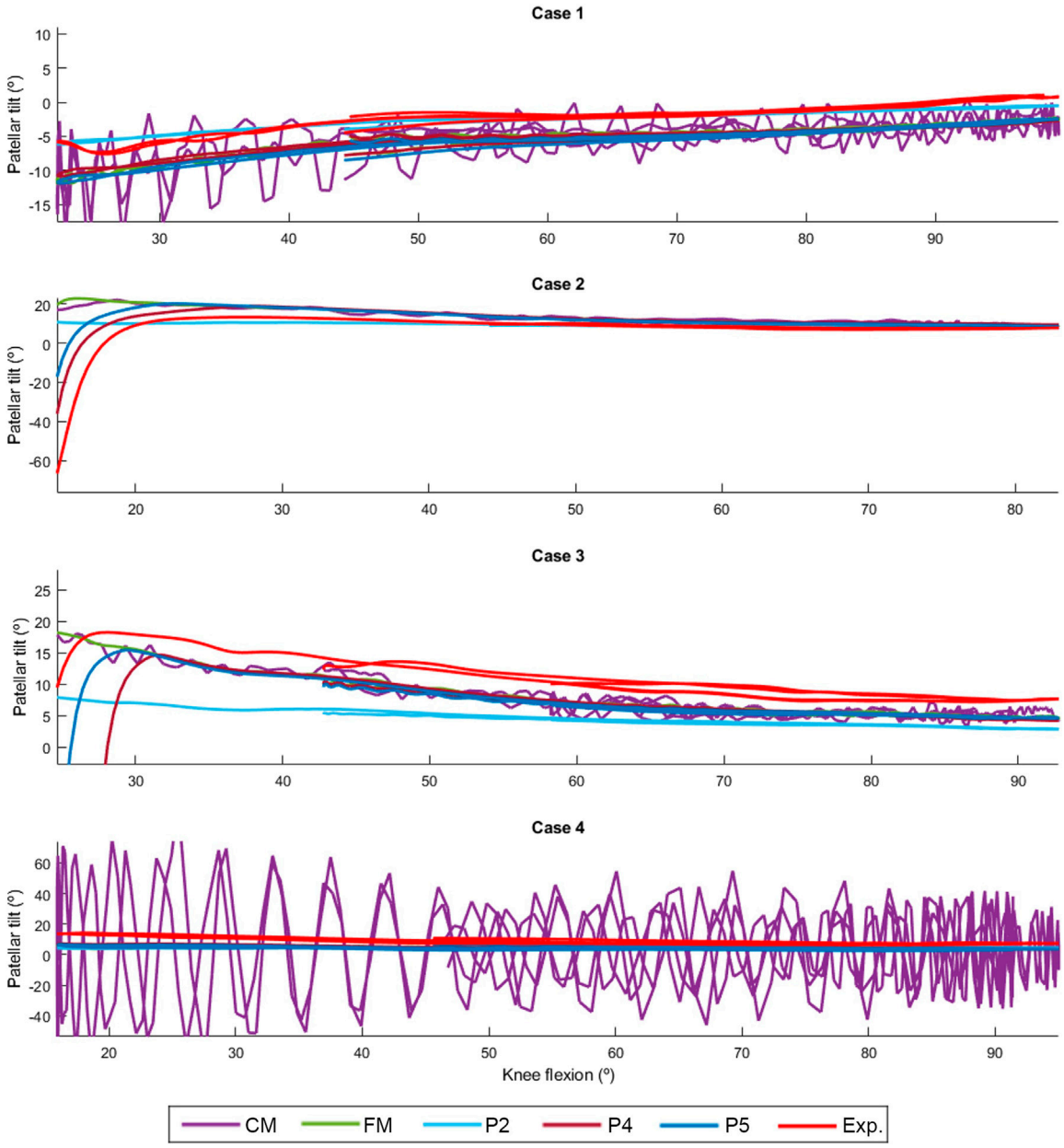

FIGURE 8
Comparison of the simulated patellar tilt using different contact detection algorithms.

As a limitation, this preliminary work focused on the simplified load case of a passive knee flexion. This choice was made to facilitate validation through a low-cost sensorized 3D-printed knee test rig, while also addressing ethical considerations (Michaud et al., 2023). Despite the seemingly simple motion, this method has proven to be relevant for assessing patellar tracking during TKR surgeries (Best et al., 2020). Authors acknowledge that muscle activity and knee loads could potentially affect patellar tracking. Nevertheless, these parameters are not expected to impact the contact detection model presented in this study. Additionally, in their recent work, the authors demonstrated their ability to perform real-time inverse dynamics and estimate individual muscle forces, instilling confidence in maintaining efficient computational time (Lugrís et al., 2023).

In future studies, the authors will intend to employ more realistic tendon models instead of linear springs to validate the applicability of the proposed approach in real-life scenarios. They will also incorporate contact interactions between tibial and femoral implants, enabling predictions for TKR treatments. Nevertheless, this presents an additional challenge in accurately applying the corresponding forces to the virtual model, given the unclear force magnitude and the application points/surfaces associated with the surgeon's maneuver. Lastly, in light of computational time performances, the authors are considering reconstructing the model motion, solving inverse dynamics and estimating contact

forces, all while offering real-time visualization of the results (Lugrís et al., 2023).

5 Conclusion

The patellofemoral digital twin and contact detection algorithms developed in this study enable the reproduction of pathological scenarios resulting in patellar instability and facilitate the prediction of post-treatment function. Computational efficiency was taken into account, and the histories of position, orientation, and contact force of the patella during its motion were validated using experimental measurements obtained from a sensorized 3D-printed test bench. The best results were achieved through a purely analytical contact detection algorithm, allowing for clinical usability and optimization of clinical outcomes.

Data availability statement

The raw data supporting the conclusion of this article will be made available by the authors, without undue reservation.

Author contributions

FM: Conceptualization, Data curation, Funding acquisition, Investigation, Methodology, Software, Validation, Writing–original draft, Writing–review and editing. AL: Data curation, Software, Supervision, Writing–review and editing. FM: Methodology, Software, Writing–review and editing. JC: Funding acquisition, Project administration, Resources, Supervision, Writing–review and editing.

Funding

The author(s) declare financial support was received for the research, authorship, and/or publication of this article. This work was funded by Pixee Medical under project OTR0123. Moreover, FM would like to acknowledge the support of the Galician Government and the Ferrol Industrial Campus by means of the postdoctoral research contract 2022/CP/048.

Conflict of interest

The authors declare that the research was conducted in the absence of any commercial or financial relationships that could be construed as a potential conflict of interest.

Publisher's note

All claims expressed in this article are solely those of the authors and do not necessarily represent those of their affiliated organizations, or those of the publisher, the editors and the reviewers. Any product that may be evaluated in this article, or claim that may be made by its manufacturer, is not guaranteed or endorsed by the publisher.

References

Aksahin, E., Kocadal, O., Aktekin, C. N., Kaya, D., Pepe, M., Yılmaz, S., et al. (2016). The effects of the sagittal plane malpositioning of the patella and concomitant quadriceps hypotrophy on the patellofemoral joint: a finite element analysis. *Knee Surg. Sport. Traumatol. Arthrosc.* 24 (3), 903–908. doi:10.1007/s00167-014-3421-7

Ateshian, G. A. (1993). A B-spline least-squares surface-fitting method for articular surfaces of diarthrodial joints. *J. Biomech. Eng.* 115 (4A), 366–373. doi:10.1115/1.2895499

Bei, Y., and Fregly, B. J. (2004). Multibody dynamic simulation of knee contact mechanics. *Med. Eng. Phys.* 26 (9), 777–789. doi:10.1016/j.medengphy.2004.07.004

Best, M. J., Tanaka, M. J., Demehri, S., and Cosgarea, A. J. (2020). Accuracy and reliability of the visual assessment of patellar tracking. *Am. J. Sports Med.* 48 (2), 370–375. doi:10.1177/0363546519895246

Bull, A., Katchburian, M., Shih, Y.-F., and Amis, A. (2002). Standardisation of the description of patellofemoral motion and comparison between different techniques. *Knee Surg. Sport. Traumatol. Arthrosc.* 10 (3), 184–193. doi:10.1007/s00167-001-0276-5

Clark, D., Walmsley, K., Schranz, P., and Mandalia, V. (2017). Tibial tuberosity transfer in combination with medial patellofemoral ligament reconstruction: surgical technique. *Arthrosc. Tech.* 6 (3), e591–e597. doi:10.1016/j.eats.2017.01.003

Cuadrado, J., Michaud, F., Lugrís, U., and Pérez Soto, M. (2021). Using accelerometer data to tune the parameters of an extended kalman filter for optical motion capture: preliminary application to gait analysis. *Sensors* 21 (2), 427. doi:10.3390/s21020427

Curreli, C., Di Puccio, F., Davico, G., Modenese, L., and Viceconti, M. (2021). Using musculoskeletal models to estimate *in vivo* total knee replacement kinematics and loads: effect of differences between models. *Front. Bioeng. Biotechnol.* 9 (Jul), 703508–712021. doi:10.3389/fbioe.2021.703508

Dopico, D. (2016). MBSLIM: multibody Systems en Laboratorio de Ingeniería Mecánica. Available at: http://lim.ii.udc.es/MBSLIM.

Dopico, D., González, F., Cuadrado, J., and Kövecses, J. (2014). Determination of holonomic and nonholonomic constraint reactions in an index-3 augmented Lagrangian formulation with velocity and acceleration projections. *J. Comput. Nonlinear Dyn.* 9 (4). doi:10.1115/1.4027671

Dopico, D., Luaces, A., Saura, M., Cuadrado, J., and Vilela, D. (2019). Simulating the anchor lifting maneuver of ships using contact detection techniques and continuous contact force models. *Multibody Syst. Dyn.* 46 (2), 147–179. doi:10.1007/s11044-019-09670-8

Dopico, D. D., Fernández, A. L., Michaud, F., and Cuadrado, J. (2012). Simulation of the anchor lifting maneuver of a ship using contact detection techniques and continuous force models. doi:10.1007/s11044-019-09670-8

Farrokhi, S., Keyak, J. H., and Powers, C. M. (2011). Individuals with patellofemoral pain exhibit greater patellofemoral joint stress: a finite element analysis study. *Osteoarthr. Cartil.* 19 (3), 287–294. doi:10.1016/j.joca.2010.12.001

Flores, P., Machado, M., Silva, M. T., and Martins, J. M. (2011). On the continuous contact force models for soft materials in multibody dynamics. *Multibody Syst. Dyn.* 25 (3), 357–375. doi:10.1007/s11044-010-9237-4

Fregly, B. J., Besier, T. F., Lloyd, D. G., Delp, S. L., Banks, S. A., Pandy, M. G., et al. (2012). Grand challenge competition to predict *in vivo* knee loads. *J. Orthop. Res.* 30 (4), 503–513. doi:10.1002/jor.22023

Gavrea, B., Negrut, D., and Potra, F. A. (2005). "The Newmark integration method for simulation of multibody systems: analytical considerations," in *Design engineering*. Editors A. Parts and B. ASMEDC (USA: IEEE), 1079–1092. doi:10.1115/IMECE2005-81770

Gay Neto, A. (2023). Framework for automatic contact detection in a multibody system. *Comput. Methods Appl. Mech. Eng.* 403, 115703. doi:10.1016/j.cma.2022.115703

Geier, A., Tischer, T., and Bader, R. (2015). Simulation of varying femoral attachment sites of medial patellofemoral ligament using a musculoskeletal multi-body model. *Curr. Dir. Biomed. Eng.* 1 (1), 547–551. doi:10.1515/cdbme-2015-0130

Hayat, Z., El Bitar, Y., and Case, J. L. (2023). Patella dislocation. Available at: https://www.ncbi.nlm.nih.gov/books/NBK538288/ (Accessed September 26, 2023).

Hippmann, G. (2004). An algorithm for compliant contact between complexly shaped bodies. *Multibody Syst. Dyn.* 12 (4), 345–362. doi:10.1007/s11044-004-2513-4

Innocenti, B., Fekete, G., and Pianigiani, S. (2018). Biomechanical analysis of augments in revision total knee arthroplasty. *J. Biomech. Eng.* 140 (11), 111006. doi:10.1115/1.4040966

Islam, K., Duke, K., Mustafy, T., Adeeb, S. M., Ronsky, J. L., and El-Rich, M. (2015). A geometric approach to study the contact mechanisms in the patellofemoral joint of normal versus patellofemoral pain syndrome subjects. *Comput. Methods Biomech. Biomed. Engin.* 18 (4), 391–400. doi:10.1080/10255842.2013.803082

Katchburian, M. V., Bull, A. M. J., Shih, Y. F., Heatley, F. W., and Amis, A. A. (2003). Measurement of patellar tracking: assessment and analysis of the literature. *Clin. Orthop. Relat. Res.* 412 (412), 241–259. doi:10.1097/01.blo.0000068767.86536.9a

Kebbach, M., Darowski, M., Krueger, S., Schilling, C., Grupp, T. M., Bader, R., et al. (2020). Musculoskeletal multibody simulation analysis on the impact of patellar component design and positioning on joint dynamics after unconstrained total knee arthroplasty. *Mater. (Basel)* 13 (no. 10), 2365. doi:10.3390/ma13102365

Khasawneh, R. R., Allouh, M. Z., and Abu-El-Rub, E. (2019). Measurement of the quadriceps (Q) angle with respect to various body parameters in young Arab population. *PLoS One* 14 (6), e0218387. doi:10.1371/journal.pone.0218387

Li, X., Song, S., Yao, J., Zhang, H., Zhou, R., and Hong, Q. (2023). Efficient collision detection using hybrid medial axis transform and BVH for rigid body simulation. *Graph. Models* 128, 101180. doi:10.1016/j.gmod.2023.101180

Lugrís, U., Pérez-Soto, M., Michaud, F., and Cuadrado, J. (2023). Human motion capture, reconstruction, and musculoskeletal analysis in real time. *Multibody Syst. Dyn.* 60, 3–25. doi:10.1007/s11044-023-09938-0

Luyckx, T., Didden, K., Vandenneucker, H., Labey, L., Innocenti, B., and Bellemans, J. (2009). Is there a biomechanical explanation for anterior knee pain in patients with patella alta? Influence of patellar height on patellofemoral contact force, contact area and contact pressure. *J. Bone Jt. Surg. - Ser. B* 91 (3), 344–350. doi:10.1302/0301-620X.91B3.21592

Marra, M. A., Vanheule, V., Fluit, R., Koopman, B. H. F. J. M., Rasmussen, J., Verdonschot, N., et al. (2015). A subject-specific musculoskeletal modeling framework to predict *in vivo* mechanics of total knee arthroplasty. *J. Biomech. Eng.* 137 (2), 020904. doi:10.1115/1.4029258

Michaud, F., Mouzo, F., Dopico, D., and Cuadrado, J. (2024). A sensorized 3d-printed knee test rig for experimental validation of patellar tracking and contact simulation after total knee replacement (Preprint). *BioRxiv*. doi:10.1101/2024.02.13.58009

Nolan, J. E., Schottel, P. C., and Endres, N. K. (2018). Trochleoplasty: indications and technique. *Curr. Rev. Musculoskelet. Med.* 11 (2), 231–240. doi:10.1007/s12178-018-9478-z

Paz, A., Orozco, G. A., Korhonen, R. K., García, J. J., and Mononen, M. E. (2021). Expediting finite element analyses for subject-specific studies of knee osteoarthritis: a literature review. *Appl. Sci.* 11 (23), 11440. doi:10.3390/app112311440

Putman, S., Boureau, F., Girard, J., Migaud, H., and Pasquier, G. (2019). Patellar complications after total knee arthroplasty. *Orthop. Traumatol. Surg. Res.* 105 (1), S43–S51. doi:10.1016/j.otsr.2018.04.028

Romero, F., Alonso, F. J. J., Cubero, J., and Galán-marín, G. (2015). An automatic SSA-based de-noising and smoothing technique for surface electromyography signals. *Biomed. Signal Process. Control* 18, 317–324. doi:10.1016/j.bspc.2015.02.005

Sharma, V., Arun, C. O., and Krishna, I. R. P. (2019). Development and validation of a simple two degree of freedom model for predicting maximum fundamental sloshing mode wave height in a cylindrical tank. *J. Sound. Vib.* 461, 114906. doi:10.1016/j.jsv.2019.114906

Shatrov, J., and Parker, D. (2020). Computer and robotic – assisted total knee arthroplasty: a review of outcomes. *J. Exp. Orthop.* 7 (1), 70. doi:10.1186/s40634-020-00278-y

Tischer, T., Geier, A., Lenz, R., Woernle, C., and Bader, R. (2017). Impact of the patella height on the strain pattern of the medial patellofemoral ligament after reconstruction: a computer model-based study. *Knee Surg. Sport. Traumatol. Arthrosc.* 25 (10), 3123–3133. doi:10.1007/s00167-016-4190-2

Van Rossom, S., Wesseling, M., Smith, C. R., Thelen, D. G., Vanwanseele, B., Dieter, V. A., et al. (2019). The influence of knee joint geometry and alignment on the tibiofemoral load distribution: a computational study. *Knee* 26 (4), 813–823. doi:10.1016/j.knee.2019.06.002

Vaughan, C. L., Davis, B. L., and O'Connor, J. C. (1999). *Dynamics of human gait*. 2nd ed. Cape Town: Kiboho Publishers.

Wang, J.-W., Chen, W.-S., Lin, P.-C., Hsu, C.-S., and Wang, C.-J. (2010). Total knee replacement with intra-articular resection of bone after malunion of a femoral fracture. *J. Bone Jt. Surg. Br.* 92-B (10), 1392–1396. doi:10.1302/0301-620X.92B10.24551

frontiers | Frontiers in Bioengineering and Biotechnology

TYPE Original Research
PUBLISHED 26 February 2024
DOI 10.3389/fbioe.2024.1335159

OPEN ACCESS

EDITED BY
Anne D. Koelewijn,
Friedrich-Alexander-Universität Erlangen-Nürnberg, Germany

REVIEWED BY
Wojciech Wolański,
Silesian University of Technology, Poland
Kaushik Mukherjee,
Indian Institute of Technology Delhi, India

*CORRESPONDENCE
Anas Ben Achour,
anas.ben.achour@iwu.fraunhofer.de

†These authors have contributed equally to this work and share first authorship

RECEIVED 08 November 2023
ACCEPTED 07 February 2024
PUBLISHED 26 February 2024

CITATION
Ben Achour A, Apfeld F, Lauer G, Bräuer C, Leonhardt H, Franke A, Lipphaus A, Teicher U, Witzel U and Schröder TA (2024), Development of a test bench for biomechanical simulation—a preliminary study of mandibular forces. *Front. Bioeng. Biotechnol.* 12:1335159. doi: 10.3389/fbioe.2024.1335159

Development of a test bench for biomechanical simulation—a preliminary study of mandibular forces

Anas Ben Achour[1*†], Florian Apfeld[1,2†], Günter Lauer[3], Christian Bräuer[4], Henry Leonhardt[3], Adrian Franke[3], Andreas Lipphaus[2], Uwe Teicher[1], Ulrich Witzel[2] and Tom Alexander Schröder[3,5]

[1]Fraunhofer Institute for Machine Tools and Forming Technology IWU, Dresden, Germany, [2]Biomechanics Research Group, Chair of Product Development, Faculty of Mechanical Engineering, Ruhr University Bochum, Bochum, Germany, [3]Department of Oral and Maxillofacial Surgery, University Hospital Carl Gustav Carus Dresden, Technische Universität Dresden, Dresden, Germany, [4]Department of Oral and Maxillofacial Surgery, Facial Plastic Surgery, University of Rostock, Rostock, Germany, [5]Else Kröner Fresenius Center for Digital Health, Technische Universität Dresden, Dresden, Germany

Purpose: The aim of this study is to develop a test bench, which integrates different complexity levels and enables in that way a flexible and dynamic testing for mid and long term intervals as well as testing of maximum loads till implant failure of different osteosynthesis systems on the mandible.

Material and Methods: For this purpose, an analysis of the state of the art regarding existing test benches was combined with interviews of clinical experts to acquire a list of requirements. Based on these requirements a design for a modular test bench was developed. During the implementation of the test stand, functional tests were continuously carried out and improvements made. Depending on the level of complexity, the test bench can be used either as an incorporated variant or as a standalone solution. In order to verify the performance and the degree of fulfilment of the requirements of these two variants of the test bench, preliminary studies were carried out for all levels of complexity. In these preliminary studies, commercially available osteosynthesis and reconstruction plates were investigated for their biomechanical behaviour and compared with data from the literature.

Results: In total, fourteen test runs were performed for the different levels of complexity. Firstly, five test runs were executed to test the simplified load scenario in the incorporated variant of the test bench. High forces could be transmitted without failure of the miniplates. Secondly a quasi-static test scenario was examined using the incorporated variant with simplified load insertion. Five experiments with a number of cycles between 40,896 and 100,000 cycles were carried out. In one case the quasi-static testing resulted in a fracture of the tested reconstruction plate with a failure mode similar to the clinical observations of failure. The last four test runs were carried out using the standalone variant of the test bench simulating complex load patterns via the insertion of forces through imitated muscles. During the test runs joint forces were measured and the amplitude and vector of the resulting joint forces were calculated for both temporomandibular joints. Differences in the force transmission depending on the implant system in comparison to the zero sample could be observed.

Conclusion: The presented modular test bench showed to be applicable for examination of the biomechanical behavior of the mandible. It is characterized by the adjustability of the complexity regarding the load patterns and enables the subsequent integration of further sensor technologies. Follow-up studies are necessary to further qualify and optimize the test bench.

KEYWORDS

biomechanics, bite forces, mandible, implant materials, experimental, test bench, osteosynthesis

1 Introduction

In oral and maxillofacial surgery many different types of osteosynthesis and reconstruction plates have been developed over the last 100 years (Sauerbier et al., 2008). The challenge is to meet very different requirements in the treatment of a variety of diseases, defects or traumas. Due to the complex anatomy (Wong et al., 2010), kinematics and force transmission (Throckmorton, 2000; van Eijden, 2000; Wieja et al., 2022) of the mandible, the highest demands are placed on the plates and their attachment. Despite approaches such as patient-specific (Goodson et al., 2019) and special three-dimensional (3D) plates (de Oliveira et al., 2018), (Ben Achour et al., 2019) complications do occur, e.g., inflammations and plate exposures (van den Bergh et al., 2012), (Dean et al., 2020) or complications due to mechanical reasons like plate fractures or screw loosening (Martola et al., 2007; Probst et al., 2012; Bagheri and Bell, 2014; Seol et al., 2014). Hence they are subject to permanent further development. In order to predict the performance of these modifications of existing plate geometries respectively the new developments of plates, tests on force transmission close to reality are essential. Those results can be used to check the physical load transmission characteristics of different implants as well as for the optimization and verification of complementary Finite Element Method (FEM) simulations. For this purpose it is necessary to mimic the complex biomechanics of the mandible in its anatomical context on a laboratory scale. FEM itself has been used more recently in oral and maxillofacial surgery (Lisiak-Myszke et al., 2020). However, test benches used today by Schupp et al. (Schupp et al., (2007), Karoglan et al., (2006), Rendenhybach et al., (2017) and Zimmermann et al., (2017) do not represent these complex relationships and simplify the biomechanics by combining the various muscle forces into a single resulting force. In addition to this similarity, however, the test benches differ in their designs for force application, specimen bearing and test dynamics. Thus the comparability is limited and no precise predictions can be made about failure cases and limitations of the individual plates. In contrast to the simplified test benches, Meyer et al., (2000) chose the approach of simulating each muscle insertion by means of taped ropes for their static test bench, which can be seen as the reference test bench for static tests for complex load patterns. However, the difficulty of this test setup is the correct bonding of the ropes and the correct selection of the muscle forces. This difficulty results from the fact that these forces acting on the mandible during movement and chewing can only be estimated and are subject to a wide range as things stand today.

Besides the applied muscle forces it should also be considered to simulate the main bite forces at different points of the dentition in order to investigate the behaviour of implants during special masticatory processes. However, the maximum bite forces measured in several studies do differ in a large range mainly due to influences such as age, sex, occlusion, position of measurement and physiological and psychological conditions of test persons (Wieja et al., 2022), (Varga et al., 2011). For biomechanical testing different types of loads can be considered and used for load transmission:

- muscle forces and
- resulting bite forces.

In addition joint forces are generated whose directional vectors can be of great importance to avoid additional joint load and wear. The aim of using osteosynthesis and reconstruction plates in the mandibular region is generally to enable load transfer equivalent to the healthy mandible with preservation of the physiological stresses on the bone and the adjoining articulations over the complete period until full regeneration (Gutwald et al., 2017), (Kumar et al., 2016). However to achieve this goal flexible and dynamic testing methods for plate systems are needed that can simulate different load profiles and cover the wide range of acting forces resulting from inter-individual variations. None of the previously published test benches and methods meet these high-performance requirements for reality-based biomechanical testing of the mandible including complex load patterns and dynamics. For that reason the authors of this paper aimed to develop a test bench as an evolution of the reference test benches, which integrates different complexity levels. This is necessary in order to investigate the mid- and longterm stability and behavior of plating systems in flexible and dynamic testing as well as testing of maximum loads till implant failure. Therefore, in addition to the simplified processes for testing the maximum loads, the goal is also to enable a quasi-static test setup with consideration of the masticatory muscles as a complex case to overcome the state of the art. The main load spectrum of this complex case is implemented in a muscularly guided mastication process, which is cyclical and adaptable in its composition. Besides of those basic functions interfaces are already provided for additional sensor systems to allow expanding the range of functions of the test bench and the number of test parameters to be adapted to individual requirements. This paper describes the design of the test bench and provides the performance of each level of complexity of the test bench using results from preliminary studies that are comparable to the state of the art.

2 Materials and methods

2.1 Requirement analysis and definition of complex test benches

A flexible and dynamic test bench is supposed to realize different load scenarios in varying degree of abstraction. Therefore, the necessary requirements for the test bench are comprehensive. The analysis of specific research publications was done to use the lessons learned for the definition of minimum requirements. To achieve a high flexibility of the test bench the concept of modularity and adaptability was chosen. Based on this the following requirements for such a test bench were set.

Initially the test bench needs to be able to test various osteosynthesis systems (e.g., miniplates, 3D plates, reconstruction-plates), which are fixed on human mandible models (natural bone or artificial bone). The test bench needs to be adaptable to the size of the model. Furthermore, it is important how the forces are introduced in the mandible and how it is mounted. This aspect is dependent on the degree of abstraction. In addition, further requirements are considered in the construction (data evaluation, reproducibility and stability of the experiments, safety aspect, usability and extension capability). Based on these requirements, a test bench with two degrees of abstractions and different test scenarios was considered:

1. Simplified test scenario in which the muscles for mouth closure are represented by one resultant force, influenced by the test benches of Schupp et al. (2007), Rendenbach et al. (2017) and Zimmermann et al. (2017). This construction can be mounted on a universal stress-strain testing machine to function as a built-in system. The following requirements must be met on that variant of the test bench:
   a) Static experiments to analyze the maximal forces until failure.
   b) Quasi-static experiments to imitate simplified exposure during the chewing process.
2. Complex test scenario in which all muscles for mouth closure are realized while loading the specimen. Therefore, a new construction is necessary to function as a standalone solution. The construction is inspired by Meyer et al., (2000), who created a static test bench. With the developed test bench even quasi-static experiments are possible. Based on this the following requirements must be met to demonstrate the functionalities of the test bench and to generate approaches for new series of experiments, which overcome the state of the art:
   a) Quasi-static experiments to imitate realistic forces during the chewing process
   b) Experimental reconstruction of published force data during the chewing process, which were calculated in mathematical or simulative computations.

2.2 Design and components of the modular test bench

Both concepts are based on the same frame made of aluminium profiles, which are resistant to bending and torsion. The frame can be mounted on a universal stress-strain testing machine for the simplified concept or in the standalone test bench for the complex scenario as seen in Figure 1.

In both cases the mandibular joint is supported by an aluminium profile, which corresponds to the form and the function of the mandibular fossa (see Figure 2 blue box—mandibular joint imitation). The support of the resulting forces at the teeth is realized with a modular counterpart to transmit the forces via single or multiple teeth (see Figure 2 orange box—modular counterpart). Therefore a unilateral, bilateral or occlusive load scenario can be tested. Moreover, the defined force of the testing machine can be divided on the mandible via a specific distributor (see Figure 2 green box—Distributor). Therefore, it is possible to induce the force equally on both halves or split it up to 70% on the healthy side without the osteosynthesis and 30% in the affected one. This idea is based on the consideration of Schupp et al., (2007), who suggested, that the resected side will load less due to missing dental support.

The simplified test scenario was integrated in a universal stress-strain testing machine TIRAtest 2720 (TIRA GmbH, Schalkau, Germany) with an integrated control technology (EDC 222, Doli Elektronik GmbH, München, Germany) and axial force sensor (Typ Kap-S, 5kN, A.S.T. GmbH, Dresden, Germany). The generated data (force, displacement, cycle number) are transferred in the computer software TIRAtest System 4.6.0.52 (TIRA GmbH, Schalkau, Germany).

For the complex and more realistic test scenario the masticatory muscles M. temporalis, M. masseter, M. pterygoideus medialis, as well as M. pterygoideus lateralis are represented via ropes with 3 mm diameter (Regatta 2000; LIROS GmbH, Berg, Germany). The physiological vectors of each muscle force were determined by calculating a resultant angle of the individual muscle pulls of each specific muscle in the sagittal and frontal planes. The ropes are glued on the muscle insertions areas with UHU Sekundenkleber Plastic (UHU GmbH and Co. KG, Bühl/Baden, Germany), which showed the best results in tests on adhesive strength. The insertion areas are based on the illustrations of Netter (2008). With the help of guide pulleys (Sprenger GmbH, Iserlohn, Germany) the ropes are orientated in the direction of the calculated physiological muscle vectors and are connected with defined and muscle specific weights. Nevertheless, the design of the test bench enables easy adjustment of the directional vectors of the muscles if needed. The weights are laid on two movable platforms, which can be lifted vertically with one linear axis (Föhrenbach GmbH, Löffingen-Unadingen, Germany) as a central load control (see Figure 3). The motor control is realized with a stepper motor (Pythron GmbH, Gröbenzell, Germany) and the software NanoPro (Nanotec Electronic GmbH and Co. KG, Feldkirchen, Germany).

In both scenarios further force sensors can be added to measure the forces located at the mandible joint. The used sensors are piezoelectrical three axis load cells (Type 9317C, Kistler Instrumente GmbH, Winterthur, Switzerland). To measure the forces resulting on the teeth, specific strain gauges for measurements of compressive and tension forces inside of screws are tested (TB21, Hottinger Brüel & Kjaer GmbH, Darmstadt, Germany).

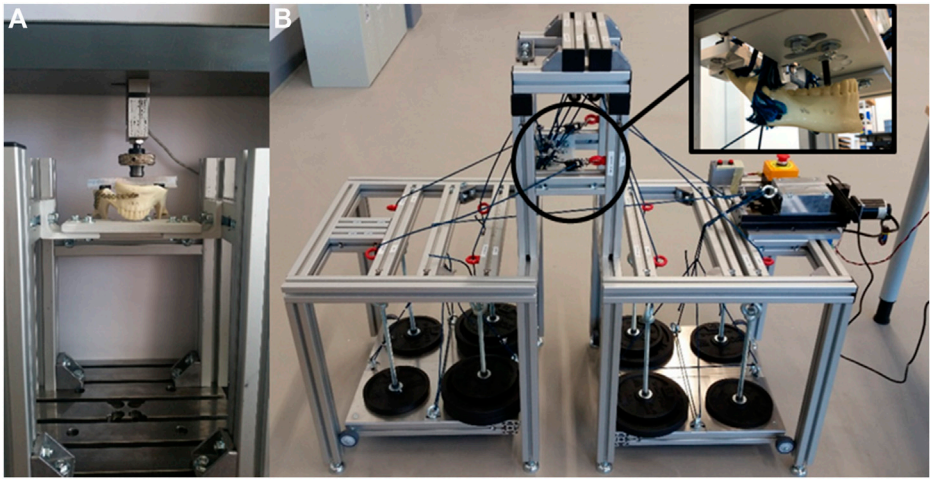

FIGURE 1
Test bench variants: **(A)** Built-in solution for simple scenarios; **(B)** Standalone solution for complex scenarios.

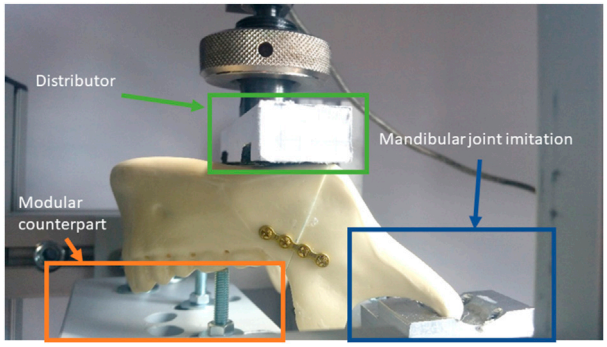

FIGURE 2
Imitation of the mandibular joint via milled aluminium part.

2.3 Experimental set-up of the preliminary studies to verify the test bench

After the implementation and pilot tests for optimizations the following test settings (see Table 1) were defined for the different test scenarios in order to investigate the degree of compliance of the requirements.

The preset parameters for each test scenario can be explained by some basic assumptions in the following way:

- **Scenario 1.1 Static tests for maximum force:**
  - o Load definition: The defined load for the test is the load the testing machine realizes.
  - o Load insertion: The teeth forces are located bilateral at the first molars, where the highest forces are predicted (Wieja et al., 2022; Varga et al., 2011; BAKKE et al., 1990)
  - o Stop criterium: A force of 2000 N was defined as a stop criterium. In case the 2000 N were induced perfectly, every side of the mandible is strained with 1000 N. This force will be distributed between the joint and the resulted teeth force. In extensive studies, the maximum bite force is between 500 and 1000 N (Varga et al., 2011; BAKKE et al., 1990; Braun et al., 1995; van der Bilt et al., 2008; Mathur et al., 2014). In the case of osteosynthesis it certainly lower and decreases to the half of the initial strength (Tate et al., 1994).
- **Scenario 1.2 Quasistatic tests for simplified exposure:**
  - o The force is split into 30% on the mandible side with the affected and 70% on the healthy mandible side with a distributor. The teeth force is located unilaterally at the first molar of the healthy side
  - o During the cycle of exposure the forces are alternating between a minimum force of 50 N and a maximum force of 400 N, 500 N or 550 N, depending on the experiment. This force should result in a physiological workload, which is comparable to the average during the chewing process.
  - o In contrast to other mandible test machines (Schupp et al., 2007; Rendenbach et al., 2017; Zimmermann et al., 2017), the force sensor is located differently. In this construction the resulting muscle forces are inserted via the testing machine instead of measuring the resulting force directly at the teeth. Nevertheless, the resulting teeth force can be determined with the help of the strain gauges in this test bench as well.
  - o The cycle time varies between 2.5 s (400 N) to 3.3 s (550 N), due to a constant rate of force increase
  - o A maximum cycle number of 100,000 is chosen. It is assumed, that only during 2.5 min per meal, the highest exposure emerges. The remaining time is used to chew the already grinded and softened food. Due to the experimental studies mentioned in the introduction, it is expected, that the low forces (<100 N) have no significant effect on the lifetime of the osteosynthesis plates. With three meals a day and a chewing cycle time of 70 times per minute this results in 96,075 cycles for half a year. The assumptions based on the ideas of Weiskopf et al. (1981) and Verplancke et al. (2011).
- **Scenario 2. Quasistatic tests for complex exposure:**
  - o The mounting of the mandible is comparable to the quasistatic test for simple exposure (in case of unilateral

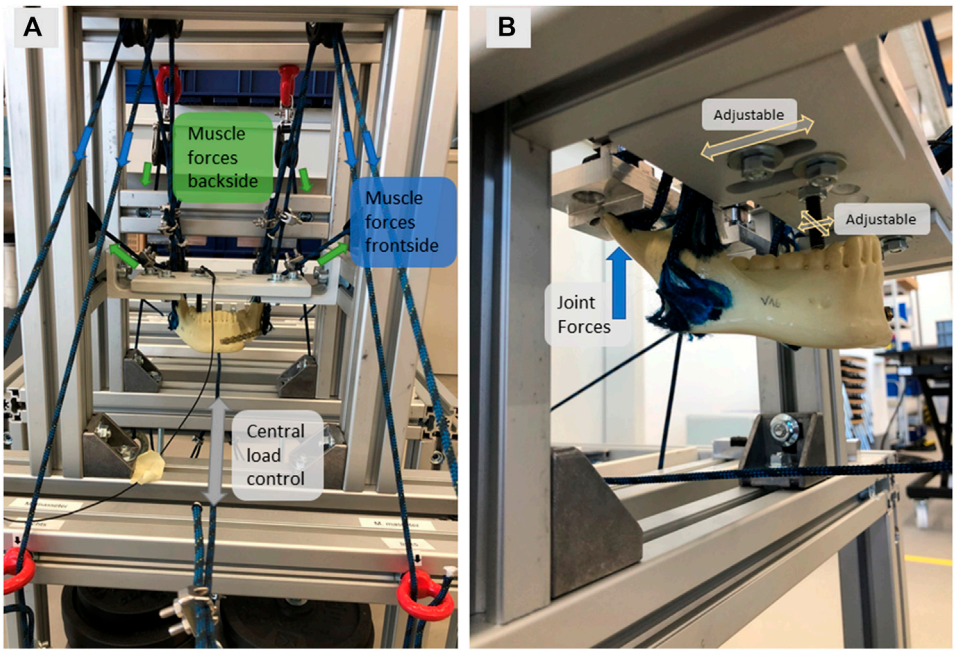

FIGURE 3
Complex load scenario with **(A)** Frontview of clamped specimen with muscle forces directing to the frontside (M.masseter, M. pt. medialis) and the backside (M.temporalis. M. pt. lateralis); **(B)** Isometric view of the clamped specimen with the adjustable position of tooth force insertion and the force transmission into the mandibular joint.

TABLE 1 Set-up of test parameters of the various test scenarios.

Scenario	Load	Distribution of force	Velocity	Stop criteria	Cycle time	Sample size n
1.1 Static	Testing machine (<2000 N)	Bilateral	5 N/s	2000 N or fracture	-	5
1.2 Quasistatic (simple)	Testing machine (400 N, 500 N, 550 N)	Unilateral	400 N/s	100.000 cycles or fracture	2.5—3.3 s	5
2. Quasistatic (complex)	Specific weights (see Table 2)	Bilateral and unilateral	Preliminary test only			

exposure: force split 70:30, otherwise 50:50 with teeth force on M1).

However, in this scenario the muscle forces of four large chewing muscles on each side are represented through individual ropes with specific weights. Different load scenarios were tested (see Table 2), based on the mathematical calculations of Rues (Rues et al., 2011), (Rues et al., 2008). The loads in the bilateral load distribution are specified for each side. As can be seen, the calculated forces of Rues already differ in the results, although the experimental assumptions (bilateral unrestricted molar biting) are the same.

For all experiments artificial mandibles were used (Mandible intact w/Easy Clip, serial number 8950, SYNBONE AG, Zizers, Switzerland). It is made of polyurethane and have related characteristics like human mandibles (Bredbenner and Haug, 2000). Afterwards, the fractures were cut with a bandsaw. With the help of silicone cutting guides, the fracture lines could be reproduced accurately. In the next step the osteosynthesis plates were fixed by an experienced surgeon. Different osteosynthesis and fracture scenarios were used to analyze the functionalities of the test bench:

- **Scenario 1.1:**
  - o Fracture along the mandibular angulus (right side), miniplate (Ti, 4 holes, 1.0 mm thickness, Anton Hipp GmbH, Fridingen a. D., Germany), 2 types of screws were tested (Ti, 2.0 × 10 mm; Ti, 2.3 × 10 mm, both Anton Hipp GmbH, Fridingen a. D., Germany)
- **Scenario 1.2:**
  - o Resection of a part of the mandibular corpus (left and right), reconstruction plate (Ti, 2.4 mm, Anton Hipp GmbH), 7 screws (Ti, 2.7 × 10 mm and 2.0 × 10 mm, Anton Hipp GmbH)
- **Scenario 2:**
  - o Fracture along the mandibular angulus (right side), miniplate (Ti, 4 holes, 1.0 mm thickness, Anton Hipp GmbH, Fridingen a. D., Germany), 2 types of screws

TABLE 2 Muscle forces (in N) for different load distributions to reconstruct published force data during the chewing process.

	Resulted force 1st molar	Musculus temporalis		Musculus masseter		Musculus pterygoideus medialis		Musculus pterygoideus lateralis		Joint force	
Bilateral D1	200	150		100		60		20		120	
Bilateral D2	300	230		140		100		25		300	
Unilateral D3	200	H	R	H	R	H	R	H	R	H	R
		145	105	90	80	25	30	2	5	110	140

D—Distribution set 1.3, H—Healthy side, R—Resected side.

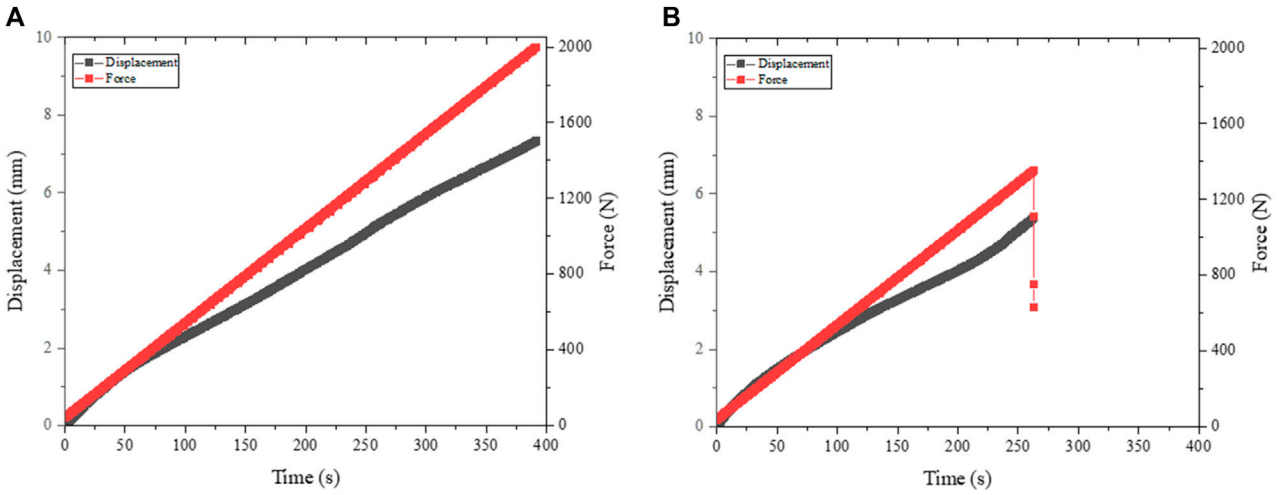

FIGURE 4
Force and displacement of static test scenarios: **(A)** Stop criterium: 2000 N and **(B)** Stop criterium: fracture.

were tested (Ti, 2.0 × 10 mm; Ti, 2.3 × 10 mm, both Anton Hipp GmbH, Fridingen a. D., Germany)Structured

- o Resection of a part of the mandibular corpus (left and right), reconstruction plate (Ti, 2.4 mm, Anton Hipp GmbH), 7 screws (Ti, 2.7 × 10 mm and 2.0 × 10 mm, Anton Hipp GmbH)Structured

3 Results

3.1 Static experiments

In total five experiments of static testing were performed. The function and performance of the test bench could be confirmed. A fracture as a stop criterium occurred twice for the second and third specimen between 1,352 and 1561 N. Thereby, instead of the miniplates, the synthetic mandibular specimen broke under the mandibular condyle, where the smallest cross-sectional area of the mandible can be found and one time the side of the tooth collapsed, where the fixation of the test bench was mounted.

In Figure 4 an example of the recorded force and displacement over time diagram can be seen. On the left graph a) the model could resist 2000 N. In contrast the right graph b) shows a fracture during the experiment. The universal testing machine is controlled by force (5 N/s), which explains the linear progress. The displacement progression thereby showed different shapes (some are more linear, others have a very thin s-shape). More experiments are necessary to create reasonable data to resolute this variation in displacement, to generate reliable statistics and for specific studies of osteosynthesis systems. Parallel to the machine data, it is also possible to observe the experiment with cameras to complement the knowledge of deformation. Afterwards the video and the developed crack can be analysed on the computer.

3.2 Quasi-static experiments for simplified exposures

Five experiments were carried out. The function and performance of the test bench could be confirmed. The force-displacement curves from tests one to four are very constant and stable (see Figure 5). It can be seen that the force curve oscillates between the set maximum value of 400 N and the unloading force of approximately 50 N. The same results can be applied to the development of the displacement.

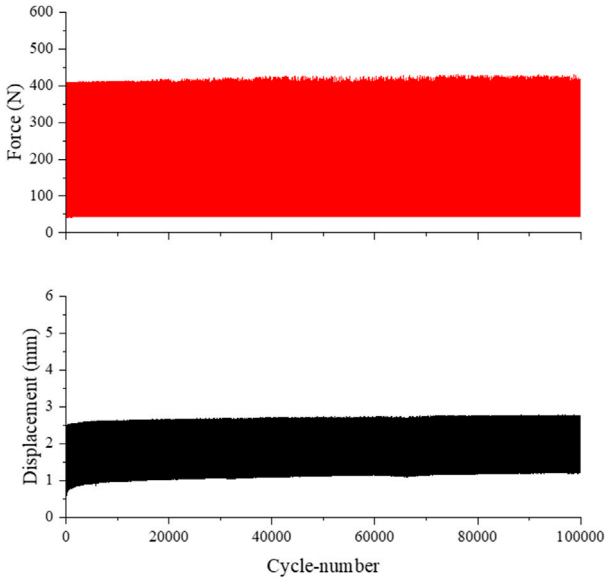

FIGURE 5
Force and displacement of the quasi-static test scenario for simplified exposure.

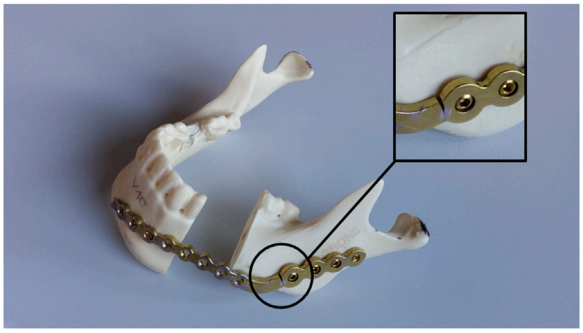

FIGURE 6
Fractured specimen and reconstruction plate of specimen 5.

No visible damage to the reconstruction plate could be identified for the test specimens one to four. As seen in Table 3, during the preliminary tests, slight adaptions about the measuring memory, frequency and sampling rate had to be done to enable artefact free tests to achieve the preset number of 100,000 cycles. Furthermore, in following analysis of the load and displacement diagram the reliability of the measured forces was compared to the defined forces. It turns out that a regular compression tension testing machine is able to realise the quasi-static test scenario. The 90% percentile of measured peak forces has a range of only 10 N. Moreover, the effect of a smaller sampling rate on the deviation of peak forces was analysed. As can be assumed, the sampling rate of 0.15 s resulted in the best outcome and can be analysed more detailed. Even smaller sampling rates do not improve the outcome. Instead, they could even lead to errors in the measurement memory due to the amount of data.

Only the results of specimen number 5 are out of line, as seen in Table 3. Of all quasi-static tests, the highest compressive force of 550 N was applied to the mandibular model. Due to the adjustment of the end criteria and the control factors for a more stable test sequence, the test had to be restarted three times. Furthermore, during the test, a part of the tooth broke off, on which the tooth force was induced. As a result, the contact area for the tooth force had to be adjusted and the test bench restarted. The test finally came to a halt after 40,896 cycles due to a crack in the osteosynthesis plate (see Figure 6). A second visible crack was also found in the mandibular model itself. This crack advanced below the broken tooth. This resulted in an increased bending of the mandible model, which could be observed via larger displacement towards the end. The greater movement also influenced the reconstruction plate. In parallel, it is conceivable that the osteosynthesis plate had already weakened slightly due to fatigue and the lower stability has led to an increasing displacement. Presumably, a combination of the two effects led to a fracture of the osteosynthesis plate at the end of this test run.

3.3 Quasi-static experiments for complex exposures

In the preliminary study of the complex test scenario various load scenarios were tested in four test runs in total, divided into two quasi-static and two static tests. Due to the different force measurements via the three axis load cell for the joint force and a one-axis strain gauges for the teeth force, all resulting forces can be

TABLE 3 Test results of quasi-static tests for simplified exposure.

Specimen Nr	Cycles	Stop	Force testing machine (N)	Time (s) per cycle	Sampling rate (s)
1	66,190*	No	400	3.78	0.5
2	100,000	No	400	2.59	0.55
3	100,000	No	400	2.5	0.52
4	100,000	No	500	2.88	0.52
					0.15**
5***	40,896	Yes	550	3.29	0.5

*Test stop due to full measurement memory of the measuring program.
** From the 82,650th cycle onwards, test with higher data resolution.
*** 3 test pauses, reasons: Adjustment end criteria, adjustment due to tooth breakage.

10.3389/fbioe.2024.1335159

TABLE 4 Results of the test runs of the complex test scenario on the standalone variant of the test bench.

Test Nr. Osteosynthesis	Distribution of muscle forces	Predicted tooth force (N)	Predicted joint force (N)	Predicted forces based on	Load modus	Tooth meshing	Measured tooth force (N)	Measured joint force (N)	Cyclenumber/ cycletime
CT1 Miniplate	D2	300	300	Rues et al. (Rues et al., 2011)	bilateral	M1	?	195.4 (left)	7,486/16.3 s/cycle
								190.7 (right)	
CT2 Reconstruction plate (left side)	D3	200	150 (left)	Rues et al. (Rues et al., 2008)	unilateral	M1	?	102.4 (left)	40,280/6 s/cycle
			120 (right)					74.4 (right)	
CT3 No plate, healthy mandible	D1	200	120	Rues et al. (Rues et al., 2011)	bilateral	M1	≈220- 245	101.1 (left)	Static test only
								87.8 (right)	
CT4 Imitation of the simplified test scenario with reconstruction plate, force distributor	Resultant force of 400 N	400	30%—70% distribution	-	unilateral	M1	?	56.6 (left)	Static test only
								71.6 (right)	

CT, Complex Test 1. . .4, D—Distribution set (Table 2).

determined. This allows to have an overall comprehension of the load condition.

The measured data (Table 4) firstly show that the measured resulting forces at the temporomandibular joint are lower than the predicted calculations from the literature. Unfortunately, the tooth forces could only be determined in one case, because the force measurement with the strain gauge inside the screw did not provide reliable data over the whole time of the test runs. Only at one test run the measurement and recording of stable data was possible. In this case the described effect can be identified. However, since the tooth force could not be reliably determined, this investigation must be validated by new tests in the future.

The difference between the bilateral and unilateral joint loads can also be inferred from the results. The ratio between the force of the healthy to injured side ranges from 86% (CT3) to 97% (CT1) for bilateral loading. For the unilateral loading, on the other hand, between 72% (CT2) and 79% (CT4). This tendency can be expected, since an asymmetric load consequently also entails an asymmetric force distribution. However, in this context, the result of test run CT3 stands out. Due to the bilateral force application, a value closer to 100% was expected. The result shows that an exact symmetrical force distribution can only be approximately achieved in a real test bench. An improvement is certainly needed here. However, the development of the forces over time was analysed. Therefore test run CT2 was chosen. The diagrams of the joint forces after 600 and 40,280 cycles were compared. The result was that in the local time area between a few cycles, the force progression is very similar as seen in Figure 7. In a global observation the force contribution changes a little bit. In the case of experiment 2, the resulting force decreases on both sides by 8.5 N, which is less than 10% of the maximum value.

Last but not least the measured joint forces in three dimensions can be analysed during the test. Therefore, a complete cycle of loading and unloading can be visualised. As expected, the largest force is in the vertical direction z (see Figure 7 blue and red line). The course of the x- and y-directions varies significantly. The values showed that the mandible twists slightly under load (tests run CT1 and CT2) or shifts forward (test run CT3) or backward (test run CT4). A direct dependence between the movements and the type of loading or osteosynthesis plates cannot be found from the data. Reasons for that different movement can be the fixation of the system - for example, in case the mandibular condyle is not sitting perfectly in the mandibular fossa. Due to the increasing load it is pushed in the direction of the geometric centre. As a last observation a trend can be detected, that the test with bilateral loads (CT1 and CT3) affects a more symmetric load distribution compared to the unilateral load. Anyhow, it is possible to calculate based on the sensor signals the amount and the vectors of the resulting joint forces at each side of the mandible as shown in Figure 8.

Comparing the calculated angles of the resultant forces shown in Table 5 it can be seen that the orientation of the vectors does not change significantly over the duration of the test runs. The slight changes indicate again that the specimen centres itself during the test run. The almost same orientation of the left and right joint of CT3 represents the unfractured specimen and fits the expectations. In comparison to that it can be seen that the fractured and fixed specimens showed different orientations of the resulting forces on the left and right side of the mandibular. The strong difference between the test run V4 in comparison to the other fractured

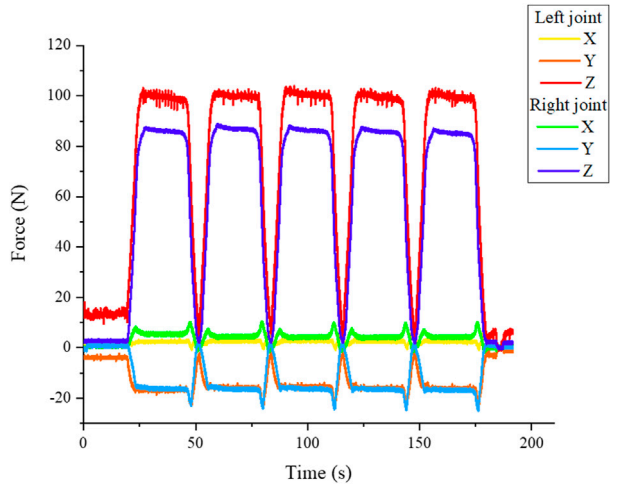

FIGURE 7
Periodic force signal of the standalone test bench shown for test run V2.

specimen can result from the mounting of the specimen in combination with higher implemented test forces. But there is a strong need to investigate these observations in further studies.

4 Discussion

The estimation of the biomechanical component behaviour of osteosynthesis systems takes on a very important role for product development and optimization, especially when used for a long time and for reconstructing large defects of the mandible. The existing test benches described in the literature must evolve to enable realistic biomechanical testing as they only cover highly simplified load scenarios or static tests. However, precise knowledge of the interacting forces and torque is a key component for the realistic simulation of these complex biomechanics. Unfortunately, the published data shows that there is still no scientific consensus on the real forces acting to the mandible during different tasks. The absolute values, which are assumed for the resulting muscle force of the published experiments must also be viewed critically. Unlike the determination of masticatory forces via food experiments (Stróżyk and Bałchanowski, 2016), muscle forces cannot be measured directly, but are determined by electromyography (Gonzalez et al., 2011). Gonzalez et al. (Gonzalez et al., 2011) have shown that EMG measurements are stable in terms of the repeatability of the results. However, with EMG measurements it should be questioned whether the signals of muscles that are more difficult to access (e.g., M. pt. medialis and M. pt. lateralis) can also be reliably recorded. These aspects were not addressed in the referenced study. The exact positioning and attachment of the transducers on the skin surface could have an effect here, as well as the correct positioning of the tooth force measurement. According to Throckmorton (Throckmorton, 2000), the maximum load in the joint is already reduced by 30% if the location shifts from P2 to M1 with the same tooth force. However, based on these data and the calculated muscle forces, the resulting forces can be determined with the aid of a linear system of equations (Rues et al., 2008), which are always subject to minor deviations of the maximum values. These are sometimes accepted to solve the following system of linear equations (Rues et al., 2008). In order to approximate reality, new studies (Wieja et al., 2022), (Rues et al., 2011) now take other factors into account (e.g., the muscle feathering). In addition, there are also major variations in the ratios of the individual muscle forces within the models used. The further development of analytical calculation methods and the addition of simulations have already improved the determination of muscle forces and will continue to approximate reality in the future. Using a static resulting force, what almost all published test benches do, does not enable a change of different ratios between the single muscle forces and with that no change of the load pattern is possible. Another critical issue is that the data are mainly biased towards male patients, as they are more often considered due to the fact that they have a higher masticatory strength and the maximum values are of interest for static testing. Nevertheless, as a result of their simplification, these test benches are easy to use and can still generate valid results for certain experiments of biomechanical behavior like the maximum force transition before failure for static testing. On the other hand, the described test bench by Meyer et al. (Meyer et al., 2000), which represents a complex but static load scenario via simulating specific muscle forces, is not dynamic and cannot emulate specific load patterns over long-term periods. Moreover, this test bench is not designed to measure all kinds of forces (tooth force/teeth forces, joint forces) to acquire a complete load pattern of the mandible and to simulate deformations accordingly. In addition, due to the complex design of the test bench, reproducibility is not given as a result of the specimen holder, which is difficult to adjust.

Based on the described pros and cons, the authors decided to take the approach of a modular test bench to combine the advantages of both loading scenarios and to significantly extend their functional range. The implemented concept of the test bench showed that, in addition to the pure static tests for the investigation of maximum transferable loads, quasi-static tests could also be carried out. Furthermore, it could be shown that the dynamic force scenarios of the test routine can be adjusted within certain limits, which opens up the possibility of direct comparability with similar test benches like Schupp et al. (Schupp et al., 2007), Karoglan et al. (Karoglan et al., 2006), Rendenbach et al. (Rendenbach et al., 2017) and Zimmermann et al. (Zimmermann et al., 2017). In addition to this comparability, the test bench can be easily adapted to modified specimen geometries and new load patterns due to its sophisticated design. It is theoretically also suitable for human mandibles (natural bone) or mandibles from animal models such as minipigs. The test bench developed is outstanding in comparison with equivalent test benches due to the fact that, in addition to the resulting muscle force, the joint forces as well as the vector of these forces can also be recorded. Furthermore, an interface for inserting additional sensors for measuring the tooth force has been provided. Unfortunately the first approach of the authors to measure this force turned out to be too unstable to record reliable data. Therefore, in a future revision, the measurement principle for recording tooth forces must be adapted and validated in further experiments. The authors decided to use artificial bone specimens for the preliminary tests first of all to ensure the reproducibility by the exclusion of inter-individual variations of the specimen as they inevitably occur in natural bone. Secondly, artificial bone was used to compare the results of preliminary testing with published results of other experiments. For that reason it can be proven that the results of the static test scenario showed a similar outcome in comparison with Zimmermann et al. (Zimmermann et al.,

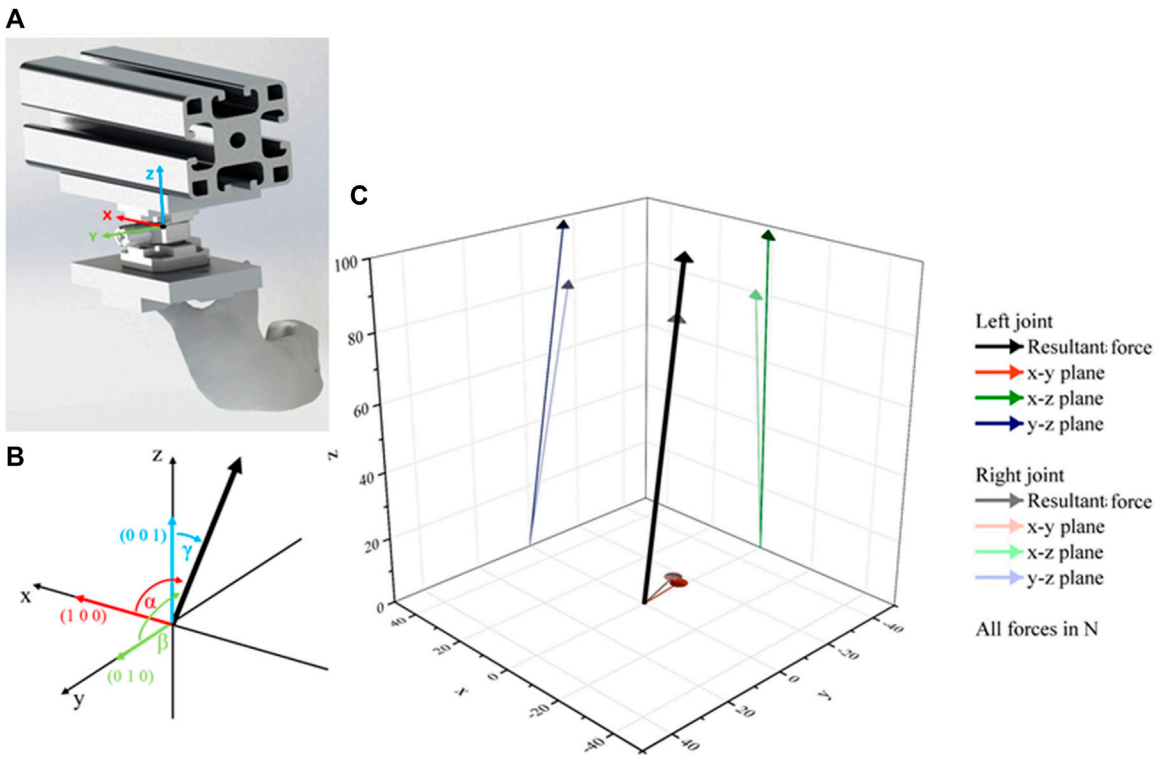

FIGURE 8
Calculation of resultant force vector with: **(A)** Location of the coordinate system, **(B)** orientation of angles and **(C)** calculated vectors of V3 at the start of measurement.

TABLE 5 Calculated angles of the vector of the resultant force.

	CT1	CT2 start	CT2 mid	CT2 end	CT3 start	CT3 end	CT4 start	CT4 end
α_{left}	97	86	87	87	89	89	97	90
β_{left}	96	95	94	94	99	100	71	75
γ_{left}	10	6	6	5	9	10	20	15
α_{right}	87	88	86	89	86	86	85	86
β_{right}	75	74	75	74	102	102	61	65
γ_{right}	16	16	15	16	13	11	30	25

2017). Only the absolute values of the calculated stiffness differ between the two test benches as a result of the different manufacturers of the osteosynthesis systems and the resulting component deviations with slightly different bearings. All mini-plates tested were able to transmit the applied forces without component failure.

Comparing the quasi-static results for simplified load patterns with published results of Schupp et al. (Schupp et al., 2007) and Karoglan et al. (Karoglan et al., 2006) it can be seen that the deformation of the mini-plate fixed specimen and the mode of failure of the reconstruction plates of this preliminary study are similar to the published ones. In order to achieve exact comparability between the test benches described in literature and this one, it would be necessary to be able to set the exact tooth force for the author's test bench. This was unfortunately not possible due to the unstable sensor system of the screw-specimen contact, so that the tooth forces had to be estimated on the basis of the system of equations from Rues et al. (Rues et al., 2008) and the directly measured joint forces. It has been shown that using a resulting force of 400 N produces approximately 150 N of tooth force and asymmetric joint forces. This resulting force was too low to cause significant failure events in the quasi-static test for all specimens. By increasing the resulting force to 550 N it could be shown that the quasi-static testing results in higher tooth forces and with that in a typical breakage of the reconstruction plates as described in Schupp et al. (Schupp et al., 2007) and Rendenbach et al. (Rendenbach et al., 2017). The reconstruction plates break mainly in the region next to the first screw hole of the tension side of the plate, where the cross section is the smallest.

The measured data of the quasi-static modus for complex load pattern firstly showed that the measured resulting forces at the temporomandibular joint are lower than the predicted calculations from the literature. The reasons for this can be manifold. Even slight deviations at the muscle insertion surfaces could lead to changes. Rues et al. (Rues et al., 2011), (Rues et al., 2008) assume a defined start and end

point for the calculations, whereas an insertion surface is used in the test model. Furthermore, it is possible that a slight deviation of the muscle angle may impact on the result. The same issue can be applied to the exact tooth insertion point on the first molar. The sum of the small deviations can ultimately lead to different results. Another important reference variable in this context is the tooth force. It is possible that in the present test bench a larger force is transmitted through the teeth, which would compensate for the lower joint forces. When comparing the force distribution of the complex scenario via measuring the joint forces it could be seen that an exact symmetrical force distribution for the unfractured and mini-plate fixed specimen can only be achieved approximately in a real test bench. In fact, these minor deviations also occurred in the simplified test rig of Karoglan et al. (Karoglan et al., 2006). Deviation from the symmetric load distribution can be caused by different factors, e.g., slight changes in the clamping of the specimen or the position of the counterpart to insert tooth forces or even material defects of the specimen. There was also a deviations between the expected and measured values of the joint forces (30%–70%) when using the force distributor while testing the reconstructed specimen. Those deviations can be caused due to the fine positioning of the distributor or counterpart. Another point is that in the case of testing a reconstruction plate with unilateral loading, the affected side absorbs a greater joint force (CT2, CT4). Since along the resected side, no force can be transferred via the teeth but only via the temporomandibular joint, the result seems quite plausible. Another very interesting point is that by imitating the simplified load pattern (CT4) on the complex standalone version of the test bench the orientation and amount of the joint forces differ notably in comparison to the complex load pattern (CT2). This clearly indicates that the force transmission through the mandible and the bearing force on the tooth-specimen-contact are dependent on the complexity of the test bench. Simplified test benches can therefore lead to a biased result with regard to the biomechanical suitability of implants in this case. This bias can be avoided by using load patterns that are close to reality. The test bench for complex load patterns presented in this paper produces load patterns which are close to reality. It can be used already for quasi-static long-term tests of implant systems in order to investigate their biomechanical behavior and represents the basic solution for upcoming evolvements.

5 Conclusion

In conclusion the presented modular test bench showed to be applicable for the examination of the biomechanics of the mandible. Based on the results of the preliminary studies it can be observed, that the published of established test benches could be viable reproduced. Furthermore, it could be proven, that using a complex load pattern via reality-based muscle forces and the measurement of all forces in quasi-static mastication processes is considered reasonable. The presented standalone solution of the test bench significantly exceeds the state of the art due to its quasi-static test execution for the simulation of long time periods as well as the flexible adjustability of muscle forces and direction vectors and the inclusion of different specimen types and geometries. For this reason, the complex experimental setup presented in this paper should be further developed for future investigations. For this purpose, the test bench must be extended to include a robust and accurate solution for measuring the tooth force as well as an integration of control loops for adaptive adjustment of the muscle forces during long-term test runs to simulate different diets during the regeneration phase of the patient.

Data availability statement

The original contributions presented in the study are included in the article/Supplementary material, further inquiries can be directed to the corresponding author.

Ethics statement

Ethical approval was not required for the study involving animals in accordance with the local legislation and institutional requirements because we exclusively used cadaveric bone coming from slaughter houses.

Author contributions

AA: Conceptualization, Investigation, Methodology, Validation, Visualization, Writing–original draft. FA: Conceptualization, Data curation, Investigation, Methodology, Validation, Visualization, Writing–original draft. GL: Resources, Validation, Writing–review and editing. CB: Conceptualization, Data curation, Visualization, Writing–review and editing. HL: Formal Analysis, Methodology, Writing–review and editing. AF: Formal Analysis, Writing–review and editing. AL: Data curation, Formal Analysis, Resources, Writing–review and editing. UT: Formal Analysis, Resources, Visualization, Writing–review and editing. UW: Data curation, Formal Analysis, Validation, Writing–review and editing. TS: Conceptualization, Investigation, Methodology, Validation, Writing–original draft.

Funding

The author(s) declare that financial support was received for the research, authorship, and/or publication of this article. The study was co-financed by the CPS project from taxes on the basis of the budget passed by the Saxon state parliament.

Acknowledgments

The authors want to acknowledge the “Else Kröner Fresenius Center for Digital Health” in Dresden for supporting the team with their network and consulting regarding regulatory affairs. Furthermore, we are grateful for the provision of testing material done by Anton Hipp GmbH.

Conflict of interest

The authors declare that the research was conducted in the absence of any commercial or financial relationships that could be construed as a potential conflict of interest.

Publisher's note

References

Bagheri, S. C., and Bell, R. B. (2014). "Reconstructive oral and maxillofacial surgery," in *Clinical review of oral and maxillofacial surgery* (Amsterdam, Netherlands: Elsevier).

Bakke, M., Holm, B., Jensen, B. L., Michler, L., and Möller, E. (1990). Unilateral, isometric bite force in 8-68-year-old women and men related to occlusal factors. *Eur. J. Oral Sci.* 98, 149–158. doi:10.1111/j.1600-0722.1990.tb00954.x

Ben Achour, A., Meißner, H., Teicher, U., Haim, D., Range, U., Brosius, A., et al. (2019). Biomechanical evaluation of mandibular condyle fracture osteosynthesis using the rhombic three-dimensional condylar fracture plate. *J. Oral Maxillofac. Surg.* 77, 1868. doi:10.1016/j.joms.2019.04.020

Braun, S., Bantleon, H. P., Hnat, W. P., Freudenthaler, J. W., Marcotte, M. R., and Johnson, B. E. (1995). A study of bite force, part 1: relationship to various physical characteristics. *Angle Orthod.* 65, 367–372. doi:10.1043/0003-3219(1995)065<0367:ASOBFP>2.0.CO;2

Bredbenner, T. L., and Haug, R. H. (2000). Substitutes for human cadaveric bone in maxillofacial rigid fixation research. *Oral Surg. Oral Med. Oral Pathol. Oral Radiol. Endod.* 90, 574–580. doi:10.1067/moe.2000.111025

Dean, A., Alamillos, F., Heredero, S., Redondo-Camacho, A., Guler, I., and Sanjuan, A. (2020). Fibula free flap in maxillomandibular reconstruction. Factors related to osteosynthesis plates' complications. *J. Cranio-Maxillofacial Surg.* 48, 994–1003. doi:10.1016/j.jcms.2020.08.003

de Oliveira, J. C. S., Moura, L., de Menezes, J., Gabrielli, M., Pereira Filho, V., and Hochuli-Vieira, E. (2018). Three-dimensional strut plate for the treatment of mandibular fractures: a systematic review. *Int. J. Oral Maxillofac. Surg.* 47, 330–338. doi:10.1016/j.ijom.2017.08.009

Gonzalez, Y., Iwasaki, L. R., McCall Jr, W. D., Ohrbach, R., Lozier, E., and Nickel, J. C. (2011). Reliability of electromyographic activity vs bite-force from human masticatory muscles. *Eur. J. Oral Sci.* 119, 219–224. doi:10.1111/j.1600-0722.2011.00823.x

Goodson, A. M., Kittur, M. A., Evans, P. L., and Williams, E. M. (2019). Patient-specific, printed titanium implants for reconstruction of mandibular continuity defects: a systematic review of the evidence. *J. Cranio-Maxillofacial Surg.* 47, 968–976. doi:10.1016/j.jcms.2019.02.010

Gutwald, R., Jaeger, R., and Lambers, F. M. (2017). Customized mandibular reconstruction plates improve mechanical performance in a mandibular reconstruction model. *Comput. Methods Biomech. Biomed. Engin.* 20, 426–435. doi:10.1080/10255842.2016.1240788

Karoglan, M., Schütz, K., Schieferstein, H., Horch, H. H., and Neff, A. (2006). Development of a static and dynamic simulator for osteosyntheses of the mandible. *Technol. Heal. Care* 14, 449–455. doi:10.3233/thc-2006-144-525

Kumar, B. P., Venkatesh, V., Kumar, K. A. J., Yadav, B. Y., and Mohan, S. R. (2016). Mandibular reconstruction: overview. *J. Maxillofac. Oral Surg.* 15, 425–441. doi:10.1007/s12663-015-0766-5

Lisiak-Myszke, M., Marciniak, D., Bieliński, M., Sobczak, H., Garbacewicz, Ł., and Drogoszewska, B. (2020). Application of finite element analysis in oral and maxillofacial surgery—a literature review. *Mater. (Basel)* 13, 3063. doi:10.3390/ma13143063

Martola, M., Lindqvist, C., Hänninen, H., and Al-Sukhun, J. (2007). Fracture of titanium plates used for mandibular reconstruction following ablative tumor surgery. *J. Biomed. Mater. Res. Part B Appl. Biomater.* 80B, 345–352. doi:10.1002/jbm.b.30603

Mathur, V., Pillai, R., Kalra, S., and Jain, V. (2014). A preliminary study to find out maximum occlusal bite force in Indian individuals. *Indian J. Dent. Res.* 25, 325. doi:10.4103/0970-9290.138330

Meyer, C., Kahn, J. L., Lambert, A., Boutemy, P., and Wilk, A. (2000). Development of a static simulator of the mandible. *J. Cranio-Maxillofacial Surg.* 28, 278–286. doi:10.1054/jcms.2000.0149

Netter, F. H. (2008). *Atlas der Anatomie, 4.* Auflage. München: Urban und Fischer Verlag in Elsevier.

Probst, F. A., Mast, G., Ermer, M., Gutwald, R., Schmelzeisen, R., Pautke, C., et al. (2012). MatrixMANDIBLE preformed reconstruction plates—a two-year two-institution experience in 71 patients. *J. Oral Maxillofac. Surg.* 70, e657–e666. doi:10.1016/j.joms.2012.06.175

Rendenbach, C., Sellenschloh, K., Gerbig, L., Morlock, M. M., Beck-Broichsitter, B., Smeets, R., et al. (2017). CAD–CAM plates versus conventional fixation plates for primary mandibular reconstruction: a biomechanical *in vitro* analysis. *J. Cranio-Maxillofacial Surg.* 45, 1878–1883. doi:10.1016/j.jcms.2017.08.024

Rues, S., Lenz, J., Türp, J. C., Schweizerhof, K., and Schindler, H. J. (2008). Forces and motor control mechanisms during biting in a realistically balanced experimental occlusion. *Arch. Oral Biol.* 53, 1119–1128. doi:10.1016/j.archoralbio.2008.06.006

Rues, S., Lenz, J., Türp, J. C., Schweizerhof, K., and Schindler, H. J. (2011). Muscle and joint forces under variable equilibrium states of the mandible. *Clin. Oral Investig.* 15, 737–747. doi:10.1007/s00784-010-0436-4

Sauerbier, S., Schön, R., Otten, J. E., Schmelzeisen, R., and Gutwald, R. (2008). The development of plate osteosynthesis for the treatment of fractures of the mandibular body – a literature review. *J. Cranio-Maxillofacial Surg.* 36, 251–259. doi:10.1016/j.jcms.2007.08.011

Schupp, W., Arzdorf, M., Linke, B., and Gutwald, R. (2007). Biomechanical testing of different osteosynthesis systems for segmental resection of the mandible. *J. Oral Maxillofac. Surg.* 65, 924–930. doi:10.1016/j.joms.2006.06.306

Seol, G.-J., Jeon, E. G., Lee, J. S., Choi, S. Y., Kim, J. W., Kwon, T. G., et al. (2014). Reconstruction plates used in the surgery for mandibular discontinuity defect. *J. Korean Assoc. Oral Maxillofac. Surg.* 40, 266. doi:10.5125/jkaoms.2014.40.6.266

Stróżyk, P., and Bałchanowski, J. K. (2016). Effect of foodstuff on muscle forces during biting off. *Acta Bioeng. Biomech.* 18, 81–91.

Tate, G. S., Ellis, E., and Throckmorton, G. (1994). Bite forces in patients treated for mandibular angle fractures: implications for fixation recommendations. *J. Oral Maxillofac. Surg.* 52, 734–736. doi:10.1016/0278-2391(94)90489-8

Throckmorton, G. S. (2000). Temporomandibular joint biomechanics. *Oral Maxillofac. Surg. Clin. North Am.* 12, 27–42. doi:10.1016/s1042-3699(20)30229-6

van den Bergh, B., Heymans, M. W., Duvekot, F., and Forouzanfar, T. (2012). Treatment and complications of mandibular fractures: a 10-year analysis. *J. Cranio-Maxillofacial Surg.* 40, e108–e111. doi:10.1016/j.jcms.2011.05.015

van der Bilt, A., Tekamp, A., Van Der Glas, H., and Abbink, J. (2008). Bite force and electromyograpy during maximum unilateral and bilateral clenching. *Eur. J. Oral Sci.* 116, 217–222. doi:10.1111/j.1600-0722.2008.00531.x

van Eijden, T. M. (2000). Biomechanics of the mandible. *Crit. Rev. Oral Biol. Med.* 11, 123–136. doi:10.1177/10454411000110010101

Varga, S., Spalj, S., Lapter Varga, M., Anic Milosevic, S., Mestrovic, S., and Slaj, M. (2011). Maximum voluntary molar bite force in subjects with normal occlusion. *Eur. J. Orthod.* 33, 427–433. doi:10.1093/ejo/cjq097

Verplancke, K., De Waele, W., and De Bruyn, H. (2011). Dental implants, what should be known before starting an *in vitro* study. *Int. J. Sustain. Constr. Des.* 2, 360–369. doi:10.21825/scad.v2i3.20534

Weiskopf, J. (1981). "Anatomie und Physiologie des orofazialen Organs," in *Prothetische stomatologie*. Editors A. Breustedt, E. Lenz, and R. Musil (Leipzig: Johann Ambrosius Barth Verlag).

Wieja, F., Jacobs, G., Stein, S., Kopp, A., van Gaalen, K., Kröger, N., et al. (2022). Development and validation of a parametric human mandible model to determine internal stresses for the future design optimization of maxillofacial implants. *J. Mech. Behav. Biomed. Mater.* 125, 104893. doi:10.1016/j.jmbbm.2021.104893

Wong, R. C. W., Tideman, H., Kin, L., and Merkx, M. (2010). Biomechanics of mandibular reconstruction: a review. *Int. J. Oral Maxillofac. Surg.* 39, 313–319. doi:10.1016/j.ijom.2009.11.003

Zimmermann, C., Henningsen, A., Henkel, K. O., Klatt, J., Jürgens, C., Seide, K., et al. (2017). Biomechanical comparison of a multidirectional locking plate and conventional plates for the osteosynthesis of mandibular angle fractures—a preliminary study. *J. Cranio-Maxillofacial Surg.* 45, 1913–1920. doi:10.1016/j.jcms.2017.05.020

frontiers | Frontiers in Bioengineering and Biotechnology

TYPE Original Research
PUBLISHED 20 March 2024
DOI 10.3389/fbioe.2024.1372669

OPEN ACCESS

EDITED BY
Fuyou Liang,
Shanghai Jiao Tong University, China

REVIEWED BY
Yann Ledoux,
Université de Bordeaux, France
Jicheng Fu,
University of Central Oklahoma, United States
Wenxin Niu,
Tongji University, China

*CORRESPONDENCE
Julie Choisne,
j.choisne@auckland.ac.nz

RECEIVED 18 January 2024
ACCEPTED 06 March 2024
PUBLISHED 20 March 2024

CITATION
Mohammadi Moghadam S, Ortega Auriol P, Yeung T and Choisne J (2024), 3D gait analysis in children using wearable sensors: feasibility of predicting joint kinematics and kinetics with personalized machine learning models and inertial measurement units.
Front. Bioeng. Biotechnol. 12:1372669.
doi: 10.3389/fbioe.2024.1372669

3D gait analysis in children using wearable sensors: feasibility of predicting joint kinematics and kinetics with personalized machine learning models and inertial measurement units

Shima Mohammadi Moghadam, Pablo Ortega Auriol, Ted Yeung and Julie Choisne*

Auckland Bioengineering Institute, The University of Auckland, Auckland, New Zealand

Introduction: Children's walking patterns evolve with age, exhibiting less repetitiveness at a young age and more variability than adults. Three-dimensional gait analysis (3DGA) is crucial for understanding and treating lower limb movement disorders in children, traditionally performed using Optical Motion Capture (OMC). Inertial Measurement Units (IMUs) offer a cost-effective alternative to OMC, although challenges like drift errors persist. Machine learning (ML) models can mitigate these issues in adults, prompting an investigation into their applicability to a heterogeneous pediatric population. This study aimed at 1) quantifying personalized and generalized ML models' performance for predicting gait time series in typically developed (TD) children using IMUs data, 2) Comparing random forest (RF) and convolutional neural networks (CNN) models' performance, 3) Finding the optimal number of IMUs required for accurate predictions.

Methodology: Seventeen TD children, aged 6 to 15, participated in data collection involving OMC, force plates, and IMU sensors. Joint kinematics and kinetics (targets) were computed from OMC and force plates' data using OpenSim. Tsfresh, a Python package, extracted features from raw IMU data. Each target's ten most important features were input in the development of personalized and generalized RF and CNN models. This procedure was initially conducted with 7 IMUs placed on all lower limb segments and then performed using only two IMUs on the feet.

Results: Findings suggested that the RF and CNN models demonstrated comparable performance. RF predicted joint kinematics with a 9.5% and 19.9% NRMSE for personalized and generalized models, respectively, and joint kinetics with an NRMSE of 10.7% for personalized and 15.2% for generalized models in TD children. Personalized models provided accurate estimations from IMU data in children, while generalized models lacked accuracy due to the limited dataset. Furthermore, reducing the number of IMUs from 7 to 2 did not affect the results, and the performance remained consistent.

Discussion: This study proposed a promising personalized approach for gait time series prediction in children, involving an RF model and two IMUs on the feet.

KEYWORDS

3D gait analysis, inertial measurement units, machine Learning, pediatric, joint kinematics, joint kinetics

1 Introduction

Children's walking patterns are distinctive from adults and evolve with age (Cigali et al., 2011; Senden et al., 2023). At a small age, gait tends to be less repetitive and will differ from those of adults (Ganley and Powers, 2005; Jain et al., 2016), emphasizing the need to build normative data for a pediatric population (Ganley and Powers, 2005). The differences in school-aged children's walking patterns are often attributed to their significant musculoskeletal changes (Bari et al., 2023), given that they are in a critical stage of growth and development (Onis et al., 2007). A recent study (Bach et al., 2021) suggested that the degree of gait maturity does not always directly relate to the chronological age of the child. This finding underscores the complexity of assessing gait development in children. Moreover, it's been shown that, compared to adults, young individuals exhibit more variable kinematic patterns when performing repetitive movements (Kuhtz-Buschbeck et al., 1996). Additionally, the observed variability in Electromyography (EMG) waveform within-session for children exhibited approximately twice the variability of EMG signals (muscle activation level) for adults (Granata et al., 2005), affecting their joint kinematics and kinetics within a single session.

Three-dimensional gait analysis (3DGA) is a valuable tool for understanding a child's gait pattern and how it compares with normative data of typically developed children's gait (Ito et al., 2022; Bari et al., 2023). The insights gained from 3DGA in children affected by lower limb movement disorders serve as a foundation for clinical assessment to target personalized treatment and improve their walking patterns (Bari et al., 2023). Considering the unique challenges and broad spectrum of motor impairments in this population, addressing developmental challenges requires a tailored approach. The current gold standard for performing 3DGA involves Optical Motion Capture (OMC) along with force plates due to its high accuracy and robustness (Chester et al., 2005). However, the high cost of OMC systems and the time-consuming data post-processing needed lead to long waitlists for patients and sometimes long-distance travel for families coming from rural areas (Aminian and Najafi, 2004).

Wearable sensors like Inertial Measurement Units (IMUs) are potential alternatives to the OMC system, enabling the potential to capture 3DGA in rural areas and natural environments (Gurchiek et al., 2019). Unlike the OMC systems, IMUs are inexpensive, small, and lightweight and can be used outside the clinic by wearing them or attaching them to the children's limbs or pelvis (Aminian and Najafi, 2004). Although IMU sensors are very promising in motion analysis, challenges such as time-increasing drift errors, which result in less accurate estimations, still need to be overcome (Aminian and Najafi, 2004). Moreover, traditional approaches, such as sensor fusion algorithms (Sabatini, 2006; Madgwick et al., 2011), as well as the tool package OpenSense (Al Borno et al., 2022), require placing an IMU on each body segment for accurate kinematics calculations and functional calibration.

The challenges associated with processing IMU data in adult populations have been addressed in previous studies (Findlow et al., 2008; Luu et al., 2014; Dorschky et al., 2020; Giarmatzis et al., 2020; Lim et al., 2020; Stetter et al., 2020; Mundt et al., 2021; Sharifi Renani et al., 2021; Tan et al., 2022; Moghadam et al., 2023a) by implementing Machine learning (ML) models. While each of these studies utilized a combination of IMUs and ML techniques, their focuses varied: some concentrated on predicting joint kinematics (Findlow et al., 2008; Luu et al., 2014; Dorschky et al., 2020; Sharifi Renani et al., 2021; Tan et al., 2022), som on joint kinetics (Giarmatzis et al., 2020; Stetter et al., 2020), and few on both kinematics and kinetics prediction (Lim et al., 2020; Mundt et al., 2021; Moghadam et al., 2023a). These ML models can establish a direct relationship between the IMUs' data and OMC derived gait time series such as, joint kinematics, joint kinetics, and muscle forces (Moghadam et al., 2023a). Prior research indicated the efficacy of this approach in adult populations, demonstrating highly accurate results with low errors during the personalized model (tested on the same individual used for training). Additionally, reliable estimations were yielded using generalized models (tested on new participants not included in the training set), even in scenarios with limited dataset availability. Among various ML models developed for the adults population, artificial neural networks (ANN) have been widely utilized for predicting gait time series. However, there is a limited body of literature exploring alternative data-driven models that may demand smaller datasets while achieving comparable results to ANNs. Building on this context, in a prior study, we demonstrated that Random Forest (RF) models can yield results comparable to more intricate machine learning models such as Convolutional Neural Networks (CNNs) for 3D Gait Analysis (3DGA) in adults (Moghadam et al., 2023a). Given the greater heterogeneity in children's gait, it will be interesting to explore whether RF or CNNs can be applied to a pediatric population with similar performances.

The primary focus of existing ML models for 3DGA in children lies in gait classification (Kamruzzaman and Begg, 2006; Zhang et al., 2009; Zhang and Ma, 2019; Choisne et al., 2020; Khaksar et al., 2021) rather than the development of models for predicting gait time series. There are only a handful of studies focused on predicting children's gait using ML techniques (Kwon et al., 2012; Vigneron et al., 2017; Morbidoni et al., 2021; Kolaghassi et al., 2022; Kolaghassi et al., 2023). A research group used EMG sensors' signals to predict children with cerebral palsy (CP) knee moment and achieved high correlation coefficients between 0.71 and 0.93 for different participants (Kwon et al., 2012). Another study proved the feasibility of using neural networks in predicting gait events from surface EMG signals in hemiplegic cerebral palsy (Morbidoni et al., 2021). Other studies have employed ML techniques to estimate one-step-ahead gait trajectories to control lower-limb robotic devices in children with CP (Kolaghassi et al., 2022; Kolaghassi et al., 2023). However, none of the mentioned studies utilized IMUs' data to develop the ML model. Given the effective performance of a combination of IMU and ML models in

FIGURE 1
Pictures of the front **(A)** and back **(B)** of a participant, illustrating markers' placement (numbered in the image) and sensor locations (IMU axes depicted in red). The study did not utilize data from the Electromyography (EMG) sensors.

adults, exploring its applicability in a heterogeneous pediatric population would be an interesting avenue for investigation.

It is noteworthy that previous studies have indicated the feasibility of predicting diverse gait time series in adults using a single IMU on the pelvis (Lim et al., 2020) or a pair of IMUs on the shanks (Sharifi Renani et al., 2020; Yeung et al., 2023) or the feet (Gholami et al., 2020). However, given the unique challenges posed by children's gait, it remains crucial to extend this inquiry to children's gait analysis by exploring the applicability of using a reduced number of IMUs. A high number of IMU sensors on the body could be impractical in real-world gait analysis, particularly for at-home applications, as it requires high computational power to monitor numerous IMUs (Sivakumar et al., 2019). Therefore, another aspect requiring investigation is to quantify the optimal number of IMUs needed for accurately estimating gait time series in children.

Therefore, this study aimed to assess the feasibility of leveraging data from IMUs to construct ML models for predicting gait time series in school-aged children. This goal was pursued through three key objectives. Firstly, we sought to explore whether personalized and generalized ML models for predicting gait time series in children could demonstrate comparable efficacy to their adult counterparts. Secondly, an evaluation was conducted to compare the accuracy of two distinct ML models–the multi-output RF and CNN models–for predicting gait time series in children. The final objective centered on exploring the potential of placing a singular IMU on each foot, as opposed to employing seven IMUs distributed across all lower limb segments.

2 Materials and methods

2.1 Participants

Seventeen typically developed (TD) children (9 Females, 8 Males; age = 10.5 ± 2.8 yr [6:15]; height = 147.2 ± 16.9 cm [119:174]; weight = 37.1 ± 11.7 kg [19.7:56.9]) were recruited for this study. Each child's legal guardian provided informed consent prior to data collection. The research strictly adhered to ethical principles outlined in the Helsinki Declaration and received approval from the University of Auckland (New Zealand) human participant ethics committee (reference number 021615).

2.2 Data collection

OMC, force plates, and IMUs data were recorded while each participant completed one static and a minimum of 15 over-ground walking trials for over 20 m at their self-selected speed. For the initial five participants, we affixed 37 reflective markers, indicated by numbers 1 to 37 in Figure 1, on their body segments. Subsequently, a paper by Bakke and Besier (2022) from our lab suggested a streamlined marker set, removing markers 6, 7, 8, 9, 10, 11, 18, 21, 32, and 33, which demonstrated equivalent accuracy in kinematics calculation. For the remaining participants, we adopted this refined marker set with 27 markers. Marker trajectories were traced by a 14-camera optical motion capture system (Vicon Motion Systems Ltd., United Kingdom) at a sampling frequency of 100 Hz for all trials. In addition, seven IMU sensors [Blue Trident, Vicon IMeasureU Ltd. (NZ)] were secured on the participants' pelvis (between left and right posterior superior iliac spine markers), thighs (1 cm above the lateral aspect of the patella), shanks (1 cm above the lateral aspect of the ankle), and feet (on the dorsal surface) as shown in Figure 1, and recorded three axes of angular velocity and linear acceleration at 2 kHz. Ground reaction forces (GRFs) were acquired at 2 kHz from three force plates (Bertec, Columbus, Ohio) embedded in the gait lab floor. The Vicon Nexus software (version 2.12) was used to collect and synchronize marker trajectory, GRF, and IMUs data and subsequently to reconstruct markers' trajectories.

2.3 Data processing

After extracting data as C3D files from Nexus, MOtoNMS, a Matlab Motion data elaboration toolbox for neuromusculoskeletal applications (Mantoan et al., 2015), was used to filter marker trajectories and ground reaction forces (GRF) using a Butterworth fourth order, 8 Hz low pass filter. Then MOtoNMS was employed for rotating and aligning the lab coordinate system to the OpenSim coordinate system, where X, Y, and Z-axes correspond to the frontal, transverse, and sagittal planes, respectively. Additionally, MOtoNMS was utilized to determine hip joint center (HJC) locations using Harrington regression equations from static trials for scaling in OpenSim (Harrington et al., 2007).

A musculoskeletal model was created for each participant by linearly scaling OpenSim gait 2392 model (Delp et al., 2007), which is a generic adult model. The Gait 2392 model is a detailed biomechanical representation, featuring 23 degrees of freedom and 92 musculotendon actuators. Within this model, the pelvis and hip joints offer three rotational degrees of freedom each, allowing for movements in the three planes of motion. The pelvis in Gait 2392 allows for movements such as tilt, obliquity, and rotation in the transverse plane, facilitated by its complex structure of joints. The hip joint is characterized as a ball-and-socket joint, enabling motions such as flexion/extension, adduction/abduction, and internal/external rotation. The knee model is a simple hinge joint with one degree of freedom allowing for flexion/extension. Additionally, the ankle (allowing for ankle dorsi/plantar flexion) and subtalar (allowing for ankle inversion/eversion) joints are simulated as frictionless revolute joints. The scaling tool in OpenSim (version 3.3) aligns virtual markers on the generic model with those placed on specific anatomical landmarks of the participant's body during the static trial. The HJCs calculated by MOtoNMS were used to scale the femur. The kinematics and kinetics of the lower limb joints, including the pelvis (3 DOF), hip (3 DOF), knee (1DOF in the sagittal plane), and ankle (2DOF; sagittal and frontal planes), were calculated for all participants using the inverse kinematics (IK) and inverse dynamics (ID) tools in OpenSim. To estimate joint kinematics and kinetics, we picked two gait cycles from each trial, resulting in a minimum of 30 gait cycles for each participant. The IK tool employs an optimization technique to ensure precise alignment between the virtual markers on the scaled model and the corresponding experimental markers in a least-squares sense (Lu and O connor, 1999; Knudson, 2007). For joint kinetics prediction, we focused on the gait cycles occurring on the force plates to allow for joint forces and moments calculation through the ID tool, which solves the equations of motion (Davis et al., 1991). We excluded trials where the participant's feet were not entirely within the force plates. Therefore, a variable number of kinetics gait cycles remained for each participant, ranging from a minimum of 8 to a maximum of 18.

This process resulted in a dataset encompassing measurements for 15 joints kinematics and 15 joints kinetics targets, including pelvis tilt, pelvis rotation, pelvis obliquity, hip rotation, hip flexion, hip abduction/adduction, knee flexion/extension, ankle dorsi/plantar flexion, and ankle inversion/eversion joints angles and moments for both legs. Finally, the IMU data were down sampled to 100 Hz to align the data's frequency with the joint kinematics and kinetics frequency. This also reduces the computational load for feature extraction and machine learning (ML) model construction.

2.4 Joint kinematics and kinetics prediction using ML models

After processing data for the 17 participants, a total of 73,364 time points for joint kinematics and 21855 time/data points for joint kinetics were used for the development of ML models. The outlined procedures (Figure 2), including windowing IMU data, feature extraction, feature selection, model development, and model evaluation, were executed as detailed in the subsequent sections.

2.4.1 Training and testing sets

We implemented two distinct data splitting methods to facilitate two types of examinations (Figure 2, Step 1); the first looked at the intra-subject examination accuracy, and the second looked at the inter-subject prediction accuracy.

Intra-subject examination: In this approach, the training dataset consisted of 70% of a participant's gait cycles, and the remaining 30% of gait cycles were allocated for the testing dataset. A total of 17 training and testing datasets were created to cover all participants and perform the intra-subject examination.

Inter-subject examination: To create training and testing datasets for this examination, we employed a leave-one-out approach for our cohort of 17 participants. The dataset was partitioned to assess the model's generalization across diverse individuals. During each iteration, one participant's gait cycles were set aside for testing, while the gait cycles from the

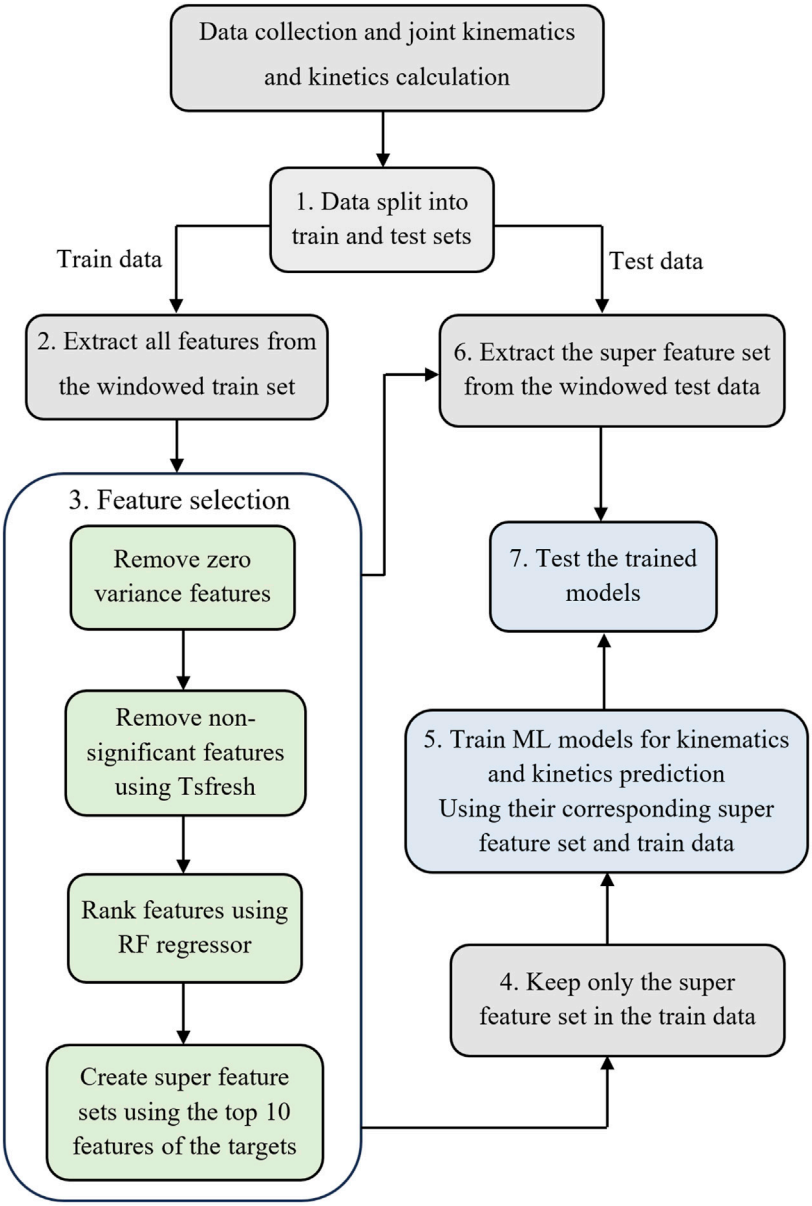

FIGURE 2
The workflow to develop the ML models. Step 1: Split the data into training and testing sets. Step 2: Window IMU data and feature extraction for the training dataset. Step 3: Feature selection. Step 4: Keep only the selected features in the training set. Step 5: Train ML models using selected features in the training set. Step 6: window IMU data and extract the super feature set (determined in step 3) for the test dataset. Step 7: Test the trained model on the testing set.

remaining 16 participants constituted the training dataset. This process was repeated 17 times, each time excluding a different participant from the training set.

2.4.2 IMU sensors data windowing and feature extraction

In our pursuit of enhancing the accuracy of the learned models and emphasizing the main characteristics of the input data (Laird and Saul, 1994), we adopted a feature engineering technique. From each IMU, we took six time series, encompassing triaxial angular velocity and linear acceleration, to extract features.Thus, we had a total of 42 data vectors from seven IMUs. We organized the input time series data into sequences of consecutive, sliding, and overlapping windows. We selected a window size of 0.75 s, as shown to be the most accurate in predicting gait time series (Moghadam et al., 2023b).

Then, we employed the Tsfresh (Christ et al., 2018) (Time Series FeatuRe Extraction on the basis of Scalable Hypothesis tests) python package to perform feature extraction on the windowed input data (Figure 2, Step 2). This process yielded a feature vector $\vec{x}_i = (f_1(x_1), f_2(x_2), \ldots, f_m(x_i))$ for each vector of input data (x_i). Tsfresh extracted 788 distinct features from each channel of IMU data, resulting in a substantial total of 33,096 features derived from the 42 channels of input data.

2.4.3 Feature selection

The presence of irrelevant and noisy features may considerably reduce the performance of the ML model. The process of removing irrelevant features and selecting the most relevant features is called feature selection (Figure 2, Step 3). We eliminated all zero-variance features to initiate the process of determining the most important features. Then, the Tsfresh feature selector's built-in function was utilized to remove any non-significant feature, using the Benjamini-Hochberg method (Benjamini and Hochberg, 1995). In the next step, the remaining features were ranked based on their Gini Importance in predicting each target using a Random Forest (RF) regressor (Hasan et al., 2016). Then, the top ten features associated with each target were selected. Our previous findings demonstrated that this selection of 10 features per target yields precise estimations in multi-output models (Moghadam et al., 2023b).

After feature selection, two comprehensive feature sets were constructed, each including 150 features. The first merged all the top features related to kinematics targets, forming the basis for a multioutput ML model dedicated to kinematics prediction. The second feature set put all the top features associated with kinetics targets together to develop a multioutput ML model tailored for kinetics prediction. We retained only the features present in the super feature set from all the extracted features for the training dataset (Figure 2, Step 4).

2.4.4 Non-linear regression ML models

We developed RF and CNN models to assess their accuracy in predicting lower limb joint kinematics and kinetics during gait (Figure 2, Step 5). The hyperparameters for both RF and CNN models were chosen based on previously optimized models (Moghadam et al., 2023a). We employed an RF model comprising 500 trees, each with a maximum depth of 25.

For the CNN model, we used a multi-output architecture with five hidden layers. The selected features were scaled using the Standard Scaler function from the Sklearn library to ensure all variables fell within the same range (between zero and one). Targets were also scaled, and post-prediction, they were rescaled to their original values using the same scaler. The model's architecture featured an input layer with a size of 150, followed by two convolutional layers, each followed by a max-pooling layer. Both convolutional layers comprised 256 filters with a kernel size of three and employed a "relu" activation function. The max-pooling layers had a pool size of two. Subsequently, the data was flattened and passed through a dense output layer with a linear activation function. The number of units in the output layer corresponded to the number of targets (15 for both CNN models utilized for kinematics and kinetics prediction). The 'Adam' solver with a learning rate of 0.01 was used for weight optimization, employing the mean squared error as the loss function. An early stopping mechanism monitored validation loss and halted training if no improvement was observed after five epochs. The batch size was set to 32, and the model was trained for a maximum of 100 epochs to achieve robust results.

2.4.5 Models' evaluation

To evaluate the performance of the CNN and RF models, we began by extracting the super feature set from the windowed test dataset (Figure 2, Step 6). Subsequently, the trained ML models were employed to predict targets, joint kinematics, and kinetics using the extracted features from test datasets (Figure 2, Step 7). Then, we computed the root mean square error (RMSE) and Normalized RMSE (NRMSE) between the OpenSim outputs and the predicted values generated by each ML model for all targets. Violin plots were utilized to illustrate the distribution of RMSEs across various IMU configurations and examinations (intra and inter-subject) for each target. These plots offer a visual representation of how data is spread out within each category. In a violin plot, the width of the shape at any given point indicates the probability of values occurring. Additionally, within the violins, the median line is depicted as a short horizontal line, providing a clear reference point for the central tendency of the data. The reported RMSEs and NRMSEs for intra-subject and inter-subject examination are average of personalized and generalized models, respectively. After determining the optimal ML model and IMU sensor configuration, we conducted additional analysis by 1) plotting average waveforms from both OpenSim and ML models' outputs, 2) calculating R2 values and creating correlation plots, and 3) generating Bland-Altman (Bland and Altman, 1986) plots to evaluate agreement between OpenSim outputs and predicted values for the selected model.

2.5 The effect of reducing IMU sensors to feet IMUs

In a prior study (Moghadam et al., 2023b), we demonstrated the feasibility of accurately estimating gait time series using machine learning models with just two IMUs positioned on the feet. To explore the applicability of this approach to children's data, we replicated the steps described in Figure 2 using two IMUs placed on the feet instead of the full set of 7 IMUs.

3 Results

3.1 Joint kinematics prediction

The distribution of predicted joint kinematics RMSE revealed similar predictive accuracy between the RF and CNN models, whether we're looking at the personalized models (intra-subject) or generalized models (inter-subject) (Figure 3). The RF model exhibited, on average, lower prediction errors of 0.22° in intra-subject examinations and 0.20° in inter-subject examinations when compared to the CNN model across all joints and planes of motion.

For the personalized models, reducing the number of IMUs to only one on each foot did not alter the prediction of joints kinematics compared to using all seven IMUs (Figure 3A). Interestingly, in the inter-subject examination, pelvis rotation, hip rotation, and ankle inversion/eversion angles experienced a decrease in their prediction errors by using only two IMUs; however, it increased the RMSE in the inter-subject evaluation for pelvis tilt and hip flexion/extension (Figure 3B). It is worth mentioning that these differences were not statistically significant.Independently of the model and the number of IMUs used, the average RMSE across all joints and planes of motion indicated considerably lower values in the intra-subject examinations compared to the inter-subject examinations. In the intra-subject evaluation, the RMSE spanned from a minimum of 1.0° (Pelvis tilt) to a maximum of 6.7° (ankle inversion/eversion). For the inter-subject evaluation, the range of

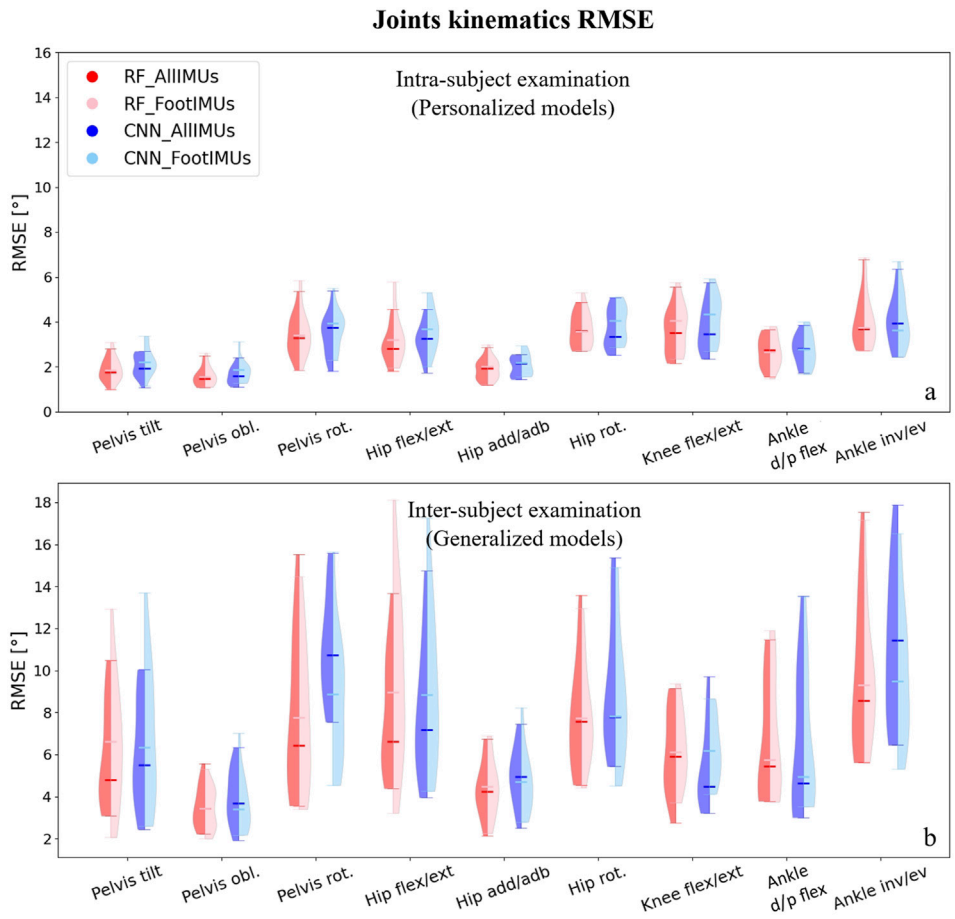

FIGURE 3
Violin plots illustrate the RMSE in degrees for joint kinematics predictions, comparing OpenSim IK outcomes with those from ML models. The red violins represent errors from the RF model, while the blue violins depict errors from the CNN model. Darker hues indicate models utilizing data from the full set of IMUs (n = 7), and lighter hues denote models using data solely from foot-mounted IMUs (n = 2). Panel **(A)** presents results from the intra-subject examination, while panel **(B)** displays the inter-subject examination results, utilizing models designed to generalize across participants.

TABLE 1 The Normalised RMSE (NMRSE) along with their corresponding standard deviation (SD) values for joint angle prediction across all joints and planes of motion in intra and inter-subject examinations, based on RF models' output using two IMUs.

Joint kinematics target	NRMSE (%) ± SD	
	Intra-subject examination	Inter-subject examination
Pelvis tilt	14.1 ± 5.1	33.1 ± 20.4
Pelvis obliquity	9.6 ± 2.7	19.7 ± 9.8
Pelvis rotation	13.8 ± 2.7	23.0 ± 13.1
Hip flexion/extension	6.1 ± 1.7	17.7 ± 8.4
Hip adduction/abduction	8.1 ± 1.9	18.4 ± 6.9
Hip rotation	11.9 ± 2.3	21.2 ± 7.1
Knee flexion/extension	5.2 ± 1.6	9.6 ± 6.6
Ankle dorsi/plantar flexion	6.7 ± 1.8	15.3 ± 5.7
Ankle inversion/eversion	10.1 ± 2.2	21.4 ± 5.9
Average	9.5 ± 3.3	19.9 ± 6.4

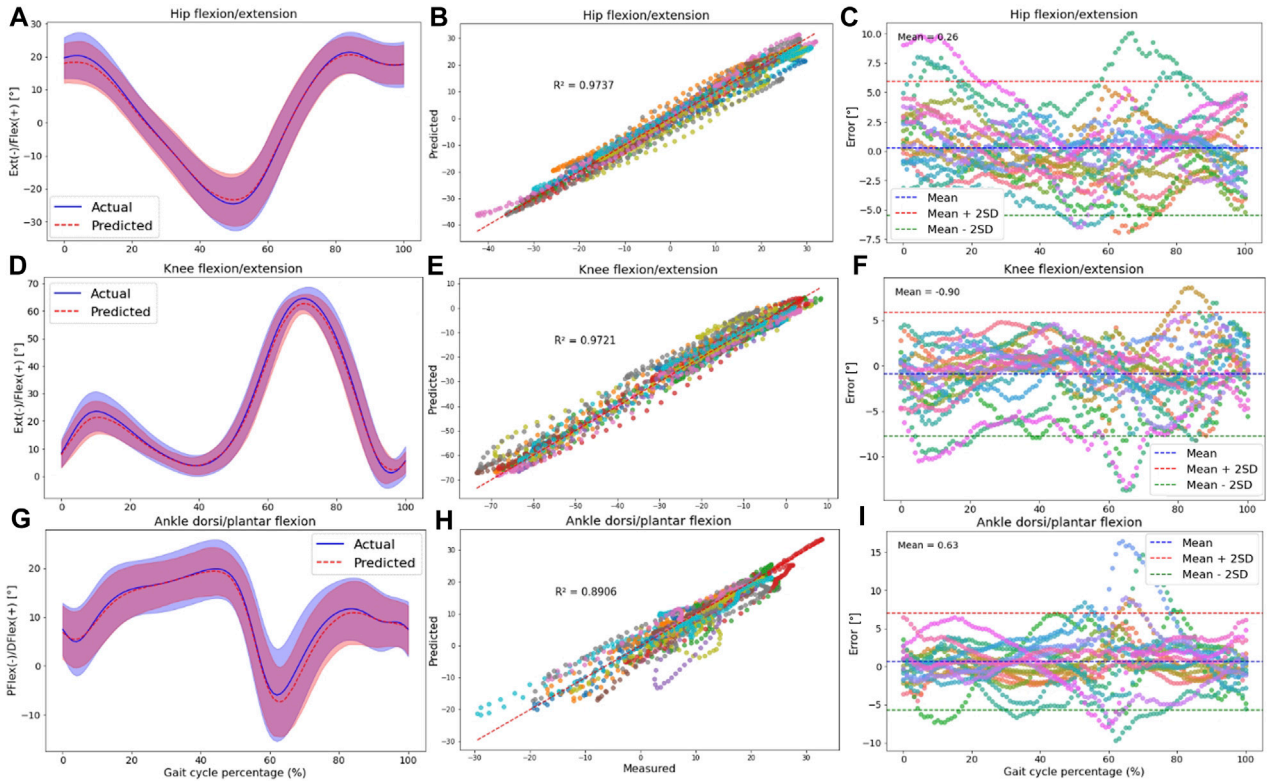

FIGURE 4
The plots are made across all participants in the intra-subject examination, specifically for hip **(A–C)**, knee **(D–F)**, and ankle **(G–I)** joint angles in the sagittal plane. Panels **(A,D,G)** present the RF model's average predictions (the dashed red line represents the average, and the red shaded area indicates the SD) for joint angles, utilizing data from IMUs placed on the feet. These predictions are compared to the joint angles derived from the OpenSim IK tool (the solid blue line represents the average, and the blue shaded area indicates the SD). Panels **(B,E,H)** illustrate the correlation and R-squared (R^2) values for the mentioned joint angle targets. In **(C,F,I)**, we utilized Bland-Altman plots to visually depict the errors throughout one gait cycle for all participants. In these plots, the dashed blue line represents the mean error, and the mean ± 2SD is depicted as dashed red and green lines. Each distinct color in these plots represents the results of one participant.

RMSE increased, covering values from 2.1° (hip adduction/abduction) to 17.5° (ankle inversion/eversion).

In our analysis, we found that overall, the RF model gave slightly better results, and the number of IMUs used (two vs. seven) did not have an impact on the results. Therefore, we concentrated on the results provided by the RF model with two IMUs for the subsequent analysis. After normalizing the RMSE values to the data range, we observed that the lowest normalized RMSE (NRMSE) was associated with knee flexion/extension angle, and the highest NRMSE value was related to the pelvis tilt angle (Table 1). In the hip and ankle joint angles prediction, the lowest error appeared in the sagittal plane; however, in the case of the pelvis, the highest error was associated with the sagittal plane. This finding held true for both intra and inter-subject examinations. Notably, the NRMSE values for all joints and planes of motion in the inter-subject results were nearly twice as high as those observed in the intra-subject examination. Specifically, the average RMSE across all targets increased from 9.5% to 19.9% (Table 1). When comparing the average NRMSE for children below 10 years with children older than 10 years, a clear trend emerges. On average, the NRMSE is lower (1.7% in intra-subject and 0.3% in inter-subject examinations) in the older age group when predicting joint kinematics (refer to Supplementary Table SA1).

To understand if the prediction accuracy is consistent across the gait cycle for the intra-subject examination, we performed further analysis for the RF model outputs encompassing: 1) Average range of motion (ROM) comparison between the OpenSim IK tool and the RF model's output. 2) Correlation plot and R-squared (R^2) Assessment, and 3) Bland-Altman Analysis to provide insights into the agreements between predicted and measured variables.

Hip, knee, and ankle joint angles in the sagittal plane are presented in Figure 4. Additional results for other targets, including pelvis angles in all planes of motion, hip joint angles in the frontal and transverse planes, and ankle joint angles in the frontal plane, are detailed in Supplementary Figure SA1.

Plotting an average ROM (standard deviation (±SD)) across all participants revealed that the predicted waveforms closely followed the measured waveforms obtained from the OpenSim IK tool. The SD area of the predicted values fell within the shaded area representing the measured values, indicating a close fit between the predicted and measured data in the intra-subject examination (Figures 4A, D, G; Supplementary Figures SA1A, D, G, J, M, P).

Furthermore, there was a strong correlation between the OpenSim IK outputs and predicted joint angles, with R^2 values exceeding 0.83 for pelvis angles in all planes of motion (Supplementary Figures SA1B, E, H), 0.76 for hip angles

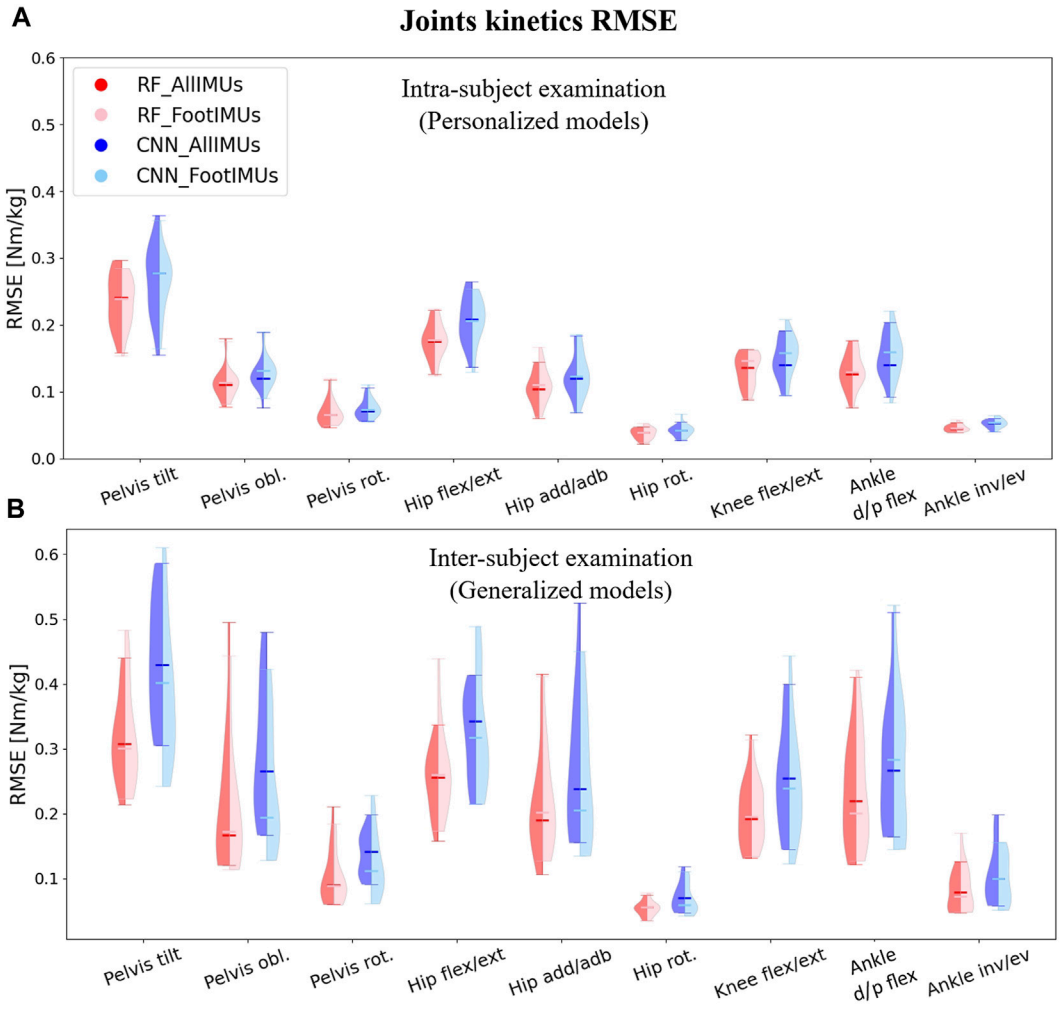

FIGURE 5
Violin plots illustrate the RMSE in degrees for joint kinematics predictions, comparing OpenSim ID outcomes with those from ML models. The red violins represent errors from the RF model, while the blue violins depict errors from the CNN model. Darker hues indicate models utilizing data from the full set of IMUs (n = 7), and lighter hues denote models using data solely from foot-mounted IMUs (n = 2). Panel **(A)** presents results from the intra-subject examination, while panel **(B)** displays the inter-subject examination results, utilizing models designed to generalize across participants.

(Supplementary Figures SA1K, N; Figure 4B), 0.97 for knee angle (Figure 4E), and 0.77 for ankle joint angles (Supplementary Figures SA1Q; Figure 4H). The high performance of the RF model in the sagittal plane was observed at the hip, knee, and ankle.

Strong agreement between the measured and predicted values was evident in the Bland-Altman plots, with the error falling within the range of two standard deviations from the mean value for most participants. No specific pattern in the error values was seen based on these plots; however, the bias between predicted and measured kinematics was around zero for all targets (Figures 4C, F, I; Supplementary Figures SA1C, F, I, L, O, R).

3.2 Joint kinetics prediction

When predicting joint kinetics, the RF model demonstrated slightly superior performance when compared to the CNN model (Figure 5). The RF model yielded lower prediction error values than the CNN model across all joints and planes of motion, with a reduction of 0.017 Nm/kg RMSE in intra-subject examinations and 0.037 Nm/kg RMSE in inter-subject examinations. The better performance of the RF model was more pronounced in the inter-subject examination (Figure 5B).

In terms of the number of IMU sensors used for joint kinetics prediction, we found nearly identical results when employing only the feet IMUs as compared to using all 7 IMUs. However, in specific kinetics targets, such as pelvis tilt and hip flexion/extension in the intra-subject examination and pelvis obliquity, hip adduction/abduction, and hip rotation in the inter-subject examination, even lower prediction errors were achieved by utilizing just two IMUs placed on the feet. It is important to highlight that irrespective of the model type and the number of IMUs employed for prediction, the RMSE values in the inter-subject examination were consistently higher than the RMSE in the intra-subject examination.

As for the kinematics, we concentrated on the results provided by the RF model with two IMUs for further analysis. After calculating the NRMSE between outputs of the RF model and the OpenSim ID tool, we observed that the highest NRMSE values were

TABLE 2 the NRMSE values along with their corresponding SD for joint moment prediction across all joints and planes of motion in intra and inter-subject examinations, based on RF models' output using feet IMUs.

Joint kinetics target	NRMSE (%) ± SD	
	Intra-subject examination	Inter-subject examination
Pelvis tilt	13.7 ± 1.9	13.9 ± 3.6
Pelvis obliquity	13.2 ± 2.1	16.8 ± 5.2
Pelvis rotation	12.8 ± 3.4	13.4 ± 3.8
Hip flexion/extension	11.8 ± 2.1	26.4 ± 14.5
Hip adduction/abduction	8.5 ± 2.1	15.1 ± 8.8
Hip rotation	9.6 ± 2.9	10.9 ± 3.3
Knee flexion/extension	8.5 ± 1.9	10.3 ± 2.6
Ankle dorsi/plantar flexion	6.4 ± 1.3	11.7 ± 9.6
Ankle inversion/eversion	12.5 ± 2.3	18.5 ± 7.3
Average	10.7 ± 2.6	15.2 ± 4.9

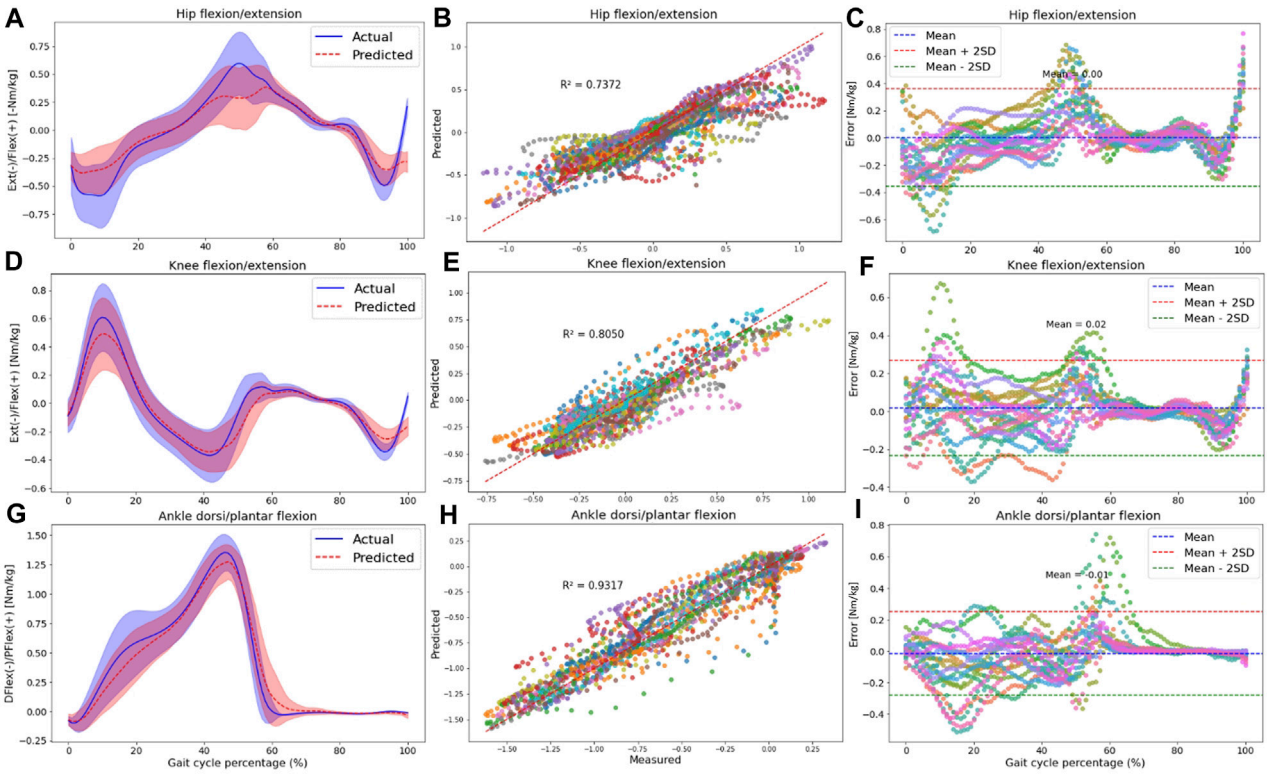

FIGURE 6
The plots are made across all participants in the intra-subject examination, specifically for hip **(A–C)**, knee **(D–F)**, and ankle **(G–I)** joint moments in the sagittal plane. Panels **(A,D,G)** present the RF model's average predictions (the dashed red line represents the average, and the red shaded area indicates one SD) for joint moments, utilizing data from IMUs placed on the feet. These predictions are compared to the joint moments derived from the OpenSim ID tool (the solid blue line represents the average, and the blue shaded area indicates one SD). Panels **(B,E,H)** illustrate the correlation and R-squared (R^2) values for the mentioned joint moment targets. In **(C,F,I)**, we utilized Bland-Altman plots to visually depict the errors throughout one gait cycle for all participants. In these plots, the dashed blue line represents the mean error, and the mean ± 2SD is depicted as dashed red and green lines. Each distinct color in correlation and error plots represents the results of one participant.

associated with the pelvis tilt in the intra-subject examination (similar to the kinematics analysis) and hip flexion/extension in the inter-subject examination. Conversely, ankle dorsi/plantar flexion exhibited the lowest NRMSE for intra-subject examination, while knee flexion/extension displayed the lowest NRMSE for inter-subject examination.

Just like with joint kinematics, the NRMSE values for all joints and planes of motion in the inter-subject results were higher than the intra-subject examination. Specifically, the average RMSE across all targets increased from 10.7% to 15.2% (Table 2). Similar to the prediction of joint kinematics, a consistent trend was noted in the prediction of joint kinetics (refer to Supplementary Table SA2). Notably, the NRMSE was lower by 1% in intra-subject and 4.3% in inter-subject examinations for older children (above 10 years old) as opposed to their younger counterparts (below 10 years old).

To understand if the prediction accuracy is consistent across the gait cycle for the intra-subject examination, we performed further analysis for the RF model outputs encompassing: 1) Average normalized moment comparison between the OpenSim IK tool and the RF model's output. 2) Correlation plot and R-squared (R^2) Assessment, and 3) Bland-Altman Analysis to provide insights into the agreements between predicted and measured variables.

The results for the hip, knee, and ankle joint moments in the sagittal plane are shown in Figure 6. Additional results for other targets, including pelvis moments in all planes of motion, hip joint moments in the frontal and transverse planes, and ankle joint moment in the frontal plane, are detailed in Supplementary Figure SA2.

Plotting the average and standard deviation waveforms for joint moments throughout a gait cycle in intra-subject examination, we observed that the RF model's predictions effectively tracked the OpenSim ID tool output. However, the SD area of the predicted values did not consistently fall within the shaded area related to the measured values across the entire gait cycle [(Figures 6A, D, G); Supplementary Figures SA2A, D, G, J, M, P]. Especially toward the end of the stance phase (50%–60% of the gait cycle), the model predicted a lower range of motion in the three joints in the sagittal plane. Also, at the beginning of the stance phase, we can observe some discrepancies in knee flexion and hip extension moment predictions.

Compared to joint angles, the correlation between the measured and predicted joint moments was lower for the pelvis, with R2 values of 0.43, 0.31, and 0.41 for pelvis tilt, obliquity, and rotation, respectively (Supplementary Figures SA2B, E, H). The R2 values for other joint kinetics were consistent with the performance seen in joint kinematics prediction. Specifically, the hip joint experienced R2 higher than 0.73 in all planes of motion (Supplementary Figures SA2K, N; Figure 6B), the R2 for the knee joint was 0.80 in the sagittal plane (Figure 6E), and the ankle displayed R2 values higher than 0.83 in both the frontal (Supplementary Figures SA2Q) and sagittal planes (Figure 6H).

According to Bland-Altman plots, there was a good agreement between the measured and predicted targets, as the errors were within a range of two SD of the mean value for most participants. Similar to joint kinematics prediction, the bias between measured and predicted variables was around zero for all kinetics targets. An interesting observation was that during the final phase of the gait cycle (swing phase), errors were almost zero for most joint kinetics (Figures 6C, F, I; Supplementary Figures SA1C, F, I, L, O, R).

4 Discussion

The aim of this study was to investigate the feasibility of using a combination of IMUs' data and ML models for predicting joint kinematics and kinetics in school-aged children. To answer this aim, the first objective was to assess the accuracy of RF and CNN ML models by quantifying both intra-subject and inter-subject prediction errors. The second objective was to evaluate the influence of using only an IMU on each foot versus seven IMUs, one on each segment of the lower limb, on kinematics and kinetics prediction performance. We employed a feature engineering technique to extract and select the most important features from the IMUs' acceleration and angular velocity data to enhance the models' performance.

4.1 ML comparison

Regarding the first objective, findings suggested that the RF and CNN models demonstrated comparable performance for predicting joint kinematics (NRMSE of 9.5% versus 10.6% for personalized and NRMSE of 19.9% versus 22.5% for generalized models, respectively) and kinetics (NRMSE of 10.7% versus 12.9% for personalized and NRMSE of 15.2% versus 17.9% for generalized models respectively) in TD children. This implies that the complexity of deep neural network structures may not be necessary for gait time series prediction. Consequently, it opens the door to more efficient and easily interpretable modeling approaches, such as the RF model (Breiman, 2001). Supporting this notion, a separate study found RF models to outperform CNN models in estimating step length, showing an absolute error of 5.09 cm for RF compared to 5.26 cm for CNN (Seifer et al., 2023). Furthermore, the superiority of RF models, with an average error of 5.57°, becomes evident in gait trajectory generation, surpassing the neural network model with an average error of 6.00° in another study (Ren et al., 2019).

The higher performance of RF models could be attributed to their resilience against overfitting. This resilience arises from their capacity to amalgamate multiple decision trees trained on bootstrapped data, coupled with the utilization of feature randomization, pruning, and averaging (Breiman, 2001). On the other hand, CNNs exhibit a notable susceptibility to overfitting, particularly when dealing with smaller datasets (Slijepcevic et al., 2023).

4.1.1 Intra-subject examination

We created 17 personalized models for predicting kinematics and kinetics based on customized feature sets specific to each participant. Our results from the RF model using two IMUs data demonstrated strong predictive accuracy, with an average RMSE ranging from 1.61° to 4.16° (NRMSE of 5.2%–14.1%) across all joint kinematics. The RMSE values for joint kinematics stayed well below the 5° error threshold, which is often considered a clinically acceptable level of deviation for assessing joint movements (Slater et al., 2018). However, the joint kinematics prediction error were higher than for adults in other studies, where observed values ranged from 1.38° to 3.96° for all targets (Findlow et al., 2008; Giarmatzis et al., 2020; Moghadam et al., 2023a; Yeung et al., 2023). Similarly, joint kinetics prediction error were higher (0.038–0.233 Nm/kg) in this study than on adult population, where the RMSE ranged from 0.042 to 0.198 Nm/kg (Dey et al., 2019; Mundt et al., 2020; Moghadam et al., 2023a). This elevated error in both kinematics

and kinetics prediction in the intra-subject evaluation of children compared to the adult models underscores the greater variability in gait time series within individual children across different trials. Different gait maturity level (Bach et al., 2021) as well as heightened variability in gait patterns (Kuhtz-Buschbeck et al., 1996) and EMG gait waveforms (Granata et al., 2005) in children compared to adults has been shown in other studies. This discrepancy may be attributed to the increased susceptibility of children to distractions during walking (Stolze et al., 1998) or to the heterogeneity in children's gait cycles compared to adults.

Despite the higher errors in the children's personalized ML model compared to adults, the Bland-Altman plots revealed a notable level of agreement between the measured and predicted values during the intra-subject examination. Most participants exhibited errors within the range of two SD from the mean error value. Additionally, average errors consistently remained near zero for all predicted targets, underlining the good overall agreement between the IMU-based and OMC-based kinematics and kinetics. It is worth noting that no discernible patterns in the error values were observed, indicating a lack of systematic bias in the predictions (Bland and Altman, 1986). These findings emphasize the practicality and suitability of employing this approach, which involves a personalized RF model utilizing IMU data for accurately estimating gait time series in children.

One interesting finding of personalized modeling (intra-subject examination) was the good model performance within the sagittal plane compared to the other planes of motion for joint kinematics prediction, especially in the case of hip and ankle joint angles. The knee angle, only computed within the sagittal plane, demonstrated a high correlation between the actual and predicted values (R2 of 0.97). The enhanced performance of the RF model in the sagittal plane (higher R2 and lower errors) can be attributed to the more prominent joint movements within this plane, which, in turn, yields more distinct signals from the IMUs. Consequently, this clarity in the IMU signals contributes to the model's improved predictive performance in the sagittal plane. While other planes of motion, such as the frontal and transverse planes, contribute to a comprehensive understanding of gait, the sagittal plane takes precedence in gait analysis due to its primary role in capturing the fundamental aspects of forward movement. We've shown that the proposed personalized method exhibits remarkable accuracy, demonstrating a clinically acceptable level of error, particularly in the sagittal plane. This notable precision positions it as exceptionally valuable for advancing the gait analysis of children.

4.1.2 Inter-subject examination

In the inter-subject examination of the RF model, the results were less promising compared to the intra-subject test, with average RMSE ranging from 3.5° to 9.6° (NRMSE of 9.6%–33.1%) for joint kinematics. When comparing the outcomes with adults cohort, it becomes apparent that the RMSE values in adults exhibit lower errors (RMSE between 2.17° and 6.53°) (Luu et al., 2014; Dorschky et al., 2020; Lim et al., 2020; Sharifi Renani et al., 2021; Moghadam et al., 2023a). Similar findings were found for joint moments with NRMSE of 10.3%–26.4% found in this study compared to 4.54%–10.74% in previous adults studies (Giarmatzis et al., 2020; Lim et al., 2020). In fact, these errors are of such magnitude that they do not provide confidence in the accurate prediction of gait time series in children not included in the training set. This contrasts with the previously demonstrated success of inter-subject modeling in predicting time series for the adult population with limited data (Giarmatzis et al., 2020; Lim et al., 2020; Stetter et al., 2020; Moghadam et al., 2023a).

The primary reason for the elevated error in the children's generalized model compared to adults can be attributed to the diverse gait patterns among individual children, given their ongoing musculoskeletal changes and developmental stages within the specified age range of six to 15 years in this study (Onis et al., 2007; Bari et al., 2023). However, as age advances, there is a reduction in variability within the gait pattern, as demonstrated in our findings revealing higher errors in gait analysis for younger children compared to older ones. When analysing the average (±SD) waveforms of targets within a gait cycle, we observed a noticeable standard deviation surrounding the average waveform for the children, reaffirming the high variability of gait patterns among children. This is comparable to a study by Fokuchi et al., where a greater deviation area for younger people compared to the adults' normative gait data is shown (Fukuchi et al., 2018). The secondary reason for the high error in generalized modeling lies in the limitations of the dataset. Effective ML models typically require access to extensive datasets comprising a wide spectrum of walking patterns. Consequently, the performance of a model trained on a small dataset featuring only 16 participants is inherently limited when applied to new, unseen subjects. The considerable errors observed in generalized modeling render this approach less advisable for children who were not part of the initial training dataset.

4.2 Number of IMUs

Concerning the second objective, we demonstrated that utilizing two IMUs on the feet, instead of a total of seven IMUs, resulted in similar accuracy of the models, specifically in intra-subject examination. Concerning the inter-subject examination, while there was a slight increase in error for some targets (pelvis tilt, hip flexion/extension angles and moments, and ankle dorsi/plantar moment), reducing the number of IMUs to feet IMUs resulted in decreased errors for specific targets such as pelvis rotation angle, hip rotation angle, ankle inversion/eversion angles, pelvis obliquity moment, hip adduction/abduction moment, and hip rotation moment.

These findings are consistent with our prior research, which suggested that in adult gait prediction, employing ML models allows us to achieve nearly identical results using only feet IMUs, as opposed to utilizing seven IMUs (one for each segment) (Moghadam et al., 2023b). This can be attributed to the proficiency of ML models in establishing a robust relationship between IMU data and targets. Another contributing factor is the identification of alternative features to raw IMU data, thereby augmenting the predictive capabilities of the ML model, even when working with a limited number of IMUs. The feasibility of employing a single IMU on the pelvis (Lim et al., 2020) or a pair of IMUs on shanks (Sharifi Renani et al., 2020; Yeung et al., 2023) or feet (Gholami et al., 2020) for predicting a diverse range of gait time series has been demonstrated in prior studies. Reducing the number

of IMUs streamlines model implementation, decreases data processing time, and lowers sensor-related costs. Additionally, the potential integration of foot IMUs within shoes, rendering them inconspicuous during community use, could enhance patient compliance.

4.3 Limitations and future work

This study presents limitations to be addressed by future research. Firstly, the utilization of a generic adult model for scaling and constructing musculoskeletal models for children. The issue lies in the potential discrepancies between generic adult models and the individual anatomical characteristics of children. Developing more precise, subject-specific models would ideally involve leveraging medical imaging data, such as MRI, CT, or X-rays, which can be both time-consuming and financially burdensome (Nolte et al., 2016). To address this limitation, future research could explore alternative methods like statistical shape modeling to build children's musculoskeletal models (Carman et al., 2022).

Another limitation of this study pertains to the omission of an investigation into the potential impact of slight variations in the placement of IMUs that may occur when different individuals are responsible for placing the IMUs. The concern here is that small variations could influence the data collected and, consequently, affect the accuracy and reliability of the results. Addressing this limitation in future research might involve conducting a sensitivity analysis or implementing standardized procedures for IMU placement to mitigate the potential impact of such variations on the study outcomes. It is noteworthy that a similar analysis was taken in an adult study and did not change the results (Moghadam et al., 2023a). So, we expect that these findings apply to children, too, meaning small changes in sensors' placement should not substantially affect the outcomes.

Our study focused on TD children to establish the models, which will differ from other populations, such as children with cerebral palsy. The choice of ML model and the number of required IMUs may differ, as children with movement disorders often exhibit more complex and diverse gait patterns. Several research groups have successfully employed regression machine learning models to estimate gait time series in specific patient cohorts. Examples of previous studies on patients include the prediction of knee joint moments during gait in individuals with CP (Kwon et al., 2012), the estimation of knee joint kinematics in patients with knee osteoarthritis (Tan et al., 2022), and the forecasting of gait parameters for patients with osteoarthritis (OA) and those undergoing total knee arthroplasty (TKA) (Sharifi Renani et al., 2020). Notably, these investigations demonstrated high correlation coefficients ranging from 0.71 to 0.99, showcasing the viability of gait time series prediction in targeted patient groups using wearable sensors and machine learning models. While the model employed in this study demonstrates robust performance with TD children, its suitability for diverse pathologies warrants exploration. Gait patterns vary significantly across different conditions, making it imprudent to apply the exact same model to a new population. Consequently, our future endeavours will involve evaluating the performance of our algorithm on additional patient cohorts, including children with cerebral palsy.

Another notable limitation is the computational resources required for the primary feature extraction and selection processes. We utilized high-performance computers with 80 GB of RAM memory to address this demand. However, once the model is trained, it can be executed on less powerful computers, focusing solely on extracting the selected features and providing inference from the model.

It is also important to acknowledge that the accuracy of estimations using data from other labs may not match the precision of our own results. This discrepancy can be related to variations in equipment and sensor usage across different laboratories. However, by incorporating data from multiple labs into the training dataset for our models, we can enhance the models' ability to generalize across different settings. In future work, it would also be valuable to consider the integration of a contactless monitoring system, akin to the innovative approach developed in a separate study (Huang et al., 2024). Integrating such systems into the ML model holds the potential for real-time prediction of gait time series in children.

4.4 Strengths and contributions

By developing an ML model for predicting gait time series in children with diverse gait patterns, we achieved results comparable to studies focused on the adult population, particularly in the context of personalized modeling. We believe that our model offers several advantages over traditional methods that rely on IMUs for gait analysis. For instance, our model can predict a comprehensive set of lower limb joint angles and moments during gait using only two IMUs attached to the feet. To the best of our knowledge, this is the first study tailored to children's gait time series prediction, leveraging a combination of IMU data and ML techniques.

Other methodologies, which would use sensor fusion algorithms rather than ML, require additional normalization steps to calculate each IMU sensors' orientation relative orientation to each body segment, leading to inaccuracies and numerical drift errors. In contrast, our personalized models have good accuracy, can be streamlined, and work independently of the user's expertise. Following a single data collection session in a gait lab, remote patient monitoring becomes feasible by placing IMUs on the patient's feet and feeding the IMU data into the model for inference. Furthermore, this workflow can be utilized in real-time, as the inference time for the RF model is on the order of milliseconds.

5 Conclusion

The current study showed that RF and CNN models exhibit comparable results in the context of gait analysis within a typically developed pediatric population. The practicality of employing only two IMUs placed on the feet for predicting a comprehensive set of lower-limb joint kinematics and kinetics was successfully demonstrated. The presented workflow, employing foot IMUs, not only reduces processing time but also streamlines the integration of wearable sensors in clinical settings. Our forthcoming research endeavors will include increasing the sample size and introducing more variability to the overground walking scenarios to enhance the accuracy of our generalized model.

Moreover, future work will be dedicated to developing ML models tailored to a cohort of children with movement disorders, specifically children with CP. This expansion promises to bring valuable insights and tools to the field of pediatric gait analysis, serving as a testament to the potential for advanced technology to benefit those with unique clinical requirements.

Data availability statement

The datasets presented in this study can be found in online repositories. The names of the repository/repositories and accession number(s) can be found below: The post-processed data, including joint kinematics, joint kinetics, as well as the raw IMU data utilized for constructing ML models in this study, are accessible on the open-source platform SimTK.org (https://simtk.org/projects/ml_sensors).

Ethics statement

The studies involving humans were approved by the research strictly adhered to ethical principles outlined in the Helsinki Declaration and received approval from the University of Auckland (New Zealand) human participant ethics committee (reference number 021615). The studies were conducted in accordance with the local legislation and institutional requirements. Written informed consent for participation in this study was provided by the participants' legal guardians/next of kin.

Author contributions

SM: Data curation, Formal Analysis, Investigation, Methodology, Software, Validation, Visualization, Writing–original draft, Writing–review and editing. PO: Data curation, Writing–original draft, Writing–review and editing. TY: Conceptualization, Funding acquisition, Methodology, Supervision, Writing–original draft, Writing–review and editing. JC: Conceptualization, Funding acquisition, Investigation, Methodology, Project administration, Resources, Supervision, Validation, Writing–original draft, Writing–review and editing.

Funding

The author(s) declare financial support was received for the research, authorship, and/or publication of this article. This study was funded by the Health Research Council NZ (grant number 19/652), the Aotearoa fellowship (philanthropic donation from the Robertson foundation), the Friedlander Foundation (philanthropic donation), and the Science for Technological Innovation NZ (grant number UOAX2005).

Acknowledgments

We express our gratitude to the participants for their valuable contributions to this study. Additionally, we acknowledge the support of the Health Research Council NZ, the Aotearoa fellowship, the Friedlander Foundation, and the Science for Technological Innovation NZ National Science Challenge for funding this research.

Conflict of interest

The authors declare that the research was conducted in the absence of any commercial or financial relationships that could be construed as a potential conflict of interest.

Publisher's note

Supplementary material

The Supplementary Material for this article can be found online at: https://www.frontiersin.org/articles/10.3389/fbioe.2024.1372669/full#supplementary-material

References

Al Borno, M., O'Day, J., Ibarra, V., Dunne, J., Seth, A., Habib, A., et al. (2022). Opensense: an open-source toolbox for inertial-measurement-unit-based measurement of lower extremity kinematics over long durations. *J. neuroengineering rehabilitation* 19 (1), 22–11. doi:10.1186/s12984-022-01001-x

Aminian, K., and Najafi, B. (2004). Capturing human motion using body-fixed sensors: outdoor measurement and clinical applications. *Comput. Animat. virtual worlds* 15 (2), 79–94. doi:10.1002/cav.2

Bach, M. M., Daffertshofer, A., and Dominici, N. (2021). The development of mature gait patterns in children during walking and running. *Eur. J. Appl. physiology* 121, 1073–1085. doi:10.1007/s00421-020-04592-2

Bakke, D., and Besier, T. (2022). Shape-model scaled gait models can neglect segment markers without consequential change to inverse kinematics results. *J. Biomechanics* 137, 111086. doi:10.1016/j.jbiomech.2022.111086

Bari, M. A., Mir, H. N., Parrey, J. A., Ateeq, A., Ajhar, A., Al Muslem, W. H., et al. (2023). Exploring variations in gait patterns and joint motion characteristics in school-aged children across different walking speeds: a comprehensive motion analysis study. *J. Med. Life* 16 (6), 895–903. doi:10.25122/jml-2023-0110

Benjamini, Y., and Hochberg, Y. (1995). Controlling the false discovery rate: a practical and powerful approach to multiple testing. *J. R. Stat. Soc. Ser. B Methodol.* 57 (1), 289–300. doi:10.1111/j.2517-6161.1995.tb02031.x

Bland, J. M., and Altman, D. (1986). Statistical methods for assessing agreement between two methods of clinical measurement. *lancet* 327 (8476), 307–310. doi:10.1016/s0140-6736(86)90837-8

Breiman, L. (2001). Random forests. *Mach. Learn.* 45 (1), 5–32. doi:10.1023/a:1010933404324

Carman, L., Besier, T. F., and Choisne, J. (2022). Morphological variation in paediatric lower limb bones. *Sci. Rep.* 12 (1), 3251. doi:10.1038/s41598-022-07267-4

Chester, V. L., Biden, E. N., and Tingley, M. (2005). Gait analysis. *Biomed. Instrum. Technol.* 39 (1), 64–74. doi:10.2345/0899-8205(2005)39[64:GA]2.0.CO;2

Choisne, J., Fourrier, N., Handsfield, G., Signal, N., Taylor, D., Wilson, N., et al. (2020). An unsupervised data-driven model to classify gait patterns in children with cerebral palsy. *J. Clin. Med.* 9 (5), 1432. doi:10.3390/jcm9051432

Christ, M., Braun, N., Neuffer, J., and Kempa-Liehr, A. W. (2018). Time series feature extraction on basis of scalable Hypothesis tests (Tsfresh–a Python package). *Neurocomputing* 307, 72–77. doi:10.1016/j.neucom.2018.03.067

Cigali, B. S., Uluçam, E., and Bozer, C. (2011). 3d motion analysis of hip, knee and ankle joints of children aged between 7-11 Years during gait. *Balkan Med. J.* (2), 197–201. doi:10.5174/tutfd.2010.04199.2

Davis, R. B., III, Ounpuu, S., Tyburski, D., and Gage, J. R. (1991). A gait analysis data collection and reduction technique. *Hum. Mov. Sci.* 10 (5), 575–587. doi:10.1016/0167-9457(91)90046-z

Delp, S. L., Anderson, F. C., Arnold, A. S., Loan, P., Habib, A., John, C. T., et al. (2007). Opensim: open-source software to create and analyze dynamic simulations of movement. *IEEE Trans. Biomed. Eng.* 54 (11), 1940–1950. doi:10.1109/tbme.2007.901024

Dey, S., Yoshida, T., Ernst, M., Schmalz, T., and Schilling, A. F. (2019). "A random forest approach for continuous prediction of joint angles and moments during walking: an implication for controlling active knee-ankle prostheses/orthoses," in 2019 IEEE International Conference on Cyborg and Bionic Systems (CBS) (IEEE), 66–71.

Dorschky, E., Nitschke, M., Martindale, C. F., Van den Bogert, A. J., Koelewijn, A. D., and Eskofier, B. M. (2020). Cnn-based estimation of sagittal plane walking and running Biomechanics from measured and simulated inertial sensor data. *Front. Bioeng. Biotechnol.* 8, 604. doi:10.3389/fbioe.2020.00604

Findlow, A., Goulermas, J., Nester, C., Howard, D., and Kenney, L. (2008). Predicting lower limb joint kinematics using wearable motion sensors. *Gait posture* 28 (1), 120–126. doi:10.1016/j.gaitpost.2007.11.001

Fukuchi, C. A., Fukuchi, R. K., and Duarte, M. (2018). A public dataset of overground and treadmill walking kinematics and kinetics in healthy individuals. *PeerJ* 6, e4640. doi:10.7717/peerj.4640

Ganley, K. J., and Powers, C. M. (2005). Gait kinematics and kinetics of 7-year-old children: a comparison to adults using age-specific anthropometric data. *Gait posture* 21 (2), 141–145. doi:10.1016/j.gaitpost.2004.01.007

Gholami, M., Napier, C., and Menon, C. (2020). Estimating lower extremity running gait kinematics with a single accelerometer: a deep learning approach. *Sensors* 20 (10), 2939. doi:10.3390/s20102939

Giarmatzis, G., Zacharaki, E. I., and Moustakas, K. (2020). Real-time prediction of joint forces by motion capture and machine learning. *Sensors* 20 (23), 6933. doi:10.3390/s20236933

Granata, K. P., Padua, D. A., and Abel, M. F. (2005). Repeatability of surface emg during gait in children. *Gait Posture* 22 (4), 346–350. doi:10.1016/j.gaitpost.2004.11.014

Gurchiek, R. D., Cheney, N., and McGinnis, R. S. (2019). Estimating biomechanical time-series with wearable sensors: a systematic review of machine learning techniques. *Sensors* 19 (23), 5227. doi:10.3390/s19235227

Harrington, M., Zavatsky, A., Lawson, S., Yuan, Z., and Theologis, T. (2007). Prediction of the hip joint centre in adults, children, and patients with cerebral palsy based on magnetic resonance imaging. *J. biomechanics* 40 (3), 595–602. doi:10.1016/j.jbiomech.2006.02.003

Hasan, M. A. M., Nasser, M., Ahmad, S., and Molla, K. I. (2016). Feature selection for intrusion detection using random forest. *J. Inf. Secur.* 7 (3), 129–140. doi:10.4236/jis.2016.73009

Huang, S., Dai, H., Yu, X., Wu, X., Wang, K., Hu, J., et al. (2024). A contactless monitoring system for accurately predicting energy expenditure during treadmill walking based on an ensemble neural network. *Iscience* 27 (3), 109093. doi:10.1016/j.isci.2024.109093

Ito, T., Noritake, K., Ito, Y., Tomita, H., Mizusawa, J., Sugiura, H., et al. (2022). Three-dimensional gait analysis of lower extremity gait parameters in Japanese children aged 6 to 12 years. *Sci. Rep.* 12 (1), 7822. doi:10.1038/s41598-022-11906-1

Jain, E., Anthony, L., Aloba, A., Castonguay, A., Cuba, I., Shaw, A., et al. (2016). Is the motion of a child perceivably different from the motion of an adult? *ACM Trans. Appl. Percept. (TAP)* 13 (4), 1–17. doi:10.1145/2947616

Kamruzzaman, J., and Begg, R. K. (2006). Support vector machines and other pattern recognition approaches to the diagnosis of cerebral palsy gait. *IEEE Trans. Biomed. Eng.* 53 (12), 2479–2490. doi:10.1109/tbme.2006.883697

Khaksar, S., Pan, H., Borazjani, B., Murray, I., Agrawal, H., Liu, W., et al. (2021). Application of inertial measurement units and machine learning classification in cerebral palsy: randomized controlled trial. *JMIR Rehabilitation Assistive Technol.* 8 (4), e29769. doi:10.2196/29769

Knudson, D. V. (2007). *Fundamentals of Biomechanics*. Springer.

Kolaghassi, R., Al-Hares, M. K., Marcelli, G., and Sirlantzis, K. (2022). Performance of deep learning models in forecasting gait trajectories of children with neurological disorders. *Sensors* 22 (8), 2969. doi:10.3390/s22082969

Kolaghassi, R., Marcelli, G., and Sirlantzis, K. (2023). Deep learning models for stable gait prediction applied to exoskeleton reference trajectories for children with cerebral palsy. *IEEE Access* 11, 31962–31976. doi:10.1109/access.2023.3252916

Kuhtz-Buschbeck, J., Boczek-Funcke, A., Heinrichs, H., Illert, M., and Stolze, H. (1996). Kinematic analysis of prehension in children. *Eur. J. Neurosci.* Suppl, 9–131.

Kwon, S., Park, H.-S., Stanley, C. J., Kim, J., Kim, J., and Damiano, D. L. (2012). A practical strategy for semg-based knee joint moment estimation during gait and its validation in individuals with cerebral palsy. *IEEE Trans. Biomed. Eng.* 59 (5), 1480–1487. doi:10.1109/tbme.2012.2187651

Laird, P., and Saul, R. (1994). "Automated feature extraction for supervised learning," in Proceedings of the First IEEE Conference on Evolutionary Computation. IEEE World Congress on Computational Intelligence (IEEE), 674–679.

Lim, H., Kim, B., and Park, S. (2020). Prediction of lower limb kinetics and kinematics during walking by a single imu on the lower back using machine learning. *Sensors* 20 (1), 130. doi:10.3390/s20010130

Lu, T.-W., and O connor, J. (1999). Bone position estimation from skin marker Co-ordinates using global optimisation with joint constraints. *J. biomechanics* 32 (2), 129–134. doi:10.1016/s0021-9290(98)00158-4

Luu, T. P., Low, K., Qu, X., Lim, H., and Hoon, K. (2014). An individual-specific gait pattern prediction model based on generalized regression neural networks. *Gait posture* 39 (1), 443–448. doi:10.1016/j.gaitpost.2013.08.028

Madgwick, S. O., Harrison, A. J., and Vaidyanathan, R. (2011). "Estimation of imu and marg orientation using a gradient descent algorithm," in 2011 IEEE international conference on rehabilitation robotics (IEEE), 1–7.

Mantoan, A., Pizzolato, C., Sartori, M., Sawacha, Z., Cobelli, C., and Reggiani, M. (2015). Motonms: a Matlab toolbox to process motion data for neuromusculoskeletal modeling and simulation. *Source code Biol. Med.* 10 (1), 12–14. doi:10.1186/s13029-015-0044-4

Moghadam, S. M., Yeung, T., and Choisne, J. (2023a). A comparison of machine learning models' accuracy in predicting lower-limb joints' kinematics, kinetics, and muscle forces from wearable sensors. *Sci. Rep.* 13 (1), 5046. doi:10.1038/s41598-023-31906-z

Moghadam, S. M., Yeung, T., and Choisne, J. (2023b). The effect of imu sensor location, number of features, and window size on a random forest model's accuracy in predicting joint kinematics and kinetics during gait. *IEEE Sensors J.* 23, 28328–28339. doi:10.1109/jsen.2023.3317366

Morbidoni, C., Cucchiarelli, A., Agostini, V., Knaflitz, M., Fioretti, S., and Di Nardo, F. (2021). Machine-learning-based prediction of gait events from emg in cerebral palsy children. *IEEE Trans. Neural Syst. Rehabilitation Eng.* 29, 819–830. doi:10.1109/tnsre.2021.3076366

Mundt, M., Johnson, W. R., Potthast, W., Markert, B., Mian, A., and Alderson, J. (2021). A comparison of three neural network approaches for estimating joint angles and moments from inertial measurement units. *Sensors* 21 (13), 4535. doi:10.3390/s21134535

Mundt, M., Thomsen, W., Witter, T., Koeppe, A., David, S., Bamer, F., et al. (2020). Prediction of lower limb joint angles and moments during gait using artificial neural networks. *Med. Biol. Eng. Comput.* 58 (1), 211–225. doi:10.1007/s11517-019-02061-3

Nolte, D., Tsang, C. K., Zhang, K. Y., Ding, Z., Kedgley, A. E., and Bull, A. M. (2016). Non-linear scaling of a musculoskeletal model of the lower limb using statistical shape models. *J. biomechanics* 49 (14), 3576–3581. doi:10.1016/j.jbiomech.2016.09.005

Onis, M. d., Onyango, A. W., Borghi, E., Siyam, A., Nishida, C., and Siekmann, J. (2007). Development of a who growth reference for school-aged children and adolescents. *Bull. World health Organ.* 85 (9), 660–667. doi:10.2471/blt.07.043497

Ren, S., Wang, W., Hou, Z.-G., Chen, B., Liang, X., Wang, J., et al. (2019). Personalized gait trajectory generation based on anthropometric features using random forest. *J. Ambient Intell. Humaniz. Comput.* 14, 15597–15608. doi:10.1007/s12652-019-01390-3

Sabatini, A. M. (2006). Quaternion-based extended kalman filter for determining orientation by inertial and magnetic sensing. *IEEE Trans. Biomed. Eng.* 53 (7), 1346–1356. doi:10.1109/tbme.2006.875664

Seifer, A.-K., Küderle, A., Dorschky, E., Moradi, H., Hannemann, R., and Eskofier, B. (2023). *Step length and gait speed estimation using a hearing aid integrated accelerometer: a comparison of different algorithms*.

Senden, R., Marcellis, R., Meijer, K., Willems, P., Lenssen, T., Staal, H., et al. (2023). Dataset of 3d gait analysis in typically developing children walking at three different speeds on an instrumented treadmill in virtual reality. *Data Brief* 48, 109142. doi:10.1016/j.dib.2023.109142

Sharifi Renani, M., Eustace, A. M., Myers, C. A., and Clary, C. W. (2021). The use of synthetic imu signals in the training of deep learning models significantly improves the accuracy of joint kinematic predictions. *Sensors* 21 (17), 5876. doi:10.3390/s21175876

Sharifi Renani, M., Myers, C. A., Zandie, R., Mahoor, M. H., Davidson, B. S., and Clary, C. W. (2020). Deep learning in gait parameter prediction for oa and tka patients wearing imu sensors. *Sensors* 20 (19), 5553. doi:10.3390/s20195553

Sivakumar, S., Gopalai, A. A., Lim, K. H., and Gouwanda, D. (2019). Artificial neural network based ankle joint angle estimation using instrumented foot insoles. *Biomed. Signal Process. Control* 54, 101614. doi:10.1016/j.bspc.2019.101614

Slater, A. A., Hullfish, T. J., and Baxter, J. R. (2018). The impact of thigh and shank marker quantity on lower extremity kinematics using a constrained model. *BMC Musculoskelet. Disord.* 19 (1), 399–410. doi:10.1186/s12891-018-2329-7

Slijepcevic, D., Zeppelzauer, M., Unglaube, F., Kranzl, A., Breiteneder, C., and Horsak, B. (2023). *Explainable machine learning in human gait analysis: a study on children with cerebral palsy*. IEEE Access.

Stetter, B. J., Krafft, F. C., Ringhof, S., Stein, T., and Sell, S. (2020). A machine learning and wearable sensor based approach to estimate external knee flexion and adduction moments during various locomotion tasks. *Front. Bioeng. Biotechnol.* 8, 9. doi:10.3389/fbioe.2020.00009

Stolze, H., Kuhtz-Buschbeck, J., Mondwurf, C., Jöhnk, K., and Friege, L. (1998). Retest reliability of spatiotemporal gait parameters in children and adults. *Gait posture* 7 (2), 125–130. doi:10.1016/s0966-6362(97)00043-x

Tan, J.-S., Tippaya, S., Binnie, T., Davey, P., Napier, K., Caneiro, J., et al. (2022). Predicting knee joint kinematics from wearable sensor data in people with knee osteoarthritis and clinical considerations for future machine learning models. *Sensors* 22 (2), 446. doi:10.3390/s22020446

Vigneron, V., Dorizzi, B., Khouri, N., and Desailly, E. (2017). Predicting postoperative gait in cerebral palsy. *Gait posture* 52, 45–51. doi:10.1016/j.gaitpost.2016.11.012

Yeung, T., Cantamessa, A., Kempa-Liehr, A. W., Besier, T., and Choisne, J. (2023). Personalized machine learning approach to estimating knee kinematics using only shank-mounted IMU. *IEEE Sensors J.* 23, 12380–12387. doi:10.1109/jsen.2023.3267398

Zhang, B., Zhang, Y., and Begg, R. K. (2009). Gait classification in children with cerebral palsy by bayesian approach. *Pattern Recognit.* 42 (4), 581–586. doi:10.1016/j.patcog.2008.09.025

Zhang, Y., and Ma, Y. (2019). Application of supervised machine learning algorithms in the classification of sagittal gait patterns of cerebral palsy children with spastic diplegia. *Comput. Biol. Med.* 106, 33–39. doi:10.1016/j.compbiomed.2019.01.009

frontiers | Frontiers in Bioengineering and Biotechnology

TYPE Brief Research Report
PUBLISHED 10 April 2024
DOI 10.3389/fbioe.2024.1346365

OPEN ACCESS

EDITED BY
Anne D. Koelewijn,
Technische Fakultät, Friedrich-Alexander-Universität Erlangen-Nürnberg, Germany

REVIEWED BY
Varun Joshi,
University of Michigan, United States
Nicos Haralabidis,
Stanford University, United States

*CORRESPONDENCE
Eline Van Der Kruk,
e.vanderkruk@tudelft.nl

RECEIVED 29 November 2023
ACCEPTED 28 March 2024
PUBLISHED 10 April 2024

CITATION
Van Der Kruk E and Geijtenbeek T (2024), Is increased trunk flexion in standing up related to muscle weakness or pain avoidance in individuals with unilateral knee pain; a simulation study.
Front. Bioeng. Biotechnol. 12:1346365.
doi: 10.3389/fbioe.2024.1346365

Is increased trunk flexion in standing up related to muscle weakness or pain avoidance in individuals with unilateral knee pain; a simulation study

Eline Van Der Kruk[1]* and Thomas Geijtenbeek[1,2]

[1]Department of Biomechanical Engineering, Faculty of Mechanical Engineering, Delft University of Technology, Delft, Netherlands, [2]Goatstream, Delft, Netherlands

The 'Timed Up and Go' test (TUG) is a widely used clinical tool for assessing gait and balance, relying primarily on timing as a measure. However, there are more observable biomechanical compensation strategies within TUG that are indicative of underlying neuromuscular issues and movement priorities. In individuals with unilateral knee osteoarthritis, an increased trunk flexion during TUG is a common phenomenon, often attributed to muscle weakness and/or pain avoidance. Unfortunately, it is difficult to differentiate between these underlying causes using experimental studies alone. This study aimed to distinguish between muscle weakness and pain avoidance as contributing factors, using predictive neuromuscular simulations of the sit-to-walk movement. Muscle weakness was simulated by reducing the maximum isometric force of the vasti muscles (ranging from 20% to 60%), while pain avoidance was integrated as a movement objective, ensuring that peak knee load did not exceed predefined thresholds (2–4 times body weight). The simulations demonstrate that a decrease in muscular capacity led to greater trunk flexion, while pain avoidance led to slower movement speeds and altered muscle recruitments, but not to greater trunk flexion. Our predictive simulations thus indicate that increased trunk flexion is more likely the result of lack of muscular reserve rather than pain avoidance. These findings align with reported differences in kinematics and muscle activations between moderate and severe knee osteoarthritis patients, emphasizing the impact of severe muscle weakness in those with advanced knee osteoarthritis. The simulations offer valuable insights into the mechanisms behind altered movement strategies, potentially guiding more targeted treatment.

KEYWORDS

predictive simulation, neuromuscular model, knee osteoarthritis, ageing, sit-to-walk, timed-up-and-go

1 Introduction

Quality of healthcare is at risk due to an increase of age-related health issues and a shortage of healthcare workers in the near future. The primary focus of many governments is to prolong the independence of older adults in their own homes. A crucial daily activity that supports this independence is the act of rising from a seated position (Dall and Kerr,

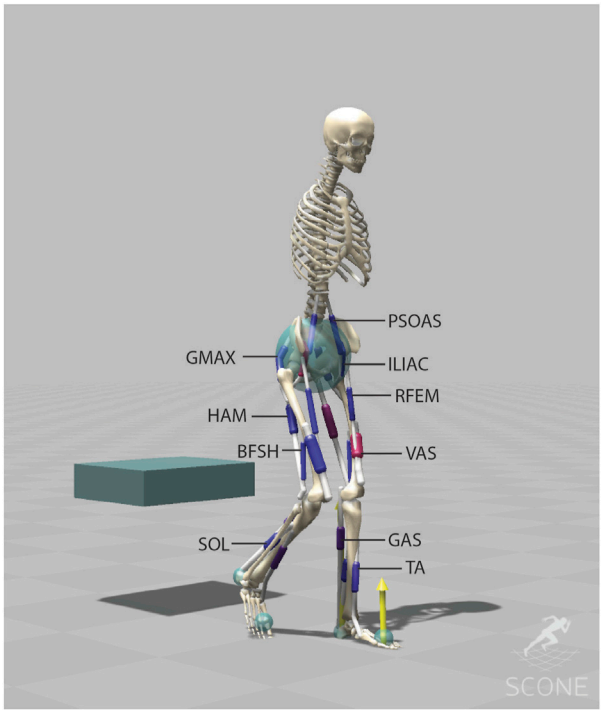

FIGURE 1
The musculoskeletal model (H1120) has 11 degrees of freedom (3 dofs between the pelvis and the ground, a pin joint (1-dof) at the hip, ankle and knee, a 1-dof lumbar joint, between the pelvis and the lumbar, and a 1-dof thoracic joint between the lumbar and the torso) and is actuated using 20 Hill-type muscle-tendon units. The H1120 model is available on (van der Kruk and Geijtenbeek, 2023b).

2010). This seemingly simple task becomes increasingly challenging as individuals age and is closely linked to a higher risk of falls (Fuller, 2000).

In Western societies, a significant percentage of individuals over the age of 65 suffer from symptomatic osteoarthritis (OA), particularly affecting the knee joint (Eysink et al., 2019). The 'Timed Up and Go' test (TUG) is a clinical evaluation of gait and balance, serving as a diagnostic tool in these individuals (Bouchouras et al., 2015). It involves a sit-to-walk exercise where individuals rise from a chair, walk a distance of 3 m, turn, walk back to the chair, and sit down. In a clinical setting, the time taken for this exercise is measured, if the exercise takes more than 30 s the patient is indicated with an high risk of falling.

Recent experimental research has demonstrated that beyond timing, biomechanical compensation strategies are indicative of the underlying age-related changes in the neuromuscular system and movement priorities in sit-to-walk (van der Kruk et al., 2022). Individuals with unilateral OA often exhibit asymmetrical movements while standing up, bearing additional weight on the unaffected side by leaning the trunk or by using asymmetric arm movements (Turcot et al., 2012; Naili et al., 2018; Davidson et al., 2013; Eitzen et al., 2014; Lamontagne et al., 2012). Additionally, they display increased maximum trunk flexion (Turcot et al., 2012; Sagawa et al., 2017). Recent systematic reviews suggest that these altered trunk flexion patterns may be related to muscle weakness and/or pain avoidance (van der Kruk and Geijtenbeek, 2023a).

Whereas experimental studies cannot distinguish between these underlying causes (van der Kruk et al., 2021), predictive simulations are a promising tool to determine the interconnectivity and interdependency of the neuromuscular capacity, reinforcement schemes, sensory integration, and adaptation strategies in standing up. We recently published the validation of a planar neuromusculoskeletal model with reflex-based muscle control that simulates the sit-to-walk movement (van der Kruk and Geijtenbeek, 2023a). This communication aims to leverage this predictive neuromuscular framework to determine whether the observed alterations in trunk flexion strategies in individuals with unilateral knee osteoarthritis are more likely attributed to muscle weakness or to pain avoidance.

2 Materials and methods

2.1 Model and controller

The design and validation of the musculoskeletal model and controller have been previously published (van der Kruk and Geijtenbeek, 2023a). We employed the H1120 model, featuring 11 degrees of freedom and 20 Hill-type muscles, which was initially developed as an OpenSim3 model and translated into Hyfydy (Figure 1) (van der Kruk and Geijtenbeek, 2023b). Peak isometric forces in this model are based on a lower limb model by (G2392) (Delp et al., 1990). The validation study showed that the simulated joint angles, muscle activation, and joint loading fell within experimental ranges with some limitations. Due to simplified contact geometries of the chair and buttocks, thighs rolling over the chair's surface is not considered in the simulation which in reality extend the contact period. Ground contact forces for the stance leg's during the initial step were underestimated due to the simplified foot contact which results in an underestimation of the ankle joint load of the stance leg during this initial step.

Contact forces between the feet and the ground and between the buttocks and the chair were modelled with a Hunt Crossley force spheres and box, respectively. The simulation of the sit-to-walk movement involved the utilization of a standing-up controller (van der Kruk and Geijtenbeek, 2023a) followed by a gait controller (Geyer and Herr, 2010). The standing-up controller operates on a reflex control principle, featuring two distinct states, each with its own set of control parameters. The reflex controller is based on monosynaptic and antagonistic proprioceptive feedback from the muscles and vestibular feedback linked to the pelvis tilt. The timing of the transition between the states is part of the optimization problem. To account for neural latencies, we incorporated data from previous studies.

States calculated from the model were muscle length (L), muscle velocity (v), muscle force (F), and pelvis tilt orientation (θ) and velocity ($\dot{\theta}$). The optimization problem encompassed a total of 551 free parameters, comprising controller gains (KC, KL+, KF±, Kp, and Kv), muscle length feedback offsets (lo), proportional feedback of θ (θo), proportional feedback of the lumbar and thoracic joints, transition times between the controllers, and stance load threshold for the gait state controller.

2.2 Objective function

We used the objective measures from the published sit-to-walk controller (van der Kruk and Geijtenbeek, 2023a). These measures encompassed the following criteria: a gait velocity measure with a minimum threshold of 0.8 m/s, range penalties designed to replicate joint limitations, including lumbar extension (−50°–0°), thorax extension (−15°–15°), pelvis tilt (−50°–30°), and ankle angle (−60°–60°), a constraint on knee limit force (500 N/m) that represents the passive knee properties when the knee exceeds the range of 120° flexion or 10° extension, and minimal head acceleration (threshold of 1 m/s^2). The selected speed was considered the minimum required speed to have a gait pattern that represents gait inside the lab and clinic. In daily life, normal gait speeds for older adults typically range around 0.9 m/s for women and 1.0 m/s for men (Kasović et al., 2021). As such, a speed of 0.8 m/s was considered a realistic minimum for measurements conducted in clinical environments.

Additionally, we included an energy estimate aimed at reducing energy consumption during the stand-up phase and minimizing the cost of transport during gait. The measure consisted of metabolic energy expenditure based on (Wang et al., 2012; Bhargava et al., 2004) (J_{mb}), and was complemented by the minimization of cubed muscle activations (J_{act}), along with torque minimization (J_T) at the lumbar and thoracic joints to serve as a proxy for the absence of trunk muscles. J_{mb} is a sum of the muscle activation rate ($\dot{A}$), the muscle maintenance heat rate ($\dot{M}$), the muscle shortening heat rate ($\dot{S}$), and the positive mechanical work rate ($\dot{W}$). $\dot{A}$ and $\dot{M}$ depend on the muscle mass, which was estimated by dividing the maximum isometric force over the muscle specific tension (25 N/cm^2) multiplied the muscle density (1.0597 g/cm^3) and optimal fiber length. Hence, when weakening the VAS muscle in the muscle weakness condition, we reduced the mass accordingly. During the optimization process, the overall energy estimate, a weighted sum between the terms ($J_{total} = \omega_{mb}J_{mb} + \omega_{act}J_{act} + \omega_T J_T$) became the sole non-zero term within the objective function. We empirically set $\omega_{mb} = 0.01$, $\omega_{act} = 0.1$ and $\omega_T = 0.0003$ for all conditions.

2.3 Optimization algorithm

The optimization process was conducted using the open source software SCONE with the Covariance Matrix Adaptation Evolutionary Strategy (CMA-ES) (Geijtenbeek, 2019). Simulations were performed using the Hyfydy simulation engine (Geijtenbeek, 2024). The population size of each generation was 10, and the number of iterations varied depending on the simulation duration. Multiple parallel optimizations were executed with the same initial guesses based on (van der Kruk and Geijtenbeek, 2023a), and the best set was subsequently employed as the starting point for the next set of optimizations, meaning the initial guesses for each condition were based on solution of the previous condition (−30% strength on −20% strength, etc.).

2.4 Conditions

2.4.1 Muscle weakness (VAS)

Muscular capacity progressively declines with age, with the largest relative decline in knee flexion-extension. Individuals with knee osteoarthritis also have pronounced decline in quadriceps strength (Slemenda et al., 1997; McAlindon et al., 1993; V Hurley et al., 1997). A recent review indicates that the Rectus Femoris (RF) exhibits the most substantial relative muscle atrophy (Naruse et al., 2023). However, imaging studies and cadaver studies in older (Ward et al., 2009) and younger adults (Handsfield et al., 2014) show that the Vasti (VAS) muscles undergo the greatest decline in absolute PCSA. Specifically, there is an approximately 85 cm^2 reduction in the combined vastus lateralis, medialis, and intermedius, compared to an approximate 21 cm^2 reduction in the RF.

To therefore simulate reduced muscular capacity in knee extension, we systematically bilaterally decreased the vasti (VAS) maximum isometric force by 20%, 30%, 40%, 50%, and 60%. We chose for a bilateral approach, since the contralateral knee in subjects with unilateral OA also show quadriceps strength deficits, although in a lesser extent (Alnahdi et al., 2012). We initiated the model with the optimized sit-to-walk controller for the standard seat (van der Kruk and Geijtenbeek, 2023a; van der Kruk and Geijtenbeek, 2023b) (neutral condition). The best set of the reduced model was then employed as the starting point for the subsequent optimization, replicating a progressive capacity decline scenario.

2.4.2 Pain avoidance

To simulate pain avoidance, we incorporated a cost function requiring the simulation to minimize the peak unilateral knee load of the stepping leg to less than 4, 3, and 2 times the body weight (BW). The joint load above the set threshold is integrated over time as measure. Individuals with symptomatic unilateral knee OA prefer to step with the affected leg first. Therefore, we implemented a cost function that becomes zero once the peak knee load on the stepping leg (left leg in simulations) was below the set threshold.

2.5 Measures

We analysed the trunk flexion, calculated as the angle between the global vertical and the trunk (sum of pelvis tilt, lumbar extension, and thoracic extension). Additionally, we assessed differences in timing, muscle activation, joint loading, and kinematics. The outcomes under various conditions were visualized using the OpenSim software (Delp et al., 2007).

3 Results

3.1 Reduced VAS muscle strength

Reducing the maximum isometric strength VAS led to an increased bilateral activation of the Vasti muscle (Figure 2). The

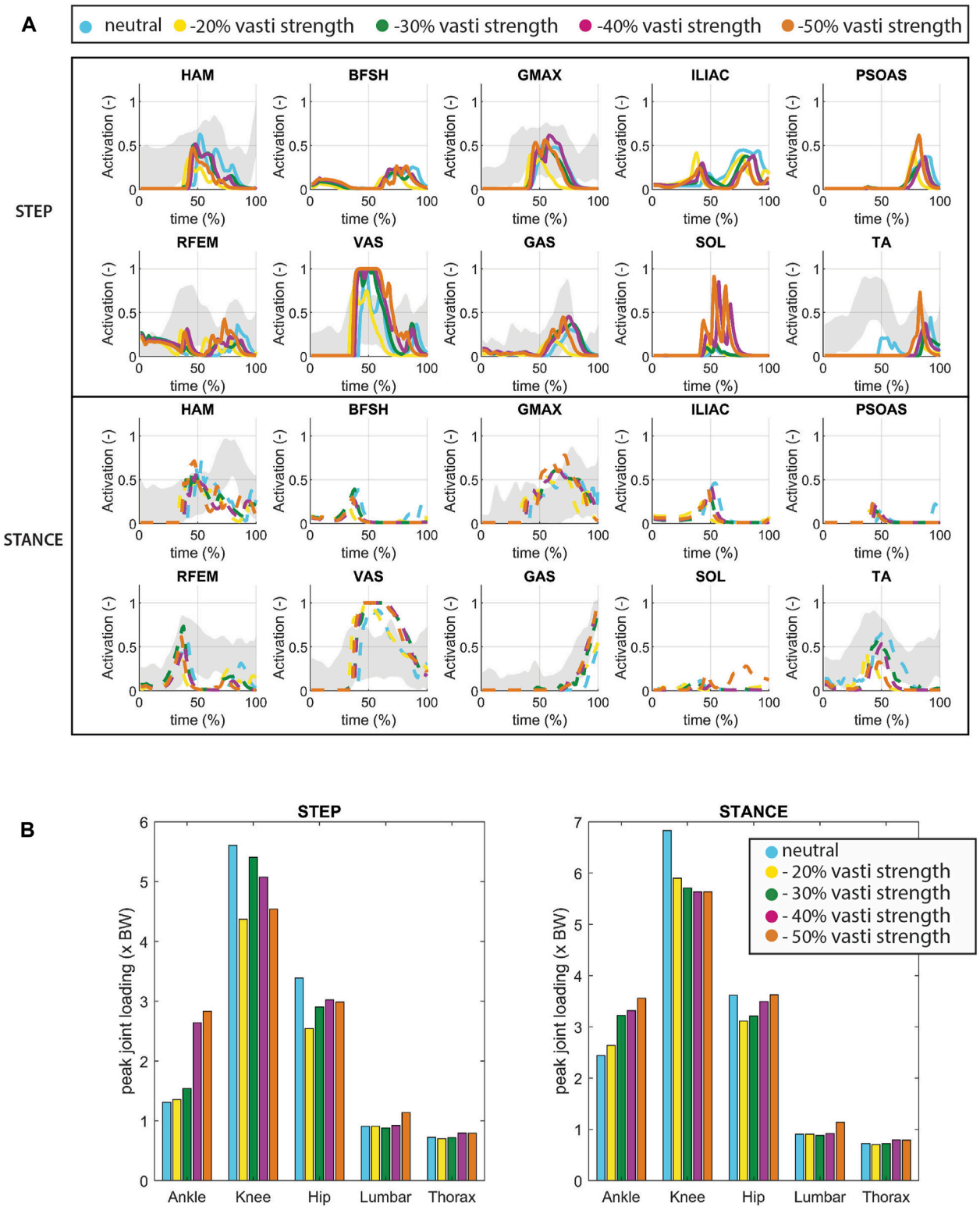

FIGURE 2
(A) Muscle activation for conditions in which VAS strength is reduced. The grey shade represents experimental sEMG data adopted from (van der Kruk and Geijtenbeek, 2023a). Note that since no Maximum Voluntary Contraction was available in this dataset, the excitation was normalized by the maximum excitation measured within the individual complete sit-to-walk trials (stand up-walk 3 m–turn–walk 3 m–sit down). As a result the activation levels indicated by the sEMG might be higher than the actual activation levels. **(B)** Joint loading for conditions in which VAS strength is reduced.

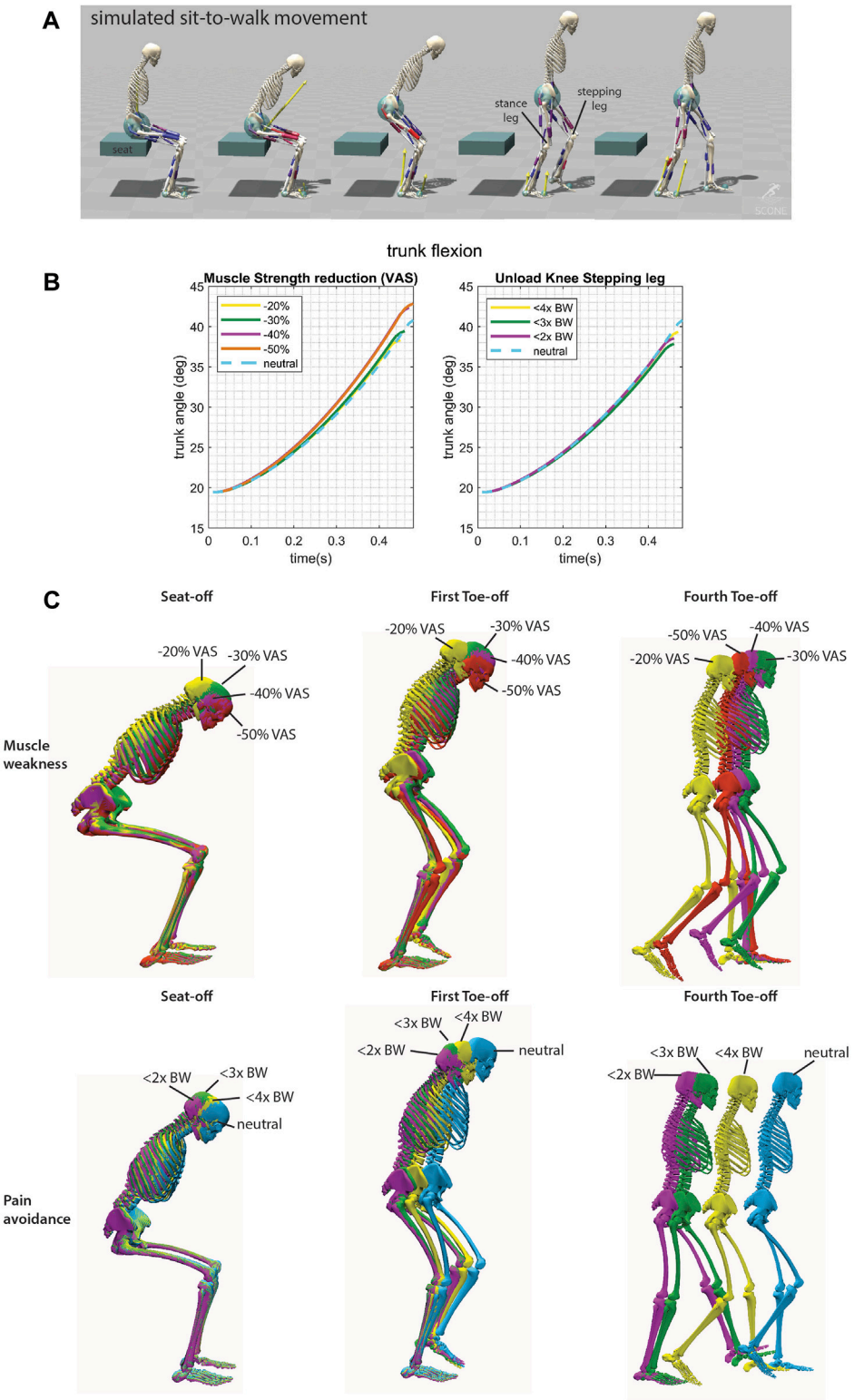

FIGURE 3
(A) Simulated sit-to-walk movement adopted from (van der Kruk and Geijtenbeek, 2023a). The stepping leg is the leg that steps first. **(B)** Trunk flexion from the initiation of the movement to initiation of seat unloading. **(C)** Conditions for the sit-to-walk simulations shown in color for seat-off, first toe off (when the ground reaction force of the stepping leg becomes zero), and fourth toe off. There is a mild increase in trunk flexion when the VAS strength was reduced. When the knee is unloaded there is a slower movement speed.

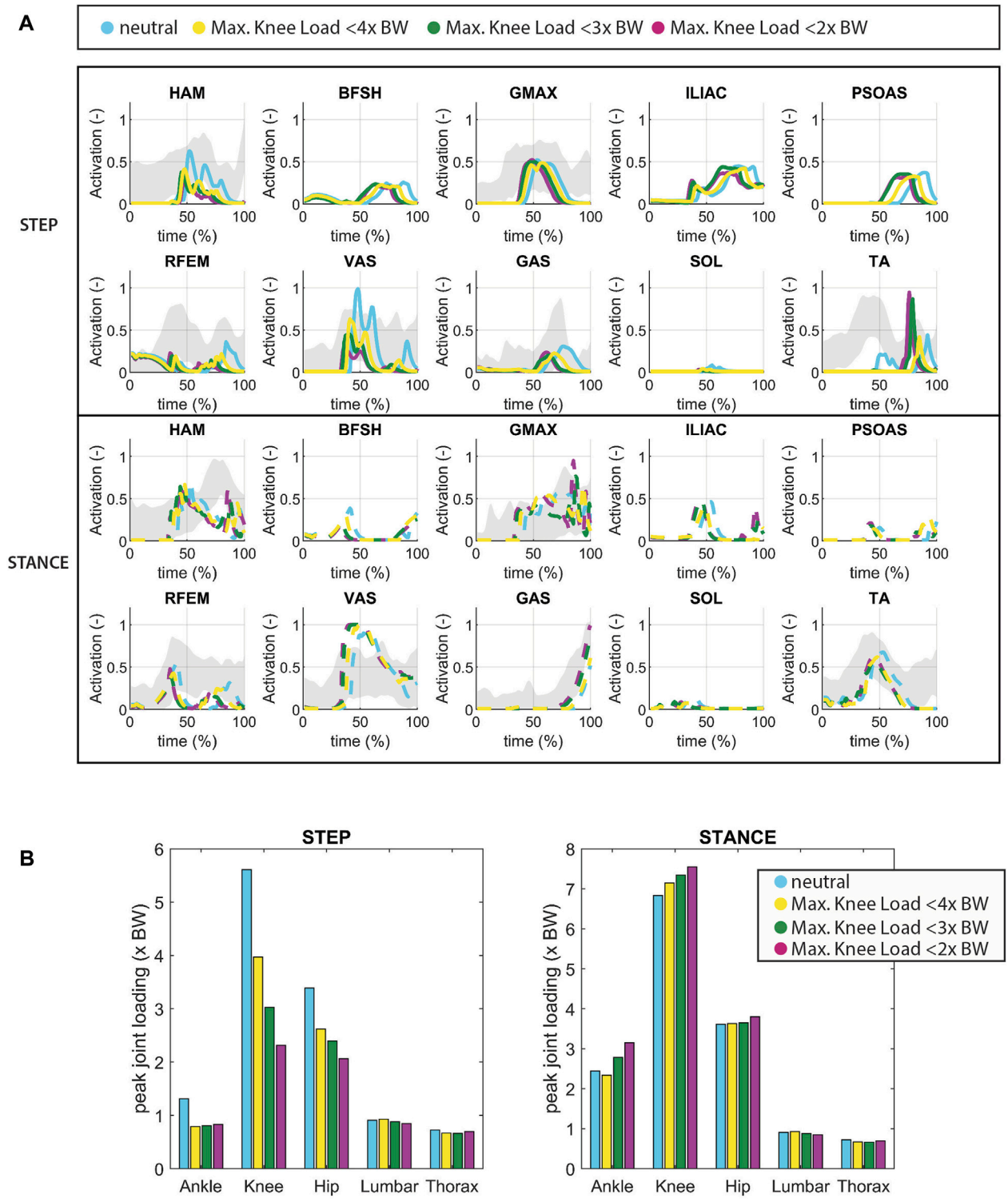

FIGURE 4
(A) Muscle activation in which the knee joint of the stepping leg is unloaded (pain avoidance). The grey shade represents experimental sEMG data adopted from (van der Kruk and Geijtenbeek, 2023a). Note that since no Maximum Voluntary Contraction was available in this dataset, the excitation was normalized by the maximum excitation measured within the individual complete sit-to-walk trials (stand up-walk 3 m–turn–walk 3 m–sit down). As a result the activation levels indicated by the sEMG might be higher than the actual activation levels. **(B)** joint loading in which the knee joint of the stepping leg is unloaded.

simulation compensates with increased hip extensor activity (HAM, GMAX) and increased plantarflexor muscle activity (GAS, SOL) in the stepping leg. This aligns with findings from experimental studies on sit-to-stand movements in older adults (Smith et al., 2020).

We found a bilateral rise increase of ankle joint loading, particularly on the stepping side which doubled in the −50% condition compared to the neutral condition. Reduced VAS muscle strength thus resulted in elevated ankle loads. When VAS strength was further reduced to −60%, the model could not find a solution to rise from the seat unaided.

A minor increase in trunk flexion was observed when VAS strength was reduced (Figure 3). Trunk flexion at seat-off reached 42.8° in the −50% condition *versus* 38.3° in the −20% condition (40.8° in the neutral condition). The timing of the movement (Figure 3C) showed no noticeable pattern with reduced muscle strength. We hypothesize that in the −20% and 30% condition, there remains sufficient physiological reserve to allow for variations in gait velocity. Consequently, standing up can be slower, as gait velocity can compensate to achieve the desired average speed. Evidently, this compensatory strategy appears to be more efficient in terms of our cost assessment. However, as the strength reduction is further decreased to 40% and 50%, patterns of reduced movement velocity begin to emerge.

3.2 Pain avoidance

In the neutral condition, the peak knee loads (stance leg: 6.8 BW, stepping leg: 5.6 BW) and hip loads (stance leg: 3.6 BW, stepping leg: 3.4 BW) manifest just after seat-off. The peak ankle load in the stepping leg occurs during the rising phase (stepping leg: 1.3 BW), and for stance leg, it arises at the end of the single stance phase (stance leg: 2.4 BW), consistent with experimental data (van der Kruk and Geijtenbeek, 2023a). Unloading of the knee is accomplished by reducing ipsilateral activation of VAS and hamstrings (HAM) (Figure 4). Following Toe-off, there is an increased ipsilateral activation of the tibialis anterior muscle (TA), resulting in increased dorsiflexion, which compensates for reduced foot-ground clearance. Unloading the knee (ranging from −29% to −59%) led to reduced load on the ipsilateral hip (ranging from −23% to −39%) and ankle (ranging from −37% to −40%). However, the ipsilateral ankle did not exhibit proportional unloading, unlike the other joints. Loading on the contralateral knee and hip increased, ranging from +5% to +11% and 0% to +5%, respectively. As for the contralateral ankle, there was a load decrease in the <4BW condition (−4%) and an increase in the other conditions (14% and 29%).

Interestingly, during knee unloading, the simulation yielded a smaller, rather than a greater, trunk angle at seat-off compared to the neutral condition (Figure 4). There was an increase in movement time observed with increased knee unloading (from initiation to heel strike of the first step: 1.1s in the neutral condition up to 1.3s in the <2x BW knee load condition) (Figure 3D).

4 Discussion

Our simulations reveal a minor increase in trunk flexion (2^{v}) in response to a decrease in maximum isometric force in VAS (representing reduced muscular capacity). The data files, simulations, and videos can be found in the repository (van der Kruk and Geijtenbeek, 2024). Experimental studies have reported an approximate increase of nine° in trunk angle during sit-to-stand movements in individuals with osteoarthritis (OA) compared to controls (46.4° *versus* 37.5°) (Turcot et al., 2012). We observed similar differences in trunk angle when simulating a low seat condition presented in (van der Kruk and Geijtenbeek, 2023a; van der Kruk and Geijtenbeek, 2023b) (51° trunk angle, approximately 10° difference with neutral condition). Low seat height increases the task demand resulting in less muscular reserve. In essence, it reflects a reduced muscular capacity (van der Kruk et al., 2021). Consequently, we suspect that the trunk angle would have exhibited greater flexion had the muscle strength of more muscles been compromised. Pain avoidance, simulated with the objective of reducing knee load, resulted in altered muscle recruitments, characterized by reduced ipsilateral activation of VAS and HAM, and slower movement speeds. However, it did not yield greater trunk flexion strategies. The predictive simulations thus support the idea that increased trunk flexion is more likely a consequence of insufficient muscular reserve than a pain avoidance mechanism.

The increase in time to perform the sit-to-walk movement is consistent with findings in the sit-to-stand (STS) task. Previous studies have reported that individuals with knee OA take significantly more time to complete the STS task and TUG compared to older adults (Turcot et al., 2012; Su et al., 1998; Patsika et al., 2011). Various authors have postulated that this time difference may be attributed to increased forward body bending (Su et al., 1998)or quadriceps muscle weakness (Alghadir et al., 2015). However, the simulations show that reducing movement velocity alone results in decreased peak knee loading, and might therefore be the result of a pain reduction strategy.

Our simulation model contains a number of limitations, which can be addressed in future studies:

- The simulations are conducted with a planar model. In reality, human movements during sit-to-walk involve lateral trunk motions and arm support (van der Kruk et al., 2022). Individuals with unilateral symptomatic knee osteoarthritis can use this to redistribute the load (van der Kruk and Geijtenbeek, 2023a). However, this aspect could not be tested in the current model. Additionally, individuals with knee OA exhibit increased antagonist muscle activation (Davidson et al., 2013; Patsika et al., 2011; Bouchouras et al., 2015; Bouchouras et al., 2020), which is linked to the medial-lateral and internal-external rotational stability of the knee. These complexities were not captured by the simplified planar joint in the model.
- In the simulations we only tested the effect of reduced VAS isometric strength. In reality, OA patients experience muscle weakness in multiple muscle groups, which could contribute to greater trunk flexion. Furthermore, regarding the musculoskeletal model, the maximum isometric forces are based on (Delp et al., 1990), where VAS muscles are relatively weak for a healthy adult, as indicated by the maximum activation of this muscle during chair rising (van der Kruk and Geijtenbeek, 2023a).

- The H1120 model represents a male adult with a height of 1.80 m and a mass of 75 kg. Body height and mass influence movement strategies in sit-to-walk. (van der Kruk and Geijtenbeek, 2023a).To ensure direct comparisons with experimental datasets, it would be beneficial to diversify musculoskeletal models and simulations.
- The feet were modelled using single rigid bodies, and the addition of a separate toe segment might allow for further unloading of the knee. We do not expect this to drastically change the results, because the placement and stiffness of the contact spheres allows for mimicking toe rolls.

While the Timed-Up-and-Go test is a commonly employed clinical assessment, only the timing of the exercise is typically reported in clinical and literature contexts. There is a scarcity of biomechanical data pertaining to OA patients' performance in this test, particularly regarding which leg they use to step out first. Our choice to reduce the peak load in the stepping leg was informed by clinical observations. Given that in the sit-to-walk movement, individuals must unload one leg to initiate gait, this assumption appears valid from a motor control perspective. We did conduct simulations where the stance leg was unloaded (available online (van der Kruk and Geijtenbeek, 2024)). Those simulations demonstrate that the energy objective costs were higher when the stance leg was unloaded compared to the stepping leg, providing further support for the idea that unloading the stepping leg is a more natural movement.

When examining published experimental data, greater trunk flexion was only observed in individuals with severe knee OA (van der Kruk and Geijtenbeek, 2023a). In contrast, individuals with moderate knee OA exhibited a similar movement trajectory to that of healthy individuals but with altered muscle recruitment patterns (van der Kruk and Geijtenbeek, 2023a). This discrepancy can be attributed to variations in muscle strength. It is plausible that individuals with severe OA, due to reduced daily activity, possess less muscular reserve compared to individuals with moderate OA. Consequently, severe OA patients may resort to increased trunk flexion during the process of standing up as a compensatory mechanism to counteract their strength limitations.

Taking this line of reasoning further, it is conceivable that in individuals with early and moderate symptomatic knee OA, unloading the knee to alleviate pain could potentially contribute to the development of muscular weakness in specific muscle groups, such as the vasti, over time. Humans stand up over 60 times a day and the simulations indicate that unloading the knee during this action is accomplished through reduced activation of the VAS. Since it is reasonable to infer that this compensation mechanism occurs in various daily activities, we can postulate the following hypothesis: individuals with early and moderate OA may unload the knee to mitigate pain, inadvertently leading to the underuse of specific muscle groups, particularly the vasti muscles. Over time, this underuse could result in a decline in vasti strength, resulting in increased trunk flexion, as observed in individuals with severe knee OA. Our interpretation for unilateral OA patients is that reduced activity leads to the bilateral muscle strength deficits while the specific compensation strategies during these activities, like reduced VAS activation, result in the unilateral muscle strength deficit in specific muscle groups in the affected limb (Figure 4). This underscores the significance of monitoring and addressing pain in individuals with early and moderate OA.

Data availability statement

The original contributions presented in the study are included in the article/Supplementary material, further inquiries can be directed to the corresponding author.

Author contributions

EV: Conceptualization, Data curation, Funding acquisition, Investigation, Methodology, Resources, Supervision, Validation, Visualization, Writing–original draft, Writing–review and editing. TG: Software, Writing–review and editing.

Funding

The author(s) declare financial support was received for the research, authorship, and/or publication of this article. This study was funded by NWO-TTW VENI Grant 18145 (2021). The funders had no role in study design, data collection and analysis, decision to publish, or preparation of the manuscript.

Conflict of interest

Author TG was employed by Goatstream.

The remaining author declare that the research was conducted in the absence of any commercial or financial relationships that could be construed as a potential conflict of interest.

Publisher's note

All claims expressed in this article are solely those of the authors and do not necessarily represent those of their affiliated organizations, or those of the publisher, the editors and the reviewers. Any product that may be evaluated in this article, or claim that may be made by its manufacturer, is not guaranteed or endorsed by the publisher.

References

Alghadir, A., Anwer, S., and Brismée, J.-M. (2015). The reliability and minimal detectable change of Timed up and Go test in individuals with grade 1–3 knee osteoarthritis. *BMC Musculoskelet. Disord.* 16, 174–177. doi:10.1186/s12891-015-0637-8

Alnahdi, A. H., Zeni, J. A., and Snyder-Mackler, L. (2012). Muscle impairments in patients with knee osteoarthritis. *Sports Health* 4 (4), 284–292. doi:10.1177/1941738112445726

Bhargava, L. J., Pandy, M. G., and Anderson, F. C. (2004). A phenomenological model for estimating metabolic energy consumption in muscle contraction. *J. Biomech.* 37 (1), 81–88. doi:10.1016/s0021-9290(03)00239-2

Bouchouras, G., Patsika, G., Hatzitaki, V., and Kellis, E. (2015). Kinematics and knee muscle activation during sit-to-stand movement in women with knee osteoarthritis. *Clin. Biomech.* 30 (6), 599–607. doi:10.1016/j.clinbiomech.2015.03.025

Bouchouras, G., Sofianidis, G., Patsika, G., Kellis, E., and Hatzitaki, V. (2020). Women with knee osteoarthritis increase knee muscle co-contraction to perform stand to sit. *Aging Clin. Exp. Res.* 32, 655–662. doi:10.1007/s40520-019-01245-z

Dall, P. M., and Kerr, A. (2010). Frequency of the sit to stand task: an observational study of free-living adults. *Appl. Ergon.* 41 (1), 58–61. doi:10.1016/j.apergo.2009.04.005

Davidson, B. S., Judd, D. L., Thomas, A. C., Mizner, R. L., Eckhoff, D. G., and Stevens-Lapsley, J. E. (2013). Muscle activation and coactivation during five-time-sit-to-stand movement in patients undergoing total knee arthroplasty. *J. Electromyogr. Kinesiol.* 23 (6), 1485–1493. doi:10.1016/j.jelekin.2013.06.008

Delp, S. L., Anderson, F. C., Arnold, A. S., Loan, P., Habib, A., John, C. T., et al. (2007). OpenSim: open-source software to create and analyze dynamic simulations of movement. *IEEE Trans. Biomed. Eng.* 54 (11), 1940–1950. doi:10.1109/tbme.2007.901024

Delp, S. L., Loan, J. P., Hoy, M. G., Zajac, F. E., Topp, E. L., and Rosen, J. M. (1990). An interactive graphics-based model of the lower extremity to study orthopaedic surgical procedures. *IEEE Trans. Biomed. Eng.* 37 (8), 757–767. doi:10.1109/10.102791

Eitzen, I., Fernandes, L., Nordsletten, L., Snyder-Mackler, L., and Risberg, M. A. (2014). Weight-bearing asymmetries during Sit-To-Stand in patients with mild-to-moderate hip osteoarthritis. *Gait Posture* 39 (2), 683–688. doi:10.1016/j.gaitpost.2013.09.010

Eysink, P. E. D., Poos, M., Gijsen, R., Kommer, G. J., and van Gool, C. H. (2019). *Epidemiologische data van Ziekten van het botspierstelsel en bindweefsel: achtergrondrapport voor Programma Zinnige Zorg.*

Fuller, G. F. (2000). Falls in the elderly. *Am. Fam. Physician* 61 (7), 2159–2168.

Geijtenbeek, T. (2019). Scone: open source software for predictive simulation of biological motion. *J. Open Source Softw.* 4 (38), 1421. doi:10.21105/joss.01421

Geijtenbeek, T. (2024). The {Hyfydy} simulation software. Available at: https://hyfydy.com.

Geyer, H., and Herr, H. (2010). A muscle-reflex model that encodes principles of legged mechanics produces human walking dynamics and muscle activities. *IEEE Trans. neural Syst. rehabilitation Eng.* 18 (3), 263–273. doi:10.1109/tnsre.2010.2047592

Handsfield, G. G., Meyer, C. H., Hart, J. M., Abel, M. F., and Blemker, S. S. (2014). Relationships of 35 lower limb muscles to height and body mass quantified using MRI. *J. Biomech.* 47 (3), 631–638. doi:10.1016/j.jbiomech.2013.12.002

Kasović, M., Štefan, L., and Štefan, A. (2021). Normative data for gait speed and height norm speed in≥ 60-year-old men and women. *Clin. Interv. Aging* 16, 225–230. doi:10.2147/cia.s290071

Lamontagne, M., Beaulieu, M. L., Varin, D., and Beaulé, P. E. (2012). Lower-limb joint mechanics after total hip arthroplasty during sitting and standing tasks. *J. Orthop. Res.* 30 (10), 1611–1617. doi:10.1002/jor.22127

McAlindon, T. E., Cooper, C., Kirwan, J. R., and Dieppe, P. A. (1993). Determinants of disability in osteoarthritis of the knee. *Ann. Rheum. Dis.* 52 (4), 258–262. doi:10.1136/ard.52.4.258

Naili, J. E., Broström, E. W., Gutierrez-Farewik, E. M., and Schwartz, M. H. (2018). The centre of mass trajectory is a sensitive and responsive measure of functional compensations in individuals with knee osteoarthritis performing the five times sit-to-stand test. *Gait Posture* 62, 140–145. doi:10.1016/j.gaitpost.2018.03.016

Naruse, M., Trappe, S., and Trappe, T. A. (2023). Human skeletal muscle-specific atrophy with aging: a comprehensive review. *J. Appl. Physiol.* 134 (4), 900–914. doi:10.1152/japplphysiol.00768.2022

Patsika, G., Kellis, E., and Amiridis, I. G. (2011). Neuromuscular efficiency during sit to stand movement in women with knee osteoarthritis. *J. Electromyogr. Kinesiol.* 21 (5), 689–694. doi:10.1016/j.jelekin.2011.05.006

Sagawa, Y., Bonnefoy-Mazure, A., Armand, S., Hoffmeyer, P., Suva, D., and Turcot, K. (2017). Individuals with knee osteoarthritis exhibit altered movement patterns during the sit-to-stand task. *Mov. Sport Sciences-Science Mot.* (98), 39–49. doi:10.1051/sm/2017004

Slemenda, C., et al. (1997). Quadriceps weakness and osteoarthritis of the knee. *Ann. Intern Med.* 127 (2), 97–104. doi:10.7326/0003-4819-127-2-199707150-00001

Smith, S. H. L., Reilly, P., and Bull, A. M. J. (2020). A musculoskeletal modelling approach to explain sit-to-stand difficulties in older people due to changes in muscle recruitment and movement strategies. *J. Biomech.* 98, 109451. doi:10.1016/j.jbiomech.2019.109451

Su, F. C., Lai, K. A., and Hong, W. H. (1998). Rising from chair after total knee arthroplasty. *Clin. Biomech.* 13 (3), 176–181. doi:10.1016/s0268-0033(97)00039-9

Turcot, K., Armand, S., Fritschy, D., Hoffmeyer, P., and Suvà, D. (2012). Sit-to-stand alterations in advanced knee osteoarthritis. *Gait Posture* 36 (1), 68–72. doi:10.1016/j.gaitpost.2012.01.005

van der Kruk, E., and Geijtenbeek, T. (2023a). A planar neuromuscular controller to simulate age-related adaptation strategies in the sit-to-walk movement. *bioRxiv*, 2011–2023. doi:10.1101/2023.11.24.568552

van der Kruk, E., and Geijtenbeek, T. (2023b). Repository sit-to-walk simulations. Available at: https://github.com/BODIES-Lab-TU-Delft/Sit-to-walk-predictive-simulations.

van der Kruk, E., and Geijtenbeek, T. (2024). Repository case study simulations. Available at: https://github.com/BODIES-Lab-TU-Delft/STW-case-study-unilateral-pain.git.

van der Kruk, E., Silverman, A. K., Koizia, L., Reilly, P., Fertleman, M., and Bull, A. M. J. (2021). Age-related compensation: neuromusculoskeletal capacity, reserve and movement objectives. *J. Biomech.* 122, 110385. doi:10.1016/j.jbiomech.2021.110385

van der Kruk, E., Strutton, P., Koizia, L. J., Fertleman, M., Reilly, P., and Bull, A. M. J. (2022). Why do older adults stand-up differently to young adults? investigation of compensatory movement strategies in sit-to-walk. *npj Aging* 8 (1), 13. doi:10.1038/s41514-022-00094-x

V Hurley, M., Scott, D. L., Rees, J., and Newham, D. J. (1997). Sensorimotor changes and functional performance in patients with knee osteoarthritis. *Ann. Rheum. Dis.* 56 (11), 641–648. doi:10.1136/ard.56.11.641

Wang, J. M., Hamner, S. R., Delp, S. L., and Koltun, V. (2012). Optimizing locomotion controllers using biologically-based actuators and objectives. *ACM Trans. Graph. (TOG)* 31 (4), 1–11. doi:10.1145/2185520.2335376

Ward, S. R., Eng, C. M., Smallwood, L. H., and Lieber, R. L. (2009). Are current measurements of lower extremity muscle architecture accurate? *Clin. Orthop. Relat. Res.* 467 (4), 1074–1082. doi:10.1007/s11999-008-0594-8

frontiers | Frontiers in Bioengineering and Biotechnology

TYPE Original Research
PUBLISHED 24 May 2024
DOI 10.3389/fbioe.2024.1384062

OPEN ACCESS

EDITED BY
Jörg Miehling,
Technische Fakultät, Friedrich-Alexander-Universität Erlangen-Nürnberg, Germany

REVIEWED BY
Alessio Gizzi,
Campus Bio-Medico University, Italy
Wojciech Wolański,
Silesian University of Technology, Poland

*CORRESPONDENCE
Robin Remus,
robin.remus@rub.de

RECEIVED 08 February 2024
ACCEPTED 22 April 2024
PUBLISHED 24 May 2024

CITATION
Remus R, Sure C, Selkmann S, Uttich E and Bender B (2024), Soft tissue material properties based on human abdominal *in vivo* macro-indenter measurements.
Front. Bioeng. Biotechnol. 12:1384062.
doi: 10.3389/fbioe.2024.1384062

Soft tissue material properties based on human abdominal *in vivo* macro-indenter measurements

Robin Remus*, Christian Sure, Sascha Selkmann, Eike Uttich and Beate Bender

Chair of Product Development, Department of Mechanical Engineering, Ruhr-University Bochum, Bochum, Germany

Simulations of human-technology interaction in the context of product development require comprehensive knowledge of biomechanical *in vivo* behavior. To obtain this knowledge for the abdomen, we measured the continuous mechanical responses of the abdominal soft tissue of ten healthy participants in different lying positions anteriorly, laterally, and posteriorly under local compression depths of up to 30 mm. An experimental setup consisting of a mechatronic indenter with hemispherical tip and two time-of-flight (ToF) sensors for optical 3D displacement measurement of the surface was developed for this purpose. To account for the impact of muscle tone, experiments were conducted with both controlled activation and relaxation of the trunk muscles. Surface electromyography (sEMG) was used to monitor muscle activation levels. The obtained data sets comprise the continuous force-displacement data of six abdominal measurement regions, each synchronized with the local surface displacements resulting from the macro-indentation, and the bipolar sEMG signals at three key trunk muscles. We used inverse finite element analysis (FEA), to derive sets of nonlinear material parameters that numerically approximate the experimentally determined soft tissue behaviors. The physiological standard values obtained for all participants after data processing served as reference data. The mean stiffness of the abdomen was significantly different when the trunk muscles were activated or relaxed. No significant differences were found between the anterior-lateral measurement regions, with exception of those centered on the linea alba and centered on the muscle belly of the rectus abdominis below the intertubercular plane. The shapes and areas of deformation of the skin depended on the region and muscle activity. Using the hyperelastic Ogden model, we identified unique material parameter sets for all regions. Our findings confirmed that, in addition to the indenter force-displacement data, knowledge about tissue deformation is necessary to reliably determine unique material parameter sets using inverse FEA. The presented results can be used for finite element (FE) models of the abdomen, for example, in the context of orthopedic or biomedical product developments.

KEYWORDS

soft tissue biomechanics, inverse FEA, surface EMG (sEMG), abdominal wall, hyperelastic material properties, human abdomen, *in vivo* indenter measurements, FEBio

1 Introduction

Understanding the functions and properties of biomechanical systems is a key success factor in computer-aided human-centered design (Neumann and Bender, 2022). The basis for this are robust and valid human body models, that allow to examine the effects of crucial biological or technical variables (Wolf et al., 2020b; Neumann et al., 2020). Product development involving user behaviors or properties of the human body has traditionally been an iterative and empirical process (Grujicic et al., 2010). CAE (computer-aided engineering) can help reduce development costs and time, as it enables early preclinical verification, ethical assurance, reduction of repetitive patient involvement, and quantification of mechanisms of action (Wolf et al., 2020a; Alawneh et al., 2022). However, the study and optimization of the interfaces between biomechanical and technical systems is particularly complex, as the transferred values are directly influenced by the interaction between the geometry and mechanical properties of both the human tissue and the technical system (Haug et al., 2004; Portnoy et al., 2008; Moerman et al., 2016; Sadler et al., 2018; Fougeron et al., 2023). In particular, this is the case in the lower part of the trunk, or the abdomen, as it consists of highly vulnerable tissue with great anatomical variations (Lamielle et al., 2008) and ensures vital bodily functions (Standring et al., 2016). Moreover, issues affecting the lower back, such as pain, are also associated with the soft tissues of the abdomen, which contribute to its stabilization (Hodges et al., 2005; Driscoll and Blyum, 2019) and unloading (Hodges et al., 2001; Stokes et al., 2010). In order to broaden the understanding of these biomechanical relationships and to improve the development of new aids using simulation models, the soft tissue behavior of the abdomen will be investigated in this study.

Recent simulation models that include the biomechanical behavior of the abdomen or parts of it differ in their implementing methods, scope, and degree of detail, depending on the requirements of their intended use case (Anderson et al., 2007; Hicks et al., 2015). Possible use cases encompass, for example, studies on 1) the effect of individual braces in scoliosis treatment (Périé et al., 2004; Clin et al., 2010; Sattout et al., 2016), or of lumbar orthoses (Molimard et al., 2019; Bonnaire et al., 2020) on the lumbosacral spine, 2) injury prevention in crash testing (King, 2018; Untaroiu et al., 2018; Grébonval et al., 2021) and stiff structure impact (Lee and Yang, 2001; Haug et al., 2004; Snedeker et al., 2007) or vertical impact load (Cox, 2020) studies, or 3) the load removal of the spine by increasing the intra-abdominal pressure (El-Monajjed and Driscoll, 2020; Guo et al., 2021). Another use case is modelling the interaction of organs (Misra et al., 2008), or the abdominal wall with surgical instruments (Hernández et al., 2011); these models are used for virtual surgical planning or support of education (Leong et al., 2022). Recently, authors analyzed the effects of muscular contractions on the biomechanics of the abdominal wall numerically (Pavan et al., 2019; Todros et al., 2020).

FEA is a standard approach in mechanics to calculate the reaction of structures to loads or interactions, but only few FE models exist that model the biomechanics for the whole abdomen (King, 2018). One aspect of biomechanical modelling are geometric shapes. While imaging data is accurate (Hayes et al., 2013a), it is not sufficient to derive material properties in terms of stress-strain data for all nonlinear responses of soft tissues (Sadler et al., 2018) and their interplay. In recent years, advancements in automatic segmentation methods, e.g., deep learning algorithms for exact and individual or statistical shape models, enabled the rapid generation of anatomical geometries (Sekuboyina et al., 2021; Ji et al., 2022; Ma et al., 2022). Geometrical data sets were generated using a large amount of imaging data, which include collections of single organs, vessels, and bones, as well as collections of body segments (Li et al., 2023).

While geometries are increasingly patient-specific and complex, the literature still lacks data on soft tissue material behavior, which is crucial for valid simulations (Kauer et al., 2002; van Loocke et al., 2006; Anderson et al., 2007). Thus, it is difficult to compile the complete data sets required for biomechanical modelling of the abdomen. Numerous invasive and non-invasive studies have been conducted to capture properties that go beyond the pure geometry of the abdomen, the abdominal wall that spans the anterior and lateral side of the abdomen, or the organs. Strategies used include, for example, the indirect and non-invasive estimation of intra-abdominal pressure (Tayebi et al., 2021) by measuring the tension of the abdominal wall via indentation (van Ramshorst et al., 2008; van Ramshorst et al., 2011). Functional responses, deformations, and kinematics of the abdominal wall were assessed during controlled muscle activity (Todros et al., 2019; Jourdan et al., 2022) or during upper body movements (Szymczak et al., 2012; Remus et al., 2023). Song et al. (2006) measured the *in vivo* elasticity of the entire abdominal wall during laparoscopic surgery and Szepietowska et al. (2023) investigated the non-homogeneous strain fields of external living human abdominal walls during peritoneal dialysis and breathing. Podwojewski et al. (2014) and Tran et al. (2014) examined abdominal walls subjected to air pressure loading *ex vivo*. Because the abdominal wall plays a crucial role in protecting the abdominal organs, moving the trunk, and stabilizing the lumbar spine (Hodges et al., 2005), other researchers used shear wave elastography (Tran et al., 2016; Wang et al., 2020) to estimate the elasticity of abdominal wall muscles, for example, to improve the treatment of hernias (Deeken and Lake, 2017). However, the biomechanical behavior of the abdomen and its elements depends strongly on the interplay of its elements. For example, muscle contractions and intra-abdominal pressure affect the biomechanics of the abdominal wall (Pavan et al., 2019), and the abdominal organs interact with neighboring organs and the walls of the abdominal cavity while undergoing large relative sliding movements (Haug et al., 2004). The mechanical properties of organs and their interactions were investigated under numerous aspects such as abdominal trauma (Viano, 1989; Lamielle et al., 2008; Ramachandra, 2016) or tool-tissue interactions (Carter et al., 2001; Davies et al., 2002; Tay et al., 2006; Sato et al., 2013).

Due to the lack of data on soft tissue behavior, in addition to an exact anatomical model, simplifications and assumptions, depending on the biomechanical modelling goals (Lee and Yang, 2001), are necessary. While it is known that abdominal muscles have a stiffening effect on the trunk (Hodges et al., 2015), it is rarely considered in abdominal interaction models and as it can only be determined *in vivo*. Modelling the macroscopic behavior requires

geometry data and force-compression functions, but the amount of *in vivo* data present in literature is limited, e.g., due to ethical implications, costs, or expenditure of time. Therefore, when creating an interaction model, it may be necessary to identify own material parameters for the macroscopic behavior. A common approach for the abdomen is to assume one linear material parameter per body region and varying body postures (Périé et al., 2004; Cooper et al., 2019; Bonnaire et al., 2020), but among others, Huang and Zheng (2015) state that one parameter pure elasticity theory is not sufficient to meet the hyperelastic properties of soft tissue (van Loocke et al., 2006).

Indentation is a common approach to determine the macroscopic behavior and properties of tissue in different body regions (Huang and Zheng, 2015), e.g., buttock (Grujicic et al., 2010), thigh (Sadler et al., 2018), shank (Moerman et al., 2016), foot (Erdemir et al., 2006), or lower arm (Moerman, 2012). If impact time and total deformation are surveilled and limited, indentation is a safe and non-invasive method for *in vivo* measurement of hyperelastic soft tissue (Huang and Zheng, 2015). Zhang et al. (1997) and Marinopoulos et al. (2020) view material property measurement of soft tissue with an indenter as an inverse problem, and Davies et al. (2002) introduced an inverse engineering approach to solve the problem. However, extracting unique material parameters from indenter measurements can be difficult (Pierrat et al., 2018), because the inverse FEA might result in several parameter sets, which lead to similar experimental and simulation data with one or none being valid (Oddes and Solav, 2023). A possible approach to solve this problem is to measure the displacement of the surrounding surface, for example, via 3D digital image correlation (Solav et al., 2018), or an optical 3D deformation analyzer (Ahn and Kim, 2010). Conducting indentations and surface displacement measurements usually requires custom technical solutions (Lister et al., 2011) that must comply with strict safety regulations while producing adequate results (Marinopoulos et al., 2020).

The assessment of hyperelastic *in vivo* material parameters of the abdomen is extensive and requires appropriate measurements, which have rarely been reported. The aim of this study is therefore to determine the mechanical *in vivo* responses of the physiological abdomen under local uniaxial compression, taking into account the activation of trunk muscles during various controlled activities, and to derive characterizing hyperelastic material properties. For this purpose, we aim to

1) obtain continuous force-displacement curves from macro-indentation experiments, including the associated surface deformations, and
2) conduct inverse FE simulations for region-specific hyperelastic material model data.

We hypothesize that the abdominal tissue responses under local compressions show significant variations between regions and with varying muscle activities. Our approach is to determine unique material parameters using inverse FEA based on data that we have recorded non-invasively with an indenter developed for this purpose, including ToF 3D measurements. In order to evaluate the influence of muscle tone on the elasticity of the abdominal soft tissue, the tests were performed on multiple participants under both activation and relaxation of the trunk muscles. sEMG signals of the main trunk muscles were measured to monitor and evaluate activation. Measurements hopefully reduce inherent variability and errors due to uncertainties and provide new possibilities for human-technology interaction simulations.

TABLE 1 Anthropometric characteristics of the participants. Body fat percentage was assessed indirectly using a 4-compartment skinfold-thickness equation (Peterson et al., 2003).

	Mean ± SD	Range	Unit
Age	31.8 ± 3.25	25–37	years
Body mass	74.1 ± 6.41	62–85	kg
Body height	181.4 ± 7.67	168–191	cm
BMI	22.52 ± 1.53	19.5–24.6	kg/m^2
Chest girth	93.7 ± 8.82	80.9–114.3	cm
Waist girth	81.7 ± 5.64	70.4–87.63	cm
Gluteal girth	99.8 ± 3.93	91.5–106.7	cm
Forearm girth	26.4 ± 1.19	23.8–28.2	mm
Abdominal skinfold	20.9 ± 8.41	7.0–32.0	mm
Suprailiac skinfold*	10.7 ± 4.03	4.5–18.0	mm
Iliac crest skinfold	17.1 ± 5.69	7.7–24.5	mm
Front thigh skinfold*	14.0 ± 5.47	4.7–21.2	mm
Triceps skinfold*	10.1 ± 3.17	4.9–15.0	mm
Subscapular skinfold*	12.8 ± 4.16	7.1–19.8	mm
Chest skinfold	9.79 ± 4.86	4.1–18.9	mm
Body fat	19.9 ± 4.49	10.3–24.1	%

The skinfold-thicknesses used for the body fat calculation are marked with *.

2 Materials and methods

The study is divided into three sections: 1) The experimental acquisition of force-displacement curves with the associated surface deformations at six different regions of the abdomen, 2) the processing of the measured data, and 3) the determination of descriptive material parameters by means of inverse FEA.

2.1 Study design and participants

A total of ten healthy males (25–37 years) participated in the study. Exclusion criteria were acute abdominal or low back pain, limited range of motion and trunk injuries, nervous system disorders, or skin diseases. All participants were fasting at least 2 h before the start of the study and wore loose pants without a restrictive waistband. Anthropometric characteristics of the participants were taken as shown in Table 1. This included body weight and skinfold thicknesses (Clauser et al., 1988; Norton, 2018). The latter was measured three times at each of seven positions (Norton, 2018) with a calibrated Harpenden

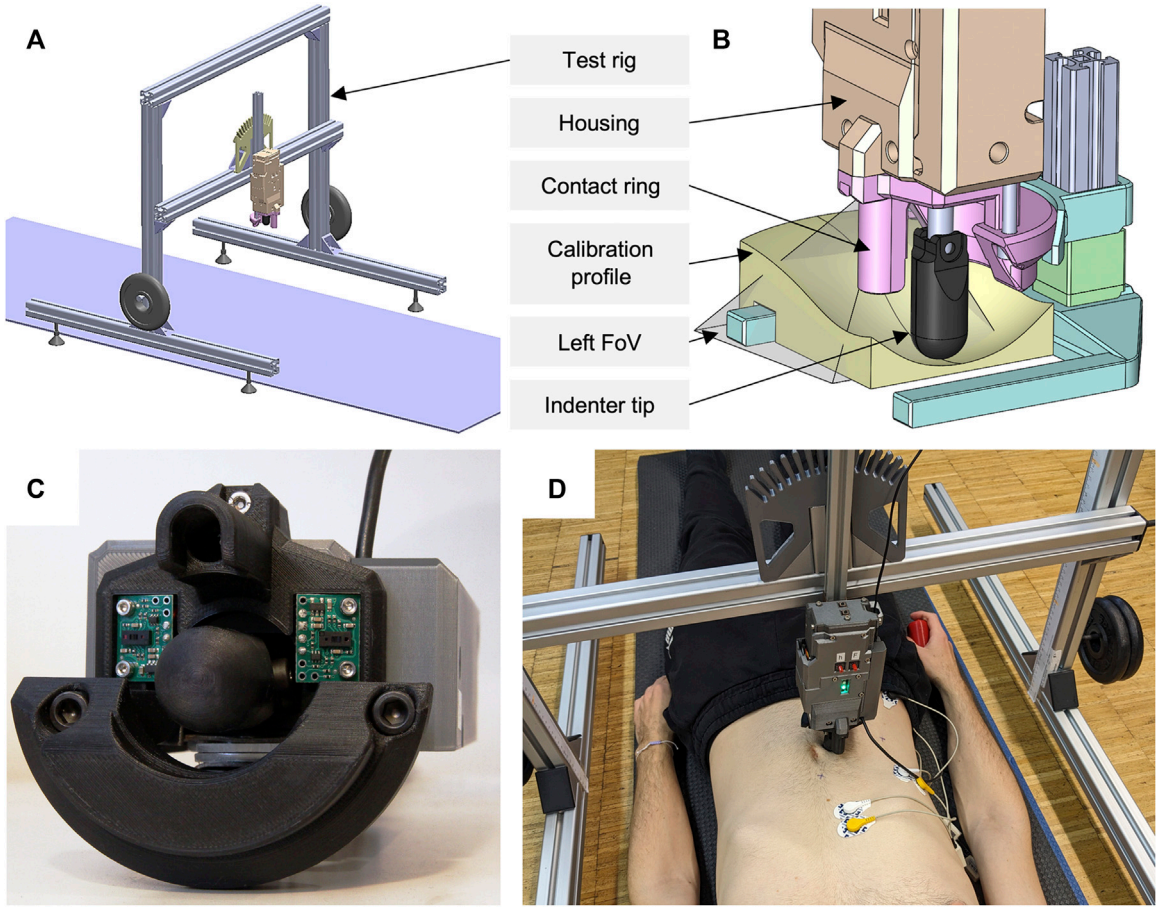

FIGURE 1
Overview of the experimental setup used. **(A)** Complete test rig with yoga mat, two additional weights, and mounted indenter in vertical position. **(B)** ToF sensor calibration setup with visualization of the left field of view (FoV) and an exemplary calibration profile. **(C)** Close-up of the mechatronic indenter (bottom view). Both ToF sensors, the contact ring with cutouts, and the indenter tip can be seen. **(D)** Participant in the experimental procedure of measurement region R2 with sEMG electrodes applied and the remote control in his right hand.

Skinfold Caliper. For consistency, all data was recorded by a single examiner. The participants' body mass index (BMI) was within the normal range (19.5–24.6 kg/m^2). The Ethics Committee of the Medical Faculty of the Ruhr-University Bochum approved the study (23-7868 08/10/23) and participants provided written informed consent.

2.2 Equipment and technical calibration

A custom-built mechatronic tissue indenter with test rig (Figure 1) was used to gather the force-displacement curves and the surface displacements simultaneously. The indenter tip was moved towards the participant through a ring [in analogy to Carter et al. (2001)] mounted on the indenter housing. The ring was not continuous, but had cutouts laterally, allowing for visual measurement of the skin deformation (Figure 1C). To define the zero position for each test and to ensure a perpendicular measurement orientation, this contact ring rested lightly on the skin so that the tissue was just visibly compressed. The plastic indenter tip had the shape of a hemisphere with radius r_t = 10 mm. The feed rate was 5 ± 1 mm/s and realized by an electronic micro linear drive. The feed force was measured with a 222.4 N (50 lbf) load cell, mounted to the side of the indenter facing away from the participant, which was subjected to the force applied by the linear drive. Maximum travel and maximum feed force were adjustable. A test rig made of torsion-resistant 40 × 40 mm aluminum profiles was used to mount the mechatronic indenter above the participant (Figure 1A). Both height and alignment of the indenter were adjustable on the test rig for each participant and measurement position. To avoid injury, the feed force was electronically and mechanically limited based on the estimated pressure between skin and indenter tip. The limits were taken from findings for the design of workplaces with collaborating robots (Muttray et al., 2014; Melia et al., 2015) and correspond to the point at which the increasing perception of pressure from an indenter tip turns into a noticeable pain. The lower pain limit for abdominal muscles was 35 N/cm^2. Because no pressure limits were known for paraspinal tissue, we used a software-controlled force limit of

110 N for all positions. A hardware force limitation was additionally implemented in case the electronic limitation failed. The dead weight of the free-standing test rig was 10% above the software-controlled force limit, so that it lifted off the ground when limits were exceeded. A wired remote control was used to allow participants to start and interrupt a measurement by themselves.

To calibrate our force-displacement test setup with tissue-like material (Wells and Liang, 2011), we used cylinders made of ballistic gelatin (GELITA BALLISTIC 3 gelatin, 255–265 g Bloom). The cylinders, 100 mm in diameter and 80 mm in height, were produced according to the preparation procedure of GELITA: Comprised of heating distilled water and gelatin to a maximum of 55°C ± 5°C, curing the mixture in molds for 24 h, demolding the specimens, and conditioning for 60 h within a moisture-sealing barrier. Conditioning temperatures for our cylinders with 10 wt% gelatin solution were 4°C according to FBI recommendations (Fackler and Malinowski, 1988; Maiden et al., 2015) and 15°C for increased compliance. Since gelatin is very sensitive to shear stress (Wells and Liang, 2011; Valliere et al., 2018), we covered the entire top of the gelatin cylinder with a rigid acrylic plate during calibration. Ultrasonic gel was applied in between. A cylinder with 10 mm radius was used as indenter tip. We compressed the differently tempered cylinders three times each at 5 mm/s up to 200 N using our experimental test setup (Figure 1A) and a materials testing machine (Zwick Z010 with GTM GmbH series K, 10 kN, 2 mV/V). Maximum deformation was 24.6 mm at 15°C. Comparing the measurement accuracy, maximum root mean square errors (RMSE) were 0.389 and 0.433 N, and percentage deviations were below 2.4% and 3.1%, for maximum compression forces of 60 and 120 N.

To optically measure the 3D surface deformations, two 8×8 Multi-Zone ToF sensors (VL53L5CX, STMicroelectronics) were used. These were mounted sagittal symmetrically to the sides of the indenter tip on the housing, each at a 12° angle to the observation plane (Figure 1C). The sensor distances perpendicular to the reference plane (zero position) were 35.1 mm. Each trapezoidal field of view, starting at the tip of the indenter, had a diagonal of 63° and a minimum length of 39.1 mm laterally to the reference plane. This resulted in a minimum observable area of approximately 16.74 cm^2. When the tissue is deformed starting from its initial state, the measurable area increases. For calibration of the ToF sensors and their data processing, we used 3D printed PLA (polylactic acid) profiles in matt white after ensuring that the optically measured distances did not differ from those of the skin [all participants had a Fitzpatrick skin type (Fitzpatrick, 1988) of I-III]. The seven profiles (including horizontal planar, bevelled at 12° and thus parallel to the sensor plane, convex or concave converging towards the sensor tip) represented continuous surface deformations from 0 to 45 mm (Figure 1B). The processing of the 15 Hz raw sensor data included a transformation of the absolute distance values for the 64 measuring zones into the 3D displacement of the trapezoidally measured surface, a calculation of the means over a sliding window of length 5 across the neighboring elements, and a linear time interpolation to 0.1 s. The comparisons to the fully known geometries resulted in absolute measurement deviations of ±1.6 mm. Maximum deviations occurred in the peripheral measurement zones. Mean RMSE and standard deviation (SD) over all profiles was 0.805 ± 0.45 mm.

2.3 Surface electromyography

During the indenter measurements, bipolar sEMG activity of the three main trunk muscles was recorded using 42 × 24 mm Ag/AgCl disposable surface electrodes with hydrogel (Kendall H93SG). Following skin preparation, three pairs of electrodes were placed on the right side of the body on the anterior abdominal (E1), the lateral abdominal wall (E2), and the paraspinal musculature (E3) (Criswell, 2011) with a center-to-center distance of 24 mm. To not interfere with the optical measurements of the skin deformations, the placements of E1, E2, and E3 were cranial to the subcostal plane. E1 was centered on the rectus abdominis and E3 was centered on the muscle belly of the erector spinae. E2 was located at the level of the most caudal palpable costa spuria in the transition between the hypochondric and right lumbar region (Figure 2). The reference electrode was placed caudally to the lateral abdominal wall muscles in the region of the anterior superior iliac spine. For sEMG signal acquisition, we used three bipolar preamplifiers of type ToMEMG V1.2 and a Tower of Measurement (DeMeTec GmbH, Langgöns, Germany). sEMG signals were sampled at 1024 Hz, filtered, quantified, visualized, and recorded using custom-built software. To mitigate the influence of electrocardiographic and power line artifacts, a band-pass filter between 45 and 500 Hz and a notch filter at 50 Hz were applied to the raw signals. For quantization, root mean square of the filtered signal was calculated on a sliding window of 200 samples (195.3 ms).

To create a frame of reference for normalization, participants performed maximum voluntary contractions (MVC) in three positions and received the following instructions:

1) MVC in supine position: Crunch with legs bent 90° and abdominal muscles actively tensed after inhaling. Arms at sides of torso, shoulders and head not touching the floor. Gaze is centered on the test bench.
2) MVC in left lateral position: Jackknife with legs and the arm on top extended. The left arm is locked behind the head, the back and neck are kept straight. Legs and head do not touch the floor.
3) MVC in prone position: Superman with arms and legs outstretched. Head, legs, and arms do not touch the ground.

For the sEMG amplitude normalization, the MVCs from the same positions as in the measurements were used in each case. The baseline sEMG activity was recorded when the participants were lying fully relaxed in all three positions before the start of the measurements.

2.4 Experimental procedure

Six measurement regions were deduced from the muscular structures and anatomical characteristics of the abdomen (Rohen et al., 2015; Netter, 2017; Schünke et al., 2018; Tayebi et al., 2021) as

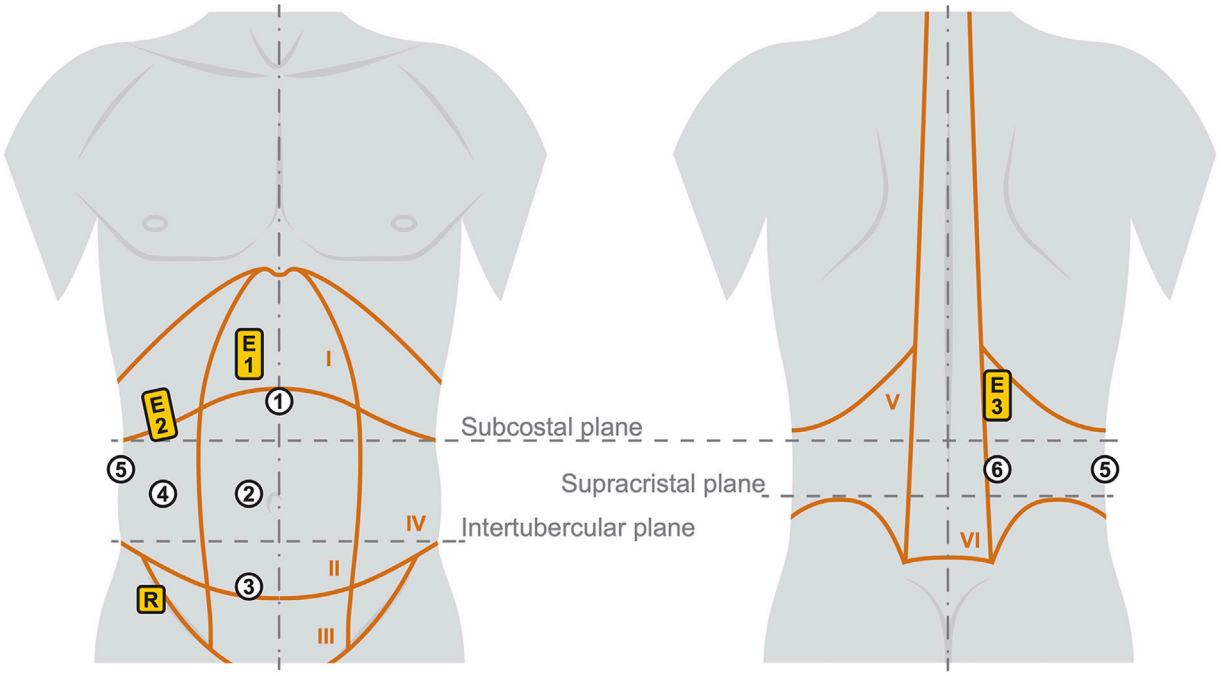

FIGURE 2
Illustration of the six measurement regions (white circles) with the three sEMG positions (yellow rectangles). The trunk with indicated anatomical characteristics is shown on the left from anterior and on the right from posterior. Details and labels of the Roman numbered body regions I-VI are given in Table 2.

visualized in Figure 2 and explained in more detail in Table 2. The regions were identified by palpation (Van Sint Jan, 2007) and marked with a water-soluble pen. To eliminate individual and uncontrollable influence of the trunk muscles to stabilize the spine (Hodges et al., 2015), the participants were lying in three positions: supine, lateral, and prone. Four measurements were taken at each region with fully relaxed (R) and controlled activated (A) musculature, leading to a total of 48 measurements per participant. The regions are numbered from 1 to 6 and measurements were carried out in the same order (for instance: indentation with fully relaxed muscles in measurement region 1 is named R1). To maximize comparability, participants were given the following instructions:

- All measurements: Exhale before starting a measurement and hold the breath while the indenter tip moves out.
- R1-R4 (Supine position): Your legs and arms are stretched out and lie flat on the yoga mat. The head lies on the pillow so that all your muscles are fully relaxed.
- R5 (Left lateral position): Your head lies on the pillow and the legs are slightly bent on top of each other on the yoga mat. The upper arm is held in front of the body. The left arm can be placed under the pillow to support the head and relax the lateral muscles.
- R6 (Prone position): The legs are stretched out and lying on the yoga mat. Your head lies sideways on the pillow and the arms are crossed next to the head. All muscles should be relaxed.
- A1-A4 (Supine position): Your legs and head do not touch the mat. The legs form a right angle. The center of your gaze is directed towards the indenter. The arms are at the side of the upper body.
- A5 (Left lateral position): Your right leg and head are not touching the mat. The right leg is fully extended and in line with the head. To stabilize the body, the right arm is held in front of the body and the left leg is slightly bent. The left arm is stretched upwards.
- A6 (Prone position): Legs and head do not touch the mat. Your legs are stretched out. The arms are folded to the side of the head and are just not touching the mat.

By comparing the monitored sEMG amplitudes to that of other participants, the postures were evaluated before and during each measurement and adjusted by interacting with the participant if necessary. To reduce tilting of the pelvis and chest in coronal plane, a folded towel was placed under the waist.

After the posture instructions, ultrasound gel was applied to the measurement region to minimize friction between skin and indenter tip. The test rig was set up so that the indenter was perpendicular to the body (Figure 1D) and the contact ring was in light contact with the skin. This was checked before each single measurement. To familiarize participants with the measurement procedure, test measurements were performed at region 1 with R and A at least once. If the patient breathed during an indentation, significant changes in muscle activity were observed, or other disturbances were detected, the respective measurement was repeated.

2.5 Data processing

Data was processed and analyzed using MATLAB R2022b (MathWorks, Inc., Natick, MA). Three measurements were

TABLE 2 Test plan of the unilateral indenter measurements. Assuming abdominal symmetry, the measurements were solely performed on the right side of the body. Each measurement was carried out with fully relaxed (R) and controlled activated (A) muscles at the six regions listed (*cf.* Figure 2).

Region number	Lying position	Body region	Description of the measurement region
1	Supine	Transition between epigastric and (I) umbilical region (II)	Centered on the linea alba, about 1 cm cranial to the subcostal plane
2	Supine	Umbilical region	Centered on the rectus abdominis, at the supracristal plane. In most cases, this was below the second tendinous intersection (fibrous band) and at the level of the umbilicus
3	Supine	Transition between umbilical and hypogastric region (III)	Centered on the rectus abdominis, about 1 cm below the intertubercular plane
4	Supine	Lateral abdominal region (IV)	On a line with the mamilla, at the supracristal plane. Thus, lateral to the rectus abdominis and central on the lateral abdominal wall
5	Left lateral	Lateral abdominal region (V)	Most lateral position of the abdomen, midway between subcostal and supracristal plane
6	Prone	Transition between lateral abdominal and lateral lumbar region (VI)	Centered on the lumbar erector spinae muscle belly, midway between subcostal and supracristal plane. In most cases, this was at the level of vertebra L3

manually selected for each participant at each measurement region. Data recorded before a detectable contact force and after maximum stroke was not considered for further data processing. For the force-displacement curves, the raw data was cleaned of recording-related outliers. Polynomial curve fits $f(\delta)$ of degree $n = 1, 2, \ldots, 5$ were used for the uniform and continuous description of the non-linear curves for each participant (Figure 3A) and as a mean for each measurement region (Figure 3B). The polynomials (1) were selected according to two criteria: the least possible degree with minimum RMSE, and validity in the range $0 \le \delta \le \delta_{max}$, based on the available cleaned measurement data.

$$f(\delta) = f_1\delta^n + f_2\delta^{n-1} + \ldots + f_n\delta + f_{n+1} \tag{1}$$

The coefficients f_n are in descending powers, and the length of f is $n + 1$. The mean force-displacement curves for each measurement region with R or A were based on all the respective raw data sets of the participants. To quantify entire test ranges, these combined data sets were also used to create conforming 2D boundaries, the upper and lower limits of which were each described by a curve fit (Figure 4). Goodness of fits (Sum of Squares Due to Error, R-Squares, and RMSEs) are provided with all coefficients f_n in Supplementary Material S1.

For the relative skin or surface displacements, we used the measuring points from the fifth row from the anterior of both ToF sensors (Figure 5A), which were synchronized in time with the force-displacement data. These two sets of eight ToF measuring points were located to the left and right of the indenter tip respectively and were used to deduce continuous surface displacement curves: In relation to the reference plane, the vertical components, as visualized in Figure 5B, served as the relative surface displacements. Offsets to the indenter tip were eliminated on the surface side. The first measurable contact force as a result of an incipient deformation was taken as reference. Assuming that measuring points close to the indenter tip are distorted, raw data in the range $-0.9\,r_t \le x \le 0.9\,r_t$ were discarded. The direct connection of the remaining most central measuring points from the left and right side resulted in two intersection points with the indenter tip profile. From these, together with the measuring points and three additional base points on the reference plane, curve fits of third degree were created separately for each side. The base points on the reference plane were introduced because the field of view of the ToF sensors did not always capture the entire displacement. Consequently, the start of the deformation on the reference plane could be unknown. To approximate it, the positions x_B of the base points located within an 8 mm interval were shifted in 5 mm steps from the outermost ToF measuring point to $|x_B| \le r_C = r_t + 100$ mm and a fit was calculated in each case. This is subject to the assumption that the surface displacements are continuous and can be described by a third degree polynomial. The selection of a participant-specific fit $v(x)$ per side and indentation depth δ_I is done by minimizing the cost function $\boldsymbol{\Theta}(x_B)$ in (2).

$$\boldsymbol{\Theta}(x_B) = RMSE_{v(x)} + Q, \tag{2}$$

$$Q = \begin{cases} 0.75\left|\dfrac{x_{xmax}}{r_C}\right| & \text{if } v(x \le r_C) \cap \text{reference plane} \neq \varnothing \\ 10 & \text{if } v(x \le r_C) \cap \text{reference plane} = \varnothing \end{cases}$$

$RMSE_{v(x)}$ is the standard error of the regression of $v(x)$ and x_{xmax} is the intersection point of $v(x)$ with the reference plane for a given x_B. If no intersection existed, the penalty factor was applied instead.

For mean surface displacement per measurement region $u(x)$ (Figure 5D), a fit of third degree was calculated over all $v(x)$ (Figure 5C) of both sides combined (mirrored left side) for one δ_I each. Each of these complete experimental surface deformations is defined for the range $0\,\text{mm} \le x \le r_C$ and includes the profile of the indenter tip in the negative z-direction for $x < x_{min}$ and the reference plane for $x > x_{max}$. With $n = 4$, $u(x)$ is analogous to (1). As part of the objective function analysis (Section 2.9), the transitions to the indenter tip and the reference plane were automatically smoothed in an x-axis section of up to 10 mm for a continuous displacement curve.

2.6 Statistical analysis

The experimental force-displacement results were statistically analyzed for T1) differences between the six measurement regions

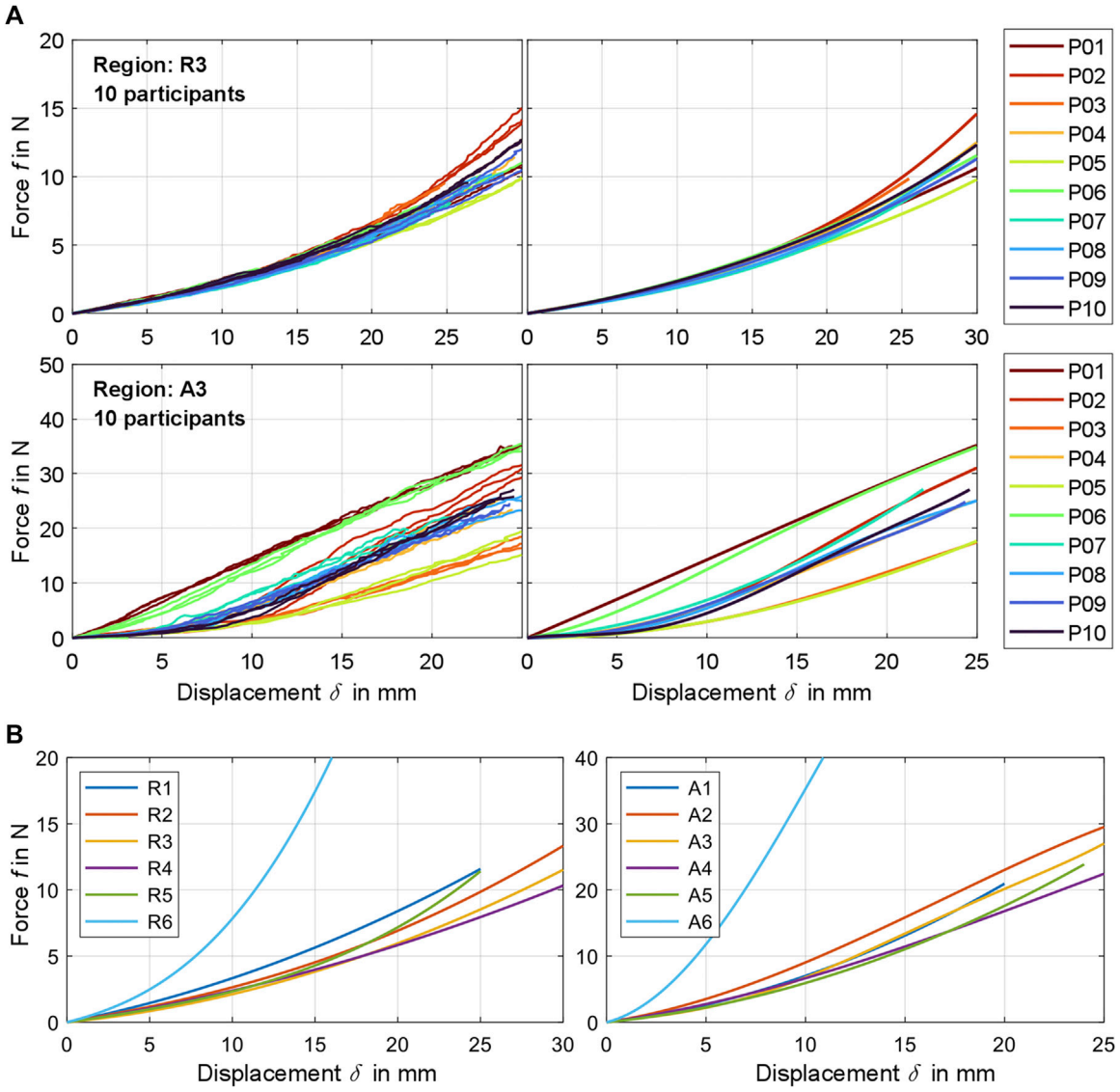

FIGURE 3
(A) Exemplary comparison of experimentally determined raw force-displacement curves (left) and the participant-related curve fits calculated from these (right) for measurement region 3 for fully relaxed (R) and controlled activated (A) musculature. A visualization for all participants and regions can be found in Supplementary Material S3. **(B)** Compilation of all mean curve fits $f(\delta)$ for the six measurement regions, each for the range $0 \leq \delta \leq \delta_{max}$.

with similar muscle activities (R or A), and T2) differences between muscle activities for the six measurement regions. A p-value of <0.05 was considered statistically significant. Statistical tests were conducted for $\delta = 7, 14$, and 20 mm where available. As a result of these multiple comparisons, Bonferroni correction factors were used. All data sets for all subjects were tested for normal distribution using the one-sample Kolmogorov-Smirnov test. Because the test was rejected for a number of data sets, we used the nonparametric Kruskal–Wallis test for T1), considering each measurement region independent from one another. Post hoc comparisons were made with Tukey's honestly significant difference procedure (multiple comparison test) for comparisons between regions. Assuming that the respective measurements from R and A are paired, we conducted a non-parametric Friedman test with a Bonferroni factor of 2 ($\alpha = 0.025$) for T2).

2.7 Axisymmetric FE model

For the inverse FEA of an axisymmetric indentation test, we utilized the framework *indentify* (https://github.com/SolavLab/indentify, v1.0.1) developed and made available by Oddes and Solav (2023) and adapted it to our needs. For pre- and postprocessing of the simulations, running in the FE solver FEBio v4.3 (Maas et al., 2012), we used MATLAB R2022b with the open-source toolbox GIBBON (Moerman, 2018). The indentation model comprises an FE cylinder with radius and height r_C and Ogden material model (*cf.* Section 2.8). No differentiations were made between the different layered abdominal tissue components. Skin, fat, muscles, and all subsequent structures were lumped and modeled as a homogeneous material. The indenter tip was modelled rigid with

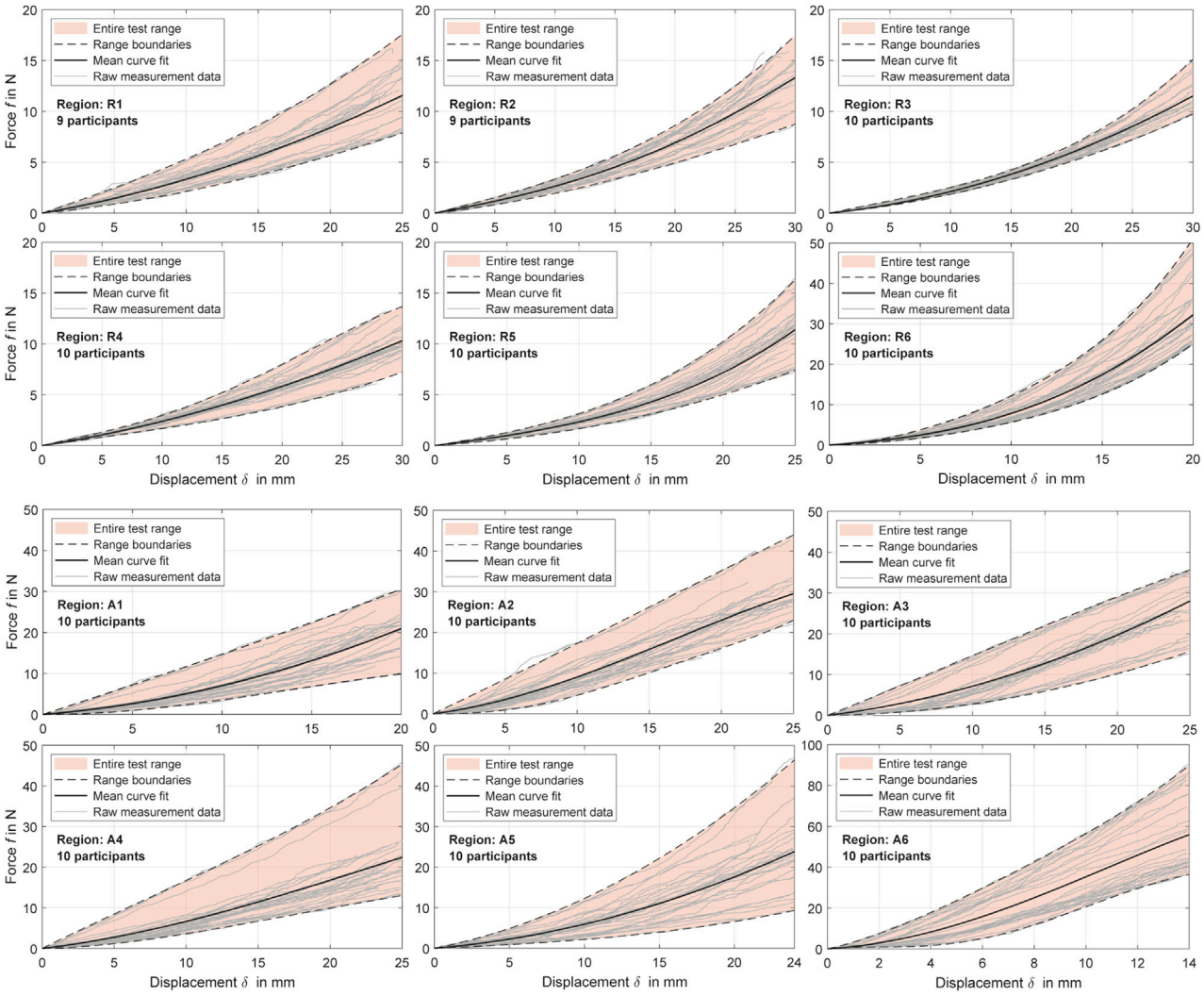

FIGURE 4
Experimental force-displacement curves for all measurement regions with distinction between relaxed and activated musculature (R and A). The polynomial curve fits (Table 4) are shown alongside the cleaned raw data for all participants and the resulting value ranges.

the same geometry as in our experiments and was displaced vertically downwards to the respective indentation depths δ_I. In the tangential section, the 90° circular sector of the indenter tip including a 20 mm cylinder section (Figure 6B) had 60 triangular shell elements. Four equally spaced δ_I were simulated for each region (Table 2) to match with the experimental data. Maximum displacement was $\delta_{max} = \delta_{I=4} = 25$ mm for R2-R5. Friction between indenter tip and cylinder surface was omitted with a friction coefficient of zero using FEBio's *sliding-elastic* contact formulation. To reduce simulation time, only a cylinder sector of 2° (Figure 6A) was solved with the meshing characteristics and boundary conditions described in detail by Oddes and Solav (2023).

An FE mesh convergence analysis was conducted to check the numerical simulation accuracy for different mesh densities. The mesh density bias was 1.1 towards the center and 0.8 towards the top of the FE cylinder. No larger mesh density bias could be set to ensure model stability until δ_{max} and mesh refinement factors $N < 7$. A fine mesh with a mesh refinement factor of $\tilde{N} = 6$ served as reference for data comparison at $\delta = 20$ mm. Target was a convergence below 1% of the relative errors for the indentation force (3) and the surface displacement (4).

$$E_F(N) = \frac{\left|F(N) - F\left(\tilde{N}\right)\right|}{\left|F\left(\tilde{N}\right)\right|} \cdot 100\% \tag{3}$$

$$E_u(N) = \sum_{i=1}^{N_n(N)} \frac{\left|\boldsymbol{u}^i(N) - \boldsymbol{u}^i\left(\tilde{N}\right)\right|}{\left|\boldsymbol{u}^i\left(\tilde{N}\right)\right|} \cdot 100\% \tag{4}$$

$F(N)$ is the maximum indentation force and the vector $\boldsymbol{u}^i(N)$ denotes the final displacement of the i^{th} node on the upper outer edge of the FE cylinder segment (*cf.* Figure 6B) using a mesh refinement factor N. $N_n(N)$ is the number of the nodes used. To take into account varying material behaviors, three material sets covering the entire parameter space were analyzed. As a result of the mesh convergence analysis (compare with Section 3.3), we used a mesh refinement factor of $N = 3$ and quadratic elements (hex20 and penta15) in the objective function

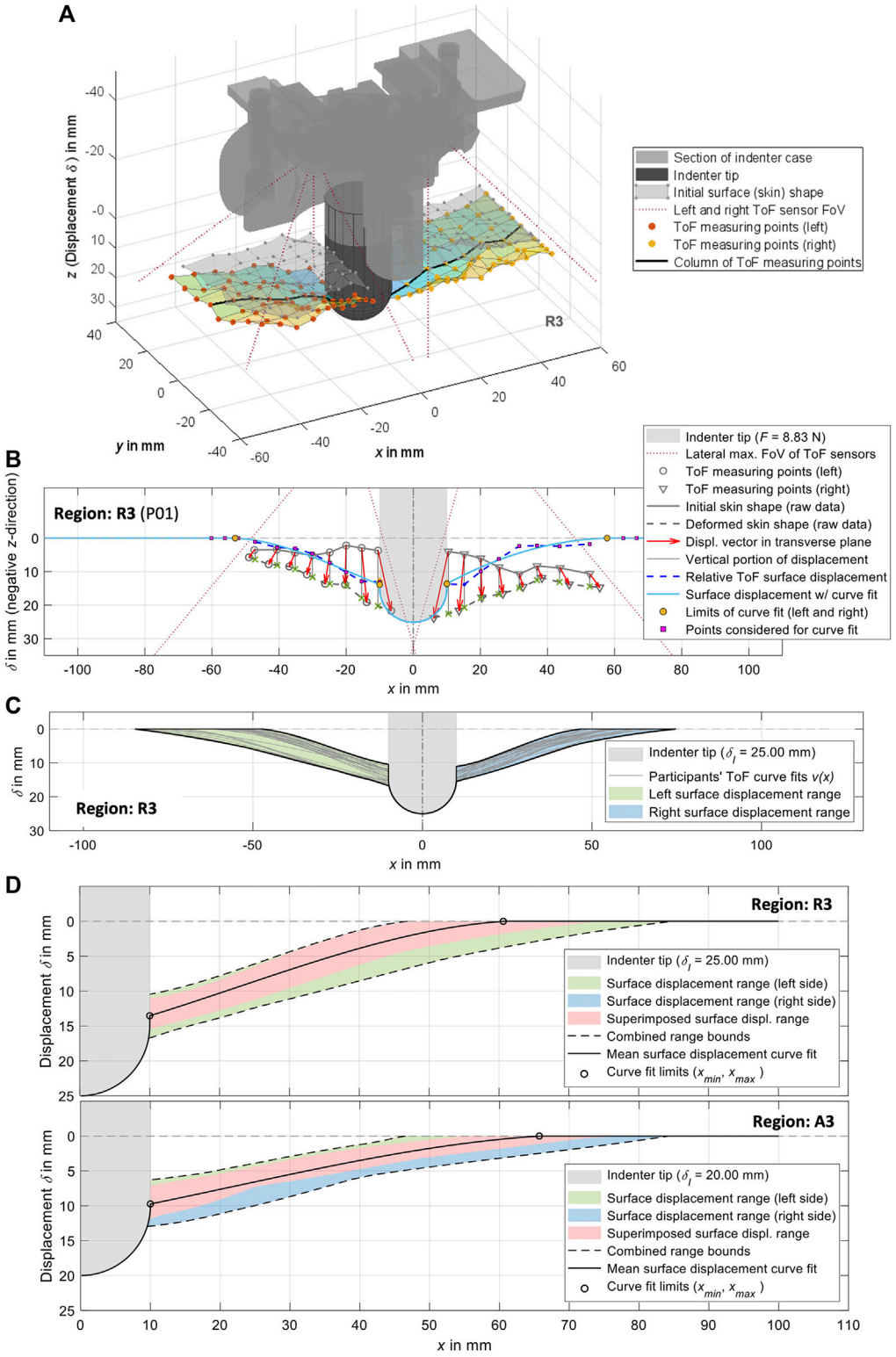

FIGURE 5
Visualizations of the experimental surface measurements and their processing exemplarily for measurement region 3. **(A)** 3D plot of the ToF measuring points from the left and right side, together with a visualization of the indenter tip and the indenter case. In addition to the initially measured undeformed skin, the deformation resulting from the measuring points is also shown. **(B)** Procedure for generating curve fits from the ToF measuring points in transverse plane (*cf.* Section 2.5). **(C)** Compilation of the left and right curve fits for all participants with visualization of the resulting ranges. **(D)** Complete surface displacements for both sides of all participants for δ_I. The mean surface displacement consists of the outer edge of the indenter tip that is in contact with the skin, the mean curve fit representing the deformation profile of the skin (Table 5), and an idealized undeformed section. The maximum radius of influence of the indentation is specified by x_{max}.

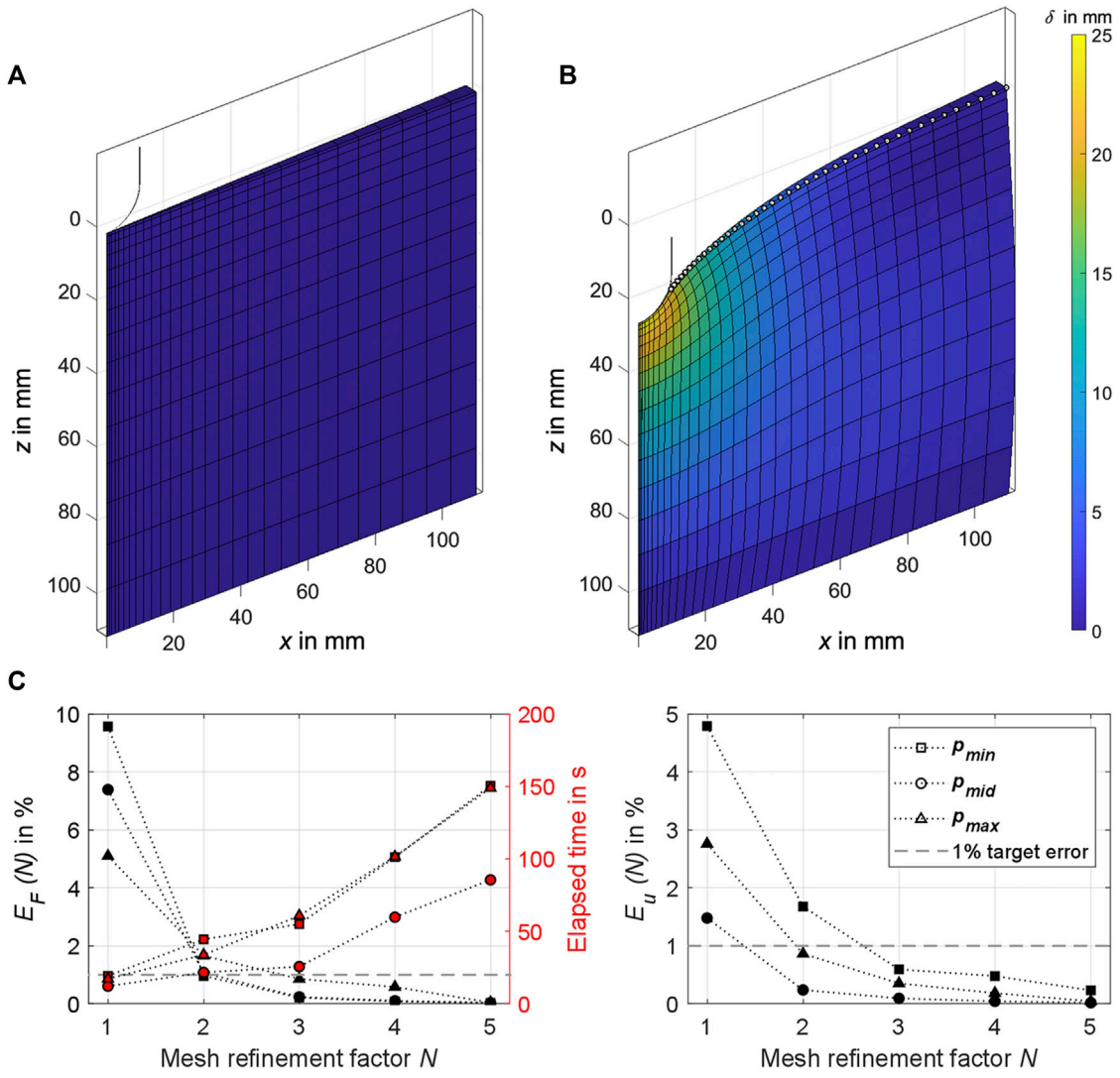

FIGURE 6
(A) The 2° sector of the axisymmetric FE cylinder as used in the analysis. The section of the hemispherical indenter tip in the initial state is also shown in the cylinder's center. **(B)** Exemplary simulation result for $\delta = 25$ mm. The displacements of the finite elements are colored, and the nodes used in the objective function F_u [Eq. (8)] are highlighted with white dots. **(C)** Results of the FE mesh convergence analysis for three material sets $\boldsymbol{p}_{min} = (1\,\text{kPa}, 4)$, $\boldsymbol{p}_{mid} = (45\,\text{kPa}, 30)$, and $\boldsymbol{p}_{max} = (140\,\text{kPa}, 60)$ each plotted against the mesh refinement factor N used. On the left are the relative errors of the indentation forces E_F [Eq. (3)] with the elapsed solution times (plotted in red), and on the right the relative errors of the surface displacements E_u [Eq. (4)]. The convergence target error for E_F and E_u is shown on both sides.

analysis (Section 2.9). This resulted in 30 elements in radial, 15 elements in axial, and one element in tangential direction.

2.8 Constitutive model

Consistent with previous mechanical descriptions of human soft tissue (Holzapfel, 2000; Erdemir et al., 2006; Flynn et al., 2011; Halloran and Erdemir, 2011; Maas et al., 2012; Moerman et al., 2017; Calvo-Gallego et al., 2018; Wang et al., 2019; Marinopoulos et al., 2020; Alawneh et al., 2022; Lohr et al., 2022), we used a hyperelastic, nearly-incompressible Ogden material model (Simo and Taylor, 1991) to describe the nonlinear force-displacement and surface deformation behaviors gathered in this study. With a set of material parameters $\boldsymbol{p} = (p_1, p_2) = (c, m)$ and the bulk-like modulus κ, the uncoupled first-order Ogden strain energy density function Ψ integrated in FEBio is defined in (5),

$$\Psi(\lambda_i) = \frac{c}{m^2}\sum_{i=1}^{3}\left(\tilde{\lambda}_i^m - 1\right) + \frac{\kappa}{2}(\ln J)^2 \tag{5}$$

where λ_i is the i^{th} deviatoric principal stretch and J represents the volume ratio. For a nearly isochoric deformation, $\kappa = \frac{c}{2}\cdot 10^3$ was selected (Moerman et al., 2017; Oddes and Solav, 2023).

2.9 Objective function analysis

Based on the objective function analysis with synthetic reference values of Oddes and Solav (2023), we defined the combined objective

function $F_{fu}(\boldsymbol{p};\delta)$ as the modulated sum of the overall normalized errors between the indentation forces $F_f(\boldsymbol{p};\delta)$ and the associated overall normalized relative errors between the surface displacements $F_u(\boldsymbol{p};\delta)$ in Eq. (6).

$$F_{fu}(\boldsymbol{p};\delta) = \eta F_f(\boldsymbol{p};\delta) + (1-\eta) F_u(\boldsymbol{p};\delta), \quad \eta \in [0,1] \tag{6}$$

The modulation factor η enables a convex combination of both residual errors. This means that $\eta = 0$ or $\eta = 1$ corresponds to a sole evaluation of the superficial displacements or the indentation reaction forces. The residual errors between the indentation forces at an indentation depth δ are defined in (7).

$$F_f(\boldsymbol{p};\delta) = \frac{\left|f(\boldsymbol{p};\delta) - f(\delta)\right|^2}{\left|f(\delta)\right|^2} \tag{7}$$

$f(\delta)$ is the experimental mean and $f(\boldsymbol{p};\delta)$ is the simulated indentation reaction force in negative z-direction, respectively. $F_u(\boldsymbol{p};\delta)$ quantifies the combined surface displacement deviations in (8).

$$F_u(\boldsymbol{p};\delta) = \sum_{i=1}^{\bar{N}_n} w_{n,i} \cdot \frac{\left|u_{(i)}(\boldsymbol{p};\delta) - u_{(i)}(\delta)\right|^2}{\left|u_{(i)}(\delta)\right|^2} \tag{8}$$

$u_{(i)}(\boldsymbol{p};\delta)$ and $u_{(i)}(\delta)$ are the simulation and the mean reference surface displacements during an indentation depth δ of the i^{th}-node in negative z-direction. No displacements in directions other than the z-direction could be tracked using our ToF measurement setup. After interpolating the mean reference displacements (Table 5) to all nodes of the simulation model, only the nodes $\bar{N}_n$ that fulfill $x_{min} \le x_n \le x_{Trim}$ were considered. x_n is the node position in x-direction and x_{min} represents the outer edge of the indenter tip. x_{Trim} in turn results from the reference displacements $\delta_{Trim} = u(x_{Trim})$, which must at least be given so that a reasonable evaluation of $F_u(\boldsymbol{p};\delta)$ is possible. Due to the processing of the measurement data (Section 2.5), $u(x \ge x_{max}) = 0$ applies to all mean displacements. For the calculation of $F_u(\boldsymbol{p};\delta)$, this leads to an underrepresentation of displacement errors near the indenter tip due to $\lim_{x \to x_{max}} u(x) = 0$, despite an inversely proportional weighting to their initial radial coordinates w_n.

$$w_n = \frac{\left(\frac{1}{r_1}, \frac{1}{r_2}, \ldots, \frac{1}{r_{\bar{N}_n}}\right)^T}{\left\|\left(\frac{1}{r_1}, \frac{1}{r_2}, \ldots, \frac{1}{r_{\bar{N}_n}}\right)^T\right\|} \tag{9}$$

The nodes visualized in Figure 6B (vertex and edge nodes in the range $x_{min} \le r_{N_n} \le r_C$) on the outer edge of the cylinder section were represented by their coordinates $r_1, r_2, \ldots, r_{N_n}$. The number of all surface nodes used in each case was $\bar{N}_n \le N_n \in \mathbb{N}$.

To analyze the objective functions combined over all indentation depths, δ_I (10) was specified for the resulting parameter space, where $\boldsymbol{p}$ is an element of the discrete parameter space $\boldsymbol{P} = \boldsymbol{C} \times \boldsymbol{M}$.

$$F_{fu}^{tot}(\boldsymbol{p}) = \frac{1}{4}\sum_{I=1}^{4} F_{fu}(\boldsymbol{p};\delta_I), \quad \text{for } I = 1,2,3,4 \tag{10}$$

Consequently, the minimum of $F_{fu}^{tot}(\boldsymbol{p})$ constitutes the resulting material parameter $\boldsymbol{p}_{res}$ for the FE model, which approximately results in the smallest error to the experimental data (best fit) over all indentation depths and the selected η. The 2D grid of $\boldsymbol{P}$ is based on $\boldsymbol{C}$ and $\boldsymbol{M}$, which comprise the evenly spaced Ogden material parameters c and m: $\boldsymbol{C}$ = 1:1:60 kPa, and $\boldsymbol{M}$ = 4:1:125.

We evaluated a trim factor δ_{Trim} in the range 0.1 − 1.2 mm best suitable for evaluating the objective function for each measurement region (Table 2) using six parameters: 1) The SD of distances between $F_{fu}^{tot}(\boldsymbol{p})$ and all $F_{fu}(\boldsymbol{p};\delta_I)$, 2) the proportion of $F_{fu}^{tot}(\boldsymbol{p}) > 1.5$ in $\boldsymbol{P}$, 3) the circularity measurement for $F_{fu}^{tot}(\boldsymbol{p}) \le 1.5$ in $\boldsymbol{P}$, 4) the relative change of mean $F_f(\boldsymbol{p};\delta)$ to $F_u(\boldsymbol{p};\delta)$ over all δ_I, and 5) and 6) the change in the resulting relative material parameters c and m. Their results were analyzed for the entire parameter space and are visualized as an example in Supplementary Material S2 over the range of δ_{Trim}. To determine the shape parameters 1–3, the parameter space was nondimensionalized using the respective $\boldsymbol{p}_{max} = (c_{max}, m_{max})$. For parameter 4, the minimum difference to 0.5 (equal weighting), assuming the lowest possible trim factor, was aimed for. Convergence was the aim for all other parameters. For 1, 2, and 3 with <2% and for 5, and 6 <1%. The rounded mean value of all six individual target trim factors resulted in the δ_{Trim} per region used in the objective function analysis.

3 Results

All participants were students or academic employees. No complications occurred during the measurement sessions, there were no interruptions, and a complete set of data was recorded in each case. The results of the sEMG measurements are summarized in Table 3. Because the MVCs primarily targeted the muscle regions over which direct measurements were conducted, the most relevant values are highlighted. With regard to the MVC in the supine position, the anterior relative muscle activities at E1 amounted to an average of 3.9% during R1-R3, and 33.2% during A1-A3 (see Figure 2 for measurement regions). The anterolateral measurement region 4 was located lateral to the rectus abdominus. The subjects were in supine position, which is why the MVC in this position was used. Because this and the active posture took place within the sagittal plane, the relative activity at E2 was higher by a factor of 6.4 and 1.5 for R and A respectively compared to E1. For the lateral MVC, the absolute muscle activity at E2 was 216.5% higher, which explains the increased relative activity at E2 during R4. In general, however, the measurement data also confirmed the experimental assessment that the anterolateral muscles measured with E2 were less well activated selectively by the participants. Except during the measurements in region 4, the relative muscle activities in the relevant regions for R were 5.3% ± 2.04% and for A 34.3% ± 7.03%. During measurements R1 and R2 only one participant was unable to fully relax his abdominal muscles (E1 ≥ 10.4%, E2 ≥ 42.1%), as a result of which the forces for $\delta > 5$ mm were up to 90% higher than the mean. With the aim of determining physiological standard values, these data sets were excluded from all subsequent evaluations.

3.1 Force-displacement curves

The processed force-displacement curves for the measured regions with distinction between R (fully relaxed musculature)

TABLE 3 Surface EMG amplitude of the participants. Electrode positions E1, E2, and E3 are displayed in Figure 2 and data is given as mean with standard deviation (mean ± SD). The most relevant values for the evaluations are printed in bold (activity of the muscle group on which the indentation was conducted).

	Body position	E1	E2	E3
Baseline activity in µV	Supine	**6.8 ± 1.04**	6.9 ± 2.30	5.0 ± 0.31
	Lateral	8.3 ± 5.09	**6.4 ± 1.42**	4.8 ± 0.41
	Prone	5.2 ± 0.42	5.0 ± 0.34	**6.1 ± 1.73**
MVC in µV	Supine	**235.4 ± 168.95**	61.7 ± 39.46	40.2 ± 35.09
	Lateral	72.7 ± 75.25	**133.6 ± 101.62**	50.5 ± 31.79
	Prone	16.1 ± 10.19	33.3 ± 18.56	**105.2 ± 45.32**
	Measurement region			
Muscle activity in %	R1	**3.9 ± 2.4**	14.1 ± 9.3	36.4 ± 30.8
	R2	**4.1 ± 2.1**	18.9 ± 16.5	36.1 ± 30.2
	R3	**3.7 ± 2.3**	14.5 ± 11.5	38.8 ± 33.3
	R4	4.0 ± 2.4	**24.8 ± 23.8**	36.2 ± 30.7
	R5	33.6 ± 41.0	**8.3 ± 5.7**	14.9 ± 10.5
	R6	42.6 ± 18.4	20.3 ± 10.3	**6.6 ± 2.8**
	A1	**30.2 ± 9.4**	40.7 ± 25.2	35.3 ± 32.3
	A2	**32.3 ± 6.6**	41.8 ± 22.7	34.6 ± 28.6
	A3	**37.2 ± 7.4**	51.6 ± 29.8	35.4 ± 29.3
	A4	34.4 ± 5.0	**51.7 ± 30.8**	38.6 ± 37.6
	A5	44.1 ± 39.8	**26.8 ± 13.2**	42.8 ± 33.3
	A6	61.6 ± 22.6	33.3 ± 17.4	**44.9 ± 5.5**

and A (controlled activated musculature) are visualized in Figure 4 and the mean curve fits $f(\delta)$ are listed in Table 4. As usual for mechanically loaded layered biological soft tissue (Zhang et al., 1997; Huang and Zheng, 2015), non-linear courses with a toe region with very small stiffnesses at low deformation, followed by tissue stiffening with increasing indentation depths, can be observed for the relaxed curves. Transitions between the two sections were on average 12.1 ± 2.5 mm for R and 4.3 ± 1.6 mm for A. The measurements for A were less compliant, and the curves were almost linear after the toe region. The activation of the muscles under the skin and subcutaneous tissue after uniaxial compression therefore resulted in a stiffer overall system that behaved less like usual soft tissue. In comparison, participant 6 (P06) had the lowest body fat percentage at 10.3% (*cf.* Table 1) and a pronounced lateral abdominal musculature due to his athletic background. The measured force at A4 was therefore more than twice as high as the average. For A1, A4, and A5, P06 forms the upper range limits (*cf.* Supplementary Material S3) but shows no deviations from the average when his muscles were relaxed. It could also be seen that the lack of subcutaneous fat <13.6% led to an approximate linearization of the overall anterolateral force-displacement curves in P01 and P06. P02 set the upper limit for A2. He had pronounced trunk muscles to prevent back pain and an average body fat percentage of 17.2%. After a toe region of less than 1.3 mm, the force-displacement curves of P02 were almost linear. The force ranges increased with greater displacements and were 14.6 ± 11.57 N at δ^*_{max}.

Overall, measurement regions 2, 3, 4, and 6 showed large linear sections with muscles activated. In the center of the linea alba and laterally (regions 1 and 5) the curve curses remained predominantly non-linear. Mean gradients of the linear sections for regions 1 to 6 with activated musculature could be approximated with 1.42, 1.39, 1.43, 1.08, 1.36, and 5.22 N/mm. For better comparability, we subdivided the curves with relaxed muscles at $0.45 \cdot \delta_{max}$ and specified a stiffness value for each segment. From region 1 to 6, these were 0.34, 0.29, 0.24, 0.26, 0.25, and 0.72 N/mm for the first segment. For the second segment, linearly approximated stiffnesses were 0.56, 0.56, 0.49, 0.41, 0.62, and 2.31 N/mm. The subjects with a body fat >21% represented the lower anterolateral limits of the ranges. For relaxed musculature, no participant represented a systematic upward or downward outlier. The lowest variance between the subject data was observed for R3 and the highest for A5. The resulting RMSEs for the mean curve fits f were 1.18 ± 0.765 N/mm and 4.97 ± 2.996 N/mm for all regions with R and A. Consequently, interindividual differences have increased due to the activation of the trunk muscles.

The Kolmogorov-Smirnov tests (T1) were statistically significant ($p < 0.001$) for the indentation depths considered across all participants. This means that neither the six measurement regions for relaxed nor for active musculature originate from the same distribution. Analysis of variances of the

TABLE 4 Coefficients of the experimental mean force-displacement curves (Figure 4). Each polynomial curve fit $f(\delta)$ describing this is defined for $0 \le \delta \le \delta_{max}$ with $f_{max} = f(\delta_{max})$. The complete data set after curve fitting for the force-displacement measurements can be found in Supplementary Material S1.

Measurement region	δ_{max} in mm	f_{max} in N	Degree (n-1)	Polynomial curve fit $f(\delta)$						
				Coefficients f_n						RMSE in N/mm
				f_1	f_2	f_3	f_4	f_5	f_6	
R1	25	11.85	2	8.684e-03	2.462e-01	0	-	-	-	1.256
R2	30	13.33	4	−2.937e-06	2.590e-04	2.479e-03	2.163e-01	0	-	0.963
R3	30	11.52	2	8.604e-03	1.260e-01	0	-	-	-	0.512
R4	30	10.33	2	5.279e-03	1.859e-01	0	-	-	-	0.660
R5	25	11.41	4	5.359e-06	1.710e-04	3.677e-03	1.740e-01	0	-	1.025
R6	20	32.25	4	−2.765e-05	2.665e-03	2.231e-02	3.214e-01	0	-	2.639
A1	20	20.94	2	3.456e-02	3.556e-01	0	-	-	-	2.913
A2	25	29.51	5	−1.119e-05	−6.415e-04	4.969e-02	5.176e-02	4.619e-01	0	3.320
A3	25	27.01	5	9.067e-06	−5.547e-04	1.047e-02	−2.882e-02	3.835e-01	0	3.922
A4	25	22.44	3	−3.641e-04	2.890e-02	4.072e-01	0	-	-	4.682
A5	24	23.86	2	2.864e-02	3.068e-01	0	-	-	-	4.037
A6	14	55.98	4	−3.118e-04	−3.885e-03	3.465e-01	7.624e-01	0	-	10.959

various measurement regions also showed that the results for R6 differed significantly ($p <$ corrected α) from R3, R4, and R5 as well as R3 from R1. Limited to $\delta = 7$ mm, this also applied for R6 to R2. For an activated musculature, only region 6 did not differ significantly from region 2 (*cf.* Figure 3B). Highly significant differences were also found in the Friedman test (T2): Depending on a relaxed or activated musculature, the group means of measurement regions 1 to 6 differ from each other ($p < 0.001$).

3.2 Surface displacements

The experimental mean surface displacements for all measurement regions at δ_I are listed in Table 5 and are visualized for region 3 in Figure 5D. All other regions and indentation depths are visualized in Supplementary Material S4. Each displacement curve was calculated using the individual curves of all participants from both body sides. As can be seen in Figure 5, the left and right sides of the measurements differ. The mean deformation curve therefore represents an approximation for the respective region. The weakest symmetry is found in regions 5 and 6 (see colored indication of the sides). Fits of third degree were suitable for describing the measured displacement in all cases. In individual cases, lower or higher degrees led to abrupt transitions, no intersection with the reference plane, or oscillations. A qualitative comparison of relaxed and activated musculature showed that curve shapes for R had greater slope, x_{min} were smaller (closer to the center of the indenter tip), and x_{max} were therefore also relatively smaller. In addition, the displacement curves for regions 3, 4, and 5 were concave and for 1, 2, and 6 they were more linear.

3.3 FE mesh convergence analysis

We ran all simulations on a PC with Windows 11 Pro, Intel Core i7-10700K 3.80 GHz CPU, and 32 GB RAM. The results for the FE mesh convergence analysis are shown in Figure 6C. Given a short calculation time of ≤60 s, the errors for $E_F(N)$ and $E_u(N)$ are convergent and <1% with $N = 3$. Lower N, however, provided a barely relevant time advantage, but increased the error for the surface displacement almost threefold, especially with more compliant material.

3.4 Hyperelastic abdominal material parameters

Four parameter spaces $\boldsymbol{P}$ with a total of 3321, 2565, 2565, and 2115 parameter sets for δ^*_{max} = 13, 16, 20, and 25 mm were calculated respectively, depending on the properties of the experimental reference data. Sets with $\delta^*_{max} = 25$ mm took an average of 69.1 ± 23.84 s each. Figure 7 shows a representative example for the numerical interim results of the objective function analysis. The resulting shapes of $F_{fu}(\boldsymbol{p}; \delta_I)$ are visualised as contour plots for each specific indentation depth step δ_I. The centers highlighted with markers define the minima of these contour plots and thus the respective parameter set $\boldsymbol{p_I}$, which represent optimal solutions for δ_I and η. The optimization results for $\eta = 0.5$ (center column) together with the intermediate results (Figure 7) are compiled in Figure 8 for each measurement region investigated. The resulting material parameter sets $\boldsymbol{p_{res}}$ at the minimum of $F^{tot}_{fu}(\boldsymbol{p})$ [see Eq. (10)] are indicated as well. All results are listed in Table 6.

From the closed shapes of $F^{tot}_{fu}(\boldsymbol{p})$, a unique $\boldsymbol{p_{res}}$ could be identified for all regions with the optimization conditions used.

TABLE 5 Experimental mean surface displacements (Figure 5) for all measurement regions with mean indentation forces $f^* = f(\delta_I)$ (Table 4) at the discrete indentation depths δ_I as reference parameters for the inverse FE analysis. Each polynomial curve fit $u(x)$ is defined for $x_{min} \leq x \leq x_{max}$ (Figure 5D) for an inverted z-axis. x_{min} and x_{max} are the intersection points with the indenter tip and the reference plane ($\delta = 0$), respectively. A visualization of all displacements can be found in Supplementary Material S4.

Measurement region	δ_I for I = 1, 2, 3, 4 in mm	f^* in N	Polynomial curve fit $u(x)$					
			Range limits in mm		Coefficients u_n			
			x_{min}	x_{max}	u_1	u_2	u_3	u_4
R1	5	1.45	6.089	42.859	−1.065e-04	6.927e-03	−3.190e-02	−2.971
	10	3.33	7.831	53.080	−4.762e-05	3.425e-03	8.567e-02	−7.078
	15	5.65	8.837	62.945	−4.873e-05	4.178e-03	1.030e-01	−10.89
	20	8.40	9.671	66.729	−6.188e-05	5.926e-03	8.836e-02	−13.9
R2	6.25	1.51	7.342	37.005	−1.993e-04	1.256e-02	−1.166e-01	−2.782
	12.5	5.53	8.943	45.946	−1.246e-04	8.224e-03	6.108e-02	−8.087
	18.75	6.27	9.756	57.187	−5.454e-05	3.227e-03	2.287e-01	−13.43
	25	9.86	10.000	65.213	−5.666e-05	4.188e-03	2.368e-01	−17.54
R3	6.25	1.12	7.566	35.484	−2.180e-04	1.351e-02	−1.365e-01	−2.433
	12.5	2.92	9.293	42.561	−1.745e-04	1.119e-02	5.990e-03	−7.075
	18.75	5.39	9.942	52.568	−6.188e-05	3.089e-03	2.467e-01	−12.52
	25	8.53	10.000	60.609	−6.175e-05	4.191e-03	2.418e-01	−16.31
R4	6.25	1.37	7.348	36.761	−1.688e-04	1.022e-02	−6.487e-02	−3.037
	12.5	3.15	9.026	49.639	−3.117e-05	3.522e-04	2.401e-01	−8.972
	18.75	5.34	9.831	61.055	−1.742e-05	−5.439e-04	3.221e-01	−13.67
	25	7.94	10.000	67.845	−1.813e-05	−4.167e-04	3.827e-01	−18.39
R5	6.25	1.28	7.331	39.196	−1.194e-04	7.065e-03	−8.779e-03	−3.318
	12.5	3.21	8.955	43.200	−1.068e-04	5.409e-03	1.698e-01	−8.818
	18.75	6.34	9.697	52.244	−4.996e-05	1.204e-03	3.545e-01	−14.68
	25	11.41	9.990	61.790	−5.988e-05	3.226e-03	3.379e-01	−19.07
R6	4	1.81	6.811	43.314	6.69e-07	−4.281e-04	5.611e-02	−1.682
	8	5.25	8.518	45.484	−4.42e-05	2.257e-03	7.747e-02	−4.033
	12	11.10	9.272	51.617	2.646e-07	−2.121e-03	2.639e-01	−8.007
	16	19.96	9.865	57.954	8.678e-06	−3.241e-03	3.435e-01	−10.71
A1	4	1.98	6.425	45.758	−7.288e-06	1.786e-04	5.058e-02	−1.99
	8	5.06	8.082	45.302	−6.09e-05	3.765e-03	5.473e-02	−4.543
	12	9.24	8.921	49.949	−8.825e-05	6.103e-03	6.618e-02	−3.34
	16	14.54	9.463	55.936	−5.966e-05	4.297e-03	1.412e-01	−10.9
A2	5	3.52	7.095	46.183	−1.724e-05	5.926e-04	6.401e-02	−2.522
	10	9.04	8.513	50.939	−3.94e-05	2.501e-03	9.710e-02	−6.23
	15	15.84	9.315	57.370	−4.751e-05	3.453e-03	1.354e-01	−10.16
	20	23.02	9.878	65.679	−3.791e-05	2.684e-03	1.961e-01	−13.72
A3	5	2.19	7.553	39.789	1.582e-06	−3.823e-04	6.318e-02	−2.008
	10	6.77	9.309	47.862	−2.645e-05	1.298e-03	9.510e-02	−4.625

(Continued on following page)

TABLE 5 (*Continued*) Experimental mean surface displacements (Figure 5) for all measurement regions with mean indentation forces $f^* = f(\delta_I)$ (Table 4) at the discrete indentation depths δ_I as reference parameters for the inverse FE analysis. Each polynomial curve fit $u(x)$ is defined for $x_{min} \le x \le x_{max}$ (Figure 5D) for an inverted z-axis. x_{min} and x_{max} are the intersection points with the indenter tip and the reference plane ($\delta = 0$), respectively. A visualization of all displacements can be found in Supplementary Material S4.

Measurement region	δ_I for I = 1, 2, 3, 4 in mm	f^* in N	Polynomial curve fit $u(x)$					
			Range limits in mm		Coefficients u_n			
			x_{min}	x_{max}	u_1	u_2	u_3	u_4
	15	13.42	9.795	56.835	−2.952e-05	1.614e-03	1.561e-01	−8.663
	20	20.12	10.000	65.710	−2.59e-05	1.704e-03	1.772e-01	−11.65
A4	5	2.74	7.252	49.359	5.653e-06	−9.252e-04	8.103e-02	−2.425
	10	6.66	8.761	49.564	−8.992e-06	−9.275e-04	1.988e-01	−6.479
	15	11.44	9.584	57.680	−7.473e-06	−1.211e-03	2.744e-01	−10.36
	20	16.80	9.981	63.514	−1.605e-05	−1.236e-04	2.837e-01	−13.41
A5	5	2.25	6.772	47.663	7.959e-06	−1.075e-03	9.514e-02	−2.954
	10	5.93	8.856	53.956	2.45e-05	−3.237e-03	2.213e-01	−6.363
	15	11.04	9.616	54.403	1.31e-05	−3.276e-03	3.356e-01	−10.67
	20	17.59	9.969	59.772	7.236e-06	−3.051e-03	3.979e-01	−14.43
A6	3.25	5.97	6.440	52.595	1.001e-05	−9.623e-04	4.477e-02	−1.149
	6.5	17.97	8.652	54.386	3.466e-05	−3.406e-03	1.263e-01	−2.373
	9.75	33.95	9.422	61.089	3.14e-05	−3.384e-03	1.605e-01	−4.337
	13	51.03	9.817	67.835	3.628e-05	−4.454e-03	2.358e-01	−6.824

The smallest absolute error occurred for R6 with $F_{fu}^{tot} = 0.12$ and the largest for R1 with $F_{fu}^{tot} = 0.43$. Partial errors of $F_f(\boldsymbol{p}; \delta_I)$ and $F_u(\boldsymbol{p}; \delta_I)$ were accumulated in F_{fu}^{tot} over all δ_I. As an example, for region 3, Figure 9 compares the FE results of the indentation FE model with the experimental data used. Deviations between the surface displacements are thus recognizable. However, their quantitative comparison for F_u was conducted solely in the surface evaluation range indicated, between the intersection of the indenter tip profile and δ_{trim} (see Section 2.9). In general, a more concave surface deformation was observed for the material model used compared to some of the experimental data. The resulting material parameters for the different abdominal regions can be characterized as follows: With relaxed musculature $c = 6.6 \pm 1.14$ kPa, $m = 18 \pm 7.04$ anterior-lateral, and $c = 25$ kPa, $m = 19$ posterior. With activated musculature $c = 17.8 \pm 1.79$ kPa, $m = 21.4 \pm 2.97$ anterior-lateral, and $c = 100$ kPa, $m = 23$ posterior. The absolute deviations between f^* and f_{sim} were maximum at δ^*_{max} with 3.4 ± 2.36 N.

4 Discussion

In this study, macro-indentation and time-of-flight skin deformation measurements were conducted to obtain data sets quantifying the *in vivo* material behavior of the physiological adult male abdomen. The data sets comprise the slow and continuous (non-ballistic) force-displacement curves of six abdominal regions, each synchronized with the displacements of the surrounding soft tissue resulting from the indentation. To account for the influence of the trunk muscles, the measurements were conducted with both fully relaxed and controlled activated muscles in various lying positions. Due to the small scatter range of the physiological parameters, standard values were calculated for all participants combined, which served as reference for inverse FEA. The inverse FEA was used to numerically estimate material parameters, which allowed the mechanical responses of the soft tissues to be simulated as a whole. All processed data sets and the material parameters of this study are described in detail or made available in the Supplementary Material S1–S4.

Our focus was on the *in vivo* characterization of the mechanical responses of the human abdominal wall and the structures it encloses in the abdominal cavity. During trunk muscle activation, the sections assumed to be linearized after foot regions of 3.5–8 mm were on average 5.2 N/mm posteriorly and 1.1–1.4 N/mm elsewhere (anterior-lateral). During relaxation, stiffnesses for small displacements were 0.72 N/mm posteriorly, and 0.24–0.34 N/mm anteriorly to laterally. The stiffnesses of the abdomen under large deformations (45% δ_{max}, see Figure 4) were approximately 0.41–0.56 N/mm anteriorly, 0.62 N/mm laterally, and 2.31 N/mm posteriorly. This is in high agreement with previous measurements of local abdominal stiffnesses in which postures and experimental procedure were different (van Ramshorst et al., 2011; Tran et al., 2016). Although not statistically significant, the compliance with relaxed muscles is reduced anterolaterally (region 4) compared to the central abdomen (linea alba).

For each measurement region (Figure 2), we conducted an objective function analysis in which the mean experimental

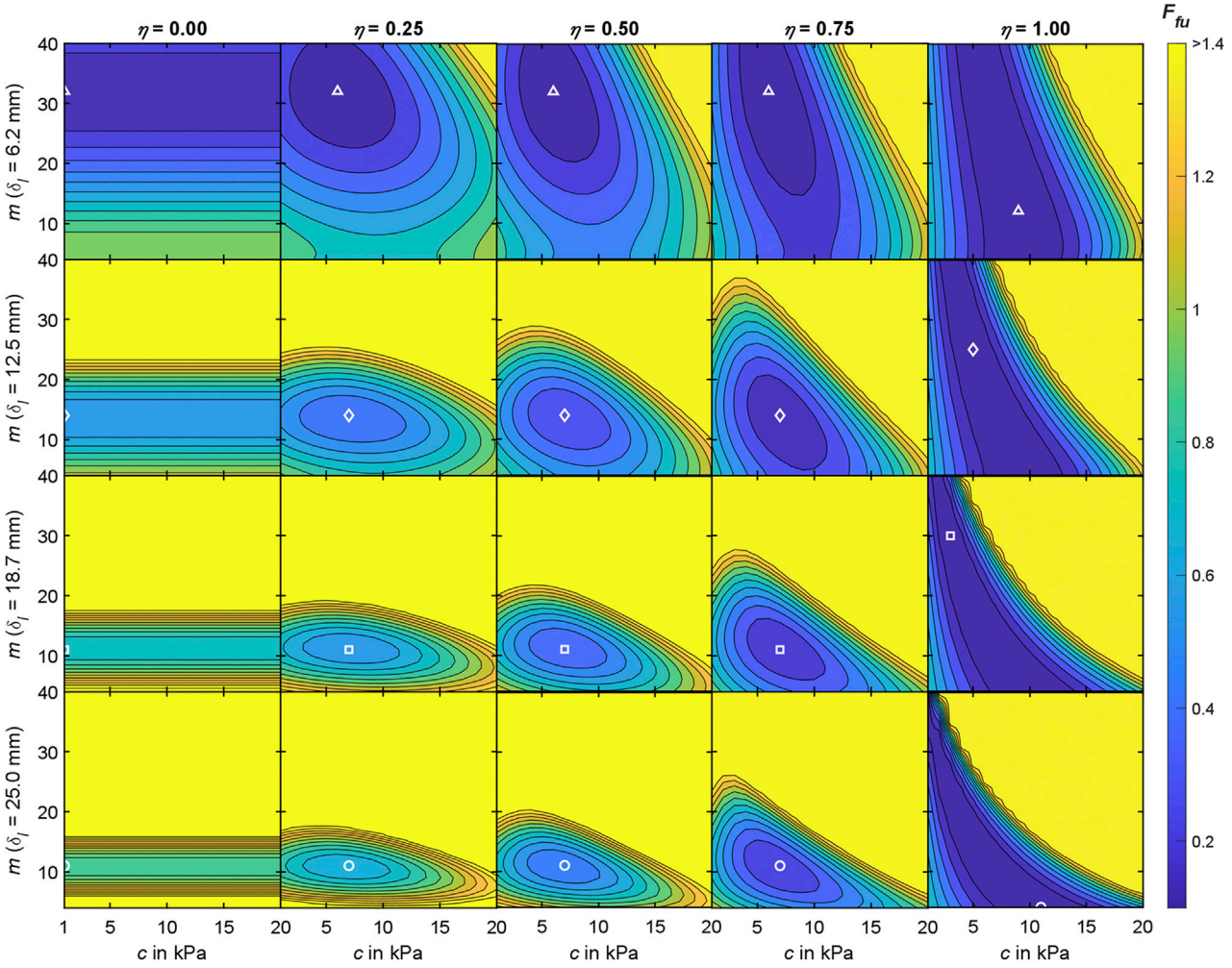

FIGURE 7
Interim results of the objective function analysis for the Ogden material model at measurement region 3 with $\boldsymbol{C}$ = 1:1:20 kPa, and $\boldsymbol{M}$ = 4:1:40. The 20 contour plots depict the resulting dimensionalized shapes of $F_{fu}(\boldsymbol{p};\delta_l)$ [*cf.* Eq. (6)] for five modulation factors η and the four indentation depth steps δ_l (Table 5). For recognizable scaling of the contours, values > 1.4 are discarded and shown in light yellow. White, unfilled markers indicate parameter sets $\boldsymbol{p}_l$ as locations of min $F_{fu}(\boldsymbol{p};\delta_l)$ for δ_l from small to large: Triangle, rhombus, square, and circle. For η = 0.5, min $F_{fu}(\boldsymbol{p};\delta_l)$ are 0.06, 0.27, 0.37, and 0.42 and $\boldsymbol{p}_l$ are (6 kPa, 32), (7 kPa, 14), (7 kPa, 11), and (7 kPa, 11).

indenter force-displacement curve (Table 4) and the mean surface displacement (Table 5) served as the optimization targets. The accumulated differences between these and the simulation results were visualized using contour plots (Figure 8) and the convergence to a minimum was marked. Regarding the material stiffness and the surface displacement, the sensitivities of m and c [see Ogden strain energy density function in (5)] become apparent in Figure 7 for η = 0 and η = 1. There is hardly any influence on the surface shape for varying c (horizontally orientated valleys). In case of η = 1, we observed vertically orientated deep valleys, which show that the material stiffness is not very sensitive to m. Only for modulation factors $0 < \eta < 1$, and thus with the superposition of tissue stiffness and surface deformation information, rounded and closed valleys resulted within the parameter space. For equal weighting, we evaluated all shapes and minima of the contour plots for η = 0.5. As already described by Oddes and Solav (2023) for synthetic material data, material parameter sets could only be determined reliably in our study with the consideration of F_f and F_u. Force-displacement data of the indenter alone is insufficient, although it is commonly used as the sole basis for parameter identification in inverse FEA (Fougeron et al., 2023). Frequently used alternatives are therefore multiple starting points optimizations, or genetic or evolutionary algorithms that are globally convergent (Oddes and Solav, 2023).

To the best of our knowledge, our study is the first of its kind, but has limitations in several aspects. Only young and healthy male participants with a similar BMI (Table 1) were involved in the study. As expected, we only found small inter-individual differences. Consequently, no general conclusions can be drawn about the entire population. However, other publications report significant differences in soft tissue behavior (Song et al., 2006; van Ramshorst et al., 2011; Sadler et al., 2018) as well as distribution of subcutaneous adipose tissue and body composition (Esparza-Ros et al., 2022) between women and men. Men's tissue is often stiffer and less deformable. In 2011, van Ramshorst et al. (2011) reported that abdominal wall tension was on average 31% higher in men than in

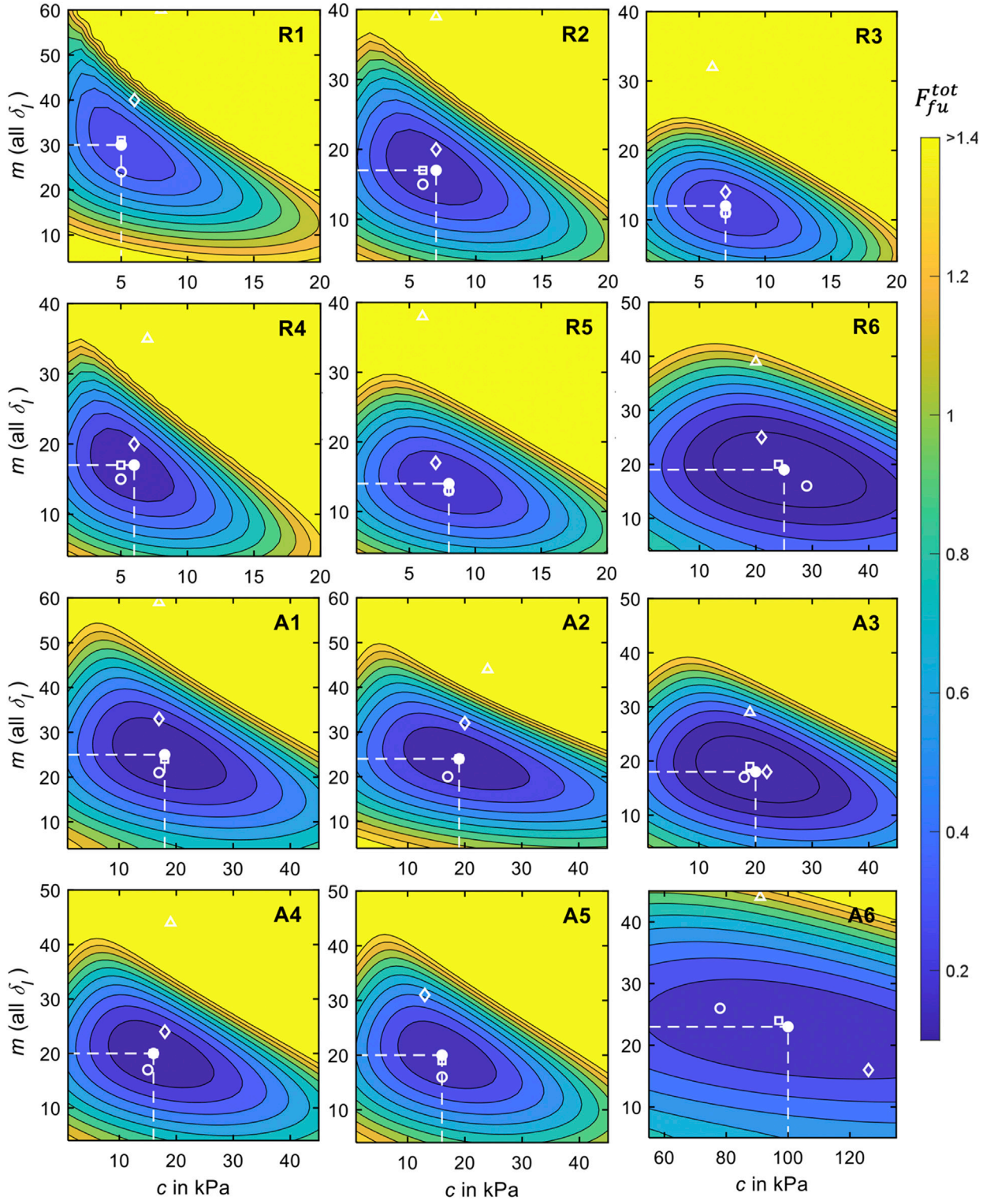

FIGURE 8
Results of the objective function analysis for all measurement regions and relaxed and activated musculature for $\eta = 0.5$. The contour plots depict the resulting shapes of $F_{fu}^{tot}(\boldsymbol{p})$ [*cf.* Eq. (10)] with white, unfilled markers indicating the resulting locations of min $F_{fu}(\boldsymbol{p};\delta_l)$ for δ_l from small to large: Triangle, rhombus, square, and circle (*cf.* Figure 7). Min $F_{fu}^{tot}(\boldsymbol{p})$ are each indicated with white, filled circles and the resulting material parameter sets $\boldsymbol{p}_{res}$ from $\boldsymbol{P}$ are listed in Table 6. Certain parameter spaces are cropped for better visualization.

TABLE 6 Resulting (best fit) Ogden material parameter sets p_{res} with the parameter sets p_I for the four simulated δ_I as ranges, and the respective values used in the inverse FE analysis. The identification of p_{res} from the discrete parameter range $P = C \times M$ was carried out using the minimum of the objective function Eq. (10) with the reference parameters from Table 5. For κ see Section 2.8.

Measurement region	δ^*_{max} in mm	δ_{trim} in mm	f_{sim} in N for δ^*_{max}	p_{res}		p_I range		$\min(F^{tot}_{fu})$
				c in kPa	m	c in kPa	m	
R1	20	0.5	10.78	5	30	5–8	24–60	0.43
R2	25	0.6	13.11	7	17	6–7	15–39	0.33
R3	25	0.5	9.62	7	12	6–7	11–32	0.38
R4	25	0.5	11.24	6	17	5–7	15–35	0.31
R5	25	0.6	12.46	8	14	6–8	13–38	0.35
R6	16	0.6	19.60	25	19	20–29	16–39	0.12
A1	16	0.6	17.08	18	25	17–18	21–59	0.26
A2	20	0.5	30.37	19	24	17–24	20–44	0.29
A3	20	0.5	23.91	20	18	18–22	17–29	0.13
A4	20	0.5	21.07	16	20	15–19	17–44	0.26
A5	20	0.6	21.07	16	20	12–16	16–60	0.33
A6	13	0.4	59.48	100	23	78–126	16–44	0.34

women, but that BMI had no significant influence. We were able to confirm this for the BMI, except for one participant with activated and pronounced abdominal muscles and the lowest percentage of body fat in regions 1, 4, and 5.

The experimental setup we developed (Figure 1) was accurate in terms of repeatability and absolute accuracy when compared to a mechanical testing machine with gelatine and 3D printed surface profiles. Overall, the test setup proved to be suitable for the aims of this study. Because the application of the test procedure is not limited to young male participants, data should also be gathered from other populations in the future, for example, women, people with a higher BMI, people with pathologies, and older people. This data could have a major impact on the computer-aided development of medical aids and products for which patient compliance is important. As only changes in the surface profile of the skin were measured using ToF, only tissue displacements in the axial direction could be captured and not, for example, strains. In addition, the initial positions and displacements of the soft tissues and organs of the abdomen were unknown in our study. Technically, these could not be determined with the current measurement setup. Supplementary MRIs or ultrasound scans can provide additional information to better categorize possible inter-individual variances, internal tissue deformations, and improve models with heterogeneous material or individual organs. The circumvention of physical limitations during MRI measurements has already been addressed and solved, for example, by Moerman (2012) by use of a custom designed, hydraulically powered, and MRI compatible soft tissue indenter.

Because both ToF sensors were mounted on the indenter housing, the field of view and thus the covered measuring range around the indenter tip was limited. As part of the data processing, we approximated laterally exceeding displacements of the skin with a multifactorial optimization using polynomial curve fits of third degree and base points (Figure 5). This procedure proved to be reliable, albeit time-consuming, because it had to be performed for each data set at the desired indentation depth. Nevertheless, in our opinion, this approach provides an accurate approximation of the total deformations under the assumption of an initially planar surface. In further studies, ToF sensors with a higher resolution could be mounted further away from the skin, or ToF sensors with a wider field of view could be used. Alternatively, laser scanning (Todros et al., 2019; Todros et al., 2020) or 3D digital image correlation (Moerman et al., 2009) would be accurate and reliable methods for superficial measurement of the abdominal wall, although they could make the experimental setup more complex. As interactions with skin are an important topic in modelling (Sanders et al., 1998; Portnoy et al., 2008), these should be examined more closely on the abdomen in the future. Detailed results from previous mechanical studies of the skin (Ní Annaidh et al., 2012) can serve as basis for this. However, due to the anisotropy of the skin, the orientation of the Langer lines is also relevant. To quantify the proportional influence of the skin on overall *in vivo* reactions, the effective movements of natural or applied surface patterns of the skin can be measured using digital image correlation (Szepietowska et al., 2023). Analyzing the displacement of the discrete structures of the overall image provides information about the anisotropic skin strains, which is not possible with ToF sensors that only return distance images.

In the current study, the sEMG signals were used to monitor whether the participants followed the instructions regarding muscle activation. Due to our primary aim of generating experimental reference data for the inverse FEA, we did not perform subject- or region-specific correlation analyses with other results. A potential shortcoming of the measurement in the anterolateral region 4 was that the supine position and movements in the lateral plane did not explicitly activate the abdominal oblique muscles (E2). Anterolateral crunches or a posterolateral position could be better suited in the future. For

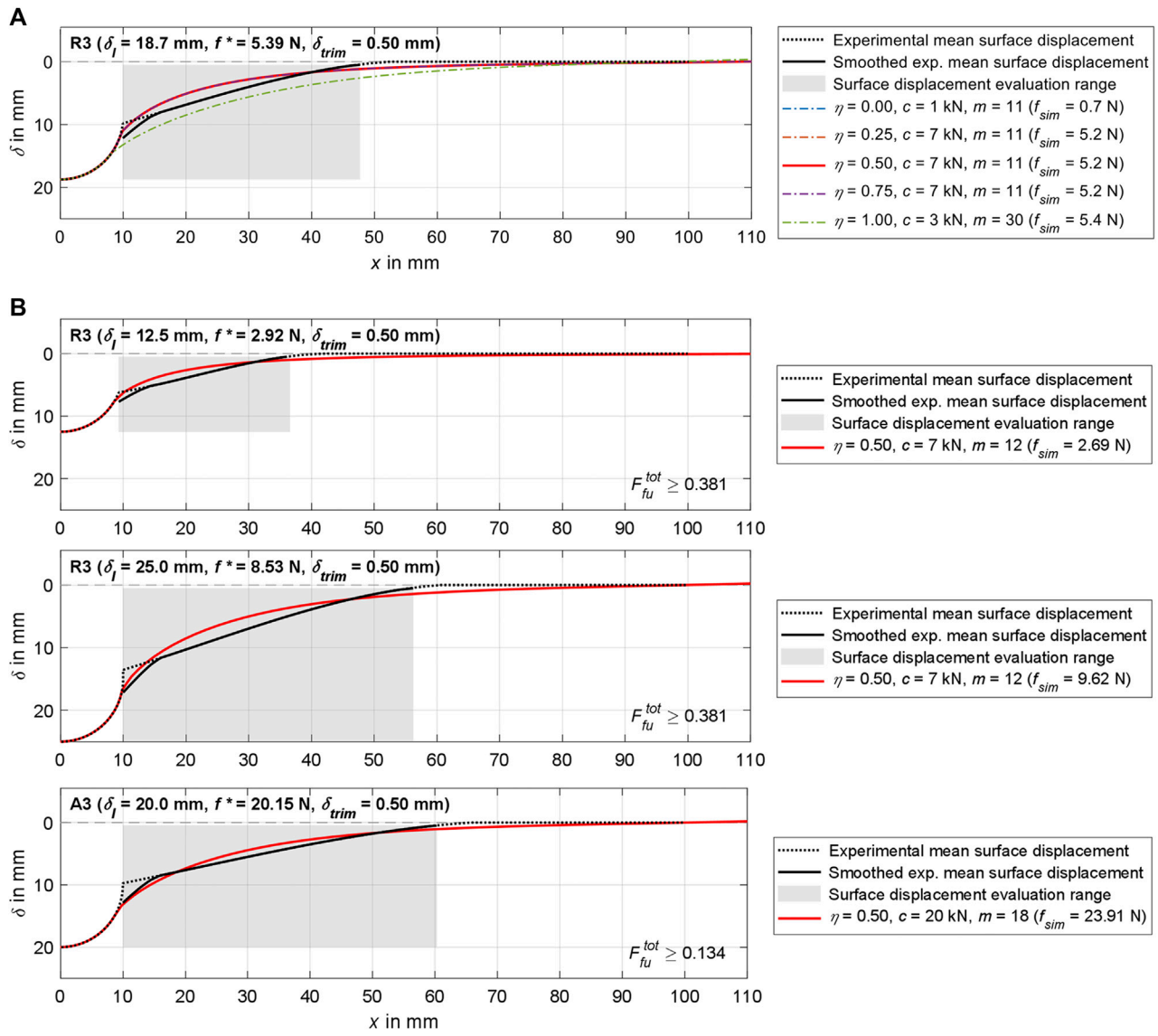

FIGURE 9
Visualization of simulation results for region 3 and various δ_I in comparison with the experimentally determined indentation forces and surface displacements. To calculate F_u, only the smoothed section of the surface displacement (solid black line) within the evaluation range, marked in gray, was considered. **(A)** Contrasting the separate preliminary results for all five η (*cf.* Figure 7), the resulting $\boldsymbol{p}_I$, and f_{sim} from which $F_{fu}(\boldsymbol{p}; \delta_I)$ was calculated. **(B)** The solid red lines represent the surface displacements with the best fit Ogden material parameter sets $\boldsymbol{p}_{res}$ from Table 6 for respective δ_I.

the anterior measurement regions 1-4, the participants were either fully extended or held their legs at a right angle with their lower legs horizontal. Due to the macroscopic nature of our study, we consider any subsequent influences on the tissue density and tension of the skin as a result of the postural changes to be negligible. The same applies to possible alterations in abdominal organ location, morphology, and rib coverage due to postural changes (Hayes et al., 2013a; Hayes et al., 2013b). The large anterior and lateral tissue deformations required ultrasound gel between indenter tip and skin, as the contact friction would otherwise have been highly unpleasant for the participants. In addition, this simplified the contact condition for the inverse FEA.

The present work is limited to one isotropic and hyperelastic material, thus the application to anisotropic and viscoelastic materials requires further research. For fat, the assumption of isotropic behavior is accurate (Dubuis et al., 2012), but the approximately 30 mm thick abdominal wall consists of numerous layers of muscles, tendinous structures, and blood vessels with fibers oriented in different directions (Song et al., 2006; Hernández et al., 2011; Deeken and Lake, 2017). However, the interaction of the layers decreases the degree of anisotropic response significantly (Hernández et al., 2011; Simón-Allué et al., 2017; Lohr et al., 2022). In addition, we used a 2° sector of an axisymmetric FE cylinder (Figure 6A). Further adaptations of the framework used in combination with FEBio and the opportunity to freely customize the codes offer a wide range of possibilities for more detailed inverse FEA. A first and already integrated approach should be the investigation of other hyperelastic material models (Mooney-Rivlin, Neo-Hookean, and

Ogden-Moerman) that can be used for soft tissue modelling (Alawneh et al., 2022) as well as higher order Ogden models. There is also potential for improvement in terms of computational efficiency and model stability. Even though our study showed that a first-order Ogden model already provides good approximations for all regions, the numerical results for larger deformations offer the potential to be closer to the experimental data (Figure 8). Because the volumetric behavior depends on the bulk-like modulus and we determined it via a ratio to the varied material parameter c, its influence on the FE surface deformation is to be analyzed systematically in further studies.

Another simplification worth mentioning is the planarization of the locally compressed abdominal surface, here in the form of a right circular cylinder. As was also evident in the ToF raw data, the undeformed measurement regions were mostly cylindrical surfaces, but were converted to a planar reference plane during data processing. This means that all $x > x_{max}$ (Table 5) were assumed not to be displaced and a comparison with the FE cylinder was made possible [*cf.* Eq. (8)]. Depending on $\boldsymbol{p}$ and δ, it could be seen that areas near the outer edge of the FE cylinder shifted in the direction opposite to the direction of indentation (*cf.* Figure 9). This material uplift was due to the compensation of the central uniaxial compression and the finite cylinder diameter. As the uplifts were <0.35 mm at the outer edge for all $\boldsymbol{p}_{res}$ and δ^*_{max}, we consider them to be negligible. To compensate for this, the cylinder radius would have to be increased, δ^*_{max} reduced, or an additional boundary condition applied to the cylindrical surfaces. For buttock compression with a plate, for example, Moerman et al. (2017) have shown that geometric differences influence the results of an inverse FEA. This is one of the reasons why an FE model with a cylindrical surface, that mimics the participant-specific curvature of the abdominal wall, could provide an even more accurate description in the future. The 3D surface shapes required for this can be obtained using the integrated ToF sensors (Figure 5A).

The use of four equidistant indentation depth steps δ_I is another shortcoming of our inverse FEA approach. For an optimal numerical approximation of the experimental material behavior, more than one material parameter set $\boldsymbol{p}_I$ for each of the four δ_I was required for all measurement regions. In the example of R3, $\boldsymbol{p}_I$ resulted in $\boldsymbol{p}_1 = (6\,\text{kPa}, 32)$ and $\boldsymbol{p}_3 = \boldsymbol{p}_4 = (7\,kPa, 11)$, among others. Assuming that the abdominal material response under compression is continuous, $\boldsymbol{p}_{res}$ is therefore only an approximation over all δ_I. A higher amount of discrete δ_I can improve the numerical accuracy of the overall result. In contrast to synthetically generated reference data (Oddes and Solav, 2023), which are based on an already known material parameter set, the experimental reference data of the surface displacements for the respective δ_I was calculated independently from all participants as an average value. The multi-criteria optimization approach [see Eq. (2)] does not ensure that the individual curve fits can be described using a material model in a way that a $\boldsymbol{p}_{res} = \boldsymbol{p}_I$ exists for $I \in \mathbb{N}^+$. In addition to a continuous determination of $\boldsymbol{p}_{res}$ over the entire indenter stroke, the surface displacement in particular should not be determined independently for the δ_I used in future.

It should be noted that we focused on the transient material response during indentation and thus did not consider tissue relaxation. All measurements were carried out with the same indentation speed. Each test run was completed quickly and continuously in less than 16 s (extension and retraction of the indenter tip with 40 mm maximum travel), so the reaction was considered as an instantaneous response (Yu et al., 2006; Lu et al., 2009). The fact that the participants had to hold their breath and purposefully activated their muscles, however, prohibited slower tests (<5 mm/s) and prolonged holding of the indenter tip at maximum stroke (>1 s). Deep inhalation lifted the abdominal wall and the muscle activity was measurably increased. Limited by the indenter being in continuous contact with the skin, no active breathing could be examined and separate runs would be necessary. We therefore assume increased abdominal stiffness during inhalation, which should be investigated in further studies.

Modelling viscoelasticity is straightforward and can be carried out, for example, using an elastic component coupled with a viscous component, which acts as a damper that delays the stress-strain response (Wells and Liang, 2011). The use of our data for the validation of complex models, that represent the abdomen in detail, is also conceivable. Along with exact anatomical models, patient-specific material that takes biological data into account, is becoming increasingly relevant in biomedical engineering and treatment (Erdemir et al., 2006; Moerman et al., 2016; Simón-Allué et al., 2017; Macron et al., 2020; Lerchl et al., 2022). By averaging over all participants and discarding the anatomical characteristics, we are not yet able to make statements beyond the physiological standard values. Further work will seek to address subject-specific material parameters from inverse FEA using *in vivo* indentation data and tissue displacements.

A long-term goal of our work is to assess biomechanical principles of action of the lower back to improve the development of biomedical products specifically in the early design phases. We aim to achieve this by simulating the interaction between a digital human body model and a virtual technical system. This facilitates the methodical variation of the properties of the technical system as part of the engineering design process with regard to ethical and economic factors. Moreover, even the latest experimental methods are limited when it comes to studying internal mechanics such as muscle forces or stress states in soft tissues, the overall context of the stabilizing functions of individual muscles, and thus the possible causes of pain (Remus et al., 2021). To support the engineering design process, a new type of digital model of the lower trunk aims to couple a muscle-driven forward dynamical active hybrid model of the lumbosacral spine (Remus et al., 2023) with the surrounding soft tissue of the abdomen. In this regard, the work presented here contributes to a better understanding and numerical quantification of abdominal *in vivo* soft tissue behavior under local compression.

5 Conclusion

In this study, we presented a novel, simple, and reliable method for *in vivo* measurement of the mechanical soft tissue behavior of the human abdomen. The force-displacement curves, the associated surface displacements of the skin, and the muscle activities of ten males were measured in a total of six regions, in each case with completely relaxed and with controlled activated muscles while lying horizontally. The experimental data allowed us to identify similarities and

significant differences between the regions and states of muscle activation. In addition, we used inverse FEA to derive unique hyperelastic material parameter sets that numerically approximate the experimentally measured soft tissue behaviors. This comprehensive *in vivo* dataset is not available in the current literature and represents an advance in our knowledge of abdominal material properties, enabling improved numerical human body models, interaction studies, and product development processes.

Data availability statement

The original contributions presented in the study are included in the article/Supplementary Material, further inquiries can be directed to the corresponding author.

Ethics statement

The studies involving humans were approved by the Ethics Committee of the Medical Faculty of the Ruhr-University Bochum (23-7868 08/10/23). The studies were conducted in accordance with the local legislation and institutional requirements. The participants provided their written informed consent to participate in this study.

Author contributions

RR: Conceptualization, Data curation, Formal Analysis, Investigation, Methodology, Project administration, Resources, Software, Validation, Visualization, Writing–original draft, Writing–review and editing. CS: Investigation, Resources, Software, Writing–review and editing. SS: Formal Analysis, Resources, Software, Validation, Writing–review and editing. EU: Validation, Writing–original draft, Writing–review and editing. BB: Funding acquisition, Supervision, Writing–review and editing.

Funding

The author(s) declare that financial support was received for the research, authorship, and/or publication of this article. We acknowledge support by the DFG Open Access Publication Funds of the Ruhr-University Bochum.

Acknowledgments

The authors would like to thank Christoph Ehlert (Chair of Product Development, RUB) for his technical support in the realization and calibration of the measurement equipment, and Letícia Mamede for conducting an explorative preliminary indenter study as part of her student thesis. Additionally, we would like to acknowledge all the volunteers who participated in this research project for devoting their time to the experimental activity.

Conflict of interest

The authors declare that the research was conducted in the absence of any commercial or financial relationships that could be construed as a potential conflict of interest.

Publisher's note

All claims expressed in this article are solely those of the authors and do not necessarily represent those of their affiliated organizations, or those of the publisher, the editors and the reviewers. Any product that may be evaluated in this article, or claim that may be made by its manufacturer, is not guaranteed or endorsed by the publisher.

Supplementary material

The Supplementary Material for this article can be found online at: https://www.frontiersin.org/articles/10.3389/fbioe.2024.1384062/full#supplementary-material

SUPPLEMENTARY MATERIAL S1
Complete data set of coefficients and goodness of fits of the polynomial curve fitted experimental force-displacement curves $f(\delta)$.

SUPPLEMENTARY MATERIAL S2
Exemplary visualization of the trim factor δ_{Trim} evaluations best suitable for the objective function analysis of measurement region 3.

SUPPLEMENTARY MATERIAL S3
Visualization of the experimentally determined raw force-displacement curves (left) and the participant-related curve fits calculated from these (right) for all regions.

SUPPLEMENTARY MATERIAL S4
Experimental mean surface displacements and ranges for all measurement regions at δ_j.

References

Ahn, B., and Kim, J. (2010). Measurement and characterization of soft tissue behavior with surface deformation and force response under large deformations. *Med. Image Anal.* 14, 138–148. doi:10.1016/j.media.2009.10.006

Alawneh, O., Zhong, X., Faieghi, R., and Xi, F. (2022). Finite element methods for modeling the pressure distribution in human body–seat interactions: a systematic review. *Appl. Sci.* 12, 6160. doi:10.3390/app12126160

Anderson, A. E., Ellis, B. J., and Weiss, J. A. (2007). Verification, validation and sensitivity studies in computational biomechanics. *Comput. Methods Biomech. Biomed. Engin* 10, 171–184. doi:10.1080/10255840601160484

Bonnaire, R., Woo-Suck, H., Calmels, P., Convert, R., and Molimard, J. (2020). "Parametric study of lumbar belts in the case of low back pain: effect of patients' specific characteristics," in *Computational biomechanics for medicine: personalisation, validation and therapy*. Editors M. P. Nash, P. M. F. Nielsen, A. Wittek, K. Miller, and G. R. Joldes (Cham, Switzerland: Springer), 43–59.

Calvo-Gallego, J. L., Domínguez, J., Gómez Cía, T., Gómez Ciriza, G., and Martínez-Reina, J. (2018). Comparison of different constitutive models to characterize the viscoelastic properties of human abdominal adipose tissue. A pilot study. *J. Mech. Behav. Biomed. Mater* 80, 293–302. doi:10.1016/j.jmbbm.2018.02.013

Carter, F. J., Frank, T. G., Davies, P. J., McLean, D., and Cuschieri, A. (2001). Measurements and modelling of the compliance of human and porcine organs. *Med. Image Anal.* 5, 231–236. doi:10.1016/S1361-8415(01)00048-2

Clauser, C., Tebbetts, I., Bradtmiller, B., McConville, J., and Gordon, C. (1988) *Measurer's handbook: U.S. Army anthropometric survey 1987-1988*: Natick, Massachusetts.

Clin, J., Aubin, C.-E., Parent, S., and Labelle, H. (2010). A biomechanical study of the Charleston brace for the treatment of scoliosis. *Spine* 35, E940–E947. doi:10.1097/BRS.0b013e3181c5b5fa

Cooper, L., Gullane, A., Harvey, J., Hills, A., Zemura, M., Martindale, J., et al. (2019). Experimental platform to facilitate novel back brace development for the improvement of spine stability. *Comput. Methods Biomech. Biomed. Engin* 22, 1163–1173. doi:10.1080/10255842.2019.1645837

Cox, C. A. (2020) *Computational modeling of the lumbar spine: active musculature and intra-abdominal pressure in compressive loading*. Dissertation: Duke University, Department of Biomedical Engineering.

E. Criswell (2011). *Cram's introduction to surface electromyography* (Sudbury, MA: Jones and Bartlett).

Davies, P. J., Carter, F. J., and Cuschieri, A. (2002). Mathematical modelling for keyhole surgery simulations: a biomechanical model for spleen tissue. *IMA J. Appl. Math.* 67, 41–67. doi:10.1093/imamat/67.1.41

Deeken, C. R., and Lake, S. P. (2017). Mechanical properties of the abdominal wall and biomaterials utilized for hernia repair. *J. Mech. Behav. Biomed. Mater* 74, 411–427. doi:10.1016/j.jmbbm.2017.05.008

Driscoll, M., and Blyum, L. (2019). Investigation of the inter-dependence between intra-abdominal pressure and spinal stability. *Clin. Biomech. (Bristol, Avon)* 69, 164–167. doi:10.1016/j.clinbiomech.2019.07.018

Dubuis, L., Avril, S., Debayle, J., and Badel, P. (2012). Identification of the material parameters of soft tissues in the compressed leg. *Comput. Methods Biomech. Biomed. Engin* 15, 3–11. doi:10.1080/10255842.2011.560666

El-Monajjed, K., and Driscoll, M. (2020). A finite element analysis of the intra-abdominal pressure and paraspinal muscle compartment pressure interaction through the thoracolumbar fascia. *Comput. Methods Biomech. Biomed. Engin* 23, 585–596. doi:10.1080/10255842.2020.1752682

Erdemir, A., Viveiros, M. L., Ulbrecht, J. S., and Cavanagh, P. R. (2006). An inverse finite-element model of heel-pad indentation. *J. Biomechanics* 39, 1279–1286. doi:10.1016/j.jbiomech.2005.03.007

Esparza-Ros, F., Moreira, A. C., Vaquero-Cristóbal, R., Barrigas, C., Albaladejo-Saura, M., and Vieira, F. (2022). Differences between four skinfold calipers in the assessment of adipose tissue in young adult healthy population. *Nutrients* 14, 2085. doi:10.3390/nu14102085

Fackler, M. L., and Malinowski, J. A. (1988). Ordnance gelatin for ballistic studies. Detrimental effect of excess heat used in gelatin preparation. *Am. J. forensic Med. pathology* 9, 218–219. doi:10.1097/00000433-198809000-00008

Fitzpatrick, T. B. (1988). The validity and practicality of sun-reactive skin types I through VI. *Arch. Dermatol* 124, 869. doi:10.1001/archderm.1988.01670060015008

Flynn, C., Taberner, A., and Nielsen, P. (2011). Modeling the mechanical response of *in vivo* human skin under a rich set of deformations. *Ann. Biomed. Eng.* 39, 1935–1946. doi:10.1007/s10439-011-0292-7

Fougeron, N., Trebbi, A., Keenan, B., Payan, Y., and Chagnon, G. (2023). Current Poisson's ratio values of finite element models are too low to consider soft tissues nearly-incompressible: illustration on the human heel region. *Comput. Methods Biomech. Biomed. Engin*, 1–10. doi:10.1080/10255842.2023.2269286

Grébonval, C., Trosseille, X., Petit, P., Wang, X., and Beillas, P. (2021). Effects of seat pan and pelvis angles on the occupant response in a reclined position during a frontal crash. *PLOS ONE* 16, e0257292. doi:10.1371/journal.pone.0257292

Grujicic, M., Pandurangan, B., Xie, X., Gramopadhye, A. K., Wagner, D., and Ozen, M. (2010). Musculoskeletal computational analysis of the influence of car-seat design/adjustments on long-distance driving fatigue. *Int. J. Industrial Ergonomics* 40, 345–355. doi:10.1016/j.ergon.2010.01.002

Guo, J., Guo, W., and Ren, G. (2021). Embodiment of intra-abdominal pressure in a flexible multibody model of the trunk and the spinal unloading effects during static lifting tasks. *Biomech. Model Mechanobiol.* 20, 1599–1626. doi:10.1007/s10237-021-01465-1

Halloran, J. P., and Erdemir, A. (2011). Adaptive surrogate modeling for expedited estimation of nonlinear tissue properties through inverse finite element analysis. *Ann. Biomed. Eng.* 39, 2388–2397. doi:10.1007/s10439-011-0317-2

Haug, E., Choi, H.-Y., Robin, S., and Beaugonin, M. (2004). "Human models for crash and impact simulation," in *Handbook of numerical analysis: computational models for the human body* (Germany: Elsevier), 231–452.

Hayes, A. R., Gayzik, F. S., Moreno, D. P., Martin, R. S., and Stitzel, J. D. (2013a). Abdominal organ location, morphology, and rib coverage for the 5(th), 50(th), and 95(th) percentile males and females in the supine and seated posture using multi-modality imaging. *Ann. Adv. Automot. Med.* 57, 111–122.

Hayes, A. R., Gayzik, F. S., Moreno, D. P., Martin, R. S., and Stitzel, J. D. (2013b). Comparison of organ location, morphology, and rib coverage of a midsized male in the supine and seated positions. *Comput. Math. Methods Med.* 2013, 1–12. doi:10.1155/2013/419821

Hernández, B., Peña, E., Pascual, G., Rodríguez, M., Calvo, B., Doblaré, M., et al. (2011). Mechanical and histological characterization of the abdominal muscle. A previous step to modelling hernia surgery. *J. Mech. Behav. Biomed. Mater* 4, 392–404. doi:10.1016/j.jmbbm.2010.11.012

Hicks, J. L., Uchida, T. K., Seth, A., Rajagopal, A., and Delp, S. L. (2015). Is my model good enough? Best practices for verification and validation of musculoskeletal models and simulations of movement. *J. Biomech. Eng.* 137, 020905. doi:10.1115/1.4029304

Hodges, P. W., Cresswell, A. G., Daggfeldt, K., and Thorstensson, A. (2001). *In vivo* measurement of the effect of intra-abdominal pressure on the human spine. *J. Biomechanics* 34, 347–353. doi:10.1016/S0021-9290(00)00206-2

Hodges, P. W., Eriksson, A. E. M., Shirley, D., and Gandevia, S. C. (2005). Intra-abdominal pressure increases stiffness of the lumbar spine. *J. Biomechanics* 38, 1873–1880. doi:10.1016/j.jbiomech.2004.08.016

Hodges, P. W., Ferreira, P. H., and Ferreira, M. L. (2015). "Chapter 14 - lumbar spine: treatment of motor control disorders," in *Pathology and intervention in musculoskeletal rehabilitation*. Editors D. J. Magee, J. E. Zachazewski, W. S. Quillen, and R. C. Manske (Germany: s.l. Elsevier Health Sciences), 520–560.

Holzapfel, G. A. (2000) *Nonlinear solid mechanics: a continuum approach for engineering*. Chichester: Wiley.

Huang, Y.-P., and Zheng, Y.-P. (2015) *Measurement of soft tissue elasticity* in vivo: *techniques and applications*. Boca Raton: CRC Press.

Ji, Y., Bai, H., Yang, J., Ge, C., Zhu, Y., Zhang, R., et al. (2022). AMOS: a large-scale abdominal multi-organ benchmark for versatile medical image segmentation. *ArXiv*. doi:10.48550/arXiv.2206.08023

Jourdan, A., Rapacchi, S., Guye, M., Bendahan, D., Masson, C., and Bège, T. (2022). Dynamic-MRI quantification of abdominal wall motion and deformation during breathing and muscular contraction. *Comput. Methods Programs Biomed.* 217, 106667. doi:10.1016/j.cmpb.2022.106667

Kauer, M., Vuskovic, V., Dual, J., Szekely, G., and Bajka, M. (2002). Inverse finite element characterization of soft tissues. *Med. Image Anal.* 6, 275–287. doi:10.1016/S1361-8415(02)00085-3

King, A. I. (2018). "Chapter 12: impact biomechanics of the abdomen," in *The biomechanics of impact injury: biomechanical response, mechanisms of injury, human tolerance and simulation*. Editor A. I. King (Cham: Springer).

Lamielle, S., Vezin, P., Verriest, J.-P., Petit, P., Trosseille, X., and Vallancien, G. (2008). 3D deformation and dynamics of the human cadaver abdomen under seatbelt loading. *Stapp Car Crash J.* 52, 267–294. doi:10.4271/2008-22-0011

Lee, J. B., and Yang, K. H. (2001). Development of a finite element model of the human abdomen. *Stapp Car Crash J.* 45, 79–100. doi:10.4271/2001-22-0004

Leong, F., Lai, C. Y., Khosroshahi, S. F., He, L., Lusignan, S. de, Nanayakkara, T., et al. (2022). A surrogate model based on a finite element model of abdomen for real-time visualisation of tissue stress during physical examination training. *Bioengineering* 9, 687. doi:10.3390/bioengineering9110687

Lerchl, T., El Husseini, M., Bayat, A., Sekuboyina, A., Hermann, L., Nispel, K., et al. (2022). Validation of a patient-specific musculoskeletal model for lumbar load estimation generated by an automated pipeline from whole body CT. *Front. Bioeng. Biotechnol.* 10, 862804. doi:10.3389/fbioe.2022.862804

Li, J., Pepe, A., Gsaxner, C., Luijten, G., Jin, Y., Ambigapathy, N., et al. (2023) *MedShapeNet – A large-scale dataset of 3D medical shapes for computer vision*.

Lister, K., Gao, Z., and Desai, J. P. (2011). Development of *in vivo* constitutive models for liver: application to surgical simulation. *Ann. Biomed. Eng.* 39, 1060–1073. doi:10.1007/s10439-010-0227-8

Lohr, M. J., Sugerman, G. P., Kakaletsis, S., Lejeune, E., and Rausch, M. K. (2022). An introduction to the Ogden model in biomechanics: benefits, implementation tools and limitations. *Philos. Trans. A Math. Phys. Eng. Sci.* 380, 20210365. doi:10.1098/rsta.2021.0365

Lu, M.-H., Yu, W., Huang, Q.-H., Huang, Y.-P., and Zheng, Y.-P. (2009). A hand-held indentation system for the assessment of mechanical properties of soft tissues *in vivo*. *IEEE Trans. Instrum. Meas.* 58, 3079–3085. doi:10.1109/TIM.2009.2016876

Ma, J., Zhang, Y., Gu, S., Zhu, C., Ge, C., Zhang, Y., et al. (2022). AbdomenCT-1K: is abdominal organ segmentation a solved problem? *IEEE Trans. Pattern Anal. Mach. Intell.* 44, 6695–6714. doi:10.1109/TPAMI.2021.3100536

Maas, S. A., Ellis, B. J., Ateshian, G. A., and Weiss, J. A. (2012). FEBio: finite elements for biomechanics. *J. Biomech. Eng.* 134, 011005. doi:10.1115/1.4005694

Macron, A., Pillet, H., Doridam, J., Rivals, I., Sadeghinia, M. J., Verney, A., et al. (2020). Is a simplified Finite Element model of the gluteus region able to capture the mechanical response of the internal soft tissues under compression? *Clin. Biomech.* 71, 92–100. doi:10.1016/j.clinbiomech.2019.10.005

Maiden, N. R., Fisk, W., Wachsberger, C., and Byard, R. W. (2015). Ballistics ordnance gelatine - how different concentrations, temperatures and curing times affect calibration results. *J. forensic Leg. Med.* 34, 145–150. doi:10.1016/j.jflm.2015.05.019

Marinopoulos, T., Zani, L., Li, S., and Silberschmidt, V. V. (2020). Modelling indentation of human lower-limb soft tissue: simulation parameters and their effects. *Contin. Mech. Thermodyn.* 35, 939–955. doi:10.1007/s00161-020-00933-w

Melia, M., Schmidt, M., Geissler, B., König, J., Krahn, U., Ottersbach, H. J., et al. (2015). Measuring mechanical pain: the refinement and standardization of pressure pain threshold measurements. *Behav. Res.* 47, 216–227. doi:10.3758/s13428-014-0453-3

Misra, S., Ramesh, K. T., and Okamura, A. M. (2008). Modeling of tool-tissue interactions for computer-based surgical simulation: a literature review. *PRESENCE Teleoperators Virtual Environ.* 17, 463–491. doi:10.1162/pres.17.5.463

Moerman, K. M. (2012) An improved Framework for the inverse Analysis of skeletal muscle tissue in-vivo. *Dissertation*. Dublin: The University of Dublin, Trinity College.

Moerman, K. M. (2018). GIBBON: the geometry and image-based bioengineering add-on. *J. Open Source Softw.* 3, 506. doi:10.21105/joss.00506

Moerman, K. M., Holt, C. A., Evans, S. L., and Simms, C. K. (2009). Digital image correlation and finite element modelling as a method to determine mechanical properties of human soft tissue *in vivo*. *J. Biomechanics* 42, 1150–1153. doi:10.1016/j.jbiomech.2009.02.016

Moerman, K. M., Solav, D., Sengeh, D., and Herr, H. (2016) Automated and data-driven computational design of patient-specific biomechanical interfaces. *engrxiv*. doi:10.31224/osf.io/g8h9n

Moerman, K. M., van Vijven, M., Solis, L. R., van Haaften, E. E., Loenen, A. C., Mushahwar, V. K., et al. (2017). On the importance of 3D, geometrically accurate, and subject-specific finite element analysis for evaluation of *in-vivo* soft tissue loads. *Comput. Methods Biomech. Biomed. Engin* 20, 483–491. doi:10.1080/10255842.2016.1250259

Molimard, J., Bonnaire, R., Han, W. S., Convert, R., and Calmels, P. (2019). In-silico pre-clinical trials are made possible by a new simple and comprehensive lumbar belt mechanical model based on the Law of Laplace including support deformation and adhesion effects. *PLoS ONE* 14, e0212681. doi:10.1371/journal.pone.0212681

Muttray, A., Melia, M., Geißler, B., König, J., and Letzel, S. (2014). Kollaborierende Roboter: Ermittlung der Schmerzempfindlichkeit an der Mensch-Maschine-Schnittstelle. *Wiss. Schlussbericht zum Vorhaben FP-0317*.

Netter, F. H. (2017) *Atlas of human anatomy*. Philadelphia: Elsevier.

Neumann, M., and Bender, B. (2022). "Challenges in the development of biomechatronic systems," in *Design methodology for future products* (Cham: Springer), 105–122.

Neumann, M., Remus, R., Sauerhoff, M., Lipphaus, A., Uttich, E., Sure, C., et al. (2020). Digitale Zwillinge in Interaktion mit Menschmodellen. *ZWF* 115, 116–120. doi:10.3139/104.112327

Ní Annaidh, A., Bruyère, K., Destrade, M., Gilchrist, M. D., and Otténio, M. (2012). Characterization of the anisotropic mechanical properties of excised human skin. *J. Mech. Behav. Biomed. Mater* 5, 139–148. doi:10.1016/j.jmbbm.2011.08.016

Norton, K. I. (2018). "Standards for anthropometry assessment," in *Kinanthropometry and exercise physiology*. Editors K. Norton and R. Eston (Boca Raton, FL: Routledge), 68–137.

Oddes, Z., and Solav, D. (2023). Identifiability of soft tissue constitutive parameters from *in-vivo* macro-indentation. *J. Mech. Behav. Biomed. Mater* 140, 105708. doi:10.1016/j.jmbbm.2023.105708

Pavan, P. G., Todros, S., Pachera, P., Pianigiani, S., and Natali, A. N. (2019). The effects of the muscular contraction on the abdominal biomechanics: a numerical investigation. *Comput. Methods Biomech. Biomed. Engin* 22, 139–148. doi:10.1080/10255842.2018.1540695

Périé, D., Aubin, C. E., Lacroix, M., Lafon, Y., and Labelle, H. (2004). Biomechanical modelling of orthotic treatment of the scoliotic spine including a detailed representation of the brace-torso interface. *Med. Biol. Eng. Comput.* 42, 339–344. doi:10.1007/BF02344709

Peterson, M. J., Czerwinski, S. A., and Siervogel, R. M. (2003). Development and validation of skinfold-thickness prediction equations with a 4-compartment model. *Am. J. Clin. Nutr.* 77, 1186–1191. doi:10.1093/ajcn/77.5.1186

Pierrat, B., MacManus, D. B., Murphy, J. G., and Gilchrist, M. D. (2018). Indentation of heterogeneous soft tissue: local constitutive parameter mapping using an inverse method and an automated rig. *J. Mech. Behav. Biomed. Mater* 78, 515–528. doi:10.1016/j.jmbbm.2017.03.033

Podwojewski, F., Otténio, M., Beillas, P., Guérin, G., Turquier, F., and Mitton, D. (2014). Mechanical response of human abdominal walls *ex vivo*: effect of an incisional hernia and a mesh repair. *J. Mech. Behav. Biomed. Mater* 38, 126–133. doi:10.1016/j.jmbbm.2014.07.002

Portnoy, S., Yizhar, Z., Shabshin, N., Itzchak, Y., Kristal, A., Dotan-Marom, Y., et al. (2008). Internal mechanical conditions in the soft tissues of a residual limb of a trans-tibial amputee. *J. Biomechanics* 41, 1897–1909. doi:10.1016/j.jbiomech.2008.03.035

Ramachandra, R. (2016) *Injury and impact responses of the abdomen subjected to seatbelt loading*. Dissertation: The Ohio State University. US.

Remus, R., Lipphaus, A., Neumann, M., and Bender, B. (2021). Calibration and validation of a novel hybrid model of the lumbosacral spine in ArtiSynth-The passive structures. *PLOS ONE* 16, e0250456. doi:10.1371/journal.pone.0250456

Remus, R., Selkmann, S., Lipphaus, A., Neumann, M., and Bender, B. (2023). Muscle-driven forward dynamic active hybrid model of the lumbosacral spine: combined FEM and multibody simulation. *Front. Bioeng. Biotechnol.* 11, 1223007. doi:10.3389/fbioe.2023.1223007

Rohen, J. W., Yokochi, C., and Lütjen-Drecoll, E. (2015) *Anatomy: a photographic atlas*. USA: Wolters Kluwer.

Sadler, Z., Scott, J., Drost, J., Chen, S., Roccabianca, S., and Bush, T. R. (2018). Initial estimation of the *in vivo* material properties of the seated human buttocks and thighs. *Int. J. Non-Linear Mech.* 107, 77–85. doi:10.1016/j.ijnonlinmec.2018.09.007

Sanders, J. E., Greve, J. M., Mitchell, S. B., and Zachariah, S. G. (1998). Material properties of commonly-used interface materials and their static coefficients of friction with skin and socks. *J. Rehabil. Res. Dev.* 35, 161–176.

Sato, F., Yamamoto, Y., Ito, D., Antona-Makoshi, J., Ejima, S., Kamiji, K., et al. (2013). "Hyper-viscoelastic response of perfused liver under dynamic compression and estimation of tissue strain thresholds with a liver finite element model," in Proceedings of the 2013 IRCOBI Conference, China, September 11-13, 2013 (IEEE), 736–750.

Sattout, A., Clin, J., Cobetto, N., Labelle, H., and Aubin, C.-E. (2016). Biomechanical assessment of providence nighttime brace for the treatment of adolescent idiopathic scoliosis. *Spine Deform.* 4, 253–260. doi:10.1016/j.jspd.2015.12.004

Schünke, M., Schulte, E., and Schumacher, U. (2018) *PROMETHEUS Allgemeine Anatomie und Bewegungssystem: LernAtlas der Anatomie*. Stuttgart: Georg Thieme Verlag.

Sekuboyina, A., Husseini, M. E., Bayat, A., Löffler, M., Liebl, H., Li, H., et al. (2021). VerSe: a Vertebrae labelling and segmentation benchmark for multi-detector CT images. *Med. Image Anal.* 73, 102166. doi:10.1016/j.media.2021.102166

Simo, J. C., and Taylor, R. L. (1991). Quasi-incompressible finite elasticity in principal stretches. Continuum basis and numerical algorithms. *Appl. Mech. Eng.* 85, 273–310. doi:10.1016/0045-7825(91)90100-k

Simón-Allué, R., Calvo, B., Oberai, A. A., and Barbone, P. E. (2017). Towards the mechanical characterization of abdominal wall by inverse analysis. *J. Mech. Behav. Biomed. Mater* 66, 127–137. doi:10.1016/j.jmbbm.2016.11.007

Snedeker, J. G., Barnstuble, B. B., Iaizzo, P. A., Farshad, M., Niederer, P., and Schmidlin, F. R. (2007). A comprehensive renal injury concept based on a validated finite element model of the human abdomen. *J. Trauma* 62, 1240–1249. doi:10.1097/01.ta.0000215531.05677.19

Solav, D., Moerman, K. M., Jaeger, A. M., Genovese, K., and Herr, H. M. (2018). MultiDIC: an open-source toolbox for multi-view 3D digital image correlation. *IEEE Access* 6, 30520–30535. doi:10.1109/ACCESS.2018.2843725

Song, C., Alijani, A., Frank, T., Hanna, G., and Cuschieri, A. (2006). Elasticity of the living abdominal wall in laparoscopic surgery. *J. Biomechanics* 39, 587–591. doi:10.1016/j.jbiomech.2004.12.019

Standring, S., Ananad, N., and Gray, H. (2016). *Gray's anatomy: the anatomical basis of clinical practice* (Philadelphia, Pa: Elsevier).

Stokes, I. A., Gardner-Morse, M. G., and Henry, S. M. (2010). Intra-abdominal pressure and abdominal wall muscular function: spinal unloading mechanism. *Clin. Biomech. (Bristol, Avon)* 25, 859–866. doi:10.1016/j.clinbiomech.2010.06.018

Szepietowska, K., Troka, M., Lichodziejewska-Niemierko, M., Chmielewski, M., and Lubowiecka, I. (2023). Full-field *in vivo* experimental study of the strains of a breathing human abdominal wall with intra-abdominal pressure variation. *J. Mech. Behav. Biomed. Mater* 147, 106148. doi:10.1016/j.jmbbm.2023.106148

Szymczak, C., Lubowiecka, I., Tomaszewska, A., and Smietański, M. (2012). Investigation of abdomen surface deformation due to life excitation: implications for implant selection and orientation in laparoscopic ventral hernia repair. *Clin. Biomech. (Bristol, Avon)* 27, 105–110. doi:10.1016/j.clinbiomech.2011.08.008

Tay, B. K., Kim, J., and Srinivasan, M. A. (2006). *In vivo* mechanical behavior of intra-abdominal organs. *IEEE Trans. Biomed. Eng.* 53, 2129–2138. doi:10.1109/TBME.2006.879474

Tayebi, S., Gutierrez, A., Mohout, I., Smets, E., Wise, R., Stiens, J., et al. (2021). A concise overview of non-invasive intra-abdominal pressure measurement techniques: from bench to bedside. *J. Clin. Monit. Comput.* 35, 51–70. doi:10.1007/s10877-020-00561-4

Todros, S., Cesare, N. de, Concheri, G., Natali, A. N., and Pavan, P. G. (2020). Numerical modelling of abdominal wall mechanics: the role of muscular contraction and intra-abdominal pressure. *J. Mech. Behav. Biomed. Mater* 103, 103578. doi:10.1016/j.jmbbm.2019.103578

Todros, S., Cesare, N. de, Pianigiani, S., Concheri, G., Savio, G., Natali, A. N., et al. (2019). 3D surface imaging of abdominal wall muscular contraction. *Comput. Methods Programs Biomed.* 175, 103–109. doi:10.1016/j.cmpb.2019.04.013

Tran, D., Mitton, D., Voirin, D., Turquier, F., and Beillas, P. (2014). Contribution of the skin, rectus abdominis and their sheaths to the structural response of the abdominal wall *ex vivo*. *J. Biomechanics* 47, 3056–3063. doi:10.1016/j.jbiomech.2014.06.031

Tran, D., Podwojewski, F., Beillas, P., Ottenio, M., Voirin, D., Turquier, F., et al. (2016). Abdominal wall muscle elasticity and abdomen local stiffness on healthy volunteers during various physiological activities. *J. Mech. Behav. Biomed. Mater* 60, 451–459. doi:10.1016/j.jmbbm.2016.03.001

Untaroiu, C. D., Pak, W., Meng, Y., Schap, J., Koya, B., and Gayzik, S. (2018). A finite element model of a midsize male for simulating pedestrian accidents. *J. Biomech. Eng.* 140. doi:10.1115/1.4037854

Valliere, M. J., Wall, P. L., and Buising, C. M. (2018). From pull to pressure: effects of Tourniquet buckles and straps. *J. Am. Coll. Surg.* 227, 332–345. doi:10.1016/j.jamcollsurg.2018.06.005

van Loocke, M., Lyons, C. G., and Simms, C. K. (2006). A validated model of passive muscle in compression. *J. Biomechanics* 39, 2999–3009. doi:10.1016/j.jbiomech.2005.10.016

van Ramshorst, G. H., Lange, J. F., Goossens, R. H. M., Agudelo, N. L., Kleinrensink, G. J., Verwaal, M., et al. (2008). Non-invasive measurement of intra-abdominal pressure: a preliminary study. *Physiol. Meas.* 29, N41–N47. doi:10.1088/0967-3334/29/8/N01

van Ramshorst, G. H., Salih, M., Hop, W. C. J., van Waes, O. J. F., Kleinrensink, G.-J., Goossens, R. H. M., et al. (2011). Noninvasive assessment of intra-abdominal pressure by measurement of abdominal wall tension. *J. Surg. Res.* 171, 240–244. doi:10.1016/j.jss.2010.02.007

Van Sint Jan, S. L. (2007) *Color atlas of skeletal landmark definitions: guidelines for reproducible manual and virtual palpations*. Edinburgh, New York: Churchill Livingstone.

Viano, D. C. (1989). Biomechanical responses and injuries in blunt lateral impact. *SAE Trans.* 98, 892432–901719. doi:10.4271/892432

Wang, X., He, K., Zhu, Y., Fu, X., Huang, Z., Ding, R., et al. (2020). Use of shear wave elastography to quantify abdominal wall muscular properties in patients with incisional hernia. *Ultrasound Med. Biol.* 46, 1651–1657. doi:10.1016/j.ultrasmedbio.2020.03.027

Wang, X., Savonnet, L., Theodorakos, I., Beurier, G., and Duprey, S. (2019). "Biomechanical human models for seating discomfort assessment," in *DHM and posturography*. Editor S. Scataglini (San Diego: Elsevier Science and Technology), 643–656.

Wells, P. N. T., and Liang, H.-D. (2011). Medical ultrasound: imaging of soft tissue strain and elasticity. *J. R. Soc. Interface* 8, 1521–1549. doi:10.1098/rsif.2011.0054

Wolf, A., Miehling, J., and Wartzack, S. (2020a). Challenges in interaction modelling with digital human models – a systematic literature review of interaction modelling approaches. *Ergonomics* 63, 1442–1458. doi:10.1080/00140139.2020.1786606

Wolf, A., Miehling, J., and Wartzack, S. (2020b). Elementary affordances: a study on physical user-product interactions. *Procedia CIRP* 91, 621–626. doi:10.1016/j.procir.2020.02.220

Yu, W., Li, Y., Zheng, Y.-P., Lim, N. Y., Lu, M. H., and Fan, J. (2006). Softness measurements for open-cell foam materials and human soft tissue. *Meas. Sci. Technol.* 17, 1785–1791. doi:10.1088/0957-0233/17/7/017

Zhang, M., Zheng, Y.-P., and Mak, A. F. (1997). Estimating the effective Young's modulus of soft tissues from indentation tests—nonlinear finite element analysis of effects of friction and large deformation. *Med. Eng. Phys.* 19, 512–517. doi:10.1016/S1350-4533(97)00017-9

frontiers | Frontiers in Bioengineering and Biotechnology

TYPE Systematic Review
PUBLISHED 11 June 2024
DOI 10.3389/fbioe.2024.1386874

OPEN ACCESS

EDITED BY
Fuyou Liang,
Shanghai Jiao Tong University, China

REVIEWED BY
Michel Mesnard,
Université de Bordeaux, France
Wenxin Niu,
Tongji University, China

*CORRESPONDENCE
Iris Wechsler,
wechsler@mfk.fau.de

RECEIVED 16 February 2024
ACCEPTED 21 May 2024
PUBLISHED 11 June 2024

CITATION
Wechsler I, Wolf A, Shanbhag J, Leyendecker S, Eskofier BM, Koelewijn AD, Wartzack S and Miehling J (2024), Bridging the sim2real gap. Investigating deviations between experimental motion measurements and musculoskeletal simulation results—a systematic review.
Front. Bioeng. Biotechnol. 12:1386874.
doi: 10.3389/fbioe.2024.1386874

Bridging the sim2real gap. Investigating deviations between experimental motion measurements and musculoskeletal simulation results—a systematic review

Iris Wechsler[1]*, Alexander Wolf[1], Julian Shanbhag[1], Sigrid Leyendecker[2], Bjoern M. Eskofier[3], Anne D. Koelewijn[3,4], Sandro Wartzack[1] and Jörg Miehling[1]

[1]Engineering Design, Department of Mechanical Engineering, Friedrich-Alexander-Universität Erlangen-Nürnberg, Erlangen, Germany, [2]Institute of Applied Dynamics, Department of Mechanical Engineering, Friedrich-Alexander-Universität Erlangen-Nürnberg, Erlangen, Germany, [3]Machine Learning and Data Analytics Lab, Department Artificial Intelligence in Biomedical Engineering (AIBE), Friedrich-Alexander-Universität Erlangen-Nürnberg, Erlangen, Germany, [4]Chair of Autonomous Systems and Mechatronics, Department of Electrical Engineering, Friedrich-Alexander-Universität Erlangen-Nürnberg, Erlangen, Germany

Musculoskeletal simulations can be used to estimate biomechanical variables like muscle forces and joint torques from non-invasive experimental data using inverse and forward methods. Inverse kinematics followed by inverse dynamics (ID) uses body motion and external force measurements to compute joint movements and the corresponding joint loads, respectively. ID leads to residual forces and torques (residuals) that are not physically realistic, because of measurement noise and modeling assumptions. Forward dynamic simulations (FD) are found by tracking experimental data. They do not generate residuals but will move away from experimental data to achieve this. Therefore, there is a gap between reality (the experimental measurements) and simulations in both approaches, the sim2real gap. To answer (patho-) physiological research questions, simulation results have to be accurate and reliable; the sim2real gap needs to be handled. Therefore, we reviewed methods to handle the sim2real gap in such musculoskeletal simulations. The review identifies, classifies and analyses existing methods that bridge the sim2real gap, including their strengths and limitations. Using a systematic approach, we conducted an electronic search in the databases Scopus, PubMed and Web of Science. We selected and included 85 relevant papers that were sorted into eight different solution clusters based on three aspects: how the sim2real gap is handled, the mathematical method used, and the parameters/variables of the simulations which were adjusted. Each cluster has a distinctive way of handling the sim2real gap with accompanying strengths and limitations. Ultimately, the method choice largely depends on various factors: available model, input parameters/variables, investigated movement and of course the underlying research aim. Researchers should be aware that the sim2real gap remains for both ID and FD approaches. However, we conclude that multimodal approaches tracking kinematic and dynamic measurements may be one possible solution to handle the sim2real gap as

methods tracking multimodal measurements (some combination of sensor position/orientation or EMG measurements), consistently lead to better tracking performances. Initial analyses show that motion analysis performance can be enhanced by using multimodal measurements as different sensor technologies can compensate each other's weaknesses.

KEYWORDS

systematic review, biomechanical modeling and simulation, sim2real gap, data tracking methods, residual minimisation, inverse dynamics, forward dynamic simulations

1 Introduction

In the virtual world, individuals are depicted by digital human models. The models can be used to simulate human properties and skills (Bullinger-Hoffmann and Mühlstedt, 2016). Musculoskeletal models are digital human models used to determine a person's internal dynamic state. They depict the human body as a multi-body system and consist of rigid bodies, joints and muscles. The models can be used to compute biomechanical parameters like muscle forces, joint torques and joint reaction forces non-invasively. Musculoskeletal simulations can address research questions that are difficult to address (well) with direct measurements, either due to the definition of the variable of interest (such as center of mass) or ethical reasons. Musculoskeletal simulations have been used in the medical context to simulate the effect of muscle or tendon surgeries (Herrmann and Delp, 1999) or to investigate abnormal gait (Arnold et al., 2005; Higginson et al., 2006; John et al., 2013). The simulations have become more prevalent in various fields, including product development and human factors engineering. For example, they have been used to aid in the development of exoskeletons (Ferrati et al., 2013; Uchida et al., 2016; Molz et al., 2022), optimize worker movement at workstations (Maurice et al., 2019), and enhance the ergonomic design of products (Rasmussen et al., 2012; Jeang et al., 2018).

The general differential equation of motion is the basis for dynamics simulations of human motion

$$M(q)\ddot{q} + C(q,\dot{q})\dot{q} + G(q) - A\tau - J^T(q)F_{ext} = 0$$

where $q, \dot{q}$ and $\ddot{q}$ describe the generalized coordinates, velocities and accelerations, respectively. For the most part, generalized coordinates describe joint angles which depict the pose of the human. Additional generalized coordinates define the position and orientation of the model's root segment (usually the trunk or pelvis) in space. M is the mass/inertia matrix dependent on the joint angles. C denotes the centrifugal/coriolis matrix, dependent on joint angles and velocities. G is the gravity matrix, dependent on the joint angles. $J^T(q)F_{ext}$ describes external forces using the Jacobian. τ describes joint moments and A is the coefficient matrix that converts joint torques to segment torques.

The general differential equation of motion can be formulated in two ways. It can either solve the equations of motion for the joint moments, called inverse dynamics (ID). For this, the generalized coordinates and external forces are needed as input. Or it can solve the equations of motion for the generalized accelerations using joint torques or muscle activations and external forces as input, called forward dynamics (FD). ID is part of the conventional musculoskeletal simulation workflow consisting of inverse kinematics (IK), ID and static optimization. IK computes the motion of the model, expressed in generalized coordinates, based on experimental measurements of body motion. ID uses the output of IK and measured external forces (e.g., ground reaction forces, GRFs) to compute corresponding joint loads. Static optimization computes muscle activations and muscle forces based on the output of ID. FD uses joint torque trajectories as input to generate body motions. Alternatively, muscle activation patterns, which in turn result in joint torques by using muscle models, can be used as input. An FD simulation problem can be solved using an open-loop optimal control problem also known as trajectory optimization (Chao and Rim, 1973; Anderson and Pandy, 2001).

However, since simulations are always simplifications of reality, errors are present in the outputs of ID and FD, which display in different ways. In ID, these errors show up as residual forces and torques (residuals). These residuals show up in the equations of motion for the generalized coordinates for which no input is available, specifically the degrees of freedom that define the position and orientation of the reference segment, typically the trunk, in space. Residuals occur because the model is expected to perform motions and produce forces that it did not perform and cannot produce by definition. This is because the dynamic model of the model is fundamentally different from the dynamics of the real system (the human). Hatze (2002) called this the fundamental problem of musculoskeletal simulations. External and inertial forces and torques are not in balance. Residuals are needed to dynamically balance the simulation (Reinbolt et al., 2011; Hicks et al., 2015) to ensure that the kinematic trajectory of the system's center of mass is physically consistent with experimentally measured GRFs (Werling et al., 2023). In contrast, such residuals are not present in FD, since the dynamics of the musculoskeletal model are followed by definition. Instead, the joint angles will be different to those calculated with IK, and have a larger deviation from the measured data. IK mostly uses optimizations to calculate joint angles by finding the best match between experimental marker positions and virtual markers placed on the model for every time step. This is then called kinematic tracking, as the model tracks the experimental data.

This review focuses on musculoskeletal simulations which analyze/track experimental data. Pure FD simulations not considering experimental data, or using experimental data only for generating an initial guess, are excluded. This article focuses on the analysis of measured motion rather than producing predictions of motion, which is the focus of these simulations.

To achieve reliable simulation results, a model that is as well adapted as possible to the individual person is a prerequisite. Model

individualization methods are used to adjust a generic musculoskeletal model to best fit measurements (e.g., marker positions in static pose or segment lengths) taken from the person. Despite this individualization process, deviations between reality and the simulation will remain. We call this deviation the sim2real gap.

The sim2real gap has two error components: the kinematic and the dynamic error. The kinematic error is the difference between joint angles of the real human and the model. As the true joint angles are usually not measurable, the kinematic error can be expressed by the sum of squared differences between measured and simulated marker trajectories or sensor positions/orientations. Kinematic errors stem from experimental errors like noisy position, orientation or acceleration measurements and soft tissue artifacts (STAs). Those experimental errors are especially crucial, since the computation of joint velocity and joint acceleration through numerical differentiation leads to an amplification of those errors (Kuo, 1998). Furthermore, despite the model individualization process, there are kinematic differences between the human and the models, such as deviations of joint axes or joint rotation centers and deviating body segment dimensions. These differences also contribute to the kinematic error. The dynamic error is the difference between joint moments, muscle activity patterns and external loads of the real human and the model. As the true joint moments are not measurable, the dynamic error can be expressed by the residuals, differences in muscle activity patterns or external loads. For FD approaches, residuals cannot be observed as they are not generated. The dynamic error arises due to discrepancies between the musculoskeletal model and the human body, such as body segment inertial parameters (BSIPs) and muscle parameters, inaccurate external load measurements, and the propagation of the kinematic error. BSIPs include the mass, position of center of mass and inertia. Despite previous model individualization, deviations between BSIPs and muscle parameters still occur due to modeling assumptions or inaccurate model parameters. BSIPs and muscle parameters are not precisely known and without the use of medical imaging methods (e.g., MRI), they can only be computed using regression equations based on cadaveric measurements (Leva, 1996) or geometric approaches (Hatze, 1980).

In this review, the sim2real gap is investigated separately from model-person consistency, which describes the consistency between musculoskeletal models and their real-life counterparts. While model person consistency does influence the sim2real gap–especially because of the influence of BSIPs–integrating model individualization methods goes beyond the scope of this review.

As musculoskeletal simulation results are used to answer (patho-) physiological research questions, simulation results should be accurate and reliable. In general, four comparative values are analyzed to evaluate simulation results. For the kinematic assessment, the level of deviations between measured and estimated marker trajectories or sensor positions/orientations are analyzed. For the dynamic assessment, the size of residuals, or the deviation between measured and estimated muscle activity patterns or external load measurements can be analyzed. These comparative values can be analyzed for both ID and FD approaches. For ID approaches, Hicks et al. (2015) presented recommendations for verification and validation measures. For marker trajectories, the overall root mean square error (RMSE) should be within the measurement error. Maximum residual forces and torques are considered valid, if the residual forces are less than 5% of the magnitude of the net external force and the residual torques are less than 1% the magnitude of net external forces multiplied by the center of mass height. Relatedly, Gupta et al. (2022) presented a physics informed approach for calculating maximum residual force/torque values. They reported maximum residual value ranges that are mostly more restrictive than the recommendations given by Hicks et al. (2015). For FD approaches, no specific recommendations exist. However, if the simulation results deviate significantly from the measurement data or IK results, it is questionable whether they should then still be used to answer research questions based on measured motion data, because of the large sim2real gap.

Consequently, for accurate and reliable simulation results, solution strategies are needed to handle the sim2real gap. Begon et al. (2018) carried out a systematic review and presented existing IK methods to compensate the effect of STAs. These methods minimize the kinematic error. Publications that were included in their work are not further analyzed in our review. To handle the dynamic error in musculoskeletal simulations, different methods have been proposed. Vaughan et al. (1982) optimized BSIPs based on kinematic data and optimization theory by minimizing the difference between measured and calculated GRFs. Riemer and Hsiao-Wecksler (2009) extended this approach by optimizing both segment-angle trajectories and BSIPs to minimize the difference between measured and calculated GRFs. Thelen and Anderson (2006) implemented a proportional-differential (PD) controller to minimize residuals for walking simulations by adjusting pelvic translations and lower back angular trajectories and van den Bogert et al. (2011) used trajectory optimization to track experimentally measured motion data without generating residuals. However, no comprehensive overview of available methods exists describing how to handle the sim2real gap in musculoskeletal simulation by minimizing both kinematic and dynamic errors to achieve reliable and accurate simulation results. Therefore, we conducted a systematic literature search to identify, classify and analyze existing methods that handle the sim2real gap in musculoskeletal simulations. Our research questions are:

RQ1: Which solution approaches exist to handle the sim2real gap in the field of musculoskeletal simulations?

We give readers an overview of available methods using both the ID and FD simulation approach that can be used to handle the sim2real gap in musculoskeletal simulations.

RQ2: What is the primary goal of the identified methods and which strengths and limitations do they have?

We describe strengths and limitations of the methods to help researchers decide which approach is most appropriate for their particular research question. In addition, we analyze if methods exist that are able to handle the sim2real gap for any arbitrary model, input parameters and investigated movements without deviation from experimental data.

This review is intended for both beginner and more experienced researchers in the field of biomechanical simulations. Beginners who are just starting out with biomechanical modeling and simulations are given a comprehensive explanation of the sim2real gap as well as an overview of possible simulation methods that are generally used in this field. More experienced researchers who are concerned about the sim2real gap of their simulation results can use the overview of identified methods to decide which method would be best for answering their individual research question.

2 Survey methodology

This review was planned following the PRISMA-P 2015 checklist (Moher et al., 2015). We followed a systematic approach to identify relevant literature. An electronic search was performed in the databases Scopus, PubMed and Web of Science (cut-off date: 24 January 2024), followed by a manual screening and selection process. Results were first screened by title and abstract. After that a full-text screening was performed to determine eligibility. Documents of the types *article* and *review* in English language were considered. Further limitations were chosen for every database based on available limitation criteria. For Scopus, the search string was applied to title, abstract and keywords. The results were limited to the following search categories: Engineering, Medicine, Computer Science, Mathematics, Physics and Astronomy, Multidisciplinary. For Web of Science, the search was performed on all fields for the Web of Science Core Collection. No further limitations were chosen. For PubMed, the search was performed only on title and abstract as there was no option to search keywords. As our goal was to identify methods that handle the sim2real gap, we applied a comprehensive search string:

(("musculoskel*") OR ("musculo-skel*") OR ("biomechan*") OR ("anthropo*") OR ("digital human")) AND (("model*")) AND (("kinemat*") OR ("dynam*") OR (" kinet*")) AND (("method*") OR ("approach*") OR ("framework*") OR (" algorithm*")) AND (("motion*") OR ("gait*") OR ("movement*")) AND (("error*") OR ("inconsisten*") OR ("miscalcu*") OR ("minim*") OR ("consisten*") OR ("incorrect*")) AND (("transfer*") OR ("track*") OR ("reconstruct*") OR ("optim*") OR ("simulation*") OR ("residual*"))

Search items included relevant terms like kinematic, dynamic, residuals, consistency and errors. We used a generic search string since the term *sim2real gap* is not an established term in the field of biomechanical simulations. Additionally, a backward search identifying further works was performed on identified relevant publications.

Results retrieved by the search string were appraised for significance according to specific inclusion and exclusion criteria, which were applied first to the title, then to the abstract, and then to the full-text. Papers describing methods handling the sim2real gap of musculoskeletal simulations using a physiological biomechanical model were included. These methods should compensate (or minimize) either the kinematic error, the dynamic error or both errors simultaneously. Papers describing model individualization methods as well as pure FD simulations that do not track experimental data are out of scope for this research and therefore excluded as this review focuses on handling the sim2real gap in musculoskeletal simulations to achieve accurate and reliable simulation results based on experimentally measured motion data. One author screened all records and decided whether a publication met the inclusion criteria. If the author was unsure whether or not to include the work, he consulted his co-authors. In the end, one other author checked all identified publications for eligibility.

To answer the aforementioned research questions the papers were analyzed according to the following aspects: problem formulation, input/output, model specifics, method evaluation, simulation software, states/controls, experimentally measured quantities and the primary goal of each method. No automation tools were used for this process. For every study, each aspect was analyzed and written in a spreadsheet. One author extracted the data. A second author checked the accuracy of the extracted data and the completeness of the spreadsheet.

To synthesise the data, the analyzed aspects were used to cluster the identified studies according to the way how the sim2real gap is handled, the mathematical method used, and the parameters/variables of the simulations which were adjusted which corresponds to RQ1.

3 Results

3.1 Search yield

Applying the search string to the three databases yielded 3,579 results. Figure 1 illustrates the identification and selection process. We used the aforementioned inclusion and exclusion criteria to exclude non-relevant publications. 1,550 duplicates were removed. After screening the results by title, 335 results remained. The abstract screening excluded a further 180 papers. In the end, 86 papers were excluded through full-text screening. In turn, 16 publications were added by performing backward search. Ultimately, 85 results fulfilled the criteria and thus were included in this review.

3.2 Identified solution approaches (RQ1)

We clustered relevant publications into eight general solution approaches (clusters), see Figure 2. These approaches differ in the way the sim2real gap is handled, which mathematical method is used and which parameters/variables of the musculoskeletal model or the simulation are adjusted to handle the sim2real gap. Table A1 in the Supplementary Material shows the cluster to which each publication is assigned. Each cluster is briefly described in terms of how the sim2real gap is handled. Furthermore, Table A2–Table A9 summarize, separately for each cluster, the proposed method. These tables include additional information for each cluster, including if and how the method was validated. If a marker-based motion tracking approach was used as reference, we stated that the method was validated using the standard approach. If the method was verified on synthetic data, we also indicated that. If it was not validated, we added information regarding the performance (e.g., kinematic RMSE) of the proposed method or information regarding the evaluation (e.g., residual size, comparison between measured and

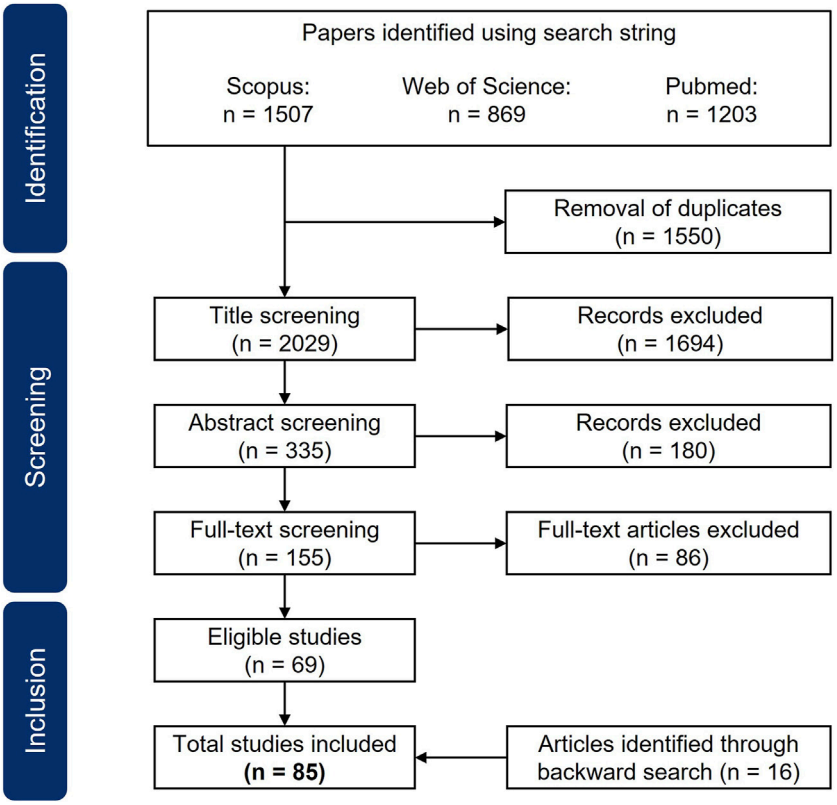

FIGURE 1
PRISMA flow diagram describing the literature search, identification, screening and selection process. The search string was applied to the three databases Scopus, Web of Science and Pubmed. It yielded 3579 results. The results were first screened by title, then by abstract and then the full-text was screened for eligibility using defined inclusion criteria. Backward search was performed on eligible results. In the end 85 papers were included in the review.

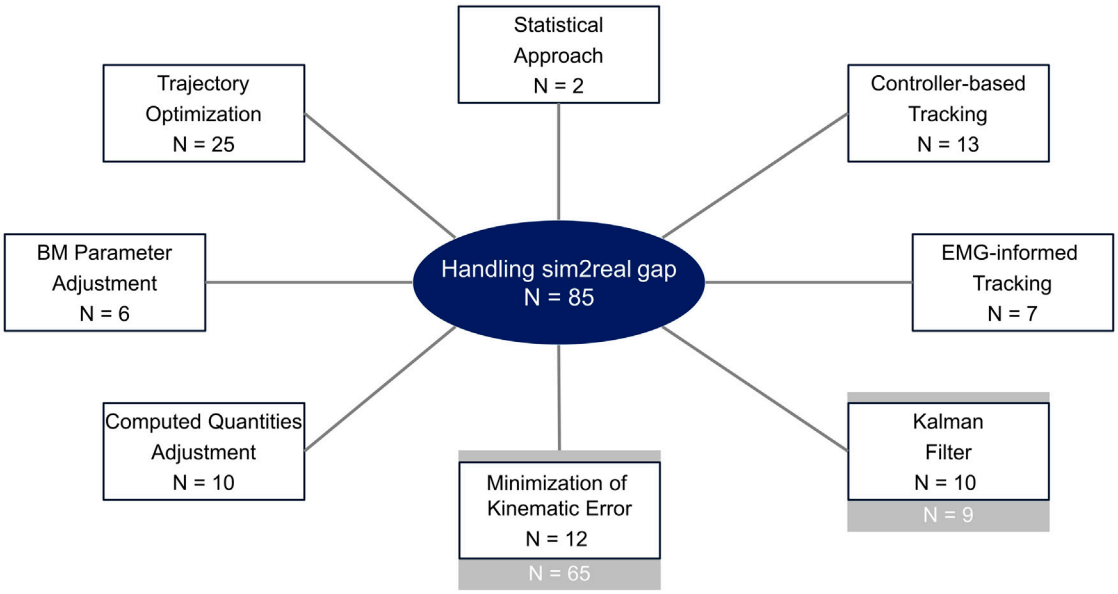

FIGURE 2
Relevant identified publications were sorted into eight different solution approaches (clusters). The approaches differ in three aspects: how the sim2real gap is handled, the mathematical method used and the parameters/ variables of the simulations which were adjusted. The grey boxes represent publications that were already analyzed by Begon et al. (2018) in their literature review regarding inverse kinematics methods. As these methods aim to minimize the kinematic error they also handle the sim2real gap.

computed GRFs) in the corresponding column. Table A10 in the Supplementary Material lists experimental measurements that were used in every publication.

Methods in the *minimization of kinematic error* cluster describe kinematic tracking methods that handle the sim2real gap by optimizing kinematic tracking performance. Based on the kinematic input being tracked, the methods either compensate noise and sensor drift (inertial measurement unit (IMU) -based methods), STAs (marker-based methods) or enhance the tracking performance by including joint constraints (depth camera-based methods). Method descriptions and information about kinematic inputs are listed in Table A2.

Methods included in the *BM parameter adjustment* cluster principally use the fact that the ID problem is overdetermined when both external forces and kinematics are measured. In this case, the sim2real gap is handled through optimization, where either BSIPs or marker positions are adjusted to reduce residuals. Method descriptions and information about optimized variables are listed in Table A3.

Methods included in the *computed quantities adjustment* cluster, generally use a similar approach like those of the *BM parameter adjustment* cluster. These methods also take advantage of the overdetermined nature of the ID approach to handle the sim2real gap. The difference between the two clusters are the input variables of the cost functions which are modified. Instead of optimizing BSIPs or marker positions, computed variables like joint angles, joint accelerations or muscle forces are adjusted. Method descriptions and information about optimized variables are listed in Table A4.

Another solution approach (cluster) is the implementation of a *Kalman Filter* to handle the sim2real gap for musculoskeletal simulations. In general, the Kalman Filter is a two-step prediction correction approach generating optimal state estimations based on erroneous measurements (Serra, 2018). It produces optimal estimates of a system state by averaging predicted and measured states using a weighted average. The covariance of both the system and the measurement noise is used to calculate the weight. Through this, random noise of measurement systems can be reduced. In case of biomechanical simulations, the state vector of the Kalman filter may include only kinematic parameters (e.g., joint angles). These approaches then minimize the kinematic error. The state vector can also include both kinematic and body segment parameters (Bonnet et al., 2017) or both kinematic and kinetic parameters (e.g., joint angles and muscle forces or joint torques) (Mohammadi et al., 2020). Or it can include uncertainty models of IMU-sensors to estimate the size of undesired errors (orientation errors, gyroscope bias and magnetic disturbances) to compensate these (Yuan et al., 2019). The choice of the state vector variables mainly depends on the underlying study aim–minimization of the kinematic error or dynamic error. Method descriptions and state vector variables for every publication classified into this cluster are listed in Table A5.

Methods in the *trajectory optimization* cluster use both the FD and ID approach to generate biomechanical simulations. FD approaches generate simulations without residual forces and torques. For approaches using ID the dynamical constraints are loosened and residuals are set to some level of tolerance. In contrast to static optimization, trajectory optimization mostly considers muscle activation and deactivation dynamics and optimizes the movement over the whole time series. This way non-physiological jumps in position and acceleration data are prevented. This aspect applies for all papers included in this cluster. A subcategory of this cluster is called inverse dynamic optimal control. Inverse dynamic optimal control uses trajectory optimization to solve the muscle redundancy problem dynamically over time. It computes neural excitations that result in given joint torques, which were computed using ID. Thus, the methods produce motion simulations that are consistent with muscle dynamics but not necessarily consistent for the external forces. Table A6 lists method descriptions as well as information about the optimization variables as these differ.

Methods in the *electromyography (EMG)-informed tracking* cluster are multimodal motion tracking methods. They use cost functions which are extended by including EMG-measurements, as an expression of neural excitations, in addition to marker or joint angle trajectory tracking. All methods use trajectory optimization to solve a forward dynamic simulation problem to dynamically track both measurements. It is assumed that tracking both marker trajectories and EMG-measurements enhances accuracy and reliability of biomechanical simulation results (Bailly et al., 2021). Table A7 lists method descriptions as well as information about the optimization variables.

Methods in the *controller-based tracking* cluster use the FD approach. They handle the sim2real gap by applying a dynamic tracking approach. Next to kinematic parameters also dynamic parameters (e.g., muscle activations) are being tracked. However, a unique feature here is the implementation of feedback into musculoskeletal simulations. Additionally, some kind of controller is used to track specific input variables. The methods use the FD approach. This way no undesired residuals are generated. Most methods included in this cluster focus on enhancing accuracy of simulations in the field of gait analysis. Some methods focus on enhancing accuracy of simulations for wrist or arm movement. Table A8 lists method descriptions and information about the controller that was used.

The last cluster includes methods using *statistical approaches* for musculoskeletal simulations and to handle the sim2real gap. Instead of minimizing specific cost functions, as was the goal in all other clusters, statistical approaches try to estimate the most likely variable values (e.g., joint angles or joint loads) given a specific set of measured kinematic parameters (e.g., marker trajectories). Method descriptions and information regarding the statistical approach are listed in Table A9.

3.3 Primary goal in relation to handling the sim2real gap, strengths, and limitations of methods (RQ2)

The primary goal varies for all listed publications and methods. Some methods aim at tracking kinematic parameters as closely as possible and thus minimizing the kinematic error (Cesic et al., 2016; Begon et al., 2017; Bonnet et al., 2017; Joukov et al., 2017; Laidig et al., 2017; Schellenberg et al., 2017; Joukov et al., 2018; Niu et al., 2018; Tagliapietra et al., 2018; Pataky et al., 2019; Inai et al., 2020; Joukov et al., 2020; Price et al., 2020; Sy et al., 2020; Halilaj et al.,

2021; Sy et al., 2021; Al Borno et al., 2022; Lefebvre et al., 2023). Alternatively, the kinematic error can be minimized by compensating sensor noise and bias (e.g., sensor drift or magnetic disturbances) which affects methods using IMU-sensors for motion analysis (Cockcroft et al., 2014; Allen et al., 2017; Laidig et al., 2017). Some methods investigate if a multimodal motion analysis approach (combination of IMU-sensors with either RGB-video- or depth-camera) enhances tracking performance thus minimizing the kinematic error (Atrsaei et al., 2016; Halilaj et al., 2021; Pearl et al., 2023). Other methods explicitly aim to generate simulation results without undesired residuals (Vaughan et al., 1982; Koopman et al., 1995; Kuo, 1998; Cahouët et al., 2002; Mazzà and Cappozzo, 2004; Riemer et al., 2008; Remy and Thelen, 2009; Riemer and Hsiao-Wecksler, 2009; Jackson et al., 2015; Samaan et al., 2016; Faber et al., 2018; Muller et al., 2018; Noamani et al., 2018; Fritz et al., 2019; Pallarès-López et al., 2019; Sturdy et al., 2022; Werling et al., 2023). Certain methods primarily target a different goal than generating simulation results without residuals. The goal can be the estimation of most accurate muscle forces or torques (Chao and Rim, 1973; Koh and Jennings, 2003; Seth and Pandy, 2007; Morrow et al., 2014; Lv et al., 2016; Bélaise et al., 2018a; Bélaise et al., 2018b; Stanev and Moustakas, 2018; Moissenet et al., 2019; Bailly et al., 2021; Ceglia et al., 2023), the determination of joint torques or muscle excitations needed to generate desired movement (Kaplan and Heegaard, 2001; Thelen et al., 2003; Thelen and Anderson, 2006; Da Silva et al., 2008; Ghafari et al., 2009; Demircan et al., 2010; Watanabe and Sugi, 2010; Lin et al., 2018; Mouzo et al., 2018; Dorschky et al., 2019; Haralabidis et al., 2021; Wang et al., 2021; Wang et al., 2022) or the development of controllers to determine muscle activity that track desired movement (Yamaguchi and Zajac, 1990; Blana et al., 2009; Arash Haghpanah et al., 2022). Handling the sim2real gap is then a secondary achievement. Some publications investigate the effect of different computational choices on computation time (Falisse et al., 2019) or robustness of convergence (Neptune, 1999; Febrer-Nafría et al., 2020). Others aim at predicting human motion (van den Bogert et al., 2011; van den Bogert et al., 2012; Meyer et al., 2016; Nitschke et al., 2020; Febrer-Nafría et al., 2022). Neptune and Hull (1998) developed a musculoskeletal model and optimization framework to best reproduce some specific movement and Nitschke et al. (2023) developed an approach for analyzing arbitrary three-dimensional motions using optimal control simulations by directly tracking marker trajectories and GRFs. Since the solution strategies (clusters) all differ quite extensively in how the authors (attempt to) handle the sim2real gap, all strategies have various limitations and potentials which are described below.

Methods in the *BM parameter adjustment* cluster complement the standard workflow consisting of model scaling, IK and ID as an extension but there is a risk that calculated parameters could be overfitted or unrealistic. Measures should be taken to prevent this (constraining the solution space). The methods are not limited to certain motions even though initially measurements of specific movements are required to adjust the BSIPs. The following limitations are associated with these methods. Although modeling errors are corrected, model assumptions (e.g., missing model segments) cannot be compensated. Furthermore, several assumptions are made which reduce the validity of computed results: bilateral symmetry, error-free measured kinematics and use of a correct objective function. The methods imply that all residuals stem only from inaccurate BSIPs. This assumption leads to the estimation of values that minimize a specific cost function but do not have to be equal to the real value. Muller et al. (2017) even state that an optimization of BSIPs based on the difference between calculated and measured GRFs is not necessary as the risk of overfitting cannot be avoided.

The work of Werling et al. (2023) is an exception to the points previously discussed. The paper presents *AddBiomechanics*, an online tool that enables the computation of motion dynamics analysis in an automated and standardized way. Marker trajectories are tracked as close as possible by optimizing joint angles, body segment parameters as well as model marker positions simultaneously. Additionally, the model's center of mass and rotational generalized coordinates of the model's root segment are adjusted to be consistent with experimentally measured GRFs. Therefore, the residuals are not assumed to be solely generated by either erroneous kinematics or BSIPs. Variables of both entities are adjusted to handle the sim2real gap without deviating too much from the kinematic input data. Nevertheless, there are still limitations. A statistical prior model is used to optimize the body segments. This prior model is based on population data of active-duty military personnel (men and women) and is therefore not reflective of the broad population. The authors state that the method may then choose body segment parameters for fitting to the marker data that are more in line to the parameters in the prior model, even though the "true" parameters are different. Additionally, the optimizer prioritizes solutions that move anatomical markers as little as possible. If the experimental markers have not been labelled correctly, this could lead to the estimation of incorrect joint angles and the model marker positions on the input model would have to be adjusted accordingly to compensate this.

Strengths and limitations of methods in the *computed quantities adjustment* cluster are similar to aspects described in the previous paragraph. The methods significantly minimize residuals but a risk of overfitting or computing unrealistic parameter values remains. One strength is that it is possible to constrain optimization parameters into physiologically reasonable ranges, as done by Riemer and Hsiao-Wecksler (2009), to prevent the estimation of unrealistic parameter values. Computed parameters are assumed to be inaccurate due to measurement noise and STAs. Different kind of errors can be compensated depending on the described method. Cahouët et al. (2002) compensate derivation errors in joint accelerations. Koopman et al. (1995) compensate errors stemming from both measurement and model segment estimation errors, whereas Kuo (1998) compensates the effect of noise on position data. While this does reduce the size of residuals in the simulation, the compensation is done by deviating from the experimental data. The assumptions made in these methods, however, limit the validity of the computed results. In most publications BSIPs and GRFs are assumed to be error-free and it is assumed that residuals stem only from inaccurate kinematic parameters. Accordingly, risk of overfitting towards the model cannot be avoided. Bonnet et al. (2017) explicitly state that unrealistic accelerations may be generated since an optimization algorithm compensates for various error types and not only for differentiation errors as intended in the work of Cahouët et al.

(2002) and Kuo (1998). In addition, some methods were developed for analyzing only one specific movement and thus are not universally applicable.

Using *trajectory optimization* to determine biomechanical parameters can lead to simulation results without residuals. However, to achieve this, simulation results will move away from marker trajectories, IMU sensor measurements or IK results. In general, the cluster has a couple of strengths. The variables are optimized dynamically over time. This way, non-physiological joint angle, velocity and acceleration trajectories are avoided because muscle activation/deactivation dynamics are generally implemented. Methods in this cluster may generate simulation results without residuals as trajectory optimization is one possible way to solve FD and the simulations adhere to the laws of physics. Moreover, the methods are flexible. States, controls, constraints as well as the objective function can be chosen to reach a specific goal. Cost functions can be extended to not only track kinematic but also kinetic parameters (e.g., GRFs) to enhance convergence performance. If a foot-ground contact model is added, GRFs can be computed and compared to measurements. Thus, force plate measuring errors and modeling assumptions can be compensated through the adjustment of GRFs. The limitations for this solution approach include that measured motion data may be smoothed significantly in order to adhere to system dynamics. A further limitation is the high computation time and the amount of computational power that is required for solving forward dynamic formulations. The simulations may have problems to converge. This may be especially true for non-cyclic movements, as periodicity constraints can then not be applied. Furthermore, choosing optimal weights for the different terms of the objective function (tracking term, regularization term, smoothing term) is challenging. Additionally, trajectory optimization methods assume that the model BSIPs are accurate and do not get adjusted, only the system kinematics and forces are optimized. Applying trajectory optimization on three-dimensional models with many degrees of freedom and muscles significantly increases the complexity and therefore computation time increases and convergence becomes even more challenging. Error propagation occurs when joint angle trajectories are directly tracked, because the reference joint angle trajectories result from an IK which is error-prone. These erroneous joint angle trajectories are then used as reference for the simulation.

Using a *Kalman Filter* minimizes the kinematic error of simulation results as error models are used to compute optimized state estimations (e.g., marker positions, sensor positions or orientations). However, the quality of the optimized state vector estimations is restricted by the accuracy of the implemented error models. The *Kalman Filter* offers unique advantages when applied for musculoskeletal modeling and simulation since the method was specifically developed to enhance state estimations (originally position location) based on erroneous observations (Serra, 2018). Mohammadi et al. (2020) produced estimates that are both consistent with the system and the measurement model. They assumed that joint angle measurements are affected by white Gaussian noise; e.g., modelled as a normal probability distribution. This noise can then be compensated by the extended Kalman Filter because the explicit noise model is known. Analogous to the computed quantities adjustment cluster, state variables can be constrained to ensure feasible parameter values (Bonnet et al., 2017). Nevertheless, a Kalman Filter has many parameters that need to be set correctly, requiring expert knowledge. Covariances have to be known to compensate measuring noise and STAs cannot yet be compensated in contrast to white gaussian measurement noise since no coherent error model exists. Further, the Kalman Filter is currently mostly applied for simulating two-dimensional models (Bonnet et al., 2017; Mohammadi et al., 2020). Bonnet et al. (2017) state that, although possible, expanding their method to include three-dimensional model estimation would require significantly more parameters and could lead to redundancy problems. Moreover, for many publications, specific assumptions are taken to enhance or enable convergence: bilateral symmetry, constant acceleration or jerk, a fixed yaw angle or periodicity in gait. This significantly reduces the validity of presented methods.

Since all reviewed *EMG-informed tracking* methods use trajectory optimization as mathematical method, strengths and limitations are analogous to previously described aspects. Besides those aspects, it is advisable to track both EMG-measurements and marker trajectories because the measurements complement each other (Bélaise et al., 2018b) and minimize both the kinematic and dynamic error simultaneously. However, EMG-measurements are error prone and thus may restrict the significance for handling the sim2real gap. The methods enable the implementation of muscle co-contraction in musculoskeletal simulations in contrast to using cost functions minimizing the sum of squared muscle activity. Furthermore, overall muscle force estimation can be enhanced (Bailly et al., 2021; Ceglia et al., 2023). Main limitations for methods of this approach are challenges related to EMG measurements, which are often noisy, while physiological cross-talk cannot be avoided. Also, surface electrodes cannot be used to measure activity in deep muscles (Sartori et al., 2014). In addition, external disturbances may interfere with the measurements and lead to inaccurate values.

Controller-based tracking methods can generate simulation results without residuals but may move away from measured parameters to achieve this (Thelen and Anderson, 2006). The methods tend to not only model the human body, but also the control of the human nervous system by incorporating feedback in the simulation. Moreover, analogous to the *trajectory optimization* cluster, kinematic parameter trajectories (e.g., joint angles) remain physiologically feasible because muscle activation and deactivation mechanics are implemented. Controller-based tracking approaches may have problems to accurately track movements that are characterized by rapid acceleration changes (e.g., jumps or running) if the feedback gains are not implemented correctly (van der Kooij et al., 2001; Koelewijn and Ijspeert, 2020). Using sensory input, the healthy human body is able to react incredibly fast to disturbances like sudden imbalance in form of tripping while walking. In this case, the postural controller reacts immediately and tries to prevent the person from falling. While some controllers are somewhat/partly able to imitate measurements of human behavior after perturbations, it is not known if the model that is used (e.g., reflex controller or a PD controller) is analogous to the control as it happens in the human body. In addition, typical limitations which are associated with controllers can also occur, including instability and loss of control.

Statistical approaches minimize the kinematic error by maximizing a specific probability (e.g., maximum likelihood of a parameter's posterior distribution) instead of minimizing specific objective functions which leads to more accurate joint angle estimates in contrast to standard approaches (Pataky et al., 2019). However, the methods are restricted by convergence problems and the required high computational effort. Lv et al. (2016) generated a data-driven prior-model which uses known information from a motion database to constrain the solution space of the inverse dynamic problem. This way, ambiguity of human motion (e.g., during double stance phase of gait) gets reduced, which occurs when there is no information available regarding the distribution of the ground reaction forces between both legs. Generally, limitations for these approaches include that analogous to the Kalman Filter cluster, convergence problems may occur when implementing three-dimensional models. Pataky et al. (2019) introduced the Bayesian IK method and state that it is impracticable for more complex models with many degrees of freedom. Furthermore, significant computational power is needed and computation time is already high for two-dimensional analyses (Pataky et al., 2019). Moreover, since the method of Lv et al. (2016) is based on a database including specific motions, only the included motion types (walking, jumping, running, turning and hopping) can be accurately analyzed. Results for other movements (e.g., stair climbing) were not accurate. A generalization to related but nevertheless different movements is therefore not possible.

4 Discussion

The literature study revealed answers to the raised research questions which are summarised next.

RQ1: For the first research question, we investigated which methods exist to handle the sim2real gap in musculoskeletal simulations and found that the results could be classified into eight clusters: *minimization of kinematic error*, *BM-parameter adjustment, computed quantity adjustment, Kalman Filter, EMG-informed tracking, controller-based tracking, trajectory optimization* and *statistical approaches*. The clusters differ in the way the sim2real gap is handled.

RQ2: For the second research question, we investigated the primary goal of the methods regarding the way the sim2real gap is handled as well as strengths and limitations of each cluster. In short, every method has a distinctive primary goal. Every cluster has a distinctive way how to deal with the sim2real gap with accompanying potentials and limitations. We could not identify a specific solution approach that is able to generate consistent simulations without introducing residuals for any arbitrary model, input variables and investigated movement without deviating from the corresponding experimental data. At this point, the automated tool AddBiomechanics presented by Werling et al. (2023) seems to be the best solution for analyzing experimental kinematic and kinetic data using ID, as it optimizes both kinematic and kinetic input and estimated parameters to handle the sim2real gap. But the method is only able to analyze marker-based motion data. For FD, methods in the *EMG-informed tracking* cluster are very promising, as these methods handle the sim2real gap by minimizing both the kinematic and dynamic error simultaneously.

The majority of the reviewed methods was designed for specific movements like human gait (e.g., Koopman et al., 1995; Thelen and Anderson, 2006; Remy and Thelen, 2009). Thus, most of the methods are not suitable for handling the sim2real gap for arbitrary movements. Although some papers offer promising methods (e.g., Kalman Filter, Bayesian IK), the majority of these are implemented for two-dimensional models. Application to three-dimensional models would require considerably more computational power. Convergence and redundancy problems could also occur (Bonnet et al., 2017; Pataky et al., 2019). Some methods focus solely on one of the reasons contributing to the sim2real gap mentioned in the introduction (e.g., measurement noise, STAs or modeling errors). This mainly includes publications from the *BM parameter adjustment* and *computed quantities adjustment* clusters. These solution approaches are problematic since residuals describe how large the dynamic error of the sim2real gap is. Often, in an optimization, it is assumed that all error is due to either the measurements or the model. The assumed source is adapted to reduce or eliminate the residuals. However, this adaptation then includes the error from the other source. Consequently, in case of musculoskeletal simulations, parameter values (e.g., BSIP, joint angle, joint acceleration trajectories) which are generated by such an approach do not have to correspond to the real values. For methods included in these clusters, there is high risk of overfitting optimization parameters. In addition, the dynamic error of the simulation may be decreased after adjusting specific values to minimize residuals, but this does not necessarily enhance the validity of the simulation. In fact, the consistency between the BM and the corresponding person can even decrease. As a result, the sim2real gap increases and thus the reliability of the simulation decreases. One way to see this, is by analyzing an independent experimental measure, e.g., muscle activity, and compare this to the corresponding model output. Furthermore, in order to gain valid simulation results without residuals with these approaches, it should be known which part of residuals stems from which error (modeling or measurement error). As there is no way to determine this distribution it seems advisable to generate a model that represents a specific person as accurately as possible before trying to reduce residuals with other solution approaches. Methods using trajectory optimization generate simulation results without residuals by definition but may significantly move away from experimental data as model parameters do not get adjusted during the optimizations. This may be less relevant if the overall aim of the investigation is to predict either novel movements or to analyze the change biomechanical variables due to changing environment or product design (e.g., for the design of running shoes as in van den Bogert et al. (2012)). However, when analyzing experimental data, this approach may lead to solutions which are not reliable or accurate for the person initially measured. This aspect mainly depends on the chosen term weights of the optimization problem. A higher tracking weight can be chosen to force the simulation to track the input data more closely but then convergence problems may arise as the solver is not able to find a

solution. Analogous, *controller-based tracking* methods also generate simulation results without residuals and may move away from experimental measurement data so that the simulation adhere to system dynamics. However, the methods may be advantageous for tracking non-periodic data as no periodic constraints are defined to enhance convergence. *EMG-informed tracking* methods track both kinematic and dynamic variables, decreasing the kinematic and dynamic error simultaneously. Through this multimodal approach, the sim2real gap is handled in a more holistic approach.

Currently, there is no universal strategy to handle the sim2real gap for an arbitrary movement while using an arbitrary model and arbitrary motion data because the problem is extensive and complex. This is also emphasized by the diverse solution approaches (clusters) which were identified in this review. There is no consensus on which method is most appropriate for achieving reliable and accurate simulation results. Hicks et al. (2015) provide recommendations for reducing and minimizing residuals in case the ID approach is used. This includes carefully executing pre-processing steps. Data collection should be well prepared and the calibration procedure should be performed diligently. Furthermore, the model should be scaled properly. If residuals are still large, parameters like inertia values or kinematics can be adjusted. These recommendations are in accordance to clusters identified in this review (*BM parameter adjustment* and *computed quantities adjustment*) and to suggestions that Hatze proposed in his work in (2002) in which he described the fundamental problem of myoskeletal inverse dynamics. He implied that sufficiently complex musculoskeletal models as well as error reduction in data measuring and processing methods are necessary to improve the accuracy of computed joint torques using ID. Analogous, Riemer et al. (2008), Riemer and Hsiao-Wecksler (2009) and Gupta et al. (2022) show that residuals have an effect on computed joint torques. In case a full-body model is used for an analysis, researchers have to take care that their residuals are not larger than values that are recommended by Gupta et al. (2022). Otherwise, the computed joint torques are neither accurate nor reliable (and should not be taken as a basis for answering (patho-) physiological questions). The online tool *AddBiomechanics,* presented by Werling et al. (2023) seems to be the most sophisticated and also holistic approach to handle the sim2real gap using the ID approach. As both kinematic and kinetic input and estimated parameters are optimized to achieve minimum residuals, this framework is consistent with the solution strategies identified in this review.

However, the aforementioned proposed recommendations apply only for ID approaches. For FD approaches used to analyze experimentally measured motion data, no specific recommendations are given in the literature on how to handle the sim2real gap. In this review this includes the *trajectory optimization*, *controller-based tracking* and *EMG-informed tracking* clusters. FD approaches generate no residuals by definition but to achieve this, the simulation may move far away from experimental measurements or IK results and the larger the sim2real gap again becomes. Researchers using FD to analyze experimental measurement data should keep this in mind if they plan to use the simulation results to answer (patho-) physiological research questions.

At this point it should be mentioned that achieving simulation results without generating residuals is not necessary or should not be tried to achieve in any case. If there was a theoretically perfect model of a person available the remaining inconsistency would stem solely from the measurement errors and could then be eliminated using a FD approach. Since perfect, fully comprehensive models are not possible to achieve, each model is only an abstraction depicting a real person in more or less detail. Based on the idea that a simulation conducted with a perfect model generates no modeling errors, one can argue that the more accurate the model is, the fewer modeling errors are expected. Greater modeling errors would be assumed when using partial models in comparison to using full-body models. For this reason, it is not appropriate to strive for handling or closing the sim2real gap when a partial model of the human body is used. Researchers have to take care how much they should strive for minimizing the kinematic and dynamic error given the accuracy of the model they use. The less complex a model is, the less clear it will be which part of the residuals is generated by each error source (modeling or measurement error). Minimization of residuals is then not advisable. On the contrary, van den Bogert and Su (2008) state that in this case, and on the condition that full ground reaction force measurements are available, more reliable ID results can be generated when the upper-body is not included because its motion cannot be measured reliably and minimizing residuals would thus introduce errors in the simulation results.

We described in the previous paragraph that removing residuals is not recommended for any model. In these cases, the size of residuals can also not be used to validate a musculoskeletal simulation as proposed by Hicks et al. (2015) and Gupta et al. (2022). Validating musculoskeletal simulation results remains a challenge because the ground truth can never be known. As optical marker tracking is the gold standard for motion capture, new measurement and simulation methods are validated using this approach. Nevertheless, the gold standard is also prone to both modeling errors and measurement noise. When a new method produces results that differ from the gold standard solution, it is hard to determine whether the results are worse or better than the gold standard approach. The problem that remains is that it is not possible to perform measurements to separate model and measurement errors. Both errors occur simultaneously and cannot be eliminated beforehand so that only one error remains. Using synthetic data (e.g., generated using optimal control) is another way to validate novel approaches. A limitation of this approach lies within the aspect that measurement noise (especially STAs) cannot yet be simulated correctly. Up to now, validation remains a key challenge of musculoskeletal simulations.

Bailly et al. (2021) hypothesise, that tracking multimodal motion measurement can lead to smaller kinematic errors, thus handling the sim2real gap. The papers we reviewed which tracked multimodal motion measurement data supported this hypothesis. Each paper sorted into the *EMG-informed tracking* cluster uses a multimodal motion measurement and tracking approach. Kinematic errors were reported to be decreased using this approach in every publication but one. Mallat et al. (2021), categorised into the *Kalman Filter* cluster, fused RGB camera data and IMU sensor data to track human gait. They hypothesise that through this approach, individual weaknesses (marker occlusion and sensor drift) of the two measurement and sensor technologies compensate each other. Analogous, Pearl et al. (2023) fused camera and IMU data to track human gait. But instead of using a Kalman Filter, the

authors used dynamic optimization to analyze experimentally measured motion. This multimodal approach outperformed single-modality approaches (using either only IMU or video data for human motion analysis). Halilaj et al. (2021) used both RGB camera data and IMU data in combination with a statistical shape model. Both the shape and the pose of the statistical shape model are optimized so that model joint centers best match estimated joint centers identified using the RGB camera. IMU and video data is then fused by adding an error term in the optimization minimizing the difference between video-based angular velocity and angular velocity values measured by the IMU sensors. Analogous to the results reported by Mallat et al. (2021), motion analysis performance was enhanced as the sensor technologies compensate each other's weaknesses. Atrsaei et al. (2016) fused depth-camera data and IMU sensor data to track human arm motion. Again, the sensor fusion led to a decrease of the kinematic error. This is in line with a proposal we made in a prior publication that multimodal motion tracking could compensate IMU-sensor inherent problems like sensor drift or calibration problems in order to gain more reliable and accurate motion measurements (Wechsler et al., 2023).

It is important to note that the classification scheme presented in this review is not strictly selective, since the individual levels of the proposed clusters are not equal. For instance, some clusters describe the mathematical method that was used in simulations (*trajectory optimization* and *Kalman Filter*) whereas others directly describe the way how the sim2real gap is handled (*Minimization of kinematic error, BM parameter adjustment*, *computed quantities adjustment*). Many methods could therefore be fitted to various clusters. For example, every paper sorted into the *EMG-informed tracking* cluster uses *trajectory optimization*. The *EMG-informed tracking* cluster could therefore also be regarded as a subcategory of the *trajectory optimization* cluster. However, we decided to list these papers separately because tracking multimodal data (marker position/joint angle trajectories and EMG-measurements) is a distinguishing feature of these papers. The same applies for publications sorted into the *Kalman Filter* cluster since these could also be sorted into the *computed quantities adjustment cluster* or the *Minimization of kinematic error* cluster.

Additionally, there are limitations regarding the applied search strategy and the screening process. Both aspects are subjective to the decision of the authors. Even though inclusion and exclusion criteria were defined, objectivity cannot be guaranteed. Furthermore, the lack of consistent and uniform nomenclature complicates the identification of relevant papers using a search string. The term *sim2real gap* is not an established term in the field of biomechanical simulation but a description of the issue addressed in this review article. Therefore, searching for and identifying articles that handle the sim2real gap is laborious and error-prone. In addition, simulations that are free of residuals, either by definition (FD) or minimisation methods (ID), are sometimes called *dynamically consistent*. We decided against using this term, as there appears to be no clear definition and mutual understanding of the term in the biomechanical community. This circumstance has further complicated the search and selection of methods relevant for this review article. Consequently, even though the literature search was performed to the best of our knowledge, completeness of the review cannot be ensured.

5 Conclusion

This review identified and analyzed methods for handling the sim2real gap, the deviation between reality and musculoskeletal simulations which occurs because of kinematic and dynamic errors. The results showed that different solution approaches exist in literature, but there is no consensus on which method is most appropriate. Generally, FD approaches always generate simulations without residuals. However, to achieve this, the simulation may move far away from experimental measurements or IK results. This includes methods included in the *trajectory optimization*, *EMG-informed tracking* and *controller-based tracking* cluster. Therefore, the sim2real gap shows up as this deviation between the recorded movement and the simulated movement. An ID approach generates residual forces and torques while usually tracking experimental measurements more closely than FD approaches. Therefore, the sim2real gap shows up through the residuals. However, there are ways to reduce the residuals by adjusting either kinematic or dynamic simulation parameters. This includes methods included in the *BM parameter adjustment* and *computed quantities adjustment* cluster. Comparing the size of residuals to given recommendations provides information on the size of the sim2real gap. However, smaller residuals do not necessarily mean that the sim2real gap is smaller. In both methods, there is a risk of overfitting to the specific experimental data used, meaning that the adjusted parameters or quantities are unrealistic. Prevention methods should be taken to reduce this risk (e.g., constraining the solution space). By using a *Kalman Filter,* the kinematic error of simulation results is minimized as error models are used to compute optimal state estimations (e.g., marker positions, sensor positions or orientations). However, the quality of the optimized state vector estimation is restricted by the accuracy of the implemented error models. *Statistical approaches* minimize the kinematic error by maximizing a specific probability (e.g., maximum likelihood of a parameter's posterior distribution) which leads to more accurate joint angle estimates in contrast to standard approaches for a two-dimensional movement. However, the methods are largely restricted by convergence problems and the required high computational effort. Ultimately, the method choice largely depends on various factors: available model, input parameters, investigated movement and of course the underlying research aim. However, we conclude that multimodal approaches tracking kinematic and dynamic measurements may be one possible solution to handle the sim2real gap as methods tracking multimodal measurements (some combination of sensor position/orientation or EMG measurements), consistently lead to better tracking performances. Initial analyses show that motion analysis performance can be enhanced by using multimodal measurements as different sensor technologies can compensate each other's weaknesses (e.g., marker occlusion and IMU drift). FD approaches (*trajectory optimization*, *controller-based tracking*, *EMG-informed tracking*) or a Kalman Filter are suitable for the simultaneous processing of multimodal measurement data.

Data availability statement

The original contributions presented in the study are included in the article/Supplementary Material, further inquiries can be directed to the corresponding author.

Author contributions

IW: Conceptualization, Data curation, Formal Analysis, Investigation, Methodology, Visualization, Writing–original draft, Writing–review and editing. AW: Conceptualization, Formal Analysis, Writing–review and editing, Methodology. JS: Conceptualization, Formal Analysis, Writing–review and editing. SL: Writing–review and editing. BE: Writing–review and editing. AK: Conceptualization, Formal Analysis, Supervision, Writing–review and editing. SW: Funding acquisition, Resources, Supervision, Writing–review and editing, Project administration. JM: Conceptualization, Formal Analysis, Funding acquisition, Methodology, Resources, Supervision, Writing–review and editing, Investigation, Project administration.

Funding

The author(s) declare that financial support was received for the research, authorship, and/or publication of this article. This work was funded by the Deutsche Forschungsgemeinschaft (DFG, German Research Foundation) - SFB 1483 - Project-ID 442419336, EmpkinS.

Conflict of interest

The authors declare that the research was conducted in the absence of any commercial or financial relationships that could be construed as a potential conflict of interest.

Publisher's note

All claims expressed in this article are solely those of the authors and do not necessarily represent those of their affiliated organizations, or those of the publisher, the editors and the reviewers. Any product that may be evaluated in this article, or claim that may be made by its manufacturer, is not guaranteed or endorsed by the publisher.

Supplementary material

The Supplementary Material for this article can be found online at: https://www.frontiersin.org/articles/10.3389/fbioe.2024.1386874/full#supplementary-material

References

Al Borno, M., O'Day, J., Ibarra, V., Dunne, J., Seth, A., Habib, A., et al. (2022). OpenSense: an open-source toolbox for inertial-measurement-unit-based measurement of lower extremity kinematics over long durations. *J. Neuroeng Rehabil.* 19, 22. doi:10.1186/s12984-022-01001-x

Allen, M., Zhong, Q., Kirsch, N., Dani, A., Clark, W. W., and Sharma, N. (2017). A nonlinear dynamics-based estimator for functional electrical stimulation: preliminary results from lower-leg extension experiments. *IEEE Trans. Neural Syst. Rehabil. Eng.* 25, 2365–2374. doi:10.1109/TNSRE.2017.2748420

Anderson, F. C., and Pandy, M. G. (2001). Static and dynamic optimization solutions for gait are practically equivalent. *J. Biomech.* 34, 153–161. doi:10.1016/s0021-9290(00)00155-x

Arash Haghpanah, S., Farrokhnia, M., Taghvaei, S., Eghtesad, M., and Ghavanloo, E. (2022). Tracking ankle joint movements during gait cycle via control of functional electrical stimulation. *Proc. Inst. Mech. Eng. H.* 236, 239–247. doi:10.1177/09544119211052365

Arnold, A. S., Anderson, F. C., Pandy, M. G., and Delp, S. L. (2005). Muscular contributions to hip and knee extension during the single limb stance phase of normal gait: a framework for investigating the causes of crouch gait. *J. Biomechanics* 38, 2181–2189. doi:10.1016/j.jbiomech.2004.09.036

Atrsaei, A., Salarieh, H., and Alasty, A. (2016). Human arm motion tracking by orientation-based fusion of inertial sensors and kinect using unscented kalman filter. *J. Biomechanical Eng.* 138, 091005. doi:10.1115/1.4034170

Bailly, F., Ceglia, A., Michaud, B., Rouleau, D. M., and Begon, M. (2021). Real-time and dynamically consistent estimation of muscle forces using a moving horizon EMG-marker tracking algorithm-application to upper limb biomechanics. *Front. Bioeng. Biotechnol.* 9, 642742. doi:10.3389/fbioe.2021.642742

Begon, M., Andersen, M. S., and Dumas, R. (2018). Multibody kinematics optimization for the estimation of upper and lower limb human joint kinematics: a systematized methodological review. *J. Biomech. Eng.* 140. doi:10.1115/1.4038741

Begon, M., Bélaise, C., Naaim, A., Lundberg, A., and Chèze, L. (2017). Multibody kinematics optimization with marker projection improves the accuracy of the humerus rotational kinematics. *J. Biomechanics* 62, 117–123. doi:10.1016/j.jbiomech.2016.09.046

Bélaise, C., Dal Maso, F., Michaud, B., Mombaur, K., and Begon, M. (2018a). An EMG-marker tracking optimisation method for estimating muscle forces. *Multibody Syst. Dyn.* 42, 119–143. doi:10.1007/s11044-017-9587-2

Bélaise, C., Michaud, B., Dal Maso, F., Mombaur, K., and Begon, M. (2018b). Which data should be tracked in forward-dynamic optimisation to best predict muscle forces in a pathological co-contraction case? *J. Biomech.* 68, 99–106. doi:10.1016/j.jbiomech.2017.12.028

Blana, D., Kirsch, R. F., and Chadwick, E. K. (2009). Combined feedforward and feedback control of a redundant, nonlinear, dynamic musculoskeletal system. *Med. Biol. Eng. Comput.* 47, 533–542. doi:10.1007/s11517-009-0479-3

Bonnet, V., Dumas, R., Cappozzo, A., Joukov, V., Daune, G., Kulić, D., et al. (2017). A constrained extended Kalman filter for the optimal estimate of kinematics and kinetics of a sagittal symmetric exercise. *J. Biomech.* 62, 140–147. doi:10.1016/j.jbiomech.2016.12.027

Bullinger-Hoffmann, A. C., and Mühlstedt, J. (2016). *Homo Sapiens Digitalis - Virtuelle Ergonomie und digitale Menschmodelle* (Berlin, Heidelberg: Springer Berlin Heidelberg). doi:10.1007/978-3-662-50459-8

Cahouët, V., Luc, M., and David, A. (2002). Static optimal estimation of joint accelerations for inverse dynamics problem solution. *J. Biomech.* 35, 1507–1513. doi:10.1016/s0021-9290(02)00176-8

Ceglia, A., Bailly, F., and Begon, M. (2023). Moving horizon estimation of human kinematics and muscle forces. *IEEE Robot. Autom. Lett.* 8, 5212–5219. doi:10.1109/LRA.2023.3291921

Cesic, J., Joukov, V., Petrovic, I., and Kulic, D. (2016). "Full body human motion estimation on lie groups using 3D marker position measurements," in 2016 IEEE-RAS 16th International Conference on Humanoid Robots (Humanoids), (Cancun, Mexico: IEEE), Mexico, 15 Nov, 2016 (IEEE), 826–833.

Chao, E. Y.-S., and Rim, K. (1973). Application of optimization principles in determining the applied moments in human leg joints during gait. *J. Biomech.* 6, 497–510. doi:10.1016/0021-9290(73)90008-0

Cockcroft, J., Muller, J. H., and Scheffer, C. (2014). A novel complimentary filter for tracking hip angles during cycling using wireless inertial sensors and dynamic acceleration estimation. *IEEE Sensors J.* 14, 2864–2871. doi:10.1109/JSEN.2014.2318897

Da Silva, M., Abe, Y., and Popović, J. (2008). Simulation of human motion data using short-horizon model-predictive control. *Comput. Graph. Forum* 27, 371–380. doi:10.1111/j.1467-8659.2008.01134.x

Demircan, E., Besier, T., Menon, S., and Khatib, O. (2010). "Human motion reconstruction and synthesis of human skills," in *Advances in robot kinematics: motion in man and machine*. Editors J. Lenarcic and M. M. Stanisic (Dordrecht: Springer Netherlands), 283–292. doi:10.1007/978-90-481-9262-5_30

Dorschky, E., Krüger, D., Kurfess, N., Schlarb, H., Wartzack, S., Eskofier, B. M., et al. (2019). Optimal control simulation predicts effects of midsole materials on energy cost of running. *Comput. Methods Biomech. Biomed. Engin* 22, 869–879. doi:10.1080/10255842.2019.1601179

Faber, H., van Soest, A. J., and Kistemaker, D. A. (2018). Inverse dynamics of mechanical multibody systems: an improved algorithm that ensures consistency between kinematics and external forces. *PLoS One* 13, 0204575. doi:10.1371/journal.pone.0204575

Falisse, A., Serrancolí, G., Dembia, C. L., Gillis, J., and Groote, F. (2019). Algorithmic differentiation improves the computational efficiency of OpenSim-based trajectory optimization of human movement. *PLoS One* 14, 0217730. doi:10.1371/journal.pone.0217730

Febrer-Nafría, M., Fregly, B. J., and Font-Llagunes, J. M. (2022). Evaluation of optimal control approaches for predicting active knee-ankle-foot-orthosis motion for individuals with spinal cord injury. *Front. Neurorobot.* 15, 748148. doi:10.3389/fnbot.2021.748148

Febrer-Nafría, M., Pallarès-López, R., Fregly, B. J., and Font-Llagunes, J. M. (2020). Comparison of different optimal control formulations for generating dynamically consistent crutch walking simulations using a torque-driven model. *Mech. Mach. Theory* 154, 104031. doi:10.1016/j.mechmachtheory.2020.104031

Ferrati, F., Bortoletto, R., and Pagello, E. (2013). "Virtual modeling of a real exoskeleton constrained to a human musculoskeletal model," in *Biomimetic and biohybrid systems*, D. Hutchison, T. Kanade, J. Kittler, J. M. Kleinberg, F. Mattern, and J. C. Mitchell, (Berlin, Heidelberg: Springer Berlin Heidelberg), 96–107. doi:10.1007/978-3-642-39802-5_9

Fritz, J., Kröll, J., and Schwameder, H. (2019). Influence of body segment parameter estimation on calculated ground reaction forces in highly dynamic movements. *J. Biomech.* 84, 11–17. doi:10.1016/j.jbiomech.2018.12.008

Ghafari, S. A., Meghdari, A., and Vossoughi, G. R. (2009). Forward dynamics simulation of human walking employing an iterative feedback tuning approach. *Proc. Institution Mech. Eng. Part I J. Syst. Control Eng.* 223, 289–297. doi:10.1243/09596518JSCE671

Gupta, D., Donnelly, C., and Reinbolt, J. (2022). Physics-based guidelines for accepting reasonable dynamic simulations of movement. *IEEE Trans. Biomed. Eng.* 69, 1194–1201. doi:10.1109/TBME.2021.3119773

Halilaj, E., Shin, S., Rapp, E., and Xiang, D. (2021). American society of biomechanics early career achievement award 2020: toward portable and modular biomechanics labs: how video and IMU fusion will change gait analysis. *J. Biomechanics* 129, 110650. doi:10.1016/j.jbiomech.2021.110650

Haralabidis, N., Serrancolí, G., Colyer, S., Bezodis, I., Salo, A., and Cazzola, D. (2021). Three-dimensional data-tracking simulations of sprinting using a direct collocation optimal control approach. *PeerJ* 9, e10975. doi:10.7717/peerj.10975

Hatze, H. (1980). A mathematical model for the computational determination of parameter values of anthropomorphic segments. *J. Biomech.* 13, 833–843. doi:10.1016/0021-9290(80)90171-2

Hatze, H. (2002). The fundamental problem of myoskeletal inverse dynamics and its implications. *J. Biomech.* 35, 109–115. doi:10.1016/S0021-9290(01)00158-0

Herrmann, A. M., and Delp, S. L. (1999). Moment arm and force-generating capacity of the extensor carpi ulnaris after transfer to the extensor carpi radialis brevis. *J. Hand Surg.* 24, 1083–1090. doi:10.1053/jhsu.1999.1083

Hicks, J. L., Uchida, T. K., Seth, A., Rajagopal, A., and Delp, S. L. (2015). Is my model good enough? Best practices for verification and validation of musculoskeletal models and simulations of movement. *J. Biomech. Eng.* 137, 020905. doi:10.1115/1.4029304

Higginson, J. S., Zajac, F. E., Neptune, R. R., Kautz, S. A., and Delp, S. L. (2006). Muscle contributions to support during gait in an individual with post-stroke hemiparesis. *J. Biomechanics* 39, 1769–1777. doi:10.1016/j.jbiomech.2005.05.032

Inai, T., Takabayashi, T., Edama, M., and Kubo, M. (2020). Algorithm to compute muscle excitation patterns that accurately track kinematics using a hybrid of numerical integration and optimization. *J. Biomech.* 107, 109836. doi:10.1016/j.jbiomech.2020.109836

Jackson, J. N., Hass, C. J., and Fregly, B. J. (2015). Residual elimination algorithm enhancements to improve foot motion tracking during forward dynamic simulations of gait. *J. Biomech. Eng.* 137, 111002. doi:10.1115/1.4031418

Jeang, A., Chiang, A. J., Chiang, P. C., Chiang, P. S., and Tung, P. Y. (2018). Robust parameters determination for ergonomical product design via computer musculoskeletal modeling and multi-objective optimization. *Comput. Industrial Eng.* 118, 180–201. doi:10.1016/j.cie.2018.02.013

John, C. T., Anderson, F. C., Higginson, J. S., and Delp, S. L. (2013). Stabilisation of walking by intrinsic muscle properties revealed in a three-dimensional muscle-driven simulation. *Comput. Methods Biomechanics Biomed. Eng.* 16, 451–462. doi:10.1080/10255842.2011.627560

Joukov, V., Bonnet, V., Karg, M., Venture, G., and Kulic, D. (2018). Rhythmic extended kalman filter for gait rehabilitation motion estimation and segmentation. *IEEE Trans. Neural Syst. Rehabil. Eng.* 26, 407–418. doi:10.1109/TNSRE.2017.2659730

Joukov, V., Cesic, J., Westermann, K., Markovic, I., Kulic, D., and Petrovic, I. (2017). "Human motion estimation on Lie groups using IMU measurements," in IEEE/RSJ International Conference on Intelligent Robots and Systems (IROS), Vancouver, 7-10 July 1992 (BC: IEEE), 1965–1972.

Joukov, V., Cesic, J., Westermann, K., Markovic, I., Petrovic, I., and Kulic, D. (2020). Estimation and observability analysis of human motion on lie groups. *IEEE Trans. Cybern.* 50, 1321–1332. doi:10.1109/TCYB.2019.2933390

Kaplan, M. L., and Heegaard, J. H. (2001). Predictive algorithms for neuromuscular control of human locomotion. *J. Biomech.* 34, 1077–1083. doi:10.1016/S0021-9290(01)00057-4

Koelewijn, A. D., and Ijspeert, A. J. (2020). Exploring the contribution of proprioceptive reflexes to balance control in perturbed standing. *Front. Bioeng. Biotechnol.* 8, 866. doi:10.3389/fbioe.2020.00866

Koh, M. T. H., and Jennings, L. S. (2003). Dynamic optimization: inverse analysis for the Yurchenko layout vault in women's artistic gymnastics. *J. Biomech.* 36, 1177–1183. doi:10.1016/S0021-9290(03)00085-X

Koopman, B., Grootenboer, H. J., and Jongh, H. J. (1995). An inverse dynamics model for the analysis, reconstruction and prediction of bipedal walking. *J. Biomech.* 28, 1369–1376. doi:10.1016/0021-9290(94)00185-7

Kuo, A. D. (1998). A least-squares estimation approach to improving the precision of inverse dynamics computations. *J. Biomech. Eng.* 120, 148–159. doi:10.1115/1.2834295

Laidig, D., Schauer, T., and Seel, T. (2017). "Exploiting kinematic constraints to compensate magnetic disturbances when calculating joint angles of approximate hinge joints from orientation estimates of inertial sensors," in 2017 International Conference on Rehabilitation Robotics (ICORR), London, 17-20 July 2017 (IEEE), 971–976.

Lefebvre, F., Rogowski, I., Long, N., and Blache, Y. (2023). Influence of marker weights optimization on scapular kinematics estimated with a multibody kinematic optimization. *J. Biomechanics* 159, 111795. doi:10.1016/j.jbiomech.2023.111795

Leva, P. (1996). Adjustments to Zatsiorsky-Seluyanov's segment inertia parameters. *J. Biomech.* 29, 1223–1230. doi:10.1016/0021-9290(95)00178-6

Lin, Y.-C., Walter, J. P., and Pandy, M. G. (2018). Predictive simulations of neuromuscular coordination and joint-contact loading in human gait. *Ann. Biomed. Eng.* 46, 1216–1227. doi:10.1007/s10439-018-2026-6

Lv, X., Chai, J., and Xia, S. (2016). Data-driven inverse dynamics for human motion. *ACM Trans. Graph.* 35, 1–12. doi:10.1145/2980179.2982440

Mallat, R., Bonnet, V., Dumas, R., Adjel, M., Venture, G., Khalil, M., et al. (2021). Sparse visual-inertial measurement units placement for gait kinematics assessment. *IEEE Trans. Neural Syst. Rehabil. Eng.* 29, 1300–1311. doi:10.1109/TNSRE.2021.3089873

Maurice, P., Padois, V., Measson, Y., and Bidaud, P. (2019). Assessing and improving human movements using sensitivity analysis and digital human simulation. *Int. J. Comput. Integr. Manuf.* 32, 546–558. doi:10.1080/0951192X.2019.1599432

Mazzà, C., and Cappozzo, A. (2004). An optimization algorithm for human joint angle time-history generation using external force data. *Ann. Biomed. Eng.* 32, 764–772. doi:10.1023/b:abme.0000030241.26857.75

Meyer, A. J., Eskinazi, I., Jackson, J. N., Rao, A. V., Patten, C., and Fregly, B. J. (2016). Muscle synergies facilitate computational prediction of subject-specific walking motions. *Front. Bioeng. Biotechnol.* 4, 77. doi:10.3389/fbioe.2016.00077

Mohammadi, H., Khademi, G., Simon, D., Bogert, A. J., and Richter, H. (2020). Upper body estimation of muscle forces, muscle states, and joint motion using an extended Kalman filter. *IET Control Theory and Appl* 14, 3204–3216. doi:10.1049/iet-cta.2020.0321

Moher, D., Shamseer, L., Clarke, M., Ghersi, D., Liberati, A., Petticrew, M., et al. (2015). Preferred reporting items for systematic review and meta-analysis protocols (PRISMA-P) 2015 statement. *Syst. Rev.* 4, 1. doi:10.1186/2046-4053-4-1

Moissenet, F., Bélaise, C., Piche, E., Michaud, B., and Begon, M. (2019). An optimization method tracking EMG, ground reactions forces, and marker trajectories for musculo-tendon forces estimation in equinus gait. *Front. Neurorobot* 13, 48. doi:10.3389/fnbot.2019.00048

Molz, C., Yao, Z., Sänger, J., Gwosch, T., Weidner, R., Matthiesen, S., et al. (2022). A musculoskeletal human model-based approach for evaluating support concepts of exoskeletons for selected use cases. *Proc. Des. Soc.* 2, 515–524. doi:10.1017/pds.2022.53

Morrow, M. M., Rankin, J. W., Neptune, R. R., and Kaufman, K. R. (2014). A comparison of static and dynamic optimization muscle force predictions during wheelchair propulsion. *J. Biomech.* 47, 3459–3465. doi:10.1016/j.jbiomech.2014.09.013

Mouzo, F., Lugris, U., Pamies-Vila, R., and Cuadrado, J. (2018). Skeletal-level control-based forward dynamic analysis of acquired healthy and assisted gait motion. *Multibody Syst. Dyn.* 44, 1–29. doi:10.1007/s11044-018-09634-4

Muller, A., Pontonnier, C., and Dumont, G. (2017). Uncertainty propagation in multibody human model dynamics. *Multibody Syst. Dyn.* 40, 177–192. doi:10.1007/s11044-017-9566-7

Muller, A., Pontonnier, C., and Dumont, G. (2018). The MusIC method: a fast and quasi-optimal solution to the muscle forces estimation problem. *Comput. Methods Biomech. Biomed. Engin* 21, 149–160. doi:10.1080/10255842.2018.1429596

Neptune, R. R. (1999). Optimization algorithm performance in determining optimal controls in human movement analyses. *J. Biomech. Eng.* 121, 249–252. doi:10.1115/1.2835111

Neptune, R. R., and Hull, M. L. (1998). Evaluation of performance criteria for simulation of submaximal steady-state cycling using a forward dynamic model. *J. Biomech. Eng.* 120, 334–341. doi:10.1115/1.2797999

Nitschke, M., Dorschky, E., Heinrich, D., Schlarb, H., Eskofier, B. M., Koelewijn, A. D., et al. (2020). Efficient trajectory optimization for curved running using a 3D musculoskeletal model with implicit dynamics. *Sci. Rep.* 10, 17655. doi:10.1038/s41598-020-73856-w

Nitschke, M., Marzilger, R., Leyendecker, S., Eskofier, B. M., and Koelewijn, A. D. (2023). Change the direction: 3D optimal control simulation by directly tracking marker and ground reaction force data. *PeerJ* 11, e14852. doi:10.7717/peerj.14852

Niu, K., Anijs, T., Sluiter, V., Homminga, J., Sprengers, A., Marra, M. A., et al. (2018). *In situ* comparison of A-mode ultrasound tracking system and skin-mounted markers for measuring kinematics of the lower extremity. *J. Biomechanics* 72, 134–143. doi:10.1016/j.jbiomech.2018.03.007

Noamani, A., Vette, A. H., Preuss, R., Popovic, M. R., and Rouhani, H. (2018). Optimal estimation of anthropometric parameters for quantifying multisegment trunk kinetics. *J. Biomech. Eng.* 140. doi:10.1115/1.4040247

Pallarès-López, R., Costa Alvim, F., Febrer-Nafría, M., Menegaldo, L. L., and Font-Llagunes, J. M. (2019). Assessment of residual reduction procedures for high-speed tasks. *Gait Posture* 73, 116–119. doi:10.1016/j.gaitpost.2019.07.191

Pataky, T. C., Vanrenterghem, J., and Robinson, M. A. (2019). Bayesian inverse kinematics vs. least-squares inverse kinematics in estimates of planar postures and rotations in the absence of soft tissue artifact. *J. Biomech.* 82, 324–329. doi:10.1016/j.jbiomech.2018.11.007

Pearl, O., Shin, S., Godura, A., Bergbreiter, S., and Halilaj, E. (2023). Fusion of video and inertial sensing data via dynamic optimization of a biomechanical model. *J. Biomech.* 155, 111617. doi:10.1016/j.jbiomech.2023.111617

Price, M. A., LaPrè, A. K., Johnson, R. T., Umberger, B. R., and Sup, F. C. (2020). A model-based motion capture marker location refinement approach using inverse kinematics from dynamic trials. *Int. J. Numer. Method Biomed. Eng.* 36, 3283. doi:10.1002/cnm.3283

Rasmussen, J., Holmberg, L. J., Sørensen, K., Kwan, M., Andersen, M. S., and Zee, M. (2012). Performance optimization by musculoskeletal simulation. *Mov. Sport Sci/Sci Mot.*, 73–83. doi:10.1051/sm/2011122

Reinbolt, J. A., Seth, A., and Delp, S. L. (2011). Simulation of human movement: applications using OpenSim. *Procedia IUTAM* 2, 186–198. doi:10.1016/j.piutam.2011.04.019

Remy, C. D., and Thelen, D. G. (2009). Optimal estimation of dynamically consistent kinematics and kinetics for forward dynamic simulation of gait. *J. Biomech. Eng.* 131, 031005. doi:10.1115/1.3005148

Riemer, R., and Hsiao-Wecksler, E. T. (2009). Improving net joint torque calculations through a two-step optimization method for estimating body segment parameters. *J. Biomech. Eng.* 131, 011007. doi:10.1115/1.3005155

Riemer, R., Hsiao-Wecksler, E. T., and Zhang, X. (2008). Uncertainties in inverse dynamics solutions: a comprehensive analysis and an application to gait. *Gait Posture* 27, 578–588. doi:10.1016/j.gaitpost.2007.07.012

Samaan, M. A., Weinhandl, J. T., Bawab, S. Y., and Ringleb, S. I. (2016). Determining residual reduction algorithm kinematic tracking weights for a sidestep cut via numerical optimization. *Comput. Methods Biomech. Biomed. Engin* 19, 1721–1729. doi:10.1080/10255842.2016.1183123

Sartori, M., Farina, D., and Lloyd, D. G. (2014). Hybrid neuromusculoskeletal modeling to best track joint moments using a balance between muscle excitations derived from electromyograms and optimization. *J. Biomech.* 47, 3613–3621. doi:10.1016/j.jbiomech.2014.10.009

Schellenberg, F., Taylor, W. R., Jonkers, I., and Lorenzetti, S. (2017). Robustness of kinematic weighting and scaling concepts for musculoskeletal simulation. *Comput. Methods Biomech. Biomed. Engin* 20, 720–729. doi:10.1080/10255842.2017.1295305

Serra, G. L. de O. (2018). Kalman filters - theory for advanced applications. *IntechOpen*. doi:10.5772/intechopen.68249

Seth, A., and Pandy, M. G. (2007). A neuromusculoskeletal tracking method for estimating individual muscle forces in human movement. *J. Biomech.* 40, 356–366. doi:10.1016/j.jbiomech.2005.12.017

Stanev, D., and Moustakas, K. (2018). Simulation of constrained musculoskeletal systems in task space. *IEEE Trans. Biomed. Eng.* 65, 307–318. doi:10.1109/TBME.2017.2764630

Sturdy, J. T., Silverman, A. K., and Pickle, N. T. (2022). Automated optimization of residual reduction algorithm parameters in OpenSim. *J. Biomech.* 137, 111087. doi:10.1016/j.jbiomech.2022.111087

Sy, L. W., Lovell, N. H., and Redmond, S. J. (2020). Estimating lower limb kinematics using a lie group constrained extended kalman filter with a reduced wearable IMU count and distance measurements. *Sensors* 20, 6829. doi:10.3390/s20236829

Sy, L. W., Lovell, N. H., and Redmond, S. J. (2021). Estimating lower body kinematics using a lie group constrained extended kalman filter and reduced IMU count. *IEEE Sensors J.* 21, 20969–20979. doi:10.1109/JSEN.2021.3096078

Tagliapietra, L., Modenese, L., Ceseracciu, E., Mazzà, C., and Reggiani, M. (2018). Validation of a model-based inverse kinematics approach based on wearable inertial sensors. *Comput. Methods Biomech. Biomed. Engin* 21, 834–844. doi:10.1080/10255842.2018.1522532

Thelen, D. G., and Anderson, F. C. (2006). Using computed muscle control to generate forward dynamic simulations of human walking from experimental data. *J. Biomech.* 39, 1107–1115. doi:10.1016/j.jbiomech.2005.02.010

Thelen, D. G., Anderson, F. C., and Delp, S. L. (2003). Generating dynamic simulations of movement using computed muscle control. *J. Biomech.* 36, 321–328. doi:10.1016/S0021-9290(02)00432-3

Uchida, T. K., Seth, A., Pouya, S., Dembia, C. L., Hicks, J. L., and Delp, S. L. (2016). Simulating ideal assistive devices to reduce the metabolic cost of running. *PLoS One* 11, 0163417. doi:10.1371/journal.pone.0163417

van den Bogert, A. J., Blana, D., and Heinrich, D. (2011). Implicit methods for efficient musculoskeletal simulation and optimal control. *Procedia IUTAM* 2, 297–316. doi:10.1016/j.piutam.2011.04.027

van den Bogert, A. J., Hupperets, M., Schlarb, H., and Krabbe, B. (2012). Predictive musculoskeletal simulation using optimal control: effects of added limb mass on energy cost and kinematics of walking and running. *Proc. Institution Mech. Eng. Part P J. Sports Eng. Technol.* 226, 123–133. doi:10.1177/1754337112440644

van den Bogert, A. J., and Su, A. (2008). A weighted least squares method for inverse dynamic analysis. *Comput. Methods Biomech. Biomed. Engin* 11, 3–9. doi:10.1080/10255840701550865

van der Kooij, H., Jacobs, R., Koopman, B., and van der Helm, F. (2001). An adaptive model of sensory integration in a dynamic environment applied to human stance control. *Biol. Cybern.* 84, 103–115. doi:10.1007/s004220000196

Vaughan, C. L., Andrews, J. G., and Hay, J. G. (1982). Selection of body segment parameters by optimization methods. *J. Biomech. Eng.* 104, 38–44. doi:10.1115/1.3138301

Wang, W., Wang, D., Falisse, A., Severijns, P., Overbergh, T., Moke, L., et al. (2021). A dynamic optimization approach for solving spine kinematics while calibrating subject-specific mechanical properties. *Ann. Biomed. Eng.* 49, 2311–2322. doi:10.1007/s10439-021-02774-3

Wang, X., Guo, J., and Tian, Q. (2022). A forward-inverse dynamics modeling framework for human musculoskeletal multibody system. *Acta Mech. Sin.* 38, 522140. doi:10.1007/s10409-022-22140-x

Watanabe, T., and Sugi, Y. (2010). Computer simulation tests of feedback error learning controller with IDM and ISM for functional electrical stimulation in wrist joint control. *J. Robotics* 2010, 1–11. doi:10.1155/2010/908132

Wechsler, I., Wolf, A., Fleischmann, S., Waibel, J., Molz, C., Scherb, D., et al. (2023). Method for using IMU-based experimental motion data in BVH format for musculoskeletal simulations via OpenSim. *Sensors* 23, 5423. doi:10.3390/s23125423

Werling, K., Bianco, N. A., Raitor, M., Stingel, J., Hicks, J. L., Collins, S. H., et al. (2023). AddBiomechanics: automating model scaling, inverse kinematics, and inverse dynamics from human motion data through sequential optimization. *PLoS ONE* 18, e0295152. doi:10.1371/journal.pone.0295152

Yamaguchi, G. T., and Zajac, F. E. (1990). Restoring unassisted natural gait to paraplegics via functional neuromuscular stimulation: a computer simulation study. *IEEE Trans. Biomed. Eng.* 37, 886–902. doi:10.1109/10.58599

Yuan, Q., Asadi, E., Lu, Q., Yang, G., and Chen, I.-M. (2019). Uncertainty-based IMU orientation tracking algorithm for dynamic motions. *IEEE/ASME Trans. Mechatron.* 24, 872–882. doi:10.1109/TMECH.2019.2892069

frontiers | Frontiers in Bioengineering and Biotechnology

TYPE Original Research
PUBLISHED 27 June 2024
DOI 10.3389/fbioe.2024.1384617

OPEN ACCESS

EDITED BY
Jörg Miehling,
Friedrich-Alexander-Universität Erlangen-Nürnberg, Germany

REVIEWED BY
Sanghoon Lee,
Daegu Gyeongbuk Institute of Science and Technology (DGIST), Republic of Korea
Michel Mesnard,
Université de Bordeaux, France

*CORRESPONDENCE
Johanna Baier,
johanna.woeste@rub.de

RECEIVED 10 February 2024
ACCEPTED 30 April 2024
PUBLISHED 27 June 2024

CITATION
Baier J, Selkmann S and Bender B (2024), Simulation of FES on the forearm with muscle-specific activation resolution. *Front. Bioeng. Biotechnol.* 12:1384617. doi: 10.3389/fbioe.2024.1384617

Simulation of FES on the forearm with muscle-specific activation resolution

Johanna Baier*, Sascha Selkmann and Beate Bender

Chair for Product Development, Institute for Product and Service Engineering, Ruhr-University Bochum, Bochum, Germany

Introduction: Functional electrical stimulation (FES) is an established method of supporting neurological rehabilitation. However, particularly on the forearm, it still cannot elicit selective muscle activations that form the basis of complex hand movements. Current research approaches in the context of selective muscle activation often attempt to enable targeted stimulation by increasing the number of electrodes and combining them in electrode arrays. In order to determine the best stimulation positions and settings, manual or semi-automated algorithms are used. This approach is limited due to experimental limitations. The supportive use of simulation studies is well-established, but existing simulation models are not suitable for analyses of selective muscle activation due to missing or arbitrarily arranged innervation zones.

Methods: This study introduces a new modeling method to design a person-specific digital twin that enables the prediction of muscle activations during FES on the forearm. The designed individual model consists of three parts: an anatomically based 3D volume conductor, a muscle-specific nerve fiber arrangement in various regions of interest (ROIs), and a standard nerve model. All processes were embedded in scripts or macros to enable automated changes to the model and the simulation setup.

Results: The experimental evaluation of simulated strength–duration diagrams showed good coincidence. The relative differences of the simulated amplitudes to the mean amplitude of the four experiments were in the same range as the inter-experimental differences, with mean values between 0.005 and 0.045. Based on these results, muscle-specific activation thresholds were determined and integrated into the simulation process. With this modification, simulated force-intensity curves showed good agreement with additionally measured curves.

Discussion: The results show that the model is suitable for simulating realistic muscle-specific activations. Since complex hand movements are physiologically composed of individual, selective muscle activations, it can be assumed that the model is also suitable for simulating these movements. Therefore, this study presents a new and very promising approach for developing new applications and products in the context of the rehabilitation of sensorimotor disorders.

KEYWORDS

electromagnetic simulation, upper limb, digital twin, individual model, selective muscle activation, product development, electrical stimulation

1 Introduction

Functional electrical stimulation (FES) has received significant attention in recent years for its positive impact on motor recovery in post-stroke patients or those with spinal cord injury. By applying electrodes to the skin of the forearm, FES can elicit hand movements that otherwise might be impossible. However, achieving precise and physiological hand movements is still challenging (Westerveld et al., 2012; Malesevic et al., 2012; Imatz-Ojanguren et al., 2016); common applications are therefore limited to simple movements such as hand opening and closing. In order to stimulate complex and functional hand movements, different wrist and finger muscles must be selectively activated in a specific pattern (Imatz-Ojanguren et al., 2016). This is particularly difficult at the forearm due to the anatomy—numerous small muscles arranged in several layers (Westerveld et al., 2012; Bao et al., 2018; Baker et al., 1993). A muscle is activated selectively when it is activated while minimizing the activation of neighboring muscles. In addition to the stimulation parameters (current amplitude, pulse width and shape, and frequency) and chosen electrodes (size and geometry), the selective activation of a muscle depends particularly on the stimulation site (Westerveld et al., 2012; Bao et al., 2018; Baker et al., 1993). The best position to stimulate a single muscle is generally referred to as the "motor point" (MP) (Baker et al., 1993; Imatz-Ojanguren et al., 2016; RaviChandran et al., 2020b).

Current research approaches in the context of selective muscle activation often attempt to enable selective stimulation at different MPs by increasing the number of electrodes. Arrays with many small electrodes are placed on the forearm in order to determine the best stimulation positions and settings using manual or semi-automated algorithms (Koutsou et al., 2016; Salchow et al., 2016a; Crema et al., 2018). The evaluation of the stimulated movement is performed either manually by an expert (Salchow et al., 2016a) or automatically by measuring movements (Malesevic et al., 2012; Bao et al., 2018; Salchow et al., 2016b) or forces (Keller et al., 2007). All previous studies use non-specific arrays (electrodes arranged in regular grids) and are based on a limited number of experiments because these are very time-consuming and are further limited by premature muscle fatigue during FES. The search algorithms are therefore not optimized—they require many repetitions and either take a long time or only cover a small range of the possible settings. Despite extensive research, these approaches have not yet succeeded in developing a system suitable for everyday use that reliably and without great additional effort enables the stimulation of selective muscle activation in the forearm as a basis for complex hand movements. It is thus evident that other or complementary methods are needed. Particularly in the field of biomedical engineering, there is great potential in coupling human-related models with digital twins using biomechanical or bioelectronic simulations (Neumann et al., 2020).

In the context of FES, simulation studies have been successfully used to enhance understanding and support the development of new FES applications (Imatz-Ojanguren et al., 2016). Existing simulation studies have primarily focused on two influencing factors: electrode configuration and fat-layer thickness. Evaluation criteria in simulation-based analyses often cover either the activation of single modeled nerve fibers or a general volume area in which fiber activation occurs (activation volume). For instance, Gomez-Tames et al. (2011) analyzed the influence of fat-layer thickness on activation volume, and five other studies have investigated the interdependency of fat thickness and electrode size (Doheny et al., 2010; Gomez-Tames et al., 2012; Gomez-Tames et al., 2013b; Kuhn and Keller, 2005; Kuhn et al., 2010), inter-electrode distance (Doheny et al., 2010; Gomez-Tames et al., 2012; 2013b), and electrode shape (Gomez-Tames et al., 2012). With respect to the electrode configuration, Kuhn et al. (2009b) analyzed the influence of electrode material properties (hydrogel resistivity) and composed electrodes (as often used with array electrodes) on the required stimulation current to achieve a defined activation (depth of activation volume). Cooper et al. (2011) also addressed electrode material properties and simulated resistivity changes during prolonged use. Two other studies have addressed just the electrode shape with respect to the nerve fiber orientation: Goffredo et al. (2014) analyzed different patterns of an electrode array; Loitz et al. (2015) rotated a rectangular single electrode. In contrast, RaviChandran et al. (2020a) analyzed the influence of electrode shape in terms of different edge length but same area. However, none of the studies analyzed the influence of stimulation settings and person-specific characteristics on the selective activation of individual muscles, taking into account the surrounding muscles. Such studies are critical to support experimental improvement and enable the transfer of these approaches to daily practice.

Existing simulation models only represent the "outer" anatomy (i.e., the different homogeneous tissue layers) and are not suitable for analyses for selective muscle activation due to missing or randomly arranged innervation areas. All models cover a 3D volume conductor with one or various embedded nerve fibers which are coupled to a nerve model. This two-step approach was first introduced by McNeal (1976). The volume conductor is used to simulate the extracellular potential distribution at the nerve fibers. On this basis, the activation of the nerve fibers is then calculated with the nerve model. All existing 3D volume conductors consist of three to five homogeneous tissue layers, mostly arranged in symmetrical cylinders. In contrast, past models differed in the arrangement of the nerve fibers: single nerve fibers at specified locations (Doheny et al., 2010; Cooper et al., 2011; Gomez-Tames et al., 2013b; RaviChandran et al., 2020a), nerve fiber bundles at specified locations (Goffredo et al., 2014; Kuhn et al., 2009b; 2010), many nerve fibers homogeneously distributed in the whole muscle layer (Kuhn and Keller, 2007), and many nerve fibers located in a specified volume representing one single muscle (Gomez-Tames et al., 2013c; a; Loitz et al., 2015). However, none of the existing models provides muscle-specific activation resolution, which is required to use the simulation to develop new applications and products that enable the stimulation of complex hand movements.

This paper introduces the design and evaluation of a new, person-specific simulation model that enables the analysis and evaluation of simulation results at the level of selective muscle activations. In contrast to previous models, our volume conductor is anatomy-based, which means that an individual anatomy given by MRI data is approximated by regular geometries. Furthermore, the nerve fibers in our model are arranged in various muscle-specific regions. This allows conclusions to be drawn about the activation of each individual muscle as the result of a stimulation pulse at a specific electrode

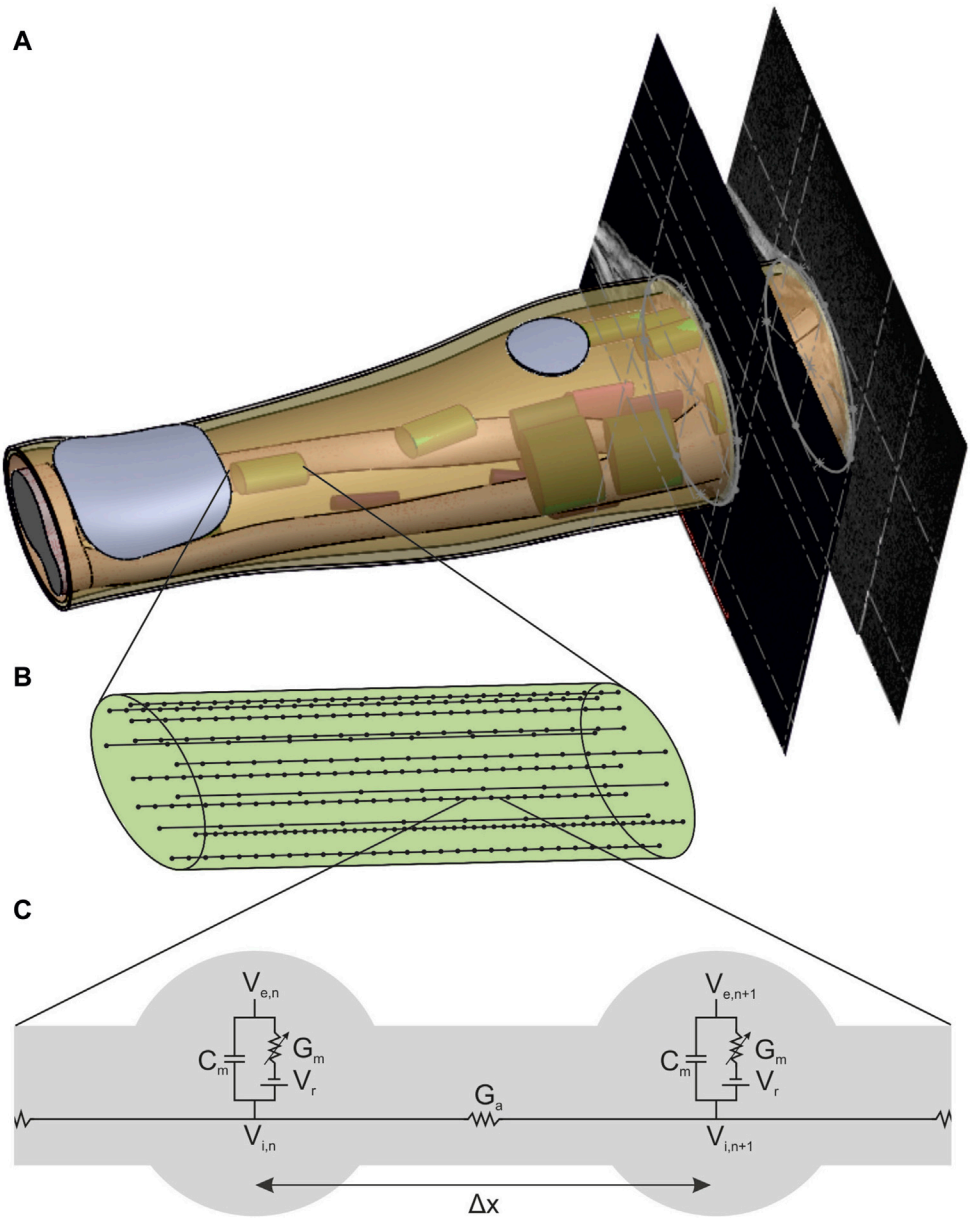

FIGURE 1
New forearm model enabling the simulation of FES with muscle-specific activation resolution. **(A)** Anatomically based volume conductor with four homogeneous tissue layers (bone, muscle, fat, and skin) and two stimulation electrodes that is extended with muscle-specific regions of interest (ROIs) to support the nerve fiber arrangement. **(B)** Detailed view of one ROI with 15 exemplary nerve fibers with random positions and random fiber diameter based on a bimodal distribution. **(C)** Detailed view of the connection of two nodes of ranvier of a nerve fiber with the linear cable model based on McNeal (1976).

position. The developed model is evaluated with experimental measurements and shows good alignment for strength–duration and force-intensity curves. Thus, the new model enables the simulation of single muscle activation, which forms the basis for complex movements and further simulation-based analysis.

The two main objectives of this paper are as follows:

- The introduction of a new modeling method to develop a digital twin of the forearm that accurately and reliably predicts real stimulated muscle activations for different electrode configurations and stimulation settings.
- The automation of model modifications and simulation workflow in order to enable the future use of the digital twin in product development with respect to optimization and AI methods.

2 Methods

The new individual model basically consists of three parts: an anatomically based 3D volume conductor with four homogeneous tissue layers and two stimulation electrodes placed on the skin

TABLE 1 Material properties (conductivity σ and relative permittivity ϵ_r) defined by Kuhn and Keller (2005) as standard materials and meshing operations for hydrogel of the electrodes and biological tissues.

Layer	Material properties		Mesh operations	
	Conductivity σ [S/m]	Relative permittivity ϵ_r [-]	Type	Maximum length [mm]
Hydrogel[a]	1/11	1	inside	2
Skin	1/700	6,000	inside	2
Fat	1/33	25,000	inside	4
Muscle (axial)	1/3	120,000	inside	7.5
Muscle (radial)	1/9	40,000		
Bone[b]	1/50	3,000	inside	10

[a]Material properties modified according to the product data sheet.
[b]Material properties from cortical bone used for the whole bone layer.

surface (Figure 1A), a muscle-specific nerve fiber arrangement in various regions of interest (ROIs) (Figure 1A, B), and a standard nerve model connected to the single nerve fibers (Figure 1C). According to the two-step approach mentioned above, the volume conductor was used to simulate the extracellular potential distribution caused by a single stimulation pulse, and the nerve model was used to simulate the activation state of the single fibers based on this potential distribution. In addition, individual muscle activations are calculated based on the simulated fiber activations, which is enabled by the muscle-specific arrangement of nerve fibers. This model and simulation setup is then evaluated by comparing simulated strength–duration (SD) diagrams with experimental measurements.

2.1 Volume conductor and potential distribution

The volume conductor consists of four anatomically based homogeneous tissue layers: a bone layer covering the two forearm ulna and radius bones as well as the elbow joint surrounded by muscle tissue and a fat and a skin layer (Figure 1A). In addition, two electrodes consisting of a hydrogel pad and an electrode sheet on the top are modeled on the skin layer. It is based on the MRI data of a healthy subject (34y, female, position of the forearm during scan: elbow flexed 90°, forearm parallel to shoulders, hand in pronation position). The subject gave her informed consent to the use of the MRI data for modeling and to the publication of the resulting model. No personal data are included, and no conclusions can be drawn. The MRI data were used exclusively as an anatomical reference for modeling; no medial application took place. Therefore, no ethical approval was required for data collection and their use for modeling.

For the design, the contours of the two bones, the muscle–fat interface, and the skin were approximated by single or composed (only at the elbow bone) ellipses in 10 MR images: 8 MR images equidistant between the lateral epicondyle of the humerus (LEH) and the radial styloid process (RSP), one additional image at the proximal end of the radius, and another 5% of the LE-RSP distance proximal to the LEH. This approach, using regular geometries to approximate the anatomic shape, ensured that the resulting volumes and surfaces were still mathematically defined and therefore that the model can be easily extended or modified. The chosen approach also implied the use of 3D design software (Solidworks, Version 2018; Dassault Systems; Velizy-Villacoublay, France) instead of, for example, an MRI viewer with rendering options. The space between LEH and RSP is the main part of the model due to the reference system for the ROI positioning (see section 2.2) and has a length of 242 mm; the proximal extension is then required to cover the most proximal ROI entirely and leads to a total model length of 254.1 mm. Five filled volumes were created using the molding feature that combines the contours of each set: radius and ulna (only until LEH), elbow bone (from LEH to end), and muscle and skin (whole length). The three bone volumes were then combined into a single volume (bone layer). In addition to the filled volume, a thin molding feature 1 mm thick was constructed from the skin contours (skin layer). The other layers were then constructed by subtraction operations: filled muscle volume minus bone volume (muscle layer) and filled skin volume minus filled muscle volume and skin layer (fat layer).

To complete the 3D volume conductor, the two electrodes were designed on the skin so that they could be modified in position, geometry, and size. In this step, changes in electrode configuration were processed automatically by incorporating a macro and a linked text-file. The position of each electrode is defined by an axial and a radial value. The axial position is the distance of the electrode along the forearm from the LEH; the radial position is the distance of the electrode from a predefined reference line along the circumference counterclockwise (looking from elbow to wrist) of the skin at that axial position. The reference line is a straight line that divides the ulna approximately in the middle. It is constructed as the intersection between a plane positioned manually at the right height and the skin surface. To construct each of the electrodes, the following steps were performed:

1) The electrode position is constructed: First, a plane parallel to the top face of the arm at the distance of the axial position was added and an intersection curve of the skin at that position was sketched. This curve was then trimmed at the end (counterclockwise) by adding a short straight line (0.5 mm).

TABLE 2 Overview of the literature values used to position the ROIs at the supposed nerve entry points (NEPs). The main study by Liu et al. (1997) examined several cadaveric forearms to determine the number and position of terminal nerve branches entering a muscle.

Muscle group	Muscle name		Proximal Max[a] [%]	Median[a] [%]	Distal Max[a] [%]
Superficial flexors	Flexor carpi radialis	FCR	16	25	37
	Flexor carpi ulnaris	FCU	6	13	51
	Flexor digitorum superficialis	FDSdist	(−5.5)	74[b]	(+5.5)
		FDSprox	(−5.5)	51.5[b]	(+5.5)
	Palmaris longus	PL	10	18	35
	Pronator teres	PT	5	16	28
Deep flexors	Flexor digitorum profundus	FDPdist	(−5.5)	36.7[c]	(+5.5)
		FDPprox	(−5.5)	26.5[c]	(+5.5)
	Flexor pollicis longus	FPL	25	40	60
	Pronator quadratus	PQ	72	85	90
Radial extensors	Brachioradialis	BR	−17	−4	12
	Extensor carpi radialis brevis	ECRB	12	25	37
	Extensor carpi radialis longus	ECRL	−8	3	15
Superficial extensors	Extensor carpi ulnaris	ECU	25	33	43
	Extensor digitorum	ED	17	33	52
	Extensor digiti minimi	EDM	34	37	60
Deep extensors	Abductor pollicis longus	APL	34	40	52
	Extensor indicis	EI	56	65	87
	Extensor pollicis brevis	EPB	41	61	70
	Extensor pollicis longus	EPL	39	52	67
	Supinator	SUP	10	19	31

[a](Liu et al., 1997).
[b](Bickerton et al., 1997).
[c](Hwang et al., 2007).

Finally, the electrode position was added by a 3D reference point that was placed on the open intersection curve at the percentage distance corresponding to the radial position.

2) The electrode geometry is constructed: The geometry was sketched, including all dimensions on a plane tangential to the skin at the constructed electrode position. To allow a full projection of that sketch onto the skin surface, a plane with 20 mm offset from the model was used.

3) The hydrogel volume is constructed: The skin layer was first copied twice. The electrode sketch was then wrapped around the outer surface of the skin copy (specifications: Spline Surface and Emboss with 1 mm thickness). The second skin copy was then subtracted from the first to obtain the hydrogel volume without the skin layer.

4) The electrode face is constructed: The outer surface of the hydrogel volume was copied. In the case of array electrodes, various surfaces were added through additional planes and sketches (not used in this study).

The resulting volume conductor, consisting of four anatomically based homogeneous tissue layers and two hydrogel electrodes, was then used to simulate the extracellular potential using the finite element method (FEM). Thereby, the simulated stimulation impulse was transmitted through the modeled electrodes. Since the propagation of the stimulation pulse in biological tissues is an electromagnetic field problem, it can be described by Maxwell's equation. By assuming quasi-stationarity (Plonsey and Heppner, 1967) and neglecting the magnetic flux, which is not of interest in the present case, Maxwell's equation simplifies thus:

$$-\nabla \cdot \left([\epsilon] \nabla \frac{\partial V}{\partial t} \right) - \nabla \cdot ([\sigma] \nabla V) = 0. \quad (1)$$

Standard simulation software uses this equation, such as Ansys Electronics Desktop (2022 R2; Ansys Inc.; Canonsburg, Pennsylvania, United States) in the Maxwell package used in this study. To set up the simulation, the material properties are first defined, and then meshing is followed by the stimulation pulse.

The connection between the electrodes and skin was modeled by a simplified electrical network based on resistive and capacitive elements. This modeling approach, proposed by

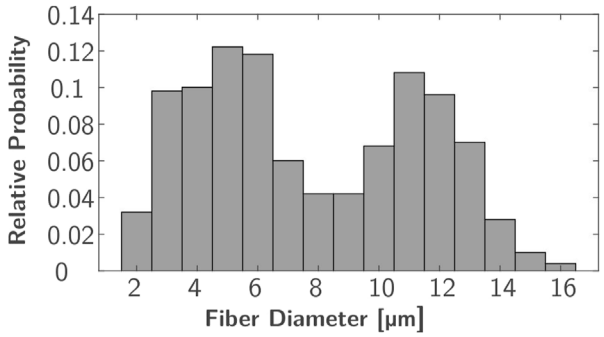

FIGURE 2
Bimodal diameter distribution used for nerve fiber modeling based on averaged distributions from Buchthal and Rosenfalck (1966) and O'Sullivan and Swallow (1968).

Keller and Kuhn (2008), provides a basis for understanding the interactions at the interface between electrode and skin. However, this approach does not account for inhomogeneities within the tissues and the electrode, such as sweat glands or blood vessels. According to Kuhn (2008), these inhomogeneities only have a significant impact on nerve activation when they are in close proximity to the nerves. For the purposes of this study, which aims to analyze nerve activation solely within the muscle volume, this simplified model proved sufficient, particularly as the anisotropic material properties of the muscle and the isotropic properties of the other tissues were considered.

The material properties cover the biological tissues of the forearm as well as the hydrogel of the electrodes. Electrical properties of biological tissue include conductivity and permittivity due to their microanatomy with closed compartments covering a liquid embedded in another liquid. Both properties depend on the exact tissue composition and structure (e.g., water content), and the experimentally determined values in the literature are inconsistent. In the context of the simulation of transcutaneous stimulation, Kuhn and Keller (2005) compared simulated surface and intramuscular potential curves of six models with different material properties with experimentally measured curves. Based on their results, the authors defined standard materials that were used in this study (Table 1), as in several previous FES simulation studies.

The meshing was realized in Ansys Electronics Desktop using tetrahedral elements and refining them by manual mesh operations for each layer. Table 1 summarizes the mesh operations and parameters used, which were selected on the basis of a convergence analysis.

The stimulation pulse was modeled by a current placed on a different electrode surface near the elbow and a sink placed on the indifferent electrode surface at the wrist. To obtain a single rectangular pulse with ramp-in and -out as used by the stimulator, a piece-wise-linear function (pwl) was used to define the current. Furthermore, Ansys autonomously selected the boundary conditions for the electrodes based on the type of excitation. The external environment (air) was neglected in solving the problem.

2.2 Muscle-specific nerve fiber arrangement

The muscle-specific arrangement of nerve fibers was realized by grouping them into distinct regions of interest (ROIs), with each ROI approximating the innervation zone (IZ) of a muscle at the nerve entry point (NEP) of the corresponding muscle. This is realized by determining first the NEP of a muscle to define the axial position of the ROI, then approximating the muscle course to define the orientation, and thirdly approximating the cross section of the muscle by an ellipse to define the size. The NEPs were determined by mapping data from studies on cadaveric human forearms to the anatomy on which this work was based (given by the MRI data). Table 2 summarizes the proximal maximum, median, and distal maximum distance of the NEPs from the lateral epicondyle of the humerus (LEH) relative to the forearm length (defined as the distance between the LEH and the radial styloid process, or RSP) for all forearm muscles. Most values are based on Liu et al. (1997). They analyzed the innervation pattern (number and position of NEPs) in ten cadaveric forearms. Their results showed that the NEPs of the two finger flexors vary along more than 50% of the forearm, so additional data were taken into account to split these ranges in two ROIs (Bickerton et al., 1997; Hwang et al., 2007). Negative values were excluded for modeling as the authors examined extended arms in contrast to the MRI data used that cover a flexed arm: the BR was not included at all and the extensor carpi radialis longus (ECRL) was designed without using the proximal maximum value. A total of 20 muscle-specific ROIs were added to the 3D forearm model by the following steps.

1) The axial distances given in Table 2 were calculated, and the nearest MR image was determined and added at the corresponding distance to the existing 3D forearm model. The median section defined the axial position of the ROI.
2) The required muscle was identified in all three MRI images. In each slice, an ellipse approximating the cross section of the required muscle was designed, where the three major axes had to be parallel. To support this step, a continuous 3D segmentation of all muscles was realized using a 3D Slicer (http://www.slicer.org). In this segmentation, the dimensions and the angle (roll) of the single ellipses were determined. The orientation of the ROI was defined then by first connecting the major axes (pitch) on the sections at the proximal and distal maximum and then the minor axes (yaw).
3) The area of the ROI was sketched on a tilted plane (at the defined axial position, perpendicular to the defined orientation) and extended 10 mm proximally and distally. Each ROI has an elliptical area with muscle-specific dimensions.

In each ROI, 500 uniformly distributed nerve fibers underlying a bimodal diameter distribution were modeled. Every nerve incorporates various fiber types that can be distinguished by diameter and differ in their characteristics, such as conduction velocity and excitability (Rattay, 1990; Hall and Guyton, 2011). The bimodal diameter distribution has been determined for myelinated fibers in peripheral nerves in animals (Prodanov and Feirabend, 2007; Rijkhoff et al., 1996) and humans (Buchthal and Rosenfalck, 1966; O'Sullivan and Swallow, 1968; Jacobs and Love,

TABLE 3 Overview of the axon and membrane characteristics used to set up the linear cable model.

Parameter		Value	References
Axon diameter	d	2–16 µm	Buchthal and Rosenfalck (1966); O'Sullivan and Swallow (1968)
Internodal distance	Δx	155–1,500 µm	McIntyre and Grill (1998)
Node length	L	2.5 µm	McNeal (1976)
Specific axon resistance	ρ_i	0.7 Ωm	McNeal (1976)
Membrane conductance/unit area	g_m	30.4 m/cm^2	McNeal (1976)
Membrane capacitance/unit area	c_m	2 $\mu F/cm^2$	McNeal (1976)
Resting potential	V_r	−70 mV	McNeal (1976); Frankenhaeser and Huxley (1964)
Threshold potential	Vth	−55 mV	

1985). In this study, diameter distributions of two median nerves (Buchthal and Rosenfalck, 1966) and a sural nerve (O'Sullivan and Swallow, 1968) (which is similar to the distributions of the analyzed radial nerves) were averaged. The resulting distribution ranges from 2 to 16 µm and has peaks at 5 and 11 µm (Figure 2); it is comparable to the fiber distributions used in previous FES simulation studies (Kuhn et al., 2009a; Gomez-Tames et al., 2013a; Loitz et al., 2015). As no 3D nerve model was incorporated but each fiber was represented by a single line with nodes at fiber-specific distances (Figure 1C, Δx), this modeling was realized in MATLAB (Version R2024a; The MathWorks, Inc.; Natick, Massachusetts, United States). To align the positions with the modeled ROIs, these were exported to MATLAB as stl-files. The modeled nodes represent the nodes of Ranvier between the myelin sheaths where the electrophysiological processes occurr in saltatory conduction (Hall and Guyton, 2011), and their distance increased with fiber diameter. The chosen Δx values were based on McIntyre et al. (2002) and the first and last nodes were of random distance to the ROI bottom and top faces.

2.3 Nerve model and muscle activation

This study used two common approaches to predict the effect of external stimulation on the nerve fibers: the linear cable model (LC) and the activating function (AF) (McNeal, 1976; Rattay, 1986; 1990). Both approaches were chosen due to their computational efficiency and have already been successfully used in the context of optimization problems (Loitz et al., 2015) and implemented in MATLAB. The linear cable model is the simplest electrical representation of a nerve fiber, first introduced in McNeal (1976). It combines all ionic currents at the Ranvier nodes into one time-invariant current and it assumes the myelin sheath to be a perfect insulator so that the internode section can be modeled by a stand-alone conductance. Eq. (2) gives the resultant mathematical description for node n (Figure 1C, left node).

$$\frac{dV_{m,n}}{dt} = \frac{1}{C_m}\left[G_a\left(V_{m,n-1} - 2V_{m,n} + V_{m,n+1} + V_{e,n-1} - 2V_{e,n} + V_{e,n+1}\right) - I_{ionic}\right]. \quad (2)$$

If the calculated membrane potential exceeds a defined threshold, the corresponding node of Ranvier is assumed to generate an action potential (McNeal, 1976) and the nerve fiber is considered activated (Kuhn, 2008; Loitz, 2019). Table 3 summarizes all axon and membrane characteristics used to build the linear cable model in MATLAB.

The AF is a simplified mathematical description for predicting the nerve fiber response defined as the second derivative of the extracellular potential along the axon course. Rattay (1986) initially showed that this is the main driver for the generation of action potentials in unmyelinated axons.

$$f(x,t) = \frac{\partial^2 V_e(x,t)}{\partial x^2}. \quad (3)$$

A positive value indicates membrane depolarization and a negative value, hyperpolarization (Rattay, 1986; 1999). Although this term was initially defined for unmyelinated axons, it has also been successfully used to predict the activation of myelinated fibers during FES simulation (Kuhn, 2008; Cooper et al., 2011; Gomez-Tames et al., 2011; 2013b; Loitz, 2019). Kuhn (2008) further introduced thresholds depending on the most important influencing factors (axon diameter and pulse width) to improve prediction accuracy when simulating FES with skin electrodes. These thresholds were used in the current study when predicting fiber activation with the activating function (for more details and the lookup values, see Kuhn, 2008).

Based on the single fiber activations, the percentage of activated fibers within one ROI was calculated, which is proportional to the muscle activation as outlined above. This was done for every ROI so that a muscle-specific activation resolution was achieved.

2.4 Experimental evaluation

The experimental evaluation was realized by comparing simulated and experimentally measured strength–duration (SD) diagrams for eight ROIs at predefined electrode positions. SD diagrams relate the required amplitude to achieve a defined motor response (mostly motor threshold) to the duration of the stimulation pulse (pulse width) for a specific muscle (Baker et al., 1993). They are a common method for evaluating the excitability of nerves or muscles in experiments (e.g., Baker et al., 1993; Imatz-Ojanguren et al., 2016) and have been used in previous studies to

TABLE 4 Overview of selected muscles, stimulation settings, and outcome criteria to evaluate the new FES simulation model.

	Simulation	Experiment
Muscles	ECU, ED, ECRB, ECRL, FCR, FDS, and FCU	
Amplitude	1–50 mA, increment 1 mA	1 – x mA, increment 1 mA, x as required to see a motor response
Pulse width	1–500 μs, continuous	20–100 μs with increment 20 μs and 150–500 μs with increment 50 μs
Motor response	Muscle-specific ROI activation	Significant increase in force

TABLE 5 Overview of selected muscles, settings, and outcome criteria to evaluate the model and simulation setup.

ROI	Different electrode		Indifferent electrode	
	Axial pos. [%]	Radial pos. [%]	Axial pos. [%]	Radial pos. [%]
ECU	33.06	9.88[a]	88.00	20.00
ED	33.06	22.03[a]		
ECRB	25.62	32.11[b]		
ECRL	3.31	30.17[a]		
FCR	25.62	65.36[a]	91.50	72.00
FDSprox	52.07	75.39[b]		
FDSdist	74.38	71.50[b]		
FCU	13.22	85.13[a]		

[a]Projection in the direction of the minor axis of the ellipse.
[b]Projection in the direction of the minor and major axes of the ellipses, position in between both points.

evaluate FES simulation setups (e.g., Kuhn et al., 2009a; Goffredo et al., 2014). The experiments were performed with the healthy subject (34y, female) who also provided the MRI data. Table 4 summarizes the selected settings and used outcome criteria to generate the SD diagrams. At each electrode position, amplitude and pulse width were varied in the specified ranges. The eight ROIs were chosen in a first step because good selective activation can be achieved for these muscles.

The predefined electrode positions correspond to the projections of the eight ROI centers onto the skin, along with one of the ellipsis axes or between them, depending on the orientation of the ROI. Table 5 summarizes these positions. For the simulations, the positioning is carried out as described above. For the experiments, the same reference system is transferred to the real forearm: a reference line along the ulna (palpable) is drawn on the forearm beginning vertically at the LE of the humerus and ending at the RSP. The axial position is then the length along this line; the radial position is the length along the circumference at height of the axial position. Since the exact dimensions of the model and the real forearm differ due to the model's simplifications, relative positions are used. To account for the variance in electrode position during the experiments, they were repeated four times. Experiment 1-0 was the initial experiment and marking of the electrode positions. Experiment 1-1 was a replication of 1–0 but included removal and reattachment of the electrodes. Experiments 2-0 and 3-0 were full replications with new marking of the electrode positions. The three new marking procedures resulted in positions within a maximum range of 1 cm.

The experimental setup is shown in Figure 3. It covers the following components and setup.

- A multichannel stimulator (KT Motion, MEDEL GmbH; Hamburg, Germany; CE0483) connected to the skin by two hydrogel electrodes (Axelgaard Manufacturing Co., Ltd.; Fallbrook, CA, United States). The different electrode is round with a diameter of 25 mm and is placed at the stimulation position at the muscle. The indifferent electrode is square with a 50 mm edge length and is placed at a neutral position near the wrist (ventral for flexors, dorsal for extensors).
- A force measurement system was used for the hand and wrist, including an adjustable forearm support and comprehensive software for data recording and stimulation control (self-developed, Chair of Product Development, Ruhr-University Bochum; Bochum, Germany): The hand-rest of the measuring system was ergonomically shaped and allowed placement, in combination with the forearm support, of the hand in a resting position for measurements to avoid forces caused by pre-tensioning of the muscles. The forces generated by isometric muscle contraction were recorded using eight force sensors: two at the base to record the forces resulting from flexion/extension and radial/ulnar abduction of the wrist (±200 N), two for the thumb to record the forces resulting from abduction/adduction (±50 N) and extension/flexion

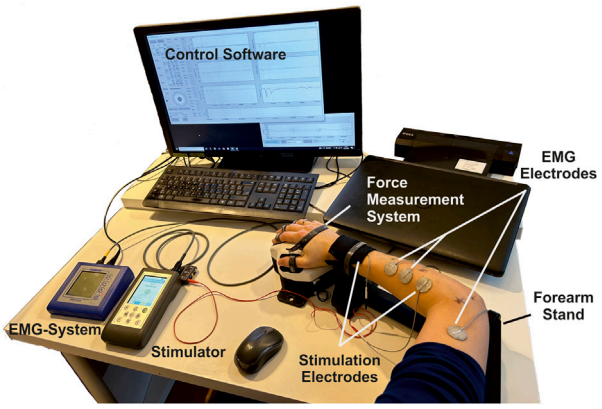

FIGURE 3
Overview of the experimental setup consisting of a stimulator with two hydrogel stimulation electrodes, a force measuring system with forearm support and control software, and an EMG system with two measuring electrodes and an additional reference electrode.

(±200 N), and one for each finger II to V to record the resulting forces from flexion/extension (±50 N). Each force sensor was previously tested for linearity and measurement deviation within the permissible measurement range using a materials-testing machine (Zwick Z010 with GTM GmbH 238 series K, 10 kN, 2 mV/V) and were then calibrated. Both the fingertip and the respective distal joint can be used as the contact point for the force measurements of fingers I to V. The measurement frequency can be set in discrete steps from 10 to 320 Hz. We chose, for our measurements, a frequency of 80 Hz. In addition to the force data, the stimulation settings frequency, pulse width, and stimulation current were recorded in parallel in the software.

- An EMG System (Novativ, MEDEL GmbH; Hamburg, Germany; CE0482) was connected to the skin by three hydrogel electrodes (Axelgaard Manufacturing Co., Ltd.; Fallbrook, CA, United States; EC No 1907/2006): two electrodes for measuring the differential muscle potential between the stimulation electrodes on the respective muscle body and one reference electrode at a neutral position at the upper arm. No exact positioning of the measurement electrodes was carried out, as the influences due to translation along the muscle fibers or rotations up to 30° mainly affect the amplitude of the signal (Duarte et al., 2016), which is not of interest here. The EMG measurements (measurement frequency: 4,500 Hz) were used during the experiments to ensure that no unintended, voluntary muscle activation was performed. A stimulated movement only leads to clearly identifiable M-waves in EMG that occur after each stimulation pulse (Merletti et al., 1992). Any other activation indicated an unintentional voluntary contraction, so the measurement was aborted and repeated.
- A defined hand to forearm to upper arm positioning reflecting the same positioning chosen during MRI data acquisition: hand in pronation position (preset by the measuring system), elbow flexed approximately 90°, upper arm parallel to palm (that is, parallel to the table).

3 Results

Previous models have been limited in simulating the activation of several single muscles, which is necessary for using them as a digital twin and supporting the development of individualized applications and new products. To demonstrate that our simulation model maps real muscle activations correctly and reliably, we generated strength–duration (SD) diagrams for various muscles, both for simulations and the experimental measurements. Typically, in experimental studies, the lowest muscle response is chosen for the creation of the SD diagram. However, in simulations, even at low intensities, individual nerve fibers are activated; such activations may not be measurable in experiments and could lead to an overestimation of activation in the simulation compared to the experiments. To ensure reproducible and comparable thresholds from both experimental measurements and simulations, we opted for the onset of the characteristic sigmoidal progression of the intensity-force curve instead of the usual first muscle twitch. For the example shown in Figure 4A, this means that the activation thresholds used to create the SD diagrams were shifted by force increases from 3–4 mA to 6–7 mA. This applied to all four repetitions of the experiment. Figure 4B shows, for the same muscle, the fitted mean curve that was used for the further comparisons to simulated SD diagrams. Additionally, the maximal variance for the four repetitions is

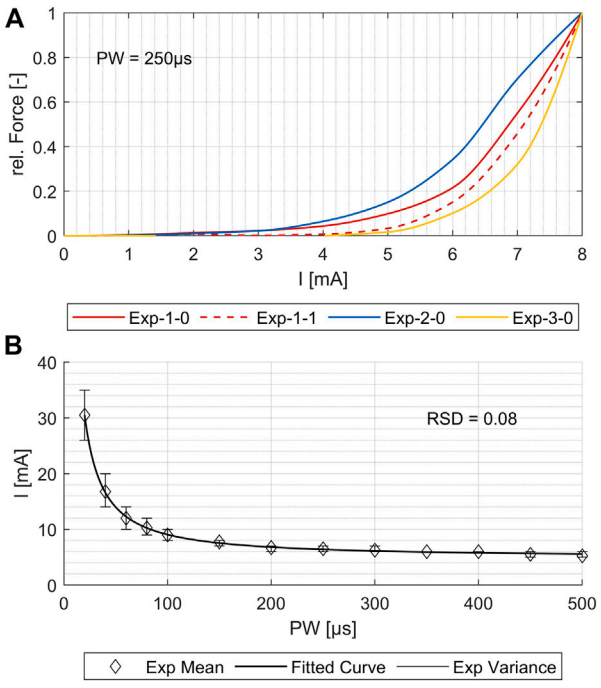

FIGURE 4
Comparison of the four experimental measurements for one exemplary muscle (flexor carpi radialis, or FCR). **(A)** Force increase over amplitude for PW = 250 µs. **(B)** Variance of the strength–duration diagrams and the resulting fit curve for the mean values. The relative standard deviation (RSD) is 0.08.

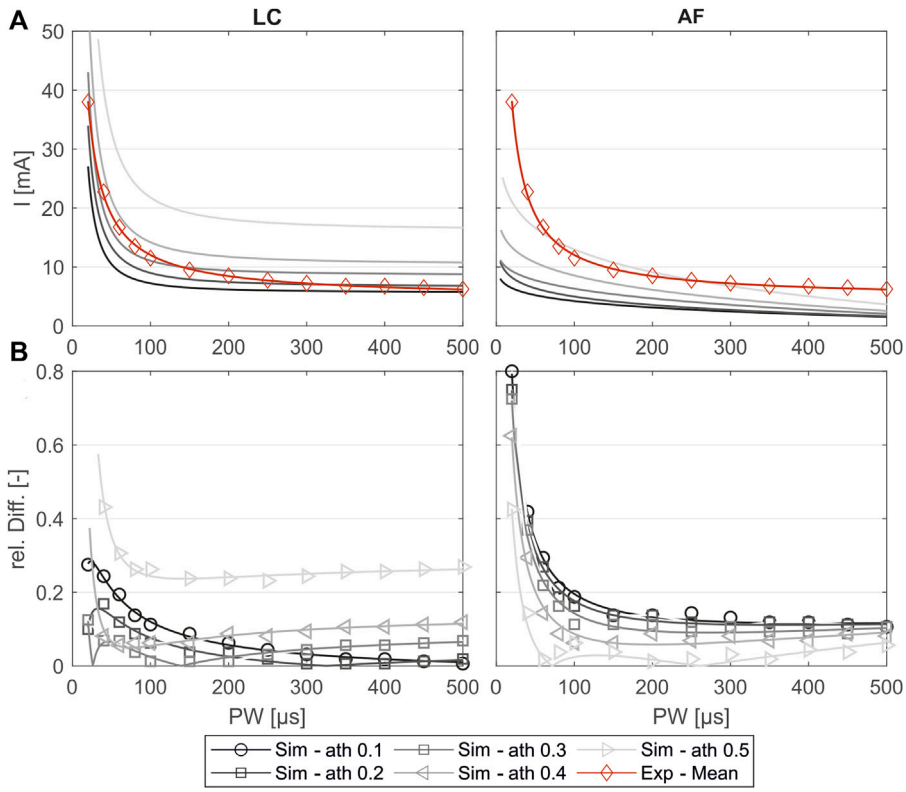

FIGURE 5
Comparison of the experimentally measured and simulated SD diagrams using the linear cable model (LC) or the activating function (AF) for one exemplary muscle (extensor carpi ulnaris, or ECU). **(A)** Simulated SD curves using different activation thresholds (ath) compared to the mean fit from the experiments. **(B)** Relative difference of the simulated and experimental SD curves: markers show the relative difference at the experimentally measured PW steps, and the lines show the relative difference of the fitted curves shown in **(A)**.

shown. Although the three electrode positions differed (<1 cm) when repeating the marking procedure, the resulting SD plots show only small differences for all muscles with relative standard deviations (RSDs) between 0.04 and 0.09, except for the ECRL, which is slightly higher at 0.14.

Figure 5A shows the simulated SD curves for one exemplary muscle (extensor carpi ulnaris, or ECU) using the linear cable model (LC) as well as the activating function (AF) compared to the experimental SD curve. The simulated SD curves vary depending on the chosen activation threshold (ath), which is defined as the percentage activation of the corresponding region of interest (ROI). To determine which activation thresholds are appropriate, we conducted the following analysis. Figure 5 includes uniformly distributed ath between 0.1 and 0.6 to illustrate the influence of this factor and the range of the resulting SD curves. In general, the graphs generated with the LC model follow the same trajectory as the experimental curve, whereas the graphs generated using the AF especially fail to map the characteristic curve for low pulse widths (PW) up to 200 µs. Therefore, we excluded the AF in further analysis. To analyze the deviations of the simulated and experimental SD curves, the relative differences were plotted for each PW in 1 µs steps. As illustrated in Figure 5B, the SD graphs for the LC model fit for either low PW or those higher. The curves of the ath with comparable overall good fit intersect at PW 200 ± 50 µs. We therefore determined muscle-specific activation thresholds for two PW ranges, 20–200 µs and 201–500 µs, based on the mean of the relative differences between the SD curves at each PW in 1 µs steps. Table 6 summarizes these values for the different muscles and activation thresholds, with the best fitting cases highlighted in bold. For the muscles that could not be selectively/experimentally validated, we chose the activation thresholds based on the average of the validated muscles for the respective pulse width ranges: 0.20 for PW = 20–200 µs and 0.12 for PW = 201–500 µs.

Figure 6 shows the distribution of the relative differences between simulated PW to the experimental mean values (A) compared to the distribution of the inter-experimental differences (single experiments to experimental mean). The comparison shows that for both pulse width (PW) intervals, the remaining differences in the simulated values are in the same range as the inter-experimental differences for all muscles. It can be assumed that for a higher number of experiments, the experimental mean converges against the simulated curve.

Figure 7 shows the comparison of the simulated intensity-force curves with (corrected) and without (default) inclusion of the muscle-specific activation threshold (ath) with the experimentally measured intensity-force curves for different PWs for one muscle (ECRB) as an example. The experiment in this case was performed additionally and was not part of the

TABLE 6 Mean relative differences between the simulated and experimental SD curves for two PW intervals: 20 – 200 *μs* and 201 –500 *μs*.

ROI	PW range [μs]	Activation threshold (ath)									
		0.05	0.10	0.15	0.20	0.25	0.30	0.35	0.40	0.45	0.50
ECU	20–200	0.171	0.139	0.120	0.083	0.050	**0.030**	0.031	0.087	0.159	0.330
	201–500	0.054	0.028	0.025	**0.010**	0.026	0.052	0.079	0.107	0.160	0.266
ED	20–200	0.085	0.041	0.027	**0.027**[a]	0.062	0.124	0.176	0.253	0.379	0.719
	201–500	**0.011**	0.034	0.061	0.069	0.096	0.145	0.171	0.225	0.288	0.478
ECRB	20–200	0.226	0.146	0.064	**0.025**	0.119	0.222	0.335	0.486	0.664	0.931
	201–500	0.108	0.052	**0.013**	0.046	0.111	0.190	0.254	0.364	0.469	0.589
ECRL	20–200	0.213	0.177	0.147	0.118	0.088	0.062	**0.029**	0.040	0.099	0.175
	201–500	0.083	0.059	0.036	0.014	**0.008**	0.013	0.045	0.084	0.130	0.180
FCU	20–200	0.093	0.038	**0.022**	0.029	0.076	0.119	0.172	0.236	0.359	0.515
	201–500	**0.013**	0.018	0.042	0.071	0.101	0.130	0.160	0.194	0.274	0.640
FDSprox	20–200	**0.045**	0.062	0.186	0.294	0.468	0.748	0.911	1.367	2.173	26.652
	201–500	**0.020**	0.095	0.179	0.241	0.371	0.483	0.634	0.762	0.900	1.071
FDSdist	20–200	0.170	0.096	**0.044**	0.050	0.144	0.242	0.369	0.517	0.713	0.937
	201–500	0.045	**0.017**	0.054	0.105	0.159	0.226	0.304	0.362	0.479	0.613
FCR	20–200	0.084	0.043	**0.013**	0.042	0.073	0.117	0.202	0.291	0.409	0.616
	201–500	0.025	**0.005**	0.033	0.062	0.082	0.105	0.167	0.229	0.294	0.429

[a]decision based on the fourth decimal (ath 0.15: 0.0272; ath 0.20: 0.0270).
The bold values indicate the smallest difference for each ROI.

determination of the activation thresholds. As can be seen, the corrected simulated curve fits well with the experimental curve for all PWs. Both curves show the characteristic onset of the sigmoidal progression of intensity-force curves. The characteristic late bending cannot be seen as the amplitude was not increased until the maximum muscle force was reached. The default simulated curve instead differs clearly from the experimental curve and does not show the characteristic sigmoidal progression.

4 Discussion

Despite the established use of FES for many years and extensive research, current applications at the forearm to stimulate hand movements are still limited to simple movements due to the difficulties of achieving selective muscle activations. Most research in this area has focused on experimentally determining motor points (MPs) using multichannel systems with electrode arrays and manual or semi-automatic search algorithms (Salchow et al., 2016a; Malesevic et al., 2012; Keller et al., 2007; Koutsou et al., 2016). However, the results and their impact are limited, mainly due to the small number of experiments (time-consuming, premature muscle fatigue). Simulations have been used successfully in the past to complement experimental research, but existing simulation models are not suitable for analyses of selective muscle activation.

This study used a new modelling approach to develop an individual forearm model that allows the analysis of FES at the level of individual muscle activation through simulations. Like existing models, our simulation model represents the "outer" anatomy by homogeneous tissue layers (bone, muscle, fat, and skin), as in, for example, Kuhn and Keller (2005), Loitz et al. (2015), RaviChandran et al. (2020b), and Gomez-Tames et al. (2013b). In contrast to these models, the shape of our tissue layers is neither fully simplified (as e.g. in Kuhn and Keller, 2005) nor fully anatomic (as e.g. in Gomez-Tames et al., 2013b). The shape of our model is anatomically based, meaning that an individual anatomy given by MRI data has been approximated with regular geometries—mostly ellipses. The advantage of this choice is that the resulting volumes and surfaces are still mathematically defined and, therefore, the model can be easily extended or modified. This is important:

- to allow the modeling of electrodes of any size and geometry (including electrode arrays in future applications) at any location on the skin;
- to allow future parameterization of the model, enabling its easy adaptation to different fat thicknesses or forearm lengths, for example.

As all changes to the electrode configuration are automatically updated via scripts and macros, the model can be easily integrated into optimization loops. Optimization loops can be used, for example, to find the best individual stimulation positions, which could then be integrated into an individual forearm sleeve.

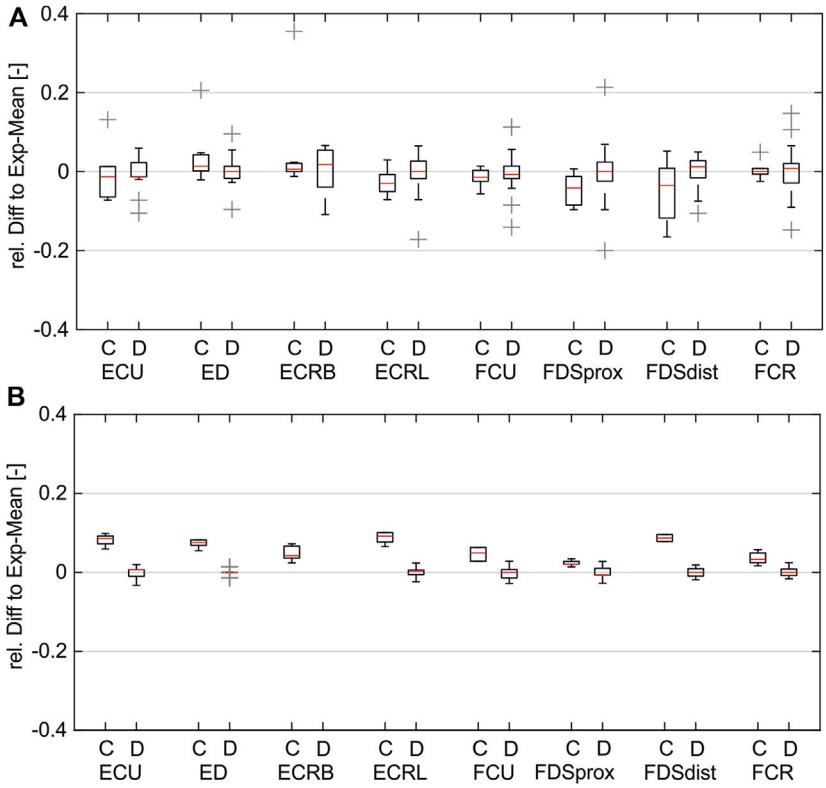

FIGURE 6
Comparison of simulated and inter-experimental distribution of relative differences: **(A)** for PW range 20–200 µs; **(B)** for PW range 201–500 µs. (C = difference between simulated data and experimental mean; D = difference between single experiments and mean).

In addition to the "outer" anatomy, our model also includes aspects of the "inner" anatomy; more precisely, it includes muscle-specific regions of interest (ROIs) that represent the muscle areas where the nerve entry point (NEP) and the innervation zone (IZ) of individual muscles are located. The nerve fibers were arranged in these various muscle-specific ROIs, which differ from existing models, which cover three main types of arrangement: single fiber or one group of fibers placed at a specific depth (e.g., Kuhn et al., 2010; Goffredo et al., 2014; RaviChandran et al., 2020b), uniform distribution of various fibers covering the whole muscle layer (e.g., Kuhn and Keller, 2007), and fibers arranged in one muscle-specific region (e.g., Gomez-Tames et al., 2013a; Loitz et al., 2015). In the latter case, this region was placed in the muscle layer based only on general anatomical information; in our model, the muscle-specific regions were placed based on the transfer of literature data regarding the position of NEPs to the underlying anatomy (MRI data). Due to the muscle-specific nerve fiber arrangement, our model enables the simulation of single muscle activations and, consequently, simulation-based analyses of selective muscle activation.

The experimental evaluation shows an overall good coincidence of the simulated and experimentally measured muscle activations. The small RSD of the different measurements indicate that the chosen reference system provides a robust method for transferring electrode positions between the digital twin and real forearm (Figure 4). The comparison of the simulated strength–duration (SD) curves with the measured curves shows that the simulations with the LC model are generally suitable for reproducing the characteristic course of the SD curves, unlike the simulations with the AF. The best fit is achieved when splitting the considered pulse width (PW) range in two intervals: 20–200 µs and 201–500 µs. For each muscle, different activation thresholds showed the best results. The definition of a global activation threshold would always lead to high differences in some muscles and is only used for the muscles not yet considered experimentally. Considering these limitations for low PWs up to 200 µs, the maximal mean relative difference between simulated and experimental curve is 0.045 and, for PWs higher than 200 µs, 0.013.

The main reason for the need to split the considered PW range in two intervals is that the measured amplitudes still decrease for high PWs. With increasing PW, the amplitude normally converges toward a minimum amplitude required to stimulate a muscle response—the rheobase (Baker et al., 1993). According to Baker et al. (1993), PW higher than 300 µs does not usually affect the stimulation amplitude. Therefore, we are currently working on evaluating a second existing person-specific model to understand whether this effect is person-specific or occurs more often and that perhaps the reporting studies have a bias, such as due to less precise measurement systems.

In addition to this experimental anomaly, there exist different simulation-based reasons that could explain the lack of the simulated curves to represent the measured curves over the full PW range.

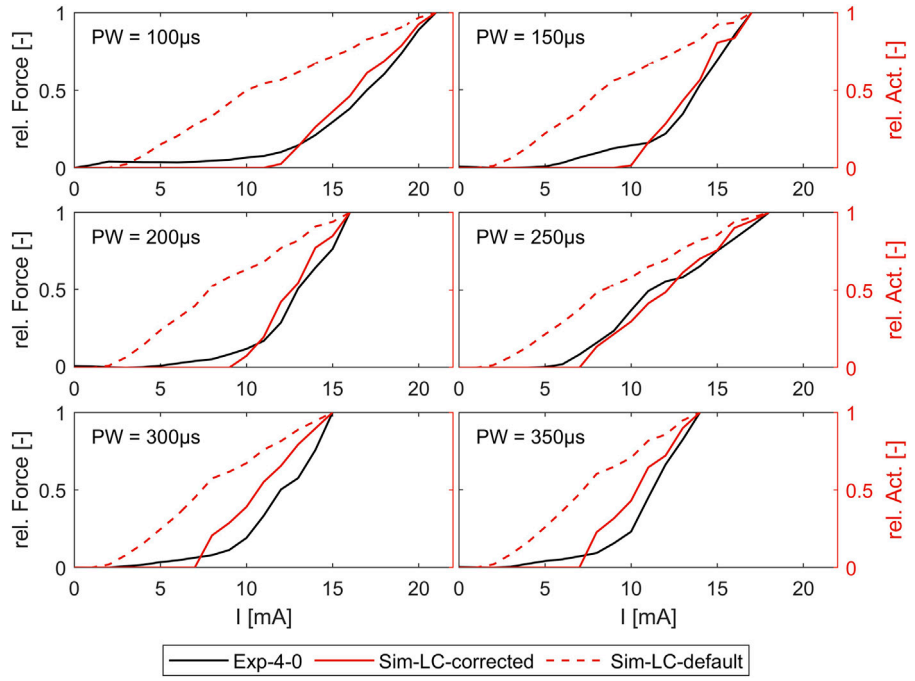

FIGURE 7
Comparison of simulated force-intensity curves (with and without, including the muscle-specific ath) with experimental curves for different PW. Example shown for the extensor carpi radialis muscle (ECRB).

- The selected nerve fiber orientation: all nerve fibers are modeled parallel to the ROI, which means parallel to the muscle course. This may not represent the actual fiber orientations with sufficient accuracy, as the terminal nerve branch splits after the NEP, and the individual fibers pull in all directions to reach all muscle fibers. It has been shown that the relative orientation of the nerve fibers to the electrode (if not rotationally symmetrical) influences activation (Loitz et al., 2015).
- The selected number of nerve fibers: the simulation is performed with a fixed number of 500 nerve fibers, which is probably higher than the real number (McComas, 1998). This number was chosen to minimize the influence of randomness.
- The selected nerve model type: the LC model is a very simplified model of a nerve fiber, assuming perfect insulation at the internodal sections. More detailed models consider the different ionic currents through membranes, such as the MRG model (McIntyre et al., 2002). These models could be integrated as well (e.g., Kuhn and Keller, 2005; RaviChandran et al., 2020b), but this increases simulation time significantly and is therefore a disadvantage when aiming for integration in optimization or AI methods.
- The selected parameters for the nerve model: changing individual model parameters influences the activation results and, consequently, also SD curves (McIntyre and Grill, 1998). The model parameters were chosen in accordance with exiting simulation studies in FES but may differ with the differing objectives of simulation models.

The first two of these simulation-based reasons may affect different muscles in different ways, and therefore might also affect the "global activation threshold" aspect mentioned above. However, an important question here is, "Is there one global activation threshold for all muscles?". Measured SD curves for different muscles show differences (Baker et al., 1993), which indicates it is not. This is consistent with anatomical studies showing that fiber type distribution differs between muscles (Hwang et al., 2007). Based on this hypothesis, the definition of mean values as realized for the muscles not measured will lead to inappropriate muscle activations for these muscles. Therefore, we are currently working on individual measurements of these models to determine muscle-specific activation thresholds.

Considering the muscle-specific activation thresholds for the two PW intervals leads to promising results in predicting muscle activation independently of the stimulation intensity, which is determined by PW and amplitude. The simulated strength-intensity curves fit additional experimental data not used in prior determination of the activation thresholds and shows the characteristic force increase at the same amplitude. As muscle activation patterns are composed of single muscle activations, it can be assumed that the model is also suitable for simulating these and enabling further conclusions on stimulated movements or forces when several muscles are activated simultaneously, as is usual.

Overall, the approach presented holds significant promise of being suitable for designing digital twins of the forearm that can

enable accurate and reliable prediction of real stimulated muscle activations. The next steps cover the two aspects mentioned above: experimental evaluation of a second individual model, which is already designed, and experimental evaluation of the remaining ROIs for the model presented. Furthermore, we aim to use the activation patterns simulated with the current model to predict the resulting movement or force. In a first step, each measured force could be related to a weighted sum of the activations of all muscles affecting this force location and direction (e.g., all extensors analyzed in these studies contribute to an extension in the wrist). In a second step, the model presented could be coupled with a biomechanical musculo-skeletal model to predict and visualize real movements. The current model is already suitable for integration into product development processes due to the automated model and simulation workflow modification: it can be integrated in optimization loops to find the best stimulation positions and design a patient-specific forearm sleeve for easy stimulation setup, or it can be used for developing optimized search algorithms for common electrode arrays with regular grids. In order to increase the benefits of this digital twin for product development, a future parameterization is planned. Such a parameterized digital twin will enable the prediction of muscle-specific activations by FES on the forearm for different forearm anatomies, which will particularly further improve the development of universal solutions using optimization or AI methods.

Data availability statement

The raw data supporting the conclusion of this article will be made available by the authors, without undue reservation.

Ethics statement

Ethical review and approval was not required for the experiments in this study in accordance with the local legislation and institutional requirements. All materials used for the experiments are either commercially available and approved for use in humans or were used exclusively for measurement. The only aim of the experiments was to evaluate the simulation results; no medical application, therapy optimization or testing of product prototypes took place. Written informed consent was obtained from the one participant for the collection of the data and for the publication of any potentially identifiable images or data included in this article.

Author contributions

JB: conceptualization, formal analysis, methodology, visualization, writing–original draft, and writing–review and editing. SS: resources, software, writing–original draft, and writing–review and editing, visualization, methodology. BB: supervision, and writing–review and editing, resources.

Funding

The author(s) declare financial support was received for the research, authorship, and/or publication of this article. We acknowledge support by the DFG Open Access Publication Funds of the Ruhr-University Bochum.

Conflict of interest

The authors declare that the research was conducted in the absence of any commercial or financial relationships that could be construed as a potential conflict of interest.

Publisher's note

References

Baker, L. L., McNeal, D. R., Benton, L. A., Bowman, B. R., and Waters, R. L. (1993). Neuromuscular electrical stimulation: a practical guide *(downey, CA: los amigos research & education institute)*. 3.

Bao, X., Zhou, Y., Wang, Y., Zhang, J., Lü, X., and Wang, Z. (2018). Electrode placement on the forearm for selective stimulation of finger extension/flexion. *PloS one* 13, e0190936. doi:10.1371/journal.pone.0190936

Bickerton, L. E., Agur, A. M., and Ashby, P. (1997). Flexor digitorum superficialis: locations of individual muscle bellies for botulinum toxin injections. *Muscle & nerve* 20, 1041–1043. doi:10.1002/(sici)1097-4598(199708)20:8<1041::aid-mus18>3.3.co;2-l

Buchthal, F., and Rosenfalck, A. (1966). Evoked action potentials and conduction velocity in human sensory nerves. *Brain Res.* 3–122. doi:10.1016/0006-8993(66)90056-4

Cooper, G., Barker, A. T., Heller, B. W., Good, T., Kenney, L. P. J., and Howard, D. (2011). The use of hydrogel as an electrode-skin interface for electrode array fes applications. *Med. Eng. Phys.* 33, 967–972. doi:10.1016/j.medengphy.2011.03.008

Crema, A., Malesevic, N., Furfaro, I., Raschella, F., Pedrocchi, A., and Micera, S. (2018). A wearable multi-site system for nmes-based hand function restoration. *IEEE Trans. neural Syst. rehabilitation Eng. a Publ. IEEE Eng. Med. Biol. Soc.* 26, 428–440. doi:10.1109/TNSRE.2017.2703151

Doheny, E. P., Caulfield, B. M., Minogue, C. M., and Lowery, M. M. (2010). Effect of subcutaneous fat thickness and surface electrode configuration during neuromuscular electrical stimulation. *Med. Eng. Phys.* 32, 468–474. doi:10.1016/j.medengphy.2010.03.004

Duarte, R., Mesnard, M., de Miollis, F., Ramos, A., Wentzy, P., and de Sèze, M. (2016). *Influence of semg electrode positioning during muscular activity tests*. Lisboa, Portugal: 10th Congresso Nacional de Mecanica Experimental.

Frankenhaeser, B., and Huxley, A. F. (1964). The action potential in the myelinated nerve fibre of xenopus laevis as computed on the basis of voltage clamp data. *J. physiology* 171, 302–315. doi:10.1113/jphysiol.1964.sp007378

Goffredo, M., Schmid, M., Conforto, S., Bilotti, F., Palma, C., Vegni, L., et al. (2014). A two-step model to optimise transcutaneous electrical stimulation of the human upper arm. *COMPEL - Int. J. Comput. Math. Electr. Electron. Eng.* 33, 1329–1345. doi:10.1108/COMPEL-04-2013-0118

Gomez-Tames, J., Gonzalez, J., and Yu, W. (2011). "Influence of subcutaneous fat thickness upon the activation volume in transcutaneous electrical stimulation to a thigh simulation model," in 14th Annual Conference of the International FES Society.

Gomez-Tames, J., Gonzalez, J., and Yu, W. (2013a). "Influence of fat thickness and femur location on nerve activity computation during electrical stimulation," in IEEE 17th International Conference on Intelligent Engineering Systems (INES), 2013 (Piscataway, NJ: IEEE), 51–54.

Gomez-Tames, J., Gonzalez, J., and Yu, W. (2013b). A simulation study on the dominance of the tissues' conductivity in the muscle recruitment. *J. Med. Imaging Health Inf.* 3, 72–78. doi:10.1166/jmihi.2013.1139

Gomez-Tames, J. D., Gonzalez, J., Nakamura, S., and Yu, W. (2013c). "Simulation of the muscle recruitment by transcutaneous electrical stimulation in a simplified semitendinosus muscle model," in *Converging clinical and engineering research on neurorehabilitation vol. 1 of biosystems & biorobotics*. Editors J. L. Pons, D. Torricelli, and M. Pajaro (Berlin, Heidelberg: Springer Berlin Heidelberg), 449–453. doi:10.1007/978-3-642-34546-3_73

Gomez-Tames, J. D., Gonzalez, J., and Yu, W. (2012). "A simulation study: effect of the inter-electrode distance, electrode size and shape in transcutaneous electrical stimulation," in Conference proceedings: Annual International Conference of the IEEE Engineering in Medicine and Biology Society. IEEE Engineering in Medicine and Biology Society. Annual Conference 2012, 3576–3579.

Hall, J. E., and Guyton, A. C. (2011). "Guyton and Hall textbook of medical physiology: student consult," in *Activate at studentconsult.com. Searchable full text online* (Philadelphia: Saunders Elsevier), 12.

Hwang, K., Jin, S., Hwang, S.-H., Lee, K.-M., and Han, S.-H. (2007). Location of nerve entry points of flexor digitorum profundus. *Surg. radiologic Anat. SRA* 29, 617–621. doi:10.1007/s00276-007-0260-y

Imatz-Ojanguren, E., Kostic, M., Chia Bejarano, N., and Keller, T. (2016). "Workshop on transcutaneous functional electrical stimulation," in *Emerging therapies in neurorehabilitation II vol. 10 of biosystems & biorobotics*. Editors J. L. Pons, R. Raya, and J. González (Cham: Springer International Publishing), 273–301. doi:10.1007/978-3-319-24901-8_11

Jacobs, J. M., and Love, S. (1985). Qualitative and quantitative morphology of human sural nerve at different ages. *Brain a J. neurology* 108, 897–924. doi:10.1093/brain/108.4.897

Keller, T., and Kuhn, A. (2008). Electrodes for transcutaneous (surface) electrical stimulation. *J. Automatic Control* 18, 35–45. doi:10.2298/JAC0802035K

Keller, T., Lawrence, M., and Kuhn, A. (2007). "Selective finger and wrist activation using multi-channel transcutaneous electrical stimulation electrodes," in 12th Annual Conference of the International FES Society 12.

Koutsou, A. D., Moreno, J. C., Del Ama, A. J., Rocon, E., and Pons, J. L. (2016). Advances in selective activation of muscles for non-invasive motor neuroprostheses. *J. neuroengineering rehabilitation* 13, 56. doi:10.1186/s12984-016-0165-2

Kuhn, A. (2008). *Modeling transcutaneous electrical stimulation*. Dissertation. ETH zürich, zürich.

Kuhn, A., and Keller, T. (2005). "A 3d transient model for transcutaneous functional electrical stimulation," in 10th Annual Conference of the International FES Society.

Kuhn, A., and Keller, T. (2007). "A selectivity measure for transcutaneous electrodes," in 12th Annual Conference of the International FES Society.

Kuhn, A., Keller, T., Lawrence, M., and Morari, M. (2009a). A model for transcutaneous current stimulation: simulations and experiments. *Med. Biol. Eng. Comput.* 47, 279–289. doi:10.1007/s11517-008-0422-z

Kuhn, A., Keller, T., Lawrence, M., and Morari, M. (2010). The influence of electrode size on selectivity and comfort in transcutaneous electrical stimulation of the forearm. *IEEE Trans. neural Syst. rehabilitation Eng. a Publ. IEEE Eng. Med. Biol. Soc.* 18, 255–262. doi:10.1109/TNSRE.2009.2039807

Kuhn, A., Keller, T., Micera, S., and Morari, M. (2009b). Array electrode design for transcutaneous electrical stimulation: a simulation study. *Med. Eng. Phys.* 31, 945–951. doi:10.1016/j.medengphy.2009.05.006

Liu, J., Pho, R. W., Pereira, B. P., Lau, H. K., and Kumar, V. P. (1997). Distribution of primary motor nerve branches and terminal nerve entry points to the forearm muscles. *Anatomical Rec.* 248, 456–463. doi:10.1002/(sici)1097-0185(199707)248:3<456::aid-ar19>3.3.co;2-a

Loitz, J. C. (2019). *Novel methods in electrical stimulation with surface electrodes*. Berlin, Germany: LOGOS VERLAG BERLIN.

Loitz, J. C., Reinert, A., Schroeder, D., and Krautschneider, W. H. (2015). Impact of electrode geometry on force generation during functional electrical stimulation. *Curr. Dir. Biomed. Eng.* 1, 458–461. doi:10.1515/cdbme-2015-0110

Malesevic, N. M., Popovic Maneski, L. Z., Ilic, V., Jorgovanovic, N., Bijelic, G., Keller, T., et al. (2012). A multi-pad electrode based functional electrical stimulation system for restoration of grasp. *J. neuroengineering rehabilitation* 9, 66. doi:10.1186/1743-0003-9-66

McComas, A. J. (1998). 1998 isek congress keynote lecture: motor units: how many, how large, what kind? international society of electrophysiology and kinesiology. *J. Electromyogr. Kinesiol.* 8, 391–402. doi:10.1016/S1050-6411(98)00020-0

McIntyre, C. C., and Grill, W. M. (1998). Sensitivity analysis of a model of mammalian neural membrane. *Biol. Cybern.* 79, 29–37. doi:10.1007/s004220050455

McIntyre, C. C., Richardson, A. G., and Grill, W. M. (2002). Modeling the excitability of mammalian nerve fibers: influence of afterpotentials on the recovery cycle. *J. neurophysiology* 87, 995–1006. doi:10.1152/jn.00353.2001

McNeal, D. R. (1976). Analysis of a model for excitation of myelinated nerve. *IEEE Trans. Biomed. Eng. BME* 23, 329–337. doi:10.1109/TBME.1976.324593

Merletti, R., Knaflitz, M., and DeLuca, C. J. (1992). Electrically evoked myoelectric signals. *Crit. Rev. Biomed. Eng.* 19, 293–340.

Neumann, M., Remus, R., Sauerhoff, M., Lipphaus, A., Uttich, E., Sure, C., et al. (2020). Digitale Zwillinge in Interaktion mit Menschmodellen. *Z. für Wirtsch. Fabr.* 115, 116–120. doi:10.3139/104.112327

O'Sullivan, D. J., and Swallow, M. (1968). The fibre size and content of the radial and sural nerves. *J. neurology, Neurosurg. psychiatry* 31, 464–470. doi:10.1136/jnnp.31.5.464

Plonsey, R., and Heppner, D. B. (1967). Considerations of quasi-stationarity in electrophysiological systems. *Bull. Math. biophysics* 29, 657–664. doi:10.1007/BF02476917

Prodanov, D., and Feirabend, H. K. P. (2007). Morphometric analysis of the fiber populations of the rat sciatic nerve, its spinal roots, and its major branches. *J. Comp. neurology* 503, 85–100. doi:10.1002/cne.21375

Rattay, F. (1986). Analysis of models for external stimulation of axons. *IEEE Trans. bio-medical Eng.* 33, 974–977. doi:10.1109/TBME.1986.325670

Rattay, F. (1990) *Electrical nerve stimulation*. Vienna: Springer Vienna. doi:10.1007/978-3-7091-3271-5

Rattay, F. (1999). The basic mechanism for the electrical stimulation of the nervous system. *Neuroscience* 89, 335–346. doi:10.1016/S0306-4522(98)00330-3

RaviChandran, N., Aw, K. C., and McDaid, A. (2020a). Characterizing the motor points of forearm muscles for dexterous neuroprostheses. *IEEE Trans. bio-medical Eng.* 67, 50–59. doi:10.1109/TBME.2019.2907926

RaviChandran, N., Teo, M. Y., Aw, K., and McDaid, A. (2020b). Design of transcutaneous stimulation electrodes for wearable neuroprostheses. *IEEE Trans. neural Syst. rehabilitation Eng. a Publ. IEEE Eng. Med. Biol. Soc.* 28, 1651–1660. doi:10.1109/TNSRE.2020.2994900

Rijkhoff, N. J., Koldewijn, E. L., d'Hollosy, W., Debruyne, F. M., and Wijkstra, H. (1996). Morphometric data of canine sacral nerve roots with reference to electrical sacral root stimulation. *Neurourol. Urodynamics* 15, 235–248. doi:10.1002/(SICI)1520-6777(1996)15:3<235::AID-NAU8>3.0.CO;2-G

Salchow, C., Valtin, M., Seel, T., and Schauer, T. (2016a). "A new semi-automatic approach to find suitable virtual electrodes in arrays using an interpolation strategy," in *In ifess 2016 Hybrid approaches of FES, ed. IFESS.*

Salchow, C., Valtin, M., Seel, T., and Schauer, T. (2016b). A new semi-automatic approach to find suitable virtual electrodes in arrays using an interpolation strategy. *Eur. J. Transl. Myology* 26, 6029. doi:10.4081/ejtm.2016.6029

Westerveld, A. J., Schouten, A. C., Veltink, P. H., and van der Kooij, H. (2012). Selectivity and resolution of surface electrical stimulation for grasp and release. *IEEE Trans. neural Syst. rehabilitation Eng. a Publ. IEEE Eng. Med. Biol. Soc.* 20, 94–101. doi:10.1109/TNSRE.2011.2178749

Frontiers in
Bioengineering and Biotechnology

Accelerates the development of therapies, devices, and technologies to improve our lives

A multidisciplinary journal that accelerates the development of biological therapies, devices, processes and technologies to improve our lives by bridging the gap between discoveries and their application.

Discover the latest Research Topics

See more →

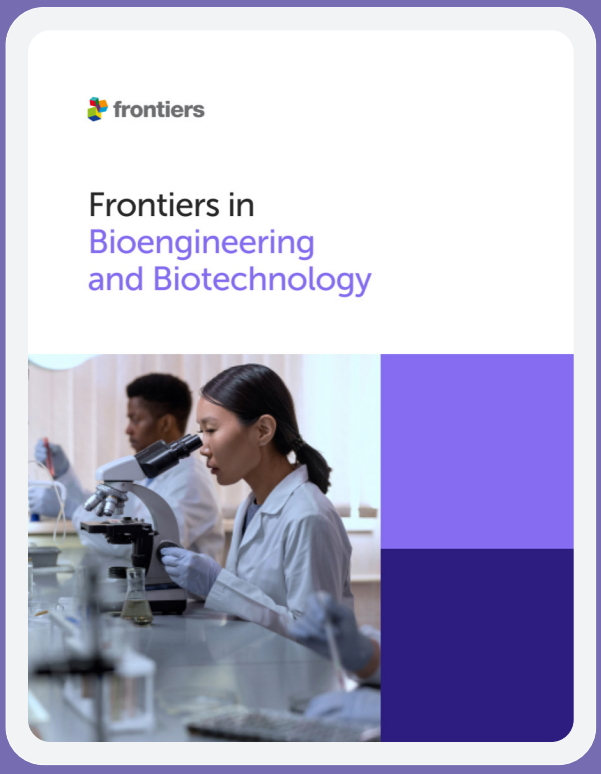

Frontiers

Avenue du Tribunal-Fédéral 34
1005 Lausanne, Switzerland
frontiersin.org

Contact us

+41 (0)21 510 17 00
frontiersin.org/about/contact